Akademiya Nauk Ukrainskoi SSR

NASA
TT
F-675
c.1

I.N. Frantsevich and D.M. Karpinos, Editors

FIBROUS COMPOSITES

TECH LIBRARY KAFB, NM
0069160

LOAN COPY: RETU
AFWL (DOU L
KIRTLAND AFB, N. M.

Translated from Russian

Published for the National Aeronautics and Space Administration
and the National Science Foundation, Washington, D.C.
by the Israel Program for Scientific Translations

TECH LIBRARY KAFB, NM
0069160

AKADEMIYA NAUK UKRAINSKOI SSR · INSTITUT MATERIALOVEDENIYA · INSTITUT MEKHAI

Academy of Sciences of the Ukrainian SSR · Institute of the Science of Materials · Institute of Mechanics

I. N. Frantsevich and D. M. Karpinos, Editors

FIBROUS COMPOSITES

(Kompozitsionnye materialy voloknistogo stroeniya)

Izdatel'stvo "Naukova Dumka"
Kiev 1970

Translated from Russian

Israel Program for Scientific Translations
Jerusalem 1972

TT 71-50050
NASA TT F-675

Published Pursuant to an Agreement with
THE NATIONAL AERONAUTICS AND SPACE ADMINISTRATION
and
THE NATIONAL SCIENCE FOUNDATION, WASHINGTON, D. C.

Copyright © 1972

Israel Program for Scientific Translations Ltd.
IPST Cat. No. 5980

ISBN 0 7065 1226 X

Translated by R. Kondor
Edited by D. Slutzkin

Printed in Jerusalem by Keter Press
Binding: Wiener Bindery Ltd., Jerusalem

Available from the
U. S. DEPARTMENT OF COMMERCE
National Technical Information Service
Springfield, Va. 22151

Contents

Preface vii

Chapter I. Equations of the Continuum Theory of Composite Materials .. 1
1. Real microstructures and models of composite fibers 2
2. Strength and elasticity of the fibers 8
3. Properties of polymer matrices under quasistatic load 12
4. Behavior of polymers at high temperatures 21
5. Properties of plastics under periodic stresses 23
6. Thermal conductivity and diffusion in the continuum 27
7. Electromagnetic field equations in continuous media 29

Chapter II. The Internal Stress Field and the Modulus of Elasticity of Composite Fibers 34
1. The problem of longitudinal shear 34
2. The optimum volume content of components in fiber composites in shear 44
3. Effect of the type of microstructure on the properties of the composite material 46
4. Longitudinal shear of multicomponent materials 48
5. Transverse shear of composite fibers 49
6. The moduli of elasticity in transverse shear for multicomponent materials 54
7. Stress in the microstructure and the elastic constants of the composite material in longitudinal tension 56
8. Longitudinal tension of multicomponent media 59
9. Transverse tension of reinforced bodies with a simple regular structure 60
10. Transverse tension of multicomponent materials 66
11. The elastic constants in areas inclined to the fiber orientation 67

Chapter III. Viscoelastic Properties of Reinforced Materials 70
1. Viscoelastic properties of reinforced plastics in shear 70
2. Viscoelasticity of reinforced plastics in longitudinal and transverse tension 73

3. Fundamental equations on the viscoelasticity theory of linearly reinforced plastics 76
4. Elastic heredity of multicomponent materials 77

Chapter IV. Thermal Conductivity and Diffusion with Absorption 84
1. Thermal conductivity of composites with solid and hollow fibers in transverse heat flux 84
2. Longitudinal thermal conductivity of reinforced materials 90
3. Thermal conductivity of multicomponent reinforced materials 91
4. Thermal conductivity equations for reinforced bodies 92
5. Diffusion in absorbing media 93

Chapter V. Thermal Expansion and Contraction 96
1. Thermoelastic expansion of composite materials with solid and hollow fibers 96
2. Effect of the type of microstructure on thermal expansion 98
3. Thermal expansion of multicomponent materials 99
4. Effect of the viscoelastic properties of the matrix on the thermal expansion and internal stress field 100
5. Contraction and residual stresses in glass-fiber reinforced plastics 101

Chapter VI. The Electromagnetic Field in Fiber Composites 104
1. Electrostatics of reinforced dielectrics 104
2. Dielectric constant in a field which changes 106
3. Magnetostatics of reinforced materials 107
4. Electromagnetostatics of dielectrics reinforced by combined or hollow fibers 108
5. Dielectric constant and permeability of multicomponent materials 109
6. Electromagnetic field equations in reinforced materials . . . 109
7. High-frequency field in materials reinforced by conductors 110
8. Longitudinally propagating waves in conductor-reinforced materials 114
9. Electromagnetic waves in dielectric fibers 116

Chapter VII. Elastic Waves in Reinforced Media 119
1. Waves in an anisotropic viscoelastic medium 119
2. Energy dissipation in a reinforced material 123
3. Elastic waves taking into account diffraction 125
4. Longitudinal shear waves 126
5. Transverse propagation of elastic waves 127
6. Longitudinal propagation of elastic waves 128

Chapter VIII. Analogies and Modeling of Composites 130
1. Analogies in the theory of disperse-reinforced composites 130
2. Analogies in the theory of composite fibers 133
3. Analogies in hereditary reinforced media 134
4. Analogies of dynamic fields in two-phase fiber composites..... 135
5. Nonlinear analogies of polymers 138
6. Mathematical modeling of composites 139

Chapter IX. Stress Concentration around Holes in Plates and Shells Made of Reinforced Materials 141
1. Stress concentration around a circular hole in plates made of glass-fiber reinforced laminated polymers 141
2. Stress distribution around an elliptic hole or crack in a plate made of glass-fiber reinforced plastic 147
3. Methods for studying stresses in stiff-core three-layer spherical shells (sandwich shells) with notches 149
4. Stress concentration around a hole in a spherical sandwich shell with a light core 154

Chapter X. The Strengthening Effect of Reinforcement in Composite Fibers 160
1. The special features of metal- or ceramic-based reinforced materials 160
2. Requirements for fibers and matrix..... 163
3. Strength of composites reinforced by continuous parallel fibers 165
4. Elastic constants of composites reinforced by oriented continuous fibers..... 170
5. Strength of materials with parallel discrete fibers 176
6. Statistical analysis of the fiber strength 182
7. Statistical model of the fracture of reinforced material in tension 185
8. Types of composite fracture 189
9. Compressive strength of composites 193
10. Thermal stresses in composite fibers..... 198

Chapter XI. Technological Processes for the Production of Composite Fibers and their Physicomechanical Properties 208
1. Production of composites by powder metallurgy 208
2. Application of coatings 213
3. Directional crystallization 214
4. Composites based on copper or copper alloys 215
5. Composites based on silver or silver alloys..... 219
6. Composites based on aluminum or aluminum alloys 222
7. Composites based on nickel or nickel alloys 225

8. Composites based on titanium 229
9. Composites based on iron, nickel, magnesium, and their alloys 231
10. Fiber-reinforced ceramic materials 231
11. Composites based on alumina and silica 234
12. Composites based on other ceramic materials 238

Chapter XII. Reinforced Plastics 242
1. Main principles of the production of reinforced plastics 242
2. Types and properties of glass fibers 243
3. Types of reinforced plastics 247
4. Plastics reinforced by high-melting fibers 253
5. Range of application of reinforced plastics 259

Chapter XIII. Filters, Transpirators, Packers, and Dampers Made of Fibrous Material 264
1. Methods for producing high-strength articles from fibers 264
2. Filter materials made from fibers 272
3. Transpiration materials with a fibrous structure 290
4. Fiber-base packing materials 309
5. Dampers of mechanical and sonic vibrations 323

Chapter XIV. Production of Reinforced Materials and their Physicomechanical Properties 330
1. Mechanical methods 330
2. Preparation of fibers from fused metals 332
3. Physicochemical methods 334
4. Metal-coated fibers 363
5. Physicomechanical properties of reinforcing materials 367

Chapter XV. Production of Fibrous Structures by Directional Crystallization of Eutectic Alloys and Heat Treatment of Solid Solutions 373
1. Properties of cast composites 373
2. Advantages and disadvantages of cast composites 380

List of abbreviations 385

PREFACE

For the design of machines and mechanisms in various branches of modern engineering (in particular, when high temperatures, high speeds, high pressure, etc. are applied), we need new materials with many different, even contradictory properties, depending on the specifications of the designer. The research worker in the science of materials can only solve such problems efficiently and quickly by a rational synthesis of materials with predetermined complex properties. For this, he must have a wide knowledge of solid-state physics, which can show him how to predict the properties of the material prepared. He must also be able to select that variant of the most flexible technique which makes it possible to synthesize or design a material combining the components with given characteristics into a homogeneous, and sometimes also into a complex, composite.

There is still another aspect of the given problem, information and its processing. In material science information is not only very complicated because of the many sources, but also because to understand the data we must have more and more additional information on other sciences, such as mathematics, physics, chemistry, and mechanics.

Therefore, the material research scientist and the designer should not obtain the information in the original form, even in a systematized one, but as data treated and analyzed by highly specialized experts and published in monographs or in reference books. Such a monograph should include a sufficiently complete and rigid representation of the physics involved in each problem, and the fundamental theoretical concepts in the given field, and also a detailed and exhaustive description of the production of both the starting substances and materials and the main applications of the materials. Finally, it must have an exhaustive and detailed bibliography, with references describing the properties of the materials of the given group, and the range of their application.

Such a monograph prepared by highly experienced experts should not be simply a compilation. It must to a certain extent be original, and give the subjective opinions of the authors. In this case, the reader joins in the author's research in the given field of modern material science. This principle was used when we wrote the monograph "Fibrous Composites," which we present to the reader.

The book deals with one of the very topical problems of modern material science. The materials which are the subject of this monograph largely determine the progress in aircraft and rocket engineering. Numerous scientific teams are participating in the development of these materials

throughout the world. From year to year the volume of publications in periodicals and as monographs is increasing. These publications, however, serve mainly for advertising purposes. Unfortunately, in the USSR and in other countries there is no general monograph of the type mentioned above. The monograph "Fibrous Composites" is an attempt to bridge this gap.

The first nine chapters of the monograph were written by G. A. Van Fo Fy. They contain original information for calculating the strength and other parameters of composites. By using continuous models, the author describes the elastic and rheonomic properties of composite fibers, their thermal conductivity, and diffusional processes in them. He also discusses problems involving thermal stresses and shrinkage in production, operation at high temperatures, and also the electromagnetic properties and the propagation of elastic waves in such materials. The methods of analogy in the theory of composite materials, and methods for designing products from them, are explained.

Chapter X was written by D. M. Karpinos and L. I. Tuchinskii, and is also theoretical. The principles of reinforcing and the strength properties of materials reinforced by continuous and discrete fibers are discussed. This chapter also describes the effect of thermal stresses on the strength characteristics, a statistical model of fracture, and defects and types of fracturing of composites.

The last chapters deal with the production of various types of composites and their properties.

The technological processes in the production of metallic and ceramic fibers, and their physicomechanical properties, are described by D. M. Karpinos, L. I. Tuchinskii, and V. G. Zil'berberg in Chapter XI.

In Chapter XII, D. M. Karpinos and V. M. Grosheva discuss reinforced materials based on plastics.

Porous fibrous materials such as filters, transpirators and dampers are described in Chapter XIII. The authors are A. G. Kostornov and I. M. Fedorchenko.

Chapter XIV was written by A. G. Kostornov, V. G. Zil'berberg, D. M. Karpinos, and A. V. Tkachenko. The technological methods for producing metallic and nonmetallic reinforcing elements, such as fibers and fabrics, are described.

The last chapter of the monograph deals with types of metallic materials, with a fibrous structure obtained by crystallization and other forms of heat treatment. It was written by D.M. Karpinos and E. N. Denbnovetskaya.

I. N. Frantsevich
Member of the Ukrainian
Academy of Sciences

Chapter I

EQUATIONS OF THE CONTINUUM THEORY OF COMPOSITE MATERIALS

By using composite fibers, with short or continuous fibers as the filler, and the material in the interstices between these fibers ensuring a monolithic composition as matrix, it is possible to create products which satisfy new qualitative requirements. The properties of composite fibers are a consequence of the properties of the individual components and the extent of the interaction in the monolithic material. The latter factor is determined mainly by the compatibility of the components and the technology used in the production of the material. These factors, however, cannot always be allowed for with the required accuracy. Therefore, to find the above characteristics of the composite materials we must make certain assumptions on the degree of interaction of the components.

The principal ideas on the integral characteristics of a composite material and the distribution of the internal field and structure can be found fairly accurately by using the continuum models of mechanics and continuum body physics.

The continuum models must describe the inhomogeneity of the structural materials, the characteristics of interaction, and the volume content and properties of the components. Also, an estimation of the effect of the filler geometry and the mutual arrangement of its elements on the integral characteristic and on the internal field are of interest.

Thus, we have the task of developing models and methods for studying the physical properties of existing composite materials and giving a theory for predicting the properties of new materials from the properties, volume content, structure type, etc., of the components.

In analogy with the crystal lattice theory, we can see that the harmonic properties of composite fibers will appear only at certain gradients of an applied external field, especially when there is only a slight change in the volume over which the data are averaged when finding the reduced material parameters. Hence, near the boundary, in the region of action of local loads, during the propagation of short waves and in other similar cases the concept of integral constants will no longer have any meaning. For these states we must introduce specifications, and carry out special research on the errors introduced when studying the fields with the reduced parameters.

If the properties of the composite fibers are studied and the external field gradient changes within permissible limits, we can set up an equation

of state for the material. This equation can serve for studying the behavior of composite products in this field.

Our book gives a variant for solving these problems for composite fibers.

Thus, as stated above, the components of the composite materials have continuum properties characterized by a limited number of averaged parameters or constants. The values of the selected constants are usually determined by experiments on macroscopic samples prepared from the components which make up the material. The dimensions of these samples should be close to those of the elements of the filler or matrix in the material, despite the fact that some parameters change to a slight degree only when the sample dimensions are changed by one or two (or more) orders of magnitude. These parameters, slightly sensitive to the structure of the constants, include the modulus of elasticity, dielectric constant, etc.

If the physical constants are found, the distribution of the field in the regions occupied by the matrix or filler is found from the appropriate equations of the continuum theory.

1. Real microstructures and models of composite fibers

The structure of composite materials is made up from strands of thin fibers combined into the monolithic material by a matrix. The fibers determine the strength and hardness of reinforced materials. The matrix protects the filler from corrosive action of the environment and ensures interactions between the fibers by mechanical and other effects.

The physicomechanical properties of composite fibers are very dependent on the mutual position of the fibers in the monolithic materials. The fiber orientation is of special importance for the properties of materials in which the components differ in strength, rigidity, thermal conductivity, and other properties, by one or several orders. Typical examples are glass-fiber reinforced plastics (GFP), in which the chief physicomechanical properties (breaking strength, Young's modulus, thermal expansion) differ by one or two orders of magnitude from the corresponding parameters of the polymer matrixes. We shall discuss later other very inhomogeneous composites. The fiber orientation is an index of the degree of anisotropy in such materials.

We shall pay special attention to composites with linearly oriented fibrous fillers; their structure is made up of a system of more or less straightened fibers.

The mutual arrangement of reinforcing fibers in the cross section has an effect on the material properties, and depends on the method of its production. In real materials we also find a scattering of the cross-sectional diameters of the fibers. Figure I.1 shows a photograph of a typical microstructure of oriented glass-fiber reinforced plastics (GFP) produced by continuous drawing. We observe a scattering in the fiber diameters and a stochastic distribution of their centers /1/. The empirical distribution of the distances between the fibers is shown in Figure I, 2 as a stepped histogram; the graph was plotted from 2,000 measurements. The authors plotted the distances between the fibers on the abscissa and the probability density on the ordinate. Most of the results refer to

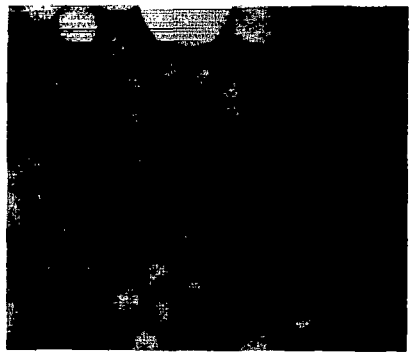

FIGURE I.1. Structure of glass-fiber reinforced plastics (× 1,000).

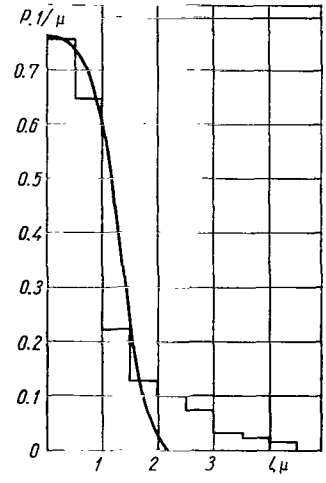

FIGURE I.2. Histogram and theoretical distribution curve of the interfiber distances.

distances of up to $1\,\mu$. In the narrow range near the zero point, where the required magnification is 10^4, the results are unreliable. This region is too narrow to have an appreciable effect on the distribution pattern of the distances between the fibers. The theoretical distribution curve (Figure I.2) is approximately described by a fractional-exponential function. The normalized probability density is given by

$$p(x) = \frac{q\lambda}{\Gamma(1/q)} e^{-(\lambda x)^q}, \qquad (I.1)$$

where x characterizes the distances between the fibers; λ, q are constants determined from the condition of optimum approximation of the theoretical and experimental curves; and $\Gamma(1/q)$ is Euler's gamma function. The mean value or the mathematical expectation of x and the corresponding statistical moments are determined by

$$\langle x^m \rangle = \int_0^\infty x^m p(x)\, dx = \frac{\Gamma\frac{1+m}{q}}{\lambda^m \Gamma(1/q)}. \qquad (I.2)$$

The standard deviation of x characterizing the scattering of x from $\langle x \rangle$ is

$$\sqrt{\langle x^2 \rangle - \langle x \rangle^2} = \frac{\sqrt{\Gamma(1/q)\,\Gamma(3/q) - \Gamma^2(2/q)}}{\lambda \Gamma(1/q)}.$$

We took $q = 4$, and $\lambda = 0.69\ 1/\mu$; the mean value and the standard deviation of the distances between the fibers are

$$\langle x \rangle = 0.71\ \mu\ ; \quad \sqrt{\langle x^2 \rangle - \langle x \rangle^2} = 0.452\ \mu\ .$$

The empirical distribution of the fiber diameters in the microsections of the given glass-reinforced fibers (GFP) is shown in Figure I.3, a as a

stepped histogram, plotted from the data of 1,050 measurements. The fiber diameters are plotted on the abscissa and the probability density of the diameters on the ordinate. The scattering of the diameters is caused by technological defects; therefore, we note a deviation of the fiber surface over the length from the constant-diameter cylindrical form. A marked break is present on the histograms for diameters slightly above $4\,\mu$. Altogether, the histogram is more or less symmetrical relative to the peak, and for this reason the distribution is governed by the Gaussian law.

$$p(x) = \frac{1}{\sigma\sqrt{2\pi}} \exp\left[-\frac{(x-\langle x\rangle)^2}{2\sigma^2}\right], \qquad (I.3)$$

where variable x determines the size of the fiber diameter in the given cross section; the standard deviation is

$$\sigma = \sqrt{\langle x^2\rangle - \langle x\rangle^2}. \qquad (I.4)$$

The histogram in Figure I. 3, b shows the distribution of the three adjacent fibers. The theoretical distribution is again Gaussian, where only x determines the angle between three adjacent fibers. The arithmetic mean and standard deviation are given by

$$\langle x\rangle = \frac{5}{18}\pi = 50°; \quad \sigma = 15.1°.$$

It can be seen that the largest number of fibers is located so that the angles between them are near to the angles characterizing a close hexagonal structure.

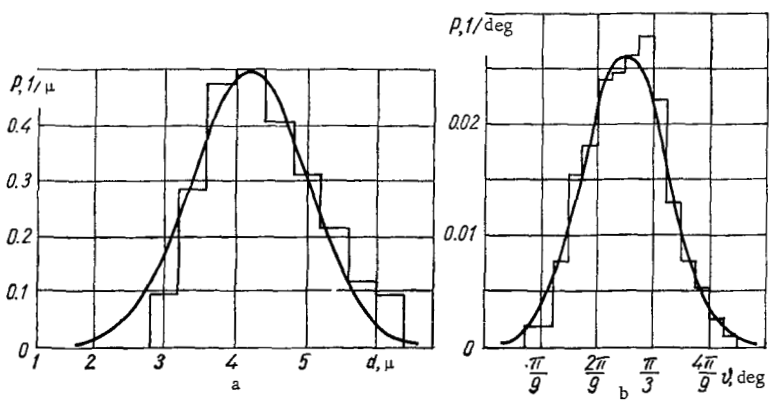

FIGURE I. 3. Distribution of fiber diameters (a) and interfiber angle (b).

In the general case the position and the changes in the fiber diameters are described by a distribution function, which cannot be represented as a product of several functions dependent on only a single variable, since the functions are correlated. After the experimental data had been processed, it was found that the type of distribution function depends on the

selected technology and other factors not readily controlled. In composite materials with a high degree of filling (about 80%), regular or near regular fiber configurations predominate. An ordered state of the microstructures is attained by various means. Thus, in a GFP ultrasonic waves are excited in the reinforced medium when the matrix is still highly fluid before hardening.

To reveal the mechanism of component interaction, and to determine the integral characteristic in the monolithic material, we isolate an elementary volume which has all the properties of the given composite, while the dimensions are the minimum permissible ones. In real materials the local structure will change within certain limits depending on the location of the elementary volume (see Figure I.1). Therefore, to evaluate the effect of the mutual fiber position on the internal field and the reduced parameters, we must study the latter for a whole set of all possible fiber structures. When the probability of finding one or other structure in a real material is known, we can determine both the mean parameter and its standard deviation from these determinations. The typical structural array is found after a study of the fiber configuration in a real material, prepared by a certain technology.

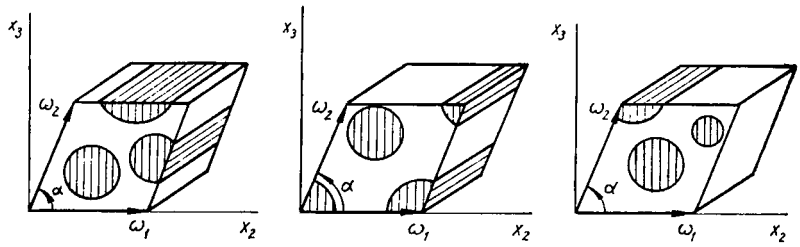

FIGURE I. 4. Models of microstructural types.

We shall consider a set of parallelepipeds of volume V (Figure I. 4) formed by a finite number of circular cylindrical bodies (fibers) and the matrix combining the fibers into a single body as a typical model of linearly reinforced materials. The cylinder axes are parallel and placed in different ways within this elementary volume. For determinancy, we assume that on the interfaces between the components the field and its gradients are continuous over the whole volume V.

Actually the fiber cross sections, for example in oriented GFP, are not circular; the fiber axes are partially warped over their length and the interfacial conditions are sometimes disturbed in individual sections. These factors alter the size and distribution of the field near the individual fibers. and their effects have the character of local disturbances, and must be allowed for by making the solutions found for the given model more accurate.

To study the field characteristics in each of the volumes, the effect of the surrounding space must be considered. In the general case this is done approximately by assuming that adjacent volumes and the whole macrostructure of the material are obtained by doubly periodic extension of the given volume. The coordinates of an arbitrary point of a macroscopic

section of the material in a plane perpendicular to the fiber direction can be expressed in terms of the lattice constants

$$x_2 + ix_3 + m\omega_1 + n\omega_2 = z + P, \qquad (I.5)$$

where $z = x_2 + ix_3$; $\omega_2 = \omega_1 be^{i\alpha}$ $(0 < b < \infty)$; $m, n = 0, \pm 1, \pm 2, \ldots \mp\infty$.

The structures considered are symmetrical because of their periodic character. In parallel translations described by fundamental vectors ω_1 and ω_2 or multiples of $|\omega_1|$ or $|\omega_2|$ the elementary volume structure is periodically repeated. The structures may also be symmetric with respect to various rotations or reflections for certain values of b and α, besides their symmetry in translation. According to /2/ and /3/, regular structures can have the symmetry axes perpendicular to the lattice plane of only the d-2nd, d-3rd, d-4th and d-6th orders, and also a mirror reflection about a straight line which will be designated by q. For two-dimensional lattices the different combinations and reflections are reduced to 10 point groups, which according to the above nomenclature may be designated by 1; 2; $1q$; $2qq$; 3; $3q$; 4; $4qq$; 6; $6qq$. The first symbol in each group characterizes the multiple of rotations d about the symmetry axis, and the second symbol indicates the mirror reflection about a line perpendicular to axis $0x_2$ and about other reflection lines associated with the given rotation. The third symbol indicates that other lines of mirror reflection are also present, which do not belong to the first line system, but are connected by additional symmetry conditions. According to current terminology, a regular structure of type $\left(b \neq 1,\ \alpha \neq \frac{\pi}{2}\right)$ belongs to the monoclinic system, characterized by point symmetry group $d = 1; 2$, with a symmetry plane perpendicular to the fiber orientation.

The requirements for an invariant structure during rotation by $\frac{2\pi}{d}$ (when $d = 3; 4; 6$) around the symmetry axis parallel to the fiber orientation or in mirror reflection, leads to restrictions in ω_1, ω_2 and α. Thus, for $b \neq 1$ and $\alpha = \frac{\pi}{2}$ the structure obtained is simple orthorhombic; if $b = 1$, and $\alpha \neq \frac{\pi}{2}$ or $\frac{2\pi}{3}$, we obtain a centered orthorhombic structure. In the last case, instead of ω_1 and ω_2, other fundamental vectors equal to the geometric sum and difference of ω_1 and ω_2 can be used. The real parts of the new vectors are not equal and are mutually perpendicular. The orthorhombic structure is characterized by the following point group symmetry $1q$; $2qq$.

The invariant structure conditions for $\alpha = \frac{\pi}{2}$ and $b = 1$ are satisfied by the tetragonal structure characterized by symmetry group 4; $4qq$. Finally, the highest symmetry is displayed by the hexagonal system where invariance is observed during rotation by $\frac{2\pi}{6}$. In this case $b = 1$ and $\alpha = \frac{2\pi}{3}$ and the symmetry group is $3.3q$; $6.6qq$.

Regular structures formed by straight fibers with the center of each placed at the lattice points have a higher point group symmetry. In this case each elementary volume contains only a single fiber. Under such conditions the monoclinic structure has the form of an oblique-angled lattice $\left(b = 1,\ \alpha \neq \frac{\pi}{2}\right)$, invariant when rotated by π with no mirror reflection

axis (Figure I. 5, a). Figure I. 5, b shows a simple orthorhombic structure $\left(b \neq 1,\ \alpha = \frac{\pi}{2}\right)$ of the highest symmetry group. A centered orthorhombic lattice of the same symmetry group is shown in Figure I. 5, c. Here also the new fundamental vectors ω_1' and ω_2' are shown, which are equal to the geometrical sum and difference of ω_1 and ω_2, respectively. The tetragonal lattice has the $4qq$ symmetry (Figure 1. 5, d), and the hexagonal lattice the $6qq$ symmetry (Figure I. 5, e).

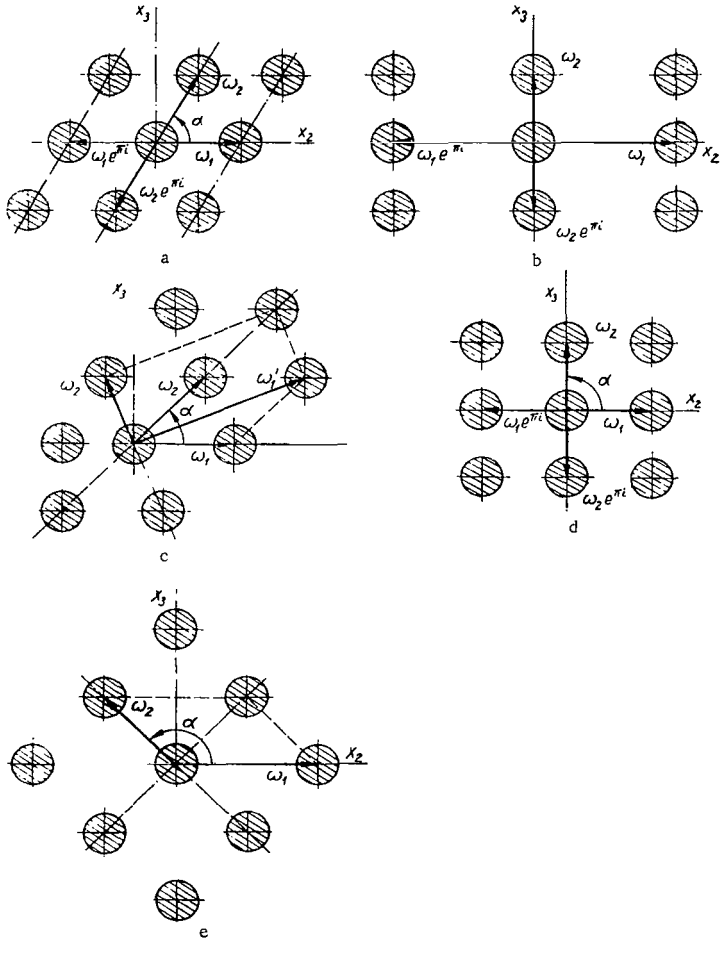

FIGURE I. 5. Monoclinic (a), simple orthorhombic (b), centered orthorhombic (c), tetragonal (d), and hexagonal (e) structures.

The area of the individual cell F, plotted from fundamental vectors ω_1 and ω_2, will consist of the cross-sectional area of the fiber F_a and the area occupied by the filler F_s:

$$F = F_a + F_s = \omega_1^2 b \sin \alpha. \qquad (I. 6)$$

Moreover, parameters are introduced which determine the relative volume content of filler ξ and matrix η in the elementary volume:

$$\xi = \frac{V_a}{V} = \frac{F_a}{F} = \frac{\pi r_0^2}{\omega_1^2 b \sin \alpha}; \quad \eta = \frac{F_s}{F} = 1 - \xi. \tag{I. 7}$$

Here V_a and V are the volumes occupied by the filler and the total volume, respectively, while r_0 is the fiber radius.

It is easily seen that closest packing of the composite material is attained when the fibers contact all the sides of the cell. This is the case when $b = 1$ and $2r_0 = \omega_1$, $\xi_{max} = \frac{\pi}{4 \sin \alpha}$. From this, for the hexagonal $\left(\alpha = \frac{\pi}{3}\right)$ and the tetragonal $\left(\alpha = \frac{\pi}{2}\right)$ lattices, we obtain

$$\xi'_{max} = \frac{\pi}{2\sqrt{3}} \approx 0.9 \quad \text{and} \quad \xi''_{max} = \frac{\pi}{4} \approx 0.78. \tag{I. 8}$$

Other regular microstructures also exist; their unit cells consist of a few fibers arranged according to a certain symmetry, which is completely determined by the spatial groups. For linearly reinforced microstructures we know 17 spatial groups; 13 of them are obtained when arranging the fibers in the symmetry determined by the 10 point groups mentioned above. Four other spatial groups determine new symmetry elements, characterizing reflections about a straight line and subsequent translation along this line by a length equal to half the corresponding lattice constant. These elements are termed slip lines g. Numerous examples of similar regular structures can be derived from crystallographic studies. Other microstructural types, which were derived from the above, will be described later.

2. Strength and elasticity of the fibers

For very thin fibers (diameter not more than a few μ), we can obtain the high-strength characteristics of perfect-structure bodies. In the ideal case the fibers are destroyed at certain critical atomic distances and therefore we have a simple formula relating the limiting tensile stress σ_B to Young's modulus: $\sigma_B = \alpha E$. The upper theoretical value $\alpha = 0.1$ was not achieved for any material; in most of the real materials α is between 0.001 and 0.1. Thus, for alumoborosilicate fibers the upper experimental limiting stress is attained at $\alpha = 0.04$.

The $\sigma - \varepsilon$ diagrams, where ε is the strain in short-time tensile tests on strong fibers at room temperature, are linear up to the moment of breaking. The fibers are broken suddenly after elastic elongation has reached its limiting value. Deviations from the proportional stress-strain law are found for fibers made of thermoplastic and some other materials in which dislocation slip is possible.

Table I.1 shows the parameters of some fiber fillers. Here ε_B is the limiting tensile strain; γ is the specific gravity; ν is the Poisson ratio; and T_m is the melting point.

TABLE I. 1. Parameters of fiber fillers

Fiber fillers	$\sigma_в$ (0.981×10^9), n/m^2	E (0.981×10^{10}), n/m^2	$\varepsilon_в$, %	γ, g/m^3	ν	T_m, °C
Cotton	0.29 – 0.88	0.43 – 1.14	7 – 9	1.53	0.4	150
High-carbon steel,	4.2	21	–	7.8	0.3	1400
$d = 5\mu$	2.2 – 3.0	–	3 – 5	–		
E-glass:						
$d = 15\mu$	1.2	7	1.5 – 2	3.54	0.2	1200
$d = 50\mu$	0.8		0.8 – 1	–		
Boron, 50 – 100μ	1.8	39	–	–	–	–
Graphite (whiskers)	24	100	–	2.2	–	3500
Al_2O_3 (whiskers)	15	53	–	4	–	–
Fe (whiskers)	13	21	–	7.8	0.3	1400

The stressed state at each volume point of a continuous medium is determined by the components of the stress tensor /4/ σ_{ik} ($\sigma_{ik} = \sigma_{ki}$, $i, k = 1; 2; 3$) or

$$\begin{vmatrix} \sigma_{11} & \sigma_{12} & \sigma_{13} \\ \sigma_{21} & \sigma_{22} & \sigma_{23} \\ \sigma_{31} & \sigma_{32} & \sigma_{33} \end{vmatrix}. \tag{I. 9}$$

Here the elements of each line determine the components on the area perpendicular to the corresponding axis (Figure I. 6). The stress vector $\overline{\sum}_n$ on any arbitrary surface with normal $\vec{n}$ will be

$$\overline{\sum}_n = \sum_{k=1}^{3} \bar{\sigma}_k n_k,$$

where n_i ($i = 1; 2; 3$) are the cosines of the angles between n and the coordinates of the axes; $\bar{\sigma}_k = \sum_{i=1}^{3} \bar{a}_i \sigma_{ki}$.

The balance equation for the elementary volume is

$$\operatorname{div} \overline{\sum} + \overline{R} = 0, \tag{I. 10}$$

where $\overline{R}$ is a vector equal to the volume force acting upon unit volume of the continuous medium.

The strained state of the small volume of the continuous medium is determined by the strain tensor given by

$$\begin{vmatrix} \varepsilon_{11} & \varepsilon_{12} & \varepsilon_{13} \\ \varepsilon_{21} & \varepsilon_{22} & \varepsilon_{23} \\ \varepsilon_{31} & \varepsilon_{32} & \varepsilon_{33} \end{vmatrix}, \tag{I. 11}$$

where $\varepsilon_{ik} = \varepsilon_{ki}$. For small strains when all the nonlinear terms can be neglected, components ε_{kk} arranged along the main diagonal determine the relative elongation of the sides of the elementary parallelepiped:

$$\varepsilon_{11} = \frac{\partial u_1}{\partial x_1}; \quad \varepsilon_{22} = \frac{\partial u_2}{\partial x_2}; \quad \varepsilon_{33} = \frac{\partial u_3}{\partial x_3}. \tag{I. 12}$$

Here u_i ($i = 1; 2; 3$) are the components of the vector indicating the displacement of the medium by the corresponding axes of Cartesian coordinates. The other elements in Table I. 1 are equal to half the angle of slide of the sides of the elementary volume

$$2\varepsilon_{21} = \frac{\partial u_1}{\partial x_2} + \frac{\partial u_2}{\partial x_1}; \quad 2\varepsilon_{32} = \frac{\partial u_2}{\partial x_3} + \frac{\partial u_3}{\partial x_2}; \quad 2\varepsilon_{13} = \frac{\partial u_1}{\partial x_3} + \frac{\partial u_3}{\partial x_1}. \tag{I. 13}$$

The six components of the strain tensor are determined by the derivatives of the three components of the displacement vector. Therefore, additional relationships called Saint Venant continuity conditions exist between the derivatives of ε_{ik}. The Saint Venant conditions are a logical consequence of the integrability conditions of equations for determining the displacement of the medium according to the strain tensor components; in Cartesian coordinates they have the following form

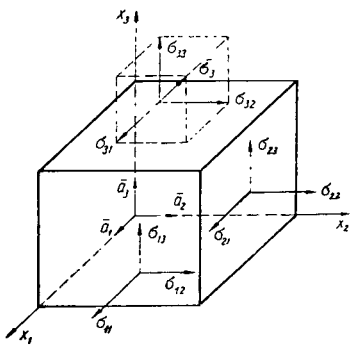

FIGURE I. 6. Distribution of the coordinate system.

$$\frac{\partial^2 \varepsilon_{11}}{\partial x_2^2} + \frac{\partial^2 \varepsilon_{22}}{\partial x_1^2} = 2\frac{\partial^2 \varepsilon_{12}}{\partial x_1 \partial x_2}; \quad \frac{\partial}{\partial x_3}\left(\frac{\partial \varepsilon_{23}}{\partial x_1} + \frac{\partial \varepsilon_{31}}{\partial x_2} - \frac{\partial \varepsilon_{12}}{\partial x_3}\right) = \frac{\partial^2 \varepsilon_{33}}{\partial x_1 \partial x_2}. \tag{I. 14}$$

The other equations are obtained by cyclical change of the subscripts.

The sum of the diagonal elements of (I. 11) determine the volume expansion of the medium

$$\varepsilon = \varepsilon_{11} + \varepsilon_{22} + \varepsilon_{33} = \operatorname{div} \bar{u}. \tag{I. 15}$$

If we assume that the material is homogeneous and isotropic, the experimental results obtained for simple tension can be generalized for the volume stressed state. The correlation between the components of the stress and strain tensors is obtained from the system of equations of Hooke's law

$$\sigma = 3K\varepsilon; \quad \sigma_{ik} - \frac{1}{3}\sigma\delta_{ik} = 2G\left(\varepsilon_{ik} - \frac{1}{3}\varepsilon\delta_{ik}\right) \ (i, k = 1; 2; 3). \tag{I. 16}$$

Here $\sigma = \sigma_{11} + \sigma_{22} + \sigma_{33}$; δ_{ik} is the Kronecker symbol and G is the modulus of elasticity in shear. The bulk modulus is determined in terms of other constants $K = \frac{E}{3(1-2\nu)}$.

By eliminating from (I. 10) according to the equations of Hooke's law, and using (I. 12) and (I. 13), we obtain a vectorial equation in terms of displacements

$$G\Delta\bar{u} + (\lambda + G)\operatorname{grad}\operatorname{div}\bar{u} + \bar{k} = 0, \tag{I. 17}$$

where $\lambda = \frac{2G\nu}{1-2\nu}$; and Δ is the Laplace operator.

The stress vector on any arbitrary area with normal $\bar{n}$ is expressed in terms of displacement by:

$$\bar{\Sigma}_n = 2G(\bar{n} \cdot \operatorname{grad})\bar{u} + \lambda\bar{n} \operatorname{div}\bar{u} + G\bar{n} \times \operatorname{rot}\bar{u}. \tag{I. 18}$$

The problem of the stress-strained state of elastic fibers is thus reduced to solving (I. 17) according to the continuum theory, provided that the given boundary conditions on the frontal and lateral fiber surfaces are satisfied. The boundary conditions are fixed, taking into account the interaction of the matrix and filler in the monolithic material.

At higher temperatures the breaking load changes much more than the modulus of elasticity of the fibers, and at certain temperatures the inelastic strain becomes appreciable. We have, however, a sufficiently wide region in which the inelastic effects can be neglected, while the mechanical state of the fibers can be fairly well represented by the thermoelasticity equations. Thus, with increase in temperature to 573° K, Young's modulus of alumoborosilicate fibers decreases by 10%, and the stressed state of such fibers can be determined from the thermoelasticity equations with satisfactory accuracy; this region is much wider for whiskers. In this case the strength of the fibers must be calculated while taking into account the decrease in the limiting stresses with increase in temperature.

If the temperature of the medium is changed by $\Theta = T - T_0$, where T_0 and T are the initial and given temperatures, elongations of the edges of the elementary volume of the filler must be equal. Therefore, in the absence of outside loads and restricting bonds for the strain of the fibers

$$\varepsilon_{kk} = \beta\Theta, \quad \varepsilon_{ik} = 0 \ (i \neq k). \tag{I. 19}$$

Here β is the linear thermal expansion coefficient. In general, the strain of the fiber is determined by thermal expansion and the action of stresses. Thus, equations connecting stress and strain in this region are given by Duhamel— Neumann

$$\sigma = 3K(\varepsilon - 3\beta\Theta); \quad \sigma_{ik} - \frac{1}{3}\sigma\delta_{ik} = 2G\left(\varepsilon_{ik} - \frac{1}{3}\varepsilon\delta_{ik}\right). \tag{I. 20}$$

If no volume forces are present allowing for thermal expansion, the balance equations in displacements are simplified to a single vectoral equation

$$G\Delta\bar{u} + (\lambda + G)\operatorname{grad}\operatorname{div}\bar{u} = 3\beta K \operatorname{grad}\Theta. \tag{I. 21}$$

Its general solution is

$$\bar{u} = \operatorname{grad}\Phi + \bar{u}_0, \tag{I. 22}$$

where $\bar{u}_0$ is the solution of (I. 21) without the right-hand side:

$$\Delta\Phi = \frac{1+\nu}{1-\nu}\beta\Theta. \tag{I. 23}$$

The displacement vector should be determined allowing for the boundary conditions on the fiber surface.

3. Properties of polymer matrices under quasistatic load

Polymers, metals, or compounds of various chemical composition, which are either plastic or brittle are used as matrices in composite materials. Polymers have been widely applied in GFP; they have more complex properties than other matrices.

In practice, phenols, polyesters, melamine, organosilicon, epoxide resins and other rigid resins, are used as matrices. Epoxide resin composites with other components are especially worth noting. The properties of the polymer matrix depend on the composition and production technology. We shall discuss a typical composite material consisting of epoxide resin ED-6 and maleic anhydride.

The stress-strain diagram of epoxide-maleic anhydride (EMA) specimens is shown in Figure I.7. The rate of loading was constant and the tests were performed at room temperature. We see that in all cases there is cleavage fracture without neck formation; the limiting strain on tension is $\varepsilon_B^+ = (2.2 - 2.5)\%$.

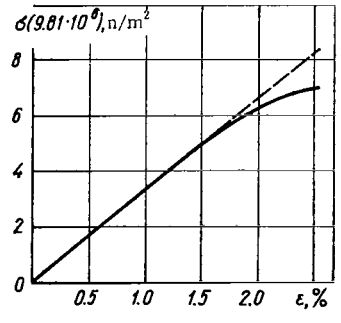

FIGURE I. 7. Stress-strain curve of the epoxide-maleic anhydride polymer.

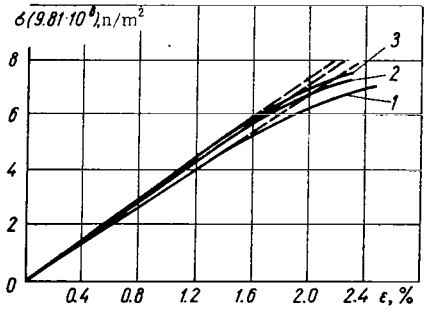

FIGURE I. 8. Effect of the loading rate on the stress-strain curve.

When the strain is about 2%, we see deviations from Hooke's law, caused by nonlinear effects and moving (time-dependent) constraints. Table I. 2 shows some elastic and strength characteristics on tension of specimens of various compositions.

TABLE I. 2. Mechanical parameters of specimens

Mechanical characteristics	Composition of		
	EBF-3*	epoxyanilinofurfurol	epoxide-maleic anhydride
E^+ $(0.981 \cdot 10^{10}$ n/m$^2)^{-1}$	0.35	0.51	0.315
ν	0.40	0.40	0.382
ε_B^+, %	2.5	2.5 – 3	2.2 – 2.5
σ_B^+ $(0.981 \cdot 10^7$ n/m$^2)^{-1}$	4.10	12	7.5

Figure I. 8 shows curves characterizing the effect of the loading rate of the polymer on the shape of the $\sigma - \varepsilon$ diagram at room temperature. Curves 1, 2, 3 were plotted for changes in the loading rate of $0.981 \cdot 10^7$ (5; 20; 40) newtons/$m^2 \cdot$ min.

The properties of polymers on compression are characterized by the curves in Figure I. 9. The slope of the straight section of the diagram characterizing the modulus of compression E^-, is 15—18% larger than the slope obtained with tension. During loading the interatomic and intermolecular bonds in the structure become oriented, and for this reason the curve is strongly convex at larger deformations. The modulus of elasticity in shear G obtained by torsion experiments was calculated from $G = \frac{E+}{2(1+\nu)}$; it differs for spatially cross-linked polymers only slightly in the elastic deformation region. Therefore, over a wide range of deformations (up to 2%) the stress-strain curves of the given polymer are described by the elasticity equations shown in section 2, provided that the loading rate is sufficiently high. Below, all the magnitudes related to the matrix will be designated by subscript s, and those relating to the filler by subscript a.

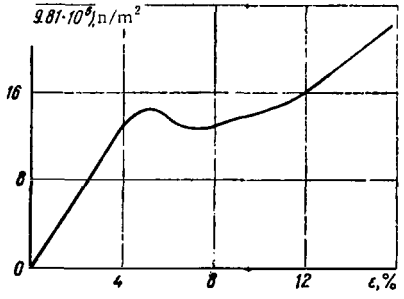

FIGURE I. 9. Compression curve of the epoxide-maleic anhydride plastic.

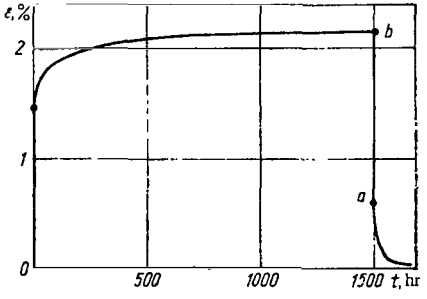

FIGURE I. 10. Loading and unloading curves for a polymer matrix.

On long-term action of mechanical loads in the polymer, we observe inelastic deformations. Their development is time-dependent. A typical curve characterizing the time-dependent deformation increase at constant tension is shown in Figure I. 10. Point c corresponds to interrupted loading and point a to load removal after a holding time of 1,500 hr. Point b corresponds to the beginning of inelastic reversible deformation. At room temperature and simple tension in a thermoreactive polymer, instantaneous elastic e_0 and viscoelastic or undeveloped highly elastic deformations e_∞ arise. These are determined by the nature of the molecular structure of the polymer, and depend on the degree of hardening of the compound and initial components, and also on other factors. Irreversible residual flow deformations of the polymer at the given temperature are sufficiently small, so that they can be neglected in our approximate treatment. Thus, the total deformation of the polymer is

$$\varepsilon = e_0 + e_\infty. \qquad (I.\ 24)$$

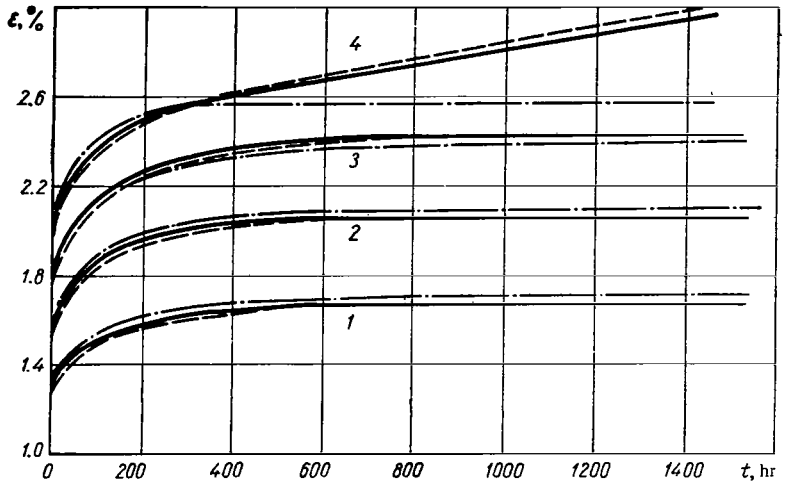

FIGURE I.11. Creep curve for the epoxide-maleic anhydride plastic.

The instantaneous elastic deformation is related to the stress by Hooke's law

$$\sigma = e_0 E_0.$$

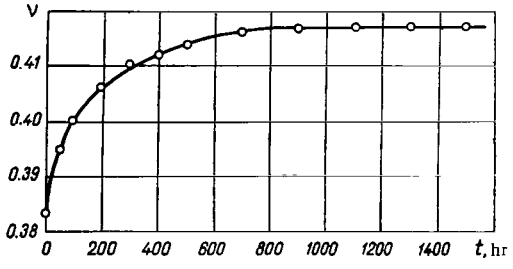

FIGURE I.12. Time dependence of the Poisson ratio.

The qualitative evaluation of the effect of the stress level on the creep process of the EMA compounds was performed by processing experimental data on tension $\sigma_{1,2,3,4} = 0.981 \cdot 10^7 (4; 5; 5.5; 6)$ newtons/m^2. The test results for 20°C and the above stress levels are represented by the continuous curves in Figure I.11. After 1,000-hr creep, a quasistable state is attained at which the rate of creep is close to zero (curves 1, 2 and 3). At higher stresses (curve 4) the creep process is also characterized by a high deformation rate after the given 1,000 hr and is terminated by cleavage fracture. The points on Figure I.12 illustrate the changes in the Poisson ratio with time. If we assume that for the given polymers the principle of strain superposition holds /6/, the effect of a stress acting at any instant will not change under the action of stresses applied at other instants. The continuous curve (Figure I,13) characterizes the growth of deformations when the stress is applied in two stages: σ_1 was $0.981 \cdot 4 \times \times 10^7$ newtons/m^2, and the specimen was subjected to this stress for 240 hr .

After this period the stress was increased to $\sigma_2 = (0.981 \cdot 5 \cdot 10^7)$ newtons/m^2, and the polymer was subjected to this stress for another 240 hr. The stress was again lowered to σ_1. The upper dashed curve 2, coinciding with the solid curve at $t > t_1$, shows the creep for σ_2; the lower curve 1 determines the creep when only σ_1 acts. It can be seen that the superposition principle applies with the necessary accuracy in the given interval of stress changes.

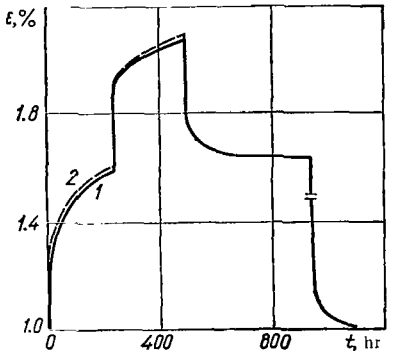

FIGURE I.13. Diagram of stepwise loading of a polymer matrix.

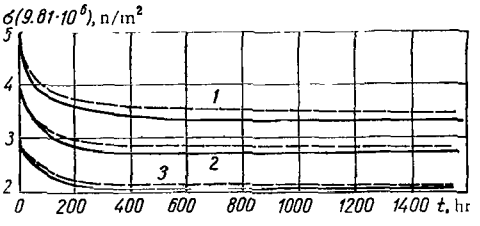

FIGURE I.14. Relaxation curve of a polymer matrix.

When fixing the deformations of polymers, we observe the relaxation of the initially applied stresses (Figure I. 14), The continuous curves illustrate the changes in the stresses for initial deformations of the material of $\varepsilon_{1,2,3} = (1.5; 1.2; 0.9)\%$.

The equation relating the inelastic strain component to the stress is best represented by applying an operator

$$e_{in} = L\sigma, \tag{I. 25}$$

where L is the operator which must satisfy the following conditions:

a) the theoretical and experimental curves of creep and stress relaxation must coincide on the initial section over the range $0 < t < t_0$ (t_0 is the time when the creep rate changes sharply);

b) the theoretical (calculated from (I. 25)) and experimental creep and relaxation curves must asymptotically coincide at $t \gg t_0$;

c) the equation must contain operator L which is governed by fairly simple transformation rules, and does not lead to additional difficulties in computations. It was found that for stable rheonomic processes when the creep rate asymptotically approaches zero, the simplest type of operation satisfying conditions a, b, and c is obtained by Volterra's integral equation using it as the kernel of a fractional-exponential function (see Rabotnov /7/)

$$L\sigma(t) = \frac{1}{\mu}\,\vartheta^*_{1-\lambda}(-\omega_\infty)\,\sigma(t) = \frac{\omega_0}{E_0}\int_0^t dt'\vartheta_{1-\lambda}(-\omega_\infty,\ t-t')\,\sigma(t'). \tag{I. 26}$$

We introduce the designations

$$\frac{1}{\mu} = \frac{\omega_\infty}{E_\infty} = \frac{\omega_0}{E_0}, \tag{I. 27}$$

where μ, ω_∞, E_∞, ω_0, E_0 and λ are rheological parameters. Their numerical values are found from experimental results on creep or stress relaxation; the physical sense of these parameters will be shown below;

$$\vartheta_{1-\lambda}(-\omega_\infty,\ t-t') = (t-t')^{\lambda-1}\sum_{n=0}^{\infty}\frac{(-\omega_\infty)^n (t-t')^{n\lambda}}{\Gamma[\lambda(n+1)]}, \tag{I. 28}$$

where $\Gamma[x]$ is Euler's second integral /8/. For $\lambda \to 1$, we have

$$\vartheta_{1-\lambda}(-\omega_\infty,\ t-t') \to e^{-\omega_\infty (t-t')}.$$

To a linear approximation according to (I. 24) and (I. 26), the stress-strain equation is

$$\varepsilon = \frac{1}{E_0}[1 + \omega_0 \vartheta^*_{1-\lambda}(-\omega_\infty)]\,\sigma(t) = \frac{1}{E^*}\sigma(t). \tag{I. 29}$$

For numerical calculations in the case of simple creep or stress relaxation, we shall use the following approximations /9/, which hold for all the argument values and make it possible to specify the lower limit

$$\vartheta^*_{1-\lambda}(-\omega_\infty)\,1 \approx \frac{1}{\omega_\infty}[1 - \exp(-\omega_\infty \lambda^\lambda t^\lambda)]. \tag{I. 30}$$

For a specification of the upper limit for $\omega_\infty (\lambda t)^\lambda \gg 1$ we use

$$\vartheta^*_{1-\lambda}(-\omega_\infty)\,1 \approx \frac{1}{\omega_\infty}\left[1 - \frac{1}{\omega_\infty t^\lambda \Gamma(1-\lambda)}\right].$$

For creep with constant stress σ_0, from (I. 29) and (I. 30) we readily obtain

$$\varepsilon \approx \frac{\sigma_0}{E_0}\left\{1 + \frac{\omega_0}{\omega_\infty}[1 - \exp(-\omega_\infty \lambda^\lambda t^\lambda)]\right\},$$

from which at $(t \to \infty)$we can find the creep modulus

$$\varepsilon \to \frac{\sigma_0}{E_0}\left(1 + \frac{\omega_0}{\omega_\infty}\right) = \frac{\sigma_0}{E_{cr}},$$

whence

$$\frac{1}{E_{cr}} = \frac{1}{E_0} + \frac{1}{E_\infty}. \tag{I. 31}$$

The modulus of instantaneous elasticity E_0 is determined from short-term tests. Therefore, by measuring the total deformation accumulated at the instant when the creep rate is equal to zero, we find E_∞ from (I. 31).

Processing the experimental data for the EMA polymer showed that

$$\lambda \approx 0.5; \quad \omega_0 \approx 0.052\, r^{-\lambda}; \quad \omega_\infty = 0.12\, r^{-\lambda};$$
$$E_\infty = 0.981 \cdot 0.73 \cdot 10^{10} \text{ newtons/m}^2.$$

For tensile stresses not exceeding $0.7\,\sigma_s$, we find a satisfactory coincidence between the experimental and theoretical values. The theoretical data are shown in Figure I.11 by the dash-dot lines. At higher stress levels (curve 4, Figure I.11), we note appreciable differences between the experimental and theoretical curves because of nonlinear effects.

To transform the expressions with the introduced operators, we use equations /10, 11, 12/:

$$\left.\begin{aligned}
&\frac{1}{1 - a\vartheta^*_{1-\lambda}(\omega)} = 1 + a\vartheta^*_{1-\lambda}(a+\omega);\\
&\vartheta^*_{1-\lambda}(x)\,\vartheta^*_{1-\lambda}(y) = \frac{\vartheta^*_{1-\lambda}(x) - \vartheta^*_{1-\lambda}(y)}{x-y}; \quad \vartheta^{*2}_{1-\lambda}(x) = \frac{\partial \vartheta^*_{1-\lambda}(x)}{\partial x};\\
&\frac{1}{1 - \sum_{k=1}^{m} a_k \vartheta^*_{1-\lambda}(x_k)} = 1 + \sum_{k=1}^{m} b_k \vartheta^*_{1-\lambda}(c_k),
\end{aligned}\right\} \qquad \text{(I. 32)}$$

where c_k $(k = 1, 2, \ldots, m)$ are the roots of

$$1 + \sum_{n=1}^{m} \frac{a_k}{x_n - c} = 0,$$

and the coefficients b_k are determined from a system of linear algebraic equations of type

$$1 + \sum_{k=1}^{m} \frac{b_k}{x_n - c_k} = 0 \quad (n = 1, 2, \ldots, m).$$

The stress relaxation processes are determined from (I.29)

$$\sigma = E^* \varepsilon(t) = E_0 [1 - \omega_0 \vartheta^*_{1-\lambda}(-\omega)]\, \varepsilon(t). \qquad \text{(I. 33)}$$

Here $\omega = \omega_0 + \omega_\infty$; the type of operator E^* was determined from (I.29) and the first equation (I.32). In the developed form the representation of (I.33) according to (I.26) can be written as

$$\sigma = E_0 \left[\varepsilon(t) - \omega_0 \int_0^t dt' \vartheta_{1-\lambda}(-\omega,\ t - t')\, \varepsilon(t') \right].$$

For simple relaxation when $\varepsilon = \varepsilon_0$, we can use approximation (I.30) to find a convenient equation

$$\sigma = \sigma_0 \left[1 - \frac{\omega_0}{\omega_0} (1 - e^{-\omega\lambda \lambda t^\lambda}) \right].$$

Here σ_0 is the initially applied stress, $\sigma_0 = \varepsilon_0 E_0$.

The data of the theoretical calculations of stress relaxation in the given polymer are shown in Figure I.14 by the dashed curves. A comparison shows that the experimental and theoretical results agree fairly well, though as seen from the curves the relaxation process proceeds at a higher

rate than described by the equations for which the rheological parameters were obtained from creep data.

For limited stress levels the stress-strain equation in the given polymers for uniaxial tension can be formally described by an equation similar to that of Hooke's law, when instead of Young's modulus E the operator E^*, determined from (I. 33), is used. In viscoelastic media, where the creep is unstable (that is, the creep rate is finite), the operators are obtained from the above equations by transition to limits $\omega_\infty \to 0$.

For the spatial stressed-strained state it is convenient to replace the elastic constants in the three-dimensional equations of Hooke's law by operators. These must be selected so that the equations obtained must not contradict available experimental data within the limits of the required accuracy. We emphasize the conditionality of this generalization because no experimental studies are available on time-depending constraints in polymers in either the plane or spatial stressed states, with simple or complex loads.

After we have carried out the necessary substitutions in (I. 16) we obtain a system of linear operator equations of the type /7/

$$\sigma = 3K^*\varepsilon;\ \sigma_{ik} - \frac{1}{3}\sigma\delta_{ik} = 2G^*\left(\varepsilon_{ik} - \frac{1}{3}\varepsilon\delta_{ik}\right). \qquad \text{(I. 34)}$$

If we neglect the viscoelastic effects on hydrostatic compression and volume expansion, that is, if we equate

$$\frac{1-2\nu^*}{E^*} = \frac{1-2\nu_0}{E_0}, \qquad \text{(I. 35)}$$

we easily obtain the Poisson ratio operator characterizing the changes in transverse deformation with time

$$\nu^* = \nu_0\left[1 + \frac{1-2\nu_0}{2\nu_0}\omega_0\vartheta^*_{1-\lambda}(-\omega)\right]. \qquad \text{(I. 36)}$$

Here and later subscript "0" denotes the instantaneous values of the Poisson ratio when the material changes according to Hooke's law. The theoretical change is the transverse effects on tension determined from (I. 35) and approximation (I. 30)

$$\nu^* \cdot 1 \approx \nu_0\left[1 + \frac{1-2\nu_0}{2\nu_0}\cdot\frac{\omega_0}{\omega}(1 - e^{-\omega\lambda_1 t})\right],$$

is shown by the continuous curve in Figure I. 12. The good agreement between the experimental and theoretical data for the EMA polymer confirms (I. 36) for simple tension. With development of viscoelastic deformations in the given polymer, the Poisson ratio increases from $\nu_0 = 0.382$ to $\nu_{cr} = 0.418$. For materials with an unstable creep ($\omega_\infty \to 0$), the limiting Poisson ratio $\nu_{cr} = 0.5$.

When directly applying the operator transformation rules, (I. 32) determines the modulus operator of shear

$$G^* = \frac{E^*}{2(1+\nu^*)} = G_0\left[1 - \frac{3\omega_0}{2+2\nu_0}\vartheta^*_{1-\lambda}\left(-\omega_\infty - \frac{3\omega_0}{2+2\nu_0}\right)\right] \qquad \text{(I. 37)}$$

and its reciprocal operator

$$\frac{1}{G^*} = \frac{1}{G_0}\left[1 + \frac{3\omega_0}{2+2\nu_0}\,\Im^*_{1-\lambda}(-\omega_\infty)\right]. \qquad \text{(I. 38)}$$

The modulus of shear in creep is obtained by the action of operator G^* on unity at $t \to \infty$

$$G_{cr} = G_0 \frac{(2+2\nu_0)\,\omega_\infty}{3\omega_0 + (2+2\nu_0)\,\omega_\infty}.$$

For the EMA polymer $G_{cr} = 0.695\,G_0$.

To process the experimental results over a wider range of creep times, we use the operators of the theory of elastic after-effects, with several kernels simultaneously. For polymers with unstable creep we introduce generalized operators 24

$$\frac{1}{E^*} = \frac{1}{E_0}\left[1 + \omega_0 \Im^*_{1-\lambda}(-\omega_\infty) + \omega_1 I^*_{1-\lambda}\right],$$

containing five rheological parameters. Here we introduce the operator with an Abel kernel acting upon the time function $f(t)$ according to

$$I^*_{1-\lambda} f(t) = \int_0^t dt' \frac{(t-t')^{\lambda-1}}{\Gamma(\lambda)} f(t'). \qquad \text{(I. 39)}$$

If we neglect the creep of the material subjected to hydrostatic tension or compression, the Poisson ratio operator in the given case is determined in the same way as (I. 36), and is equal to

$$\nu^* = \nu_0\left[1 - \frac{1-2\nu_0}{2\nu_0}\sum_{k=1}^{2} \alpha_k \Im^*_{1-\lambda}(c_k)\right].$$

In this expression the following symbols are used

$$\alpha_1 + \alpha_2 = \omega_0 - \omega_1;$$

$$\alpha_1 - \alpha_2 = \frac{\omega_\infty(\omega+\omega_1) - (\omega+\omega_1)^2 + 2\omega_1\omega_\infty}{\sqrt{(\omega+\omega_1)^2 - 4\omega_1\omega_\infty}};$$

$$c_1 + c_2 = -\omega - \omega_1; \quad c_1 - c_2 = -2\sqrt{(\omega+\omega_1)^2 - 4\omega_1\omega_\infty}.$$

Transformations according to (I. 32) give the other operators

$$\frac{1}{G^*} = \frac{1}{G_0}\left[1 + \frac{3\omega_0}{2+2\nu_0}\Im^*_{1-\lambda}(-\omega_\infty) + \frac{3\omega_1}{2+2\nu_0} I^*_{1-\lambda}\right];$$

$$E^* = E_0\left[1 + \sum_{k=1}^{2} \alpha_k \Im^*_{1-\lambda}(c_k)\right];$$

$$G^* = G_0\left[1 + \sum_{k=1}^{2} \beta_k \Im^*_{1-\lambda}(\delta_k)\right].$$

Here

$$\beta_1 = \frac{\delta_1(\delta_1 + \omega_\infty)}{\delta_1 - \delta_2};\ \beta_2 = -\frac{\delta_2(\delta_2 + \omega_\infty)}{\delta_1 - \delta_2};$$

$$\delta_1 + \delta_2 = -\omega_\infty - 3\frac{\omega_0 + \omega_1}{2 + 2\nu_0};$$

$$\delta_1 - \delta_2 = \sqrt{\left(\omega_\infty + 3\frac{\omega_0 + \omega_1}{2 + 2\nu_0}\right)^2 - 3\frac{4\omega_1\omega_\infty}{2 + 2\nu_0}}.$$

An analysis of data on the creep of polymers at different stress levels shows that there is a limit of stable creep (with reference to the stress) /13/. When it exceeds this limit the creep curve has a point of inflection, and its shape is changed, depending on the stress level. The creep process is terminated by cleavage fracture of the material, without any neck being formed. This creep limit for the EMA polymer is not higher than 0.7 σ_B. At stress levels less than those corresponding to the creep limit, the creep rate asymptotically approaches zero. In the study of the creep of spatially cross-linked polymers for various stress levels, we considered the possible solutions of the nonlinear differential equation which describes the development of the high-elastic component of the strain tensor

$$\frac{de_\infty}{dt} = Ce^{pe_\infty} - qe_\infty, \qquad \text{(I. 40)}$$

where q and c are temperature and stress dependent, and p is temperature dependent only. The total deformation rate of the polymer depends on the rate of elastic deformation and the rate determined from (I. 40). The solution of (I. 40) is

$$qt = \int_0^{pe_\infty} \frac{dx}{\frac{c}{c_k}e^{x-1} - x},$$

where $\frac{1}{c_k} = \frac{pe}{q}$.

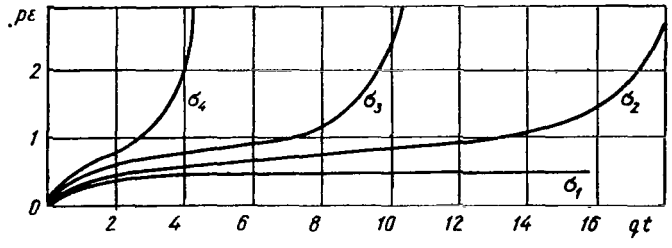

FIGURE I.15. Typical creep curves for various stress levels.

We shall consider various values of the parameters in the integrand:

a) if $\frac{c}{c_k} > 1$ and $0 < pe_\infty < \infty$, by expanding the integrand into a series and integrating by parts, we obtain

$$qt = \sum_{n=0}^{\infty}\left(\frac{e}{c/c_k}\right)^{n+1}\left\{\frac{n!}{(n+1)^{n+1}} - e^{-pe_\infty(n+1)}\left[\frac{(pe_\infty)^n}{n+1} + \frac{n(pe_\infty)^{n+1}}{(n+1)^2} + \ldots\right]\right\},$$

the integral qualitatively indicates unstable creep;

b) if $\frac{c}{c_k} = 1$ and $0 < pe_\infty < 1$, allowing for $e^{pe_\infty - 1} > pe_\infty$, over this range the above expansion holds and case b corresponds to the limit of stable creep;

c) if $\frac{c}{c_k} < 1$ and $0 < pe_\infty < b_0$, where b_0 is the root with the smallest real part of the equation $\frac{c}{c_k} e^{x-1} - x = 0$, the integral is calculated as shown in case a, and describes the stable creep curves. The nonlinear equation (I. 40) satisfactorily describes the creep of polymers at any stress conditions. To process the experimental data, we use

$$q = q_0 e^{\alpha\sigma}, \quad c/c_k = (c/c_k)_0 e^{\beta\sigma}.$$

α and β are taken from experimental data. Figure I. 15 shows typical curves for various stress levels ($\sigma_4 > \sigma_3 > \sigma_2 > \sigma_1$).

4. Behavior of polymers at high temperatures

The physicomechanical properties of polymer matrices appreciably change when the matrix is subjected to higher temperatures. Heating results in an increase in the creep rate and stress relaxation, and to a decrease in the modulus of elasticity. Finally, the polymer chains are destroyed and cross-linking sets in. The deterioration in the mechanical and other characteristics is especially noticeable at the vitrification temperature of the polymer (for the EMA compound, this is about 353°K).

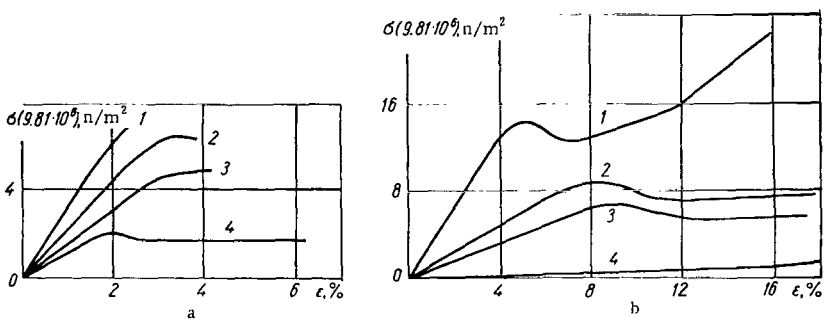

FIGURE I. 16. Tension (a) and compression (b) curves at various temperatures.

The changes in the $\sigma - \varepsilon$ curves on tension and compression with temperature increase is shown in Figure I. 16 for the given polymer (curves 1, 2, 3 and 4 were plotted for 293, 323, 348, and 373°K, respectively).

The change in the moduli of elasticity in tension and compression of this polymer is shown by curves 1 and 3, respectively, in Figure I. 17. The decrease in the ultimate strengths in tension and compression is characterized by curves 2 and 4, respectively. The last curve was plotted from the first peak of the $\sigma - \varepsilon$ diagram in compression.

The creep curves of the EMA polymer at various stress levels at 323 (a) and 348°K (b) are shown in Figure I. 18. The continuous curves were plotted for stresses $\sigma_{1,2,3,4,5} = 981 \cdot 10^7 (2; 3; 4; 5; 5.5)$ newtons/m^2 (Figure I. 18, a)

and $\sigma_{1,2,3} = 981 \cdot 10^7$ (1, 2, 3) newtons/m^2 (Figure I.18, b). The limits of stable creep at these temperatures are $0.981 \cdot 3 \cdot 10^7$ newtons/m^2 (323°K) and $0.981 \cdot 1.2 \cdot 10^7$ newtons/m^2 (348°K). The theoretical results obtained from (I.40) are represented by the dashed lines in Figures I.11 and I.18. The following temperature dependence of the parameters was taken

$$q = \bar{q}e^{+\alpha\sigma+kT}; \quad c/c_k = (c/c_k)_0 e^{\gamma T+\beta\sigma}; \quad p = \bar{p}e^{-\gamma T}.$$

The nonlinear equation investigated satisfactorily describes the creep process at different stress and temperature levels. After removal of the load in the given case no complete elastic aftereffect is observed, and the accumulated deformation only disappears on further increase in temperature.

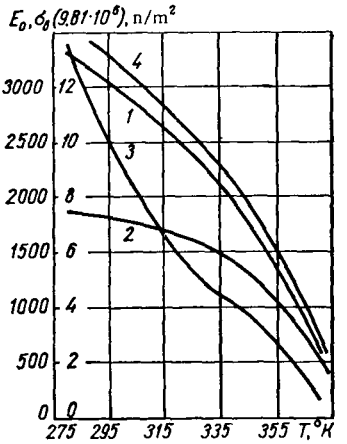

FIGURE I.17. Temperature dependence of the moduli of elasticity in tension and compression.

At fairly low stress levels and elevated temperatures it is possible to use a linear equation for the stress-strain curves over a certain range; the equations can be represented in the form

$$\sigma = 3K_0(\varepsilon - \beta_s\Theta), \quad \sigma_{ik} - \frac{1}{3}\sigma\delta_{ik} = 2G^*\left(\varepsilon_{ik} - \frac{1}{3}\varepsilon\delta_{ik}\right). \qquad \text{(I.41)}$$

The coefficient of linear expansion β_s for polymers does not remain constant with increase in temperature. Thus, close to the vitrification temperature T_v, β_s, the specific heat, and other parameters change jumpwise. Figure I.19 shows the β_s vs temperature graph for the EMA polymer. Near the vitrification point β_s increases by a factor higher than two.

If we allow for the fact that the creep of polymers at elevated temperatures is unstable over a wide range of change in the rheonomic parameters, and also take into account that these parameters are temperature dependent, the operator form of the modulus of rigidity is

$$G^* = G_0\left[1 - \frac{3\omega_0}{2+2\nu_0}\vartheta^*_{1-\lambda}\left(-\frac{3\omega_0}{2+2\nu_0}\right)\right], \qquad \text{(I.42)}$$

where

$$\omega_0 = \omega_1 e^{bT}; \quad G_0 = Ge^{-gT}. \qquad \text{(I.43)}$$

When we processed the data on creep at elevated temperatures, we found approximate values of reduced parameters for the EMA

$$\omega_0 \approx \exp(-10.87 + 0.0306T)\,r^{-\lambda}, \quad \lambda \approx 0.3;$$
$$G_0 \approx 0.981 \cdot 4.19 \cdot 10^{10}e^{-0.00925T} \text{ [newtons/m}^2\text{]}.$$

Here the temperature is given in centigrades.

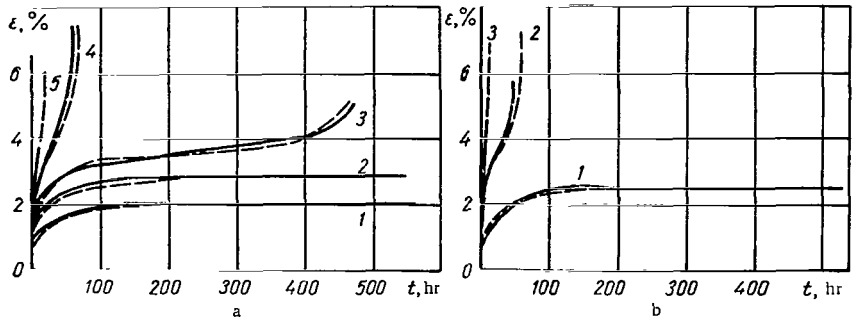

FIGURE I.18. Experimental and theoretical creep curves for various stress and temperature levels.

For polymer matrices which are thermorheologically simple, the temperature change can be allowed for by introducing the arbitrary time function $q = \varphi(t)$. Function $\varphi(t)$ is found from experimental results. In this case the integral operator acts according to /14/

$$G^*f(t) = G_0\left\{f(t) - \frac{3\omega_0}{2+2\nu_0}\int_{\varphi(t_1)}^{\varphi(t_2)} d\varphi(t')\,\vartheta_{1-\lambda}\left[-\frac{3\omega_0}{2+2\nu_0},\ \varphi(t)-\varphi(t')\right]f(t')\right\}.$$

For $f = f_0$, if $q^\lambda = a_1 \ln t/t_1$, we have the approximation

$$\vartheta^*_{1-\lambda}(-\omega)\,1 \approx \frac{1}{\omega}\left[1-\left(\frac{t}{t_1}\right)^{-\lambda\lambda a_1 \omega}\right] \quad (a_1 > 0,\ t \geqslant t_1 > 0).$$

The form of the other operators can be readily determined in analogy with the above equations.

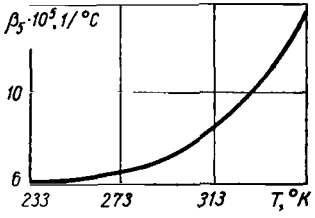

FIGURE I.19. Temperature dependence of the linear expansion coefficient of a polymer matrix.

5. Properties of plastics under periodic stresses

Under periodic stresses, the dissipation of mechanical energy in polymers is stronger than in other materials, and is appreciably affected by their moving constraints. The dissipation parameters are found from the

integral operators which have been discussed in section 3. To determine the rheological parameters used in those operators, and to give a more accurate description of the effective properties of polymers, it is best to use experimental data on the damping of the free vibrations of the specimens or the resonant hysteresis loop.

To a linear approximation, the processes of energy dissipation in tension-compression are described by a single operator. If the medium is under a unilateral stress changing with time according to the sine curve $\sigma = \mathrm{Re}\,\sigma^0 e^{i\Omega t}$, then after a certain period sufficient to enable us to neglect the effect of the initial conditions, the time-dependent change in deformation will be

$$\varepsilon = E^{*-1}\,\mathrm{Re}\,\sigma^0 e^{i\Omega t},$$

where according to our convention the lower limit should tend to

$$E^{*-1} = E_0^{-1}\left[1 + \omega_0 \int_{-\infty}^{t} dt' \vartheta_{1-\lambda}(-\omega_\infty,\ t - t')\right].$$

By applying integrals of type

$$\int_0^\infty dt\, e^{-i\Omega t} t^{\lambda-1} = \Gamma(\lambda)/(i\Omega)^\lambda$$

and (I. 44)

$$\vartheta^*_{1-\lambda}(-\omega_\infty)\, e^{i\Omega t} = \frac{e^{i\Omega t}}{\omega_\infty + i^\lambda \Omega^\lambda},$$

the deformation of the medium is expressed in terms of storage compliance I' and loss compliance I'':

$$\varepsilon = \mathrm{Re}\,(I' + iI'')\,\sigma = \sigma^0 \sqrt{I'^2 + I''^2}\cos(\Omega t - \varphi),$$

where

$$\left.\begin{aligned} &\mathrm{tg}\,\varphi = I''/I';\\ &E_0 I' = 1 + \frac{\omega_0}{\omega_\infty}\cdot\frac{1 + \Omega^\lambda/\omega_\infty \cos\pi\lambda/2}{1 + 2\Omega^\lambda/\omega_\infty \cos\pi\lambda/2 + \Omega^{2\lambda}/\omega_\infty^2};\\ &E_0 I'' = \frac{\omega_0}{\omega_\infty}\cdot\frac{1 + \Omega^\lambda/\omega_\infty \sin\pi\lambda/2}{1 + 2\Omega^\lambda/\omega_\infty \cos\pi\lambda/2 + \Omega^{2\lambda}/\omega_\infty^2}. \end{aligned}\right\} \qquad \text{(I. 45)}$$

The pattern of the dependence of the compliance values on the frequency is shown in Figure I. 20. Over a wide frequency range a monotonic dependence is found. The data in the audiofrequency range show local anomalies in the compliance curves, which are explained by high-frequency resonant dispersion in various polymers /15/. The resonant character of the dispersion is illustrated by the curves in Figure I. 21. The curves were plotted from experimental data on the changes in the compliances of polythene between 100 and 4,500 Hz. The material was preliminarily subjected to a static deformation of about 1%. Resonance occurs only once at 2,720 Hz.

To study polymers at frequencies where the dynamic characteristics are changed because of high-frequency dispersion, integral-differential operators /16/ of type

$$\Im^*_{1-\lambda}[-\omega_\infty(1+D^2/\Omega_a^2)]f(t) = \int_{-\infty}^{t} dt'(t-t')^{\lambda-1}\sum_{n=0}^{\infty}\frac{(t-t')^{n\lambda}[-\omega_\infty(1+D^2/\Omega_a^2)]^n}{\Gamma[\lambda(n+1)]}f(t'),$$

are employed. Here $D^2 = \frac{\partial^2}{\partial t^2}$. The operator is applied as follows: first $f(t)$ is differentiated with respect to t, and then integration is carried out. Frequency Ω_a is determined from the critical value Ω_{cr}, at which resonant dispersion is observed. If $\lambda \approx 1$, then $\Omega_a \approx \Omega_{cr}$. The transformation equations of the operators are similar to (I. 32). The operator modulus of the first kind and its reciprocal are given by

$$E^* = E_0\{1 - \omega_0\Im^*_{1-\lambda}[-\omega(1+D^2/\Omega_a^2)]\};$$
$$E^{*-1} = E_0^{-1}\{1 + \omega_0\Im^*_{1-\lambda}[-\omega_\infty(1+D^2/\Omega_a^2)]\}$$

etc.

If we allow for resonant dispersion, the storage compliance and loss compliance are given by

$$E_0I'_a = 1 + \frac{\omega_0}{\omega_\infty}\cdot\frac{1 - \Omega^2/\Omega_a^2 + \Omega^\lambda/\omega_\infty\cos\pi\lambda/2}{(1-\Omega^2/\Omega_a^2)^2 + 2(1-\Omega^2/\Omega_a^2)\Omega^\lambda/\omega_\infty\cos\pi\lambda/2 + \Omega^{2\lambda}/\omega_\infty^2};$$
$$E_0I''_a = \frac{\omega_0}{\omega_\infty}\cdot\frac{\Omega^\lambda/\omega_\infty\sin\pi\lambda/2}{(1-\Omega^2/\Omega_a^2)^2 + 2(1-\Omega^2/\Omega_a^2)\Omega^\lambda/\omega_\infty\cos\pi\lambda/2 + \Omega^{2\lambda}/\omega_\infty^2}. \qquad \text{(I. 46)}$$

Ω_{cr} can be estimated from the approximate equation

$$\Omega_{cr} \approx \Omega_a\sqrt{1 + \Omega_{cr}^2/\omega_\infty\cos\pi\lambda/2}.$$

Figure I. 22 shows the characteristic dependence of $\operatorname{tg}\varphi_a$, $E_0I'_a$ and $E_0I''_a$ on the frequency at a resonant frequency $\Omega_{cr} = 260$ Hz. In the limiting case $\Omega_a \to \infty$, formula (I. 46) degenerates into (I. 45).

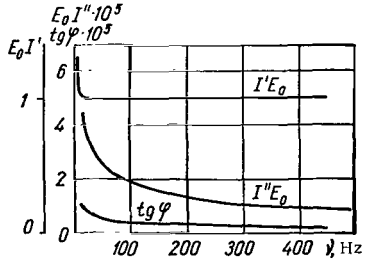

FIGURE I. 20. Frequency dependence of the compliance.

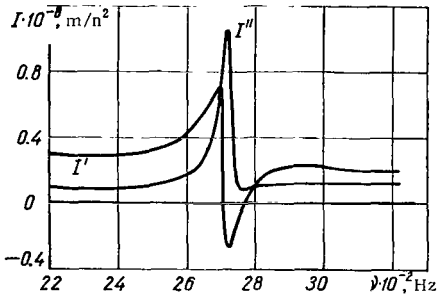

FIGURE I. 21. Frequency dependence of the compliance of polythene.

The thermal conductivity of polymers is two or three orders of magnitude lower than that of metals. For this reason, at comparatively low frequencies a state may arise in the polymers in which the quantity of

heat released by the material into the environment is less than the quantity of heat evolved by dissipation. This phenomenon is termed vibroheating. For a body of volume V, bounded by surface s, the energy balance equation can be written as

$$pC_V \frac{d}{dt}\int_V T\,dV = -\oint_s (\bar{q}\cdot\bar{n})\,ds + \int_V \Psi\,dV + \int_V \frac{\delta a}{\delta t}\,dV,$$

where C_V is the specific heat at constant volume; p is the specific gravity; $\bar{q}$ is the heat flux vector; $\bar{n}$ is the vector of the external normal to s; Ψ is the quantity of energy dissipated by the polymer per unit time from unit volume; $\frac{\delta a}{\delta t}$ is the specific work of the external field.

At boundary s, heat is transferred from the specimen to the environment

$$\varkappa(\bar{n}\cdot\operatorname{grad})T + \alpha(T - T_0)|_s = 0,$$

where T_0 is the environmental temperature; α is the heat transfer coefficient, and $\varkappa$ is the thermal conductivity coefficient.

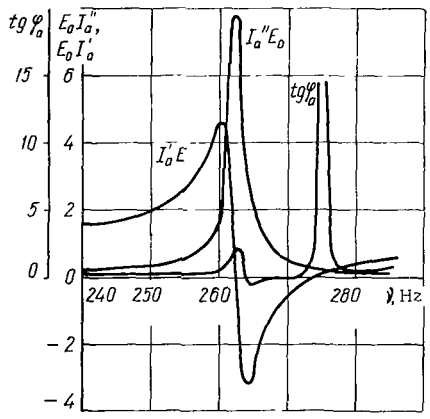

FIGURE I. 22. Frequency dependence of the storage compliance and the loss compliance with allowance for resonant dispersion.

The problem is approximately solved by assuming that period τ_0 is required for temperature equalizing in a sufficiently small volume. This is much longer than the period during which the applied stresses change, or mathematically $\tau_0 \gg 2\pi/\Omega$. In this approximation /17/ the stressed-strained state and the temperature of the specimen are best expressed in terms of the "slow" time function τ, and their changes over the range $0 < t < \tau_0$ can be neglected. Since for numerous polymers the temperature dependence of function Ψ is approximate over a restricted range /16/

$$\Psi = \Psi_0 e^{p\Theta} \quad (\Theta = T - T_0),$$

we obtain

$$pC_V \frac{d}{d\tau} \int_V \Theta \, dv = \int_V \Psi_0 e^{\gamma\Theta} \, dv - \frac{1}{\varkappa} \oint_S \alpha\Theta \, ds \qquad (I.47)$$

by averaging the energy balance equation over time range $0 \leqslant t < \frac{2\pi}{\Omega}$. We allowed for the heat transfer from the specimen to the environment, and for the fact that the reverse mechanical work completed by the stresses over the range for which the average was taken is equal to zero. (I. 47) can be further simplified if Θ is represented by a product of functions, one of which depends on time only and the other on the spatial variables

$$\Theta = \Theta_0(\tau)\,\Theta_1(x_1, x_2, x_3).$$

In some cases, by integration in (I. 46) we can obtain a nonlinear equation for $\Theta_0(\tau)$

$$\frac{d\Theta_0}{d\tau} + g\Theta_0 = Ee^{\beta\Theta_0},$$

where g, E and β are constants. The solution of this equation is discussed in section 3. Depending on the parameters, in this case, there are either stable temperature conditions, or the material is in a state of vibroheating when the temperature of the specimens increases indefinitely.

6. Thermal conductivity and diffusion in the continuum

Thermal conductivity is a result of temperature gradients. The intensity and direction of the heat flux passing through unit area is determined by vector $\bar{q}$, which according to Fourier's law is proportional to the temperature gradient /18/

$$\bar{q} = -\varkappa \operatorname{grad} T, \qquad (I.48)$$

where $\varkappa$ is the thermal conductivity coefficient.

The temperature distribution in time is obtained from the thermal conductivity equation

$$\frac{\partial T}{\partial t} - a\,\Delta T = \frac{1}{c\rho} f, \qquad (I.49)$$

where c and ρ are the specific heat and the density of the medium, respectively; f is the power of the heat source, and $a = \frac{\varkappa}{c\rho}$. The T function on the surface of the medium must be governed by the boundary conditions.

If the temperature distribution over s is known, we have boundary conditions of the first type

$$T|_s = T(x_1, x_2, x_3, t).$$

Boundary conditions of the second type are expressed in terms of the heat flux q_0 through the boundary surface:

$$-\varkappa(\bar{n} \cdot \operatorname{grad}) T|_s = q_0(x_1, x_2, x_3, t).$$

In accordance with the boundary conditions of the third type, the temperature gradient on s is proportional to the difference between the temperature of the material T and of the environment T_0

$$(\bar{n} \cdot \operatorname{grad}) T|_s = \frac{k}{\varkappa} (T - T_0),$$

where k is the overall heat transfer coefficient obtained by experiment.

If the temperature distribution is unsteady, the initial temperature distribution in the given body is obtained from

$$T(x_1, x_2, x_3, 0) = T_1(x_1, x_2, x_3).$$

Activated diffusion leads to penetration of particles through material which contains pores or other fissures /19/. If we designate by C the concentration of the diffusing matter, the diffusion equation follows directly from (I. 49), if T is substituted for C, and other coefficients are inserted:

$$\frac{\partial C}{\partial t} - D \Delta C = 0,$$

where D is the diffusivity. The flux vector Q determining the direction and amount of diffusing matter passing through unit area in unit time is given by

$$\bar{Q} = -D \operatorname{grad} C. \tag{I. 50}$$

The diffusivity D is more or less dependent on the particle concentration C. The boundary and initial conditions are obtained from the above equations by substituting C for T. The values of D for particles of various chemical composition in glasses are given in /19/ and /20/.

If the diffusing particles are absorbed in the given medium, for example, neutron diffusion, the above equations must be generalized. Neutrons move along a straight line until collision. Absorption by the nucleus or neutron scattering can occur. The absorption and scattering of neutrons are stochastic processes.

If the probability of interaction between neutrons and nuclei of the substances in unit volume be measured by the macroscopic cross section, then

$$\mu = \mu_0 + \mu_1, \tag{I. 51}$$

where μ_0 and μ_1 are cross sections of particle absorption and scattering, respectively. By designating the neutron diffusivity by $\left(D = \frac{\mu_1}{3\mu^2}\right)$, the velocity of their propagation by v, and the number of neutrons in unit volume by N, we obtain the particle flux

$$\Phi = Nv.$$

According to the balance equation for monoenergetic neutrons /21/

$$\frac{1}{v} \cdot \frac{\partial \Phi}{\partial t} = \operatorname{div}(D \operatorname{grad} \Phi) - \mu_0 \Phi + Q, \tag{I. 52}$$

where Q is the number of neutrons formed in unit volume of the medium in unit time.

When deriving (I. 52), it was assumed that μ and Φ change slightly over distances of the order of the mean free path of the particles. In this case, the particle flux vector $\overline{I}$ satisfies Fick's equation

$$\overline{I} = -D \operatorname{grad} \Phi. \tag{I. 53}$$

The conditions when (I. 52) is applicable are disturbed near the boundaries of the medium. In this case, the equation is considered to be approximate, and the concept of extrapolated boundaries is introduced to reduce errors. The solution of the diffusion equations gives better approximation to the accurate solution of the kinetic equations if conditions

$$\Phi\Big|_s = 0.7104 \frac{\partial \Phi}{\partial n}\Big|_s$$

have to be satisfied on the free boundary of the body.

For the majority of the elements of the periodic table, the cross sections of neutron absorption μ_0 and scattering μ_1 are shown in /22/.

7. Electromagnetic field equations in continuous media

The electromagnetic field in a continuous medium is described by four vectors: $\overline{E}$ and $\overline{H}$ are electric and magnetic field vectors; $\overline{D}$ is the displacement vector; and $\overline{B}$ is the magnetic induction vector /23/.

These vectors satisfy a system of the electromagnetic field equations

$$\begin{aligned} &\operatorname{rot} \overline{E} = -\frac{\partial \overline{B}}{\partial t}; \quad \operatorname{rot} \overline{H} = \frac{\partial \overline{D}}{\partial t} + \overline{j}; \\ &\operatorname{div} \overline{B} = 0; \qquad \operatorname{div} \overline{D} = \rho, \end{aligned} \tag{I. 54}$$

where ρ is the charge density; vector $\overline{j}$ determines the conduction current density, and indicates the direction of the charge movement. To a linear approximation the vectors for an isotropic medium are correlated by the equation of state

$$\overline{B} = \mu \overline{H}; \quad \overline{D} = \varepsilon \overline{E}; \quad \overline{j} = \sigma \overline{E}, \tag{I. 55}$$

where μ and ε are the permeability and dielectric constant, respectively; and σ is the conductivity.

The conductivity of polymers, glasses and other nonmetallic components is usually low, and therefore these materials are considered to be dielectrics. The dielectric constant for polymers may change appreciably because of the presence of inpurities, inclusion of bubbles, etc. If there are only a few air bubbles the dielectric constant of such a medium is described by /24/.

$$\tilde{\varepsilon} \approx \varepsilon \left(1 - \frac{3\xi}{\xi + \frac{2\varepsilon + 1}{\varepsilon - 1}}\right),$$

where ξ is the relative volume content of voids in the medium.

At high frequencies of change in the electromagnetic field, we find a large lag between $\overline{D}$ and $\overline{E}$ accompanied by energy dissipation in the

dielectric. To allow for the phase shift in the phenomenological approximation, instead of the dielectric constant, we introduce its operator, using as the kernel the fractional-exponential functions

$$\overline{D} = \varepsilon^* \overline{E} = [\varepsilon_\infty + \Omega_0^\lambda (\varepsilon^0 - \varepsilon_\infty) \partial^*_{1-\lambda} (-\Omega_0^\lambda)] \overline{E}. \tag{I.56}$$

Here, ε^0 and ε_∞ are the dielectric constants at zero and upper limit frequencies of change in the electromagnetic field; parameters Ω_0^λ and λ are obtained by experiment. For a periodically changing field, when $\overline{E} = \overline{E}_0 e^{i\Omega t}$; $\overline{D} = \overline{D}_0 e^{i(\Omega t - \varphi)}$ (φ is the phase angle), if we allow for (I.44), the real and imaginary parts of the complex dielectric constant $\varepsilon = \varepsilon' - i\varepsilon''$, are established, where

$$\varepsilon' = \varepsilon_\infty + (\varepsilon^0 - \varepsilon_\infty) \frac{1 + (\Omega/\Omega_0)^\lambda \cos \pi\lambda/2}{1 + 2(\Omega/\Omega_0)^\lambda \cos \pi\lambda/2 + (\Omega/\Omega_0)^{2\lambda}};$$

$$\varepsilon'' = \frac{(\varepsilon^0 - \varepsilon_\infty)(\Omega/\Omega_0)^\lambda \sin \pi\lambda/2}{1 + 2(\Omega/\Omega_0)^\lambda \cos \pi\lambda/2 + (\Omega/\Omega_0)^{2\lambda}}. \tag{I.57}$$

The tangent of the loss angle is determined directly from the complex dielectric constant

$$\operatorname{tg} \varphi = \varepsilon''/\varepsilon'. \tag{I.58}$$

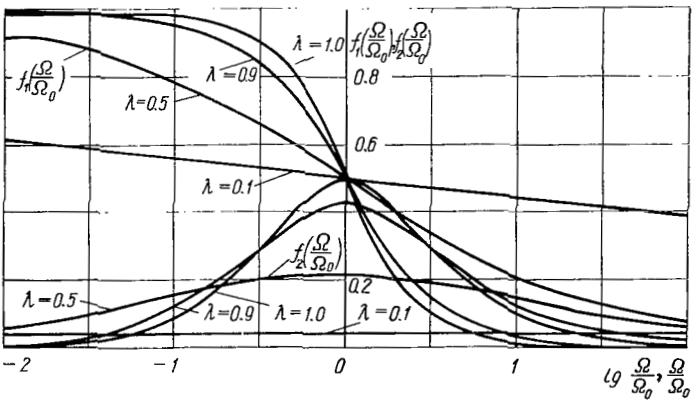

FIGURE I. 23. Dependence of f_1 and f_2 on the frequency ratio.

From these equations it is possible to process experimental data with an accuracy higher than that of the conventional formulas derived from the above equations when $\lambda = 1$. Figure I. 23 shows the curves characterizing the changes in functions f_1 and f_2 depending on the argument $\frac{\Omega}{\Omega_0}$, where

$$f_1 = \frac{1 + (\Omega/\Omega_0)^\lambda \cos \pi\lambda/2}{1 + 2(\Omega/\Omega_0)^\lambda \cos \pi\lambda/2 + (\Omega/\Omega_0)^{2\lambda}}; \quad f_2 = \frac{(\Omega/\Omega_0)^\lambda \sin \pi\lambda/2}{1 + 2(\Omega/\Omega_0)^\lambda \cos \pi\lambda/2 + (\Omega/\Omega_0)^{2\lambda}}.$$

The curves are plotted for $\lambda = 1$ (upper curve); 0.9; 0.5; and 0.1.

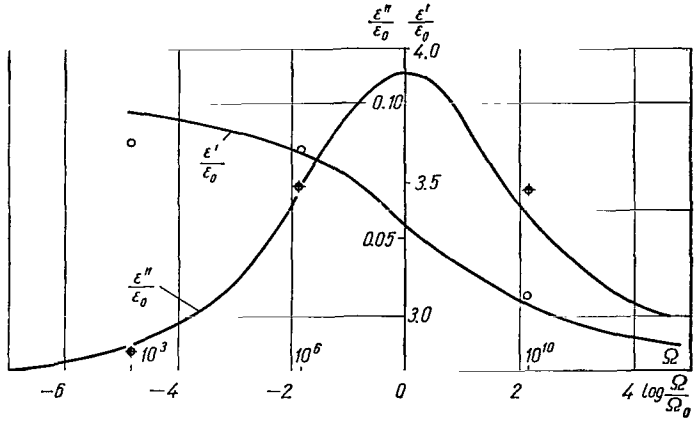

FIGURE I. 24. Dependence of the real and imaginary parts of the dielectric constant on frequency.

Figure I. 24 shows curves illustrating the changes in $\frac{\varepsilon'}{\varepsilon_0}$, $\frac{\varepsilon''}{\varepsilon_0}$ (ε_0 is the dielectric constant of a vacuum) depending on the frequency of the alternating field for the EMA polymer. The values of the parameters were taken from Kisel' /25/, who measured ε' and tan φ at 10^3, 10^6, and 10^{10} Hz; the values were $\lambda = 0.3294$; $\Omega_0 = 0.705 \cdot 10^8$ Hz, $\frac{\varepsilon^0}{\varepsilon_0} = 3.775$, $\frac{\varepsilon^\infty}{\varepsilon_0} = 2.9342$.

In the high (optical frequency) range, resonance is observed in some polymers. This phenomenon is similar to the resonance observed at mechanical vibrations (see section 5). When approaching resonant frequency Ω_{cr}, the dielectric constant increases, and at the critical frequency ε' drops to values below unity. On the other hand, with increase in frequency ε' asymptotically approaches its value in a vacuum /26/. Transition to resonant frequency is accompanied by strong absorption. The phenomenological description of these effects is given by integral-differential operators (see section 5). The operator of the dielectric constant is written as

$$\varepsilon^* = \varepsilon_a + \Omega_0^\lambda \varepsilon_b \vartheta^*_{1-\lambda}[-\Omega_0^\lambda (1 + D^2/\Omega_a^2)],$$

where ε_a, ε_b, Ω_0^λ, Ω_a are determined by processing the data of experiments carried out at Ω_{cr}. In the case of a periodically changing field the real and imaginary parts of the dielectric constant are given by

$$\varepsilon' = \varepsilon_a + \varepsilon_b \frac{1 - (\Omega/\Omega_a)^2 + (\Omega/\Omega_0)^\lambda \cos \pi\lambda/2}{(1 - \Omega^2/\Omega_a^2)^2 + 2(1 - \Omega^2/\Omega_a^2)(\Omega/\Omega_0)^\lambda \cos \pi\lambda/2 + (\Omega/\Omega_0)^{2\lambda}};$$
$$\varepsilon'' = \frac{\varepsilon_b (\Omega/\Omega_0)^\lambda \sin \pi\lambda/2}{(1 - \Omega^2/\Omega_a^2)^2 + 2(1 - \Omega^2/\Omega_a^2)(\Omega/\Omega_0)^\lambda \cos \pi\lambda/2 + (\Omega/\Omega_0)^{2\lambda}}. \quad \text{(I. 59)}$$

For a rough approximation of experimental data, we can take $\lambda = 1$.

The electromagnetic field vectors must satisfy not only the Maxwell equations (I. 54), but also the boundary conditions for the body surface.

In particular, on the fiber-matrix interface, when no changes take place on surface s, the tangential components of the electric and magnetic field vectors must be equal:

$$\bar{n} \times \bar{E}_a|_s = \bar{n} \times \bar{E}_s|_s; \quad \bar{n} \times \bar{H}_a|_s = \bar{n} \times \bar{H}_s|_s, \tag{I.60}$$

where subscripts a and s denote vectors relating to the filler and matrix, respectively.

If the electric field is time independent, and no currents are present ($\bar{j} = 0$), the main system of the electromagnetic field equations is divided into two completely independent systems: the electrostatic

$$\text{rot}\,\bar{E} = 0; \quad \text{div}\,\bar{D} = \rho; \quad \bar{D} = \varepsilon\bar{E}; \tag{I.61}$$

and the magnetostatic equations

$$\text{rot}\,\bar{H} = 0; \quad \text{div}\,\bar{B} = 0; \quad \bar{B} = \mu\bar{H}. \tag{I.62}$$

If the electromagnetic field vectors are determined, it is easy to find the values of the permeability and dielectric constants, as well as those of other parameters of the medium.

Bibliography

1. Van Fo Fy, G.A., V.V. Klyavlin, and V.P. Gordienko. Issledovanie raspredeleniya volokon v orientirovannykh stekloplastikakh (Study of Fiber Distribution in Oriented GFP). — Mekhanika Polimerov, 2. 1969.
2. Bhagavantam, S. and T. Venkatarayudu. Theory of Groups and its Application to Physical Problems. Waltair (India), Andhra University. 1948.
3. Kittel, Ch. Introduction to Solid-State Physics. New York, J. Wiley. 1955.
4. Lur'e, A.I. Prostranstvennye zadachi teorii uprugosti (Spatial Problems of Elastic Theory). Moskva, GITTL. 1955.
5. Van Fo Fy, G.A. and V.I. Ozerov. Vyazkouprugie deformatsii nekotorykh termoreaktivnykh polimerov (Viscoelastic Deformations of Some Thermoreactive Polymers). — Prikladnaya Mekhanika, 1 : 8. 1953.
6. Tobolsky, A.Y. Properties and Structure of Polymers. New York, Wiley. 1960.
7. Rabotnov, Yu. N. Ravnovesie uprugoi sredy s posledstviem (Balance of Elastic Medium with Aftereffect). — PMM, **12** : 1. 1948.
8. Bateman, H. Higher Transcendental Functions, compiled by A. Erdēlyi et al. New York, McGraw-Hill. 1953—55.
9. Rozovskii, M.I. O nekotorykh osobennostyakh uprugo-nasledstvennykh sred (Some Features of Hereditary Elastic Media). — Izvestiya AN SSSR, OTN, Mekhanika i Mashinostroenie, **2**. 1961.
10. Rabotnov, Yu. N. Polzuchest' elementov konstruktsii (Creep in Construction Elements). Moskva, Nauka. 1966.

11. Rozovskii, M.I. Ob odnom integral'nom uravnenii s singulyarnym yadrom (An Integral Equation with a Singular Kernel). — Ukrainskii Matematicheskii Zhurnal, 14:1. 1962.
12. Rozovskii, M.I. Integro-operatornyi metod nasledstvennoi teorii polzuchesti (The Integral Operator Method in the Hereditary Theory of Creep). — DAN SSSR, 160:4. 1965.
13. Van Fo Fy, G.A. and V.I. Ozerov. K osnovam teorii nelineinoi termovyazkoi uprugosti nekotorykh polimerov (Fundamentals of the Theory on Nonlinear Thermoviscous Elasticity of Some Polymers). — In: Teplovye napryazheniya v elementakh konstruktsii, Kiev, Naukova Dumka. 1969.
14. Rozovskii, M.I. O vliyanii vida konturnogo nagruzheniya na protsess deformirovaniya plastinki s krugovym vklyucheniem pri polzuchesti (The Effect of the Type of Circumferential Stresses on the Deformation of a Plate with Circular Inclusion During Creep). — In: Teoriya plastin i obolochek. Kiev, Naukova Dumka. 1962.
15. Fitzgerald, E. Mechanical Resonance Dispersion in Crystalline Polymers at Audiofrequencies. — J. Chem. Phys., 27:1180. 1957.
16. Van Fo Fy, G.A. Odnorodnye i armirovannye plastiki pri periodicheskikh vozdeistviyakh (Homogeneous and Reinforced Plastics during Periodic Action). — Prikladnaya Mekhanika, 11:8. 1966.
17. Galin, L.A. O deistvii vibratsionnoi nagruzki na polimernye materialy (Action of Vibrational Loads on Polymer Materials). — Izvestiya AN SSSR, Mekhanika, 6. 1965.
18. Gröber, H. and S. Erk. Die Grundgesetze der Wärmeübertragung. 3. völlig neubearb. Aufl. von U. Grigull, Berlin, Springer. 1955.
19. Barrer, R.M. Diffusion in and Through Solids. Cambridge University Press. 1941 (2nd Edition, 1951).
20. Gertsriken, S. and I. Dekhtyar'. Diffuziya v metallakh i splavakh v tverdoi faze (Solid-Phase Diffusion in Metals and Alloys). Moskva, Fizmatgiz. 1960.
21. Ch'iang Hsüeh-sên. Fizicheskaya mekhanika (Physical Mechanics). Moskva, Mir. 1965.
22. Atlas neitronnykh effektivnykh sechenii elementov (Atlas of the Effective Neutron Cross Sections of the Elements). Moskva, Izdatel'stvo AN SSSR. 1955.
23. Vlasov, A.A. Makroskopicheskaya elektrodinamika (Macroscopic Electrodynamics). Moskva, GITTL. 1955.
24. Lewin, L. Advanced Theory of Waveguides. London, Published for Wireless Engineer by Iliffe. 1951.
25. Kisel', B.A. Stekloplastiki (Glass-Fiber Reinforced Plastics). Moskva, Goskhimizdat. 1961.
26. Houwink, R. and A.T. Staverman (editors). Chemie und Technologie der Kunststoffe. 4 verb. und erweiterte Aufl., Leipzig. Geest und Portig. 1962—63.

Chapter II

THE INTERNAL STRESS FIELD AND THE MODULUS OF ELASTICITY OF COMPOSITE FIBERS

We shall now consider a composite formed by a strand of straightened elastic fibers and a matrix. The composite is acted on by an external field of force. To study the optimum volume content of filler in the composite, the effect of the type of fiber packing in the material and of the properties of the initial components on the internal stress field in the microstructure, the changes in the field as a function of the conditions at the fiber-matrix interface, cleavage fracture of the material, and other problems, we use a reinforced body model. The models have a discrete structure, and reflect more or less accurately the contours of the filler elements and their mutual arrangement. To simplify our task we shall neglect the effect of bending of the fibers, the inhomogeneous conditions at the interfacial area, and the edge effect for short fibers. We shall assume that the external field of force changes only slightly over the given structural cell, and that this change can be neglected.

To simplify an analysis of the internal stress field, the general solution of the problem is separated into partial solutions for the components of the field of force applied.

1. The problem of longitudinal shear

If the reinforced body has a simple hexagonal or tetragonal microstructure, the elementary volume is a prism of unit length, with a base which is either a rhombohedron or a square. Each cell contains only one fiber. We shall assume that the given volume is subjected to nondilatational strain in two mutually perpendicular planes, parallel to the orientation of the fibers, and that the average shearing stresses are given (Figure II. 1). If we direct the axes x_2, x_3 of the Cartesian coordinates perpendicular to the fiber orientation, we find the coordinates of the center of the mn-th fiber

$$x_2 + ix_3 = \omega_1 (m + ne^{i\alpha}),$$

where $\alpha = \frac{\pi}{3}$ or $\frac{\pi}{2}$, $m, n = 0, \pm 1, \ldots, \pm\infty$.

For nondilatational strain in the given planes, the three balance equations of the elementary volume of the continuum (I. 10) are reduced to

$$\frac{\partial \sigma_{12}}{\partial x_2} + \frac{\partial \sigma_{13}}{\partial x_3} = 0; \quad \frac{\partial \sigma_{12}}{\partial x_1} = \frac{\partial \sigma_{13}}{\partial x_1} = 0. \qquad \text{(II. 1)}$$

For this reason the angles of slide γ_{12} and γ_{13} are determined from (see (I. 13))

$$2\varepsilon_{12} = \gamma_{12} = \frac{\partial u_1}{\partial x_2};\ 2\varepsilon_{13} = \gamma_{13} = \frac{\partial u_1}{\partial x_3}. \tag{II. 2}$$

It follows from the above equations and Hooke's law (I. 16) that u_1 satisfies a two-dimensional Laplace equation. Therefore, the displacement function is a holomorphic function of complex variables $z = x_2 + \imath x_3$ and $\bar{z} = x_2 - ix_3$, or

$$u_1 = \varphi(z) + \overline{\varphi(z)}, \tag{II. 3}$$

where the bar on the top denotes an adjoint function. The shearing stresses are determined directly by the $\varphi(z)$ function introduced, using

$$\sigma_{12} - i\sigma_{13} = G\left(\frac{\partial u_1}{\partial x_2} - \imath\frac{\partial u_1}{\partial x_3}\right) = 2G\varphi'(z) = 2G\Phi(z). \tag{II. 4}$$

Here the prime denotes the derivative with reference to the above argument. Equations (II. 1)—(II. 4) refer to both filler and matrix, considered as a continuum. For this reason no subscripts are given for the magnitudes introduced.

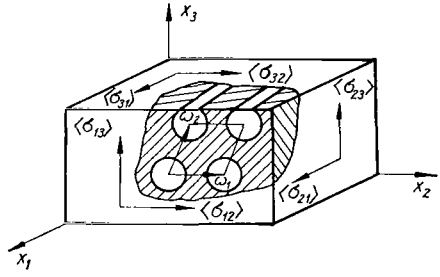

FIGURE II. 1. Elementary volume under the action of average shearing stresses.

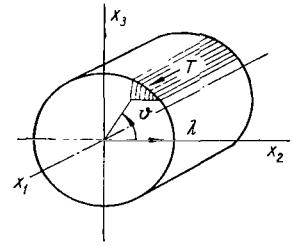

FIGURE II. 2. Fiber element under the action of shearing stresses.

The type of (II. 3) is determined with allowance for the boundary conditions on the filler-matrix interface, the interaction of the isolated volume of the reinforced medium with the surrounding space, and the mean shearing stresses or mean displacements. For determinacy, we assume ideal contact, when the displacements and stresses on the interfacial area s between the matrix and filler are equal. Deviations from these conditions are local in character and can be considered to be disturbances.

Because of the balance of the elementary prism (Figure II. 2), the shearing stresses on contour T are expressed in terms of the function introduced as

$$T = \sigma_{12}\cos\vartheta + \sigma_{13}\sin\vartheta = -iG\frac{d}{ds}[\varphi(z) - \overline{\varphi(z)}].$$

The boundary conditions on the lateral surface of each fiber are reduced to a system of functional equations, if we allow for the above expressions /1/

$$\varphi_a(\tau) + \overline{\varphi_a(\tau)} = \varphi_s(\tau) + \overline{\varphi_s(\tau)};$$
$$G_a[\varphi_a(\tau) - \overline{\varphi_a(\tau)}] = G_s[\varphi_s(\tau) - \overline{\varphi_s(\tau)}]. \qquad \text{(II. 5)}$$

We use here a local system of polar coordinates with the center on the fiber axis. According to this, the points of the contour are expressed as

$$z = \tau = \lambda e^{i\theta},$$

where $\lambda = \frac{2r_0}{\omega_1}$ is the dimensionless fiber radius. Because the stressed state along the fiber orientation is homogeneous, equations (II. 5) are satisfied over the whole fiber length.

The conditions are given which determine the correlation between the stresses or displacements distributed and averaged over the area of a single cell. For the stresses, the conditions are written as

$$\langle\sigma_{12}\rangle - i\langle\sigma_{13}\rangle = F^{-1}\iint_F dF(\sigma_{12} - i\sigma_{13}), \qquad \text{(II. 6)}$$

where the left-hand side contains known magnitudes; F is the area of the cell determined for $b = 1$ and $\alpha = \frac{\pi}{3}$ or $\frac{\pi}{2}$. Formula (II. 6) is transformed with the help of Green's theorem to the contour integrals of the unknown displacement function. The final result is

$$\langle\sigma_{12}\rangle - i\langle\sigma_{13}\rangle = \frac{iG_s}{F}\oint_{L_s}\varphi_s(z)\,d\bar{z} + \frac{iG_a}{F}\oint_{L_a}\varphi_a(z)\,d\bar{z}. \qquad \text{(II. 7)}$$

Here L_s and L_a are the contours bounding the area occupied by filler and matrix within a single cell. To allow for the interaction of the isolated volume with the surrounding space, we assume that the structure of the reinforced medium is obtained by a doubly periodic continuation of the given cell in the plane perpendicular to the fiber orientation. It is assumed that interaction occurs if the conditions of double periodicity of the stressed state, and aperiodicity (quasiperiodicity) of longitudinal displacement in the reinforced medium with periods ω_1 and $\omega_2 = \omega_1 e^{i\alpha}$, equal to the sides of the individual cell, are observed. The first condition requires that

$$(\sigma_{12} - i\sigma_{13})|_z = (\sigma_{12} - i\sigma_{13})|_{z+\omega_j} \quad (j = 1, 2). \qquad \text{(II. 8)}$$

The second condition will be automatically satisfied in this case, as will be shown below. Evidently (II. 8) holds if

$$\varphi_s'(z) = \Phi_s(z) = \Phi_s(z + \omega_j), \qquad \text{(II. 9)}$$

that is, $\Phi_s(z)$ must be an elliptic function of z /1, 2/.

The harmonic displacement function u_a with a regular period is expressed in terms of function $\varphi_a(z)$ written as a series with odd powers of z:

$$\varphi_a(z) = \sum_{k=0}^{\infty} a_{2k} \frac{z^{2k+1}}{2k+1}; \quad a_{2k} = a'_{2k} + ia''_{2k}. \tag{II. 10}$$

A doubly periodic function $\Phi_s(z)$ is built as a series according to the elliptic Weierstrass function $\wp(z)$:

$$\wp(z) = z^{-2} + \sum_{m,\,n}{}' [(z - P)^{-2} - P^{-2}]. \tag{II. 11}$$

The prime denotes that the items are left out for $m = n = 0$. From (I. 5)

$$P = m\omega_1 + n\omega_2 \quad (m, n = 0, \pm 1, \ldots, \pm\infty).$$

The required expansion is found as

$$\Phi_s(z) = C_0 + \sum_{k=0}^{\infty} \frac{\lambda^{2k+2} C_{2k+2}}{(2k+1)!} \wp^{(2k)}(z), \tag{II. 12}$$

where $\wp^{(2k)}(z)$ is the $2k$-th derivative of $\wp(z)$.

Direct integration of (II. 12) gives

$$\varphi_s(z) = C_0 z - C_2 \lambda^2 \zeta(z) + \sum_{k=1}^{\infty} C_{2k+2} \frac{\lambda^{2k+2} \wp^{(2k-1)}(z)}{(2k+1)!}. \tag{II. 13}$$

Here the Weierstrass zeta function is introduced

$$\zeta(z) = -\int dz\, \wp(z) = z^{-1} + \sum_{m,\,n}{}' [(z - P)^{-1} + P^{-1} + zP^{-2}]. \tag{II. 14}$$

The conditions of the aperiodicity of the displacement function are directly fulfilled. It is clear that the increment of $\varphi_s(z)$ on one of the lattice constants is

$$\varphi_s(z + \omega_j) - \varphi_s(z) = \omega_j C_0 - C_2 \lambda^2 \delta_j \quad (j = 1, 2), \tag{II. 15}$$

where

$$\delta_j = \zeta(z + \omega_j) - \zeta(z).$$

For the hexagonal and tetragonal lattices, we can put

$$\delta_1 = \frac{\pi}{\omega_1 \sin\alpha}; \quad \delta_2 = \frac{\pi e^{-i\alpha}}{\omega_1 \sin\alpha}. \tag{II. 16}$$

The coefficients of expansion of (II. 10) and (II. 12) are expressed in terms of the given mean stresses $\langle\sigma_{12}\rangle$ and $\langle\sigma_{13}\rangle$ by equations derived from (II. 5) and (II. 7).

The results of the calculation of the internal elastic shearing stresses as applied to the microstructure of some composites are shown by the curves in Figures II. 3 and II. 4. Figure II. 3 relates to a material with a filler of aluminoborosilicate fibers and a matrix of EMA. The curves for the metallic (steel) fibers-polymer matrix composites are shown in Figure II. 4. Figures II. 3, a, and b and II. 4, a and b show the distribution of the shearing stress concentration factors k_{12}, which characterize the

ratio of the true stress at the given point to the average stress $\langle\sigma_{12}\rangle$ ($\langle\sigma_{13}\rangle = 0$) acting in plane $x_1 = \text{const}$. Figures II. 3, c and d and II. 4, c and d show the concentration factors $k'_{13} = \frac{\sigma_{13}}{\langle\sigma_{12}\rangle}$ in the same plane. The continuous curves were plotted for the hexagonal structure and the dotted curves for the tetragonal structure. Figures II. 3, a and c and II. 4, a and c show data for materials with a relative volume content of the filler ξ of 0.636 for the tetragonal and 0.734 for the hexagonal structures, while in Figures II. 3, b and d and II. 4, b and d the curves were plotted for reinforced media, with $\xi = 0.283$ and $\xi = 0.326$ for the tetragonal and hexagonal structures, respectively. Curves c and d (Figures II. 3 and II. 4) characterize the distribution of the shearing stresses acting along the radius, and form an angle of $\vartheta = 0$ with the abscissa. The stress concentration factors are plotted on the ordinate.

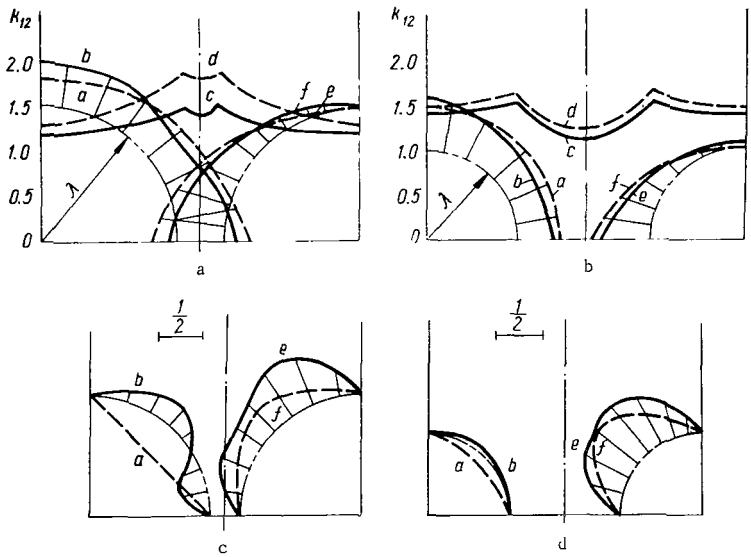

FIGURE II. 3. Distribution of stresses σ_{12} and σ'_{13} in the microstructure of glass-fiber reinforced plastics.

These curves illustrate the nonuniform distribution of the shearing stresses in the microstructure. The highest stress concentration is on the fiber-matrix interface. The stress distribution on the boundary of the medium at various points of the contour is characterized by curves a and b (in the fiber) and e and f (in the matrix) in Figures II. 3 and II. 4. The factors k_{12} and k'_{13} are read off for each radial point of the fiber circumference. In longitudinal shear the fiber is in an almost homogeneous stressed state, as seen in Figures II. 3 and II. 4, a and b; a certain stress gradient is found near the fiber boundary only.

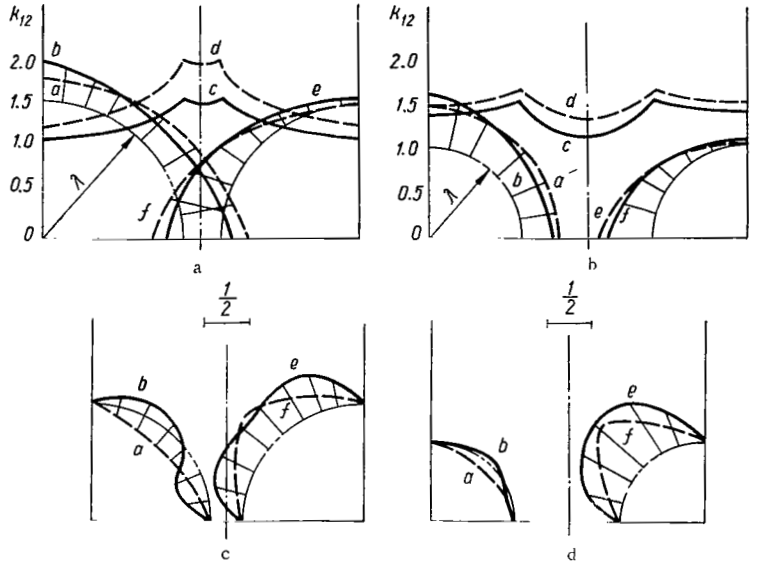

FIGURE II. 4. Distribution of stresses σ_{12} and σ'_{13} in the microstructure of solid metal-fiber reinforced plastics.

Shearing strain is determined at each point of the medium, according to (II. 2). The displacement in nondilatational strain is:

$$u_1 = \gamma_{12}x_2 - \gamma_{13}x_3 = \frac{z+\bar{z}}{2}\gamma_{12} - i\frac{z-\bar{z}}{2}\gamma_{13}.$$

The increment of elastic displacements in adjacent cells in nondilatational strain of a reinforced body is

$$u_1(z + \omega_j) - u_1(z) = \frac{\omega_j + \bar{\omega}_j}{2}\langle\gamma_{12}\rangle - i\frac{\omega_j - \bar{\omega}_j}{2}\langle\gamma_{13}\rangle =$$

$$= \omega_j C_0 + \omega_j \bar{C}_0 - C_2\lambda^2\delta_j - \bar{C}_2\lambda^2\bar{\delta}_j. \qquad \text{(II. 17)}$$

Here the last expression is derived from (II. 3) and (II. 15). By equating $j = 1, 2$, we easily see that

$$\langle\gamma_{12}\rangle = \frac{\langle\sigma_{12}\rangle}{G_{12}} = C_0 + \bar{C}_0 + \xi(C_2 + \bar{C}_2);$$

$$\langle\gamma_{13}\rangle = \frac{\langle\sigma_{13}\rangle}{G_{13}} = i(C_0 - \bar{C}_0) + i\xi(C_2 - \bar{C}_2). \qquad \text{(II. 18)}$$

These equations make it possible to determine qualitative relationships between the shear moduli of the medium G_{12} and G_{13} and the properties of the components

$$\frac{1}{G_{12}} = \frac{\eta + (1+\xi)G_s/G_a}{1 + \xi + \eta G_s/G_a} \cdot \frac{1}{G_\varepsilon} - \frac{2\xi(1 - G_s/G_a)}{1 + \xi + \eta G_s/G_a} \cdot \frac{1}{G_s}\sum_{k=0}^{\infty} C'_{2k+2}\lambda^{2k+2}\alpha_{0,k};$$

$$\frac{1}{G_{13}} = \frac{\eta + (1+\xi)\,G_s/G_a}{1+\xi+\eta G_s/G_a} \cdot \frac{1}{G_s} + \frac{\gamma\xi\,(1-G_s/G_a)}{1+\xi+\gamma_1 G_s/G_a} \cdot \frac{1}{G_s} \sum_{k=0}^{\infty} C''_{2k+2}\,\zeta^{2k+2}\alpha_{0,k}. \qquad \text{(II. 19)}$$

Here $\alpha_{0,k}$ is the coefficient for the zero power of z when $\delta^{(2k)}(z)$ is expanded into a Laurent series:

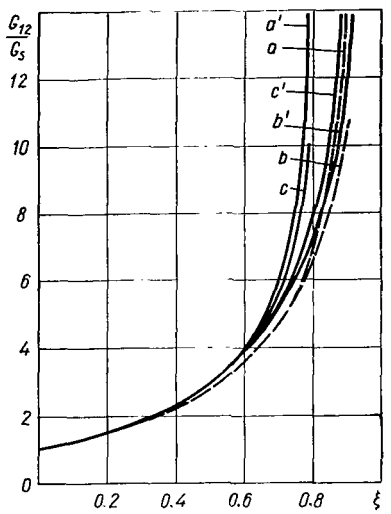

FIGURE II. 5. Dependence of the longitudinal shear modulus on the volume content of the filler.

$$C_{2k} = \frac{\langle \sigma_{12} \rangle}{2G_s} C'_{2k} + i \frac{\langle \sigma_{13} \rangle}{2G_s} C''_{2k}.$$

It follows for both the tetragonal and hexagonal systems that

$$G_{12} = G_{13}.$$

Curves a and b in Figure II. 5 characterize the change in $\frac{G_{12}}{G_s}$ as a function of ξ for the given GFP for hexagonal and tetragonal fiber arrangements; curves c' and a' are plotted for the metallic fibers. Curves b (glass fibers) and b' (metal fibers) are plotted from the results obtained from the approximate formula

$$G_{12} = G_{13} \approx G_s \frac{1+\xi+\gamma_1 G_s/G_a}{\gamma_1 + (1+\xi) G_s/G_a}. \qquad \text{(II. 20)}$$

By comparing the data it can be seen that according to (II. 20) the shear modulus can be determined to within ± 5% if the amount of fibers is low. For a higher fiber concentration the discrepancies are as high as 15—17%.

Besides solid fibers, hollow glass fibers can be used. The problem of studying the stressed-strained state of a medium reinforced by hollow fibers is in this case one of finding functions $\varphi_a(z)$ and $\varphi_s(z)$ from the boundary conditions (II. 5) and the absence of stresses in a hollow of radius ε /3/

$$\varphi_a(\tau_0) - \overline{\varphi_a(\tau_0)} = 0, \qquad \text{(II. 21)}$$

where $\tau_0 = \varepsilon e^{i\vartheta}$, and also from the given mean stresses (II. 7) (in this case contour L_a also includes the inner fiber boundary /4/). Function $\varphi_a(z)$ is written in a Laurent's series

$$\varphi_a(z) = \sum_k a_{2k} \frac{z^{2k+1}}{2k+1}. \qquad \text{(II. 22)}$$

Here and later, in the symbol for the sum we will show only the index according to which the summation is carried out if the index changes from $-\infty$ to $+\infty$. The function is constructed according to expansion (II. 13).

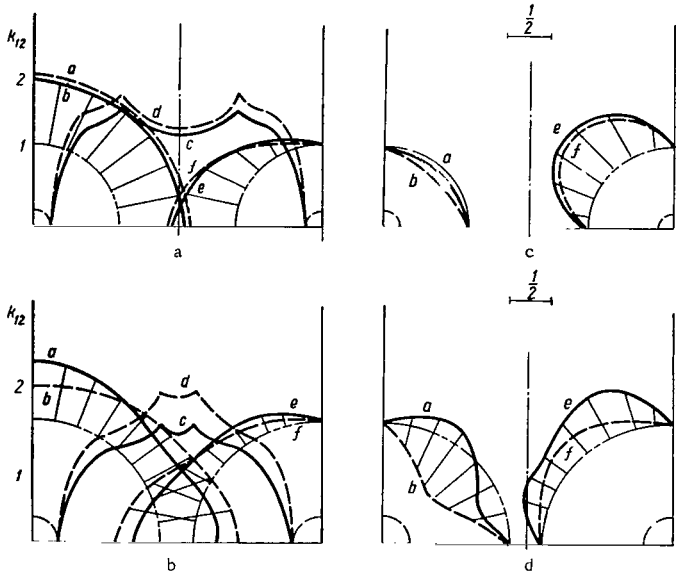

FIGURE II. 6. Concentration factors of stresses σ_{12} (a, b) and σ'_{13} (c, d) in the microstructure of hollow glass-fiber reinforced plastics ($q = 0.2$).

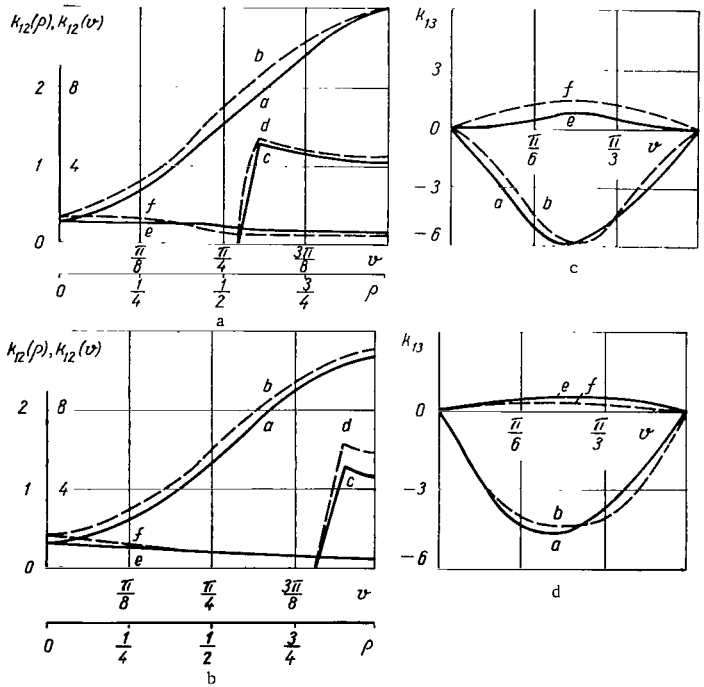

FIGURE II. 7. Concentration factors of stresses σ_{12} (a, b) and σ'_{13} (c, d) in the microstructure of hollow glass-fiber reinforced plastics.

The stress distribution in the structure of GFP with hollow fibers in the case $\langle \sigma_{13} \rangle = 0$ is illustrated in Figures II. 6 and II. 7, and the stress distribution in metal-fiber reinforced plastics is shown in Figure II. 8 for the following filler parameters: Figure II. 6, a, c— $\lambda = 0.6$, $q = 0.2$; Figure II. 6, b, d— $\lambda = 0.9$, $q = 0.2$; Figure II. 7, a, c— $\lambda = 0.6$, $q = 0.9$; Figure II. 7, b, d— $\lambda = 0.9$, $q = 0.9$; Figure II. 8, a, c— $\lambda = 0.6$, $q = 0.9$; Figure II. 8, b, d— $\lambda = 0.9$, $q = 0.9$. Curves a, b, and e, f in Figures II. 6, a, b; II. 7, a, b; and II. 8, a, b characterize the distribution of k_{12a} and k_{12s} for fiber matrix contour. The distribution curves of k'_{13a} and k'_{13s} for $\rho = \lambda$ are characterized by curves a, b and e, f (Figure 11.6, c, d; Figure II. 7, c, d and Figure II. 8, c, d).

If the hollow has a small radius and the fiber a low modulus (curves a, b in Figure II. 6, a, c), the stresses in the fiber are almost constant and the maximum stresses on the boundary are obtained for $\vartheta = 0$ (curves a, b, c and d in Figure II. 6, a, b). With increase in the volume content of filler, if the radius of the hollow remains the same, the stresses in the structure are redistributed. For fibers with comparatively large hollows (Figures II. 7, a, b) the stresses in the fiber change considerably (curves a, b). In this case the stresses change almost according to the parabolic law, which also holds during action on the cross sections of thin-walled tubes.

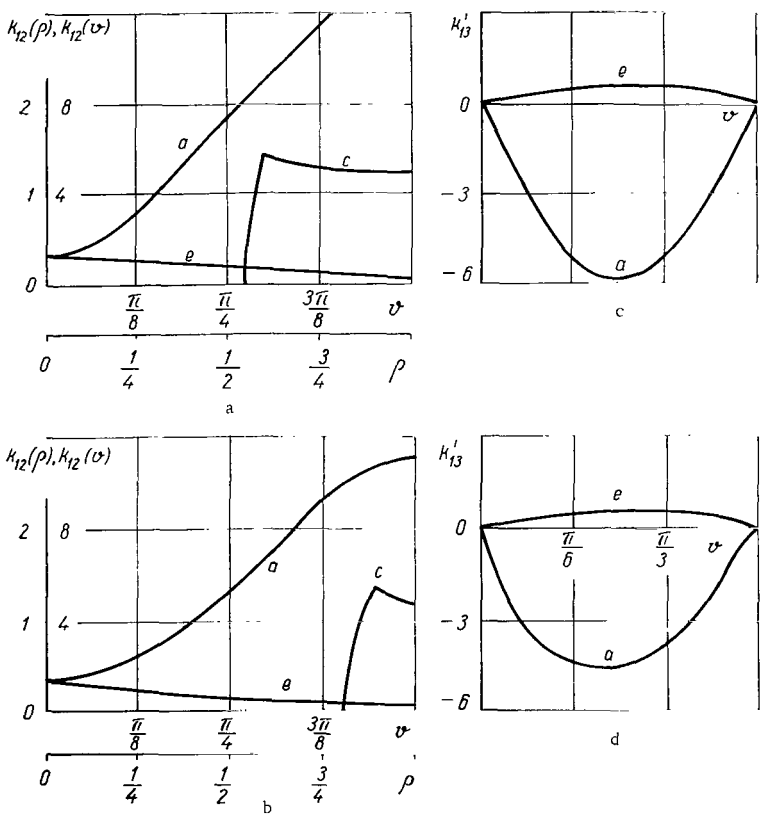

FIGURE II. 8. Concentration factors of stresses σ_{12} (a, b) and σ'_{13} (c, d) in the microstructure of hollow metal-fiber reinforced plastics ($q = 0.9$).

For comparison, in Figure II. 8 we show the curves of the structural stress concentration factors in MFP.

The equations for determining the moduli of elasticity are obtained in analogy to (II. 19)

$$\frac{1}{G_{12}} = \frac{\eta_1(1-q^2)+(1+\xi)(1+q^2)\,G_s/G_a}{(1+\xi)(1-q^2)+\eta(1+q^2)\,G_s/G_a}\cdot\frac{1}{G_s} -$$

$$-2\xi\frac{1-q^2-(1+q^2)\,G_s/G_a}{(1+\xi)(1-q^2)+\eta(1+q^2)\,G_s/G_a}\cdot\frac{1}{G_s}\sum_{k=1}^{\infty}C'_{2k+2}\lambda^{2k+2}a_{0,k};$$

$$\frac{1}{G_{13}} = \frac{\eta_1(1-q^2)+(1+\xi)(1+q^2)\,G_s/G_a}{(1+\xi)(1-q^2)+\eta(1+q^2)\,G_s/G_a}\cdot\frac{1}{G_s}+ \qquad \text{(II. 23)}$$

$$+2\xi\frac{1-q^2-(1+q^2)\,G_s/G_a}{(1+\xi)(1-q^2)+\eta_1(1+q^2)\,G_s/G_a}\cdot\frac{1}{G_s}\sum_{k=1}^{\infty}C''_{2k+2}\lambda^{2k+2}a_{0,k}.$$

For approximate calculations to within ± 5%, it is suggested that only the first term in (II. 23) be used when $\xi < 0.7$. The change in $\frac{G_{12}}{G_s}$ in GFP as a function of the volume content of the fibers ξ at various values of q are shown in Figure II. 9. Letters a, b, c, d, e and f denote the curves for $q = 0.1,\ 0.4,\ 0.6,\ 0.7,\ 0.8,$ and 0.9, respectively.

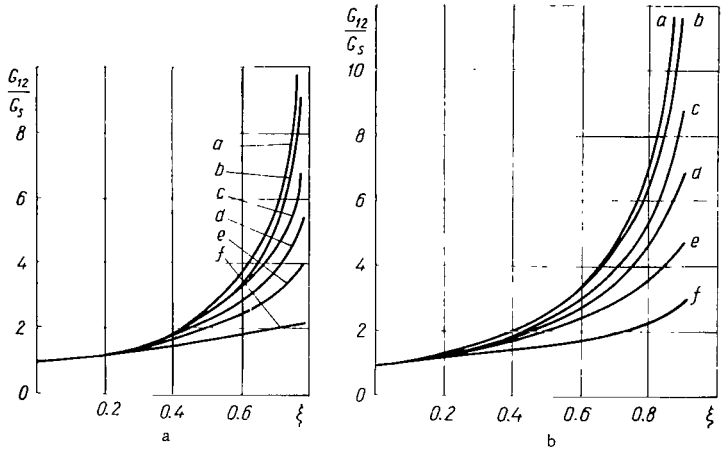

FIGURE II. 9. Dependence of the longitudinal shear modulus on the volume content of filler for different inner fiber radii:

a — tetragonal structure; b — hexagonal structure.

According to the above data, when $\xi > 0.7$ and at equal volume concentrations of fibers, with decrease in q we note that the rigidity in materials with a tetragonal structure is higher than in materials with a hexagonal arrangement of the fibers. This is explained by the second term in (II. 23) characterizing mutual fiber approach and other factors.

2. The optimum volume content of components in fiber composites in shear

In practice, the optimum volume content of the components is determined by analyzing data of breaking tests on linearly reinforced GFP with different fiber levels. According to such data /5/, the highest strengths in these glass fibers is obtained when $\xi = 0.6-0.7$. A further increase in the filler content leads to a decrease in the breaking strength of the glass fiber. Thus, at a low volume content of the fibers the ultimate strength is proportional to the filler level, but when $\xi > 0.7$, the interaction, because of the insufficient volume of the matrix, between the nonuniformly tensioned fibers becomes weaker so that the strength decreases. Redistribution between the fibers in tension is achieved to an appreciable extent by means of the matrix, which is under almost nondilatational strain. For this reason it is interesting to study the changes in the shearing stresses in the matrix subjected to shear as a function of ξ. Maximum stresses arise on the fiber-matrix interface and are determined by the sum of stresses:

$$\sigma_{12} = \frac{2\langle\sigma_{12}\rangle}{1+\xi+(G_s/G_a)} + \sigma'_{12},$$

where the first term indicates the stress change with increasing ξ. When $\xi \to 1$, the first term decreases to $\langle\sigma_{12}\rangle$; the g and k curves in Figure II. 10 characterize this change in GFP with tetragonal and hexagonal structures. The second term σ'_{12} characterizes the effect of the interaction of fibers when they approach one another. Curves e and f in Figure II. 10 show the increase in shearing stresses for materials with hexagonal and tetragonal structures.

The change in the coefficient of maximum stress concentrations in two microstructures of GFP is illustrated by curves c and d. With increase in ξ the maximum stresses decrease to a certain limit, but when the fibers approach one another their interaction increases, which then leads to a stress increase. The curves characterizing the change in k_{12} have a distinct minimum, which is very dependent on the microstructure. A similar phenomenon is observed for a polymer-metal composite (curves a, b in Figure II. 10).

According to published data, the lowest structural stresses are attained when $\xi \leq 0.6$ for the hexagonal microstructure. These ξ values may in a certain sense be considered as the optimum volume content of filler in longitudinal shear /6/.

The disturbing effect of the stressed state on the fiber boundaries is very dependent on the matrix rigidity. This is confirmed by the character of the curves (Figure II. 11) showing the change in k_{12} as a function of for hollow GFP. The fibers are placed at the points of a triangular (continuous curves) or square (dashed curves) lattice. The curves a, b, c, d, e, f, g, h and k are for q values of 0.1, 0.2, 0.3, 0.4, 0.5, 0.6, 0.7, 0.8, and 0.9 respectively.

With increase in the hollow dimensions in the fiber, the minimum stresses in longitudinal shear arise at a value of ξ which is higher than in materials with continuous fibers, though the stress concentration

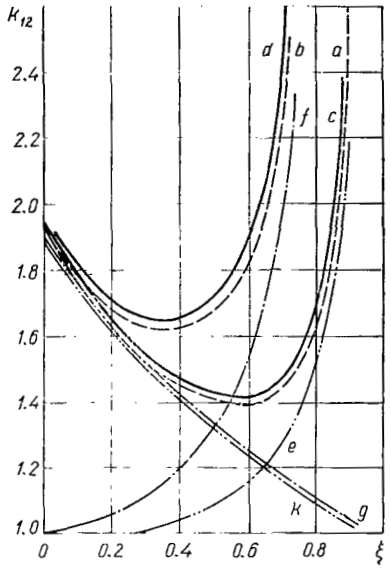

FIGURE II. 10. Dependence of the maximum stress concentration factor during longitudinal shear on the amount of filler in the case of solid fibers.

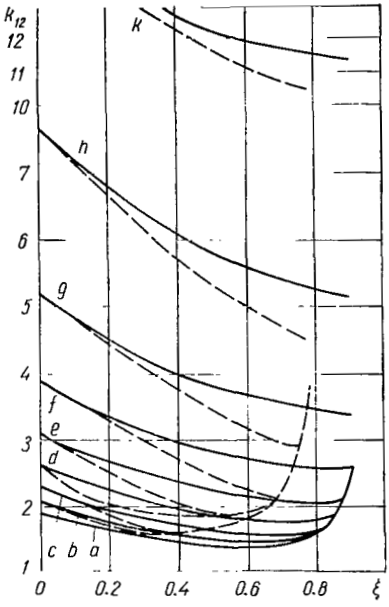

FIGURE II. 11. Dependence of the maximum stress concentration factor during longitudinal shear on the amount of filler at various inner radii of the hollow fibers.

factor increases several times. The values of K during shear as a function of the dimensions of the hollows of the fibers and the logarithm of the modulus of shear ratio is shown in Figure II. 12. The data refer to materials with hexagonal (continuous curves) and tetragonal (dashed curves) microstructures. The curves in Figure II. 12 refer to the range from $q = 0$ to $q = 0.9$.

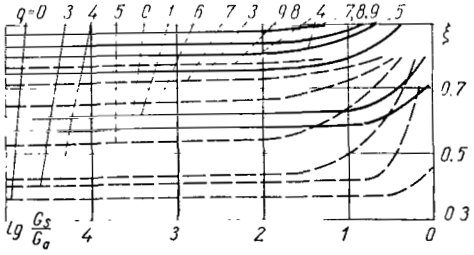

FIGURE II. 12. Dependence of the optimum amount of filler on $\frac{G_s}{G_a}$ in longitudinal shear at various inner radii of the hollow fibers.

These data cover almost all the interesting composite materials. For solid fibers tetragonally arranged a change in $\frac{G_s}{G_a}$ of three orders of magnitude leads to an increase in the optimum volume of filler from 0.25 to 0.38, and for hexagonally arranged to an increase from 0.56 to 0.8. Such an increase is mainly attained when changing $\frac{G_s}{G_a}$ by one order of magnitude.

3. Effect of the type of microstructure on the properties of the composite material

The most general microstructure of an elementary volume of a reinforced medium contains an arbitrary finite number of fibers of various diameters /7/. The mutual arrangement and the dimensions of the fiber cross section may be selected when examining a real microstructure (Figure I. 1).

Let the given volume be subjected to longitudinal shear, and let it contain p hollow fibers of various diameters. We designate by s_k and s_k' the outer and inner surfaces of the k-th fibers ($k = 1, 2, \ldots, p$), their center has the coordinate a_k; λ_k and ε_k denote the outer and inner dimensionless fiber radii.

To allow for the interaction of the isolated volume with the environment, we shall assume that the arrangement of the fibers in the whole space is obtained by a double periodic prolongation of the fundamental cell. The holomorphic function $\Phi_s(z)$ for the given volume is selected starting from the general representation of an elliptic function, according to which

$$\Phi_s(z) = C_0 - \sum_{k=1}^{p}\sum_{s=1}^{\infty} \frac{(-1)^s}{(s-1)!} C_{k,s}\zeta^{(s-1)}(z - a_k). \qquad \text{(II. 24)}$$

To satisfy the periodicity condition (II. 9), we require that

$$\sum_{k=1}^{p} C_{k,1} = 0. \qquad \text{(II. 25)}$$

Direct integration yields the displacement function on shear

$$\varphi_s(z) = C_0 z - \sum_{k=1}^{n}\sum_{s=2}^{\infty} \frac{(-1)^s}{(s-1)!} C_{k,s}\zeta^{(s-2)}(z - a_k) + \sum_{k=1}^{n} C_{k,1} \ln \sigma(z - a_k), \qquad \text{(II. 26)}$$

where $\sigma(z)$ is the Weierstrass sigma function /8/.

Solving the problem of the shear of the filler elements is reduced to the setting up of p holomorphic functions of type

$$\varphi_{a,k}(z) = \sum_{m} a_{m,k}(z - a_k)^m \quad (k = 1, 2, \ldots, p). \qquad \text{(II. 27)}$$

When the contact between fibers and matrix is ideal, p equations of type (II. 5) are satisfied. After subtracting one from another, we obtain

$$(1 + G_a/G_s)\varphi_{a,k}(\tau_k) + (1 - G_a/G_s)\overline{\varphi_{a,k}(\tau_k)}|_{s_k} = 2\varphi_s(\tau_k)|_{s_k} \quad (k = 1, 2, \ldots p), \qquad \text{(II. 28)}$$

where

$$\tau_k = z - a_k = \lambda_k e^{i\theta_k}.$$

The second system of equations follows from the given system when substituting into it adjoint complex functions. On the internal surfaces of the fibers, p conditions of type (II. 21) must be satisfied. The mean stresses must be given as

$$\langle\sigma_{12}\rangle - i\langle\sigma_{13}\rangle = \frac{iG_s}{F}\oint_{L_s}\varphi_s(z)\,d\bar{z} + \frac{iG_a}{F}\sum_{k=1}^{p}\oint_{L_k}\varphi_{a,k}(z)\,d\bar{z}. \qquad \text{(II. 29)}$$

The symbols are the same as above. The conditions of displacement aperiodicity are, as it is easy to see, transformed into

$$\varphi_s(z+\omega_j) - \varphi_s(z) = \omega_j C_0 - \delta_j\sum_{k=1}^{p} C_{k,2} - \delta_j\sum_{k=1}^{p} C_{k,1}a_k. \qquad \text{(II. 30)}$$

Constants C_k and $a_{m,k}$ are fixed when satisfying boundary conditions (II. 28).

Hooke's law for nondilatational strain and general structural type of a reinforced body can be written as

$$\begin{aligned}\langle\gamma_{31}\rangle &= X_{44}\langle\sigma_{31}\rangle + X_{45}\langle\sigma_{21}\rangle;\\ \langle\gamma_{21}\rangle &= X_{45}\langle\sigma_{31}\rangle + X_{55}\langle\sigma_{21}\rangle.\end{aligned} \qquad \text{(II. 31)}$$

If we use the technical constants, we have to equate

$$X_{44} = \frac{1}{G_{13}};\quad X_{55} = \frac{1}{G_{12}};\quad X_{45} = \frac{\mu_{31,21}}{G_{12}} = \frac{\mu_{12,31}}{G_{13}},$$

where $\mu_{31,21}$ and $\mu_{12,31}$ are termed Chentsov coefficients and characterize the shears in plane x_1x_3 produced by stresses $\langle\sigma_{12}\rangle$, or in plane x_1x_2 produced by $\langle\sigma_{31}\rangle$.

The constants and the properties of components are correlated by a system of equations

$$\begin{aligned}\langle\gamma_{12}\rangle = C_0 + \bar{C}_0 - \frac{\delta_1}{\omega_1}\sum_{k=1}^{p}(C_{k,2} + C_{k,1}a_k) - \frac{\bar{\delta}_1}{\omega_1}\sum_{k=1}^{p}(\bar{C}_{k,2} + \bar{C}_{k,1}\bar{a}_k);\\ \langle\gamma_{12}\rangle\cos\alpha + \langle\gamma_{13}\rangle\sin\alpha = e^{i\alpha}C_0 + e^{-i\alpha}\bar{C}_0 -\\ -\frac{\delta_1}{\omega_1 b}\sum_{k=1}^{p}(C_{k,2} + C_{k,1}a_k) - \frac{\bar{\delta}_2}{\omega_1 b}\sum_{k=1}^{p}(C_{k,2} + \bar{C}_{k,1}\bar{a}_k).\end{aligned} \qquad \text{(II. 32)}$$

According to these formulas, by successively equating $\langle\sigma_{12}\rangle = 1$, and $\langle\sigma_{13}\rangle = 0$; and $\langle\sigma_{12}\rangle = 0$, and $\langle\sigma_{13}\rangle = 1$, we obtain values of the angles of slide and of the corresponding constants in (II. 31).

If the centers are placed at the points of a rectangular lattice $b \neq 1$ and $\alpha = \frac{\pi}{2}$, the structure is symmetrical about three coordinate planes, C_n are real numbers, and $X_{45} = 0$. Such a structure is termed orthorhombic (section 1). The number of elastic constants in longitudinal shear remains unchanged for the orthorhombic structure when $b = 1$, $\alpha \neq \frac{\pi}{2}$ or $\frac{\pi}{3}$. When

$b = 1$ and $\alpha = \frac{\pi}{2}$, we have a tetragonal structure, for which $X_{44} = X_{55}$; $X_{45} = 0$. These equations also apply to hexagonal structures.

4. Longitudinal shear of multicomponent materials

We shall consider the shear of bodies reinforced by types of fibers of various diameters. It is assumed that the elementary volume contains $p (p \geqslant l)$ fibers, and at least one of each kind. Such materials are prepared from fibers obtained from metals, glass, polymers, or various compounds and a single matrix.

The stressed-strained state of the matrix is determined from (II. 24) observing (II. 25). The stressed-strained state of the filler is determined from (II. 27). The introduced functions must satisfy p boundary conditions of type

$$(1 + G_k/G_s)\,\varphi_k(\tau_k) + (1 - G_k/G_s)\,\overline{\varphi_k(\tau_k)} = 2\varphi_s(\tau_k) \quad (k = 1, 2, \ldots, p). \tag{II. 33}$$

The average stresses for the given volume are obtained in analogy to (II. 29):

$$\langle \sigma_{12} \rangle - i \langle \sigma_{13} \rangle = \frac{iG_s}{F} \oint_{L_s} \varphi_s(z)\, d\bar{z} + \frac{i}{F} \sum_{k=1}^{p} G_k \oint_{L_k} \varphi_{a,k}(z)\, d\bar{z}. \tag{II. 34}$$

The equations for determining moduli of shear are formally the same as (II. 32).

If the structure is formed by hexagonal cells, we can obtain shortened formulas for determining the modulus of shear. If we designate by ξ_k the relative volume content of the k-th type of fiber in the cell, and by $\eta = 1 - \sum_{k=1}^{p} \xi_k$ the volume content of the matrix, we obtain the approximate equation for the modulus of shear

$$\frac{G_{13}}{G_s} = \frac{G_{12}}{G_s} \approx \frac{\eta + 2\sum_{k=1}^{p} \dfrac{\xi_k}{1 + G_s/G_k}}{1 - \sum_{k=1}^{p} \dfrac{1 - G_s/G_k}{1 + G_s/G_k}}. \tag{II. 35}$$

At equal volume fractions of the components and low values of $\sum_{k=1}^{p} \xi_k$, this approximate formula becomes more accurate.

For materials reinforced by t types of hollow fibers, the approximate formula for the modulus of shear is obtained analogously to (II. 35)

$$\frac{G_{13}}{G_s} = \frac{G_{12}}{G_s} \approx \frac{\eta + 2\sum_{k=1}^{p} \dfrac{(1 - q_k^2)\,\xi_k}{1 - q_k^2 + (1 + q_k^2)\,G_s/G_k}}{1 - \sum_{k=1}^{p} \xi_k \dfrac{1 - q_k^2 - (1 + q_k^2)\,G_s/G_k}{1 - q_k^2 + (1 + q_k^2)\,G_s/G_k}}. \tag{II. 36}$$

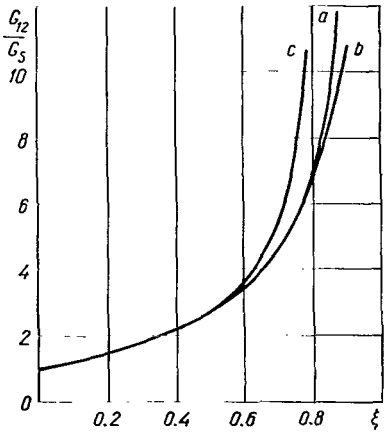

FIGURE II. 13. Dependence of the modulus of longitudinal shear of multicomponent materials on the extent of reinforcement.

Here $q_k = \varepsilon_k/\lambda_k$.

The curves of II. 13 characterize the changes in $\frac{G_{12}}{G_s}$ for GFP which consist of aluminoborosilicate and boron fibers and EMA matrix as a function of the boron (ξ_2) and aluminoborosilicate (ξ_1) levels. Curves a, b and c apply to $\xi_2 = 0$, $\xi_2 = \xi_1$ and $\xi_2 = 0.7\xi_1$, respectively. With increase in the level of boron fibers, the shear rigidity increases appreciably. From the above formulas we can find the corresponding volume content and characteristics of the components, if G_{12} is given.

5. Transverse shear of composite fibers

If the given reinforced medium has three planes of symmetry, no deformations along the fiber orientation will be present if the shear acts in the plane perpendicular to the fiber orientation. Therefore, the stress-strain state of the composite will be a function of x_2 and x_3 only.

The plane stressed state is determined from the function of complex variables using the equations in /9/:

$$\left.\begin{aligned} &\sigma_{33} + \sigma_{22} = 2[\Phi(z) + \overline{\Phi(z)}];\\ &\sigma_{33} - \sigma_{22} + 2i\sigma_{23} = 2[\bar{z}\Phi'(z) + \Psi(z)];\\ &\sigma_{11} = 2\nu[\Phi(z) + \overline{\Phi(z)}];\\ &2G(u_2 + iu_3) = \varkappa\varphi(z) - z\overline{\Phi(z)} - \overline{\psi(z)}, \end{aligned}\right\} \qquad \text{(II. 37)}$$

where

$$\varkappa = 3 - 4\nu;\ \varphi''(z) = \Phi(z);\quad \psi'(z) = \Psi(z).$$

The problem of the stress-strain state in plane $x_1 = \text{const}$ can then be simplified to the finding of two functions $\Phi(z)$ and $\Psi(z)$, which are holomorphic in the given domain.

The conditions of the ideal contact of the components is given by the following system of equations /4/:

$$\begin{gathered}\Phi_a(\tau) + \overline{\Phi_a(\tau)} - e^{2i\theta}[\bar{\tau}\Phi_a'(\tau) + \Psi_a(\tau)] = \Phi_s(\tau) + \\ + \overline{\Phi_s(\tau)} - e^{2i\theta}[\tau\Phi_s'(\tau) + \Psi_s(\tau)]; \\ (1 - G_s/G_a)\Phi_a(\tau) + (1 + \varkappa_a G_s/G_a)\overline{\Phi_a(\tau)} - (1 - G_s/G_a)e^{2i\theta}[\bar{\tau}\Phi_a'(\tau) + \\ + \Psi_a(\tau)] = (\varkappa_s + 1)\overline{\Phi_s(\tau)}.\end{gathered} \qquad \text{(II. 38)}$$

The first equation follows from the stress equality on the interfacial areas of the components, and the second from the equality of displacements at the same points. Conditions (II. 7) in this problem are replaced by restrictions imposed onto the resultant force vector and the moment of all forces acting on the elementary volume of the reinforced body. If we denote by X, Y and M the components of the resultant force in the vector projections onto axes $0x_2$, $0x_3$, and the couples acting on section AB, respectively, the above requirements can be written as

$$\begin{gathered}X + iY = -i[\varphi_s(z) + \overline{\psi_s(z)} + z\overline{\Phi_s(z)}]_A^B; \\ M = \operatorname{Re}[g_s(z) - z\psi_s(z) - z\bar{z}\Phi_s(z)]_A^B,\end{gathered} \qquad \text{(II. 39)}$$

where $g_s'(z) = \psi_s(z)$.

The condition of double periodicity of the stressed state according to (II. 37) in analogy to (II. 9) requires that

$$\begin{gathered}\Phi_s(z + \omega_j) = \Phi_s(z); \\ \bar{\omega}_j\Phi_s'(z + \omega_j) + \Psi_s(z + \omega_j) = \Psi_s(z).\end{gathered} \qquad \text{(II. 40)}$$

For reinforced bodies of hexagonal or tetragonal structure the type of $\Phi_s(z)$ is fixed by (II. 12). $\Psi_s(z)$ can be represented by the series /10/

$$\Psi_s(z) = d_0 + \sum_{k=0}^{\infty} \frac{\lambda^{2k+2}}{(2k+1)!}[d_{2k+2}\Upsilon^{(2k+1)}(z) + C_{2k+2}\gamma_i^{(2k+2)}(z)] + \Psi_0, \qquad \text{(II. 41)}$$

where $\Psi_0 = \langle \sigma_{r3} \rangle$ is the average transverse shear stress:

$$\gamma_i'(z) = -\sum_{m,n}{}' [\bar{P}(z - P)^{-2} - 2z\bar{P}P^{-3} - \bar{P}P^{-2}]. \qquad \text{(II. 42)}$$

The internal stress field in GFP and MFP is illustrated by the curves in Figures II. 14 and II. 15. The continuous curves were plotted for the hexagonal structure and the dashed curves for the tetragonal. Figures II. 14, a and b, and II. 15, a and b, show the changes in the concentration factors of the normal N and the tangential T (to the circumference) stresses for $\lambda = 0.6$ and $\lambda = 0.9$. Letters a and a' denote the curves corresponding to normal stresses, and b and b' to shearing stresses on the fiber-matrix interface. The curves in Figures II. 14, c and II. 15, c are the graphs of N and T plotted against ρ. The numbers at N and T are the values of the angular coordinates; a and b designate the curves plotted for $\lambda = 0.6$ and $\lambda = 0.9$.

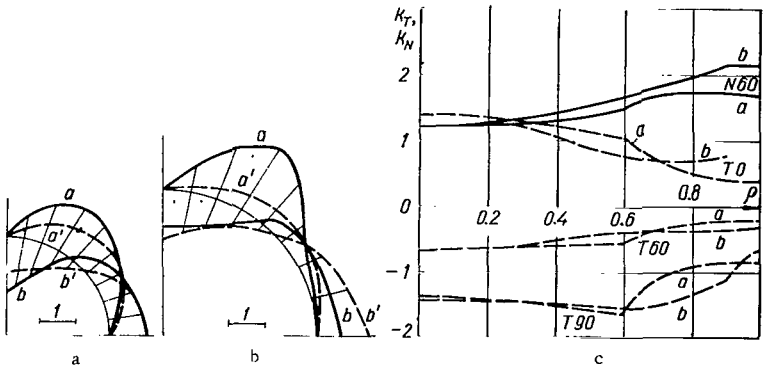

FIGURE II. 14. Normal and shearing stress concentration factors on the outside circumference of hollow fibers (a, b) and along the radius (c) in the structure of GFP.

It follows from the above that the stresses increase with increase in the distance from the fiber center, and reach their maximum on the component interface. An increase in ξ leads to a certain stress redistribution; the maximum normal stresses N arise at points closest to the adjacent fibers which are not arranged at an angle $\vartheta = \frac{\pi}{4}$ (as in a homogeneous medium), but at ϑ value, close to $\frac{\pi}{3}$. The dependence of $k_{N\,\max}$ and $k_{T\,\max}$ on ξ for GFP and MFP is shown in Figure II. 16. The maximum of the shearing

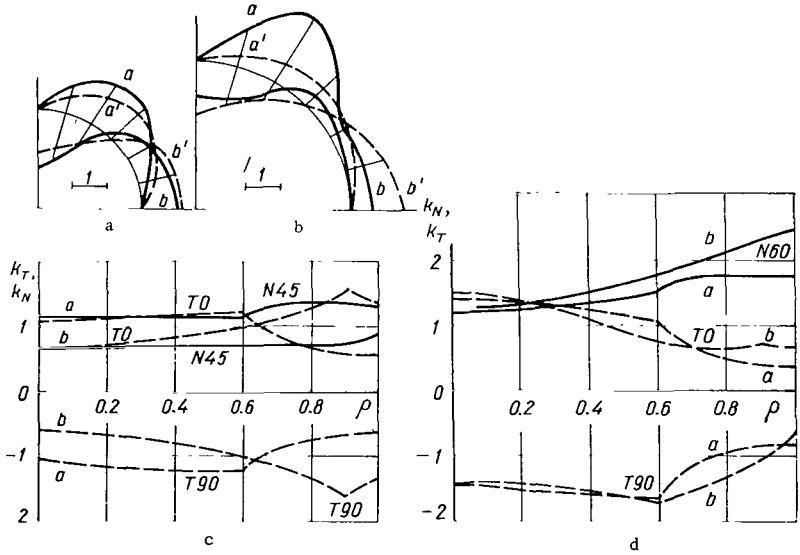

FIGURE II. 15. Normal and shearing stress concentration factors on the outside circumference of hollow fibers (a, b) and along the radius (c, d) in the structure of MFP at $\alpha = \frac{\pi}{2}$ (Figure c) and at $\alpha = \frac{\pi}{3}$ (Figure d).

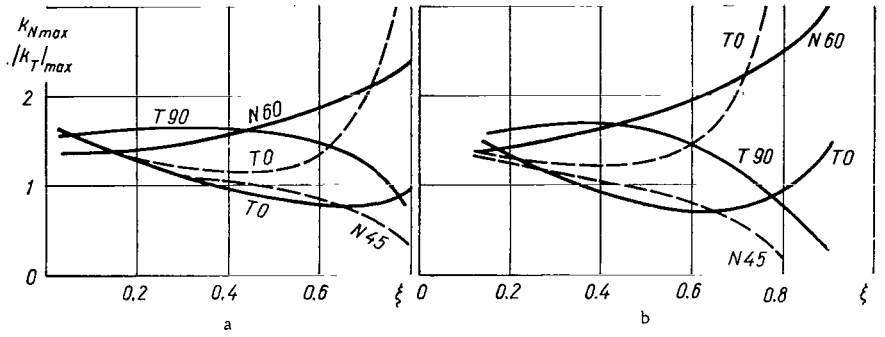

FIGURE II. 16. Dependence of the maximum stress concentration factors (N and T) on the filler level: a — GFP; b — MFP.

stresses in the hexagonal structure is at $\vartheta = \frac{\pi}{2}$, provided that $\xi < 0.78$, and in other cases at $\vartheta = 0$. When $\xi \approx 0.78$, the shearing stresses are the most uniformly distributed and their value is the lowest. When $\xi < 0.45$, the normal stresses are lower than the shearing for the closest-packed structure.

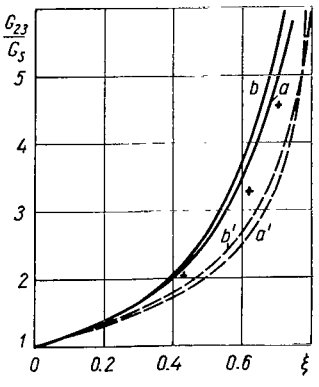

FIGURE II. 17. Dependence of the modulus of transverse shear on the filler level.

The equation for the dependence of the reduced modulus of transverse shear on the component properties is

$$G_{23} = \frac{\varkappa_s + \xi + \eta G_s/G_a}{\eta\varkappa_s + (1+\xi\varkappa_s)\,G_s/G_a} G_s + \ldots; \qquad \text{(II. 43)}$$

for the hexagonal structure, and

$$G_{23} = \frac{\varkappa_s + \xi + \eta G_s/G_a}{\eta\varkappa_s + (1+\xi\varkappa_s)G_s/G_a} G_s + \ldots . \qquad \text{(II. 44)}$$

for the tetragonal structure.

In these formulas we omitted the complicated terms which characterize the effect of fiber interaction and other factors. The dependence of $\frac{G_{23}}{G_s}$ on ξ for the two structural types $\left(\alpha = \frac{\pi}{3} \text{ and } \frac{\pi}{2}\right)$ are characterized by curves a, a' and b, b' (Figure II. 17) for GFP and MFP. The dashed curves characterize $\frac{G_{23}}{G_s}$ as a function of ξ for the hexagonal structure. The crosses denote the $\frac{G_{23}}{G_s}$ ratio for the GFP, calculated from the approximate equation (II. 43). The errors obtained by using this equation are not higher than ±10% for $\xi \leqslant 0.75$.

The stress concentration factors on the circumference of the hollow fibers in GFP for the hexagonal structure are shown in Figure II. 18. The

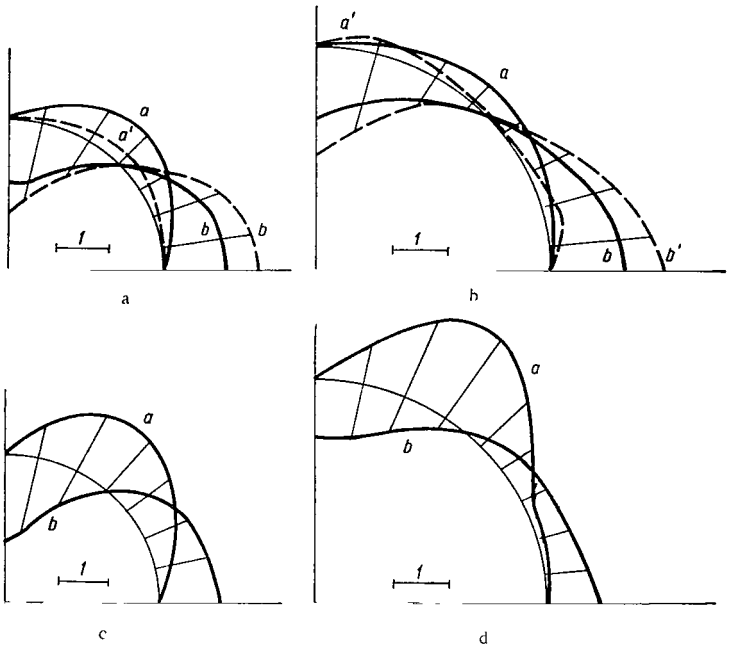

FIGURE II. 18. Stress concentration factors on the outside circumference of hollow fibers (for explanation see text).

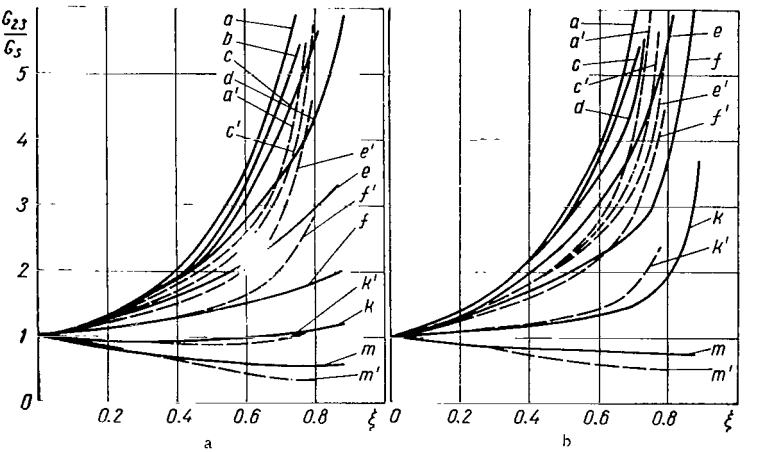

FIGURE II. 19. Dependence of the modulus of transverse shear in materials reinforced by hollow fibers on the filler level:

a — GFP; b — MFP.

concentration of stresses normal to the circumference are characterized by curves a ($q = 0.5$) and a' ($q = 0.7$), and the concentration of shearing stresses by curves b ($q = 0.5$) and b' ($q = 0.7$). The curves in Figure II. 18, a were plotted for $\xi = 0.33\,(\lambda = 0.6)$, and in Figure II. 18, b for $\xi = 0.74\,(\lambda = 0.9)$. With increase in the dimensions of the hollow, the stresses are redistributed. The normal stresses decrease and the shearing stresses increase. This increase is found on those sections of the fibers which operate on "shear."

When the fiber is approached by another adjacent fiber (Figure II. 18, b) the stresses are slightly redistributed, but there are no qualitative changes. The stress concentrations on the fiber-matrix interface for the tetragonal structure are shown in Figure II. 18, c, d. The results of the calculation for $\xi = 0.283\,(\lambda = 0.6)$ are shown in Figure II. 18, c, and for $\xi = 0.64\,(\lambda = 0.9)$ in Figure II. 18, d.

The modulus of transverse shear of the body reinforced by hollow fibers is determined from

$$\frac{G_s}{G_{23}} = 1 - \xi(\varkappa_s + 1)C_2, \tag{II. 45}$$

where

$$C_2^{-1} \approx -\eta + \frac{(\varkappa_s + 1)(1 - q^2)}{1 - q^2 - (1 + \varkappa_a q^2)\frac{G_s}{G_a}} + \cdots.$$

The values of $\frac{G_{23}}{G_s}$ when $q = 0.1$, 0.3, 0.4, 0.5, 0.6, 0.7, 0.8, and 0.9 are illustrated by the curves a, b, c, d, e, f, k, and m in Figure II. 19, a for GFP of hexagonal structure, and by the curves a', b', c', d', e', f', k', and m' for the tetragonal structure. For MFP the analogous curves are shown in Figure II. 19, b.

6. The moduli of elasticity in transverse shear for multicomponent materials

The elementary volume of a multicomponent material must contain at least one fiber of each kind. For the regular structure of the general type, when the cell contains p fibers of various diameters and properties, and the dimensions are such that $b \neq 1$ and $\alpha \neq \frac{\pi}{2}$ or $\frac{\pi}{3}$, $\Phi_s(z)$ is defined by (II. 24). The second function $\Psi_s(z)$ for the region occupied by the matrix can be taken in the form of an expansion (see II. 41):

$$\Psi_s(z) = d_0 - \sum_{k=1}^{p}\sum_{s=1}^{\infty}\frac{(-1)^s}{(s-1)!}\left[d_{k,s}\zeta^{(s-1)}(z - a_k) - C_{k,s}\eta^{(s)}(s - a_k)\right] + \Psi_0, \tag{II. 46}$$

where

$$\sum_{k=1}^{p} d_{k,1} = 0.$$

Functions $\Phi_{a,k}(z)$ and $\Psi_{a,k}(z)$ for the filler elements are established by a series of the Laurent type (II. 22). The boundary conditions are applied

to p by an equation of type (II.38), where we substitute G_k for G_a, and take into account a new expansion of the complex potentials. The arbitrary constants are determined from the boundary conditions and equations (II.39). In the case of transverse shear of a material with the most general regular structure (only one plane of symmetry exists $x_1 = \text{const}$), elongations in the longitudinal and transverse sections arise. The amount of elongation is determined, in particular, by the differences in the Poisson ratios of the matrix and filler. Therefore, the reduced elongations and the angle of transverse slide are expressed in terms of stresses as follows /7/:

$$\left.\begin{aligned}
\langle\varepsilon_{11}\rangle &= X_{11}\langle\sigma_{11}\rangle + X_{12}\langle\sigma_{22}\rangle + X_{13}\langle\sigma_{33}\rangle + X_{16}\langle\sigma_{23}\rangle;\\
\langle\varepsilon_{22}\rangle &= X_{21}\langle\sigma_{11}\rangle + X_{22}\langle\sigma_{22}\rangle + X_{23}\langle\sigma_{33}\rangle + X_{26}\langle\sigma_{23}\rangle;\\
\langle\varepsilon_{33}\rangle &= X_{31}\langle\sigma_{11}\rangle + X_{32}\langle\sigma_{22}\rangle + X_{33}\langle\sigma_{33}\rangle + X_{36}\langle\sigma_{23}\rangle;\\
\langle\gamma_{23}\rangle &= X_{61}\langle\sigma_{11}\rangle + X_{62}\langle\sigma_{22}\rangle + X_{63}\langle\sigma_{33}\rangle + X_{66}\langle\sigma_{23}\rangle.
\end{aligned}\right\} \qquad \text{(II.47)}$$

The following relationship exists between the elastic constants:

$$X_{12} = X_{21};\ X_{13} = X_{31};\ X_{23} = X_{32};\ X_{16} = X_{61};\ X_{26} = X_{62};\ X_{36} = X_{63}.$$

If the technical constants are used, we must take

$$\left.\begin{gathered}
X_{11} = \frac{1}{E_{11}};\ X_{22} = \frac{1}{E_{22}};\ X_{33} = \frac{1}{E_{33}};\ X_{66} = \frac{1}{G_{23}};\ X_{12} = -\nu_{12}X_{22};\\
X_{21} = -\nu_{21}X_{11};\\
X_{13} = -\nu_{13}X_{33};\ X_{31} = -\nu_{31}X_{11};\ X_{16} = \nu_{16}X_{66};\\
X_{23} = -\nu_{23}X_{33};\ X_{32} = -\nu_{32}X_{22};\\
X_{26} = \nu_{26}X_{66};\ X_{61} = \nu_{61}X_{11};\ X_{62} = \nu_{62}X_{22};\ X_{36} = \nu_{36}X_{66};\\
X_{63} = \nu_{63}X_{33}.
\end{gathered}\right\} \qquad \text{(II.48)}$$

In the case of plane deformation $\langle\varepsilon_{11}\rangle = 0$, and therefore

$$\langle\sigma_{11}\rangle = \nu_{21}\langle\sigma_{22}\rangle + \nu_{31}\langle\sigma_{33}\rangle + \nu_{61}\langle\sigma_{23}\rangle,$$

while the deformation in plane $x_1 = \text{const}$ is determined from

$$\begin{aligned}
\langle\varepsilon_{22}\rangle &= (X_{22} + \nu_{21}X_{12})\langle\sigma_{22}\rangle + (X_{23} + \nu_{31}X_{12})\langle\sigma_{33}\rangle + (X_{26} + \nu_{61}X_{12})\langle\sigma_{23}\rangle;\\
\langle\varepsilon_{33}\rangle &= (X_{23} + \nu_{21}X_{13})\langle\sigma_{22}\rangle + (X_{33} + \nu_{31}X_{13})\langle\sigma_{33}\rangle + (X_{66} + \nu_{61}X_{16})\langle\sigma_{23}\rangle;\\
\langle\gamma_{23}\rangle &= (X_{26} + \nu_{21}X_{16})\langle\sigma_{22}\rangle + (X_{36} + \nu_{31}X_{16})\langle\sigma_{33}\rangle + (X_{66} + \nu_{61}X_{16})\langle\sigma_{23}\rangle.
\end{aligned}$$

For bodies with a monoclinic symmetry, when no average stresses $\langle\sigma_{22}\rangle$ and $\langle\sigma_{33}\rangle$ are present and the angle of slide is known, the modulus of shear can be expressed by other constants only

$$\frac{1}{G_{23}} = -\nu_{61}X_{16} + \frac{1}{G_s} + \frac{\varkappa_s + 1}{G_s}\operatorname{Im}\left[C_0 - \frac{\delta_1}{\omega_1}\sum_{k=1}^{p}(C_{k,2} + C_{k,1}a_k)\right]. \qquad \text{(II.49)}$$

Here the first term characterizes the effects of deformational constraint, the second the compliance of the homogeneous matrix and the third the compliance allowing for the filler. It follows from the above equations that ν_{61} and X_{16} must be determined from the solution of other problems. The equations for the other constants are found by analogy

$$X_{26} = -\nu_{61}X_{12} + \frac{\varkappa_s + 1}{G_s}\operatorname{Re}\left[C_0 - \frac{\delta_1}{\omega_1}\sum_{k=1}^{p}(C_{k,2} + C_{k,1}a_k)\right];$$

$$(X_{36} + \nu_{61}X_{13})\sin\alpha + (X_{26} + \nu_{61}X_{12})\cos\alpha =$$

$$= \frac{\sin\alpha}{G_s} + \frac{\varkappa_s + 1}{G_s}\operatorname{Re}\left[e^{i\alpha}C_0 - \frac{\delta_2}{\omega_1 b}\sum_{k=1}^{p}(C_{k,2} + C_{k,1}a_k)\right]. \qquad \text{(II. 50)}$$

For materials with three symmetry planes, we equate

$$\nu_{61} = 0;\ X_{16} = 0;\ X_{26} = 0;\ X_{36} = 0.$$

The equations can be simplified further for materials with hexagonal microstructure. This case is of practical importance, since real microstructures with a sufficiently close packing of the filler are the closest to this type of regular microstructure. The approximate equations for expressing the modulus of transverse shear of a multicomponent material in terms of the component parameters for the hexagonal structure are

$$G_{23} \approx G_s \frac{1 + \sum_{k=1}^{p} \xi_k \frac{1 - G_s/G_k}{\varkappa_s + G_s/G_k}}{1 - \varkappa_s \sum_{k=1}^{p} \xi_k \frac{1 - G_s/G_k}{\varkappa_s + G_s/G_k}}. \qquad \text{(II. 51)}$$

Here the same symbols are used as in (II. 35).

If the fibers are hollow so that $q_k = \frac{\epsilon_k}{\gamma_k}$, the modulus of longitudinal shear is

$$G_{23} \approx G_s \frac{1 + \sum_{k=1}^{p} \xi_k \frac{1 - q_k^2 - (1 + \varkappa_k q_k^2) G_s/G_k}{(1 - q_k^2)\varkappa_s + (1 + \varkappa_k q_k^2) G_s/G_k}}{1 - \varkappa_s \sum_{k=1}^{p} \xi_k \frac{1 - q_k^2 - (1 + \varkappa_k q_k^2) G_s/G_k}{(1 - q_k^2)\varkappa_s + (1 + \varkappa_k q_k^2) G_s/G_k}}. \qquad \text{(II. 52)}$$

If the t-th component is represented by solid fibers then $q_t = 0$. For two-phase components ($p = 1$), from the above formula the approximate equations are obtained, with the accuracy estimated above.

7. Stresses in the microstructure and the elastic constants of the composite material in longitudinal tension

The stress-strain state of a reinforced medium in longitudinal tension is determined by solving the problem of tension by unknown stresses without allowing for the interaction between matrix and filler. We also assume that section $x_1 = \text{const}$ remains plane. Moreover, the stress-strain state of such a medium is also determined by solving the problem of the plane strained state when the longitudinal deformations are equal to zero, and the transverse displacements on the fiber-matrix interface are given. The transverse displacements are selected so that the difference in the displacements of the components make it possible to combine the boundary conditions of the matrix and the filler, while the longitudinal elongation remains zero /10/. The average tensile stresses must be given:

$$\langle \sigma_{11} \rangle = (\xi E_a + \eta E_s) \langle \varepsilon_{11} \rangle + 4\mathrm{Re}[\nu_a \langle \Phi_a(z) \rangle + \nu_s \langle \Phi_s(z) \rangle].$$

The stresses and displacements are related to the complex potentials by (II. 37). The conditions on the component interfaces, that is, the equality of the stresses for given displacement difference are given by the first equation of (II. 38), and an equation of type

$$(1 - G_s/G_a)\Phi_a(\tau) + (1 + \varkappa_a G_s/G_a)\overline{\Phi_a(\tau)} - e^{2i\theta}[\tau\Phi_a'(\tau) + \Psi_a(\tau)] = \\ = (\varkappa_s + 1)\overline{\Phi_s(\tau)} + 2G_s(\nu_a - \nu_s)\langle \varepsilon_{11} \rangle. \qquad \text{(II. 53)}$$

If we assume that $\langle \sigma_{11} \rangle' = (\xi E_a + \eta E_s)\langle \varepsilon_{11} \rangle = 1$, the stresses on the fiber-matrix interface will be distributed as shown in Figure II. 20, where along the radius of the fiber circumference, the concentration factors of the normal (curves a and a') and shearing (curves b and b') stresses are plotted. The continuous curves apply to the hexagonal and the dashed curves to the tetragonal structures. In Figure II. 20, a and c, $\lambda = 0.5$ and in Figure II. 20, b and d, $\lambda = 0.9$. In Figure II. 20, a and b apply to GFP, and c and d to MFP (steel fibers). On the surface of straightened fibers, small stresses arise caused by the difference in the values ν_a and ν_s. At the sites where the fibers approach each other compressive stresses are produced, while the stresses at the other points of the circumference are tensile.

The modulus of elasticity in longitudinal tension is given by

$$E_{11} = \xi E_a + \eta E_s + 8\xi G_s(\nu_a - \nu_s)^2 \frac{\eta + (\varkappa_s + 1)\sum_{k=1}^{\infty} C_{2k+2}\lambda^{2k+2}a_{0,k}}{1 \quad \eta + \xi\varkappa_s + \eta(\varkappa_a - 1)G_s/G_a}. \qquad \text{(II. 54)}$$

The increase in the stiffness, determined by the third and subsequent terms of (II. 54), and hence by $\nu_a - \nu_s$, is very small, as shown by calculations. For GFP the correction is only fractions of a percent. Figure II. 21, a shows $\frac{E_{11}}{E_s}$ as a function of ξ for GFP and MFP (curves b, a).

For hexagonal and tetragonal structures the Poisson ratios are equal: $\nu_{21} = \nu_{31}$ and $\nu_{12} = \nu_{13}$. The equation for expressing these ratios in terms of the component parameters is

$$\nu_{21} = \nu_s - \xi(\varkappa_s + 1)(\nu_s - \nu_a) \frac{1 - [1 - \varkappa_s + (\varkappa_s + 1)G_s G_a] \sum_{k=1}^{\infty} C_{2k+2}\lambda^{2k+2}a_{0,k}}{1 + \eta + \xi\varkappa_s + \eta(\varkappa_a - 1)G_s/G_a}.$$

These calculations show that the Poisson ratios for existing compositions can be calculated within fractions of a percent from the approximate formula

$$\nu_{21} = \nu_{31} \approx \nu_s - \frac{\xi(\varkappa_s + 1)(\nu_s - \nu_a)}{1 + \eta + \xi\varkappa_s + \eta(\varkappa_a - 1)G_s/G_a}. \qquad \text{(II. 55)}$$

The dependence of ν_{21} on ξ for GFP is represented by curve b, and for MFP by curve a (Figure II. 21. b).

If the fibers are hollow, Young's modulus is determined with a high degree of accuracy from

$$E_{11} \approx \xi(1 - q^2)E_a + \eta E_s + \cdots. \qquad \text{(II. 56)}$$

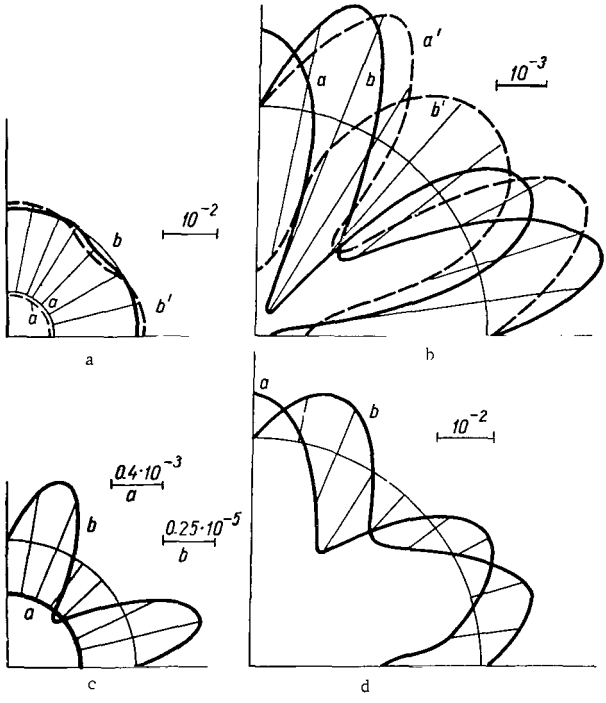

FIGURE II. 20. Normal and shearing stress concentration factors on the fiber circumference during longitudinal tension of the composite material.

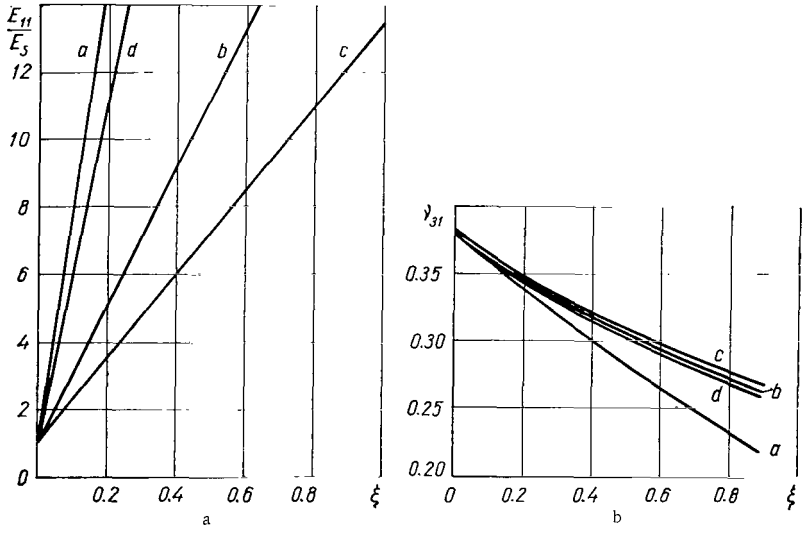

FIGURE II. 21. Dependence of Young's modulus of the composite material (a) and of the Poisson ratio in longitudinal tension (b) on the filler level.

Transverse effects for the given structural types are accurately determined from

$$\nu_{21} = \nu_{31} \approx \nu_s - \frac{\xi(\nu_a - \nu_s)(\varkappa_s + 1)(1 - q^2)}{(1 - q^2)(1 + \eta + \xi\varkappa_s) + \eta(\varkappa_a - 1 + 2q^2)\, G_s/G_a}. \qquad \text{(II. 57)}$$

In Figure II. 21, a the curves d and c plotted for GFP and MFP when $q = 0.5$ characterize changes in $\frac{E_{11}}{E_s}$ with increase in ξ; curves c and d (Figure II. 21, b) illustrate the change in ν_{21} with increase in ξ when $q = 0.5$ for GFP and MFP.

8. Longitudinal tension of multicomponent media

For multicomponent media with a general type structure, when the individual cell contains p fibers with different properties and $b \neq 1$, $\alpha \neq \frac{\pi}{2}$ or $\frac{\pi}{3}$, we can obtain equations for some of the elastic constants in the form (II. 46). The stress-strain state of the medium is determined as in the last section.

The transverse effects for structures with a monoclinic symmetry are found by expanding the complex potentials according to

$$\left.\begin{aligned}
\nu_{61} &= 2(\varkappa_a + 1)\,\mathrm{Im}\left[C_0 - \frac{\delta_1}{\omega_1}\sum_{k=1}^{p}(\nu_k - \nu_s)(C_{k,2} + C_{k,1}a_k)\right];\\
\nu_{21} &= \nu_s - (\varkappa_s + 1)\,\mathrm{Re}\left[C_0 - \frac{\delta_1}{\omega_1}\sum_{k=1}^{p}(\nu_k - \nu_s)(C_{k,2} + C_{k,1}a_k)\right];\\
\nu_{31} &= \nu_s - (\varkappa_s + 1)\,\mathrm{Im}\left[C_0\omega_1\omega_2/F - \omega_1\delta_2/F\sum_{k=1}^{p}(\nu_k - \nu_s)(C_{k,2} + C_{k,1}a_k)\right].
\end{aligned}\right\} \qquad \text{(II. 58)}$$

Here C_0 is also proportional to the difference in the Poisson ratios for the components. ν_{61} characterizes the angle of slide arising in the transverse plane in longitudinal tension, i. e., elongation in shear. It depends on $\nu_k - \nu_s$, and hence on $\nu_k = \nu_s$. This effect is equal to zero for any arrangement of the fibers in the cell. Constants $C_{k,n}$ in the above expressions are determined when boundary conditions of the matrix-filler interface are satisfied.

For a hexagonal structure of the composite materials, the equations are considerably simplified, and ν_{61} is equal to zero. The simplified equations make it possible to determine the elastic constants directly with a fair accuracy in the form

$$\nu_{21} = \nu_{31} \approx \nu_s - \frac{\sum_{k=1}^{p}\xi_k \frac{(\varkappa_s + 1)(\nu_s - \nu_k)}{2 + (\varkappa_k - 1)\, G_s/G_k}}{\eta + \sum_{k=1}^{p}\frac{(\varkappa_s + 1)\,\xi_k}{2 + (\varkappa_k - 1)\, G_s/G_k}}. \qquad \text{(II. 59)}$$

If the medium is reinforced by hollow fibers, the approximate equations for determining Young's modulus and the Poisson ratios will be

$$E_{11} \approx \sum_{k=1}^{p} \xi (1 - q_k^2) E_k + \eta E_s;$$

$$\nu_{21} \approx \nu_s - \frac{\sum_{k=1}^{p} \frac{\xi_k (1 - q_k^2)(\nu_s - \nu_k)(\varkappa_s + 1)}{2(1 - q_k^2) + (\varkappa_s - 1 + 2q_k^2) G_s/G_k}}{\eta + \sum_{k=1}^{p} \frac{\xi_k (1 - q_k^2)(\varkappa_s + 1)}{2(1 - q_k^2) + (\varkappa_k - 1 + 2q_k^2) G_s/G_k}}. \qquad (II.60)$$

Equation (II.53) is a particular case derived for $q_k = 0$.

9. Transverse tension of reinforced bodies with a simple regular structure

Let the reinforced body with a tetragonal or hexagonal structure be subjected to triaxial tension. The material will be in the plane strained state if the transverse tensile stresses are determined from (II.37). The type of complex potentials is determined according to the structure selected. We must add functions corresponding to the homogeneous stressed state of the material to (II.12) and (II.41) satisfying the conditions of equality to zero of the resultant force vector and the momentum of all forces acting upon the elementary cell:

$$\Phi_0 = \frac{1}{4}(\langle\sigma_{22}\rangle + \langle\sigma_{33}\rangle); \quad \Psi_0 = \frac{1}{2}(\langle\sigma_{33}\rangle - \langle\sigma_{22}\rangle).$$

The distribution of normal N and shearing T tensile stresses $\langle\sigma_{22}\rangle = 1$ ($\langle\sigma\rangle = 0$) of GFP and MFP is shown in Figure II.22. The continuous curves correspond to the hexagonal and the dashed curves to the tetragonal structures. The change in the stress concentration factors N (curves a, a', c, c') and T (curves b, b', d, d') over the fiber circumference as a function of ϑ are shown in Figure II.22, a, c. Curves b, d (Figure II.22, b, d) characterize the changes in the stresses with increase in the radial distance from the fiber center. The calculations were carried out for $\lambda = 0.6$ (curves a, b, a', b') and $\lambda = 0.9$ (curves c, c', d, d').

The maximum normal stresses arise on the fiber-matrix interface at the sites where adjacent fibers approach one another. Shearing stresses may attain their maximum values in the bulk of the fibers also, but they differ little from the maximum stresses on the contour (about 10%). In hexagonal composites the maximum T on the contour is displaced from angle $\vartheta = \frac{\pi}{3}$ to $\vartheta = \frac{\pi}{6}$ with increase in the filler content. In the tetragonal structure the maximum T arises when $\vartheta \approx \frac{\pi}{4}$. The changes in k_N and k_T as a function of ρ at values of ϑ when they have a maximum value are illustrated by the curves in Figure II.22, b and d.

The stress concentration is caused by differences in the moduli of elasticity of the components and by fiber interaction when the fibers approach

one another. Thus, for example, in GFP the local stresses arising in the structure are more than twice the average stresses.

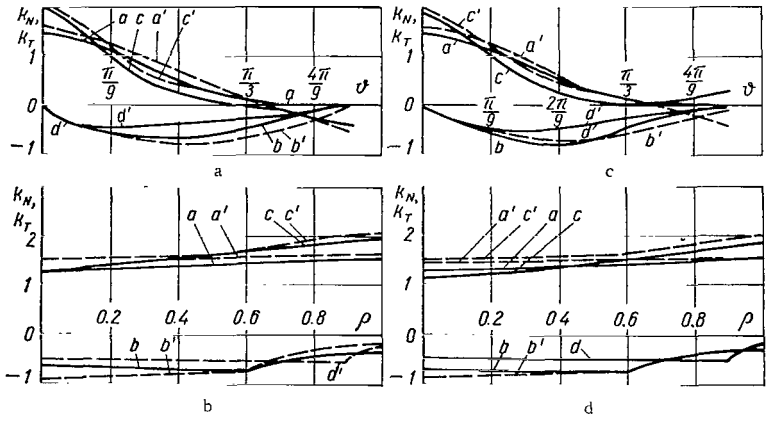

FIGURE II. 22. Stress concentration factors on the circumference (a, c) and along the radius (b, d) in MFP (Figures a, b) and GFP (Figures c, d) in transverse tension.

The approximate formula for determining $1/E_{22}$ an be obtained if we neglect the auxiliary terms

$$\frac{1}{E_{22}} \approx \nu_{21}^2 X_{11} + \frac{\varkappa_s + 1}{8G_s}\left[\frac{2 + (\varkappa_a - 1)\,G_s/G_a}{1 + \eta + \xi\varkappa_s + \eta(\varkappa_a - 1)\,G_s/G_a} - \frac{2\xi(1 - G_s/G_a)}{\xi + \varkappa_s + \gamma_1 G_s/G_a}\right]. \qquad \text{(II. 61)}$$

Here we must equate $\gamma_1 = 0$, if $\alpha = \frac{\pi}{3}$ (hexagonal lattice) and $\mathrm{Re}\,\bar{\gamma}_1 = 1.3634$, if $\alpha = \frac{\pi}{2}$. The results of the calculations of $\frac{E_{22}}{E_s}$ with increase in ξ for the glass fibers (curve a) and metal fibers (curve a') are illustrated in Figure II. 23, a $\left(\alpha = \frac{\pi}{3}\right)$ and Figure II. 24, a $\left(\alpha = \frac{\pi}{2}\right)$. The approximate equation (II. 61) makes it possible to calculate E_{22} within $\pm 10\%$, if $\xi \leqslant 0.75$. The value of E_{22} obtained is too high if $\alpha = \frac{\pi}{3}$, and too low if $\alpha = \frac{\pi}{4}$.

The simplified equation for calculating transverse effects (within $\pm 15\%$ for $\alpha = \frac{\pi}{3}$) is

$$\frac{\nu_{23}}{E_{33}} = -\nu_{31}^2 X_{11} + \frac{1}{8G_s}\left[4\nu_s + (\varkappa_s + 1)\,\xi\left(\frac{\varkappa_s - 1 - (\varkappa_a - 1)\,G_s/G_a}{1 + \gamma_1 + \xi\varkappa_s + \gamma_1(\varkappa_a - 1)\,G_s/G_a} - \frac{2(1 - G_s/G_a)}{\xi + \varkappa_s + \gamma_1 G_s/G_a}\right)\right]. \qquad \text{(II. 62)}$$

The changes in ν_{23} with increase in ξ are illustrated by curves a (glass fibers) and a' (metal fibers) in Figure II. 23, b for a hexagonal structure and in Figure II. 24, b for a tetragonal lattice. Curves e and f in Figure II. 25

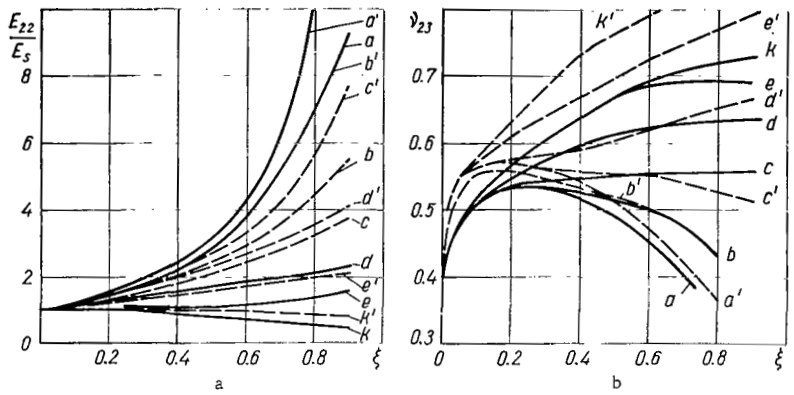

a b

FIGURE II. 23. Dependence of Young's modulus (a) and Poisson ratio (b) in transverse tension on the volume content of filler for a fiber composite with a hexagonal structure at various values of q.

characterize the changes in ν_{12} with increase in ξ for hexagonal and tetragonal structures of the GFP when $q = 0$, and curves e' and f' characterize the same when $q = 0.9$.

For the hexagonal structure of a reinforced medium there exists an additional correlation between the above elastic constants, which is a logical consequence of the invariance conditions of the mechanical properties of the medium when the coordinate system is rotated around x_1. This correlation makes it possible to determine the modulus of transverse shear in terms of the constants found in transverse tension

$$\frac{1}{G_{23}} = 2\frac{1+\nu_{23}}{E_{22}}. \qquad \text{(II. 63)}$$

For hexagonal and tetragonal structures we have $E_{22} = E_{33}$; $\nu_{23} = \nu_{32}$; $\nu_{21} = \nu_{31}$, following from the equivalent properties of the medium rotated around x_1 by $\frac{\pi}{2}$.

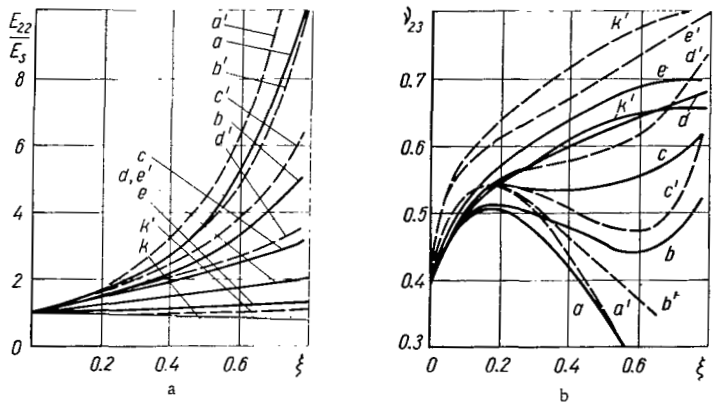

a b

FIGURE II. 24. Dependence of Young's modulus (a) and Poisson ratio (b) in transverse tension on the volume content of filler for a fiber composite with a tetragonal structure at various values of q.

For composites with hollow fibers Figures II. 26 and II. 27 show the concentration factor of normal k_N (curves a, a', c, c') and shearing k_T stresses (curves b, b', d, d') for $q = 0.4$ (Figure II. 26) and $q = 0.9$ (Figure II. 27). The continuous curves were plotted for hexagonal structures and the dashed for tetragonal. The data in Figures II. 26, a, b and II. 27, a, b refer to metal fibers, and those in Figure II. 26, c, d and II. 27, c, d to glass fibers. The changes in the stresses on the fiber-matrix interface are shown by curves a, a', b, b', c, c', d, d' (Figure II. 26, a, c and Figure II. 27, a, c). On the ordinate the concentration factors of the normal (curves a, a', c, c') and shearing (b, b', d, d') stresses are plotted, and the values of ϑ are plotted on the abscissa. The highest normal stresses arise on the component interface at $\vartheta = 0$ if $q \leq 0.75$. If $q > 0.75$ the stresses are redistributed, and the maximum is produced at $\vartheta \approx \frac{\pi}{2}$. The highest shearing stresses arise at $\vartheta \approx \frac{2\pi}{9}$ and $\frac{\pi}{4}$ for hexagonal and tetragonal structures, respectively.

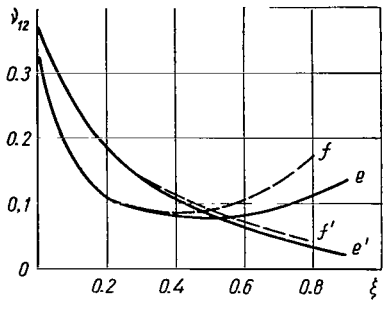

FIGURE II. 25. Dependence of the transverse effect on the filler level.

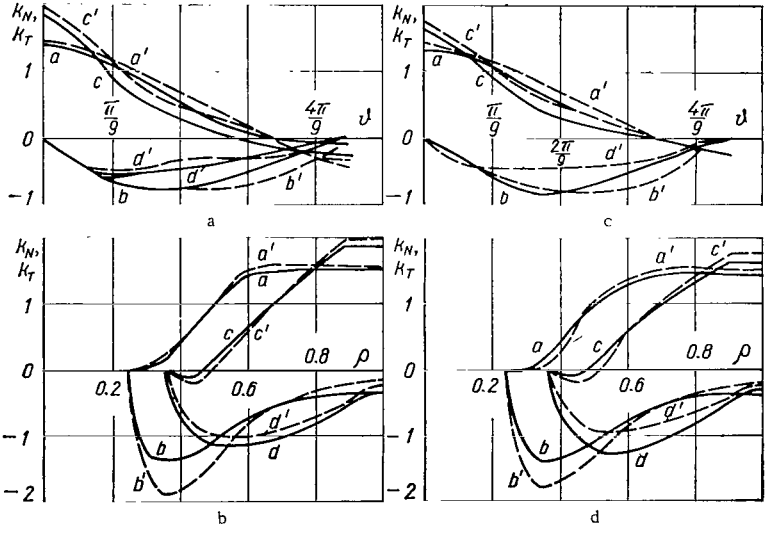

FIGURE II. 26. Stress concentration factors on the outer circumference of the fiber and along the radius in MFP and GFP in transverse tension of the material ($q = 0.4$) (for specifications, see text).

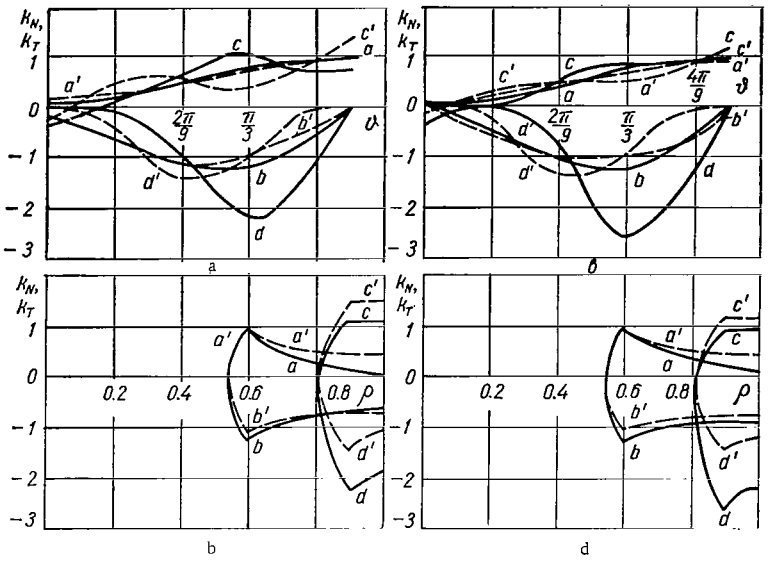

FIGURE II. 27. Stress concentration factors along the outer circumference and along the radius in MFP and GFP in transverse tension of the material ($q = 0.9$) (for specifications, see text).

The changes in the normal (curves a, a', c, c') and shearing (curves b, b', d, d') stresses as a function of the radius ρ are shown in Figures II. 26, b, d and II. 27, b, d. The curves are plotted for values of ϑ at which the corresponding stresses reach maximum values on the fiber circumference. The shearing stresses reach their maximum values in the fiber bulk, where they are about twice those on the circumference. With increase in the radius of the hollow space in the fibers, the maximum values of normal stresses decrease and those of shearing stresses increase.

The dependences of k_N (curves a, b, c, d) and k_T (curves a', b', c', d') on ξ when $q = 0$ for MFP and GFP are shown by curves a, a', c, c' and b, b', d, d' in Figure II. 28, a. Curves a, a', b, b' refer to hexagonal microstructure and curves c, c', d, d' to tetragonal. Figures II. 28, b $\left(\alpha = \frac{\pi}{3}\right)$ and II. 28, c $\left(\alpha = \frac{\pi}{2}\right)$ show the same properties for materials with $q = 0.4$ (curves a, b, c, d) and $q = 0.9$ (curves a', b', c', d'). The normal stress curves are designated by letters a, a', c, c' and the shearing stress curves by letters b, b', d, d'.

The approximate formula for determining the modulus is

$$\frac{1}{E_{22}} \approx \nu_{21}^2 X_{11} + \frac{\varkappa_s + 1}{8G_s}\left(\frac{2(1-q^2) + (\varkappa_a - 1 - 2q^2)\, G_s/G_a}{(1+\eta+\xi\varkappa_s)(1-q^2) + \eta(\varkappa_a - 1 - 2q^2)\, G_s/G_a} - \xi C_2\right), \qquad \text{(II. 64)}$$

where we equate

$$C_2 \approx \frac{2[1 - q^2 - (1 + \varkappa_a q^2)\, G_s/G_a]}{(1-q^2)(\xi + \varkappa_s) + \eta(\varkappa_a q^2 + 1)\, G_s/G_a + \frac{\xi\omega_1}{\pi}[1 - G_s/G_a - (1+\varkappa_a G_s/G_a)\, q^2\, \mathrm{Re}\,\bar{\gamma}_{11}]}.$$

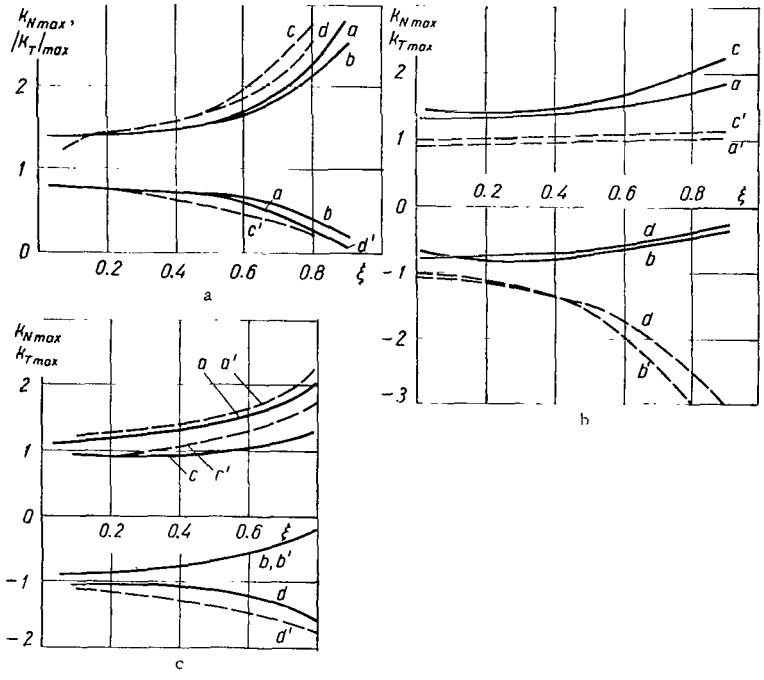

FIGURE II. 28. Dependence of the maximum stress concentration factor on the filler level (for specifications, see text).

The curves in Figures II. 23, a and II. 24, a characterize changes in $\frac{E_{23}}{E_s}$ with increase in ξ for materials with hexagonal and tetragonal structures. The continuous curves b, c, d, e, and k are plotted for GFP and the dashed ones b', c', d', e', and k' for the MFP.

The curve pairs b and b', c and c', d and d', e and e', and k and k', correspond to $q = 0.5, 0.6, 0.7, 0.8$, and 0.9, respectively. By using the approximate equation (II. 64), the errors do not exceed ± 12%. The errors decrease with decrease in ξ and increase in q.

The approximate equation for calculating ν_{23} is

$$\frac{\nu_{23}}{E_{23}} \approx -\frac{\nu_{31}^2}{E_{11}} + \frac{1}{8G_s}\left[4\nu_s + (\varkappa_s + 1)\,\xi\left(\frac{(1-q^2)(\varkappa_s - 1) - (\varkappa_a - 1 - 2q^2)\frac{G_s}{G_a}}{1 + \eta + \xi\varkappa_s + \eta(\varkappa_a - 1)\frac{G_s}{G_a}} - C_2\right)\right]. \quad \text{(II. 65)}$$

The curve pairs b and b', c and c', d and d', e and e', k and k', in Figures II. 23, b $\left(\alpha = \frac{\pi}{3}\right)$ and II. 24, b $\left(\alpha = \frac{\pi}{2}\right)$, illustrate ν_{23} as a function of ξ when $q = 0.5, 0.6, 0.7, 0.8$, and 0.9, respectively. The continuous curves were plotted for the glass fibers and the dashed curves for the metal fibers. A comparison of the results obtained from the accurate and approximate equations showed that (II. 65) is suitable if results accurate to within ± 10% are satisfactory.

10. Transverse tension of multicomponent materials

The number of elastic constants in the equations of Hooke's law (II. 47) depends on the unit cell type. According to our assumption this must contain fibers of p kinds. If $b \neq 1$, $\alpha \neq \frac{\pi}{2}$ or $\frac{\pi}{3}$, the complex potentials for the matrix are selected according to (II. 24) and (II. 46). In this case the constants are determined from

$$\left.\begin{aligned}
&\frac{1}{E_{22}} = \frac{\nu_{21}^2}{E_{11}} + \frac{\varkappa_s+1}{8G_s} + \frac{\varkappa_s+1}{2G_s}\operatorname{Re}\left[C_0 - \frac{\delta_1}{\omega_1}\sum_{k=1}^{p}(C_{k,2} + C_{k,1}a_k)\right];\\
&\frac{\nu_{23}}{E_{22}} = -\frac{\nu_{21}\nu_{31}}{E_{11}} + \frac{\nu_s}{2G_s} - \frac{\varkappa_s+1}{2G_s}\operatorname{Im}\left[C_0 - \frac{\delta_{2\omega_1}}{F}\sum_{k=1}^{p}(C_{k,2} + C_{k,1}a_k)\right];\\
&\frac{\nu_{26}}{G_{23}} = -\frac{\nu_{21}\nu_{61}}{G_{23}} + \frac{\varkappa_s+1}{G_s}\operatorname{Im}\left[C_0 - \frac{\delta_1}{\omega_1}\sum_{k=1}^{p}(C_{k,2} + C_{k,1}a_k)\right];\\
&\frac{1}{E_{33}} = \frac{\nu_{31}^2}{E_{11}} + \frac{\varkappa_s+1}{8G_s} + \frac{\varkappa_s+1}{2G_s}\operatorname{Im}\left[C_0 - \frac{\delta_{2\omega_1}}{F}\sum_{k=1}^{p}(C_{k,2} + C_{k,1}a_k)\right];\\
&\frac{\nu_{36}}{G_{23}} = -\frac{\nu_{31}\nu_{61}}{G_{23}} + \frac{\varkappa_s+1}{G_s}\operatorname{Im}\left[C_0 - \frac{\delta_1}{\omega_1}\sum_{k=1}^{p}(C_{k,2} + C_{k,1}a_k)\right].
\end{aligned}\right\} \qquad \text{(II. 66)}$$

For a hexagonal microstructure, which is the most important, we can derive approximate equations with which it is possible to determine the elastic constants directly:

$$\left.\begin{aligned}
&\frac{1}{E_{22}} \approx \frac{\nu_{21}^2}{E_{11}} + \frac{\varkappa_s+1}{8G_s}\left(\frac{1}{R} - \frac{2P}{1+P}\right) + \cdots;\\
&\frac{\nu_{23}}{E_{22}} = -\frac{\nu_{21}^2}{E_{11}} + \frac{\nu_s}{2G_s} + \frac{\varkappa_s+1}{8G_s}\left(\frac{R-1}{R} - \frac{2P}{1+P}\right) + \cdots
\end{aligned}\right\} \qquad \text{(II. 67)}$$

Here we use

$$R = \tau_l + \sum_{k=1}^{p}\frac{(\varkappa_s+1)\,\xi_k}{2 + (\varkappa_k - 1)\,G_s/G_k}, \qquad P = \sum_{k=1}^{p}\xi_k\,\frac{1 - G_s/G_k}{\varkappa_s + G_s/G_k}.$$

For materials with a tetragonal structure, the elastic constants are determined in a similar manner

$$\left.\begin{aligned}
&\frac{1}{E_{22}} \approx \frac{\nu_{21}^2}{E_{11}} + \frac{\varkappa_s+1}{8G_s}\left(\frac{1}{R} - \frac{2P'}{1+P'}\right) + \cdots;\\
&\frac{\nu_{23}}{E_{22}} \approx -\frac{\nu_{21}^2}{E_{11}} + \frac{\nu_s}{2G_s} + \frac{\varkappa_s+1}{8G_s}\left(\frac{R-1}{R} - \frac{2P'}{1+P'}\right) + \cdots,
\end{aligned}\right\} \qquad \text{(II. 68)}$$

where

$$P' = \sum_{k=1}^{p}\xi_k\,\frac{1 - G_s/G_k}{\varkappa_s + G_s/G_k}.$$

For multicomponent reinforced bodies with hollow fibers, for a hexagonal microstructure we can obtain the following approximate equations

$$\frac{1}{E_{22}} \approx \frac{\nu_{21}^2}{E_{11}} + \frac{\varkappa_s + 1}{8G_s}\left(\frac{1}{N} - \frac{2Q}{1+Q}\right) + \cdots;$$
$$\frac{\nu_{23}}{E_{22}} = -\frac{\nu_{21}^2}{E_{11}} + \frac{\nu_s}{2G_s} + \frac{\varkappa_s + 1}{8G_s}\left(\frac{N-1}{N} - \frac{2Q}{1+Q}\right) + \cdots \qquad \text{(II. 69)}$$

Here we take

$$N = \eta + \sum_{k=1}^{p} \frac{(\varkappa_s + 1)\,\xi_k (1 - q_k^2)}{2(1 - q_k^2) + (\varkappa_k - 1 + 2q_k^2)\,G_s/G_k};$$
$$Q = \sum_{k=1}^{p} \xi_k \frac{1 - q_k^2 - (1 + \varkappa_k q_k^2)\,G_s/G_k}{(1 - q_k^2)\,\varkappa_s + (1 + \varkappa_k q_k^2)\,G_s/G_k}.$$

The equations for determining the moduli of multicomponent bodies with a tetragonal structure can be derived analogously.

11. The elastic constants in areas inclined to the fiber orientation

The elastic energy stored by an individual cell on deformation of the material is independent of the rotation of the coordinate axes. For this reason, the elastic constants when, for example, tensioning the medium at an angle to the fiber direction may be expressed in terms of the parameters of the main areas which are perpendicular or parallel to the fiber direction. It follows from the above equations which hold for a certain distance from the edge of the specimen and for local disturbances that on rotation of the coordinate axis the elastic constants are transformed as components of tensors of fourth rank. For a hexagonal structure, when the coordinate system rotates around $0x_3$ by angle φ we have

$$\left.\begin{aligned}
\frac{1}{E'_{11}} &= \frac{1}{E_{11}}\cos^4\varphi + \left(\frac{1}{G_{12}} - 2\frac{\nu_{21}}{E_{11}}\right)\cos^2\varphi\sin^2\varphi + \frac{1}{E_{22}}\sin^4\varphi;\\
\frac{1}{E'_{22}} &= \frac{1}{E_{11}}\sin^4\varphi + \left(\frac{1}{G_{12}} - 2\frac{\nu_{21}}{E_{11}}\right)\cos^2\varphi\sin^2\varphi + \frac{1}{E_{22}}\cos^4\varphi;\\
\frac{1}{G'_{12}} &= \frac{1}{G_{12}} + \left(\frac{1}{E_{11}} + \frac{1}{E_{22}} + \frac{1}{G_{12}} + \frac{2\nu_{21}}{E_{11}}\right)\sin^2 2\varphi;\\
\frac{\nu'_{21}}{E'_{11}} &= \frac{\nu_{21}}{E_{11}} - \frac{1}{4}\left(\frac{1}{E_{11}} + \frac{1}{E_{22}} - \frac{1}{G_{12}} + \frac{2\nu_{21}}{E_{11}}\right)\sin^2 2\varphi \text{ etc.}
\end{aligned}\right\} \qquad \text{(II. 70)}$$

There are additional equations connecting the parameters, which are invariant with reference to coordinate transformation:

$$\frac{1}{E'_{11}} + \frac{1}{E'_{22}} - 2\frac{\nu_{21}}{E'_{11}} = \frac{1}{E_{11}} + \frac{1}{E_{22}} - 2\frac{\nu_{21}}{E_{11}};$$
$$\frac{1}{G'_{12}} + 4\frac{\nu'_{21}}{E'_{11}} = \frac{1}{G_{12}} + 4\frac{\nu_{21}}{E_{11}}.$$

The results of the theoretical calculations of the mechanical parameters of reinforced materials were compared with experimental data obtained with linearly reinforced specimens of various GFP. As a matrix we used an epoxide-phenol-butyral polymer ($E_s = 0.981 \cdot 0.25 \cdot 10^{10}$ newtons/m^2, $\nu_s = 0.37$), and the fiber consisted of aluminoborosilicate material. The continuous

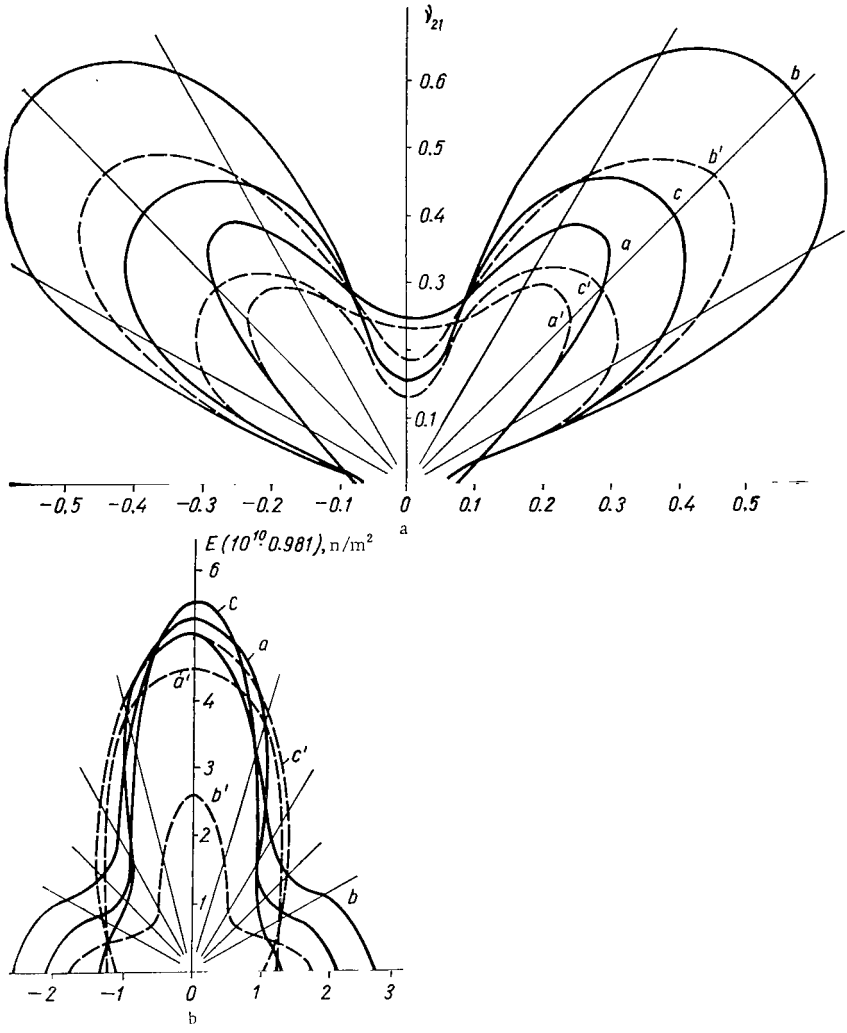

FIGURE II. 29. Dependence of the Poisson ratio (a) and Young's modulus (b) on the orientation angle of the fibers.

curves a, b, c on the polar diagrams (Figure II. 29) characterize the dependence of Young's modulus and the Poisson ratio in tension on the orientation angle of the glass fibers. These data were obtained from the above equations for linearly reinforced (curve a) and laminated GMF (the parameters of the latter material are easily expressed in terms of the linearly reinforced fibers if we assume that the cross sections are plane). The number of longitudinally reinforced layers expressed as a ratio of the number of transversely reinforced layers is 1 : 2 (curve b) or 1 : 4 (curve c). The dashed curves a', b', c' are plotted from experiments. The deviations found in the continuous and dashed curves are caused by some bending of the fibers, opening of fissures during the experiments, or other factors.

Bibliography

1. Van Fo Fy, G.A. Napryazhennoe i deformirovannoe sostoyanie sinteticheskikh materialov pri sdvige (Stressed and Strained States of Synthetic Materials in Shearing). — Prikladnaya Mekhanika, 1:5. 1965.
2. Van Fo Fy, G.A. and V.V. Klyavlin. K teorii stekloplastikov orientirovanno armirovannykh polymi voloknami. Inzhenernaya mekhanika polimerov i primenenie plastmass v promyshlennosti (The Theory of Hollow Orientated Glass-Fiber Reinforced Plastics. Engineering Mechanics of Polymers and Application of Plastics in Industry). Tbilisi, Metsniereba. 1969.
3. Klyavlin, V.V. Tsilindricheskaya obolochka odnonapravlenno armirovannaya polymi voloknami pri kruchenii v ploskosti armirovaniya (Cylindrical Shells Reinforced by Hollow Fibers in one Direction in Torsion in the Reinforcement Plane). — Prikladnaya Mekhanika, 5:5. 1969.
4. Van Fo Fy, G.A. Osnovnye sootnosheniya teorii orientirovannykh stekloplastikov s polymi voloknami (Fundamental Equations of the Theory of Oriented GFP). — Mekhanika Polimerov, 5. 1966.
5. Andrievskaya, G.D. Vysokoprochnye orientirovannye stekloplastiki (High-Strength GFP). Moskva, Nauka. 1967.
6. Van Fo Fy, G.A. and V.V. Klyavlin. Issledovanie zavisimosti mekhanicheskikh svoistv i vnutrennego polya napryazhenii pri sdvige ot vida mikrostruktury armirovannykh sred (Study of the Dependences of the Mechanical Properties and the Internal Stress Field during Shearing on the Microstructure of Reinforced Media). — Mekhanika Polimerov, 4. 1967.
7. Van Fo Fy, G.A. Uprugie postoyannye i teplovoe rasshirenie nekotorykh tel s neodnorodnoi regulyarnoi struktoroi (The Elastic Constants and Thermal Expansion of Some Bodies with an Inhomogeneous Regular Structure). — DAN SSSR, 166:4. 1966.
8. Akhiezer, I.I. Elementy teorii ellipticheskikh funktsii (Elements of the Theory of Elliptic Functions). Moskva, Gostekhizdat. 1948.
9. Muskhelishvili, N.I. Nekotorye osnovnye zadachi matematicheskoi teorii uprugosti (Some Fundamental Equations of the Mathematical Elasticity Theory). Moskva, Izdatel'stvo AN SSSR. 1954.
10. Van Fo Fy, G.A. Uprugie postoyannye i napryazhennoe sostoyanie steklolenty (Elasticity Constants and the Stressed State of Glass-Fiber Reinforced Tape). — Mekhanika Polimerov, 4. 1966.

Chapter III

VISCOELASTIC PROPERTIES OF REINFORCED MATERIALS

The inelastic properties of composite materials are caused by the inelasticity of the component and disturbances in the continuity of the material. If the stresses do not exceed a certain limit on long-term loading, we observe not only instantaneous elastic, but also viscoelastic deformations which progress with time and are almost completely reversible. The inelastic deformation is proportional to the applied stress, and depends on the microstructure of the material. The relationship between the stresses and strains in this region are determined by the equations of the linear theory of viscoelasticity.

The linear viscoelasticity theory is almost useless for studying the creep and stress relaxation processes in metals where this region is very narrow and near the elasticity limits. On the other hand, for polymer materials the linear theory gives results which agree with experimental data, provided that the stresses are not too large. This region is apparently of fundamental interest for evaluating moving constraints in GFP, where the inelastic deformations are caused mainly by undeveloped viscoelastic deformations of the polymer matrix (see Chapter I).

1. Viscoelastic properties of reinforced plastics in shear

Approximate expressions for the viscoelasticity operators of linearly reinforced materials and materials derived from them are obtained from simplified equations determining the dependence of the reduced elastic constants on the properties of the original components if the Volterra principle is applied /1/. According to this principle, the elastic constants are replaced by the integral viscoelasticity operators (see section 3 of Chapter I).

For composite materials in which the viscoelastic properties are caused by the matrix only, we have to carry out conversions of type

$$E_s \to E^*; \quad \nu_s \to \nu^*; \quad G_s \to G^*.$$

The compliance operator in transverse shear is

$$\frac{1}{G_{12}^*} \approx \frac{\gamma_1 + (1+\xi)\, G^*/G_a}{1 + \xi + \gamma_1 G^*/G_a} \cdot \frac{1}{G^*}.$$

For most of the known composites the operator established should be transformed, allowing for inequality $\left|\frac{G_\xi}{G_a}\right| \ll 1$. This considerably simplifies the equation, while the required accuracy is retained. The operators are transformed in accordance with the rules reported in section 3 of Chapter I. We shall transform operator

$$\frac{1}{1+\xi+\gamma_1 G^*/G_a} = \frac{1}{1+\xi+\gamma_1 G_0/G_a} \cdot \frac{1}{1-\frac{\gamma_1 a G_0/G_a}{1+\xi+\gamma_1 G_0/G_a} \Im^*_{1-\lambda}(-\omega_\infty - a)} =$$

$$= \frac{1}{1+\xi+\gamma_1 G_0/G_a}\left[1+\frac{\gamma_1 a G_0/G_a}{1+\xi+\gamma_1 G_0/G_a} \Im^*_{1-\lambda}\left(-\omega_\infty - \frac{a(1+\xi)}{1+\xi+\gamma_1 G_0/G_a}\right)\right],$$

where $a = \frac{3\omega_0}{2+2\nu_0}$, and (I. 37) and (I. 32) are taken into account. If the operator acts on a magnitude (unit) which is time independent, from (I. 30) we obtain

$$\frac{1}{1+\xi+\gamma_1 G^*/G_a} \cdot 1 \approx \frac{1}{1+\xi+\gamma_1 G_0/G_a}\left\{1+\frac{\gamma_1 a G_0/G_a}{(1+\xi)a+\omega_0(1+\xi+\gamma_1 G_0/Ga)}\left[1-\right.\right.$$

$$\left.\left. - \exp\left\{-(\lambda t)^\lambda\left(\omega_\infty + \frac{(1+\xi)a}{1+\xi+\gamma_1 G_0/G_a}\right)\right\}\right]\right\}.$$

If we consider the numerical values of the input parameters of GFP, we can find asymptotic estimates, according to which the given operators can be replaced by constants equal to the instantaneous elasticity, within the limits of the accuracy required.

Such estimates make it possible to obtain approximate values for the shear operators in the form

$$\frac{1}{G^*_{12}} \approx \frac{1}{G^0_{12}}[1+\Omega'\Im^*_{1-\lambda}(-\omega_\infty)];$$

$$G^*_{12} \approx G^0_{12}[1-\Omega'\Im^*_{1-\lambda}(-\omega_\infty-\Omega')]. \qquad \text{(III. 1)}$$

Here and later the superscripts "0" denote instantaneous elastic values, for example

$$G^0_{12} \approx G_0 \frac{1+\xi+\gamma_1 G_0/G_a}{\gamma_1+(1+\xi)G_0/G_a},$$

and also

$$\Omega' = \frac{a\gamma_1}{\gamma_1+(1+\xi)G_0/G_a}.$$

The operators (III. 1) make it possible to describe the creep and relaxation processes in longitudinal shear. Thus, the relaxation of the shearing stresses on nondeformational strain of a reinforced medium is governed by the law

$$\langle\sigma_{12}\rangle = G^*_{12}\langle\gamma_{12}\rangle = G^0_{12}\left[\langle\gamma_{12}\rangle - \Omega'\int_0^t dt'\Im_{1-\lambda}(-\omega_\infty-\Omega',\ t-t')\langle\gamma_{12}\rangle\right].$$

The approximate equations describing the time-dependent stress changes in the case of $\langle\gamma_{12}\rangle = \text{const}$ are determined by using approximations (see section 3 of Chapter I)

$$\langle\sigma_{12}\rangle \approx \langle\sigma_{12}^0\rangle \left\{1 - \frac{\Omega'}{\omega_\infty + \Omega'}\left[1 - e^{-(\omega_\infty + \Omega')(\lambda t)^\lambda}\right]\right\},$$

where $\langle\sigma_{12}^0\rangle$ is the stress applied at the initial moment of time. The creep modulus of longitudinal shear of the reinforced medium is obtained by transition to the limits ($t = \infty$) and the action of the modulus operator on the unit. The final form of the equation is

$$(G_{12})_{\text{CT}} \approx G_{12}^0 \frac{\iota_i + (1+\xi)\, G_0/G_a}{\eta_i (a + \omega_\infty) + \omega_\infty (1+\xi)\, G_0/G_a}\, \omega_\infty.$$

The modulus operator of transverse shear and the compliance operator are constructed analogously

$$\frac{1}{G_{23}^*} \approx \frac{1}{G_{23}^0}\left[1 + a\left(1 - \frac{\xi\eta\,(1 - G_0/G_a)^2\, b}{(\omega_0 - b)\,[\eta\varkappa_0 + (1+\xi\varkappa_0)\, G_0/G_a]}\right)\vartheta_{1-\lambda}^*(-\omega_\infty) + \right.$$
$$\left. + \frac{\xi\eta_i\,(1 - G_0/G_a)^2\, b}{\varkappa_0\eta_i + (1+\xi\varkappa_0)\, G_0/G_a}\left(\frac{\omega_0 - d}{\omega_0 - a - d}\right)\vartheta_{1-\lambda}^*(-\omega + d)\right]. \qquad \text{(III. 2)}$$

Here

$$\left.\begin{aligned} &\omega = \omega_0 + \omega_\infty; \quad \varkappa_0 = 3 - 4\nu_0; \\ &b = \frac{(\varkappa_0 - 1)\,\omega_0}{\varkappa_0 + \xi + \eta G_0/G_a}; \quad d = \frac{(\varkappa_0 - 1)\,\omega_0\,(\eta + \xi G_0/G_a)}{\eta\varkappa_0 + (1+\xi\varkappa_0)\, G_0/G_a}; \\ &G_{23}^* \approx G_{23}^0\left[1 - a\frac{\omega_0 - b - a}{\omega_0 - d - a}\vartheta_{1-\lambda}^*(-\omega_\infty - a) + \right. \\ &\left. + \frac{(d-b)\,(\omega_0 - d)}{\omega_0 - d - a}\vartheta_{1-\lambda}^*(-\omega + d)\right]. \end{aligned}\right\} \qquad \text{(III. 3)}$$

The operator of elastic heredity for GFP with hollow fibers is determined from the equations of section 3 Chapter I

$$\frac{1}{G_{12}^*} \approx \frac{1}{G_{12}^0}\left[1 + a\frac{a - \Omega_0}{a - \Omega_1}\vartheta_{1-\lambda}^*(-\omega_\infty) + \Omega_1\frac{\Omega_0 - \Omega_1}{a - \Omega_1}\vartheta_{1-\lambda}^*(-\omega_\infty - a + \Omega_1)\right];$$
$$G_{12}^* \approx G_{12}^0\left[1 - a\frac{\Omega_1}{\Omega_0}\vartheta_{1-\lambda}^*(-\omega_\infty - a) + (\Omega_0 - a)\left(1 - \frac{\Omega_1}{\Omega_0}\right)\times\right. \qquad \text{(III. 4)}$$
$$\left.\times\,\vartheta_{1-\lambda}^*(-\omega_\infty - a + \Omega_0)\right],$$

where

$$\Omega_0 = \frac{a\,(1+\xi)\,(1+q^2)\, G_0/G_a}{\eta\,(1-q^2) + (1+\xi)\,(1+q^2)\, G_0/G_a};$$
$$\Omega_1 = \frac{a\eta\,(1+q^2)\, G_0/G_a}{(1+\xi)\,(1-q^2) + \eta\,(1+q^2)\, G_0/G_a}.$$

The transverse shear operators of linearly reinforced GFP with hollow fibers are

$$\frac{1}{G_{23}^*} \approx \frac{1}{G_{23}^0}\left[1 + a\frac{\omega_0 - \beta}{\omega_0 - \beta_0}\vartheta_{1-\lambda}^*(-\omega_\infty) - (\beta - \beta_0)\left(1 - \frac{a}{\omega_0 - \beta_0}\right)\vartheta_{1-\lambda}^*(-\omega + \beta_0)\right];$$

$$G_{23}^{*} \approx G_{23}^{0}\left[1+(\beta-\beta_0)\frac{\omega_0-\beta}{\omega_0-a-\beta}\,\vartheta_{1-\lambda}^{*}(-\omega+\beta)-a\,\frac{\omega_0-a-\beta_0}{\omega_0-a-\beta}\times\right.$$
$$\left.\times\,\vartheta_{1-\lambda}^{*}(\omega_\infty-a)\right], \qquad \text{(III. 5)}$$

where

$$\beta=\omega_0\,\frac{\eta(1-q^2)+\xi(1+\varkappa_a q^2)\,G_0/G_a}{\eta(1-q^2)\varkappa_0+(1+\varkappa_a q^2)(1+\xi\varkappa_0)\,G_0/G_a}(\varkappa_0-1);$$

$$\beta_0=\frac{(\varkappa_0-1)(1-q^2)\,\omega_0}{(\varkappa_0+\xi)(1-q^2)+\eta(1+\varkappa_a q^2)\,G_0/G_a}.$$

2. Viscoelasticity of reinforced plastics in longitudinal and transverse tension

The approximate value of the operators of the modulus in longitudinal tension follows from (II. 54), where we need only the first two terms

$$E_{11}^{*} \approx E_{11}^{0}\left[1-\frac{\omega_0\gamma_1 E_0}{\xi E_a-\gamma_1 E_0}\,\vartheta_{1-\lambda}^{*}(-\omega)\right]. \qquad \text{(III. 6)}$$

For materials in which $\frac{E_0}{E_a} \ll 1$, as for instance in GFP, the correction introduced by the second term is only fractions of one percent. For this reason it can be said that in longitudinal tensions the creep deformations are small, and the material is elastic. The development of transverse effects is determined from the Poisson ratio operator

$$\nu_{21}^{*}=\nu_{31}^{*} \approx \nu_{21}^{0}\,[1+(\Omega_a-\Omega_b)\,\vartheta_{1-\lambda}^{*}(-\omega+\Omega_a)]. \qquad \text{(III. 7)}$$

Here

$$\Omega_a=\frac{\xi(\varkappa_0-1)\,\omega_0}{1+\gamma_1+\xi\varkappa_0+\eta(\varkappa_a-1)\,G_0/G_a};$$

$$\Omega_b=\omega_0(\varkappa_0-1)\,\frac{\xi\nu_a-\eta/4\,[2+(\varkappa_a-1)\,G_0/G_a]}{\xi\nu_a(\varkappa_0+1)+\eta\nu_0[2+(\varkappa_a-1)G_0/G_a]}.$$

The Poisson ratio in creep is determined by letting t approach infinity

$$(\nu_{21})_{cr} \approx \nu_{21}^{0}\,\frac{\omega-\Omega_b}{\omega-\Omega_a}.$$

For GFP (with EMA matrix) by calculation we obtain

$$\nu_{21}^{0}=0.24; \quad (\nu_{21})_{cr} \approx 1.05\nu_{21}^{0}.$$

The viscoelastic properties of media with a hexagonal structure in tension are characterized by the modulus operator $E_{22}^{*}=E_{33}^{*}$. The approximate values of the inverse operators are

$$\frac{1}{E_{22}^{*}} \approx \frac{1}{E_{22}^{0}}[1+A_1\vartheta_{1-\lambda}^{*}(-\omega_\infty)+A_2\vartheta_{1-\lambda}^{*}(-\omega+\Omega_a)+A_3\vartheta_{1-\lambda}^{*}(-\omega+b)], \qquad \text{(III. 8)}$$

where the symbols b and Ω_a are given above:

$$A_1 = \frac{2aE_{22}^0}{8G_0}\left(\frac{2+(\varkappa_a-1)\,G_0/G_a}{1+\eta+\xi\varkappa_0+\eta\,(\varkappa_a-1)\,G_0/G_a}\cdot\frac{\omega_0}{\omega_0-\Omega_a}-\frac{2\xi\,(1-G_0/G_a)}{\xi+\varkappa_0+\eta G_0/G_a}\cdot\frac{\omega_0}{\omega_0-b}\right);$$

$$A_2 = \frac{(\varkappa_0+1)\,E_{22}^0}{8G_0}\cdot\frac{2+(\varkappa_a-1)\,G_0/G_a}{1+\eta+\xi\varkappa_0+\eta\,(\varkappa_a-1)\,G_0/G_a}\left(\frac{a\,(\varkappa_0-1)^2}{b\,(\varkappa_0+1)}+\right.$$

$$\left.+\Omega_a-\frac{2a}{\varkappa_0+1}\cdot\frac{\Omega_a}{\omega_0-\Omega_a}\right);$$

$$A_3 = \frac{(\varkappa_0+1)\,E_{22}^0}{8G_0}\cdot\frac{2\xi\,(1-G_0/G_a)}{\xi+\varkappa_0+\eta G_0/G_a}\left(\frac{2a}{\varkappa_0+1}\cdot\frac{b}{\omega_0-b}-b-\frac{(\varkappa_0-1)^2}{\varkappa_0+1}\cdot\frac{a}{b}\right).$$

The modulus operator in transverse tension is

$$E_{22}^* \approx E_{22}^0\left[1+\sum_{k=1}^{3}B_k\vartheta_{1-\lambda}^*(C_k)\right], \qquad \text{(III. 9)}$$

where C_k $(k=1,\ 2,\ 3)$ are the roots of

$$1+\frac{A_1}{\omega_\infty+C}+\frac{A_2}{\omega-\Omega_a+C}+\frac{A_3}{\omega-b+C}=0,$$

while the coefficients B_k are determined from

$$\sum_{k=1}^{3}\frac{B_k}{\omega_\infty+C_k}=1;\quad \sum_{k=1}^{3}\frac{B_k}{\omega-\Omega_a+C_k}=1;\quad \sum_{k=1}^{3}\frac{B_k}{\omega-b+C_k}=1.$$

The reduction in area of the fibers in longitudinal tension is determined from

$$\nu_{12}^* \approx \nu_{12}^0\left[1+\sum_{k=1}^{3}B_k\frac{C_k+\omega-\Omega_0}{C_k+\omega-\Omega_a}\vartheta_{1-\lambda}^*(C_k)\right]. \qquad \text{(III. 10)}$$

The operator characterizing the reduction in area of the medium in the longitudinal plane is determined from

$$\frac{\nu_{23}^*}{E_{22}^*}=\frac{\nu_{21}^0}{E_{22}^0}[1+Q_1\vartheta_{1-\lambda}^*(-\omega_\infty)+Q_2\vartheta_{1-\lambda}^*(-\omega+\Omega_a)+Q_3\vartheta_{1-\lambda}^*(-\omega+b)]. \qquad \text{(III. 11)}$$

Here

$$Q_1=-\frac{E_{22}^0}{\nu_{23}^0}\left(\frac{A_1}{E_{22}^0}-\frac{a}{2G_0}+\frac{a\xi\omega_0\,(1-G_0/G_a)}{G_0\,(\omega_0-b)\,(\varkappa_0+\xi+\eta G_0/G_a)}\right);$$

$$Q_2\equiv\frac{A_2}{\nu_{23}^0};$$

and

$$Q_3\equiv\frac{E_{22}^0}{\nu_{23}^0}\left[\frac{A_3}{E_{22}^0}+\frac{\xi\,(\varkappa_0+1)\,(1-G_0/G_a)}{2G_0\,(\varkappa_0+\xi+\eta G_0/G_a)}\left(b-\frac{2ab}{(\varkappa_0+1)\,(\omega_0-b)}+\frac{(\varkappa_0-1)^2\,a}{6\,(\varkappa_0+1)}\right)\right].$$

The other symbols have been explained above.

The modulus operator in longitudinal tension of the medium reinforced by hollow fibers is

$$E_{11}^* \approx E_{11}^0\left[1-\frac{\omega_0\eta E_0}{E_{11}^0}\vartheta_{1-\lambda}^*(-\omega)\right]. \qquad \text{(III. 12)}$$

The development of transverse effects in these areas in longitudinal tension is determined by means of the operator

$$\nu_{21}^{*} \approx \nu_{21}^{0}[1 + (\Pi_a - \Pi_b)\,\vartheta_{1-\lambda}^{*}(-\omega + \Pi_a)], \qquad \text{(III. 13)}$$

where

$$\Pi_a = \frac{(1-q^2)\,\xi\,(\varkappa_0 - 1)\,\omega_0}{(1-q^2)(1+\eta+\xi\varkappa_0) + \eta(\varkappa_a - 1 + 2q^2)\,G_0/G_a};$$

$$\Pi_b = \omega_0(\varkappa_0 - 1)\,\frac{(1-q^2)\,\xi\nu_a - \eta/4\,[2(1-q^2) + (\varkappa_a + 1 - 2q^2)\,G_0/G_a]}{(1-q^2)\,\xi\nu_a(\varkappa_0+1) + \eta\nu_0\,[2(1-q^2) + (\varkappa_a + 1 + 2q^2)G_0/G_a]}.$$

In transverse tension of materials with hollow fibers the viscoelastic properties are determined by means of the operator

$$\frac{1}{E_{22}^{*}} \approx \frac{1}{E_{22}^{0}}[1 + I_1\vartheta_{1-\lambda}^{*}(-\omega_\infty) + I_2\vartheta_{1-\lambda}^{*}(-\omega + \Pi_a) + I_3\vartheta_{1-\lambda}^{*}(-\omega + \beta_0)];$$

$$E_{22}^{*} \approx E_{22}^{0}\Big[1 + \sum_{k=1}^{3}\varepsilon_k\vartheta_{1-\lambda}^{*}(g_k)\Big], \qquad \text{(III. 14)}$$

where

$$I_1 = \frac{2aE_{22}^{0}}{8G_a}\Big[\frac{2(1-q^2) + (\varkappa_0 - 1 + 2q^2)\,G_0/G_a}{(1-q^2)(1+\eta+\xi\varkappa_0) + \eta(\varkappa_a - 1 + 2q^2)\,G_0/G_a}\cdot\frac{\omega_0}{\omega_0 - \Pi_a} -$$
$$- \frac{2\xi[1-q^2-(1+\varkappa_a q^2)\,G_0/G_a]}{(1-q^2)(\xi+\varkappa_0) + \eta(1+\varkappa_a q^2)\,G_0/G_a}\cdot\frac{\omega_0}{\omega_0 - \beta_0}\Big];$$

$$I_2 = \frac{E_{22}^{0}(\varkappa_0+1)}{8G_0}\cdot\frac{2(1-q^2) + (\varkappa_0 - 1 + 2q^2)\,G_0/G_a}{(1-q^2)(1+\eta+\xi\varkappa_0) + \eta(\varkappa_a - 1 + 2q^2)\,G_0/G_a}\Big[\frac{(\varkappa_0-1)^2}{\varkappa_0+1}\cdot\frac{a}{b} +$$
$$+ \Pi_a - \frac{2a}{\varkappa_0+1}\cdot\frac{\Pi_a}{\omega_0 - \Pi_a}\Big];$$

$$I_3 = \frac{E_{22}^{0}(\varkappa_0+1)}{8G_0}\cdot\frac{2\xi[1-q^2-(1+\varkappa_a q^2)\,G_0/G_a]}{(1-q^2)(\xi+\varkappa_0) + \eta(1+\varkappa_a q^2)\,G_0/G_a}\Big[\frac{2a}{\varkappa_0+1}\cdot\frac{\beta_0}{\omega_0 - \beta_0} -$$
$$- \beta_0 - \frac{(\varkappa_0-1)^2}{\varkappa_0+1}\cdot\frac{a}{b}\Big].$$

Parameters g_k are determined from the roots of the algebraic equation

$$1 + \frac{I_1}{\omega_\infty + g} + \omega - \frac{I_2}{\Pi_a + g} + \frac{I_3}{\omega - \beta_0 + g} = 0,$$

while constants ε_k are solutions of the following system of equation:

$$\sum_{k=1}^{3}\frac{\varepsilon_k}{\omega_\infty + g_k} = 1; \quad \sum_{k=1}^{3}\omega - \frac{\varepsilon_k}{\Pi_a - g_k} = 1; \quad \sum_{k=1}^{3}\omega - \frac{\varepsilon_k}{\beta_0 + g_k} = 1.$$

The time-dependent longitudinal reduction in area in transverse tension of a medium reinforced with hollow fibers is determined by means of the operator

$$\nu_{12}^{*} = \nu_{12}^{0}\Big[1 + \sum_{k=1}^{3}\varepsilon_k\frac{g_k + \omega - \Pi_b}{g_k + \omega - \Pi a}\,\vartheta_{1-\lambda}^{*}(g_k)\Big]. \qquad \text{(III. 15)}$$

The transverse effects of GFP with hollow fibers in transverse tension are found from

$$\frac{\nu_{23}^{*}}{E_{22}^{*}} \approx \frac{\nu_{23}^{0}}{E_{22}^{0}}[1 + L_1\vartheta_{1-\lambda}^{*}(-\omega_\infty) + L_2\vartheta_{1-\lambda}^{*}(-\omega + \Pi_a) + L_3\vartheta_{1-\lambda}^{*}(-\omega + \beta_0)], \qquad \text{(III. 16)}$$

where the following new symbols are introduced:

$$L_1 = -\frac{E_{22}^0}{\nu_{23}^0}\left[\frac{I_1}{E_{22}^0} - \frac{a}{2G_0} + \frac{a\xi\omega_0\,[1-q^2-(1+\varkappa_a q^2)\,G_0/G_a]}{G_0\,(\omega_0-\beta_0)\,[(1-q^2)\,(\varkappa_0+\xi)+\eta\,(1+\varkappa_a q^2)\,G_0/G_a]}\right];$$

$$L_2 = -\frac{I_2}{\nu_{23}^0};$$

$$L_3 = -\frac{E_{22}^0}{\nu_{23}^0}\left[\frac{I_3}{E_{22}^0} + \frac{\xi\,(\varkappa_0+1)\,[1-q^2-(1+\varkappa_a q^2)\,G_0/G_a]}{2G_0\,[(1-q^2)\,(\varkappa_0+\xi)+\eta(1+\varkappa_a q^2)G_0/G_a]}\left(\beta_0 - \frac{2a\beta_0}{(\varkappa_0+1)(\omega_0-\beta_0)} + \right.\right.$$

$$\left.\left. + \frac{(\varkappa_a-1)^2\,a}{6\,(\varkappa_0+1)}\right)\right].$$

In the limiting case ($q = 0$) these equations are converted to equations for solid fibers.

3. Fundamental equations on the viscoelasticity theory of linearly reinforced plastics

The integral operators of the viscoelasticity theory are used to find relationships between the average deformations and the reduced stresses. The operators are very dependent on the orientation of the elastic fillers. If an accuracy of within $\pm 10-15\%$ is sufficient, some operators can be replaced by the elastic constants in materials of hexagonal structure (in other words, in certain areas creep and stress relaxation processes can be neglected). In this approximation we assume that

$$\left.\begin{aligned}
\langle\varepsilon_{11}\rangle &= \frac{1}{E_{11}}\langle\sigma_{11}\rangle - \frac{\nu_{21}}{E_{11}}\langle\sigma_{22}\rangle - \frac{\nu_{21}}{E_{11}}\langle\sigma_{23}\rangle, \qquad \langle\gamma_{12}\rangle = \frac{1}{G_{12}^*}\langle\sigma_{12}\rangle;\\
\langle\varepsilon_{22}\rangle &= -\frac{\nu_{21}}{E_{11}}\langle\sigma_{11}\rangle + \frac{1}{E_{22}^*}\langle\sigma_{22}\rangle - \frac{\nu_{23}^*}{E_{22}^*}\langle\sigma_{33}\rangle, \quad \langle\gamma_{13}\rangle = \frac{1}{G_{12}^*}\langle\sigma_{13}\rangle;\\
\langle\varepsilon_{33}\rangle &= -\frac{\nu_{21}}{E_{11}}\langle\sigma_{11}\rangle - \frac{\nu_{23}^*}{E_{22}^*}\langle\sigma_{22}\rangle + \frac{1}{E_{22}^*}\langle\sigma_{33}\rangle, \quad \langle\gamma_{23}\rangle = 2\frac{1+\nu_{23}^*}{E_{22}^*}\langle\sigma_{23}\rangle.
\end{aligned}\right\} \qquad \text{(III. 17)}$$

The creep and stress relaxation phenomena are described in this approximation by three independent operators only, that is linearly reinforced materials with elastic fibers display anisotropic viscoelastic properties. Equations (III. 17) are suitable for expressing creep in reinforced plastics. To study stress relaxation the reduced stresses are expressed in terms of strain.

For an experimental estimation of the anisotropic effects of the viscoelastic properties of reinforced plastics, we studied the creep of specimens tensioned at various angles to the glass fiber orientation. Figure III. 1, a shows the creep curves for GFP along various (filler) orientations for different stress levels at room temperature. Curves 1, 2, 3, 4, and 5 were plotted at stresses $\sigma = 0.981 \cdot 50 \cdot 10^7$ newtons/m^2 — $0.981 \cdot 90 \cdot 10^7$ newtons/m^2 (the interval between the individual stress levels was $0.981 \cdot 10 \cdot 10$ newtons/m^2). The creep deformations in tension in the direction of fiber orientation were small, and their limiting values were reached after a short time. Therefore, the material in these areas can be considered as being elastic. A certain creep at the initial moments of time can be

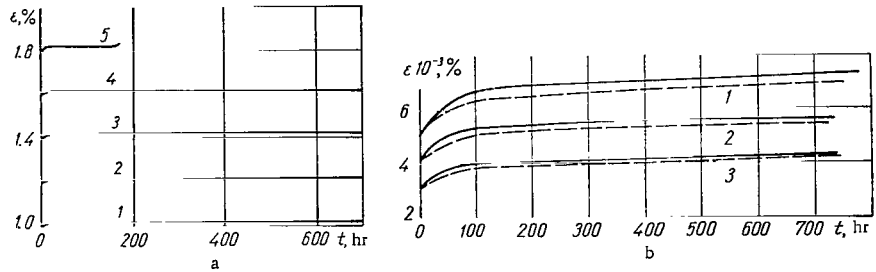

FIGURE III. 1. Creep curves for GFP along (a) and across (b) the filler orientation for different stress levels at room temperature.

explained by the matrix inelasticity, stress redistribution, and bending and other effects. Figure III. 1, b shows the creep curves of GFP in a direction perpendicular to the fiber orientations for $\sigma_3 = 0.981 \cdot 35 \cdot 10^5$ newtons/m^2, $\sigma_2 = 0.981 \cdot 50 \cdot 10^5$ newtons/m^2 and $\sigma_1 = 0.981 \cdot 60 \cdot 10^5$ newtons/m^2. The continuous curves were obtained from experimental data, and the dashed curves were calculated from

$$\langle \varepsilon_{22} \rangle = \langle \varepsilon_{22}^0 \rangle [1 + A_1 \Im_{1-\lambda}^* (-\omega_\infty) + A_2 \Im_{1-\lambda}^* (-\omega + \Omega_a) + A_3 \Im_{1-\lambda}^* (-\omega + b)] 1,$$

where the values of the instantaneous elastic deformations $\langle \varepsilon_{22}^0 \rangle$ were taken from experimental data. Because of the low strength of the material in transverse tension, the instantaneous elastic deformations selected in the experiments were sufficiently small.

The operator equations found for the main areas of the reinforced medium make it possible to study the viscoelastic properties, since on rotation of the coordinate system these operators are transformed as the components of a tensor of the fourth rank (see section 18 of Chapter II). Thus, for example, the creep deformation of material at a constant tensile stress under an angle φ to the fiber orientation is /2/

$$\langle \varepsilon_{\varphi\varphi} \rangle \approx \langle \varepsilon_{\varphi\varphi}^0 \rangle \left[\cos^4 \varphi + \left(\frac{E_{11}}{G_{12}^*} - 2\nu_{21} \right) \cos^2 \varphi \sin^2 \varphi + \frac{E_{11}}{E_{22}^*} \sin^4 \varphi \right].$$

When $\varphi = 0$ only elastic deformations arise in the material (for the given approximation), and when $\varphi = \frac{\pi}{2}$, inelastic deformations reach their maximum.

The viscoelastic properties of crosswise reinforced structures are found from the data of linearly reinforced materials.

4. Elastic heredity of multicomponent materials

We shall consider a multicomponent material with p kinds of fibers distributed over its microsection. The material has a single matrix and the material structure is hexagonal. The operator of elastic heredity is constructed by means of the Volterra principle, and simplified equations for the reduced parameters of the multicomponent reinforced material.

If the matrix is viscoelastic and the filler elastic, the compliance operator in longitudinal shear is

$$\frac{1}{G_{12}^*} \approx \frac{1}{G_{12}^0}\left[1 + a\left(1 - \sum_{j=1}^{p} \frac{x_j}{\alpha_j + \omega_\infty}\right) \Im_{1-\lambda}^*(-\omega_\infty) + \right.$$
$$\left. + \sum_{j=1}^{p} x_j \left(1 + \frac{a}{\alpha_j + \omega_\infty}\right) \Im_{1-\lambda}^*(\alpha_j)\right]. \qquad \text{(III. 18)}$$

Here

$$x_j = \alpha_j^* \left(1 - \sum_{k=1}^{p} \frac{\tau_k}{\alpha_j + \omega_\infty + \frac{a}{1 + G_0/G_k}}\right),$$

where

$$\tau_k = \frac{2a\xi_k G_0/G_k}{(1 + G_0/G_k)^2 \left(\eta + \sum_{k=1}^{p} \frac{2\xi_k G_0/G_k}{1 + G_0/G_k}\right)}.$$

Here $\alpha_j (j = 1, \ldots, p)$ are the roots of the algebraic equation

$$1 + \sum_{k=1}^{p} \frac{\lambda_k}{\omega_\infty + \frac{a}{1 + G_0/G_k} + \alpha_k} = 0,$$

where

$$\lambda_k = \frac{2a\xi_k G_0/G_k}{(1 + G_0/G_k)^2 \left(\eta + \sum_{k=1}^{p} \frac{2\xi_k}{1 + G_0/G_k}\right)},$$

while the constants α_k^* are found from the system

$$1 - \sum_{k=1}^{p} \frac{\alpha_k^*}{\omega_\infty + \frac{a}{1 + G_0/G_j} + \alpha_k} = 0 \quad (j = 1, 2, \ldots, p).$$

The modulus operator in longitudinal shear is

$$G_{12}^* \approx G_{12}^0 \left[1 - a\left(1 - \sum_{j=1}^{p} \frac{y_j}{\omega_\infty + a + \rho_j}\right) \Im_{1-\lambda}^*(-\omega_\infty - a) + \right.$$
$$\left. + \sum_{j=1}^{p} y_j \frac{\omega_\infty + \rho_j}{\omega_\infty + a + \rho_j} \Im_{1-\lambda}^*(\rho_j)\right]. \qquad \text{(III. 19)}$$

The operators introduced are found from

$$y_j = k_j \left(1 + \sum_{k=1}^{p} \frac{\lambda_k}{\omega_\infty + \frac{a}{1 + G_0/G_k} + \rho_j}\right),$$

where ρ_j are the roots of

$$1 - \sum_{k=1}^{p} \frac{\tau_k}{\omega_\infty + \dfrac{a}{1 + G_0/G_k} - \rho} = 0,$$

while constants k_j are determined from p equations of type

$$1 - \sum_{j=1}^{p} \frac{k_j}{\omega_\infty + \dfrac{a}{1 + G_0/G_k} + \rho_j} = 0.$$

The compliance operator of a multicomponent material in transverse shear can be given as the sum of operators

$$\frac{1}{G_{23}^*} \approx \frac{1}{G_{23}^0}\left[1 - a\left(1 - \sum_{j=1}^{p} \frac{N_j}{\mu_j + \omega_\infty}\right) \Im_{1-\lambda}^*(-\omega_\infty) + \right.$$
$$\left. + \sum_{j=1}^{p} N_j \left(1 + \frac{a}{\mu_j + \omega_\infty}\right) \Im_{1-\lambda}^*(\mu_j)\right]. \qquad \text{(III. 20)}$$

Here

$$N_j = S_j\left(1 - \sum_{k=1}^{p} \frac{r_k}{\mu_j + \omega - \delta_k}\right),$$

where μ_j are the roots of

$$1 + \sum_{k=1}^{p} \frac{P_k}{\omega + \mu - \delta_k} = 0,$$

while the constants S_j introduced satisfy a simultaneous system of p equations

$$1 + \sum_{j=1}^{p} \frac{S_j}{\delta_k - \omega - \mu_j} = 0 \quad (k = 1, \ldots, p).$$

Above, we adopted the following symbols for the abbreviated forms of the equations

$$P_k = \frac{\xi_k \delta_k \dfrac{1 - G_0/G_k}{\varkappa + G_0/G_k}}{1 + \sum_{k=1}^{p} \xi_k \dfrac{1 - G_0/G_k}{\varkappa_0 + G_0/G_k}}; \quad \delta_k = \frac{\varkappa_0 - 1}{\varkappa_0 + G_0/G_k}\omega_0;$$

$$r_k = \frac{\xi_k \varkappa_0 \left(\delta_k - \dfrac{\varkappa_0 - 1}{\varkappa_0}\omega_0\right) \dfrac{1 - G_0/G_k}{\varkappa_0 + G_0/G_k}}{1 + \sum_{j=1}^{p} \xi_j \varkappa_0 \dfrac{1 - G_0/G_j}{\varkappa_0 + G_0/G_j}}.$$

The modulus operator of transverse shear is

$$G_{23}^{*} \approx G_{23}^{0}\left[1 - a\left(1 - \sum_{j=1}^{p} \frac{U_j}{\varepsilon_j + \omega_\infty + a}\right) \Im_{1-\lambda}^{*}(-\omega_\infty - a) + \right.$$

$$\left. + \sum_{j=1}^{p} U_j \frac{\varepsilon_j + \omega_\infty}{\varepsilon_j + \omega_\infty + a} \Im_{1-\lambda}^{*}(\varepsilon_j)\right]. \qquad \text{(III. 21)}$$

Here

$$U_j = Z_j\left(1 + \sum_{k=1}^{p} \frac{p_k}{\varepsilon_j + \omega - \delta_k}\right).$$

The values ε_j are found from the roots of

$$1 + \sum_{j=1}^{n} \frac{r_j}{\delta_j - \omega - \varepsilon} = 0 \quad (j = 1, \ldots, p).$$

The constants Z_j satisfy the following system

$$1 - \sum_{j=1}^{p} \frac{Z_j}{\omega - \delta_k + \varepsilon_j} = 0 \quad (k = 1, \ldots, p).$$

The transverse reduction in area of the multicomponent material in longitudinal tension is given by operator

$$\nu_{21}^{*} \approx \nu_{21}^{0}[1 + (v + w)\,\Im_{1-\lambda}^{*}(-\omega + v)], \qquad \text{(III. 22)}$$

where

$$v = \frac{\sum_{k=1}^{p} \omega_0 (\varkappa_0 - 1) f_k}{\eta + \sum_{k=1}^{p} (\varkappa_0 + 1) f_k}; \quad w = (\varkappa_0 - 1)\,\omega_0 \frac{\eta/4 - \sum_{k=1}^{p} \nu_k f_k}{\nu_0 \eta + \sum_{k=1}^{p} \nu_k f_k (\varkappa_0 + 1)};$$

$$f_k = \frac{\xi_k}{2 + (\varkappa_k - 1)\, G_0/G_k}.$$

The modulus operator in longitudinal tension

$$E_{11}^{*} \approx E_{11}^{0}\left[1 - \frac{\omega_0 \eta_1 E_0}{E_{11}^{0}} \Im_{1-\lambda}^{*}(-\omega)\right]. \qquad \text{(III. 23)}$$

For fibers which are more rigid than the matrix $\left(\frac{E_k}{E_0} \gg 1\right)$ the coefficient before the operator is very small and can frequently be neglected.

The inelastic properties in transverse tension are described by operator

$$\frac{1}{E_{22}^{*}} \approx \frac{1}{E_{22}^{0}}\left[1 + W_1 \Im_{1-\lambda}^{*}(-\omega_\infty) + W_2 \Im_{1-\lambda}^{*}(-\omega + v) + W_3 \Im_{1-\lambda}^{*}(-\omega) + \sum_{j=1}^{p} T_j \Im_{1-\lambda}^{*}(\sigma_j)\right]. \qquad \text{(III. 24)}$$

In this equation

$$W_1 = E_{22}^{0}\left[\frac{2a}{\varkappa_0 + 1} \cdot \frac{\omega_0}{\omega_0 - v} - \frac{h}{2G_0(1 + h)}\left(1 - \sum_{j=1}^{p} \frac{V_j}{\omega_\infty + \sigma_j}\right)\right];$$

$$W_2 = \frac{(\varkappa_0+1)E_{22}^0}{8G_0\left(\eta+\sum_{k=1}^{p}\frac{(\varkappa_0+1)\xi_k}{2+(\varkappa_k-1)G_0/G_k}\right)}\left[\frac{(\varkappa_0-1)^2}{(\varkappa_0+1)}\cdot\frac{a}{b}+\upsilon-\frac{\upsilon}{\omega_0-\upsilon}\cdot\frac{2a}{\varkappa_0+1}\right];$$

$$W_3 = -\frac{(\varkappa_0-1)^2E_{22}^0}{24G_0}\cdot\frac{ah}{1+h}\left(1-\sum_{j=1}^{p}\frac{V_j}{\omega_\infty+\sigma_j}\right),\quad h=\sum_{k=1}^{p}\frac{\xi_k(1-G_0/G_k)}{\varkappa_0+G_0/G_k};$$

$$T_j = -\frac{(\varkappa_0+1)E_{22}^0}{4G_0}\cdot\frac{h}{1+h}V_j\left(1+\frac{2a}{\varkappa_0+1}\cdot\frac{1}{\omega_\infty+\sigma_j}+\frac{(\varkappa_0-1)^2}{\varkappa_0+1}\cdot\frac{a/6}{\omega_\infty+\sigma_j}\right),$$

where

$$V_j = Y_j\left(1+\sum_{k=1}^{n}\frac{F_k}{\sigma_j+\omega-\delta_k}\right);\quad F_k=\frac{1}{h}\cdot\frac{\delta_k\xi_k(1-G_0/G_k)}{\varkappa_0+G_0/G_k}.$$

Parameters Y_j are determined from the solution of system

$$1-\sum_{j=1}^{p}\frac{Y_j}{\omega-\sigma_j}=0,$$

where $\sigma_j - j$ is the j-th root of

$$1+\sum_{k=1}^{p}\frac{\delta_k\xi_k(1-G_0/G_k)}{(\omega-\delta_k+\sigma)(\varkappa_0+G_0/G_k)}\cdot\frac{1}{1+h}=0.$$

The formula for E_{22}^* is analogously introduced. Because it is very long and can be derived with comparative ease, we shall not report it here.

The effect of the moving constraints of the matrix on the time-dependent changes in the lateral reduction in area in tension in the plane perpendicular to fiber orientation is determined by means of the operator

$$\frac{\nu_{23}^*}{E_{22}^*}=\frac{\overset{0}{\nu}_{23}}{E_{22}^0}[1+S_1\Im_{1-\lambda}^*(-\omega_\infty)+S_2\Im_{1-\lambda}^*(-\omega)+$$
$$+S_3\Im_{1-\lambda}^*(-\omega+\upsilon)+\sum_{j=1}^{p}B_j\Im_{1-\lambda}^*(\sigma_j)]. \qquad \text{(III. 25)}$$

Here

$$S_1=\frac{E_{22}^0}{\overset{0}{\nu}_{23}}\left[\frac{a}{4G_0}\left(1+\frac{1-\eta-l}{(\upsilon-\omega_0)[\eta+(\varkappa_0-1)l]}\right)-\frac{2h}{1+h}\left(1-\sum_{j=1}^{p}\frac{V_j}{\sigma_j+\omega_\infty}\right)\right];$$

$$S_2=\frac{(\varkappa_0+1)E_{22}^0}{8\overset{0}{\nu}_{23}G_0}\left\{\omega_0-a+(\varkappa_0+1)\frac{a}{6}\left[\frac{l\omega_0}{\upsilon}\cdot\frac{\varkappa_0-1}{\eta+(\varkappa_0-1)l}-\right.\right.$$
$$\left.\left.-\frac{2h}{1+h}\left(1-\sum_{j=1}^{p}\frac{V_j}{\sigma_j+\omega_\infty}\right)\right]\right\};$$

$$S_3=\frac{(\varkappa_0+1)E_{22}^0}{8\overset{0}{\nu}_{23}G_0}\left(\upsilon-\frac{l\omega_0(\varkappa_0-1)}{1-\eta-l}\right)\left[\frac{1-\eta-l}{\eta+(\varkappa_0-1)l}\left(1+\right.\right.$$
$$\left.\left.+\frac{2a}{(\varkappa_0+1)(\upsilon-\omega_0)}\right)+\frac{(\varkappa_0-1)^2}{\varkappa_0+1}\cdot\frac{a}{6\upsilon}\right];$$

$$B_j=-\frac{\varkappa_0+1}{8\overset{0}{\nu}_{23}G_0}\cdot\frac{2E_{22}^0V_jh}{1+h}\left[1+\frac{2a}{(\varkappa_0+1)(\sigma_j+\omega_\infty)}+\frac{(\varkappa_0-1)^2a/6}{(\varkappa_0+1)(\sigma_j+\omega)}\right];$$

$$l=\sum_{k=1}^{p}\frac{\xi_k}{2+(\varkappa_k-1)G_0/G_k}.$$

TABLE III. 1. Composite parameters

Components of composite	E, n/m^2	G, n/m^2	ω_0, $\eta^{-\lambda}$	ω_∞, $\eta^{-\lambda}$	λ	η	ξ_1	ξ_2
Matrix	$9.8 \cdot 10^9$	$3.5 \cdot 10^9$	0.153	0.734	0.5	0.5	–	–
I Reinforced element	$17.35 \cdot 10^9$	$6.67 \cdot 10^9$	0.286	1.05	0.5	–	0.3	–
II Reinforced element	$16.7 \cdot 10^9$	$7.26 \cdot 10^9$	–	–	–	–	–	0.2

If the fiber elements have elastic properties also, the type of the operators becomes more complicated, and the equations are then cumbersome. Since the building up of operators of elastic heredity does not involve any difficulties, these operators will not be reported here. As an illustration we shall discuss the changes in the moving constraints for a three-component material. We will study two cases: a) when only the matrix shows moving constraints; b) when the matrix and one of the reinforcing components are inelastic.

The parameters of the composites studied are shown in Table III. 1.

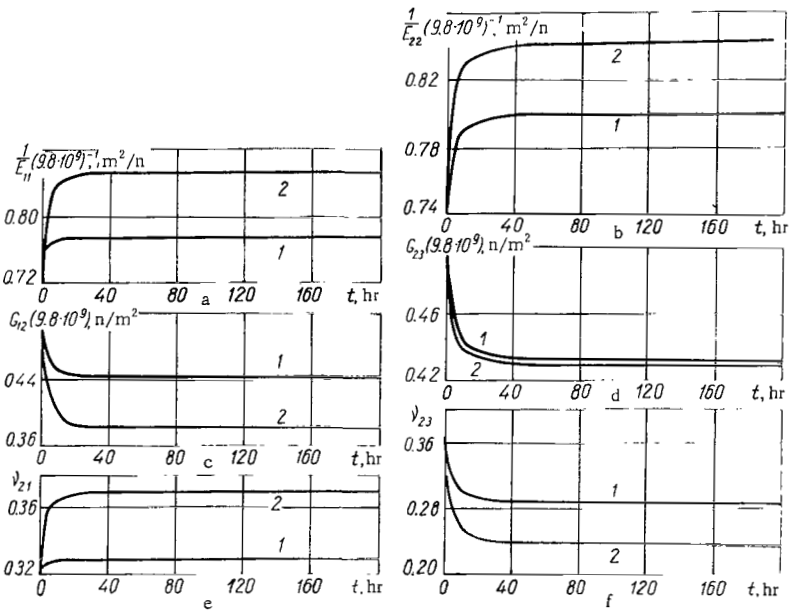

FIGURE III. 2. Time dependence of the compliances in longitudinal (a) and transverse (b) tension.

The curves illustrating the time-dependent changes in parameters $(E_{11}^*)^{-1} \cdot 1$; $(E_{22}^*)^{-1} \cdot 1$; $G_{12}^* \cdot 1$; $G_{23}^* \quad 1$; $\nu_{21}^* \cdot 1$; $\nu_{23}^* \cdot 1$ are shown in Figure III. 2, a, b, c, d, e, f, where 1 and 2 are the curves for the first and second composites, respectively.

Bibliography

1. Rabotnov, Yu. P. Polzuchest' elementov konstruktsii (Creep of Constructional Elements). Moskva, Nauka. 1966.
2. Van Fo Fy, G. A. K teorii anizotropnoi polzuchesti steklolenty (The Theory of Anisotropic Creep of a Glass-Fiber Reinforced Tape). — Mekhanika Polimerov, 2. 1965.

Chapter IV

THERMAL CONDUCTIVITY AND DIFFUSION WITH ABSORPTION

The pattern of the heat transfer process between the components of the reinforced material depends on their interfacial area. If on the interface of materials with differing thermophysical properties an ideal thermal contact exists, the temperature of the individual bodies and the heat flux between them must be continuous functions. Otherwise, we generally use the concept of contact thermal resistance on the fiber-matrix interface. Heat fluxes are equal even if the conditions of contact are imperfect, but the condition of the continuous temperature field is replaced by the condition that the temperature difference between the components is proportional to the heat flux supplied.

A complete picture of the thermal conductivity in reinforced materials is obtained by studying the temperature distribution in the microstructures when the longitudinal and transverse heat fluxes change slightly. In this case the reduced thermal conductivity coefficients are expressed in terms of the thermophysical parameters of the components.

Matter is transferred in reinforced materials as a result of the concentrational difference in the diffusing particles in adjacent volumes. If the particles diffuse in a nonabsorbing medium, the effective diffusion parameters are determined in the same way as the reduced thermal conductivity coefficients. In absorbing media the reduced parameters are found by more complicated parameters.

1. Thermal conductivity of composites with solid and hollow fibers in transverse heat flux

We shall consider a composite fiber with a simple (hexagonal or tetragonal) structure formed by continuous, straight circular fibers when the transverse heat flux is constant in time. If no longitudinal heat flux along the fiber orientation is present, the temperature T of each component will, in accordance with (I.49), satisfy the Laplace operator

$$\nabla^2 T = \frac{\partial^2 T}{\partial x_2^2} + \frac{\partial^2 T}{\partial x_3^2} = 0. \qquad \text{(IV.1)}$$

It is assumed that the axes of Cartesian coordinates $(0x_2,\ 0x_3)$ are perpendicular to the fiber orientation and no internal thermal source is present.

The solution of (IV. 1) is obtained from the complex variables theory as (see Chapter II)

$$T = \varphi(z) + \overline{\varphi(z)}. \tag{IV. 2}$$

According to the Fourier law, the vectorial components of the transverse heat flux (q^2, q^3) directed along the corresponding axes of the coordinate systems are related to the temperature by

$$q^2 - iq^3 = -2\varkappa\varphi'(z). \tag{IV. 3}$$

On the interface the introduced functions must be governed by the established boundary conditions allowing for the character of the thermal contact between the components. For ideal thermal contact

$$T_s|_{S_{mn}} = T_a|_{S_{mn}}, \quad \varkappa_s \frac{\partial T_s}{\partial n}\Big|_{S_{mn}} = \varkappa_a \frac{\partial T_a}{\partial n}\Big|_{S_{mn}} \tag{IV. 4}$$

must apply.

The reduced conditions of contact are equivalent to

$$\begin{gathered}\varphi_s(\tau) + \overline{\varphi_s(\tau)} = \varphi_a(\tau) + \overline{\varphi_a(\tau)};\\ \varkappa_s \frac{\partial}{\partial n}[\varphi_s(\tau) + \overline{\varphi_s(\tau)}] = \varkappa_a \frac{\partial}{\partial n}[\varphi_a(\tau) + \overline{\varphi_a(\tau)}],\end{gathered} \tag{IV. 5}$$

where $\tau = \lambda e^{i\theta}$ are the coordinates of the contour points.

The heat flux averaged over the cell chosen must be given beforehand /1/:

$$\langle q^2\rangle - i\langle q^3\rangle = -\frac{i\varkappa_s}{F}\oint_{L_s}\varphi_s(z)\,d\bar{z} - \frac{i\varkappa_a}{F}\oint_{L_a}\varphi_a(z)\,d\bar{z}. \tag{IV. 6}$$

Here L_s and L_a are the contours bounding the matrix and filler in plane $x_1 = \text{const}$; F is the cell area in the same plane: $F = \omega_1^2 \sin\alpha$.

For hollow fibers, not only (IV. 5) but also another equation must be given, which determines the pattern of heat transfer in the fiber hollow. However, here and later we shall assume that no heat transfer takes place in hollows.

The heat transfer between the regular structures at a constant mean flux is allowed for if the true heat flux is a doubly periodic function of z. It is evident that the periods will be equal to the sides of the unit cell, that is, ω_1 and $\omega_2 = \omega_1 e^{i\alpha}\left(\alpha = \frac{\pi}{3},\ \frac{\pi}{2}\right)$, and therefore the requirement is given by

$$(q_s^2 - iq_s^3)|_z = (q_s^2 - iq_s^3)|_{z+\omega_j} \quad (j = 1, 2) \tag{IV. 7}$$

or according to (IV. 3) by

$$\varphi_s'(z) = \Phi_s(z) = \Phi_s(z + \omega_j).$$

Function (II. 13) satisfies the above conditions for a material of the given structure. Function $\varphi_a(z)$ is selected in accordance with (II. 10).

The temperature distribution in the microstructure of a GEP with a phenol resin matrix, when only a single vector component of transverse heat flux is present ($q^2 \neq 0$) is shown in Figure IV. 1. The continuous curves

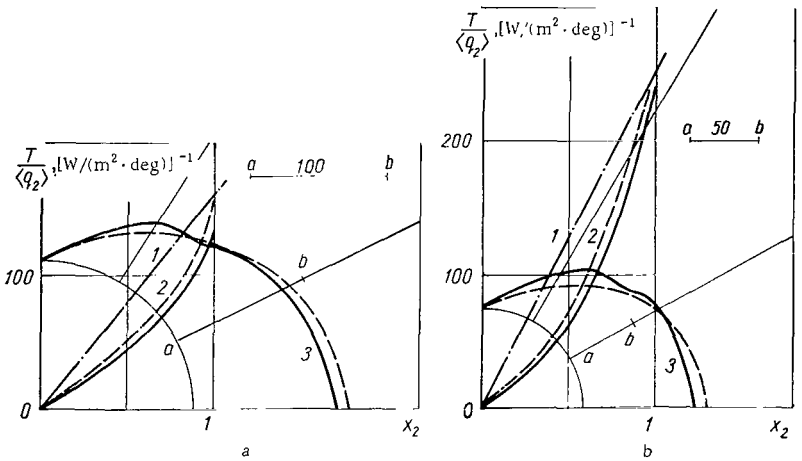

FIGURE IV. 1. Temperature distribution in the microstructure of a GFP with a volume content of filler $\zeta = 0.74$ (a) and $\zeta = 0.33$ (b).

characterize the temperature field in a material with hexagonal structure, and the dashed curves in a material with a tetragonal structure. The temperature difference $T - T_0$ is plotted on the ordinate and the distance between the given point and the fiber center on the abscissa on an enlarged scale (T_0 is the mean temperature of the cell). Curves 1 characterize the temperature distribution in a homogeneous anisotropic medium with equivalent reduced thermophysical parameters. Curves 2 determine the true temperature in the structure in plane $x_3 = \text{const}$, which passes through the fiber diameter parallel to the heat flux direction q_0^2. Because of the higher thermal conductivity of the fibers, the relative temperature increase in the fibers is on an average half that in the equivalent homogeneous medium. Curves 3 characterize the temperature distribution on the fiber-matrix interface. The temperature at each contour point is read off along the radius from the interface. If the fibers are close to one another a local temperature increase is observed at the points on the contour which are closest to the adjacent fiber (Figure IV. 1, a). For the tetragonal structure no peak arises, because the heat flows along OX_2. The calculations were carried out with the following parameters.

$$\varkappa_s = 0.35 \text{ W/m} \cdot \text{deg}$$
$$C_s = 1.55 \cdot 9.8^{-1} \text{ kjoule/newtons} \cdot \text{deg}$$
$$\varkappa_a = 1 \text{ W/m} \cdot \text{deg}$$
$$C_a = 0.796 \cdot 9.8^{-1} \text{ kjoule/newtons} \cdot \text{deg}$$

The temperature distribution in the polymer-aluminum fiber composites, for which

$$\varkappa_a = 222 \text{ W/m} \cdot \text{deg}; \quad C_a = 0.922 \cdot 9.8^{-1} \text{ kjoule/newtons} \cdot \text{deg}$$

is shown by the curves in Figure IV. 2. The data were obtained for $\zeta = 0.74$ (Figure IV. 2) and $\zeta = 0.33$ (Figure IV. 2). It can be seen from the graph that we have a nonuniform field in the given structure.

The temperature distribution in the glass fiber-aluminum matrix composite is illustrated by the curves in Figure IV. 3.

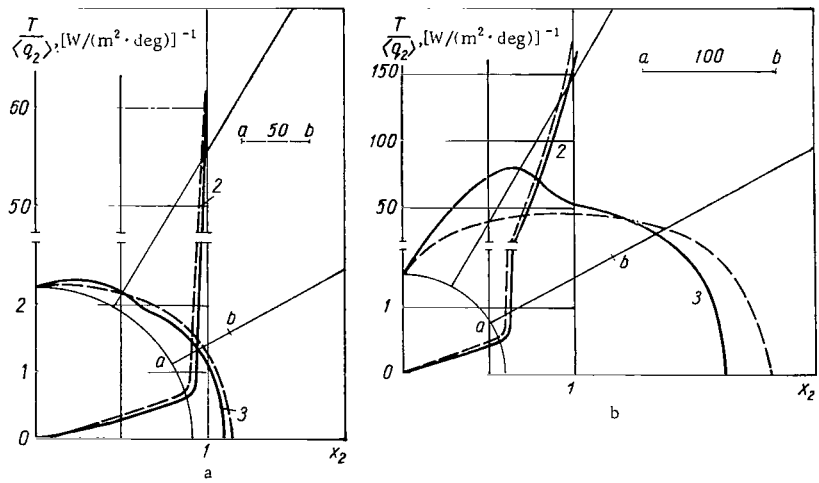

FIGURE IV. 2. Temperature distribution in polymer-aluminum fiber composite.

The symbols used in Figures IV. 2 and IV. 3 are the same as in Figure IV. 1.

The reduced transverse thermal conductivity coefficient $\varkappa_{22}$ is determined from

$$\frac{\varkappa_s}{\varkappa_{22}} = \frac{\eta + (1+\xi)\,\varkappa_s/\varkappa_a}{1+\xi+\eta\varkappa_s/\varkappa_a} + 2\,\frac{1-\varkappa_s/\varkappa_a}{1-\xi+\eta\varkappa_s/\varkappa_a}\sum_{k=1}^{\infty} C'_{2k+2}\lambda^{2k+2}\alpha_{0,\,k}. \qquad \text{(IV. 8)}$$

For the given tetragonal and hexagonal structures, we can equate $\varkappa_{22} = \varkappa_{33}$; $\varkappa_{23} = 0$; $\varkappa_{32} = 0$.

It is interesting that for inhomogeneous media the symmetry condition $\varkappa_{23} = \varkappa_{32}$ follows directly from the solution of the problem, without using Onsager's reciprocity relation.

In (IV. 8), the first term predominates; the second term characterizes the effect of fiber interaction, and depends on the microstructure of the material. The curves in Figure IV. 4 illustrate the changes in the coefficient of transverse thermal conductivity with increase in the volume content of the fibers and with change in their relative positions. The continuous curves are plotted for the hexagonal structure and the dashed ones for the tetragonal. The calculations were carried out for a composite with temperature-independent properties; this however restricts the applicability of the equations derived, since in polymers we note a decrease in $\varkappa_s$ values with increase in temperature. Curves 1, 2, and 3 are plotted for glass fiber-polymer (phenol resin), aluminum fiber-polymer, and glass fiber-aluminum composites, respectively.

According to our calculations, the approximate formula for the reduced coefficients of transverse thermal conductivity

$$\varkappa_{22} \approx \varkappa_s \frac{1+\xi+\eta\varkappa_s/\varkappa_a}{\eta+(1+\xi)\,\varkappa_s/\varkappa_a} \qquad \text{(IV. 9)}$$

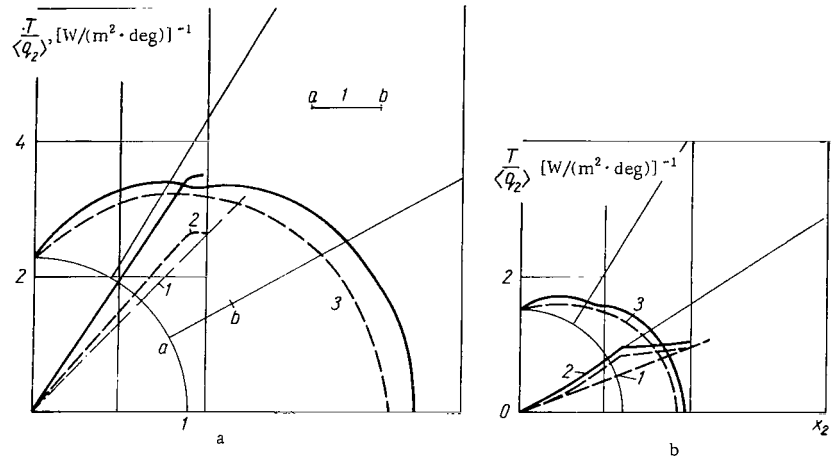

FIGURE IV. 3. Temperature distribution in glass fiber-aluminum matrix composite.

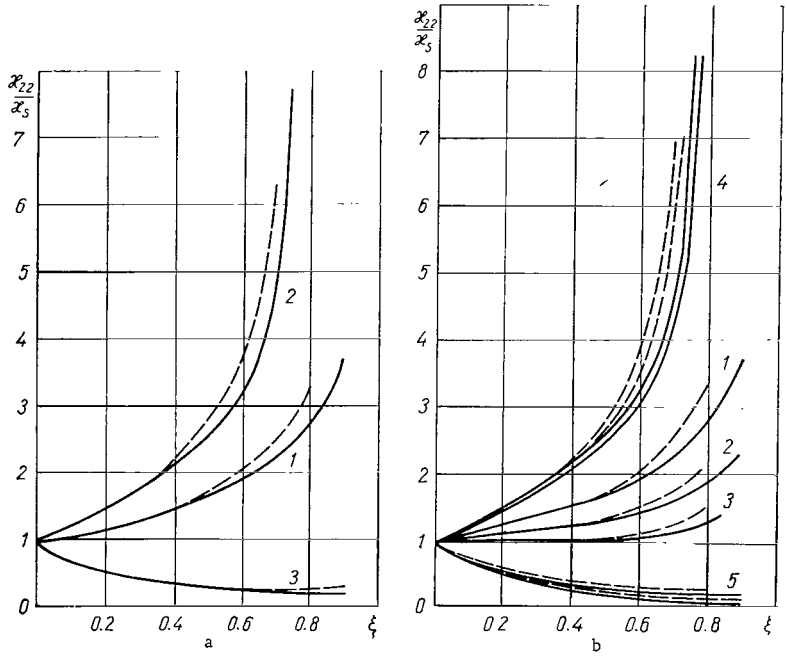

FIGURE IV. 4. Dependence of the coefficient of transverse thermal conductivity on the filler level and inner radii q.

is suitable if the component parameters differ by not more than one or two orders of magnitude (the error is not more than 1% in this case). For the aluminum fiber-polymer composite the error may be as high as 17% if the fiber content is maximum and the fibers do not contact one another.

Hollow fibers make it possible to reduce the thermal conductivity of the reinforced materials.

The temperature distribution in GFP consisting of hollow aluminoborosilicate fibers and a phenol resin matrix, with a transverse heat flux, is shown in Figure IV. 5 (Figure IV. 5,a shows the curves for $\xi = 0.74$ and Figure IV. 5,b for $\xi = 0.33$). The continuous curves show the field for the hexagonal structure and the dashed for the tetragonal. Curves 1, 2 refer to composites with solid fibers, and curves 3, 4 and 5, 6 to composites with hollow fibers for $q = 0.5$ and 0.7. The dashed lines characterize the temperature distribution in a homogeneous medium with equivalent reduced thermophysical properties. The temperature distribution in the fiber and matrix in plane $x_3 = \text{const}$ passing through the fiber diameter is shown by curves 1, 3, and 5. In the left-hand side of the cell the curves are arranged in inverse symmetry relative to the reduced curves. Curves 2, 4, and 6 characterize the temperature distribution on the fiber boundary. We see that the temperature increase is local at the points positioned nearest to the contour of the adjacent fiber. Hollows in the fibers produce some redistribution of the temperature fields in the material structure, though even in the absence of heat transfer in the hollows we do not see large differences between the curves for the hollow and solid fibers.

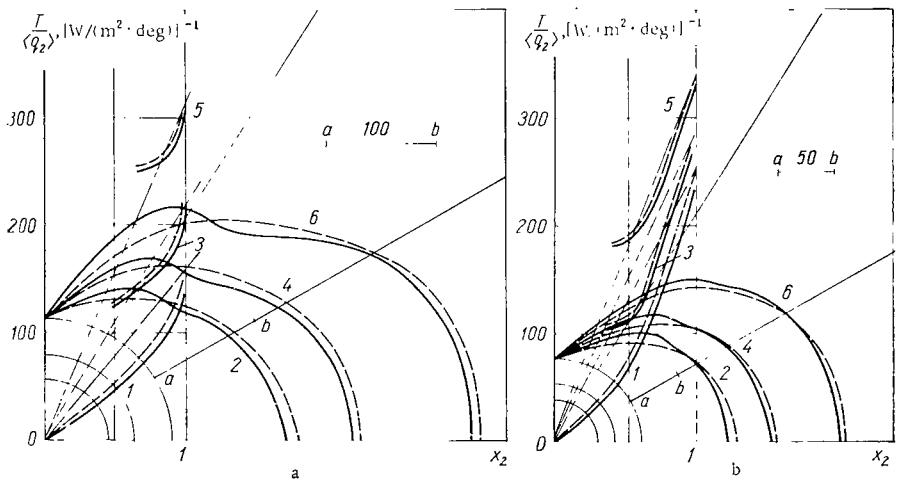

FIGURE IV. 5. Temperature distribution in the microstructure of GFP for different values of q.

The reduced coefficient of transverse thermal conductivity of a reinforced material with a simple regular structure is determined from the properties of the initial components by

$$\frac{\varkappa_s}{\varkappa_{22}} = \frac{\eta(1-q^2)+(1+\xi)(1+q^2)\varkappa_s/\varkappa_a}{(1+\xi)(1-q^2)+\eta(1+q^2)\varkappa_s/\varkappa_a} - 2\xi \frac{1-q^2-(1+q^2)\varkappa_s/\varkappa_a}{(1+\xi)(1-q^2)+\eta(1+q^2)\varkappa_s/\varkappa_a} \sum_{k=1}^{\infty} C'_{2k+2}\lambda^{2k+2}\alpha_{0,\,k}, \qquad \text{(IV. 10)}$$

where $q = \frac{\varepsilon}{\lambda}$ is the ratio of the radius of the circular cylindrical hollow to the inner fiber radius.

The curves in Figure IV.4, b illustrate the changes in $\varkappa_{22}/\varkappa_s$ with increase in the hypothetical volume content of the fibers ξ for different hollow dimensions. Curves 1, 2, and 3 were plotted for $q = 0$, $q = 0.5$ and 0.7 for the hexagonal (continuous curve) and the tetragonal (dashed curve) structures. The same diagram shows the dependence of $\frac{\varkappa_{22}}{\varkappa_s}$ on q for the aluminum fiber-polymer composite (curve 4) and for the glass fiber-aluminum composite (curve 5); q was 0.7 in both cases. If in (IV.10) only the first term is used, the maximum error is ±17% under the most unfavorable conditions (aluminum fiber-polymer composite).

2. Longitudinal thermal conductivity of reinforced materials

We shall suppose that the heat flux vector be parallel to the fibers and the transverse gradient of the temperature field averaged over the cell be zero. With such assumptions the temperature field will be a doubly periodic function of variables x_2 and x_3; the periods will coincide with the structure periods. The longitudinal heat flux in the components will differ because of the different thermophysical parameters. Therefore, the isothermal surface in each cell will reach its maximum in a region occupied by the filler or in the matrix with higher thermal conductivity coefficients, while the minimum will be in the other parts of the cell. Because of the curvature of the isothermal surface, a local transverse heat flux is produced in each cell, which leads to temperature equalization in the components. The determination of the true temperature field with a variable longitudinal flux is a very complex problem, because the function must be expanded again over the surfaces of the components.

If, on the other hand, we admit that the temperature field in a part of the material is equalized, and the isothermal curved surface degenerates into a plane perpendicular to the fiber orientation, the temperature will be a linear function of coordinate x_1, if the heat flux is constant. In this case the reduced coefficient of longitudinal thermal conductivity is proportional to the volume content of the components

$$\varkappa_{11} = \varkappa_s \tau_1 + \varkappa_a \xi. \tag{IV.11}$$

For hollow fibers the equation is transformed into

$$\varkappa_{11} = \xi (1 - q^2) \varkappa_a + \tau_1 \varkappa_s. \tag{IV.12}$$

These equations are applicable only if the isothermal surface degenerates into a plane. This is usually not the case, especially when the gradient of the longitudinal heat flux is high.

If inside the hollows heat is transferred and the longitudinal heat flux is constant, the isothermal surfaces will depend on the coordinates of the points in the cell, and a local transverse temperature gradient will exist. In this case, $\varkappa_{11}$ will depend on the heat transfer conditions in the hollows.

3. Thermal conductivity of multicomponent reinforced materials

If we start from solutions for materials with a general-type microstructure, we can study the effect of the relative positions and dimensions of the fibers in the cell on the thermal conductivity of a two-phase or multiphase composite. In each cell filler elements of each kind must be present to enable us to obtain the integral characteristics. If the microstructure of the material can be obtained by a double prolongation of the given cell, the temperature field is determined from (IV. 2), (II. 26), and (II. 27), when the transverse flux is constant and the longitudinal flux is zero. The conditions of ideal thermal contact are defined by satisfying (IV. 4) in the individual cell. For hollow fibers it is assumed that no heat is transferred inside the hollow. The transverse heat flux averaged over the cell is given by

$$\langle q^2\rangle - i\langle q^3\rangle = -\frac{i\varkappa_s}{F}\oint_{L_s}\varphi_s(z)\,d\bar{z} - \frac{i}{F}\sum_{k=1}^{p}\varkappa_{a,k}\oint_{L_k}\varphi_{a,k}(z)\,d\bar{z}, \qquad \text{(IV. 13)}$$

where $\varkappa_{a,k}$ are the thermal conductivity coefficients of the k-th filler element.

For general-type structures we find all three reduced thermal conductivity coefficients $\varkappa_{22}$, $\varkappa_{23}=\varkappa_{32}$, $\varkappa_{33}$ when solving the above problem.

For hexagonal and tetragonal structures of the composites we can find simplified equations for determining the effective thermal conductivity coefficients from the component parameters, if we neglect auxiliary factors. The coefficient of transverse thermal conductivity of a multicomponent material with a hexagonal or tetragonal structure and solid fibers is given by

$$\varkappa_{22} = \varkappa_{33} \approx \varkappa_s \frac{\eta + 2\sum_{k=1}^{p} \frac{\xi_k}{1+\varkappa_s/\varkappa_{a,k}}}{1-\sum_{k=1}^{p}\xi_k\frac{1-\varkappa_s/\varkappa_{a,k}}{1+\varkappa_s/\varkappa_{a,k}}}. \qquad \text{(IV. 14)}$$

The equation for a two-phase body ($p = 1$) coincides with (IV. 9) which, as shown above, gives a satisfactory accuracy for numerous composites.

The reduced coefficients of transverse thermal conductivity of multicomponent materials with the closest packing of hollow fibers are determined from the parameters of the individual components by

$$\varkappa_{22} = \varkappa_{33} \approx \varkappa_s \frac{\eta + 2\sum_{k=1}^{p} \frac{\xi_k(1-q_k^2)}{1-q_k^2+(1+q_k^2)\varkappa_s/\varkappa_{a,k}}}{1+\sum_{k=1}^{p}\xi_k\frac{1-q_k^2-(1+q_k^2)\varkappa_s/\varkappa_{a,k}}{1-q_k^2+(1+q_k^2)\varkappa_s/\varkappa_{a,k}}}. \qquad \text{(IV. 15)}$$

The symbols utilized above are used here. The above equations are generalized approximate formulas. Their correctness was proved for materials with an equal volume content of the components.

The reduced coefficients of longitudinal thermal conductivity of multicomponent materials are determined from

$$\varkappa_{11} \approx \eta \varkappa_s + \sum_{k=1}^{p} \xi_k (1 - q_k^2) \varkappa_{a,\,k}. \qquad \text{(IV. 16)}$$

When $q_k = 0$ we have equations for the thermal conductivity coefficient of materials with solid fibers.

4. Thermal conductivity equations for reinforced bodies

In materials reinforced by fibers of different thermophysical properties, the temperature distribution in the microstructure, as shown above, is characterized by an appreciable inhomogeneity, so that the gradient of the temperature field may vary considerably even within a single cell. Apparently, composites such as the aluminum fiber-polymer differ greatly in their thermophysical properties because of the differences in the temperature gradients in the structural elements in the inhomogeneous temperature field. This leads to local temperature increase in one of the material components, while the mean temperature gradient remains comparatively low. If the mean heat flux changes to a negligible extent within a few adjacent cells of the material structures, by introducing the reduced thermal conductivity coefficients we can establish how the mean temperature is distributed over the whole body. The true temperature distribution in the material structure is proportional to the heat flux averaged over the cell

$$T = k(x_2, x_3)\langle q \rangle,$$

where function $k(x_2, x_3)$ characterizes the temperature changes within a single cell. The temperature distribution in the material structure has been considered above. The results can also be extended to unsteady temperature fields if we neglect the time-dependent temperature redistribution within the individual cell structure. With this approximation, it is apparently possible to introduce more or less definite effective thermal conductivity coefficients.

The distribution of $\langle T \rangle$ in time in the reinforced material, with the accepted restrictions, is determined by the heat conductivity equation

$$\frac{\partial \langle T \rangle}{\partial t} = \frac{\varkappa_{11}}{\langle c \rangle \langle \rho \rangle} \cdot \frac{\partial^2 \langle T \rangle}{\partial x_1^2} + \frac{\varkappa_{22}}{\langle c \rangle \langle \rho \rangle} \cdot \frac{\partial^2 \langle T \rangle}{\partial x_2^2} + \frac{\varkappa_{33}}{\langle c \rangle \langle \rho \rangle} \cdot \frac{\partial^2 \langle T \rangle}{\partial x_3^2}. \qquad \text{(IV. 17)}$$

Here the reduced specific heat $\langle c \rangle$ and density $\langle \rho \rangle$ of the reinforced composite are found from

$$\langle c \rangle = \sum_{k=1}^{p} \xi_k (1 - q_k^2) C_k^d + \eta C_s^d; \quad \langle \rho \rangle = \sum_{k=1}^{p} \xi_k (1 - q_k^2) \rho_k + \eta \rho_s,$$

where C_k^d and C_s^d are the constant-pressure specific heats of the k-th fiber component and the matrix, respectively. As usual, it is assumed that $0x_1$ is directed along the fibers of the linearly reinforced material.

The reduced thermal conductivity of a reinforced material with a general-type structure is characterized by the symmetric heat conductivity tensor $\varkappa_{ik}$, and its matrix representation is

$$\begin{Bmatrix} \varkappa_{11} & 0 & 0 \\ 0 & \varkappa_{22} & \varkappa_{23} \\ 0 & \varkappa_{23} & \varkappa_{33} \end{Bmatrix}.$$

By rotating the coordinate axis around $0x_1$, the tensor can be reduced to the main axes, and the number of intrinsically different components is decreased to three:

$$\begin{Bmatrix} \varkappa_{11} & 0 & 0 \\ 0 & \varkappa_{22} & 0 \\ 0 & 0 & \varkappa_{33} \end{Bmatrix}.$$

For real materials where the fibers form a near hexagonal structure, and the difference between the components of the tensor of transverse heat conductivity is very small, we can write $\varkappa_{22} = \varkappa_{33}$.

The reduced thermal conductivity coefficients in planes inclined at angles φ and $\varphi + \frac{\pi}{2}$ to the fiber orientation can be calculated from the formula for transformation of the components of a tensor of the second rank:

$$\tilde{\varkappa}_{11} = \varkappa_{11} \cos^2 \varphi + \varkappa_{22} \sin^2 \varphi;$$
$$\tilde{\varkappa}_{22} = \varkappa_{22} \cos^2 \varphi + \varkappa_{11} \sin^2 \varphi.$$

At the boundary of the reinforced material, the mean temperature must conform to the corresponding boundary conditions. However, near the edge, the introduction of the reduced thermal conductivity coefficients is not justified, because of the sharp change in the gradient of the temperature field. In the approximate formulation, the boundary conditions for the mean temperature or the mean heat flux cannot be formulated more accurately than is customary in the thermal conductivity theory of solid bodies.

5. Diffusion in absorbing media

Diffusional phenomena in nonabsorbing media are described by equations analogous to those used in the heat conductivity theory. We only have to replace the thermal conductivity coefficients of the components by particle diffusivities. Therefore, the equations for the reduced diffusivities in reinforced materials can be immediately obtained by using the above substitution (see Chapter I).

For determinacy, the problem of diffusion in absorbing media is considered to be the study of the propagation of monoenergetic thermal neutrons in reinforced materials /2/. If the probability of neutron-nucleus interaction, measured in terms of the macroscopic cross section μ and the particle flux Φ, changes only slightly in distances of the order of the mean free path, the process of particle diffusion is described by equations (I.52) /3, 4/. In the simpler case of steady diffusion the monoenergetic neutron flux in a homogeneous medium will be determined from

$$\frac{\partial^2\Phi}{\partial x_1^2}+\frac{\partial^2\Phi}{\partial x_2^2}+\frac{\partial^2\Phi}{\partial x_3^2}-\frac{\mu_0}{D}\Phi=0 \qquad \text{(IV. 18)}$$

for the corresponding boundary conditions. In our approximation, it is assumed that on the boundaries of the component the flow function and the neutron flux must be continuous

$$\Phi_a=\Phi_s;\quad D_a\frac{\partial\Phi_a}{\partial n}=D_s\frac{\partial\Phi_s}{\partial n}.$$

The flow vector of particles $\bar{I}$ is decomposed into the transverse $\bar{I}_2$ and the longitudinal $\bar{I}_1$ components. By equating the flow vector components alternately to zero, we obtain the solution of the problem of diffusion processes in materials in the presence of a transverse or longitudinal flux.

In the first case, the flux in fibers in materials with a primitive hexagonal structure is obtained by expansion

$$\Phi_a=\sum_j B_{00}^j I_j(k'r)\,e^{ij\theta}\quad (j=0,\ \pm1,\ \ldots,\ \pm\infty),$$

where $k=\frac{\mu_{0,a}}{D_a}$, $k^2=\frac{\mu_{0,s}}{D_s}$, $I_j(x)$ are modified Bessel functions.

The flux in the fibers in the matrix is found as the series

$$\Phi_s=C_0\exp\{a\omega_1[m\cos\varphi+nb\cos(\alpha-\varphi)]\}\sum_j g_j(a)[I_j(kr)-Z_jK_j(kr)]\,e^{ij\theta}. \qquad \text{(IV. 19)}$$

Here $K_j(x)$ is the MacDonald function /5/; r, Θ are the cylindrical coordinates with the origin on the fiber axis; φ is the slope of vector $\bar{I}_2$ to axis $0x_2$; ω_1, $\omega_2=\omega_1 be^{i\alpha}$; and α is the lattice constant. The parameter a is the root of the infinite determinant

$$|\delta_{jt}+Z_tG_{t-j}|=0\quad (t,\ j=0;\ \pm1,\ \ldots,\ \pm\infty),$$

where δ_{jt} is the Kronecker symbol,

$$G_{t-j}=i^{(t-j)}e^{i(t-j)\varphi}\sum_{(\rho,\ \vartheta)}{\sum}'{\sum}' K_{t-j}(\omega_1k\rho)\,e^{a\omega_1\rho\sin\vartheta-i(t-j)\vartheta}. \qquad \text{(IV. 20)}$$

The position of the cells in the structure is determined from ρ and ϑ, which are expressed in terms of m and n by the equation $\rho e^{i\left(\varphi-\vartheta+\frac{\pi}{2}\right)}=m+bne^{i\alpha}$.

The connection between C_j and C_0 is found by solving

$$C_j+\sum_t Z_tG_{t-j}C_t=0\quad (j,\ t=0,\ \pm1,\ \ldots,\ \pm\infty),$$

whence $C_j=g_j(a)C_0$.

The constants introduced are expressed in terms of the component parameters

$$Z_j=\frac{I_j(x')I_j'(x)-\frac{k'D_a}{kD_s}I_j(x)I_j'(x')}{I_j(x')K_j'(x)-\frac{k'D_a}{kD_s}I_j'(x')K_j(x)};$$

$$B_{00}^jI_j(x)=\frac{I_j(x)-Z_jK_j(x)}{I_j(x')}C_j\exp\{a\omega_1[m\cos\varphi+bn\cos(\alpha-\varphi)]\}.$$

Here $x = kr_0$; $x' = k'r_0$ (r_0 is the fiber radius).

If the flux changes slightly within a single cell, we can integrate instead of summing up (IV.20), and for $k > a$, $D_a = D_s$, we find that

$$a = -\frac{\sqrt{\gamma_i\mu_{0i} + \xi\mu_{0a}}}{\sqrt{D}} = -\frac{\sqrt{\langle\mu\rangle}}{\sqrt{D}}, \qquad \text{(IV.21)}$$

that is, the reduced absorption coefficient in this equation is found from the component-displacement function. To obtain more accurate results from (IV.21), we must take more terms in the infinite determinant.

It is worth noting that for $D_a = D_s$ and $\mu_{0a} < \mu_{0s}$ there is no solution of the given problem by means of which the reduced parameters of the reinforced material can be found.

In our approximation, the mean flux distribution is found from

$$\frac{\partial^2\langle\Phi\rangle}{\partial x_2^2} + \frac{\partial^2\langle\Phi\rangle}{\partial x_3^2} - \frac{\langle\mu\rangle}{D}\langle\Phi\rangle = 0.$$

In the presence of a longitudinal neutron flux, when the field changes slightly, the reduced parameters can be determined by assuming that there exist an infinite number of particle sources, with doubly periodic distribution in the transverse plane of the reinforced material. For this approximation

$$\begin{aligned} \langle\mu_0\rangle &\approx \xi\mu_{0a} + \gamma_i\mu_{0s}; \\ \langle D\rangle &\approx \xi D_a + \gamma_i D_s. \end{aligned} \qquad \text{(IV.22)}$$

The damping of the mean longitudinal neutron flux in time when the sources act instantaneously is determined from

$$\langle\Phi\rangle \approx e^{-x_1\sqrt{\langle\mu\rangle/\langle D\rangle}} - \frac{2}{\pi}\, e^{-\frac{\langle\mu\rangle}{\langle 1/v\rangle}t} \int_0^\infty \frac{u\,du}{u^2 + \langle\mu\rangle/\langle D\rangle}\, e^{-\frac{\langle D\rangle tu^2}{\langle 1/v\rangle}} \sin x_1 u. \qquad \text{(IV.23)}$$

In the limiting case, $t \to \infty$, the longitudinal flux tends to its steady-state value, determined by the first term of (IV.23).

Bibliography

1. Van Fo Fy, G.A. Teploprovodimost' armirovannykh sred (Thermal Conductivity of Reinforced Media). — Mekhanika Polimerov, 4. 1968.
2. Van Fo Fy, G.A. Rasprostranenie neitronov v armirovannykh plastinakh (Neutron Propagation in Reinforced Plastics). — DAN Ukr RSR, 2. 1968.
3. Beckwits, K.H. and K. Wirtz. Neutron Physics. Berlin, Springer Verlag. 1964.
4. Ch'iang Hsüeh-sên. Fizicheskaya mekhanika (Physical Mechanics). Moskva, Mir. 1965.
5. Watson, G.N. A Treatise on the Theory of Bessel Functions. Cambridge Univ. Press. 1944.

Chapter V

THERMAL EXPANSION AND CONTRACTION

An increase in the temperature of the composite is accompanied by an increase in its volume, determined by the thermal expansion coefficients of the matrix and filler. In a monolithic inhomogeneous material thermal expansion produces internal thermal stresses. The magnitude of these stresses is proportional to the differences between the thermal expansion coefficients of the components. In existing compounds these coefficients may differ by as much as one or two orders of magnitude. Thus, the thermal expansion of glass fibers is only 1/15 to 1/12 of the thermal expansion of the epoxide resin matrix between room temperature and the point of vitrification ($T_v \approx 353°$ K). With further increase in temperature, the difference between the thermal expansions increases. In materials with oriented fibers, thermal expansion will be anisotropic because of the above effects. In composites with inelastic properties, the parameters in the stress-strain equations will be replaced by the corresponding linear integral operators if the temperature is high. The above effects are especially noticeable in GFP where the temperature increase is not more than 10—20°C, and the decrease in the moduli of instantaneous elasticity leads to an accelerated relaxation of thermal stresses because viscoelastic deformations develop, and the above moduli of the matrix decrease. The thermal stress relaxation in GFP need not be allowed for in the given approximation.

The components of composites combine at high temperatures, and the process itself is produced by mutual diffusion of the components and the adhesive forces acting between matrix and filler. If the temperature of the prepared composite is decreased, we observe volume contraction. Experimental data indicate that the volume contracts mainly because of negative thermal expansion.

1. Thermoelastic expansion of composite materials with solid and hollow fibers

We shall suppose that the reinforced material with a primitive hexagonal or tetragonal structure is at an elevated temperature $\Theta = T - T_0$. We shall assume that at a certain distance from the edge of the material the cross section ($x_1 = \text{const}$) is plane. In bounded bodies at a sufficient distance from the edge, where the fibers are cut, the cross section averaged over the cell will be plane because of stress redistribution between filler and

matrix. Therefore, the total longitudinal strain of the reinforced material will consist of the pure thermal deformation proportional to Θ and the mechanical deformation produced by the difference between the thermal expansion coefficients of the components. The deformations in question must, on the average, be equal, and therefore

$$\langle \varepsilon_{11} \rangle = \beta_s \Theta + \langle \varepsilon_{11} \rangle_s = \beta_a \Theta + \langle \varepsilon_{11} \rangle_a, \tag{V. 1}$$

where $\langle \varepsilon_{11} \rangle_s$ and $\langle \varepsilon_{11} \rangle_a$ are the mean longitudinal deformations of the matrix and fibers arising because of stress redistribution near the fiber edges.

In our approach, the distribution of the longitudinal tangential stresses near the fiber ends are not taken into account, and therefore an indefinite region remains where the plane cross sections are distorted when the temperature is increased. If no external stresses are applied, it follows from the balance conditions of the isolated elementary volume that both the longitudinal normal components

$$\iint_{F_a} dx_2\, dx_3\, \sigma_{11} + \iint_{F_s} dx_2\, dx_3\, \sigma_{11} = 0, \tag{V. 2}$$

and other components of the mean stress tensor are equal to zero.

The solution of the problem on thermal stresses and thermal expansion of elastic reinforced materials consists in the solution of the problem of homogeneous longitudinal tension of the components at elevated temperatures, found without taking into account the filler-matrix interaction and this interaction under conditions when there is no average longitudinal deformation.*

The first problem is solved by means of

$$\begin{gathered} \langle \sigma_{11} \rangle_a = E_a \langle \varepsilon_{11} \rangle_a; \quad u_1 = x_1 \langle \varepsilon_{11} \rangle_a + \beta_a \Theta x_1; \\ u_2 + i u_3 = -\nu_a \langle \varepsilon_{11} \rangle_a z + \beta_a z \Theta. \end{gathered} \tag{V. 3}$$

Analogous equations are set up for the matrix.

The difference between the transverse displacement in filler and matrix will be

$$(u_2 + i u_3)_a - (u_2 + i u_3)_s = -(\beta_s - \beta_a)(1 + \nu_a) z \Theta - (\nu_a - \nu_s) z \langle \varepsilon_{11} \rangle_s. \tag{V. 4}$$

The solution of the second problem is very similar to that of the problem of longitudinal tension of a reinforced material (see Chapter II).

The reduced coefficient of linear thermal expansion of a reinforced material in the longitudinal direction is determined from

$$\beta_{11} = \beta_s - (\beta_s - \beta_a) \frac{(1 + \nu_s) \xi E_a - (1 + \nu_a)(E_{11} - \eta E_s)}{(\nu_s - \nu_a) E_{11}}. \tag{V. 5}$$

The reduced coefficients of thermal expansion in the transverse directions are given by

$$\begin{aligned} \beta_{22} &= \beta_s + (\beta_s - \beta_{11}) \nu_{21} - (\beta_s - \beta_a)(1 + \nu_a) \frac{\nu_s - \nu_{21}}{\nu_s - \nu_a}; \\ \beta_{33} &= \beta_s + (\beta_s - \beta_{11}) \nu_{31} - (\beta_s - \beta_a)(1 + \nu_a) \frac{\nu_s - \nu_{31}}{\nu_s - \nu_a}. \end{aligned} \tag{V. 6}$$

* Van Fo Fy, G. A. Temperaturnye smeshcheniya i napryazheniya v stekloplastike (Thermal Displacements and Stress in Glass-Fiber Reinforced Plastics). – PMTF, 4. 1968.

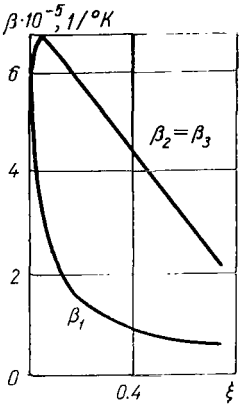

FIGURE V.1. Change in the thermal expansion coefficient of linearly reinforced GFP.

For materials with a hexagonal or tetragonal structure, $\nu_{21} = \nu_{31}$ and $\beta_{22} = \beta_{33}$ and the number of intrinsically different thermal expansion coefficients is reduced to two.

These equations also hold for materials reinforced by hollow fibers, only the corresponding values of E_{11} and ν_{21}, ν_{33} must be introduced into (V.5) and (V.6).

The pattern of thermal stress distribution on the fiber-matrix interface completely agrees with the data obtained for longitudinal tension. The thermal stresses are proportional to the difference between the thermal expansion coefficients of matrix and filler. The sign of the stresses is determined by the sign of these differences. Thus, for example, in GFP at elevated temperature the fibers are extended in the longitudinal direction, while the matrix is subjected to longitudinal compressive stresses.

Figure V.1 shows the graph of the thermal expansion coefficient plotted against the volume content of the filler ξ for linearly reinforced GFP. β_{11} is about $\frac{1}{4}$ of β_{22}, on the average, as the result of the reinforcing action of the fibers. For small ξ, the lateral thermal expansion of the composite is higher than β_s because of the action of longitudinal compressive stresses.

2. Effect of the type of microstructure on thermal expansion

We shall assume that an elementary volume of a reinforced material contains p fibers of various diameters, with their axes arbitrarily arranged within the cell. The internal stress field and the reduced thermal expansion coefficients are studied, using the general-type complex potentials.

The reduced thermal expansion coefficient is expressed in terms of the component characteristics by

$$\beta_{11} = \beta_s - \frac{\beta_s - \beta_a}{\nu_s - \nu_a}\left[(1+\nu_s)\frac{E_a}{E_{11}}\sum_{k=1}^{p}\xi_k - (1+\nu_a)(1-\eta E_s/E_{11})\right]. \qquad (V.7)$$

The equations for determining the coefficients of lateral thermal expansion of a reinforced material can be obtained in a closed form:

$$\left.\begin{aligned}
\beta_{22} &= \beta_s - (\beta_s - \beta_a)(1+\nu_a)\frac{\nu_s - \nu_{21}}{\nu_s - \nu_a} + (\beta_s - \beta_{11})\nu_{21};\\
\beta_{33} &= \beta_s - (\beta_s - \beta_a)(1+\nu_a)\frac{\nu_s - \nu_{31}}{\nu_s - \nu_a} + (\beta_s - \beta_{11})\nu_{31};\\
\beta_{23} &= \nu_{61}\left[\beta_s - \beta_{11} + (\beta_s - \beta_a)\frac{1+\nu_a}{\nu_s - \nu_a}\right].
\end{aligned}\right\} \qquad (V.8)$$

β_{23} characterizes the curving of the angles of the elementary volume at elevated temperatures. This effect is produced by the influence of nonsymmetric arrangement of the fibers in the cell, and is proportional to

the difference between the Poisson ratios of the components. For components with $\nu_s = \nu_a = \nu$, we can state

$$\left.\begin{aligned} &\beta_{23} = 0; \\ &\beta_{22} = \beta_{33} = \beta_s + (\beta_s - \beta_a)\left(\frac{\nu E_a}{E_{11}} \sum_{k=1}^{p} \xi_k - 1 - \nu\right); \\ &\beta_{11} = \beta_s - (\beta_s - \beta_a)\frac{E_a}{E_{11}} \sum_{k=1}^{p} \xi_k, \end{aligned}\right\} \qquad (V.9)$$

that is, an increase in the number of thermoelastic constants is determined mainly by the difference between the Poisson ratios of the components. If these ratios differ little for all the components (which occurs rather frequently), the thermal expansion is determined from two completely independent coefficients β_{11} and β_{22}. For materials with hollow fibers we have

$$\beta_{11} = \beta_s - \frac{\beta_s - \beta_a}{\nu_s - \nu_a}\left[(1 + \nu_s)\frac{E_a}{E_{11}} \sum_{k=1}^{p} \xi_k (1 - q_k^2) - (1 + \nu_a)(1 - \eta E_s/E_{11})\right]. \qquad (V.10)$$

The other equations remain unchanged when the corresponding values of ν_{21} and E_{11} are introduced.

3. Thermal expansion of multicomponent materials

The thermal expansion of a material reinforced by p kinds of fibers is determined from two equations:

a) from the reduced coefficients of the longitudinal thermal expansion given in terms of the component parameters

$$\beta_{11} \approx \beta_s - \sum_{k=1}^{p} \xi_k (\beta_s - \beta_k) E_k/E_{11} + \ldots, \qquad (V.11)$$

where β_k denotes the thermal expansion coefficient of the k-th kind of fiber;

b) from the reduced coefficients of lateral thermal expansion for hexagonal or tetragonal materials, given by the following approximate relationship

$$\beta_{22} \approx \beta_s + (\beta_s - \beta_{11})\nu_{21} - \frac{(\varkappa_s + 1)\sum_{k=1}^{p} \xi_k \frac{(1 + \nu_k)(\beta_s - \beta_k)}{2 + \varkappa_k G_s/G_k}}{\eta + \sum_{k=1}^{p} \frac{\xi_k (\varkappa_s + 1)}{2 + \varkappa_k G_s/G_k}}. \qquad (V.12)$$

This formula can be generalized for materials with hollow fibers where $\frac{G_s}{G_k} \ll 1$.

Within the limits of permissible error, we can use

$$\beta_{11} \approx \beta_s - \sum_{k=1}^{p} \xi_k (1 - q_k^2)(\beta_s - \beta_k) E_k/E_{11};$$

$$\beta_{22} \approx \beta_s + (\beta_s + \beta_{11})\nu_{21} - \frac{(\varkappa_s + 1)\sum_{k=1}^{p} \frac{\xi_k (1 - q_k^2)(1 + \nu_k)(\beta_s - \beta_k)}{2(1 - q_k^2) + (\varkappa_k - 1 + 2q_k^2) G_s/G_k}}{\eta + \sum_{k=1}^{p} \frac{\xi_k (1 - q_k^2)(\varkappa_s + 1)}{2(1 - q_k^2) + (\varkappa_k - 1 + 2q_k^2) G_s/G_k}}, \quad (V.13)$$

where the values of E_{11} and ν_{21} are found for hollow-fiber materials.

4. Effect of the viscoelastic properties of the matrix on the thermal expansion and internal stress field

In composite materials of the reinforced plastic type, at elevated temperatures we observe an increase in the creep rate and stress relaxation and a decrease in the modulus of instantaneous elasticity. This leads to a change in the reduced thermal expansion coefficient and stress distribution in time. To estimate the inelastic properties of the matrix according to the Volterra principle, we substitute the corresponding integral operators, allowing for the dependence of moving constraints on temperature, for the elastic constants. The calculations showed that β_{11} for reinforced polymers changes very little in time, because of the development of viscoelastic strains in the matrix. By replacing the elastic constants in (V.6) by operators, and neglecting the changes in time in magnitudes which contribute little, we obtain

$$\beta_{22}^* \approx \beta_{22}^0 \left\{1 + \frac{\beta_s - \beta_a}{\beta_{22}^0}\left[\frac{\xi E_a}{E_{11}}\nu_{21}^0 (\Omega_a - \Omega_b) + \right.\right.$$

$$\left.\left. + \frac{\tau_1 \Omega_a (1 + \nu_a)[2 + (\varkappa_a - 1) G_0/G_a]}{1 + \tau_1 + \xi\varkappa_0 + \tau_1 (\varkappa_0 - 1) G_0/G_a} \Im_{1-\lambda}^* (-\omega + \Omega_a)\right]\right\}, \quad (V.14)$$

where β_{22}^0 is the coefficient of lateral thermal expansion in a purely elastic matrix; the other symbols have been explained above (see Chapter III).

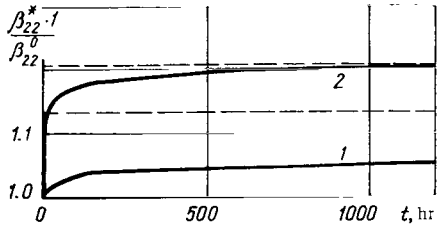

FIGURE V.2. Time dependence of the thermal expansion coefficients when the matrix is viscoelastic.

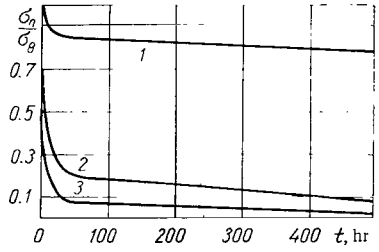

FIGURE V.3. Stress relaxation curves at various temperatures.

Curves 1 and 2 in Figure V.2 illustrate the increase in β_{22} in time in a steady-state temperature field due to the development of elastic strains in the polymer matrix. The effect of the increase in β_{22} is explained by

the fact that the matrix in the reinforced material is under the influence of limiting compressive stresses, which lead to a change in β_{22} in time. On the x-axis we plotted the time of observation in hours, and on the y-axis the ratio $\frac{\beta_{22}^{*}}{\beta_{22}^{0}} - 1$. Curve 1 is plotted for the EMA composite when the creep process at room temperature is stable (in this case the viscoelastic deformations cause an increase in β_{22} of almost 5%). Curve 2 is plotted for GFP at temperatures of about 348°K, when the creep of the matrix is unstable. At these temperatures, β_{22} increases by as much as 20%. All the calculations were performed for $\xi = 0.74$, assuming that both β_s and β_a are temperature-independent.

The change in the mechanical properties of the matrix leads to stress redistribution in the microstructure of the reinforced plastic.

The relaxation of the normal thermal stresses in the structure was determined from equations in which the integral operators of the theory of elastic heredity, taking into account the temperature-dependence of the parameters, were substituted for the elastic constants. The results are shown in Figure V. 3. Curves 1, 2 and 3 correspond to stress relaxation at 298, 323, and 348°K, respectively. The calculations were carried out after the material had been heated. On the y-axis we plotted the ratio between the stresses subject to relaxation and all the stresses in GFP found without allowing for the moving constraints in the matrix. With increase in T the rate of stress relaxation increases, while the absolute values of the stress relaxation decrease because of the decrease in the modulus of elasticity of the matrix. When $T > 348$°K, the structural stresses in the given GFP will be completely relaxed during the heating period of the individual cell.

5. Contraction and residual stresses in glass-fiber reinforced plastics

Contraction and residual stresses are observed in all composites produced at elevated temperatures and especially in GFP. We know that the glass fiber and the polymer matrix combine at polymerization (polycondensation) temperatures, when a spatial microstructure of the polymer is formed. If we assume that at the beginning of the cooling process of the reinforced material the polymerization reaction has completely terminated, with this approximation contraction and formation of residual stresses are equivalent to thermal expansion and thermal stress formation in the inhomogeneous viscoelastic medium when the temperature decreases. It was experimentally confirmed that the main residual stresses in epoxide resin matrices are due to the differences between the thermal expansions of the fibers and polymer matrix. According to the Arrhenius equation, the chemical reaction rate decreases exponentially with decrease in temperature, so that the assumption that no reactions take place during cooling is true to a first approximation.

We distinguish two types of shrinkage stresses in composites: a) structural stresses, arising in the material itself because of the differences in the physical properties of the components; and b) stresses due

to the product geometry, temperature gradient over the product thickness etc. On contraction, the sign of the structural stresses is opposite to that of the stresses arising on thermal expansion. The fibers are subjected to longitudinal compression on contraction of the matrix, while the matrix is subjected to longitudinal tension. For this reason, to remove the compressive stresses and to avoid bending of the fibers the material must be formed with preliminarily extended fibers.

A simplified solution of the shrinkage problem can be obtained with stepwise cooling conditions if we neglect stress relaxation in the individual cell during the cooling process, and consider only relaxation processes in the temperature field. These assumptions do not lead to appreciable errors in the calculation if the relaxation time considerably exceeds the cooling period of the cell.

As an example, we shall study the relaxation of normal stresses on the fiber-matrix interface; their time-dependent change is approximately described by

$$\sigma_r \approx Ae^{-gT}\left[1 - \frac{3\omega_0 e^{bT}}{2+2\nu_0}\,\Im^*_{1-\lambda}\left(-\frac{3\omega_0 e^{bT}}{2+2\nu_0}\right)\right]\Theta(t).$$

We shall assume that the cell temperature decreases jumpwise to Θ_1, and that in its initial state the material was at temperature T_n. The stresses on the fiber contour will be

$$\sigma_r \approx Ae^{-g(T_n-\Theta_1)}\left[1 - \frac{3\omega_0 e^{b(T_n-\Theta_1)}}{2+2\nu_0}\,\Im^*_{1-\lambda}\left(-\frac{3\omega_0 e^{b(T_n-\Theta_1)}}{2+2\nu_0}\right)\right]\Theta_1(t).$$

By using the approximation in Chapter I, we obtain

$$\sigma_r^{(1)} \approx A\Theta_1 \exp\left[-g(T_n-\Theta_1) - \frac{3\omega_0 e^{b(T_n-\Theta_1)}}{2+2\nu_0}(\lambda t)^\lambda\right].$$

Then, we find the stresses after their relaxation in time t_1 at $T_n - \Theta_1$, with subsequent stepwise temperature decrease to Θ_2. The additional stresses arising because of temperature changes will be

$$Ae^{-g(T_n-\Theta_1-\Theta_2)}\left[1 - \frac{3\omega_0 e^{b(T_n-\Theta_1-\Theta_2)}}{2+2\nu_0}\,\Im^*_{1-\lambda}\left(-\frac{3\omega_0 e^{b(T_n-\Theta_1-\Theta_2)}}{2+2\nu_0}\right)\right]\Theta_2 \approx$$
$$\approx Ae^{-g(T_n-\Theta_1-\Theta_2)}\exp\left[-\frac{3\omega_0 e^{b(T_n-\Theta_1-\Theta_2)}}{2+2\nu_0}(\lambda t)^\lambda\right]\Theta_2,$$

etc.

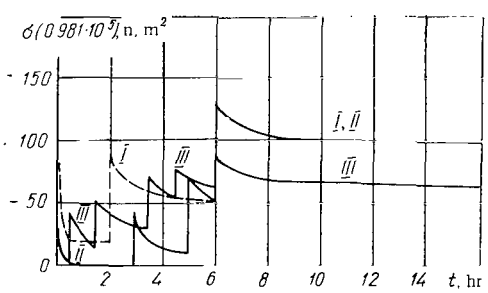

FIGURE V.4. Effect of the cooling conditions on the stress relaxation processes.

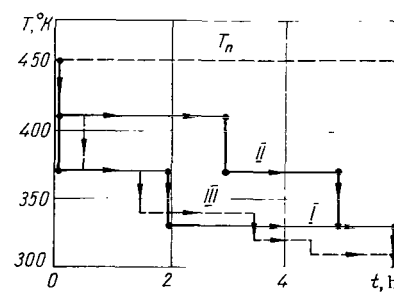

FIGURE V 5. Diagram of the cooling conditions.

Figure V.4 shows curves illustrating the effect of three cooling conditions (I, II, III — Figure V.5) on the stress relaxation in the structure of GFP.

We see from curve III of Figure V.4 corresponding to conditions III in Figure V.5 that the accelerated cooling process at high temperatures leads to a stronger stress relaxation than under conditions I and II in Figure V.5.

Chapter VI

THE ELECTROMAGNETIC FIELD IN FIBER COMPOSITES

Reinforced materials can be divided into dielectrics and conductors, depending on the component properties. The first group includes glass-fiber reinforced plastics and the second group consists of composites with current-conducting fibers and a matrix. Mixed types of composite materials also exist.

The electromagnetic properties of materials are characterized by the dielectric constant, permeability, conductivity, etc. Therefore, one of the main tasks is the determination of the reduced dielectric constant and permeability of reinforced composites from the given properties of the components, type of microstructure, and relative volume content of filler.

1. Electrostatics of reinforced dielectrics

We shall suppose that the reinforced medium with a simple regular structure is in a stationary electric field (the electrostatic equations of a homogeneous isotropic medium are reported in Chapter I).

If we introduce the electric field potential

$$\bar{E} = -\text{grad}\,\Phi, \tag{VI. 1}$$

it follows from the second equation of (I. 61) that

$$\text{div grad}\,\Phi = \nabla^2\Phi = 0. \tag{VI. 2}$$

The transverse field (the longitudinal component E_1 is absent) is of the greatest interest. For an external electric field which changes only slightly within the cell limits, the transverse components of vector $\bar{E}_s$ will be a doubly periodic function of z with structural periods ω_1 and $\omega_2 = \omega_1 e^{i\alpha}\left(\alpha = \frac{\pi}{3},\ \frac{\pi}{2}\right)$. The transverse components of the field are determined in terms of the potential function according to

$$E_2 - iE_3 = -2\Phi'(z). \tag{VI. 3}$$

The electrostatic field averaged over the cell is expressed as

$$\langle E_2\rangle - i\langle E_3\rangle = \frac{i}{F}\oint_{L_s}\Phi_s(z)\,d\bar{z} - \frac{i}{F}\oint_{L_a}\Phi_a(z)\,d\bar{z}. \qquad \text{(VI. 4)}$$

Here the symbols explained in Chapter I, section 8 are retained.

On the interface of the components the tangential components of the electrostatic field vector and the normal components of the displacement vector must be equal. These conditions are expressed in terms of potential (VI. 1) as

$$\Phi_s(\tau) = \Phi_a(\tau); \quad \varepsilon_s\frac{\partial}{\partial n}\Phi_s(\tau) = \varepsilon_a\frac{\partial}{\partial n}\Phi_a(\tau). \qquad \text{(VI. 5)}$$

The components of the displacement vector averaged over the cell will be

$$\langle D_2\rangle - i\langle D_3\rangle = -\frac{i\varepsilon_s}{F}\oint_{L_s}\Phi_s(z)\,d\bar{z} - \frac{i\varepsilon_a}{F}\oint_{L_a}\Phi_a(z)\,d\bar{z}. \qquad \text{(VI. 6)}$$

For a convenient transformation we introduce function

$$\Phi(z) = \varphi(z) + \overline{\varphi(z)}. \qquad \text{(VI. 7)}$$

The type of function $\varphi(z)$ relative to the components of the material is established either according to the requirements of the double periodicity of the field $\varphi_s'(z) = \varphi_s'(z + \omega_j)$, or are taken from (II. 10). For bodies of hexagonal or tetragonal structure, we can equate $\varepsilon_{22} = \varepsilon_{33}$ according to Neumann's principle /1/ where /2/

$$\varepsilon_{22} = \varepsilon_s\frac{1 + \xi + \gamma_1\varepsilon_s/\varepsilon_a}{\gamma_1 + (1+\xi)\varepsilon_s/\varepsilon_a} - 4\xi\varepsilon_s\eta + \frac{1 - \varepsilon_s/\varepsilon_a}{(1+\xi)\varepsilon_s/\varepsilon_a}\sum_{k=1}^{\infty}C'_{2k+2}\lambda^{2k+2}\alpha_{0,k}. \qquad \text{(VI. 8)}$$

Here again we use the symbols explained in Chapter I, section 8.

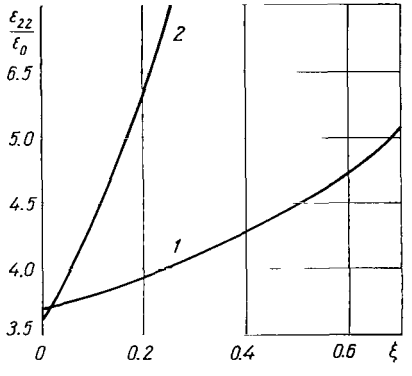

FIGURE VI. 1. Dependence of the relative dielectric constant on the filler level.

Figure VI. 1 shows curves illustrating the dependence of the relative dielectric constants of linearly reinforced GFP $\frac{\langle\varepsilon_{22}\rangle}{\varepsilon_0}$ with a PhN matrix

$\left(\frac{\varepsilon_s}{\varepsilon_0} = 3.6\right)$ on the volume content of the filler ξ. Curve 1 corresponds to aluminoborosilicate fibers, and curve 2 to fibers with a dielectric constant $\frac{\varepsilon_a}{\varepsilon_0} \approx 10^4$. The calculations show that for GFP equation (VI. 8) can be simplified to

$$\varepsilon_{22} \approx \varepsilon_s \frac{1 + \xi + \gamma_1 \varepsilon_s/\varepsilon_a}{\gamma_1 + (1 + \xi)\,\varepsilon_s/\varepsilon_a}. \qquad \text{(VI. 9)}$$

The last equation is accurate to within $\pm 5\%$.

For materials where $\frac{\varepsilon_s}{\varepsilon_a} \ll 1$, the error in this equation is higher, but remains within the permissible limits provided that the fibers do not touch one another.

From this equation we determine the transverse dielectric constant for materials in which the matrix is a dielectric and the fibers are conductors. These equations can be derived from the above equation if $\frac{\varepsilon_s}{\varepsilon_a} \to 0$.

2. Dielectric constant in a field which changes

In the case of an electromagnetic field which changes slightly, if its structure in a reinforced material is determined from the electrostatic equations with acceptable accuracy, the relationships obtained hold for a certain interval of frequency change of the electromagnetic field. To account for energy dissipation in the components in (IV. 9), instead of ε_s and ε_a we use the complex magnitudes obtained from (I. 57).

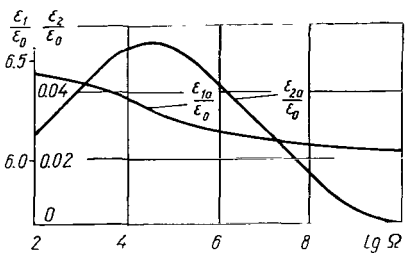

FIGURE VI. 2. Frequency dependence of the real and imaginary parts of the dielectric constant for glass-fiber reinforced plastics.

Energy dissipation in the fibers is determined by analogous equations. The parameters used in the equations are determined from a given ε_a for three frequencies. The dependence of the real and imaginary parts of ε_a on the frequency for glass fibers is shown in Figure VI. 2 $\left(\mathrm{Re}\,\frac{\varepsilon_a}{\varepsilon_0} = \frac{\varepsilon_{1a}}{\varepsilon_0};\ \mathrm{Im}\,\frac{\varepsilon_a}{\varepsilon_0} = \frac{\varepsilon_{2a}}{\varepsilon_0}\right)$.

In the approximate equations (VI. 9) if we separate the real from the imaginary parts of the dielectric constant of the reinforced material on the frequency and component properties.

$$\begin{aligned} \varepsilon'_{22} &= M\,[\varepsilon_s(\infty) + A_s] - N\varepsilon_s(\Omega_2); \\ \varepsilon''_{22} &= M\varepsilon_s(\Omega_2) + N\,[\varepsilon_s(\infty) + A_s]. \end{aligned} \qquad \text{(VI. 10)}$$

Here $\varepsilon(\infty)$ and $\varepsilon(\Omega_k)$ are the dielectric constants of the components at the maximum permissible frequency and frequency Ω_k, which are determined by experiment,

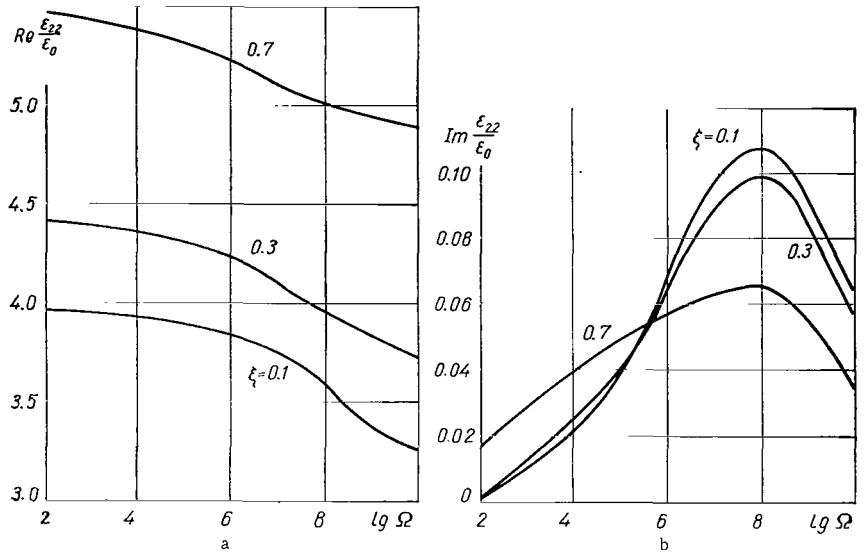

FIGURE VI.3. Frequency dependence of Re $\frac{\varepsilon_{22}}{\varepsilon_0}$ (a) and Im $\frac{\varepsilon_{22}}{\varepsilon_0}$ (b).

$$A = \varepsilon(\Omega_1) - \varepsilon(\infty);$$
$$M(g_1^2 + g_2^2) = g_1[(1+\xi)[A_a + \varepsilon_a(\infty)] + g_2[(1+\xi)\varepsilon_a(\Omega_2) + \eta_1\varepsilon_s(\Omega_2)];$$
$$N(g_1^2 + g_2^2) = g_1[(1+\xi)\varepsilon_a(\Omega_2) + \eta_1\varepsilon_s(\Omega_2)] - g_2\{(1+\xi)[A_a + \varepsilon_a(\infty)] + \eta_1[A_s + \varepsilon_s(\infty)]\},$$

where

$$g_1 = (1+\xi)[A_s + \varepsilon_s(\infty)] + \eta_1[A_a + \varepsilon_a(\infty)];$$
$$g_2 = \eta_1\varepsilon_a(\Omega_2) + (1+\xi)\varepsilon_s(\Omega_2).$$

Figure VI.3 shows the frequency dependence of Re $\frac{\varepsilon_{22}}{\varepsilon_0}$ and Im $\frac{\varepsilon_{22}}{\varepsilon_0}$ for a given volume content of glass fibers.

3. Magnetostatics of reinforced materials

For a reinforced material with a regular structure in a stationary magnetic field (see Chapter I, section 7) the magnetic field vector is expressed by the potential gradient, as in the above electrostatic problems,

$$\bar{H} = -\text{grad}\,\Phi. \qquad \text{(VI.11)}$$

We shall suppose that the longitudinal component of $\bar{H}$ is zero. The components of $\bar{H}_s$ in the tranverse plane at a constant external magnetic field will be a doubly periodic function.

The magnetostatic field averaged over the cell, which is independent of longitudinal coordinate x_1, is supposedly given by

$$\langle H_2\rangle - i\langle H_3\rangle = -\frac{i}{F}\oint_{L_s}\Phi_s(z)\,d\bar{z} - \frac{i}{F}\oint_{L_a}\Phi_a(z)\,d\bar{z}. \qquad \text{(VI. 12)}$$

The transverse components of $\bar{H}$ are determined in terms of the potential according to $H_2 - iH_3 = -2\Phi'(z)$.

On the interface of the components the tangential components of the transverse magnetic field vector and the normal components of the magnetic induction vector must be equal:

$$\Phi_a(\tau) = \Phi_s(\tau), \quad \mu_a\frac{\partial\Phi_a(\tau)}{\partial n} = \mu_s\frac{\partial\Phi_s(\tau)}{\partial n}.$$

The reduced permeability coefficients are determined from (see VI. 8):

$$\mu_{22} = \mu_{33} = \mu_s\frac{1+\xi+\eta\mu_s/\mu_a}{\eta+(1+\xi)\mu_s/\mu_a} - \frac{4\xi\mu_s(1-\mu_s/\mu_a)}{\eta+(1+\xi)\mu_s/\mu_a}\sum_{k=1}^{\infty}C'_{2k+2}\lambda^{2k+2}\omega_{0,k}. \qquad \text{(VI. 13)}$$

For approximate calculations of composite materials, in which the permeabilities of the components differ little from unity, only the first term of (VI. 13) can be used.

4. Electromagnetostatics of dielectrics reinforced by combined or hollow fibers

We shall consider a dielectric matrix reinforced by combined or hollow fibers forming a simple regular structure. The combined fibers have a cylindrical hollow, filled with other material. If the composite material is in an electrostatic field, its dielectric constant and permeability are established as for a three-phase medium. For each homogeneous and isotropic phase we introduce the electric field potential according to the above methods.

The boundary conditions for (VI. 5) for a transverse field are supplemented by analogous equations at the fiber-hollow interface. The field averaged over the cell is obtained from

$$\langle E_2\rangle - i\langle E_3\rangle = -\frac{i}{F}\oint_{L_s}\Phi_s(z)\,d\bar{z} - \frac{i}{F}\oint_{L_a}\Phi_a(z)\,d\bar{z} - \frac{i}{F}\oint_{L_r}\Phi_r(z)\,d\bar{z}.$$

Subscript r denotes magnitudes referring to the material filling the hollows.

If we omit the intermediate transformations we obtain an approximate expression for the reduced transverse dielectric constant in terms of the parameters and the volume content of the components

$$\varepsilon_{22} \approx \varepsilon_s\frac{1+\xi+\eta\varepsilon_s/\varepsilon_a-(1-\varepsilon_s/\varepsilon_a)\dfrac{1+\varepsilon_r/\varepsilon_a}{1-\varepsilon_r/\varepsilon_a}\eta q^2-2\xi q^2\dfrac{1-\varepsilon_r/\varepsilon_a}{1+\varepsilon_r/\varepsilon_a}}{\eta+(1+\xi)\varepsilon_s/\varepsilon_a-(1-\varepsilon_s/\varepsilon_a)\dfrac{1+\varepsilon_r/\varepsilon_a}{1-\varepsilon_r/\varepsilon_a}\eta q^2+2\xi q^2\dfrac{1-\varepsilon_r/\varepsilon_a}{1+\varepsilon_r/\varepsilon_a}\varepsilon_s/\varepsilon_a}. \qquad \text{(VI. 14)}$$

Here $q = \frac{\varepsilon}{\lambda}$, where ε is the radius of the hollow.

The reduced coefficient of the transverse permeability of the medium with combined or hollow fibers is determined from

$$\mu_{22} = \mu_{33} \approx \mu_s \frac{1 + \xi + \eta\mu_s/\mu_a - (1 - \mu_s/\mu_a)\frac{1 + \mu_r/\mu_a}{1 - \mu_r/\mu_a}\eta q^2 - 2\xi q^2 \frac{1 - \mu_r/\mu_a}{1 + \mu_r/\mu_a}}{\eta + (1 + \xi)\mu_s/\mu_a - (1 - \mu_s/\mu_a)\frac{1 + \mu_r/\mu_a}{1 - \mu_r/\mu_a}\eta q^2 + 2\xi q^2 \frac{1 - \mu_r/\mu_a}{1 + \mu_r/\mu_a}\mu_s/\mu_a}. \quad \text{(VI. 15)}$$

In the limiting case ($q = 0$), the equations obtained are the same as the above permeability equations.

5. Dielectric constant and permeability of multicomponent materials

We shall consider a composite reinforced by p kinds of fibers which are on the average uniformly distributed. An investigation of the electrostatic field in the multicomponent material is carried out by using the general representation of complex potential $\Phi_s(z)$ (see (II. 26)). Otherwise, establishing the solution of the problem is completely similar to the mathematical operations considered above. For materials with the closest packing, we found an approximate equation which expresses the reduced transverse dielectric constant in terms of the component properties

$$\varepsilon_{22} = \varepsilon_{33} \approx \varepsilon_s \frac{\eta + 2\sum_{k=1}^{p} 1 \frac{\xi_k}{+ \varepsilon_s/\varepsilon_k}}{1 - \sum_{k=1}^{p} \xi_k \frac{1 - \varepsilon_s/\varepsilon_k}{1 + \varepsilon_s/\varepsilon_k}}, \quad \text{(VI. 16)}$$

where ε_k is the dielectric constant of the k-th kind of fiber; the other symbols are the same as those reported in Chapter I, section 11.

The equation for the reduced transverse permeability of a multicomponent reinforced material with a hexagonal lattice is obtained by formally substituting μ_s, μ_k (permeabilities of the components) for ε_s, ε_k in (VI. 16):

$$\mu_{22} = \mu_{33} \approx \mu_s \frac{\eta + 2\sum_{k=1}^{p} 1 \frac{\xi_k}{+ \mu_s/\mu_k}}{1 - \sum_{k=1}^{p} \xi_k \frac{1 - \mu_s/\mu_k}{1 + \mu_s/\mu_k}}. \quad \text{(VI. 17)}$$

These transformations are justified by the similarity of the solutions of the electrostatic and magnetostatic equations.

To a first approximation, the reduced longitudinal dielectric constants ε_{11} and permeabilities μ_{11} can be found from the equations following from the law of mixing.

6. Electromagnetic field equations in reinforced materials

Vectors $\bar{E}$, $\bar{H}$ and $\bar{D}$, $\bar{B}$ characterizing the electromagnetic field in the material satisfy Maxwell's equations (I. 54), and are interconnected by the equations of state. For homogeneous isotropic media, the equations of state are reduced to (I. 55).

The equations of state for reinforced materials, taking into account the above discussion on the electromagnetic vectors averaged over the cell, are represented in matrix form

$$\begin{Bmatrix}\langle D_1\rangle\\ \langle D_2\rangle\\ \langle D_3\rangle\end{Bmatrix} = \begin{bmatrix}\varepsilon_{11} & 0 & 0\\ 0 & \varepsilon_{22} & \varepsilon_{23}\\ 0 & \varepsilon_{23} & \varepsilon_{33}\end{bmatrix}\begin{Bmatrix}\langle E_1\rangle\\ \langle E_2\rangle\\ \langle E_3\rangle\end{Bmatrix};\quad \begin{Bmatrix}\langle B_1\rangle\\ \langle B_2\rangle\\ \langle B_3\rangle\end{Bmatrix} = \begin{bmatrix}\mu_{21} & 0 & 0\\ 0 & \mu_{22} & \mu_{23}\\ 0 & \mu_{23} & \mu_{33}\end{bmatrix}\begin{Bmatrix}\langle H_1\rangle\\ \langle H_2\rangle\\ \langle H_3\rangle\end{Bmatrix}. \qquad \text{(VI. 18)}$$

In the majority of cases, if the volume content of the polymer matrix is low, the structure of the fibers of real materials is almost hexagonal. Therefore, within the limits of the required accuracy, we can equate

$$\begin{Bmatrix}\langle D_1\rangle\\ \langle D_2\rangle\\ \langle D_3\rangle\end{Bmatrix} = \begin{bmatrix}\varepsilon_{11} & 0 & 0\\ 0 & \varepsilon_{22} & 0\\ 0 & 0 & \varepsilon_{33}\end{bmatrix}\begin{Bmatrix}\langle E_1\rangle\\ \langle E_2\rangle\\ \langle E_3\rangle\end{Bmatrix};\quad \begin{Bmatrix}\langle B_1\rangle\\ \langle B_2\rangle\\ \langle B_3\rangle\end{Bmatrix} = \begin{bmatrix}\mu_{11} & 0 & 0\\ 0 & \mu_{22} & 0\\ 0 & 0 & \mu_{33}\end{bmatrix}\begin{Bmatrix}\langle H_1\rangle\\ \langle H_2\rangle\\ \langle H_3\rangle\end{Bmatrix}. \qquad \text{(VI. 19)}$$

Such representations of the equations of state for reinforced materials are possible under the following conditions:

a) the external electromagnetic field changes slightly in space, so that within a single cell these changes can be neglected;

b) the external electromagnetic field alternates with such a low frequency that the structure in the reinforced material can be determined by the electrostatic laws with sufficient accuracy.

The reduced dielectric constants and permeabilities on planes inclined to the fiber orientation can be determined by transformation equations of the components of the tensor of the second rank by rotating the coordinate aces. Thus, for example, if the coordinate system is rotated about axis $0x_3$ by angle α in the direction of the orientation, we can equate

$$\varepsilon'_{11} = \varepsilon_{11}\cos^2\alpha + \varepsilon_{22}\sin^2\alpha;$$
$$\varepsilon'_{22} = \varepsilon_{22}\cos^2\alpha + \varepsilon_{11}\sin^2\alpha.$$

The boundary conditions imposed onto the vector components of the averaged electromagnetic field are established over the cell, and therefore near the edge (VI. 19) becomes approximate. However, at some distance from the material boundaries, we can find the internal field at any point of the microstructure from the averaged field vector.

7. High-frequency field in materials reinforced by conductors

We shall suppose that the reinforced material in which identical circular fibers form the simplest monoclinic structure be in an electromagnetic field which changes at an arbitrary frequency Ω. The coordinates of the fiber centers are determined in the given structure from

$$x_2 + ix_3 = \omega_1(m + bne^{i\gamma}) \quad (m,\ n = 0,\ \pm 1,\ \ldots,\ \pm\infty).$$

If we assume that no side currents are present, we can find the solutions of the Maxwell equations (I. 54) and (I. 55) for each material component when the field is periodic

$$\overline{H} = \overline{\mathrm{H}}e^{-i\Omega t};\quad \overline{E} = \overline{\mathrm{E}}e^{-i\Omega t};\quad \overline{D} = \overline{d}e^{-i\Omega t},\quad \overline{B} = \overline{b}e^{-i\Omega t}.$$

By the method of complex amplitudes, the system of electromagnetic equations is reduced to a system of vectorial equations

$$\operatorname{rot} \bar{H} = -i\Omega\dot{\varepsilon}\bar{E}; \quad \operatorname{rot} \bar{E} = i\Omega\dot{\mu}\bar{H}, \tag{VI. 20}$$

where the complex dielectric constant is given by

$$\dot{\varepsilon} = \varepsilon + i\frac{\sigma}{\Omega} = \varepsilon + i\varepsilon. \tag{VI. 21}$$

The imaginary part of ε determines the dissipation of electromagnetic energy. For GFP material, where the conductivity is very low, we can neglect the dissipation in short-term processes, and omit $\dot{\varepsilon}$. If we allow for energy dissipation occurring on magnetization, in the second equation of (VI. 20) by $\dot{\mu}$ we denote the complex permeability

$$\dot{\mu} = \mu + i\mu'. \tag{VI. 22}$$

At high frequency, the imaginary part of (VI. 21) characterizing the lag of $\bar{D}$ relative to $\bar{E}$ is determined by the conductivity and other electric processes.

The solution of (VI. 20) is expressed in terms of the electric ($\bar{\pi}$) and magnetic (π^*) Hertz vectors satisfying the same Helmholtz equation

$$\frac{\partial^2\bar{\pi}}{\partial x_1^2} + \frac{\partial^2\bar{\pi}}{\partial x_2^2} + \frac{\partial^2\bar{\pi}}{\partial x_3^2} + \Omega^2\dot{\varepsilon}\dot{\mu}\bar{\pi} = 0.$$

The electric and magnetic field vectors are determined in terms of the Hertz vector, according to /3/

$$\begin{aligned} \bar{E} &= \Omega^2\dot{\varepsilon}\dot{\mu}\bar{\pi} + \operatorname{grad}\operatorname{div}\bar{\pi} + i\Omega\dot{\mu}\operatorname{rot}\bar{\pi}^*; \\ \bar{H} &= -i\Omega\dot{\varepsilon}\operatorname{rot}\bar{\pi} + \Omega^2\dot{\varepsilon}\dot{\mu}\bar{\pi}^* + \operatorname{grad}\operatorname{div}\bar{\pi}^*. \end{aligned} \tag{VI. 23}$$

We shall assume that the dielectric matrix is reinforced by ideal electric conductors inside which the field is zero. This condition holds for metals at low field frequencies. On the conductor surface there must be no tangential components of the electric and magnetic field vectors, and therefore the boundary conditions of the component interface are reduced to

$$\bar{n} \times \bar{E} = 0; \quad \bar{n} \cdot \bar{H} = 0, \tag{VI. 24}$$

where the second condition is formulated in analogy to an ideal magnetic conductor. In the given formulation, the problem consists in determining the electromagnetic field in the matrix only.

To satisfy boundary conditions (VI. 24), into each cell we introduced a local system of cylindrical coordinates r and θ, where it is sufficient to retain the longitudinal component of the Hertz vector

$$\bar{\pi} = \bar{e}_1\pi; \quad \bar{\pi}^* = \bar{e}_1\pi^*,$$

where $\bar{e}_1$, $\bar{e}_r$, $\bar{e}_\theta$ are the singular loci of the local cylindrical systems of coordinates with their origin at the center of the fiber.

For boundary conditions (VI. 24), the vectors $\bar{\pi}$ and $\bar{\pi}^*$ are not related to each other, and are determined independently. The first vector determines the propagation of the transverse magnetic waves (TM), and the second the propagation of the transverse electric waves (TE).

We know that in a homogeneous medium, a plane wave of the general type can be expanded into a series of cylindrical waves /3/

$$e^{ihx_3+i\lambda(x_1\cos\varphi+x_2\sin\varphi)} = e^{ihx_3}\sum_{\tau} i^{\tau}e^{i\tau(\varphi-\theta)}J_{\tau}(\lambda r), \qquad \text{(VI. 25)}$$

where ($h = \Omega\cos\beta$; $\lambda^2 = \Omega^2\varepsilon\mu - h^2$; $J_{\tau}(\lambda r)$) are cylindrical functions of the first kind; β and φ are the angles between the direction of wave propagation and axes $0x_1$ and $0x_2$.

In a reinforced body the wave field consists of the incident and reflected fields. In analogy with (VI. 25), it is assumed that in a composite the incident field in the cell is decomposed into Bessel functions with unknown coefficients

$$\pi_0 = \sum_{\tau} V_{00}^{\tau} J_{\tau}(\lambda r)\, e^{i\tau\theta+ihx_3}; \quad \pi_0^* = \sum_{\tau} W_{00}^{\tau} J_{\tau}(\lambda r)\, e^{i\tau\theta+ihx_3}. \qquad \text{(VI. 26)}$$

The field reflected from each fiber must correspond to the radiation conditions in infinity, and therefore it is represented as a series consisting of Hankel functions of the first kind ($H_{\tau}(\lambda r)\, e^{i\tau\theta}$). The sum of the incident and reflected fields satisfying the boundary conditions on the fiber circumference is the required solution of the diffraction problem. The incident field (VI. 26) can always be represented as the sum of the waves reflected from all the fibers. Therefore, by using the theorem of addition of Bessel functions

$$H_{\tau}(\lambda r)\, e^{i\tau\theta} = \sum_{n} H_{\tau+n}(\lambda R)\, I_n(\lambda r)\, e^{in\alpha}.$$

From this it is possible to reexpand the cylindrical waves in local systems of cylindrical coordinates with the origin in each cell, and by summing the waves reflected from all boundaries we find the finite-difference equations /4/ for determining V^{τ} and W^{τ}.

To obtain clear results, we must separate the general case into partial cases. We shall consider wave propagation in transverse and longitudinal directions to the fiber orientation. For the first type of wave propagation, we equate $h = 0$. The Hertz vector components in any cell are given by

$$\begin{aligned}\pi &= C_0 \exp\{ia_k\omega_1[m\cos\varphi + bn\cos(\alpha-\varphi)]\}\sum_{\tau} g_{\tau}(a_k)\,[J_{\tau}(\lambda r) - \\ &\qquad - Z_{\tau}H_{\tau}(\lambda r)]\, e^{i\tau\theta}; \qquad \text{(VI. 27)}\\ \pi^* &= S_0 \exp\{ib_k\omega_1[m\cos\varphi + bn\cos(\alpha-\varphi)]\}\sum_{\tau} g'_{\tau}(b_k)\,[J_{\tau}(\lambda r) - \\ &\qquad - Y_{\tau}H_{\tau}(\lambda r)]\, e^{i\tau\theta}.\end{aligned}$$

Here

$$Z_{\tau} = J_{\tau}(\lambda r_0)/H_{\tau}(\lambda r_0); \quad Y_{\tau} = J'_{\tau}(\lambda r_0)/H'_{\tau}(\lambda r_0);$$

where a_k and b_k are the k-th roots of the infinite matrices

$$|\delta_{j\tau} + Z_j G_{j-\tau}| = 0; \quad |\delta_{j\tau} + Y_j G'_{j-\tau}| = 0 \quad (j,\ \tau = 0, \pm 1, \ldots \pm\infty), \qquad \text{(VI. 28)}$$

where

$$G_{j-\tau} = (-i)^{j-\tau} e^{i(j-\tau)\varphi} \sum_{(\rho,\,\vartheta)} \sum' H_{j-\tau}(\lambda\omega_1\rho) \exp[a_k i\omega_1\rho \sin\vartheta - i(j-\tau)\vartheta];$$
$$G'_{j-\tau} = (-i)^{j-\tau} e^{i(j-\tau)\varphi} \sum_{(\rho,\,\vartheta)} \sum' H_{j-\tau}(\lambda\omega_1\rho) \exp[b_k i\omega_1\rho \sin\vartheta - i(j-\tau)\vartheta]. \quad \text{(VI. 29)}$$

The summation is carried out with respect to these discrete magnitudes ρ and ϑ which satisfy $m + ne^{i\alpha} = \rho e^{i\vartheta}$.

The parameters $g_\tau(a_k)$ and $g'_\tau(b_k)$ connect C_τ and S_τ with C_0 and S_0

$$C_\tau = g_\tau(a_k) C_0; \quad S_\tau = g'_\tau(b_k) S_0,$$

following from the solution of the system of algebraic equations

$$C_\tau + \sum_j Z_j G_{j-\tau} C_j = 0; \quad S_\tau + \sum_j Y_j G'_{j-\tau} S_j = 0 \quad (\tau,\ j = 0, \pm 1, \ldots, \pm\infty).$$

For the last representation of (VI. 27), the derivatives of which characterize the electromagnetic field in the reinforced medium when the waves propagate transversely, the "macroscopic" coordinates $x_2 + ix_3 = m\omega_1 + bne^{i\alpha}$ are introduced.

Using the "macroscopic" coordinates the solution of (VI. 27) is written as

$$\pi = Ce^{i\alpha_k(x_2\cos\varphi + x_3\sin\varphi)} \sum_{\tau} g_\tau(a_k)[J_\tau(\lambda r) - Z_\tau H_\tau(\lambda r)] e^{i\tau\Theta};$$
$$\pi^* = Se^{i\beta_k(x_2\cos\varphi + x_3\sin\varphi)} \sum_{\tau} g_\tau(b_k)[J_\tau(\lambda r) - Z_\tau H_\tau(\lambda r)] e^{i\tau\Theta}. \quad \text{(VI. 30)}$$

Thus, the total field in a reinforced material with regular structure can be represented as the product of the functions characterizing the wave field between the cells (exponent in (VI. 30)) and the field inside each cell.

For sufficiently long waves, when the field inside the cell is changed to a slight extent, we can introduce the reduced dielectric constant and permeability expressed by the roots of (VI. 28).

For waves with lengths commensurable with the interfiber distance, we can expect an increase in the contribution introduced by the field inside the cell. More information is obtained from the solutions found when calculating (VI. 28).

To find the reduced parameters, we examine the equations describing the propagation of electromagnetic fields in the longwave approximation* by using the equation of state (VI. 29) and the averaged parameters of the field vectors

$$\left.\begin{aligned}
&\frac{\partial\langle E_3\rangle}{\partial x_2} - \frac{\partial\langle E_2\rangle}{\partial x_3} = i\Omega\mu_{11}\langle H_1\rangle, \quad \frac{\partial\langle H_3\rangle}{\partial x_2} - \frac{\partial\langle H_2\rangle}{\partial x_3} = -i\Omega\varepsilon_{11}\langle E_1\rangle;\\
&\frac{\partial\langle E_1\rangle}{\partial x_3} - \frac{\partial\langle E_3\rangle}{\partial x_1} = i\Omega\mu_{22}\langle H_2\rangle, \quad \frac{\partial\langle H_1\rangle}{\partial x_3} - \frac{\partial\langle H_3\rangle}{\partial x_1} = -i\Omega\varepsilon_{22}\langle E_2\rangle;\\
&\frac{\partial\langle E_2\rangle}{\partial x_1} - \frac{\partial\langle E_1\rangle}{\partial x_2} = i\Omega\mu_{22}\langle H_3\rangle, \quad \frac{\partial\langle H_2\rangle}{\partial x_1} - \frac{\partial\langle H_1\rangle}{\partial x_2} = -i\Omega\varepsilon_{22}\langle E_2\rangle.
\end{aligned}\right\} \quad \text{(VI. 31)}$$

In the transverse magnetic field the components $\langle E_1\rangle$, $\langle H_2\rangle$ and $\langle H_3\rangle$ will differ from zero if the waves propagate transversely. The solution of the system in the form of polarized waves is

* The time factor is omitted here.

$$\langle E_1' \rangle = C \exp [i\Omega \sqrt{\varepsilon_{11}\mu_{22}} (x_2 \cos\varphi + x_3 \sin\varphi)];$$
$$\frac{\langle H_3' \rangle}{\langle E_1' \rangle} - i \frac{\langle H_2' \rangle}{\langle E_1' \rangle} = -e^{i\varphi} \sqrt{\varepsilon_{11}/\mu_{22}}. \qquad \text{(VI. 32)}$$

Here the above symbols are retained.

By comparing the exponents in (VI. 30) and (VI. 32), in the limiting case for long waves, we find

$$a = \Omega \sqrt{\varepsilon_{11}\mu_{22}}. \qquad \text{(VI. 33)}$$

In the transverse electric field the solution of (VI. 31) is

$$\langle H_1^* \rangle = C \exp [i\Omega \sqrt{\varepsilon_{22}\mu_{11}} (x_2 \cos\varphi + x_3 \sin\varphi)];$$
$$\frac{\langle E_3^* \rangle}{\langle H_1^* \rangle} - i \frac{\langle E_2^* \rangle}{\langle H_1^* \rangle} = e^{i\varphi} \sqrt{\mu_{11}/\varepsilon_{22}}, \text{ откуда } b \approx \Omega \sqrt{\varepsilon_{22}\mu_{11}}. \qquad \text{(VI. 34)}$$

For the longwave approximation, in (VI. 29) we integrate instead of summing, and neglect the imaginary parts $\dot{\varepsilon}$ and $\dot{\mu}$. Integration gives

$$G_{j-\tau} \approx \frac{4i}{F} \cdot \frac{(-1)^{j-\tau} e^{i(j-\tau)\varphi}}{\lambda^2 - a^2} \begin{cases} (a/\lambda)^{j-\tau} & (\lambda > a); \\ (\lambda/a)^{j-\tau} & (\lambda < a); \end{cases}$$
$$G'_{j-\tau} \approx \frac{4i}{F} \cdot \frac{(-1)^{j-\tau} e^{i(j-\tau)\varphi}}{\lambda^2 - v^2} \begin{cases} (v/\lambda)^{j-\tau} & (\lambda > v); \\ (\lambda/v)^{j-\tau} & (\lambda < v). \end{cases} \qquad \text{(VI. 35)}$$

In asymptotic approximation we obtain the following estimates of parameters present in (VI. 28):

$$Z_0 \approx 0, \quad Z_\tau \approx \frac{\pi i}{\Gamma(\tau)\Gamma(1+\tau)} \left(\frac{\lambda r_0}{2}\right)^{2\tau};$$
$$Y_0 \approx \pi i \left(\frac{\lambda r_0}{2}\right)^2, \quad Y_\tau \approx -\frac{\pi i}{\Gamma(\tau)\Gamma(1+\tau)} \left(\frac{\lambda r_0}{2}\right)^{2\tau}.$$

From these equations we can successively specify a and v in (VI. 28). For the transverse electric field, in the first approximation, using only one element in the second determinant, we find

$$v \approx \lambda \sqrt{\tau_1} = \Omega \sqrt{\tau_1 \varepsilon \mu}.$$

The successive approximations take the dispersion phenomena into account. By comparing the data found with those calculated from (VI. 9), we see the differences between the parameters determined by the electrostatic and electrodynamic equations.

8. Longitudinally propagating waves in conductor-reinforced materials

We shall consider a wave propagating in the direction of fiber orientation. The equations required can be obtained from (VI. 20).

We shall assume that both longitudinal components of the electromagnetic field are absent, that is $E_1 = 0$, $H_1 = 0$.

The field obtained is termed transverse electromagnetic field (TEM) and is realized when

$$\bar{E} = \bar{E}(x_2,\ x_3)\, e^{i\omega\sqrt{\varepsilon\mu}x_1}; \quad \bar{H} = \bar{H}(x_2,\ x_3)\, e^{i\omega\sqrt{\varepsilon\mu}x_1}. \tag{VI. 36}$$

The main wave of TEM is simultaneously the transverse electric and transverse magnetic wave, and propagates as a plane wave in a homogeneous matrix. From (VI. 20) and (VI. 36), we obtain

$$\begin{gathered}\sqrt{\varepsilon}E_2 = \sqrt{\mu}H_3, \quad \sqrt{\varepsilon}E_3 = -\sqrt{\mu}H_2; \\ \frac{\partial E_3}{\partial x_2} - \frac{\partial E_2}{\partial x_1} = 0, \quad \frac{\partial H_3}{\partial x_2} - \frac{\partial H_2}{\partial x_3} = 0.\end{gathered} \tag{VI. 37}$$

It follows from (VI. 37) that $\bar{E}$ and $\bar{H}$ satisfy the Laplace operator. The field structure in the cross section is determined from the solution of the corresponding electromagnetic problems (section 1 of Chapter VI) when the boundary conditions (VI. 24) on the matrix-dielectric interface are observed.

When the TE and TM waves propagate in the longitudinal direction, the wave field is determined from the components of the Hertz vector.

For a periodic field in the transverse plane the components of the Hertz vector are expanded into a series analogous to (VI. 27):

$$\begin{aligned}\pi &= C\exp\left[ihx_1 + 2\pi i\left(\frac{mp}{f} + b\frac{nq}{l}\right)\right]\sum_j g_j(h)\,[J_j(\lambda r) - Z_j H_j(\lambda r)]\, e^{ij\vartheta}; \\ \pi^* &= S\exp\left[ih'x_1 + 2\pi i\left(\frac{mp}{f} + b\frac{nq}{l}\right)\right]\sum_j g_j'(h')\,[J_j(\lambda r) - Y_j H_j(\lambda r)]\, e^{ij\vartheta},\end{aligned} \tag{VI. 38}$$

where p, q and l are the natural numbers characterizing the field periods in the cross section. The propagation parameters h and h' in the two wave types are found from (VI. 28), where we equate

$$G'_{j-\tau} = G_{j-\tau} = (-i)^{j-\tau} e^{i(j-\tau)\varphi} \sum_{(r,\,s)}{}' H_{j-\tau}(\lambda\omega_1\rho)\exp[2\pi i d\rho\sin\vartheta - i(j-\tau)\vartheta]. \tag{VI. 39}$$

Here $d\cos\varphi = \frac{p}{f}$; $d\cos(\alpha - \varphi) = \frac{q}{l}$ $(p,\ q,\ f,\ l = 1,\ 2,\ \ldots)$.

In the longwave approximation in (VI. 39), we integrate instead of summing. The following equations were set up:

$$G_{j-\tau} \approx \frac{4i}{F}\cdot\frac{(-1)^{j-\tau}e^{i(j-\tau)\varphi}}{\lambda^2 - \left(\frac{2\pi d}{\omega_1}\right)^2}\begin{cases}\left(\frac{2\pi d}{\omega_1\lambda}\right)^{j-\tau} & \left(\lambda > \frac{2\pi d}{\omega_1}\right) \\ \left(\frac{\omega_1\lambda}{2\pi d}\right)^{j-\tau} & \left(\lambda < \frac{2\pi d}{\omega_1}\right)\end{cases}.$$

In the assumed approximation, the expressions for Z_τ and Y_τ are replaced by asymptotic expansions. By using the representations found we can solve the determinant (VI. 28) and find an estimate for the propagation constants h and h'. Thus, for instance, for the TE field we determine to a first approximation

$$h = \sqrt{\Omega^2\varepsilon\mu - \frac{4\pi^2 d^2}{\omega_1^2}}, \tag{VI. 40}$$

using only one element of the corresponding determinant.

If $\Omega^2\varepsilon\mu < 4\pi^2 d^2 \Big/ \gamma_0 \omega_1^2$ the longitudinal waves are exponentially damped (they do not propagate any longer); and the damping becomes more rapid as it increases.

With increase in Ω the number of propagating waves increases.

As we have seen, dielectrics reinforced by fibers have the properties of guiding systems (waveguides), and hence their reduced electromagnetic parameters are a function of the propagating wave frequency.

9. Electromagnetic waves in dielectric fibers

We shall suppose that the components of the reinforced material are dielectrics. GFP are typical illustrations. It is supposed that the material structure is formed by a system of straightened identical fibers, with their axes arbitrarily placed $\left(b \neq 1,\ \alpha \neq \frac{\pi}{3},\ \frac{\pi}{2}\right)$.

We shall consider the simultaneous propagation of TM and TE waves. The electric and magnetic field vectors are expressed in terms of the Hertz vectors according to (VI. 23). On the interface conditions (VI. 24) are satisfied.

The total field in the individual cell consists of the incident and the reflected fields. The former consist of the fields reflected from all the fibers except the given one, while the latter must correspond to radiation conditions. The required representation of the Hertz vector for the matrix is in the form

$$\begin{aligned} \pi_s &= \sum_j \{V_{00}^j [J_j(\lambda_s r) - Z_j H_j(\lambda_s r)] - W_{00}^j Y_j^* H_j(\lambda_s r)\} e^{ij\theta + ihx_1}; \\ \pi_s^* &= \sum_j \{W_{00}^j [J_j(\lambda_s r) - Y_j H_j(\lambda_s r)] - V_{00}^j Z_j^* H_j(\lambda_s r)\} e^{ij\theta + ihx_1}. \end{aligned} \tag{VI. 41}$$

For filler elements, we have the following equations

$$\begin{aligned} \pi_a &= \sum_j (\lambda_s/\lambda_a)^2 \{V_{00}^j [J_j(\lambda_s r_0) - Z_j H_j(\lambda_s r_0)] - W_{00}^j Y_j^* H_j(\lambda_s r_0)\} \frac{J_j(\lambda_a r)}{J_j(\lambda_a r_0)} e^{ij\theta + ihx_1}; \\ \pi_a^* &= \sum_j (\lambda_s/\lambda_a)^2 \{W_{00}^j [J_j(\lambda_s r_0) - Y_j H_j(\lambda_s r_0)] - V_{00}^j Z_j^* H_j(\lambda_s r_0)\} \times \\ &\qquad \times \frac{J_j(\lambda_a r)}{J_j(\lambda_a r_0)} e^{ij\theta + ihx_1}. \end{aligned} \tag{VI. 42}$$

The subscripts of V_{00}^j and W_{00}^j denote the number of the cell in which the field is considered, and in which the origin of the local cylindrical coordinate system is placed. The expressions for Z_j, Z_j^*, Y_j and Y_j^* are very cumbersome and for this reason they are not reported here. The values of V^j and W^j in the different cells are interrelated by an infinite system of finite-difference equations

$$\begin{aligned} V_{00}^k + \sum_{m\neq 0,} \sum_{n\neq 0} \sum_j (-1)^{j-k} (Z_j V_{mn}^j + Y_j^* W_{mn}^j) H_{j-k}(\lambda_s R_{mn}) e^{i\theta'_{mn}(j-k)} = 0; \\ W_{00}^k + \sum_{m\neq 0,} \sum_{n\neq 0,} \sum_j (-1)^{j-k} (Y_j W_{mn}^j + Z_j^* V_{mn}^j) H_{j-k}(\lambda_s R_{mn}) e^{i\theta'_{mn}(j-k)} = 0, \end{aligned} \tag{VI. 43}$$

where R_{mn} is the distance between the mn-th cell and the considered cell, while Θ_{mn} is the angle at which the center of the mn-th cell is observed.

We shall now consider a particular case, that is, TEM waves which are independent of arbitrary coordinate x_1. The required equations are obtained by equating h_0 to zero

$$Y_j^* = Z_j^* = 0, \tag{VI. 44}$$

and expanding the system (VI. 43) into two completely independent equation groups determining the existence of the two types of transverse waves. The solution of the equation systems obtained is in the form of traveling waves

$$\begin{aligned} V_{mn}^h &= C_h \exp\{ia\omega_1 [m\cos\varphi + bn\cos(\alpha - \varphi)]\}; \\ W_{mn}^h &= S_h \exp\{iv\omega_1 [m\cos\varphi + bn\cos(\alpha - \varphi)]\}, \end{aligned} \tag{VI. 45}$$

where φ is the angle between the direction of the waves and the $0x_2$-axis, while a and v are unknown parameters. By substituting (VI. 45) into (VI. 43), and taking into account (VI. 44), we get two independent infinite systems for the arbitrary constants C_h and S_h. From the conditions of simultaneousness of the system it follows that both determinants are equal to zero, from which a and v are determined. Equations (VI. 45) determine the transverse wave field in the reinforced material. For the longwave approximation, parameters $G_{j-\tau}$ and $G'_{j-\tau}$ are given by (VI. 35), while the other parameters are transformed into

$$\begin{aligned} &Z_0 \approx \pi i (1 - \varepsilon_a/\varepsilon_s)\left(\frac{\lambda_s r_0}{2}\right)^2; \quad Y_0 \approx \pi i (1 - \mu_a/\mu_s)\left(\frac{\lambda_s r_0}{2}\right)^2; \\ &Z_j \approx \frac{\pi i}{\Gamma(j)\,\Gamma(1+j)}\left(\frac{\lambda_s r_0}{2}\right)^{2j} \frac{1 - \mu_s/\mu_a}{1 + \mu_s/\mu_a}; \quad Y_j \approx -\frac{\pi i}{\Gamma(j)\,\Gamma(1+j)}\left(\frac{\lambda_s r_0}{2}\right)^{2j} \frac{1 - \varepsilon_s/\varepsilon_a}{1 + \varepsilon_s/\varepsilon_a}. \end{aligned} \tag{VI. 46}$$

Thus, in the given case two types of waves exist. The reduced parameters are determined when investigating infinite determinants of type (VI. 28).

A strict solution of the problem of longitudinally propagating TE and TM waves requires an expansion of the functions while the boundary conditions are satisfied, since the propagation constants in the matrix and filler differ in the general case. However, at some distances from the faces these effects can be neglected, and the parameters V^h and W^h are determined as periodic functions

$$\begin{aligned} V_{mn}^h &= C_h \exp\{2\pi i d [m\cos\varphi + bn\cos(\alpha - \varphi)]\}; \\ W_{mn}^h &= S_h \exp\{2\pi i d [m\cos\varphi + bn\cos(\alpha - \varphi)]\}; \end{aligned} \tag{VI. 47}$$

$d\cos\varphi = \frac{p}{f}$; $d\cos(\alpha - \varphi) = \frac{q}{l}$ and p, f, q, l form a series of natural numbers characterizing the field periods in the transverse plane. The dispersion formula for determining h follows from the differences in equations (VI. 43) when (VI. 47) is substituted. In this case the medium displays wave properties, and therefore a set of frequencies exists at which energy transfer is possible.

A similar effect can be achieved if the material is enclosed between two reflecting longitudinal walls so as to prevent energy dissipation due to the formation of transverse fluxes.

When electromagnetic waves propagate over inclined areas, to a certain approximation the field is divided into the components obtained during the propagation of the TE and TM waves in the longitudinal and transverse directions.

Bibliography

1. Nye, J.F. Physical Properties of Crystals. Oxford, The Clarendon Press. 1955.
2. Van Fo Fy, G.A. Elektromagnitostatika armirovannykh polimerov (Electromagnetostatics of Reinforced Polymers). — Mekhanika Polimerov, 6. 1968.
3. Stratton, J.A. Electromagnetic Theory. New York—London, McGraw-Hill. 1941.
4. Van Fo Fy, G.A. — DAN Ukrainskoi SSR, 3. 1968.

Chapter VII

ELASTIC WAVES IN REINFORCED MEDIA

We distinguish three characteristic cases when studying the propagation of elastic waves in composites: a) propagation of long waves; the wave length is larger than the distance between the individual fibers, and the stress gradient averaged over the cell changes only slightly within the field; b) shortwave motion when the wavelength is commensurable with the lattice constant ω_1 of the given material structure; and c) high-frequency disturbances when the length of the elastic waves is much smaller than the fiber diameter. This classification is rather arbitrary, since there is no fixed boundary between the individual cases, but it is nevertheless useful. Of course, when waves of the first type propagate the stress field in the structure of the reinforced material is almost static, and therefore it is sufficient to consider the wave motion of the centers of gravity of the cells with the reduced mass. In this case, the simplest model of a reinforced material is a homogeneous anisotropic continuum with parameters obtained from the solutions of the static problems mentioned in Chapter II, while the number of intrinsically differing reduced constants is selected according to the symmetry type of the reinforced material. At these frequencies the process of energy dissipation can be studied on the basis of the viscoelasticity theory, using the Volterra principle, if the energy scattering in the components is satisfactorily described by linear expressions. This fairly simple approximation makes it possible to study dynamic phenomena in various applied problems of the theory of reinforced material.

To study the propagation of waves of the second type, we must resort to methods allowing for diffraction phenomena in the material structure. In this case, the dispersion effects become appreciable, that is, the dependence of the propagation velocity on the wavelength or wave frequency. Every cell of the reinforced material at the given frequencies behaves like a system with an infinite number of degrees of freedom, and also frequency ranges may exist at which the waves cannot propagate because of intense dissipation. Wave propagation in the third case is studied by means of asymptotic expansions, constructed for application to high-frequency disturbances in the reinforced material.

1. Waves in an anisotropic viscoelastic medium

We shall suppose that waves propagate through an unlimited viscoelastic medium reinforced by parallel fibers placed at the lattice points of a

hexagonal system. The wavelength L is much larger than the distance between the fibers ω_1 ($L \gg \omega_1$). We shall omit the dynamic phenomena in the individual cell (their effect is appreciable only when the wavelength is of the same order of magnitude as ω_1) and study wave propagation in a homogeneous anisotropic (transversely isotropic) viscoelastic continuum, where the strains are related to the stresses by

$$\varepsilon_{ik} = \overline{X}_{ik}^{\tau j}\sigma_{ij} = X_{ik}^{\tau j}\left[1 - \sum_{n=1}^{m} a_n \Im_{1-\lambda}^{*}(-\omega_n)\right]\sigma_{\tau j}. \qquad \text{(VII. 1)}$$

The type of operators as applied to several concrete reinforced materials is determined from the equations in Chapter III. For a transversely isotropic medium, it is best to represent (VII. 1) in matrix form

$$\begin{Bmatrix} \varepsilon_{11} \\ \varepsilon_{22} \\ \varepsilon_{33} \\ \varepsilon_{12} \\ \varepsilon_{13} \\ \varepsilon_{23} \end{Bmatrix} = \begin{Bmatrix} \overline{X}_{11}^{11}, & \overline{X}_{11}^{22}, & \overline{X}_{11}^{22}, & . & . & . \\ \overline{X}_{11}^{22}, & \overline{X}_{22}^{22}, & \overline{X}_{22}^{33}, & . & . & . \\ \overline{X}_{11}^{22}, & \overline{X}_{22}^{33}, & \overline{X}_{22}^{22}, & . & . & . \\ . & . & . & \overline{X}_{12}^{12}, & . & . \\ . & . & . & . & \overline{X}_{12}^{12}, & . \\ . & . & . & . & . & 2(\overline{X}_{22}^{22} - X_{22}^{33}) \end{Bmatrix} \begin{Bmatrix} \sigma_{11} \\ \sigma_{22} \\ \sigma_{33} \\ \sigma_{12} \\ \sigma_{13} \\ \sigma_{23} \end{Bmatrix}. \qquad \text{(VII. 2)}$$

The equations inverse to (VII. 1) are

$$\sigma_{ik} = E_{ik}^{\tau j}\left[1 + \sum_{n=1}^{m} b_n \Im_{1-\lambda}^{*}(-g_n)\right]\varepsilon_{\tau j} = \overline{E}_{ik}^{\tau j}\varepsilon_{ij}. \qquad \text{(VII. 3)}$$

Here, as usual, the axis $0x_1$ of the Cartesian system is directed along the fiber orientation, and the index numbers of stress and strain tensor components correspond to the selected coordinate system.

From the balance equation of the elementary volume (section 2, Chapter V) and Cauchy's equation for deformations, and also taking (VII. 3) into account, we obtain a system of three dynamic equations in terms of displacement

$$\sum_{\tau,\, n,\, k=1}^{3} E_{ik}^{\tau n}\frac{\partial^2 u_\tau}{\partial x_n\, \partial x_k} = \rho\frac{\partial^2 u_i}{\partial t^2}, \qquad \text{(VII. 4)}$$

where ρ is the density of the continuum.

We shall consider the propagation of plane waves

$$u_\tau = \operatorname{Re} A_\tau e^{i(\Omega t - \bar{k}\cdot\bar{r})}, \qquad \text{(VII. 5)}$$

where $\bar{e}_k$ ($k = 1, 2, 3$) are the singular loci; $\bar{r} = \bar{e}_k x_k$, $\bar{k} = \bar{e}_k k_k$ the wave vectors; and A_τ are arbitrary constants, correlated by a system of three algebraic equations

$$\sum_{\tau,\, n,\, m=1}^{3} E_{pm}^{\tau n}(i\Omega)\, k_n k_m A_\tau - \rho\Omega^2 A_p = 0 \quad (p = 1, 2, 3).$$

It follows from the simultaneity of the homogeneous system that the determinant which presents the frequency equation /1/ is equal to zero

$$\left| \sum_{m,\, n=1}^{3} E_{pm}^{\tau n}(i\Omega)\, k_n k_m - \rho\Omega^2\delta_{p\tau} \right| = 0. \qquad \text{(VII. 6)}$$

When deriving these equations we used (see section 5, Chapter I)

$$\overline{E}_{pm}^{\tau n} e^{i\Omega t} = e^{i\Omega t} E_{pm}^{\tau n}(i\Omega).$$

We shall study the particular cases of wave propagation. We shall assume that the wave vector is decomposed in plane (x_1, x_3) when

$$k_2 = 0;\ k_3 + ik_1 = ke^{i\Theta},$$

where

$$k = \sqrt{k_1^2 + k_3^2};\quad \operatorname{tg}\Theta = k_1/k_3.$$

(VII. 6) can be decomposed into two equations:

$$\begin{gathered} E_{12}^{12}k_1^2 + \frac{1}{2}(E_{22}^{22} - E_{22}^{33})k_3^2 - \rho\Omega^2 = 0; \\ (E_{11}^{11}k_1^2 + E_{12}^{12}k_3^2)(E_{22}^{22}k_3^2 + E_{12}^{12}k_1^2) - \rho\Omega^2(E_{11}^{11}k_1^2 + E_{12}^{12}k_3^2 + \\ + E_{22}^{22}k_3^2 + E_{12}^{12}k_3^2) + \rho^2\Omega^4 - (E_{11}^{22} + E_{12}^{12})^2 k_1^2 k_3^2 = 0. \end{gathered} \qquad \text{(VII. 7)}$$

Here and later we omit argument $(i\Omega)$ at parameters $E_{ik}^{\tau n}$. By joining the wave vector to locus $\bar{e}_1$, we obtain

$$k_3 = 0;\ k_1 = \pm\sqrt{\frac{\rho\Omega^2}{E_{11}^{11}}};\ k_{(2)} = \pm\sqrt{\frac{\rho\Omega^2}{E_{12}^{12}}};\ k_{(2)} = k_{(3)}. \qquad \text{(VII. 8)}$$

The k values found correspond to independent plane elementary waves of type

$$u_\tau = \operatorname{Re} A_\tau e^{i(\Omega t \pm k_{(\tau)} x_1)}. \qquad \text{(VII. 9)}$$

It follows from the above equations that in the given medium there exist a longitudinal tension-compression wave along the fiber orientation propagating with velocity v_1, and two longitudinal shear waves. The propagation velocity and damping factor of the latter two waves are equal because of the viscoelastic properties of the material. The two differing wave velocities are

$$v_1 = \operatorname{Re}\sqrt{E_{11}^{11}/\rho};\ v_2 = v_3 = \operatorname{Re}\sqrt{E_{12}^{12}/\rho}. \qquad \text{(VII. 10)}$$

The damping factors of the waves in the material are determined from

$$\alpha_1 = -\Omega \operatorname{Im}\sqrt{\rho/E_{11}^{11}};\ \alpha_2 = \alpha_3 = -\Omega \operatorname{Im}\sqrt{\rho/E_{12}^{12}}. \qquad \text{(VII. 11)}$$

By joining the wave vector to $\bar{e}_3$, and taking $k_1 = 0$, from (VII. 7) we obtain

$$k_{(1)} = \pm\sqrt{\frac{\rho\Omega^2}{E_{12}^{12}}};\ k_{(2)} = \pm\sqrt{\frac{2\rho\Omega^2}{E_{22}^{22} - E_{22}^{23}}};\ k_{(3)} = \pm\sqrt{\frac{\rho\Omega^2}{E_{22}^{22}}}. \qquad \text{(VII. 12)}$$

The k values found correspond to plane wave motion of type

$$u_\tau = \operatorname{Re} A_\tau e^{i(\Omega t \pm k_{(\tau)} x_3)}.$$

Here the wave velocities will differ appreciably

$$v_2 = \operatorname{Re}\sqrt{(E_{22}^{22} - E_{22}^{33})/2\rho};\quad v_3 = \operatorname{Re}\sqrt{E_{22}^{22}/\rho}. \tag{VII. 13}$$

The damping factor of these waves is determined from the imaginary part

$$\alpha_2 = -\Omega \operatorname{Im}\sqrt{\frac{2\rho}{E_{22}^{22} - E_{22}^{33}}};\quad \alpha_3 = -\Omega \operatorname{Im}\sqrt{\frac{\rho}{E_{22}^{22}}}. \tag{VII. 14}$$

If the wave vector is placed in other coordinate planes, it is easy to see that there are no velocities of elementary waves appreciably differing from the given ones.

In the more general case ($k_2 = 0$, $k_1 \neq 0$, $k_3 \neq 0$), the wave displacements according to (VII. 5) and (VII. 7) are

$$u_\tau = \operatorname{Re} A_\tau e^{i[\Omega t \pm (k_1 x_1 + k_3 x_3)]}.$$

Here

$$k_1^2 = \frac{1}{E_{12}^{12}}\left[\rho\Omega^2 - \frac{k_3^2}{2}(E_{22}^{22} - E_{22}^{33})\right];$$

$$k_3^2 = \rho\Omega^2 \frac{(E_{12}^{12} + E_{11}^{22})^2 - \frac{1}{2}(E_{11}^{11} - E_{12}^{12})(E_{22}^{22} + E_{22}^{33})}{E_{22}^{22}(E_{12}^{12})^2 + D - \frac{1}{4}E_{11}^{11}|(E_{22}^{22})^2 - (E_{22}^{33})^2|},$$

where

$$D = (E_{22}^{22} - E_{22}^{33})\left[E_{11}^{22}E_{12}^{12} - \frac{1}{2}(E_{11}^{22})^2\right].$$

The general case of plane wave propagation is studied in a similar way. To go over to technical constants we use equations

$$E_{12}^{12} = G_{12};\quad \frac{1}{2}(E_{22}^{22} - E_{22}^{33}) = G_{23},$$

$$E_{11}^{11} = \frac{1 - \nu_{23}}{1 - \nu_{23} - 2\nu_{21}\nu_{12}}E_{11};\quad E_{22}^{22} = \frac{1 - \nu_{21}\nu_{12}}{1 - \nu_{23} - 2\nu_{21}\nu_{12}}2G_{23};$$

$$E_{11}^{22} = \frac{\nu_{12}}{1 - \nu_{23} - 2\nu_{21}\nu_{12}}E_{11};\quad E_{22}^{33} = \frac{\nu_{23} + \nu_{21}\nu_{12}}{1 - \nu_{23} - 2\nu_{21}\nu_{12}}2G_{23}.$$

For composites in which the elastic parameters of the fillers are considerably higher than those of the matrix, that is, in GFP, we can estimate the wave velocity. In particular, for linearly reinforced GFP

$$\operatorname{Re} E_{11}^{11} > \operatorname{Re} E_{22}^{22} > \operatorname{Re}\frac{1}{2}(E_{22}^{22} - E_{22}^{33}) > \operatorname{Re} E_{12}^{12},$$

whence the maximum and minimum velocities of disturbance propagation are

$$v_{\max} = \operatorname{Re}\sqrt{E_{11}^{11}/\rho};\quad v_{\min} = \operatorname{Re}\sqrt{E_{12}^{12}/\rho}.$$

If we allow for the dissipative properties only in the polymer matrix (EMA), then $v_{\min}$ for a GFP is

$$v_{\min} \approx v_0 \operatorname{Re}\sqrt{1 - P\frac{\omega_\infty + P + \Omega^\lambda \cos\pi\lambda/2 - i\Omega^\lambda \sin\pi\lambda/2}{(\omega_\infty + P)^2 + 2(\omega_\infty + P)\Omega^\lambda \cos\pi\lambda/2 + \Omega^{2\lambda}}},$$

where

$$P = \frac{3\eta\omega_0}{(2+2\nu_0)[\eta+(1+\xi)G_0/G_a]}, \qquad \text{(VII. 15)}$$

$v_0 = \sqrt{G_{12}^0/\rho}$ is the limiting wave velocity in longitudinal shear. The other symbols have been described before, with increase in the frequency, the propagation velocity increases and tends to its limit value $v_0 \approx 0.532 \cdot 10^3$ m/sec.

The maximum propagation velocity of longitudinal waves in the direction of orientation of linearly reinforced GFP is

$$v_{\max} = \operatorname{Re}\sqrt{E_{11}^{11}/\rho} \approx 1{,}61 \cdot 10^3 \text{ m/sec}.$$

We see that the anisotropic effects in the given material are considerable. Our calculations show that the effect of inelastic properties of the matrix on the wave velocity is negligibly small.

2. Energy dissipation in a reinforced material

Energy dissipation during the propagation of long waves in reinforced materials is caused by the dissipative parameters of the components and by their interaction. In this chapter we shall estimate the energy dissipated in media formed by an inelastic matrix and an ideal elastic filler. Such an approximation qualitatively reflects the dissipation processes and can be generalized for other cases by analogy.

We shall assume that the reinforced medium with fibers that form a hexagonal structure is acted upon by periodic stresses $\operatorname{Re}\langle\sigma_{ik}\rangle e^{i\Omega t}$. We shall also assume that $(L \gg \omega_1)$

The dissipative properties of a reinforced medium, to a linear approximation, is determined by the five considerably differing integral operators defined in Chapter III. For materials with components intrinsically differing in their dissipative properties, only a few of the five operators can contribute appreciably to energy dissipation, that is, the reinforced medium is characterized by reinforced dissipative parameters. Thus, for example, in linearly reinforced GFP only G_{12}^*, E_{22}^* and ν_{23}^* appreciably depend on the viscoelastic properties. To a first approximation, if we neglect energy dissipation in fibers, and assume that no dry friction exists on the component interface, we obtain the complex compliance of the reinforced medium in longitudinal shear /2/

$$I_{12}' - iI_{12}'' \approx \frac{1}{G_{12}^0}\left(1 + P\,\frac{\omega_\infty + \Omega^\lambda \cos\pi\lambda/2 - i\Omega^\lambda \sin\pi\lambda/2}{\omega_\infty^2 + 2\omega_\infty\Omega^\lambda \cos\pi\lambda/2 + \Omega^{2\lambda}}\right).$$

In the case of transverse tension-compression of the given medium, the complex shear compliance is

$$I_{22}' - iI_{22}' \approx \frac{1}{E_{22}^0}\left(1 + \sum_{j=1}^{3} A_j\,\frac{\omega_j + \Omega^\lambda \cos\pi\lambda/2 + i\Omega^\lambda \sin\pi\lambda/2}{\omega_j^2 + 2\omega_j\Omega^\lambda \cos\pi\lambda/2 + \Omega^{2\lambda}}\right),$$

where the following designations are used

$$\omega_1 = \omega_- ;\ \omega_2 = \omega_0 + \omega_- - b_1 ;\ \omega_3 = \omega_0 + \omega_- - b_2 ;$$

$$A_1 = \frac{3\omega_0^2}{(2+2\nu_0)(1+c)}\left(\frac{1}{\omega_0 - b_1} + \frac{c}{\omega_0 - b_2}\right);\quad A_2 = \frac{b_1}{1+c}\left(1 - \frac{3\omega_0}{(2+2\nu_0)(\omega_0 - b_1)}\right);$$

$$A_3 = \frac{b_2 c}{1+c}\left(1 - \frac{3\omega_0}{(2+2\nu_0)(\omega_0 - b_2)}\right);$$

$$b_1 = \frac{2\xi\omega_0(1-2\nu_0)}{1+\eta+\xi\varkappa_0+\eta(\varkappa_a-1)G_0/G_a};\quad b_2 = \frac{2\omega_0(1-2\nu_0)}{1+\varkappa_0-\eta(1-G_0/G_a)};$$

$$c = -\frac{2\xi^2(1-G_0/G_a)\,b_2/b_1}{2+(\varkappa_a-1)G_0/G_a};\quad \varkappa = 3-4\nu.$$

The dependence of the dynamic moduli and dissipative characteristics on the angular frequency $\nu = 2\pi\Omega$ is shown in Figure VII. 1. The dependence of the moving constraints of the polymer matrix on the dynamic moduli is very small. The loss compliances I''_{12} and I''_{22} characterizing the dissipative properties of the material reach their maxima at a certain frequency, and afterwards decrease with increase in frequency. The specific work of the dissipative forces Ψ in a single cell is given by

$$\Psi = \frac{\delta\Omega}{2\pi V}\int_0^{2\pi/\Omega} dt \int_{V_s+V_a} dV \left[\sigma_{11}\frac{\partial \dot{u}_1}{\partial x_1} + \sigma_{22}\frac{\partial \dot{u}_2}{\partial x_2} + \sigma_{33}\frac{\partial \dot{u}_3}{\partial x_3} + \right.$$
$$\left. + \sigma_{23}\left(\frac{\partial \dot{u}_3}{\partial x_2} + \frac{\partial \dot{u}_2}{\partial x_3}\right) + 2\sigma_{12}\frac{\partial \dot{u}_1}{\partial x_2} + 2\sigma_{13}\frac{\partial \dot{u}_1}{\partial x_3}\right]. \qquad \text{(VII. 16)}$$

Here the dots on top denote the derivative with respect to time of the displacement vector components; δ is the heat equivalent of the mechanical work; V is the cell volume representing a parallelepiped of unit height and base area $V = V_s + V_a$.

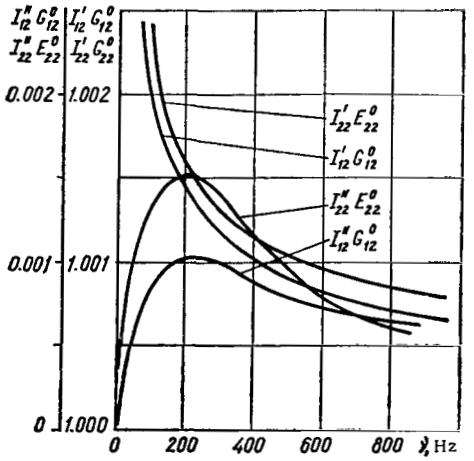

FIGURE VII. 1. Dependence of the dynamic moduli and dissipative parameters on the angular frequency.

When calculating x_1 we must remember that the period required for temperature equalization in a single cell is longer than the vibration period of the medium. For this reason the change in the temperature field during this period can be neglected. If we consider the homogeneity of the stressed-strained state along x within the separate cell, we can substitute the integral over the cell surface F for the integral over the cell volume in (VII. 16). Our calculations show that the contribution of structural stresses in energy dissipation is negligibly small /2/. It is therefore sufficient to use the reduced parameters for an approximate calculation of the dissipated energy. With this approximation

$$\Psi \approx \frac{\delta\Omega}{2\pi}\int_0^{2\pi/\Omega} dt \sum_{i,k=1}^{3} \langle \sigma_{ik}\rangle \beta_{ik}\delta_{ik}\dot{\theta} + \frac{\delta\Omega}{2\pi}\int_0^{2\pi/\Omega} dt \sum_{i,k,p,n} (X_{ik}^{pn})_0 \times$$
$$\times \left[1 + \sum_{j=1}^{m} A_j \vartheta_{1-\lambda}^{*}(-\omega_j)\right] \langle \sigma_{ik}\rangle \langle \sigma_{pn}\rangle,$$

where $\beta_{ik}\dot{\theta}$ characterizes the thermal deformation rate of the medium. In the majority of cases the first integral can be neglected. For media with a very small work of the dissipative forces during longitudinal tension-compression, from the foregoing equation we obtain

$$\Psi \approx \frac{\delta\Omega}{2} I_{22}'' [\langle \sigma_{22}^0\rangle^2 + \langle \sigma_{33}^0\rangle^2 - 2\nu_{23}^0 \langle \sigma_{22}^0\rangle \langle \sigma_{33}^0\rangle + 2(1+\nu_{23}^0)\langle \sigma_{23}^0\rangle^2] +$$
$$+ \frac{\delta\Omega}{2} I_{12}'' (\langle \sigma_{12}^0\rangle^2 + \langle \sigma_{13}^0\rangle^2). \qquad \text{(VII. 17)}$$

We use here the symbols introduced above. The accumulated energy will evolve because of the thermal conductivity processes given by

$$\gamma C_v \frac{\partial \langle T\rangle}{\partial \tau} + \varkappa_{11}\frac{\partial^2 \langle T\rangle}{\partial x_1^2} + \varkappa_{22}\left(\frac{\partial^2 \langle T\rangle}{\partial x_2^2} + \frac{\partial^2 \langle T\rangle}{\partial x_3^2}\right) = \Psi(\tau).$$

We should note that Ψ is a "slow" time function (see section 5, Chapter 1).

3. Elastic waves taking into account diffraction

If the length of the propagating elastic wave is commensurable with the interfiber distance, we must allow for energy dissipation by the fibers. The elastic displacement vector $\bar{u}$ of each component of the reinforced medium satisfies equation (see section 2 of this chapter)

$$G\Delta\bar{u} + (\lambda + G)\,\mathrm{grad}\,\mathrm{div}\bar{u} = \rho\frac{\partial^2\bar{u}}{\partial t^2},$$

where ρ is the density of the components.

The solution of the equation is a sum of functions /3/

$$\bar{u} = \bar{e}_1 u_1 + \mathrm{grad}'\,\Psi + \mathrm{rot}'\,\bar{e}_1\Phi, \qquad \text{(VII. 18)}$$

where the primes denote that the equation is differentiated with respect to variables x_2 and x_3. In the general case, the waves propagate at an angle to the fibers. For this reason the function is established in the form of traveling waves

$$u_1 = u_0 e^{i(\varkappa x_1 - \Omega t)};\ \Psi = \Psi_0 e^{i(\varkappa x_1 - \Omega t)};\ \Phi = \Phi_0 e^{i(\varkappa x_1 - \Omega t)}, \tag{VII. 19}$$

where the unknown parameter $\varkappa$ is taken as equal for all the components. Because of this assumption we do not consider the wave phenomena near the fiber boundary, when deviations from the given representation of the solution are possible. The newly introduced functions satisfy a system of equations

$$\left.\begin{aligned} &\nabla^2\Phi_0 + (\Omega^2/c_v^2 - \varkappa^2)\,\Phi_0 = 0; \\ &[\nabla^2 + (\Omega^2/c_v^2 - \varkappa^2)]\,[\nabla^2 + \Omega^2/c_0^2 - \varkappa^2)]\,\Psi_0 = 0; \\ &i\varkappa(1 + \lambda/G)\,u_0 = -(2 + \lambda/G)\,\nabla^2\Psi_0 - (\Omega^2/c_v^2 - \varkappa^2)\,\Psi_0, \end{aligned}\right\} \tag{VII. 20}$$

where ∇^2 is the Laplace operator for variables x_2 and x_3; c_0 and c_v are symbols for the velocity of longitudinal and transverse elastic waves, respectively, for each component

$$c_0 = \sqrt{\frac{\lambda + 2G}{\rho}};\quad c_v = \sqrt{\frac{G}{\rho}}.$$

We shall consider the particular cases of wave propagation. We equate Ψ and Φ to zero, that is, we assume that no displacement of the transverse plane exists. In this case it follows from the above that the transverse displacements u_1 are independent of x_1 and satisfy equation

$$\nabla^2 u_1 - \frac{1}{c_v^2} \cdot \frac{\partial^2 u}{\partial t^2} = 0. \tag{VII. 21}$$

In this case only transverse waves propagate in the medium.

If u_1 values are zero, and Φ and Ψ independent of x_1, both types of waves exist, which propagate in the transverse plane. The potentials satisfy

$$\nabla^2\Phi - \frac{1}{c_v^2} \cdot \frac{\partial^2\Phi}{\partial t^2} = 0;\quad \nabla^2\Psi - \frac{1}{c_0^2} \cdot \frac{\partial^2\Psi}{\partial t^2} = 0. \tag{VII. 22}$$

The simpler third type of elastic wave propagation is caused by longitudinal displacement along $0x_1$. According to the cases considered, the problems of wave propagation in reinforced media are solved.

4. Longitudinal shear waves

Transverse displacements of each component satisfy a wave equation of type (VII. 21), where the magnitudes relating to the matrix are denoted by "s" and those related to the fibers by "a".

On the fiber-matrix interface the conditions for stress-displacement equality are given by

$$u_s(\tau) = u_a(\tau);\quad G_s \frac{\partial u_s(\tau)}{\partial n} = G_a \frac{\partial u_a(\tau)}{\partial n}. \tag{VII. 23}$$

The wave field in the matrix is determined as the sum of the fields incident upon the given cell and reflected from the fiber boundary. The incident wave is obtained by superposition of the cylindrical waves

satisfying (VII. 21) in a local coordinate system. The reflected field satisfies Sommerfeld's radiation condition. The general solution is found by separation of the plane traveling wave

$$u_s = C_0 \exp\{ia\omega_1 [m\cos\varphi + bn\cos(\alpha - \varphi)]\} \sum_\tau g_\tau(a)\,[J_\tau(kr) - Z_\tau H_\tau(kr)]\, e^{i\tau\theta - \Omega t};$$

while the field in the fibers is analogously represented

$$u_a = C_0 \exp\{ia\omega_1 [m\cos\varphi + bn\cos(\alpha - \varphi)]\} \sum_\tau g_\tau(a)\, J_\tau(kr_0) - Z_\tau H_\tau(kr_0) \frac{J_\tau(k'r)}{J_\tau(k'r_0)} e^{i\tau\theta - i\Omega t}.$$

Here $k = \frac{\Omega}{c_{vs}}$; $k' = \frac{\Omega}{c_{va}}$. The other parameters are readily found by satisfying boundary conditions (VII. 23) for an arbitrary field. The unknown parameter a is obtained from the equality of the determinant to zero

$$|\delta_{j\tau} + Z_j G_{j-\tau}| = 0 \quad (j, \tau = 0, \pm 1, \ldots, \pm\infty). \tag{VII. 24}$$

The equation for $G_{j-\tau}$ is formally the same as (VI. 24) if λ is replaced by letter k. (VII. 24) is a dispersion equation.

In the longwave approximation, in the expression for $G_{j-\tau}$ we integrate instead of summing (see (VI. 35)) and use

$$Z_0 \approx \pi i \left(\frac{kr_0}{2}\right)^2 (1 - \rho_a/\rho_s); \quad Z_\tau \approx \frac{\pi i}{\Gamma(\tau)\,\Gamma(1+\tau)} \left(\frac{kr_0}{2}\right)^{2\tau} \frac{1 - G_s/G_a}{1 + G_s/G_a}.$$

In this case we can follow the effect of the component properties on a. The structure of (VII. 24) is such that the central column in the longwave approximation characterizes the effect of ρ_a/ρ_s on the wavelength. The other columns of the determinant depend on G_s/G_a and kr_0, that is, the wavelength depends on the frequency Ω. When $G_s/G_a = 1$, in this approximation

$$a = \pm k_s \sqrt{\eta + \xi\rho_a/\rho_s} = \pm \Omega \sqrt{\frac{\eta\rho_s + \xi\rho_a}{G}}, \tag{VII. 25}$$

and the phase velocity is frequency-independent. The field in the cell is symmetric, and the disturbances propagate as wave

$$\langle u \rangle = C \exp\{ia\omega_1 [m\cos\varphi + bn\cos(\alpha - \varphi)] - i\Omega t\}.$$

To allow for the dissipative phenomena, we substitute the corresponding integral operators, and consider the action of these operators upon the exponential time function (see section 5).

5. Transverse propagation of elastic waves

If no longitudinal displacements u_1 exist, we observe transverse wave propagation in the medium. We have shown in the preceding section that in this case longitudinal (c_0) and shear (c_v) waves exist. Functions Φ and Ψ

satisfy (VII. 22) and ideal contact conditions between filler and matrix. They are obtained in the form

$$\Psi_s = \sum_\tau \{V_{00}^\tau [J_\tau(k_{0s}r) - Z_\tau H_\tau(k_{0s}r)] - W_{00}^\tau Y_\tau^* H_\tau(k_{0s}r)\} e^{i\tau\theta - i\Omega t};$$
$$\Phi_s = \sum_\tau \{W_{00}^\tau [J_\tau(k_{vs}r) - Y_\tau H_\tau(k_{vs}r)] - V_{00}^\tau Z_\tau^* H_\tau(k_{vs}r)\} e^{i\tau\theta - i\Omega t}, \quad \text{(VII. 26)}$$

where $k_0 = \frac{\Omega}{C_0}$; $k_v = \frac{\Omega}{C_v}$.

The equations for the filler elements are similar. We shall not discuss the cumbersome equations for Y_τ, Z_τ and Y_τ^*, Z_τ^*, but give the system of finite difference equations for determining V^τ and W^τ:

$$V_{00}^\tau + \sum_{m\neq 0,} \sum_{n\neq 0,} \sum_j (Z_j V_{mn}^j + Y_j^* W_{mn}^j)(-1)^{j-\tau} H_{j-\tau}(k_{0s}R_{mn}) e^{i(j-\tau)\theta'_{mn}} = 0;$$
$$W_{00}^\tau + \sum_{m\neq 0,} \sum_{n\neq 0,} \sum_j (Y_j W_{mn}^j + Z_j^* V_{mn}^j)(-1)^{j-\tau} H_{j-\tau}(k_{vs}R_{mn}) e^{i(j-\tau)\theta'_{mn}} = 0. \quad \text{(VII. 27)}$$

The solution of the system obtained in the form of "macroscopic" traveling waves is

$$V_{mn}^\tau = C_\tau \exp\{ia\omega_1 [m\cos\varphi + nb\cos(\alpha - \varphi)]\};$$
$$W_{mn}^\tau = S_\tau \exp\{ia\omega_1 [m\cos\varphi + nb\cos(\alpha - \varphi)]\}.$$

By inserting this function into (VII. 27), we obtain an infinite system of homogeneous algebraic equations for C_τ and S_τ. The dispersion equation for a follows from the compatibility condition of this system.

6. Longitudinal propagation of elastic waves

To simplify our explanations, we shall consider a wave field far from the ends of the fibers, and assume that the material points in the transverse plane remain in one plane during motion (hypothesis of plane cross sections). The elastic displacement vector of each component is determined from (VII. 18), where the dependence of the introduced function on the longitudinal coordinate is given in the form of (VII. 19).

The boundary conditions with ideal contact are reduced to the equality of the displacement vectors and three components of the stress tensor in matrix and fillers.

The functions required for the matrix are constructed by Bessel functions

$$\Phi_{0s} = \sum_\tau [U_{00}^\tau J_\tau(\alpha_s r) + B_{00}^\tau H_\tau(\alpha_s r)] e^{i\tau\theta};$$
$$\Psi_{0s} = \sum_\tau [V_{00}^\tau J_\tau(\alpha_s r) + S_{00}^\tau H_\tau(\alpha_s r) + W_{00}^\tau J_\tau(\beta_s r) + E_{00}^\tau H_\tau(\beta_s r)] e^{i\tau\theta}, \quad \text{(VII. 28)}$$

where

$$\alpha = \sqrt{\Omega^2/C_v^2 - \varkappa^2}; \quad \beta = \sqrt{\Omega^2/c_v^2 - \varkappa^2}.$$

The other cumbersome expressions are omitted.

Transverse displacements u_0 are found by simple differentiation according to (VII. 20). For the filler, the solution is given by a series of Bessel functions of the first kind. Constants B^τ, S^τ and E^τ are expressed in terms of parameters U^τ, V^τ, and W^τ according to

$$B^\tau_{mn} = -Z^\tau_{11}U^\tau_{mn} - Z^\tau_{12}V^\tau_{mn} - Z^\tau_{13}W^\tau_{mn};$$
$$S^\tau_{mn} = -Z^\tau_{21}U^\tau_{mn} - Z^\tau_{22}V^\tau_{mn} - Z^\tau_{23}W^\tau_{mn};$$
$$E^\tau_{mn} = -Z^\tau_{31}U^\tau_{mn} - Z^\tau_{32}V^\tau_{mn} - Z^\tau_{33}W^\tau_{mn}.$$

The wave propagation parameters are interrelated by a system of homogeneous finite-difference equations

$$\left.\begin{aligned} U^\tau_{00} + \sum_{m\neq 0,}\sum_{n\neq 0,}\sum_{j}(Z^j_{11}U^j_{mn} + Z^j_{12}V^j_{mn} + \\ + Z^j_{13}W^j_{mn})(-1)^{j-\tau}H_{j-\tau}(\alpha_s R_{mn})\,e^{i(j-\tau)\theta'_{mn}} = 0; \\ V^\tau_{00} + \sum_{m\neq 0,}\sum_{n\neq 0,}\sum_{j}(Z^j_{21}U^j_{mn} + Z^j_{22}V^j_{mn} + \\ + Z^j_{23}W^j_{mn})(-1)^{j-\tau}H_{j-\tau}(\alpha_s R_{mn})\,e^{i(j-\tau)\theta'_{mn}} = 0; \\ W^\tau_{00} + \sum_{m\neq 0,}\sum_{n\neq 0,}\sum_{j}(Z^j_{31}U^j_{mn} + Z^j_{32}V^j_{mn} + \\ + Z^j_{33}W^j_{mn})(-1)^{j-\tau}H_{j-\tau}(\beta_s R_{mn})\,e^{i(j-\tau)\theta'_{mn}} = 0. \end{aligned}\right\} \qquad \text{(VII. 29)}$$

If we remember that for longitudinally propagating waves the displacement and stresses in the reinforced material will be doubly periodic functions of x_2 and x_3, we obtain the solution of (VII. 29) as periodic functions

$$\left.\begin{aligned} U^\tau_{mn} &= C_\tau \exp\{2\pi id[m\cos\varphi + nb\cos(\alpha-\varphi)]\}; \\ V^\tau_{mn} &= S_\tau \exp\{2\pi id[m\cos\varphi + nb\cos(\alpha-\varphi)]\}; \\ W^\tau_{mn} &= T_\tau \exp\{2\pi id[m\cos\varphi + nb\cos(\alpha-\varphi)]\}, \end{aligned}\right\} \qquad \text{(VII. 30)}$$

where

$$d\cos\varphi = \frac{p}{g}; \quad d\cos(\alpha-\varphi) = \frac{q}{l} \quad (p,\ q,\ l,\ g = 1,\ 2,\ \ldots).$$

By introducing (VII. 30) into (VII. 29) we obtain a system of algebraic equations. For the compatibility condition we obtain a dispersion equation for the propagation constant.

In the longwave approximation, for a known value of $\varkappa$, we can directly obtain the dependence of the reduced parameters of the reinforced medium on the properties of the components, with allowance for dispersion.

Bibliography

1. Van Fo Fy, G.A. Rasprostranenie voln v armirovannykh sredakh (Wave Propagation in Reinforced Media). — Prikladnaya Mekhanika, 3 : 4. 1967.
2. Van Fo Fy, G.A. Odnorodnye i armirovannye plastiki pri periodicheskikh vozdeistviyakh (Homogeneous and Reinforced Plastics under Periodic Action). — Prikladnaya Mekhanika, 11 : 8. 1966.
3. Van Fo Fy, G.A. — DAN URSR, RSR, 9. 1967.

Chapter VIII

ANALOGIES AND MODELING OF COMPOSITES

Analogies are the basis of mathematical modeling of various phenomena. Electroanalogies are especially useful since they make it possible to solve mechanical and physical problems.

In this chapter we shall discuss some analogies in the theory of composites, establish the generalized variables, and consider potential models of composites.

1. Analogies in the theory of disperse-reinforced composites

We shall consider composites with the two most general microstructures. They comprise materials strengthened by distributed dispersed particles of various shapes (see Figure VIII. 1), and also composites reinforced by short or continuous fibers.

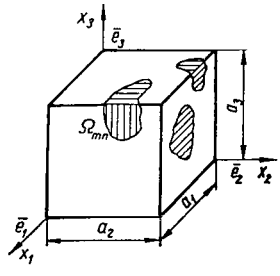

FIGURE VIII. 1. Model of a material reinforced by disperse particles.

To generalize the problem, we assume that the microstructures of both types are formed by g kinds of fibers. In the center of the first type we separate a volume (cell) v shaped as a paralleliped. It contains at least one disperse particle of each kind, and has all the macroscopic characteristics of the composite. We shall assume that the structure of the remaining part is formed by a periodic prolongation of the given cell in three ways, while the maxtrix and filler properties are indicated with sufficient accuracy by continuum models.

We have proved above that a stationary temperature, and electromagnetic or other field in a homogeneous medium can be determined by means of a potential function satisfying the Laplace equation

$$\Delta\Phi = 0. \qquad \text{(VIII. 1)}$$

If, for example, we consider a stationary temperature field, the temperature of the medium is compared to the potential

$$T \equiv \Phi,$$

and the heat flow vector $\bar{q}$ is related to the temperature gradients by Fourier's law

$$\bar{q} = -\varkappa \operatorname{grad} T, \tag{VIII. 2}$$

where $\varkappa$ is the thermal conductivity coefficient.

We shall assume that the cell contains $n (g \leqslant n)$ particles. Hence, inside the m-th disperse particle, bounded by the outer surface Ω_m $(m = 1, 2, \ldots, n)$, or in the matrix filling the space between the inclusions, the temperature and heat flow are determined from (VIII. 1) and (VIII. 2). In our discussion the magnitudes relating to the matrix and to the m-th disperse particle in the given cell will be given subscripts s and m, respectively, $(m = 1, 2, \ldots, n)$.

On the filler-matrix interface the conditions of thermal contact must be given. For determinacy, we give here conditions of ideal thermal contact

$$\begin{gathered} T_s|_{\Omega_m} = T_m|_{\Omega_m}; \\ \varkappa_s (\bar{n} \cdot \operatorname{grad}) T_s|_{\Omega_m} = \varkappa_m (\bar{n} \cdot \operatorname{grad} T_m)|_{\Omega_m} \quad (m = 1, 2, \ldots, n). \end{gathered} \tag{VIII. 3}$$

Here $\bar{n}$ is the unit vector normal to Ω_m. Moreover, additional conditions on the temperature or heat flow distribution averaged over the selected cell must be given. This restriction depends on the mean gradient of the temperature field which encloses the given body. In our problem, it is sufficient to consider a changing temperature field, when the mean heat flow does not change in the adjacent cells of the composite, and the mean temperature increases linearly. For this reason, the heat flow vector in the matrix must be a trebly periodic function of spatial variables x_1, x_2, and x_3 (see Figure VIII. 1) with periods a_1, a_2, and a_3 equal to the sides of the given parallelepiped. It is easy to see that this requirement is reduced to the following conditions:

$$\operatorname{grad} T_s(x_1, x_2, x_3) = \operatorname{grad} T_s(x_1 + a_1, x_2 + a_2, x_3 + a_3), \tag{VIII. 4}$$

which must be applied to Φ. If (VIII. 4) is satisfied, the boundary conditions on the filler-matrix interface in all the other cells into which the composite is divided will be automatically fulfilled. With the assumed approximation, it is sufficient to give the mean flow

$$\langle \bar{q} \rangle = -\frac{1}{V} \int_{V_s} \varkappa_s \operatorname{grad} T_s \, dv - \sum_{m=1}^{n} \frac{1}{V} \int_{V_m} \varkappa_m \operatorname{grad} T_m \, dv, \tag{VIII. 5}$$

where V_s and V_m are the volumes occupied by the matrix and m-th filler, respectively, in the separated cell. With this relation, we can express the temperature in the composite in terms of the components of the mean heat flux vector.

To determine the reduced thermal conductivity coefficients characterizing the intercell thermal conductivity, we shall consider heat exchange in a homogeneous anisotropic cell with an infinitely small volume corresponding

to the separated cell. According to the above the change in the mean temperature between the cells will be given by

$$\langle T \rangle = \sum_{i=1}^{3} \alpha_i x_i,$$

where α_i are constant proportionality factors.

The corresponding heat flux is given by

$$\langle \bar{q} \rangle = \sum_{i,k=1}^{3} \bar{e}_i \alpha_k \varkappa_{ik}. \qquad \text{(VIII. 6)}$$

Here $\bar{e}_i$ are the singular loci, and $\varkappa_{ik}$ are the components of the tensor of the reduced thermal conductivity coefficient. Its dyadic representation is

$$\bar{\varkappa} = \sum_{i,k}^{3} \bar{e}_i \bar{e}_k \varkappa_{ik}.$$

Equation (VIII. 6) is used for expressing α_k by $\langle q_i \rangle$ and $\varkappa_{ik}$.

By comparing the temperature gradients in a homogeneous anisotropic medium and in the composite between cells, and allowing for the fact that to simplify the computation the gradient is replaced by finite-difference equations connecting the temperatures in adjacent cells, we obtain an algebraic equation

$$\sum_{i=1}^{3} \alpha_i (x_i + a_h) = T_s(x_h + a_h) - T_s(x_h) \quad (k = 1, 2, 3). \qquad \text{(VIII. 7)}$$

From (VIII. 7), $\varkappa_{ik}$ can be expressed in terms of the thermophysical parameters and volume content of the components.

We should note that the symmetry conditions of the coefficients

$$\varkappa_{ik} = \varkappa_{ki} \qquad \text{(VIII. 8)}$$

for composite media is a direct consequence of the solution of (VIII. 7) without Onsager's reciprocity principle.

The solution of the problem of the electrostatic or magnetostatic field in the filled dielectric can be solved on the basis of analogy. Naturally, the electric $\bar{E}$ and magnetic $\bar{H}$ field vectors are expressed by the corresponding potential functions using $\bar{E} = -\operatorname{grad} \Psi$; $\bar{H} = -\operatorname{grad} \Phi$. The electric displacement $\bar{D}$ and magnetic induction $\bar{B}$ vectors are determined from the equations of state $\bar{D} = \varepsilon \bar{E}$; $\bar{B} = \mu \bar{H}$ (see Chapter I).

On the interface the tangential components of $\bar{E}$ and the normal components of $\bar{D}$ must be equal, that is

$$\bar{n} \times \bar{E}_s|_{\varrho_m} = \bar{n} \times \bar{E}_m|_{\varrho_m}; \quad \bar{n} \cdot \bar{D}_s|_{\varrho_m} = \bar{n} \cdot \bar{D}_m|_{\varrho_m}.$$

These conditions are equivalent to:

$$\Psi_s|_{\varrho_m} = \Psi_m|_{\varrho_m}; \quad \varepsilon_s (\bar{n} \cdot \operatorname{grad}) \Psi_s|_{\varrho_m} = \varepsilon_m (\bar{n} \cdot \operatorname{grad}) \Psi_m|_{\varrho_m}.$$

For the magnetostatic field, we obtain

$$F_s|_{\Omega_m} = F_m|_{\Omega_m}; \quad \mu_s(\bar{n}\cdot\operatorname{grad})F_s|_{\Omega_m} = \mu_m(\bar{n}\cdot\operatorname{grad})F_m|_{\Omega_m}.$$

In contrast to the above case, in this problem the average values of the field are given

$$\langle\bar{E}\rangle = \frac{1}{V}\int_{V_s}\operatorname{grad}\Psi_s\,dV + \sum_{m=1}^{n}\frac{1}{V}\int_{V_m}\operatorname{grad}\Psi_m\,dV; \qquad \text{(VIII. 9)}$$

$$\langle\bar{H}\rangle = \frac{1}{V}\int_{V_s}\operatorname{grad}F_s\,dV + \sum_{m=1}^{n}\frac{1}{V}\int_{V_m}\operatorname{grad}F_m\,dV.$$

In the other features, there is complete analogy between the given problems if the following transformations are applied:

$$\Psi \to T \to F; \quad \bar{E} \to \operatorname{grad}T \to \bar{H}; \quad D \to \bar{q} \to \bar{B}, \qquad \text{(VIII. 10)}$$

and also $\varepsilon \to \varkappa \to \mu$

The analogy in the determination of the reduced parameters of the composite $\varepsilon_{ik} \to \varkappa_{ik} \to \mu_{ik}$ is used in the same way.

This analogy makes it possible to determine the reduced parameters of the composite medium and the distribution of a field in the selected material from experimental data or calculations of a field of another physical nature. It is, however, necessary to observe the geometric similarity of these materials, and to use the following dimensionless numbers

$$\frac{\varepsilon_{ik}}{\varepsilon_s} = \frac{\varkappa_{ik}}{\varkappa_s} = \frac{\mu_{ik}}{\mu_s}; \quad \frac{\varepsilon_m}{\varepsilon_s} = \frac{\varkappa_m}{\varkappa_s} = \frac{\mu_m}{\mu_s} \quad \begin{pmatrix} m = 1, 2, \ldots, n; \\ i, k = 1, 2, 3. \end{pmatrix}. \qquad \text{(VIII. 11)}$$

For two-phase composites $m = 1$.

2. Analogies in the theory of composite fibers

For linearly reinforced composite fibers, it is convenient to decompose vectors $\bar{q}$, $\bar{E}$, and $\bar{H}$, into longitudinal and transverse components. The first component is directed along the orientation, and is independent of the longitudinal coordinate x_1, and the second component is directed across the fiber orientation. The number of intrinsically differing components for the composites is thus decreased. For example the tensor of the reduced thermal conductivity coefficients is characterized by the following components

$$\begin{Vmatrix} \varkappa_{11}, & 0 & 0 \\ 0, & \varkappa_{22}, & \varkappa_{23} \\ 0, & \varkappa_{32}, & \varkappa_{33} \end{Vmatrix}.$$

A special role is played in these materials by the reduced composite parameters during transverse flow.

The above analogies and dimensionless numbers (VIII. 11) for transverse flow hold in this case also. We can add to these the mechanical analogy on the stress distribution and reduced moduli of rigidity in pure shear of the composite fiber in the planes passing through the fiber axes. Equations (VIII. 10) and (VIII. 11) are generalized in the following way:

$$\Psi \to T \to F \to u_1; \quad \overline{E} \to \text{grad}' T \to \overline{H} \to \text{grad}' u_1;$$
$$D_2 - iD_3 \to q_2 - iq_3 \to B_2 - iB_3 \to \sigma_{12} - i\sigma_{13}, \qquad \text{(VIII. 12)}$$

where σ_{12}, σ_{13} are the longitudinal shearing stresses; $u_1(x_2, x_3)$ is the elastic displacement of the material in the longitudinal direction; the prime denotes double differential operations.

The dimensionless numbers have the following form

$$\frac{\varepsilon_{\alpha\beta}}{\varepsilon_s} = \frac{\gamma_{\alpha\beta}}{\gamma_s} = \frac{\mu_{\alpha\beta}}{\mu_s} = \frac{G'_{\alpha\beta}}{G_s}; \quad \frac{\varepsilon_m}{\varepsilon_s} = \frac{\gamma_m}{\gamma_s} = \frac{\mu_m}{\mu_s} = \frac{G_m}{G_s} \begin{pmatrix} m = 1, 2, \ldots, n; \\ \alpha, \beta = 2, 3. \end{pmatrix}. \qquad \text{(VIII. 13)}$$

Here G_m, G_s, and $G'_{\alpha\beta}$ are the moduli of shear of the components and the matrix, and also

$$G'_{22} = G_{12}; \quad G'_{33} = G_{13}; \quad G'_{23} = G'_{32} = \frac{G_{12}}{\mu_{31,21}} = \frac{G_{13}}{\mu_{12,31}},$$

where $\mu_{31,21}$ and $\mu_{12,31}$ are the Chentsov factors.

In real materials, the effects caused by nonsymmetries in the microstructure are very small, and therefore in most cases in practice we can assume

$$\varepsilon_{\alpha\beta} = \mu_{\alpha\beta} = \varkappa_{\alpha\beta} = G'_{\alpha\beta} = 0, \quad \text{if} \quad \alpha \neq \beta, \text{ and}$$
$$\varepsilon_{22} = \varepsilon_{33}, \ \mu_{22} = \mu_{33}, \ \varkappa_{22} = \varkappa_{33}, \ G_{12} = G_{13}. \qquad \text{(VIII. 14)}$$

Due to these simplifications, the dimensionless numbers (VIII. 13) are in the form

$$\frac{\varepsilon_{22}}{\varepsilon_s} = \frac{\gamma_{22}}{\gamma_s} = \frac{\mu_{22}}{\mu_s} = \frac{G_{12}}{G_s}; \quad \frac{\varepsilon_m}{\varepsilon_s} = \frac{\gamma_m}{\gamma_s} = \frac{\mu_m}{\mu_s} = \frac{G_m}{G_s}. \qquad \text{(VIII. 15)}$$

3. Analogies in hereditary reinforced media

It was found by experiment that the equations of state (II. 4) and similar equations do not allow for the hereditary properties of real material. Thus, when mechanical stresses act, elastic strains are observed, but their development in time lags behind the stress changes. In some materials creep, stress relaxation, and dissipative processes can be described to a first approximation by linear equations, provided that integral or even integral-differential operators are substituted for the equation constants. A good approximation of the viscoelastic properties of polymers and other materials is given by the following operator acting upon the time function, according to the law (see section 2, Chapter I):

$$G^*f(t) + G_0[1 - a\partial^*_{1-\lambda}(-\omega_\infty - a)]f(t) =$$

$$= G_0 f(t) - aG_0 \int_{-\infty}^{t} dt' f(t') \partial_{1-\lambda}(-\omega_\infty - a,\ t - t'). \qquad \text{(VIII. 16)}$$

Here, as the kernel we used the fractional-exponential function of Rabotnov.

Constants G_0, a, ω_∞, and λ are found from experimental data.

The dielectric constant operator is also introduced in a similar way. This operator makes it possible to describe processes of lag and dissipation of electromagnetic energy in real materials (see (I. 56))

$$\varepsilon^* = \varepsilon_\infty + \Omega_0^\lambda(\varepsilon^0 - \varepsilon_\infty)\partial^*_{1-\lambda}(-\Omega_0^\lambda), \qquad \text{(VIII. 17)}$$

where ε_∞ and ε^0 are the dielectric constants at very high and low frequencies, while Ω^λ, λ are experimentally determined constants.

In a periodically alternating field, the dielectric constant like the modulus of shear becomes complex. With high frequencies of the alternating field, high-frequency resonant dispersion is observed in the field; it is expressed by an increased energy absorption at a certain frequency, and changes in the material compliance. For a description of these phenomena integral-differential operators are applied (see section 5, Chapter I).

For linearly reinforced media the analogy between longitudinal shear and the transverse electric field is retained if the dimensionless numbers are used with allowance for the operator equations (VIII. 16) and (VIII. 17).

When taking into account the hereditary properties of the material components, the correspondence principle (the Volterra principle in viscoelastic media) must be used. According to this principle the constants are replaced by the corresponding integral operators

$$G_s \to G_s^*;\quad G_m \to G_m^*;\quad \varepsilon_s \to \varepsilon_s^*;\quad \mu_s \to \mu_s^*;\quad \varepsilon_m \to \varepsilon_m^*;\quad \mu_m \to \mu_m^*, \qquad \text{(VIII. 18)}$$

and also

$$G_{12} \to G_{12}^*;\quad \varepsilon_{22} \to \varepsilon_{22}^*;\quad \mu_{22} \to \mu_{22}^*.$$

A similar generalization is apparently possible in the theory of thermal conductivity also, but up to the present no experimental data confirming this assumption are available.

For hereditary media, the generalized variables are in the form (VIII. 15), where we have only to substitute the constant by the corresponding integral operators.

4. Analogies of dynamic fields in two-phase fiber composites

We shall consider the analogy of the propagation of stationary waves of longitudinal shear and TM or TE waves in linearly reinforced material.

The wave field in the components of the medium is found by solving

$$\nabla^2 u_s - \frac{1}{C_s^2} \cdot \frac{\partial^2 u_s}{\partial t^2} = 0, \quad \nabla^2 u_a - \frac{1}{C_a^2} \cdot \frac{\partial^2 u_a}{\partial t^2} = 0$$

while observing the correct boundary conditions on the component interface. Here u is the longitudinal elastic displacement; $C^2 = G/\rho$; and ρ is the density.

The solution of wave equations under conditions of ideal contact between the components and regular arrangement of circular fibers is found in local cylindrical coordinates Θ, r (see Chapter VII):

$$\begin{aligned} u_s &= \sum_{k=-\infty}^{\infty} V_{mn}^k e^{ik\Theta_{mn} - i\omega t} [I_k(k_s r_{mn}) - Z_k H_k(k_s r_{mn})]; \\ u_a &= \sum_{k=-\infty}^{\infty} V_{mn}^k e^{ik\Theta_{mn} - i\omega t} [I_k(k_s r_0) - Z_k H_k(k_s r_0)] \frac{I_k(k_a r_{mn})}{I_k(k_a r_0)}, \end{aligned} \tag{VIII. 19}$$

where subscripts mn ($mn = 0, \pm 1, \ldots, \pm\infty$) indicate the number of the cell in which the field is considered; V_{mn}^k are parameters characterizing the field changes between the cells, $k = \frac{\omega}{C}$;

$$Z_k = \frac{I_k(k_a r_0) I_k'(k_s r_0) - \frac{k_a G_a}{k_s G_s} I_k(k_s r_0) I_k'(k_a r_0)}{I_k(k_a r_0) H_k'(k_s r_0) - \frac{k_a G_a}{k_s G_s} I_k'(k_a r_0) H_k(k_s r_0)}. \tag{VIII. 20}$$

Parameters V_{mn}^k satisfy an infinite system of finite-difference equations

$$V_{mn}^k + \sum_{p \neq m,\, q \neq n} \sum_{\tau} \sum (-1)^{\tau - k} Z_\tau V_{pq}^\tau H_{\tau - k}^{(1)}(k_s R_{pq}^{mn}) e^{i(\tau - k)\theta_{pq}^{mn}} = 0 \tag{VIII. 21}$$
$$(k,\ m,\ n = 0, \pm 1, \ldots, \pm\infty).$$

The solution of this system is given in the form of traveling waves

$$V_{mn}^k = C_k \exp\{i\zeta\omega_1 [m \cos\varphi + nb \cos(\alpha - \varphi)]\}, \tag{VIII. 22}$$

where ω_1 is a constant; α is the lattice angle; φ is the slope of the wave with reference to $0x_2$. Parameter ζ is found from (VIII. 21) by substituting (VIII. 22) into it.

The two-dimensional electromagnetic field in the reinforced medium in the presence of transverse waves is described by (see Chapter VI)

$$\begin{aligned} \overline{E} &= \omega^2 \varepsilon\mu \bar{e}_1 \pi + i\omega\mu \operatorname{rot} \bar{e}_1 \pi^*; \\ \overline{H} &= -i\omega\varepsilon \operatorname{rot} \bar{e}_1 \pi + \omega^2 \varepsilon\mu \bar{e}_1 \pi^*. \end{aligned}$$

For ideal contact, the boundary conditions are reduced to the requirement that the tangential components of $\overline{E}$ and $\overline{H}$ be equal on the interface

$$\begin{aligned} &\varepsilon_s \mu_s \pi_s|_{\Omega_k} = \varepsilon_a \mu_a \pi_a|_{\Omega_k}, \quad \varepsilon_s \mu_s \pi^*|_{\Omega_k} = \varepsilon_a \mu_a \pi_a^*|_{\Omega_k}; \\ &\varepsilon_s \frac{\partial \pi_s}{\partial n}\bigg|_{\Omega_k} = \varepsilon_a \frac{\partial \pi_a}{\partial n}\bigg|_{\Omega_k}, \quad \mu_s \frac{\partial \pi_s^*}{\partial n}\bigg|_{\Omega_k} = \mu_a \frac{\partial \pi_a^*}{\partial n}\bigg|_{\Omega_k}. \end{aligned} \tag{VIII. 23}$$

This problem is solved by means of

$$\pi_s = \sum_{\tau=-\infty}^{\infty} V_{mn}^{\tau} [I_\tau(\lambda_s r_{mn}) - Z_\tau H_\tau(\lambda_s r_{mn})] e^{i\tau\theta_{mn} - i\omega t};$$

$$\pi_a = (\lambda_s/\lambda_a)^2 \sum_{\tau=-\infty}^{\infty} V_{mn}^{\tau} \left[I_\tau(\lambda_s r_0) - Z_\tau H(\lambda_s r_0) \frac{I_\tau(\lambda_a r_{mn})}{I_\tau(\lambda_a r_0)} \right] e^{i\tau\theta_{mn} - i\omega t},$$

and also

$$\pi_s^* = \sum_{\tau=-\infty}^{\infty} U_{mn}^{\tau} [I_\tau(\lambda_s r_{mn}) - Y_\tau H_\tau(\lambda_s r_{mn})] e^{i\tau\theta_{mn} - i\omega t};$$

$$\pi_a^* = (\lambda_s/\lambda_a)^2 \sum_{\tau=-\infty}^{\infty} U_{mn}^{\tau} [I_\tau(\lambda_s r_0) - Y_\tau H_\tau(\lambda_s r_0)] \frac{I_\tau(\lambda_a r_{mn})}{I_\tau(\lambda_a r_0)} e^{i\tau\theta_{mn} - i\omega t}.$$

Here

$$\lambda^2 = \omega^2 \varepsilon\mu;$$

$$Z_k = \frac{I_k(\lambda_a r_0) I_k'(\lambda_s r_0) - \frac{\lambda_s \varepsilon_a}{\lambda_a \varepsilon_s} I_k(\lambda_s r_0) I_k'(\lambda_a r_0)}{I_k(\lambda_a r_0) H_k'(\lambda_s r_0) - \frac{\lambda_s \varepsilon_a}{\lambda_a \varepsilon_s} I_k'(\lambda_a r_0) H_k(\lambda_s r_0)};$$

$$Y_k = \frac{I_k(\lambda_a r_0) I_k'(\lambda_s r_0) - \frac{\lambda_s \mu_a}{\lambda_a \mu_s} I_k(\lambda_s r_0) I_k'(\lambda_a r_0)}{I_k(\lambda_a r_0) H_k'(\lambda_s r_0) - \frac{\lambda_s \mu_a}{\lambda_a \mu_s} I_k'(\lambda_a r_0) H_k(\lambda_s r_0)}. \qquad \text{(VIII. 24)}$$

Parameters V_{mn}^k and U_{mn}^k are written as

$$V_{mn}^k = C_k \exp\{i\zeta\omega_1 [m\cos\varphi + nb\cos(\alpha - \varphi)]\};$$
$$U_{mn}^k = S_k \exp\{i\zeta_1\omega_1 [m\cos\varphi + nb\cos(\alpha - \varphi)]\},$$

where ζ and ζ_1 are found by substituting U and V into the following system of independent equations

$$V_{mn}^k + \sum_{p\neq m,} \sum_{q\neq n,} \sum_{\tau} (-1)^{\tau-k} Z_\tau V_{pq}^{\tau} H_{\tau-k}^{(1)}(\lambda_s R_{pq}^{mn}) e^{i(\tau-k)\theta_{pq}^{mn}} = 0;$$

$$U_{mn}^{\tau} + \sum_{p\neq m,} \sum_{q\neq n,} \sum_{\tau} (-1)^{\tau-k} Y_\tau U_{pq}^{\tau} H_{\tau-k}^{(1)}(\lambda_s R_{pq}^{mn}) e^{i(\tau-k)\theta_{pq}^{mn}} = 0. \qquad \text{(VIII. 25)}$$

For the given fields, the vibrational frequencies must be equal, and the material structures must be geometrically similar.

If we consider TM wave propagation when $\pi^* = 0$, the dimensionless numbers for the elastic displacement and electric fields will be

$$\frac{\rho_a}{\rho_s} = \frac{\varepsilon_a}{\varepsilon_s}; \quad \frac{G_a}{G_s} = \frac{\mu_s}{\mu_a}. \qquad \text{(VIII. 26)}$$

For the TE and elastic fields when $\pi = 0$, the following dimensionless numbers are determined:

$$\frac{\rho_a}{\rho_s} = \frac{\mu_a}{\mu_s}; \quad \frac{G_a}{G_s} = \frac{\varepsilon_s}{\varepsilon_a}. \qquad \text{(VIII. 27)}$$

When the dissipative losses due to the hereditary properties of the media have to be taken into account, the corresponding operators are used instead of the constants in the second formula of (VIII. 27). In the longwave approximation, the mean components of the electric fields and the averaged displacements are related by

$$\frac{\langle E_1\rangle}{\omega^2\varepsilon_s\mu_s}\approx\langle u_1\rangle \text{ and } \frac{\langle H_1\rangle}{\omega^2\varepsilon_s\mu_s}\approx\langle u_1\rangle.$$

5. Nonlinear analogies of polymers

The creep of thermoreactive polymers used as matrix in composites is satisfactorily described by (section 3, Chapter I)

$$\frac{d\mathrm{E}}{dt}=\frac{1}{E_0}\cdot\frac{d\sigma}{dt}+\frac{d\varepsilon}{dt},$$

where the first term characterizes the elastic part of the polymer deformation and the second term the viscoelastic component, whose time-dependent development is given by

$$\frac{d\varepsilon}{dt}=Ce^{\nu\sigma}-q\varepsilon. \qquad \text{(VIII. 28)}$$

This equations holds for all stress levels up to the breaking stress, and for different temperatures.

The solution of this equation is given in section 3 and 4 of Chapter I.

The curves for the most interesting parameters are shown in Figure I. 15. At higher temperatures and different stress levels, the temperature and stress dependences of the parameters are given by

$$q=q_0e^{kT+\alpha\sigma};\quad p=p_0e^{-\lambda T};\quad C/C_k=(C/C_k)_0\,e^{fT+\beta\sigma}.$$

The problem of vibroheating of the material under the effect of the applied periodic stresses, with allowance for the dependence of the mechanical parameters, is similar to the case given above. * For the sake of simplicity, we shall discuss only a one-dimensional case.

We shall assume that the temperature of the specimen exceeds the environmental temperature by an average of Θ. During periodic tensile-compressive stresses, the heat evolved will be proportional to the square of the applied stress, for example, under nonrigid loading conditions, and inversely proportional to the modulus of the specimen. We shall consider a material for which the modulus increases exponentially, or almost exponentially, with increase in Θ. Then, the dissipative energy is equal to $\beta e^{g\Theta}$, while the heat released by the specimen into the environment will be proportional to $-b\Theta$. If we designate by u the specific heat, from the energy balance equation we obtain (section 5, Chapter I)

$$u\frac{d\Theta}{dt}=\beta e^{g\Theta}-b\Theta.$$

* Franz, W. Dielectric Breakdown [Russian translation 1961].

By equating $C = \frac{\beta}{u}$, $g = p$, $q = \frac{b}{u}$, we obtain a relationship like (VIII. 28). These symbols can be used to set up dimensionless numbers.

The problem of the development of thermal dielectric breakdown is similar to the above problems. According to modern concepts, the conductivity of dielectrics increases with increase in temperature almost exponentially, but with increase in conductivity the temperature of the insulator increases. At a certain critical value of the applied field, the amount of heat evolved in the material will be larger than the heat transferred from the specimen to the environment, and this will lead to temperature increase until the specimen is destroyed (fused). Below this critical field value, thermal equilibrium is established in the dielectric.

For some dielectrics the conductivity σ is a function of the temperature according to the law $\sigma = \sigma_0 e^{\alpha\Theta}$.

For a constant electric field, the amount of heat released in the dielectric is $\sigma_0 E^2 e^{\alpha\Theta}$, while the heat supplied to the environment will be proportional to $-\lambda\Theta$. Therefore, the heat balance equation is

$$u\frac{d\Theta}{dt} = \sigma_0 E^2 e^{\alpha\Theta} - \lambda\Theta.$$

The compatibility conditions of this equation related to (VIII. 28) will be

$$C = \sigma_0 \frac{E^2}{u};\ \alpha = p;\ q = \frac{\lambda}{u}, \qquad \text{(VIII. 29)}$$

from which it is easy to find the dimensionless numbers for the last two problems of this section.

6. Mathematical modeling of composites

These analogies make it possible to study the reduced parameters and internal fields in composites with different microstructure from experimental data obtained for models of these materials in fields of entirely differing physical nature. The electromagnetic analogy is of special interest, since in such a field it is much less laborious to perform experiments than in stress or temperature fields.

For such experiments we must produce an analogous model of the given composite with a given microstructure and composition. Theoretical calculations for linearly reinforced materials with a tetragonal or hexagonal structure show that the type of the composite microstructure (in the case of the most indicative case, longitudinal shear) gives 17% of the contribution introduced by other factors. Thus, the formula for the transverse coefficient of thermal conductivity is

$$\varkappa_{22} = \varkappa_s \frac{1 + \xi + \eta\varkappa_s/\varkappa_a}{\eta + (1+\xi)\varkappa_s/\varkappa_a} + \frac{2\xi\varkappa_s(1 - \varkappa_s/\varkappa_a)}{\eta + (1+\xi)\varkappa_s/\varkappa_a} \sum_{k=1}^{\infty} C_{2k+2}\lambda^{2k+2}\alpha_{0,k},$$

where ξ and η are the relative volume contents of the filler and matrix, respectively, and $\eta = 1 - \xi$; C'_{2k}, λ^{2k+2}, $\alpha_{0,k}$ are parameters depending on

the relative fiber arrangement. In this formula the first term predominates. Therefore, in cases when the reduced parameters of the composite are established, we can get sufficiently accurate data if the model is produced so as to correspond to the material studied as far as the volume content of the component is concerned, and the similarity of the relative positions of the filler elements is established. * However, to study the internal field in the material, the relative arrangement of the filler element is of decisive importance. The component properties in the model are selected so as to correspond to the similarity criteria found above. If we allow for the edge effects, the model size must be selected so that the disturbances are damped near the edge over a distance equal, for example, to a few lattice constants.

* Except when the filler elements are in direct contact.

Chapter IX

STRESS CONCENTRATION AROUND HOLES IN PLATES AND SHELLS MADE OF REINFORCED MATERIALS

As an application of the fundamental equations in the theory of reinforced materials, we shall consider the problem of stress distribution around holes in plates and shells. We have mentioned above that in the study of composites it is convenient to separate two types of stresses:

a) structural stresses arising because of hard fiber inclusions in a comparatively soft matrix;

b) averaged (reduced) stresses with their distribution governed by the hole geometry, reduced anisotropy of the material, surface curvature, etc.

Therefore, in a reinforced material stress concentrations arising because of holes, grooves and other factors act in addition to non-homogeneous stress /1/. An increased stress concentration is especially pronounced on the matrix-fiber interface. For composites in which one or more components have viscoelectric properties, we can expect a time-dependent stress redistribution of certain areas, and this may lead to an increased stress concentration.

Because the strength of the reinforced material is anisotropic, we must reestimate the magnitude of the stresses around holes, cracks, etc., since a comparatively small shearing stress in the matrix is frequently more dangerous than the maximum normal stresses at the circumference of the holes.

1. Stress concentration around a circular hole in plates made of glass-fiber reinforced laminated polymers

We shall assume that a plate of linearly reinforced materials, with its straightened fibers forming a hexagonal microstructure, is weakened by a circular hole placed a few diameters from the plate edge. The position of the hole in the Cartesian coordinate system is selected in accordance with Figure IX. 1. It is assumed that the plate is under plane stress. In this case the mean stresses in the plate satisfy two balance equations

$$\frac{\partial \langle \sigma_{11} \rangle}{\partial x_1} + \frac{\partial \langle \sigma_{12} \rangle}{\partial x_2} = 0; \quad \frac{\partial \langle \sigma_{12} \rangle}{\partial x_1} + \frac{\partial \langle \sigma_{22} \rangle}{\partial x_2} = 0. \qquad \text{(IX. 1)}$$

The mean strains are given by the single equation of compatibility of the strain in the center of the plane of the plate

$$\frac{\partial^2 \langle \varepsilon_{11} \rangle}{\partial x_2^2} + \frac{\partial \langle \varepsilon_{22} \rangle}{\partial x_1^2} - 2\frac{\partial^2 \langle \varepsilon_{12} \rangle}{\partial x_1 \partial x_2} = 0. \qquad \text{(IX. 2)}$$

The equations of the linear viscoelastic theory relating ε_{ik} to σ_{ik} for a hexagonal structure under plane stress are transformed into (see Chapter III),

$$\left.\begin{aligned} \langle \varepsilon_{11} \rangle &= \frac{1}{E_{11}} \langle \sigma_{11} \rangle - \frac{\nu_{21}}{E_{11}} \langle \sigma_{22} \rangle; \\ \langle \varepsilon_{22} \rangle &= -\frac{\nu_{21}}{E_{11}} \langle \sigma_{11} \rangle + \frac{1}{E_{22}^*} \langle \sigma_{22} \rangle; \\ \langle \varepsilon_{12} \rangle &= \frac{1}{2G_{12}^*} \langle \sigma_{12} \rangle. \end{aligned}\right\} \qquad \text{(IX. 3)}$$

With the accepted accuracy, the inelastic properties of a composite are described by two operators only, E_{22}^* and G_{12}^*, when the linearly reinforced layer is under plane stress, and the fibers are ideally elastic and have a stiffness which is one order higher than the stiffness of the viscoelastic matrix. To satisfy the balance equation (IX. 1), we introduce Airy's stress function

$$\left.\begin{aligned} \langle \sigma_{11} \rangle = \frac{\partial^2 U}{\partial x_2^2}; \quad \langle \sigma_{22} \rangle = \frac{\partial^2 U}{\partial x_1^2}; \\ \langle \sigma_{12} \rangle = -\frac{\partial^2 U}{\partial x_1 \partial x_2}. \end{aligned}\right\} \qquad \text{(IX. 4)}$$

Its form is determined by its domain of definition, and by an equation derived from (IX. 2) – (IX. 4),

$$\frac{1}{E_{22}^*} \cdot \frac{\partial^4 U}{\partial x_1^4} + \left(\frac{1}{G_{12}^*} - \frac{2\nu_{21}}{E_{11}}\right) \frac{\partial^4 U}{\partial x_1^2 \partial x_2^2} + \frac{1}{E_{11}} \cdot \frac{\partial^4 U}{\partial x_2^4} = 0. \qquad \text{(IX. 5)}$$

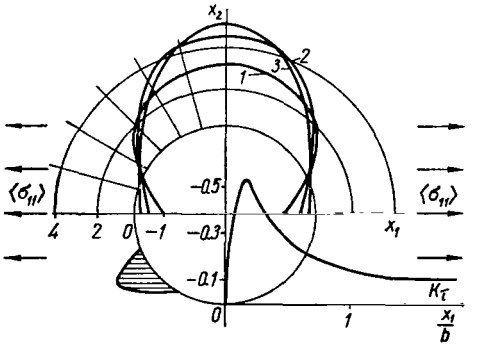

FIGURE IX. 1. Stress concentration around a circular hole when the plate is under two-dimensional stress.

The solution of (IX. 5) with constant coefficients is discussed in /2/ and /3/, when the authors studied the stress concentration at holes in orthotropic plates. To find a solution allowing for the viscoelastic properties of the matrix in the reinforced material, we use the Volterra principle (see Chapter III). The general integral of (IX. 5) depends on the roots of the characteristic equation

$$\frac{s}{E_{11}}+\left(\frac{1}{G_{12}^*}-\frac{2\nu_{21}}{E_{11}}\right)s^2+\frac{1}{E_{22}^*}=0, \qquad \text{(IX. 6)}$$

where

$$-\sqrt{E_{11}/E_{22}^*}=s_1s_2;$$
$$s_1+s_2=i\sqrt{2\left(\sqrt{E_{11}/E_{22}^*}-\nu_{21}\right)+E_{11}/G_{12}^*}. \qquad \text{(IX. 7)}$$

We shall assume that the hole circumference is free of external forces, and that a homogeneous stress is given at a distance from the hole. For determinacy, it is assumed that the plate is uniformly tensioned over its thickness by tensile stresses $\langle\sigma_a\rangle$ directed at a angle α to the $0x_1$ axis, while the fiber orientation coincides with the $0x_1$ axis.

The mean stress distribution about the hole is determined by the Volterra principle, with the aid of functions of complex variables ($z_1=x_1+s_2x_2$) and ($z_2=x_1+s_2x_2$) defined for the elastic homogeneous orthotropic material /2, 4/ by:

$$\left.\begin{aligned}\langle\sigma_{11}\rangle&=\langle\sigma_a\rangle\cos^2\alpha+2\,\mathrm{Re}\,[s_1^2\varphi'(z_1)+s_2^2\psi'(z_2)];\\ \langle\sigma_{22}\rangle&=\langle\sigma_a\rangle\sin^2\alpha+2\,\mathrm{Re}\,[\varphi'(z_1)+\psi'(z_2)];\\ \langle\sigma_{12}\rangle&=\langle\sigma_a\rangle\sin\alpha\cos\alpha-2\,\mathrm{Re}\,[s_1\varphi'(z_1)+s_2\psi'(z_2)]\end{aligned}\right\} \qquad \text{(IX. 8)}$$

(here $a=b$ for a circular hole, where a is the hole diameter);

$$\varphi(z_1)=-\frac{i\langle\sigma_a\rangle(a-is_1b)}{4(s_1-s_2)}\left[\frac{b(s_2\sin2\alpha-2\cos^2\alpha)}{z_1+\sqrt{z_1^2-(a^2+s_1^2b^2)}}+\frac{ia(2s_2\sin^2\alpha+\sin2\alpha)}{z_1+\sqrt{z_1^2-(a^2+s_1^2b^2)}}\right];$$
$$\psi(z_2)=\frac{i\langle\sigma_a\rangle(a-is_2b)}{4(s_1-s_2)}\left[\frac{b(s_1\sin2\alpha+2\cos^2\alpha)}{z_2+\sqrt{z_2^2-(a^2+s_2^2b^2)}}+\frac{ia(2s_1\sin^2\alpha+\sin2\alpha)}{z_2+\sqrt{z_2^2-(a^2+s_2^2b^2)}}\right]. \qquad \text{(IX. 9)}$$

To analyze the effect of the inelastic properties on the time-dependent stress distribution, the integral operators in (IX. 7) are selected so that they apply to GFP with a EMA matrix (see section 3, Chapter I) with a filler level $\xi=0.74$.

If the fiber orientation coincides with the direction of tension of the plate ($\alpha=0$), the mean normal stress $\langle\sigma_\theta\rangle$ on the areas located on the circumference along the path $\theta=\text{const}$ is

$$\langle\sigma_\theta\rangle=\frac{1}{s_1s_2}\langle\sigma_0\rangle=-\sqrt{E_{22}^*/E_{11}}\langle\sigma_0\rangle;$$
$$\langle\sigma_\theta\rangle=\left(1+\sqrt{2\left(\sqrt{E_{11}/E_{22}^*}-\nu_{21}\right)+E_{11}/G_{12}}\langle\sigma_0\rangle\right). \qquad \text{(IX. 10)}$$

Here angle θ is read from the axis $0x_1$; the first component characterizes the stresses in the unweakened plastic, while the second term characterizes

the effects of disturbances introduced by the hole. The circumferential stresses at points $x_1 = a$, $x_2 = 0$ and $x_1 = 0$, $x_2 = a$ are

$$\langle \sigma_\theta \rangle = \langle \sigma_0 \rangle \left\{ \sin^2 \theta + \operatorname{Re} \left[\frac{e^{-i\theta}}{s_1 - s_2} \left(\frac{s_1 \sin\theta + \cos\theta)^2}{\sin\theta - s_1 \cos\theta} - \frac{(s_2 \sin\theta + \cos\theta)^2}{\sin\theta - s_2 \cos\theta} \right) \right] \right\}.$$

Thus, the mean stress distribution around a hole can be written as

$$\langle \sigma_{ii} \rangle = k_0 \langle \sigma_0 \rangle, \tag{IX. 11}$$

where k_{ii} is a factor, which for viscoelastic bodies is the operator of the mean stress concentration factor around the hole. It was shown in Chapter II that structural stresses are related to the mean stresses by the structural stress concentration factor k_c, therefore

$$\sigma_{ik} = k_c \langle \sigma_{ik} \rangle. \tag{IX. 12}$$

In the structure of the reinforced materials according to (IX. 11) and (IX. 12), the total stress concentration factor is expressed by the product of k_0 and k_c /4/

$$k = k_c k_0. \tag{IX. 13}$$

The time-dependent changes in the concentration factor k_0 of the mean stresses $\langle \sigma_\theta \rangle$ around a circular hole for reinforced materials are plotted in Figure IX. 1. The values of k_0 for the corresponding θ are read from the circumference along the radius; curve 1 characterizes the dependence of k_0 on θ for an isotropic plate. The stress distribution for an elastic linearly reinforced polymer (GFP) is shown by curve 2; curve 3 illustrates the time-dependent change in the stresses occurring because of the viscoelastic properties of the matrix in the GFP at a stable creep, when the time the stresses act tends to infinity. The data in the last case are obtained by substituting the creep moduli for the elastic constants in the stress equations (see section 3, Chapter I). The direction of the hatching near the hole circumference shows the fiber orientation.

The maximum stresses due to anisotropic effects in the material are higher than the maximum stresses for an isotropic plate. Because of the development of viscoelastic deformations the anisotropic effects increase with time, which in turn leads to a stress increase on reinforced areas, and a stress decrease on areas not reinforced by fibers ($\theta = 0, \pi$). In general, the effects of the viscoelasticity of the oriented GFP on the stressed state is equivalent to stress redistribution because of the time-dependent changes in the anisotropy of the material. The distribution of shearing stresses on the areas arranged parallel to the $0x_1$ axis, and at a distance of radius a from this axis, is given by curve k_τ. The stress concentration factor is read from the straight line in the direction of the ordinate, on which the numerical values are plotted. The shearing stresses are equal to zero when $x_1 = 0$, then rapidly reach their maximum and decrease again. For a linearly reinforced material the shearing stresses are received by the matrix only. The shearing strength of the matrix is

very low and for this reason the stresses are very dangerous. If we take into account the stress concentration in the material and the absence of bonds preventing the propagation of cracks, it is possible to estimate the ultimate stress as $\langle\sigma_0\rangle$, at which breaking of the material is possible

$$\sigma_{12} = k_c k_\tau \langle\sigma_0\rangle < [\tau_b],$$

where τ_b is the maximum permissible shearing stress in the matrix. The mean stress distribution on the areas shown is given by

$$\langle\sigma_{12}\rangle = -\frac{\langle\sigma_0\rangle}{\beta_1-\beta_2}\left(\frac{\beta_1}{1-\beta_1}\cdot\frac{x_1\sin\frac{\xi_1}{2}-\beta_1 a\cos\frac{\xi_1}{2}}{\sqrt{(x_1^2-a^2)^2+(2\beta_1 x_1)^2}}-\right.$$

$$\left.-\frac{\beta_2}{1-\beta^2}\cdot\frac{x_1\sin\frac{\xi_2}{2}-\beta_2 a\cos\frac{\xi_2}{2}}{\sqrt{(x_1^2-a^2)^2+(2\beta_2 x_1)^2}}\right),$$

where

$$i\beta_1 = s_1;\quad i\beta_2 = s_2;$$

$$\beta_1 = \sqrt{\frac{E_{11}}{2G_{12}^*}-\nu_{21}-\sqrt{\left(\frac{E_{11}}{2G_{12}^*}-\nu_{21}\right)^2-\frac{E_{11}}{E_{22}^*}}};$$

$$\beta_2 = \sqrt{\frac{E_{11}}{2G_{12}^*}-\nu_{21}+\sqrt{\left(\frac{E_{11}}{2G_{12}^*}-\nu_{21}\right)^2-\frac{E_{11}}{E_{22}}}};$$

$$\frac{a\beta_1 x_1}{\sqrt{(x_1^2-a^2)^2+(2\beta_1 x_1)^2}} = \sin\frac{\xi_1}{2}\cos\frac{\xi_1}{2};\quad 1+\frac{x_1^2-a^2}{\sqrt{(x_1^2-a^2)^2+(2\beta_1 x_1)^2}} = 2\cos^2\frac{\xi_1}{2};$$

$$\frac{a\beta_2 x_1}{\sqrt{(x_1^2-a^2)^2+(2\beta_2 x_1)^2}} = \sin\frac{\xi_2}{2}\cos\frac{\xi_2}{2};\quad 1+\frac{x_1^2-a^2}{\sqrt{(x_1^2-a^2)^2+(2\beta_2 x_1)^2}} = 2\cos^2\frac{\xi_2}{2}.$$

According to the above calculation, the "shear" of the material on the areas (II') must lead to conditions when the part of the plate shown hatched in Figure IX. 2, a is no longer able to operate, while the remaining part of the material of the plate will be homogeneously stressed without any stress concentration around the hole.

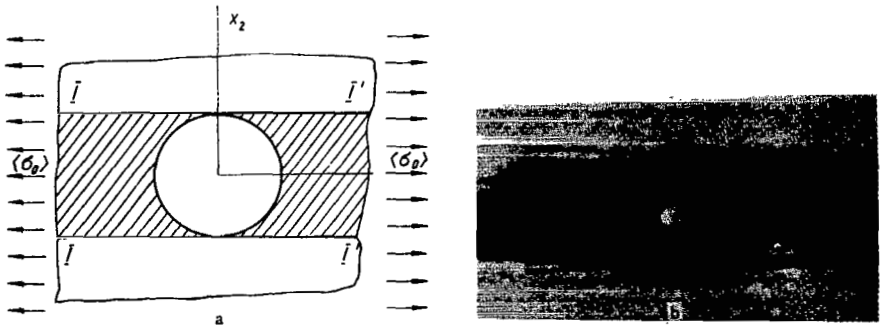

FIGURE IX. 2. Fracture pattern of a reinforced plate weakened by a circular hole.

The boundary conditions on the hole circumference were satisfied on an average only, and therefore the stress distribution in the material near the hole will differ from the values reported in Chapter II. However, the stress redistribution is so local in character that it has no effect even at a small distance (a few diameters) from the circumference. The experimental data shown in Figure IX. 2 more or less confirm the above conclusion on the fracture pattern of the plate.

If the plate consists of crosswise glass-reinforced layers of equal thickness arranged symmetrically about the central plane, the reduced mechanical parameters can easily be determined for the whole layer assembly. For this determination we use the plane section hypothesis, and the known reduced parameters for the linearly reinforced layer. By observing the compatibility conditions for the layer deformations, we establish the operators

$$\bar{E}_{11}^* = \bar{E}_{22}^* = \frac{E_{11}}{2} \cdot \frac{(1 + E_{22}^*/E_{11})^2 - 4\nu_{21}^2 (E_{22}^*/E_{11})^2}{(1 + E_{22}^*/E_{11})(1 - \nu_{21}^2 E_{22}^*/E_{11})};$$
$$\bar{\nu}_{21}^* = \nu_{21} \frac{2E_{22}^*/E_{11}}{1 + E_{22}^*/E_{11}}; \quad \bar{G}_{12}^* = G_{12}^*. \tag{IX. 14}$$

The operational moduli for the linearly reinforced layer are reported in Chapter III.

We shall assume that the given plate is weaked by a circular hole of radius a and tensioned in one of the main anisotropic directions (Figure IX. 3). The mean tangential stress distribution $\langle \sigma_\theta \rangle$ on the hole circumference is determined by (IX. 10), where we have to equate

$$s_1 s_2 = -1;$$
$$s_1 + s_2 = i\sqrt{2(1 - \bar{\nu}_{21}^*) + \bar{E}_{11}^*/G_{12}^*}.$$

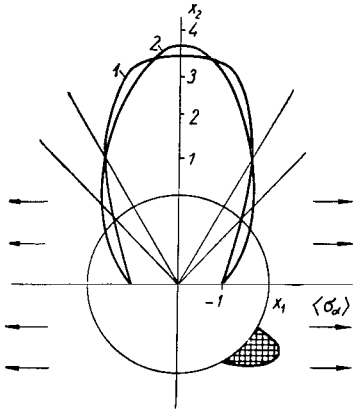

FIGURE IX. 3. Stress concentration around a circular hole in a plate tensioned along one of the main anisotropic directions.

It is worth noting that in the given case $\langle \sigma_\theta \rangle$ does not change with time when $\theta = 0$, as follows from (IX. 10). The change in the stress concentration factor $\langle \sigma_\theta \rangle$ along the hole circumference at the first instant the external stress $\langle \sigma_\alpha \rangle$ is applied is illustrated by curve 1 in Figure IX. 3. Curve 2 shows the change in the stress concentration factor $\langle \sigma_\theta \rangle$ after a long period when $t \to \infty$. We see an increase in the stresses in the maximum value region, and a stress redistribution along the hole circumference in correspondence to the scale represented on the ordinate. At unstable creep of the polymer matrix ($\omega_- \to 0$), the stresses $\langle \sigma_\theta \rangle$ on area $\theta = 0$ are time independent, and for the area $\theta = \frac{\pi}{2}$ they increase without limit.

2. Stress distribution around an elliptic hole or crack in a plate made of glass-fiber reinforced plastic

We shall assume that a plate made of linearly reinforced GFP is tensioned along the fiber orientation. Axis $0x_1$ is placed in the direction of the major axis of the elliptic hole and the fiber orientation. The distribution of tangential stresses along the circumference of the free elliptic hole with semiaxes a, $b(a > b)$ is found according to (IX. 8) and (IX. 9) from

$$\langle \sigma_\theta \rangle = \langle \sigma_0 \rangle \left\{ \frac{\sin^2 \theta}{\sin^2 \theta + \lambda^2 \cos^2 \theta} + \frac{\lambda}{\sin^2 \theta + \lambda^2 \cos^2 \theta} \times \right.$$
$$\left. \times \operatorname{Re} \left[\frac{e^{-i\theta}}{s_1 - s_2} \left(\frac{s_1 \sin \theta + \lambda \cos \theta}{\sin \theta - s_1 \lambda \cos \theta} - \frac{(s_2 \sin \theta + \lambda \cos \theta)^2}{\sin \theta - s_2 \lambda \cos \theta} \right) \right] \right\}. \qquad \text{(IX. 15)}$$

Here $\lambda = \frac{b}{a}$. The curves in Figure IX. 4 illustrate the change in the stress concentration $\langle \sigma_\theta \rangle$ on the circumference when $\frac{a}{b} = 2$ at the first instant (curve 1), and after creep when $t \to \infty$ (curve 2). The concentration factors are read along the radius from the circumference. We see that the stress concentration factor on the areas reinforced by fibers increases because of the matrix creep.

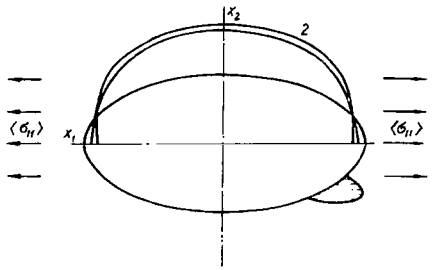

FIGURE IX. 4. Stress concentration around an elliptic hole in a plate tensioned along the major axis.

The time-dependent changes in the stress concentration factor $\langle \sigma_\theta \rangle$ on the circumference of the hole $\left(\frac{a}{b} = 2\right)$, when the plate made of linearly reinforced GFP is tensioned along the minor axis and the fiber orientation, is illustrated by the curves in Figure IX. 5.

Curve 1 characterizes the stress distribution (or the stress concentration factors) on the circumference at the instant the load is applied, while curve 2 shows these parameters after long-term stress application. We see the effect of the curvature of the circumference and of the anisotropy on the absolute value of the stress concentration factor (at $\theta = 0$ and $\theta = \pi$), and a decrease in the absolute magnitude of the negative stresses $\left(\theta = \frac{\pi}{2}\right)$.

The time-dependent stress distribution in plates with crosswise reinforcement subjected to the same loading pattern shows other features.

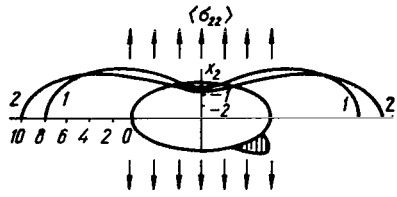

FIGURE IX. 5. Stress concentration around an elliptic hole in a plate tensioned along the minor axis.

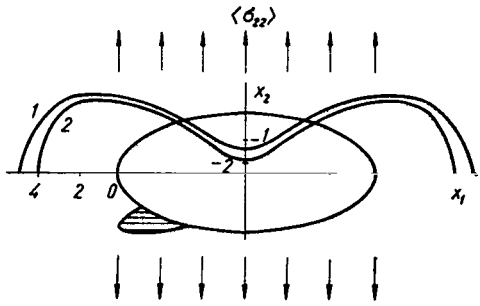

FIGURE IX. 6. Time-dependent stress redistribution for crosswise reinforced plates.

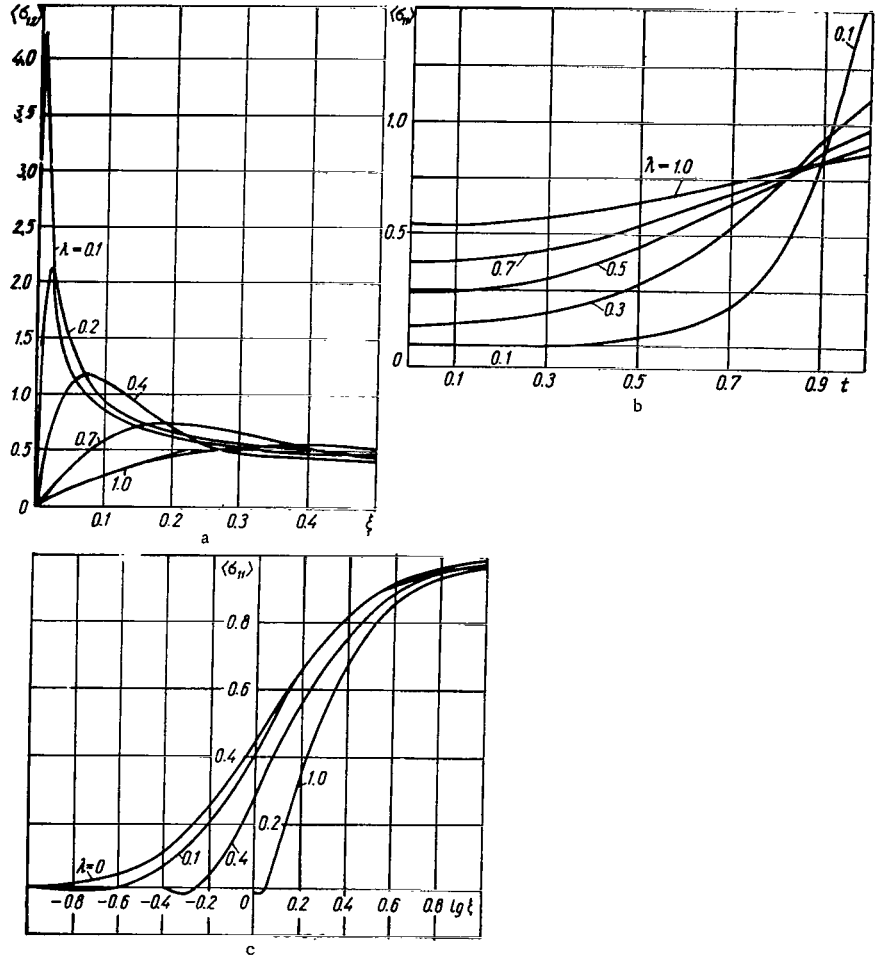

FIGURE IX. 7. Change in the maximum stresses (a) for GFP in the elastic stage, maximum normal stresses (b), and normal stresses σ_{11} (c) with increase in the distance from the crack edge.

The initial stress distribution (curve 1 in Figure IX. 6) is transformed by creep processes, so that a time-dependent decrease in the stress concentration factors occurs (curve 2).

The stress distribution around a crack in a linearly reinforced plate tensioned along the fiber orientation perpendicular to the major axis of the crack is of interest. The investigation of this would make it possible to some extent to study the stressed state at the edge of broken fibers, estimate the effective length of short fibers, and also observe the effect of crack elongation on the stress distribution in the material. The solution to this problem can be obtained directly from (IX. 8) and (IX. 9). The curves in Figure IX. 7 illustrate stress redistribution with increase in $\lambda = \frac{b}{a}$. The curves in Figure IX. 7, a show changes in the magnitude and position of the maximum of shearing stresses in section $x_2 = \pm a$ for GFP in the elastic stage. Point $\xi = \frac{x_1}{a} = 0$ is located at the edge of the ellipse. The curves in Figure IX. 7, b characterize the changes in the normal stresses $\langle \sigma_{11} \rangle$ at a distance 2λ for various λ values as a function of $t = \frac{x_2}{a}$. The changes in the stresses $\langle \sigma_{11} \rangle$ at $x_2 = 0$ and increase in the distance from the crack edge is illustrated by the curves in Figure IX. 7, c. The values of $\ln \xi^*$ are plotted on the abscissa. From the shape of the curves we can see the equalization of the stresses in the plate. Section $0 < \frac{x_1}{a} < 10^{0.4}$ characterizes the length of the cut fibers, which scarcely participate in the tensile stress transmission.

3. Methods for studying stresses in stiff-core three-layer spherical shells (sandwich shells) with notches

The wall structure in shells (sandwich shells) made from reinforced materials consists of the top and bottom load-carrying layers of oriented fiber-reinforced materials (for example glass-fiber reinforced tape), and an intermediate layer of the required stiffness and strength. The intermediate layer ensures interaction between the carrying layers. If the intermediate layer, usually termed core, is sufficiently strong and stiff to absorb stresses and moments, requiring consideration, it is called stiff; otherwise it is called light.

Light core materials are foam plastics, porous flexible materials, (rubber, etc.). Stiff cores consist of materials in the form of thin-walled isolated cells made of glass-fiber reinforced tapes, or materials obtained by stacking GFP packings of various structures, etc.

Spherical shells are generally designed to withstand uniform pressure. Therefore, both the carrying layers and core are reinforced in such a way that the stiffness and strength of the material are independent of the selected direction. This is achieved by crosswise reinforcement of the layers, which makes it possible, with a certain error, to apply isotropic body models

* [In Figure IX 7, c, log ξ].

for studying spherical shells. In this case, the reduced parameters for the whole assembly are determined from the known layer parameters.

We shall assume that a spherical sandwich shell made of isotropic material with a stiff filler is in static equilibrium under the action of a transverse load q, and weakened by a circular or elliptic hole (Figure IX. 8). The stressed state near the hole is characterized by a higher variability factor, and the study in the region can be performed on the basis of the conical shell theory. Therefore, with the given approximation, the deformation of each layer is found from /5, 6/.

$$\varepsilon_n = \frac{\partial U_n}{\partial n} - \frac{w}{R}; \quad \varepsilon_s = \frac{\partial U_s}{\partial s} + \frac{1}{\rho} U_s - \frac{w}{R}, \quad \varepsilon_{sn} = \frac{\partial U_n}{\partial s} + \frac{\partial U_s}{\partial n} - \frac{1}{\rho} U_s, \qquad \text{(IX. 16)}$$

where U_n, U_s, and w are the components of the elastic displacement vector in the normal and tangential directions to the contour, and in the perpendicular direction to the layer surface; R is the radius of the shell; $\frac{\partial}{\partial n}$ and $\frac{\partial}{\partial s}$ are the derivatives with respect to the normal and arc of the circumference of the hole; and ρ is the radius of curvature of L.

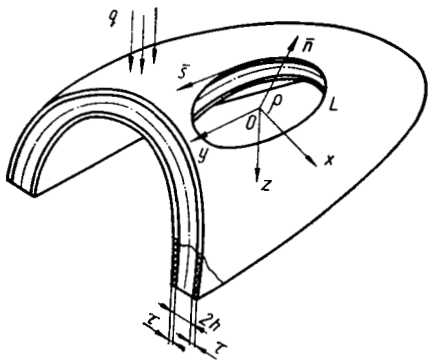

FIGURE IX. 8. Spherical sandwich shell weakened by a hole.

If we assume that the displacements are linear in both the load-carrying layers and cores of the shell walls, the equations relating the reduced stresses and moments for the whole assembly are transformed into

$$\left.\begin{aligned} N_n &= 2(B + B_0)\left(\frac{\partial U_n}{\partial n} + \nu\frac{\partial U_s}{\partial s} + \frac{\nu}{\rho}U_n - \frac{1+\nu}{R}w\right); \\ N_s &= 2(B + B_0)\left(\frac{\partial U_s}{\partial s} + \nu\frac{\partial U_n}{\partial n} + \frac{1}{\rho}U_n - \frac{1+\nu}{R}w\right); \\ N_{ns} &= (1-\nu)(B + B_0)\left(\frac{\partial U_n}{\partial s} + \frac{\partial U_s}{\partial n} - \frac{1}{\rho}U_s\right). \end{aligned}\right\} \qquad \text{(IX. 17)}$$

Here N_n, N_s, and N_{ns} are the reduced stresses for the whole assembly acting in the plane tangential to the shell ($2U_n = u_n^{(1)} + u_n^{(2)}$; $2U_s = u_s^{(1)} + u_s^{(2)}$), where indices "1" and "2" denote the displacements in the upper and lower load-carrying layers of the wall

$$B = \frac{E\tau}{1-\nu^2}; \quad B_0 = \frac{E_0 h}{1-\nu^2},$$

where E and E_0 are the moduli of elasticity of the load-carrying layer and core; τ and h are the thicknesses of the load-carrying layer and core; ν is the Poisson ratio, which is the same for all the elements of the assembly.

We shall introduce the following abbreviations for the diplacement differences

$$2V_n = u_n^{(1)} - u_n^{(2)}; \quad 2V_s = u_s^{(1)} - u_s^{(2)}$$

and the new functions Φ and Ψ given by

$$\frac{\partial V_n}{\partial n} + \frac{1}{\rho} V_n + \frac{\partial V_s}{\partial s} = \Phi; \quad \frac{\partial V_s}{\partial n} + \frac{1}{\rho} V_s - \frac{\partial V_n}{\partial s} = -\Psi. \tag{IX. 18}$$

The reduced moments in the corresponding sections of the sandwich shell are determined from

$$\left.\begin{aligned}
M_n &= -\left(2D - \frac{B_0 h\tau}{3}\right)\left(\frac{\partial^2 w}{\partial n^2} + \frac{\nu}{\rho}\cdot\frac{\partial w}{\partial n} + \nu\frac{\partial^2 w}{\partial s^2}\right) - \\
&- \left[\left(h + \frac{\tau}{2}\right)B + \frac{hB_0}{3}\right]\left[(1+\nu)\Phi + (1-\nu)\left(\frac{\partial V_n}{\partial n} - \frac{1}{\rho}V_n - \frac{\partial V_s}{\partial s}\right)\right]; \\
M_s &= -\left(2D - \frac{B_0 h\tau}{3}\right)\left(\frac{\partial^2 w}{\partial s^2} + \frac{1}{\rho}\cdot\frac{\partial w}{\partial n} + \nu\frac{\partial^2 w}{\partial n^2}\right) - \left[\left(h + \frac{\tau}{2}\right)B + \right. \\
&\left. + \frac{hB_0}{3}\right]\left[(1+\nu)\Phi + (1-\nu)\left(\frac{\partial V_s}{\partial s} + \frac{1}{\rho}V_n - \frac{\partial V_n}{\partial n}\right)\right]; \\
M_{ns} &= -(1-\nu)\left(D - \frac{B_0 h\tau}{3}\right)\left(\frac{\partial^2 w}{\partial n\,\partial s} + \frac{\partial^2 w}{\partial s\,\partial n} - \frac{1}{\rho}\cdot\frac{\partial w}{\partial s}\right) - \\
&- (1-\nu)\left[\left(h + \frac{\tau}{2}\right)B + \frac{hB_0}{3}\right]\left(\frac{\partial V_s}{\partial n} + \frac{\partial V_n}{\partial s} - \frac{1}{\rho}V_s\right),
\end{aligned}\right\} \tag{IX. 19}$$

where $D = \frac{E\tau^3}{12(1-\nu^2)}$ is the cylindrical stiffness of the individual load-carrying layer. The transverse stresses for the whole assembly in the cross section are given by

$$\left.\begin{aligned}
Q_n &= -2D\frac{\partial}{\partial n}\nabla^2 w - 2G_0\left[V_n - \left(h + \frac{\tau}{2}\right)\frac{\partial w}{\partial n}\right] - B\tau\left(\frac{\partial \Phi}{\partial n} + \frac{1-\nu}{2}\cdot\frac{\partial \Psi}{\partial s}\right); \\
Q_s &= -2D\frac{\partial}{\partial s}\nabla^2 w - 2G_0\left[V_s - \left(h + \frac{\tau}{2}\right)\frac{\partial w}{\partial n}\right] - B\tau\left(\frac{\partial \Phi}{\partial s} - \frac{1-\nu}{2}\cdot\frac{\partial \Psi}{\partial n}\right).
\end{aligned}\right\} \tag{IX. 20}$$

Here G_0 is the shear modulus of the filler; in the given system of curvilinear coordinates

$$\nabla^2 = \frac{\partial^2}{\partial n^2} + \frac{1}{\rho}\cdot\frac{\partial}{\partial n} + \frac{\partial^2}{\partial s^2}.$$

The equilibrium equations of the shell element obtained by transformation and using symbols (IX. 18) are given by the following system /6/:

$$\left.\begin{gathered}\left(B+\frac{B_0}{3}\right)\frac{h}{G_0}\nabla^2\Phi-\Phi=\frac{B_0h\tau}{6G_0}\nabla^2\nabla^2w-\left(h+\frac{\tau}{2}\right)\nabla^2w;\\ \left[2B\left(h+\frac{\tau}{2}\right)+\frac{2}{3}B_0h\right]\nabla^2\Phi+\left(2D-\frac{B_0h\tau}{3}\right)\nabla^2\nabla^2w-\frac{1}{R}\nabla^2F=q;\\ \nabla^2\nabla^2F+2(B+B_0)\frac{1-\nu^2}{R}\nabla^2w=0;\ \nabla^2\Psi-\frac{2G_0}{\left(B+\frac{B_0}{3}\right)(1-\nu)h}\Psi=0.\end{gathered}\right\}\quad\text{(IX. 21)}$$

The introduced stress function F is expressed in terms of stress by

$$N_n=\frac{\partial^2F}{\partial s^2}+\frac{1}{\rho}\cdot\frac{\partial F}{\partial n};\ N_s=\frac{\partial^2F}{\partial n^2};\ N_{ns}=-\frac{\partial^2F}{\partial n\,\partial s}+\frac{1}{\rho}\cdot\frac{\partial F}{\partial s}.\qquad\text{(IX. 22)}$$

Six boundary conditions must be given on the circumference of the hole L, and among the possible solutions of (IX. 21) we select the one satisfying the damping conditions with increase in the distance from L.

In particular, if circumference L is free of external loads, the boundary conditions require that the normal and shearing stresses, the bending moment and torques, be equal to zero, while the shearing forces must balance the reaction of the lid over the hole. These conditions are equivalent to the following system of equations:

$$\left.\begin{gathered}\left[B\left(1+\frac{\tau}{2h}\right)+\frac{B_0}{3}\right)\left(\frac{\partial V_n}{\partial s}+\frac{\partial V_s}{\partial n}-\frac{1}{\rho}V_s\right)-\frac{B_0\tau}{6}\left(\frac{\partial^2w}{\partial n\,\partial s}+\frac{\partial^2w}{\partial s\,\partial n}-\frac{1}{\rho}\cdot\frac{\partial w}{\partial s}\right)\Big]_L=0;\\ \frac{\partial^2F}{\partial s^2}+\frac{1}{\rho}\cdot\frac{\partial F}{\partial n}\Big|_L=0;\ -\frac{\partial^2F}{\partial n\,\partial s}+\frac{1}{\rho}\cdot\frac{\partial F}{\partial s}\Big|_L=0;\\ \frac{\partial^2w}{\partial n^2}+\frac{\nu}{\rho}\cdot\frac{\partial w}{\partial n}+\nu\frac{\partial^2w}{\partial s^2}\Big|_L=0;\\ (1+\nu)\Phi-(1-\nu)\left(\frac{\partial V_s}{\partial s}+\frac{1}{\rho}V_n-\frac{\partial V_n}{\partial n}\right)\Big|_L=0;\ Q_n=-\frac{qr_0}{2},\ \ldots\end{gathered}\right\}\quad\text{(IX. 23)}$$

In the last equation, if the hole is not circular, we use additional terms (r_0 is the radius of the circular hole). If r is the distance between the center of the hole and an arbitrary point on the shell it is necessary that

$$|r|\to\infty\ \left(\frac{\partial^2F}{\partial s^2}+\frac{1}{\rho}\cdot\frac{\partial F}{\partial n}\right)\to0;\ \left(-\frac{\partial^2F}{\partial n\,\partial s}+\frac{1}{\rho}\cdot\frac{\partial F}{\partial s}\right)\to0;\ w\to0;\ \Phi\to0;\ \Psi\to0.$$

Displacements V_n and V_s are determined as particular solutions of the inhomogenous equations (IX. 18). The solution of homogeneous equations must be disregarded, since they do not correspond to the physically permissible conditions of shell operation near the hole circumference.

Thus, (IX. 21) is reduced to the solution of a single inhomogeneous equation for Φ

$$L\Phi=-\frac{1}{a}\left(h+\frac{\tau}{2}\right)\nabla^2q+\frac{B_0h\tau}{6aG_0}\nabla^4q,\qquad\text{(IX. 24)}$$

where

$$\begin{gathered}L=\left[\frac{B_0h\tau}{6G_0}-\frac{h\beta}{G_0a}\left(B+\frac{B_0}{3}\right)\right]\nabla^6-\left(h+\frac{\tau}{2}-\frac{\beta}{a}\right)\nabla^4+\\ +\frac{2(1-\nu^2)}{aR^2G_0}h(B+B_0)\left(B+\frac{B_0}{3}\right)\nabla^2-\frac{2(1-\nu^2)}{aR^2}(B+B_0)=\\ =a\nabla^6-b\nabla^4+c\nabla^2-d.\end{gathered}$$

Here

$$\alpha = 2B\left(h + \frac{\tau}{2}\right) + \frac{2}{3}B_0 h; \quad \beta = \frac{B_0 h\tau}{3} - 2D.$$

The solution of the homogeneous equation (IX. 24) within the limits of accuracy of the proportionality factor is compatible with the solution of the equations for functions $\nabla^2 F$ and $\nabla^2 W$. The homogeneous solution of (IX. 24) is made up of the sum of functions

$$\Phi = \sum_{j=1}^{3} f_j,$$

where f_j satisfies the damping conditions at infinity, and the three Helmholtz equations of type

$$\nabla^2 f_j - \lambda_j^2 f_j = 0.$$

The parameters λ_j^2 are found as the roots of the algebraic equation

$$a\lambda_j^6 - b\lambda_j^4 + c\lambda_j^2 - d = 0.$$

Two groups of other arbitrary constants, necessary for satisfying the six boundary conditions, are revealed when integrating the Laplace equation for F and w. The sixth group of constants is obtained from the solution of the last equation of (IX. 21) for Ψ. For a circular or an elliptic hole, the Helmholtz equation is solved in terms of Bessel or Mathieu functions, which satisfy the damping conditions. In these cases, when the circumference of the hole is described by curvilinear coordinates (ellipse, triangle or quadrangle with curved corners), we introduce the transformation

$$x + \iota y = \zeta + \frac{\varepsilon}{\zeta^N}; \quad \zeta = \xi + \iota\eta = re^{i\theta} (\varepsilon < 1, \ N > 0);$$

the solution is obtained by the method of the small parameter ε. If we allow for

$$\frac{\partial}{\partial n} = \frac{1}{\varkappa} \cdot \frac{\partial}{\partial r}; \quad \frac{\partial}{\partial s} = \frac{1}{r\varkappa} \cdot \frac{\partial}{\partial \theta}; \quad \varkappa^2 = 1 - 2\varepsilon N r^{-N-1} \times$$
$$\times \cos(N+1)\theta + \varepsilon^2 N^2 r^{-2N-2},$$

Helmholtz's equation is transformed into

$$\left(\frac{\partial^2}{\partial r^2} + \frac{1}{r} \cdot \frac{\partial}{\partial r} + \frac{1}{r^2} \cdot \frac{\partial^2}{\partial \theta^2}\right) f_j - \lambda_j^2 f_j = \varepsilon_0 L_0 f_j,$$

where L_0 is the differential operator with variable coefficients. For this reason, the solution is written as

$$f_j = \sum_{s=0}^{\infty} \varepsilon^s f_{js}.$$

An analogous expansion by powers of ε is carried out in (IX. 19) and (IX. 20). To a first approximation ($s = 0$), the solution is found in Bessel functions for a certain circular hole, and in the subsequent approximations the results are made more accurate.

4. Stress concentration around a hole in a spherical sandwich shell with a light core

For a sandwich shell with a light core, the fundamental equations follow as a particular case from the formulas of the preceding section. In practice, the solutions of the problem of stress concentration around a hole in shells with a light core, when the load-carrying layers do not receive shearing stresses, are most frequently encountered. The above restrictions require that $B_0 = 0$ and $D = 0$. In this case, the solution of (IX. 21) can be represented in various forms, depending on the actual shell parameters /6/.

Thus, if inequality

$$1 - \nu^2 - E^2 > 0 \tag{IX. 25}$$

applies, where

$$E = \frac{\tau E}{2RG_0\left(1 + \frac{\tau}{2h}\right)},$$

(IX. 21) is reduced by complex transformation to three equations

$$\left.\begin{aligned} \nabla^2(\nabla^2\varphi - \varkappa^2\varphi) &= \frac{q}{2B\left(h + \frac{\tau}{2}\right)^2} - \frac{h\nabla^2 q}{2G_0\left(h + \frac{\tau}{2}\right)^2}; \\ \Phi = \left(h + \frac{\tau}{2}\right)\nabla^2 w + \frac{h}{2RG_0\left(h + \frac{\tau}{2}\right)}\nabla^2 F + \frac{qh}{2G_0\left(h + \frac{\tau}{2}\right)}&; \\ \nabla^2\Psi - \frac{2G_0}{(1-\nu)hB}\Psi &= 0. \end{aligned}\right\} \tag{IX. 26}$$

Here, we introduce the complex function

$$\varphi = w + gF,$$

where

$$g = \frac{1}{2\tau E\left(h + \frac{\tau}{2}\right)}\left[E + i\sqrt{1 - \nu^2 - E^2}\right], \quad \varkappa^2 = \frac{2\tau E}{R}\bar{g}.$$

In the system of boundary conditions (IX. 23), the fourth equation is disregarded. The general solution of the first equation of (IX. 26) is a sum of three functions $\varphi_k\,(k = 1, 2, 3)$, where φ_3 is the particular solution of the inhomogeneous equation, while

$$\nabla^2\varphi_1 = 0, \quad \nabla^2\varphi_2 - \varkappa^2\varphi_2 = 0.$$

For the circular hole in a polar coordinate system, for $q = \text{const}$ we take as acceptable solutions satisfying the damping conditions

$$F_n = -\frac{qRr^2}{4};$$

$$\varphi_1 = iA_0 \ln r + \sum_{n=1}^{\infty} (A_n + iB_n) r^{-n} \cos n\theta;$$

$$\varphi_2 = \sum_{n=0}^{\infty} (c_n + is_n) K_n(\varkappa r) \cos n\theta,$$

where the odd functions of θ are omitted. $K_n(\varkappa r)$ is the MacDonald function. The asymptotic mapping of this function for a large argument and the condition $(\arg \varkappa r) < \pi$ has the form

$$K_n(\varkappa r) \approx \sqrt{\frac{\pi}{h\varkappa r}} e^{-\varkappa r} + \ldots$$

Parameter $\varkappa$ is best represented as

$$\varkappa = \alpha - i\beta = \sqrt{\frac{\sqrt{1-\nu^2}}{hR(1+\tau/2h)}} e^{-i\sigma/2}$$

where

$$0 < \operatorname{tg} \sigma \leqslant E^{-1} \sqrt{1-\nu^2-E^2} \leqslant \infty, \qquad \text{(IX. 27)}$$

and for this reason $0 < \sigma \leqslant \frac{\pi}{2}$. The equality sign in (IX. 27) applies to the limiting case of a homogeneous shell when $G_0 \to \infty$. For numerical calculations, it is convenient to apply

$$K_n(\varkappa r) = -\frac{\pi}{2} \operatorname{ger}_n(\rho e^{i\lambda}) + \frac{\pi i}{2} \operatorname{gei}_n(\rho e^{i\lambda}).$$

The following functions are used here

$$\operatorname{ger}_n(x) = \cos\frac{n\pi}{2} [\operatorname{Im} J_n(x) + \operatorname{Re} Y_n(x)] + \sin\frac{n\pi}{2} [\operatorname{Re} J_n(x) - \operatorname{Im} Y_n(x)]$$

(where $Y_n(x)$ is Neumann's function) and also

$$i\varkappa r = \rho e^{i\lambda} = r \sqrt{\frac{\sqrt{1-\nu^2}}{hR\left(1+\frac{\tau}{2h}\right)}} e^{i\lambda},$$

and

$$1 \leqslant \operatorname{tg} \lambda = \operatorname{ctg} \frac{\sigma}{2} = \frac{\sqrt{1-\nu^2-E^2}}{hR(1+\tau/2h) - E} < \infty \left(\frac{\pi}{4} \leqslant \lambda \leqslant \frac{\pi}{2}\right).$$

The difference in the displacement through which the stresses and moments in the shells are established are obtained from (IX. 18). To simplify calculation in polar coordinates, we use new functions introduced by substitution

$$(V_n - iV_s) e^{-i\theta} = \frac{v_n - iv_\theta}{r} e^{-i\theta}.$$

By putting

$$\Phi = \Phi_n K_n(\varkappa r) \cos n\theta; \quad \Psi = \Psi_n K_n(\lambda r) \sin n\theta,$$

and also

$$v_r = \sum_{n=0}^{\infty} v_r^{(n)} \cos n\theta; \quad v_\theta = \sum_{n=1}^{\infty} \tilde{v}_\theta^{(n)} \sin n\theta$$

and using (IX. 18), we obtain an equation of type

$$\frac{1}{r} \cdot \frac{dv_r^{(n)}}{dr} + \frac{n}{r^2} \tilde{v}_\theta^{(n)} = \Phi_n K_n(\varkappa r); \quad \frac{1}{r} \cdot \frac{d\tilde{v}_\theta^{(n)}}{dr} + \frac{n}{r^2} v_r^{(n)} = -\Psi_n K_n(\varkappa r),$$

from which by direct integration we obtain

$$v_r^{(n)} = \Phi_n \frac{r}{\varkappa} K_n'(\varkappa r) + \Psi \frac{n}{\lambda^2} K_n(\lambda r);$$

$$\tilde{v}_r^{(n)} = -\Phi_n \frac{n}{\varkappa^2} K_n(\varkappa r) - \Psi_n \frac{r}{\lambda} K_n'(\lambda r).$$

The other components of the functions are obtained in a similar way.

If inequality (IX. 25) is not observed, that is

$$1 - \nu^2 - E^2 < 0, \tag{IX. 28}$$

the complex transformation of the equations becomes impossible, and the problem is reduced to integration of the resolving equation

$$\nabla^4 \Phi - \frac{Bh(1-\nu^2)}{G_0 R^2 (h+\tau/2)^2} \nabla^2 \Phi - \frac{1-\nu^2}{R^2 (h+\tau/2)^2} \Phi = \frac{\nabla^2 q}{2B(h+\tau/2)}. \tag{IX. 29}$$

It is easy to express the other functions in terms of Φ. For a circular hole the solution of the equation is obtained as a series of the true argument, in accordance with the MacDonald function

$$\Phi = \sum_{n=0}^{\infty} [C_n K_n(\varkappa_1 r) + S_n K_n(\varkappa_2 r)] \cos n\theta,$$

where we equate

$$\varkappa_{1,2}^2 = \frac{1}{R(h+\tau/2)} (E \pm \sqrt{E^2 - 1 + \nu^2}).$$

In this case the solution is found in terms of an exponentially damped nonoscillating function. Figure IX. 9 shows the dependence of the reduced stress concentration factor N_θ about the hole circumference on $\frac{a}{R}$ for various stiffnesses of the material components.

The pattern of disturbance damping with increase in the radial distance from the hole for $\frac{a}{R} = 0.1$ and 0.01* is illustrated by the curves in Figure IX. 10.

In the intermediate case when

$$1 - \nu^2 - E^2 = 0, \tag{IX. 30}$$

* [In Figure IX.10, $\frac{a}{R}$ is 0.1 and 0.04.]

as the resolving function we take

$$\Phi = \sum_{n=0}^{\infty} [C_n K_n(\varkappa_0 r) + rS_n K_n'(\varkappa_0 r)] \cos n\theta,$$

where

$$\varkappa_0^2 = \frac{2(1-\nu^2)\,G_0}{h\pi E}.$$

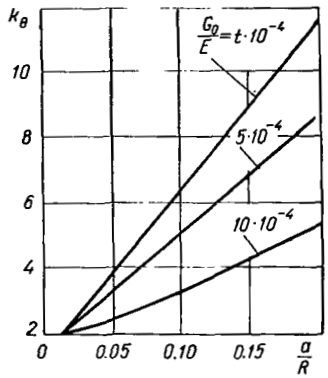

FIGURE IX. 9. Reduced stress concentration factor at various hardnesses of the material components.

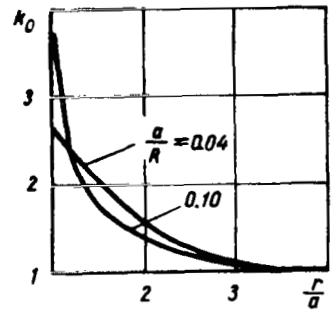

FIGURE IX. 10. Pattern of disturbance damping for various hardness values.

If the spherical surface is weakened by an elliptic hole with semiaxes a and b, the accurate solution of (IX. 26) is built up in elliptic coordinates ξ and η, which are introduced with the aid of transformations

$$x + iy = c\,\mathrm{ch}\,(\xi + i\eta)\,(c^2 = a^2 - b^2;\ \xi_0 < \xi < \infty,\ 0 \leqslant \eta \leqslant 2\pi).$$

For determinacy, we assume that the mechanical parameters of the shell satisfy (IX. 25). In other cases the solution of the problem is obtained in complete analogy with the above case. The required solution of the equation ($q = \mathrm{const}$) is constructed as modified Mathieu functions of the third kind

$$\varphi_1 = iA_0 \ln(\mathrm{ch}\,2\xi + \cos 2\eta) + \sum_{n=1}^{\infty} (A_{2n} + iB_{2n})\, e^{-2n\xi} \cos 2n\eta;$$

$$\varphi_2 = \sum_{n=0}^{\infty} (C_{2n} + iS_{2n})\,\mathrm{Fek}_{2n}(\xi_1 - q_0)\,\mathrm{Cl}_{2n}(\eta_1 - q_0);$$

$$\Psi = \sum_{n=0}^{\infty} D_{2n}\,\mathrm{Fek}_{2n}(\xi_1 - \lambda_0)\,\mathrm{Cl}_{2n}(\eta_1 - \lambda_0),$$

where

$$q_0 = \frac{\varkappa^2 c^2}{4};\quad \lambda_0 = \frac{\lambda^2 c^2}{4}.$$

For transformation of (IX. 19) and (IX. 20) we use

$$\frac{\partial}{\partial n} = \frac{1}{\varkappa} \cdot \frac{\partial}{\partial \xi}; \quad \frac{\partial}{\partial s} = \frac{1}{\varkappa} \cdot \frac{\partial}{\partial \eta}; \quad \varkappa^2 = \frac{c^2}{2} (\operatorname{ch} 2\xi - \cos 2\eta); \quad \frac{1}{\rho} = \frac{\operatorname{sh} \xi}{\varkappa (\operatorname{ch} 2\xi - \cos 2\eta)}.$$

The above Mathieu functions satisfy the damping conditions of the disturbed stressed-strained state of the shell to infinity, and to be expressed in terms of Bessel functions /7/

$$\mathrm{Fek}_{2n} (\xi_1 - q_0) = \frac{p_{2n}}{\pi A_0^{(2n)}} \sum_{r=0}^{\infty} A_{2r}^{(2n)} I_r (\sqrt{q_0} e^{-\xi}) K_r (\sqrt{q_0} e^{\xi});$$

$$\mathrm{Cl}_{2n} (\eta_1 - q_0) = (-1)^n \sum_{r=0}^{\infty} (-1)^2 A_{2r}^{(2n)} \cos 2n\eta.$$

This expansion is especially convenient for small q_0 and large ξ.

The method of solving the problem of stress concentration around a single hole can be directly applied to the case of several holes located in the region where the stressed states interact. This problem is solved immediately by superposition of the solutions for each separate hole. For expansion of the Bessel functions in various systems of polar coordinates, we have to use the theorem of the addition of Bessel functions /8/.

For (IX. 30) we must use the generalized theorem of the addition of Bessel functions that we derived from

$$z_0^p Z_n^{(p)} (z_0) e^{in\omega} = \sum_{\nu=-\infty}^{\infty} e^{i\nu\varphi} j_\nu (z) Z_{n+\nu} (R) \left[R \frac{Z_{n+\nu}^{(\,)} (R)}{Z_{n+\nu} (R)} + z \frac{j_\nu^{(\,)} (z)}{j_\nu (z)} \right]^p. \qquad \text{(IX. 31)}$$

Here, when using the binomial formula of Newton we have to introduce R and Z raised to the power corresponding to the coefficients; the Bessel functions in the numerator are differentiated according to the power of R and Z, while the functions in the denominator are neither raised to the power nor differentiated. Thus, for example, if $p = 2$, we obtain

$$e^{in\psi} z_0^2 Z_n^{(2)} (z_0) = \sum_{\nu=-\infty}^{+\infty} e^{i\nu\varphi} [j_\nu (z) Z_{n+\nu}^{(2)} (R) R^2 +$$

$$+ 2Rz j_\nu' (z) Z_{n+\nu}' (R) + z^2 j_\nu^{(2)} (z) Z_{n+\nu} (R)].$$

The addition theorem of Graf follows from (IX. 31) — as a particular case when $p = 0$. The application of (IX. 31) makes it possible to build up problems on stress concentration around several holes in spherical sandwich shells at various wall parameters.

Bibliography

1. Van Fo Fy, G. A. O kontsentratsii napryazhenii v stekloplastikakh (Stress Concentration in Glass-Fiber Reinforced Plastics). — In: Kontsentratsiya napryazhenii, 1. Kiev, Naukova Dumka. 1965.

2. Savin, G. N. Kontsentratsiya napryazhenii okolo otverstii (Stress Concentration Around Holes). Moskva, GITTL. 1949.
3. Lekhnitskii, S. G. Anizotropnye plastinki (Anisotropic Plates), GITTL. 1957.
4. Savin, G. N. and G. A. Van Fo Fy. Raspredelenie napryazhenii okolo ellipticheskogo otverstiya v plastinke iz voloknistykh materialov (Stress Distribution Around an Elliptical Hole in a Plate of Fibrous Materials). — Prikladnaya Mekhanika, 2:5. 1966.
5. Vol'mir, A. S. Ustoichivost' uprugikh sistem (Stability of Elastic Systems). Moskva, Fizmatgiz. 1963.
6. Van Fo Fy, G. A. Kontsentratsiya napryazhenii okolo otverstii v trekhsloinykh obolochkakh (Stress Concentration Around Holes in Sandwich Shells). — Prikladnaya Mekhanika, 4:2. 1969.
7. McLachlan, U. W. Theory and Application of Mathieu Functions. Oxford. The Clarendon Press. 1949.
8. Bateman, H. Higher Transcendental Functions Compiled by A. Erdélyi et al. New York, McGraw-Hill. 1953 — 1955.

Chapter X

THE STRENGTHENING EFFECT OF REINFORCEMENT IN COMPOSITE FIBERS

1. The special features of metal- or ceramic-based reinforced materials

The development of engineering sciences requires the creation of new materials suitable for ensuring the operation of the construction over a wide range of temperatures.

High strength and refractoriness, heat resistance, thermal stability, and a low specific gravity give a far from complete list of the properties which are necessary in modern materials used in nuclear and rocket and power engineering, electronics, and many other branches of the national economy.

Pure metals or their alloys can no longer completely satisfy the requirements of the new engineering sciences, because their high-temperature and creep strengths are comparatively low, while the existing ceramic materials have a low specific gravity and a good high-temperature strength, but in most cases are not sufficiently heat-resistant and their toughness is low.

To obtain all these necessary parameters we must produce composites which combine all the good properties of the different components.

Metals with a high strength at both room and elevated temperatures can be obtained by two methods, differing in principle.

The first method is to produce barriers to prevent spread of the dislocation. This includes the traditional methods of strengthening-cold hardening, alloying, heat and thermomechanical treatments, etc. The same principle is used when particles of approximately equiaxial form are introduced into the metal matrix (reinforcement by dispersed particles). In this case the dislocation density in the matrix is increased, and at the same time the matrix is strengthened without utilizing the strength of the particles themselves. The actual strength of disperse-particle reinforced material is much lower than that expected from theoretical calculations.

The second method consists in reinforcement of the metals with high-strength fibers, and is much more promising.

In a regularly arranged system, during the action of an external load the plastic flow of the matrix charges threadlike particles. Here the strength of the composite is directly dependent on the particle strength. Since numerous materials in the form of thin threads have very good mechanical properties over a wide temperature range, it is possible to

obtain almost ideally strong composites. The strength and high-temperature strength of reinforced metals depend mainly on the fiber properties and the bonding forces on the fiber-matrix interface, and are much higher than in metals strengthened by disperse particles. The modern disperse-particle reinforced materials are weakened at high temperatures because of dissolution and coagulation of disperse particles. If the disperse phase consists of high-strength ceramic whiskers, there is less tendency for the disperse phase to coagulate, since in the matrix-fiber composite the surface to volume ratio, and hence the level of the free surface energy, are lower.

Reinforced metals have numerous other advantages also over alloys strengthened by disperse particles.

Table X.1 /42/ compares various properties of materials reinforced by disperse particles and fibers.

The reinforcement of ceramic materials with fibers does not always lead to an ultimate strength above that of the pure ceramic. The low relative elongation of the ceramic and its high Young's modulus are frequently insufficient to transfer the stress to the fibers. However, in this case reinforcement leads to a strong increase in the toughness and heat resistance. The fibers do not protect the ceramic against cracking, but restrict crack propagation. The constructions retain their efficiency regardless of cracks in the matrix.

The principle of the beneficial effect of reinforcement is confirmed in Nature. Numerous natural designs have an oriented structure. The bones of animals, trunks of trees, bamboos, and skeletons of insects have a fibrous structure. Reinforcement has already been used in engineering (reinforced concrete, glass-fiber reinforced plastics).

The theory of reinforced media has been developed by the Soviet scientists, Yu. N. Rabotnov, A. L. Rabinovich, G. A. Van Fo Fy, V. V. Bolotin, E. S. Umanskii, Yu. M. Tarnopol'skii, and A. M. Skudra, etc. Among the non-Russian scientists we shall mention A. Kelly, B. W. Rosen, W. Sutton, N. I. Parrat, and others.

The reinforcement of metals and ceramics by fibers is of comparatively recent data, that is, the last 15 — 20 years. In the Soviet Union, the first research was carried out in the fifties /1/, but composite fibers have become popular during the last few years only.

Fiber composites are a new group of materials which are very much in demand in modern engineering.

TABLE X.1. Comparative strengthening of metals by particles and fibers*

Parameters compared	Strengthening	
	by particles	by fibers
Matrix	Matrix carries main load	Transfers load to fibers
Deformational strengthening	Fundamental strengthening mechanism, rate of strengthening depends on particle shape and interparticle distance	Secondary strengthening factor, effect limited by interfiber space
Disperse phase	Prevents movement of dislocation (slip)	Fibers carry main load, but at the same time this prevents, as it were, crack propagation

* We assume that the disperse particles and the fibers are hard, chemically inert, and firmly bound to the matrix. The particles are larger than the disperse particles of the precipitated phase ($d_{part} \approx 0.01$), while the fibers are fragments oriented along the direction of the applied load.

TABLE X.1. (cont.)

Parameters compared	Strengthening	
	by particles	by fibers
Maximum stress on disperse phase	Much lower than ultimate strength of reinforcing particles	Not much less than or equal to ultimate strength of fibers
Strengthening parameters	Ultimate strength of composite is very dependent on inter-particle distance and particle diameter. Volume fraction of disperse phase varies between 0.01 and 0.15; particle diameter and interparticle distance are $0.01-0.1\,\mu$.	Ultimate strength of composite is very dependent on volume fraction of fibers, their length and orientation, and little dependent on interfiber distance. Range of variation in volume fraction is $0.01-0.91$. Range of variation in length to diameter ratio is 2 to ∞;
Ratio of the composite strength to matrix strength at room temperature	$3-15$	$20-50$
Strength of composite	Changes proportionally to V_{part} when $0.0005 < V_{part} < 0.2$ (V_{part} is volume fraction of particle)	Changes proportionally to V_f in range $0.01 < V_f < 0.91$ (V_f is volume fraction of fiber)
Strengthening at elevated temperatures	Temperature ratio equal to $0.75-0.79$*	Temperature ratio equal to $0.80-0.98$*
Stability at high temperatures (high-temperature creep strength)	Depends on ability of dislocations to pass particles and particle aggregates	Depends on retention of the fibers in initial state; (weak chemical interaction and no diffusion)
Stress-strain dependence in composite	Yield peak present (elongation on fracture from 0.1 to 15%)	Elastic failure or a yield peak may be observed (depending mainly on volume content of fibers V_f, their properties and arrangement)
Properties of composite	Isotropic	Anisotropic
Bond on matrix-disperse phase interface	May be large, but not decisive with reference to $(\sigma_B)_C$, where $(\sigma_B)_C$ is ultimate strength of composite	Is very important
Methods of production	Powder metallurgy, internal oxidation, electrothermal method and crystallization from melt	Powder metallurgy, crystallization of fibers from melts, and method of applying coatings
Range of application	Where high-temperature strength and stability, and good electric and thermal conductivities at high temperatures, are required	Where materials with given properties, materials with a high specific strength at normal and elevated temperatures are required (matrix is selected according to properties, that is resistance to oxidation and chemical corrosion, hardness, ductility, etc., while the fibers only carry load)

* The temperature ratio (t. r.) is equal to T/T_m (T is the test temperature; T_m is the melting point), when the strength of the composite at the test temperature is 14 kg/mm^2.

2. Requirements for fibers and matrix

Fiber reinforcement has the following advantages: a) the composite becomes very strong; b) the matrix can be reinforced in the required direction by the design which ensures the maximum utilization of the fiber properties.

Filamentary reinforcements have, however, a disadvantage; the fibers are able to transmit the load only in the directions of their axis and there is no strengthening effect in the direction perpendicular to the axis, and in some cases even weakening may occur.

The reinforcing fibers used must have the following properties: high melting point, low specific gravity, high strength over the whole range of working temperatures, minimum solubility in the matrix, high chemical stability, absence of phase transformations over the whole range of working temperatures, and nontoxicity during production and service.

Three types of fibers are usually applied for reinforcement of metals: filamentary crystals, metal fibers, and nonmetallic, polycrystalline fibers.

Fiber crystals are the most promising material for reinforcing metals. The wide application of metal whiskers as a reinforcing element may be open to doubt because of their active interaction with numerous metal matrices, and the appreciable decrease in their strength at high temperatures, but the usefulness of ceramic whiskers is evident. The very high strength over a wide temperature range combined with the low specific gravity, chemical inertia to numerous metals, high refractoriness and resistance to corrosion of crystal fibers of alumina, magnesia, silicon carbide, etc., make these fibers irreplacable as reinforcing elements. Unfortunately, their practical application involves some difficulties, We have to solve the problem of their industrial production (as yet, the amount of available whiskers is still insufficient to carry out even large scale laboratory experiments), the selection of serviceable whiskers (usually the yield of such whiskers is not more than 10—15%), their orientation in the matrix, etc.

High-strength metallic fibers made of steel, tungsten, molybdenum, and other metals are less promising because of their higher specific gravity and lower strength. Nevertheless, because they are produced in industry in large quantities and are comparitively cheap, metallic fibers are used more than other fibers in research.

Polycrystalline metallic fibers, like metallic fibers, can be produced in large quantities. Their main drawback is their sensitivity to mechanical damage, On the other hand, due to the low specific gravity and the high chemical resistance of quartz, quartzoid, zirconia and aluminosilicate fibers, these fibers will no doubt be used in the near future for reinforcing metals as widely as for reinforcing polymers.

The matrix in reinforced composites imparts the required shape to the product, and forms the monolithic material. By combining the numerous fibers into an assembly, the matrix makes it possible for the composite to receive external loads of various types (tension, compression, bending,

shear, etc.). At the same time, the matrix itself helps to ensure the load-bearing capacity of the composite and the transmission of stresses to the fibers. A plastic matrix also aids in the transmission of stresses from destroyed or discrete fibers to adjacent ones, and the absorption of stress concentrations near various defects.

The matrix is used as a coating to protect the fibers from mechanical damage and oxidation. Moreover, the matrix ensures the strength and stiffness of the system when tensile or compressive stresses act perpendicular to the fiber orientation. If the tensile load is directed along the axis of parallelly arranged fibers, the limiting relative elongation of the matrix must be at least equal to the relative elongation of the fiber to ensure a monolithic system. But if the load acts perpendicular to the fiber axis this requirement does not suffice, as was shown by Kies /2/.

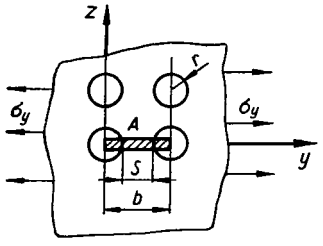

FIGURE X.1. Model of reinforced composite with rectangular arrangement of fibers (load applied perpendicular to fibers).

We shall consider the strained state of element A of a composite in which the fibers are rectangularly arranged in a simple manner. The tensile force acts in the direction of the y-axis, perpendicular to the fibers (Figure X.1). We shall assume that both matrix and fibers are subject to elastic strain. We can then write

$$E_f \varepsilon_f = \sigma_f; \tag{X.1}$$
$$E_m \varepsilon_m = \sigma_m \tag{X.2}$$

where E_f and E_m are Young's moduli of fibers and matrix; ε_f and ε_m are the unit strains in tension of the fibers and matrix; and σ_f and σ_m are the stresses arising in the fibers and matrix because of the external load.

If the matrix and fibers are simultaneously strained, the stresses in the components will be identical

$$\sigma_{yf} = \sigma_{ym} = \sigma_y, \tag{X.3}$$

where σ_{yf} and σ_{ym} are the stresses in the fibers and matrix in the direction of the y-axis, and σ_y is the external tensile stress applied to the composite in the direction of the y-axis.

The deformation ε_{yc} of element A in the composite is expressed in terms of the deformation of the components by

$$2b\varepsilon_{yc} = d_f \varepsilon_{yf} + S\varepsilon_{ym} \tag{X.4}$$

where ε_{yc}, ε_{yf} and ε_{ym} are the unit strains in tension of the composite, fibers, and matrix, respectively, while d_f is the fiber diameter.

The simultaneous solution of (X.1)–(X.4) gives an equation relating the matrix deformation to the composite deformation.

$$\varepsilon_{ym} = \varepsilon_{yc}\left(\frac{d_f}{2b} \cdot \frac{E_m}{E_f} + \frac{S}{2b}\right). \tag{X.5}$$

Since for the given fiber arrangement the approximate equation

$$V_f = 0.8\left(\frac{4b}{d_f} - 1\right)^{-1} \qquad (X.\ 6)$$

holds, (X. 5) can be transformed into

$$\varepsilon_{vm} = \varepsilon_{vc}\left[\frac{2V_f}{V_f + 0.8}\left(\frac{E_m}{E_f} - 1\right) + 1\right]^{-1}. \qquad (X.\ 7)$$

Thus, the matrix deformation is a function of the ratio of Young's moduli of the matrix and fibers and the volume fraction of the fibers V_f. In the limiting case when $V_f \to 1$, the matrix deformation must be $\frac{E_f}{E_m}$ times the total deformation. In reinforced plastics $\frac{E_f}{E_m}$ is usually between 5 and 20, and for metals it is between 1 and 10. Thus, to ensure a monolithic reinforced system, we need a matrix with a relative elongation several times the average deformation of the composite. With an elastic-plastic matrix the deformation must be larger than with a purely elastic component /2/.

By increasing the volume fraction of the fibers we can obtain a maximum strength of the composite. However, it follows from (X. 7) that if the relative matrix elongation is limited, the monolithic properties of the system may be impaired at sufficiently high V_f. Therefore, when selecting the optimum composition of the material we must allow for the decrease in the strength of the composite because of the limiting of the fiber level, and the undesired effects (separation into layers, crack formation) which may appear if the fiber packing is very close

3. Strength of composites reinforced by continuous parallel fibers

We shall consider an orthotropic single-layer plate consisting of parallel fibers uniformly distributed over the matrix (Figure X. 2). The tensile load is applied parallel to the fibers.

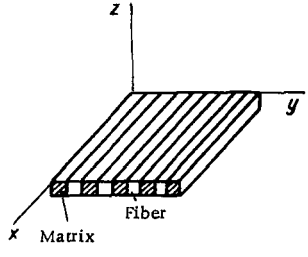

FIGURE X. 2. Fiber distribution in the matrix over the cross section of the composite.

We shall assume that the bond strength on the interface is sufficient for simultaneous deformation of the matrix and fibers up to complete destruction of the filler, that is, the mean deformation of the fibers before destruction ε_f is equal to the matrix deformation ε_m and deformations of the whole composite ε_c (these are the main preliminary conditions of the so-called "combined action theory"):

$$\varepsilon_f = \varepsilon_m = \varepsilon_c. \qquad (X.\ 8)$$

According to the additivity law, the external load received by the plate is equal to the sum

of the loads pertaining to the components. Hence, it can be concluded that the ultimate strength of the composite is expressed by

$$(\sigma_в)_c = (\sigma_в)_f V_f + \sigma'_m(1 - V_f), \tag{X.9}$$

where $(\sigma_в)_f$ is the ultimate tensile strength of the fibers and σ'_m is the stress in the matrix at the moment the fibers break.

In all cases discussed below it is assumed that the plasticity of the fibers is smaller and the modulus of elasticity larger than the corresponding matrix parameters.

In this case the tension curve of the reinforced material must, in principle, consist of four sections: I — the matrix and fiber are elastically deformed; II — the matrix passes into the elastic-plastic state, while the fiber continues to be elastically deformed; III — both system components are under plastic deformation; IV — the composite is fractured.

Depending on the properties of the components, sections II and III may be absent.

The strength of the composite cannot be expressed by (X.9) at all values of V_f. It is impossible from a purely geometrical point of view to increase the volume fraction of cylindrical fibers to more than 0.91. Also, if the volume fraction of the fibers is very low, the fibers cannot hinder the elongation of the matrix, so that the matrix will be rapidly deformed up to the ultimate strength and then fractured. In this case the reinforcement will not strengthen the composite but weaken it; its introduction is equivalent to an increase in threadlike pores.

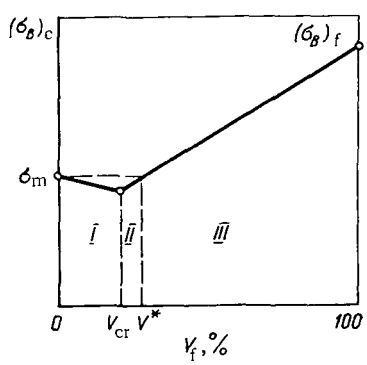

FIGURE X.3. Dependence of the tensile strength of composites reinforced by continuous parallel fibers on the volume fraction of the fibers.

The dependence of the strength on the volume content of the filler is shown in Figure X.3. If $V_f < V_{cr}$, the strength of the composite will decrease proportionally to the volume fraction of the fibers, and if $V_f > V_{cr}$, it will increase. The value of the critical volume fraction of the fibers V_{cr} can be found from the equality of the ultimate strength of the composite determined from (X.9) and the strength of the matrix, allowing for its volume fraction in the composite.

When $V_f = V_{cr}$

$$(\sigma_в)_f V_{cr} + \sigma'_m(1 - V_{cr}) = (\sigma_в)_m(1 - V_{cr}), \tag{X.10}$$

where $(\sigma_в)_m$ is the ultimate tensile strength of the matrix.

By solving (X.10), we obtain

$$V_{cr} = \frac{(\sigma_в)_m - \sigma'_m}{(\sigma_в)_f + (\sigma_в)_m - \sigma'_m}. \tag{X.11}$$

Thus, when $V_f = V_{cr}$, the strength of the composite is at its minimum. If the volume content of the fibers is equal to V^*, the ultimate strength of the composite is the initial ultimate strength of the unreinforced matrix,

$$(\sigma_в)_f V^* + \sigma'_m(1 - V^*) = (\sigma_в)_m \qquad (X.12)$$

where V^* is the volume content of the fibers at which the ultimate strength of the composite is equal to the ultimate strength of the pure matrix.

By solving (X.12) for V^* we obtain

$$V^* = \frac{(\sigma_в)_m - \sigma'_m}{(\sigma_в)_f - \sigma'_m}. \qquad (X.13)$$

To give rational reinforcement it is convenient to have the smallest possible values of V_{cr} and V^*, so that the material is strengthened at a low volume content of the filler. This can be achieved in practice by introducing fibers into the matrix which have an ultimate strength much higher than the stress in the matrix at the moment the material is destroyed (σ'_m for plastic matrixes is usually near their yield point).

TABLE X.2. Dependence of V_{cr} on the ultimate strength of the fibers

Material and mechanical properties of matrix, kg/mm²	V_{cr}, % for σ_f, kg/mm²			
	70	170	350	700
Aliminum, $\sigma'_m = 3$; $(\sigma_в)_m = 8.5$	8.3	3.2	1.6	0.8
Copper, $\sigma'_m = 4$; $(\sigma_в)_m = 21$	25.5	9.8	4.9	2.4
Nickel, $\sigma'_m = 6.5$; $(\sigma_в)_m = 31.5$	39.6	15.0	7.3	3.6
Stainless steel, $\sigma'_m = 17.5$; $(\sigma_в)_m = 45.5$	59.4	17.8	8.4	4.1

Table X.2 shows calculated data on the critical volume content of fibers for aluminum-, copper-, nickel-and stainless steel-based composites reinforced by fibers with a different tensile strength /7/. It can be seen from this table that at low strength of the fibers V_{cr} may be higher than 50%.

Ivanova and Ustinov /26/ analyzed the dependence of the specific strength on the volume fraction of the fibers, and found that V_{cr} is independent of the matrix and fiber densities, and in all cases can be determined from (X.11).

When $1 > V_f > V_{cr}$, the specific strength of a reinforced system is given by

$$\rho_{cl} = \{\sigma'_m + [(\sigma_в)_f - \sigma'_m] V_f\}/[\gamma_m + (\gamma_f - \gamma_m) V_f]; \qquad (X.14)$$

while when $V_{cr} > V_f > 0$, then

$$\rho_{c2} = (\sigma_в)_m(1 - V_f)/[\gamma_m + (\gamma_f - \gamma_m)V_f], \qquad (X.15)$$

where ρ_{c1} and ρ_{c2} are the specific strength of the composite for $V_f > V_{cr}$ and $V_f < V_{cr}$; γ_m and γ_f are the densities of the matrix and fibers.

The value of V_1^* at which the specific strength of the component becomes equal to the specific strength of the matrix depends, in contrast to V_{cr}, on the strength parameters of the components and their density, and is expressed by

$$V_1^* = \{1 + [(\sigma_в)_f - (\sigma_в)_m]\gamma_f/\gamma_m[(\sigma_t)_m - \sigma'_m]\}^{-1}. \qquad (X.16)$$

If $\gamma_f \neq \gamma_m$, V_1^* increases when the fiber density increases relative to the matrix density. When $\gamma_f/\gamma_m \to 0$ $V_1^* \to V_{cr}$. If the specific strengths of the matrix and fiber are equal ($\rho_m = \rho_f$), $V_1^* = 1$. This means that from the point of view of the specific strength, no strengthening will take place over the whole range of V_f values. If $\rho_m > \rho_f$, (X. 6) cannot be applied.

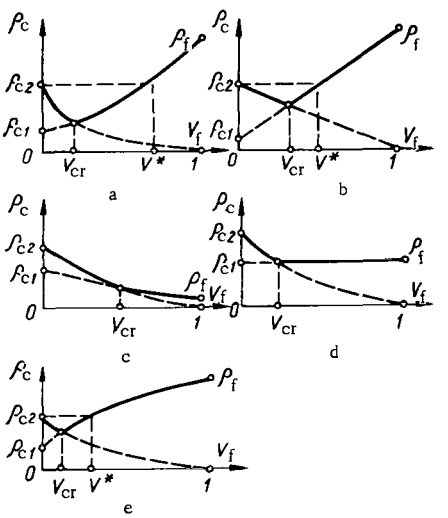

FIGURE X.4. Dependence of the specific strength of the composite on the volume content under the following conditions:

a – $\gamma_f < \gamma_m$; b – $\gamma_f = \gamma_m$; c – $\gamma_f > \gamma_m$ and $\frac{(\sigma_в)_f}{\gamma_f} < \frac{\sigma'_m}{\gamma_m}$; d – $\gamma_f > \gamma_m$ and $\frac{(\sigma_в)_f}{\gamma_f} = \frac{\sigma'_m}{\gamma_m}$; e – $\gamma_f > \gamma_m$ and $\frac{(\sigma_в)_f}{\gamma_f} > \frac{\sigma'_m}{\gamma_m}$.

If we assume that the ultimate strength of the fibers is higher than the ultimate strength of the matrix, then, depending on the density ratio and strength parameters, five different curves showing the dependence of the specific strength of the fibers on the volume content of the fibers can be obtained (Figure X. 4). The curves shown in Figure X. 4 were plotted by analyzing the first and second derviatives of (X. 14) and (X. 15).

From the five curves in Figure X. 4, only cases a, b and e are of practical interest. In these cases, with increase in the volume content of the fibers, the specific strength of the composite increases when $V_f > V_{cr}$.

The efficiency of reinforcement decreases in the following sequence

$$\gamma_f < \gamma_m;\ \gamma_f = \gamma_m;\ \gamma_f > \gamma_m$$
$$\text{and } (\sigma_в)_f/\gamma_f > \sigma_m'/\gamma_m.$$

For the ratios of the component strengths and densities shown in Figures X. 4, c and d, the specific strength of the system cannot be increased by reinforcement. The fracturing mechanism of the composite at $V_f > V_{cr}$ and $V_f < V_{cr}$ differ.

In the first case, the strength of the total material is determined by the strength of the fibers, and according to the given model, the breaking of only a small fraction of the fibers has catastrophic consequences for the whole composite.

If the material contains fibers in an amount below the critical, the breaking of a certain fraction of the fibers does not produce immediate destruction of the material. At the instant the individual fibers break, the stress decreases. However, afterwards the matrix is strengthened, and the load reverts to its former value. The whole composite is broken only when the safety factor of plasticity is exhausted. In other words, the total strain of the material is determined by the plastic properties of the matrix. At the same time, the fibers are fractured during loading.

Ustinov /9/ studied the process of this breakdown on a model of a single fiber enclosed into a matrix. It was assumed that the maximum tensile stress arises in the center of the fiber. The fiber is fractured as long as its final mean length after breaking by tension Δl_{av} is not between

$l_{cr} > \Delta l_{av} > \frac{1}{2} l_{cr}$ where l_{cr} is the critical fiber length

$$l_{cr} = \frac{(\sigma_в)_f d_f}{2\tau}. \qquad (X.\ 17)$$

To a first approximation, the final length of the sections can be assumed to be equal to

$$\Delta l_{av} \approx \frac{3}{4} l_{cr}. \qquad (X.\ 18)$$

The length of the fiber Δl_n before the n_i-th fracturing cycle is determined from

$$\Delta l_n = L/2^{n-1}, \qquad (X.\ 19)$$

where L is the initial length of the fiber.

The number of sections formed at the instant of the last n-th fracturing cycle (where n is the number of fracturing cycles to which the fibers are subjected) is expressed by

$$N_n = 2^{n-1}. \qquad (X.\ 20)$$

Before the last fracturing cycle, the mean length of the fiber sections is

$$\Delta l = 2\Delta l_{av} = \frac{3}{2} l_{cr} = \frac{3}{4} \cdot \frac{(\sigma_в)_f d_f}{\tau}. \quad (X.\ 21)$$

The number of sections formed up to the moment of the last fracturing cycle can be expressed by

$$N_n = \frac{L}{\Delta l} = \frac{4}{3} \cdot \frac{L\tau}{(\sigma_в)_f d_f}. \quad (X.\ 22)$$

The result of the simultaneous solution of (X. 20) and (X. 22) is a formula for the number of fracturing cycles for the fibers

$$n \approx 1 + 3.3 \lg \left[\frac{4}{3} \cdot \frac{L\tau}{(\sigma_в)_f d_f} \right]. \quad (X.\ 23)$$

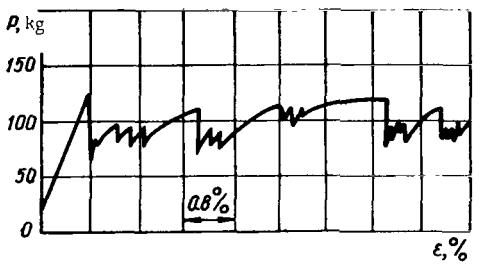

FIGURE X. 5. Stress-strain diagram of a copper-tungsten fiber composite. Volume content of fibers 10%.

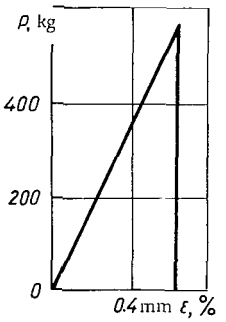

FIGURE X. 6. Tensioning diagram of a copper-tungsten fiber composite. Volume content of fibers 63%.

The fracturing of fibers is characterized by a stress-strain diagram of the reinforced system for $V_f < V_{cr}$ (Figure X. 5). When the fiber is broken first, the load which should be received by the fibers is instantly transmitted to the matrix, and a peak appears on the diagram which is proportional to the load. With proceeding deformations, the matrix is locally cold hardened, and the stress increases to such a value that the matrix is able to load new fiber parts until they are broken in another cross section. Therefore, the stress-strain diagram will have a jagged appearance, unlike that for systems in which the volume fraction of the fibers is higher than V_{cr} (Figure X. 6).

4. Elastic constants of composites reinforced by oriented continuous fibers

We shall now consider the model of a single-layer, orthotropic plate, represented in Figure X. 2, and explain the effect of the volume fraction

of the fibers and of the matrix and fiber characteristics on the elastic constants /1, 2, 8/.

Young's modulus. The tensile load is applied along the x-axis. We shall assume that the isotropic matrix and the fibers are simultaneously deformed, that is

$$\varepsilon_{xm} = \varepsilon_{xf} = \varepsilon_{xc}, \tag{X. 24}$$

where ε_{xm} ε_{xf}, and ε_{xc}, are the relative deformations on tensioning of the matrix, fibers, and composite, in the direction of the x-axis.

According to the theory of combined action, Young's modulus of the selected model in the direction of the x-axis is described by

$$E_{xc} = E_f V_f + E_m(1 - V_f). \tag{X. 25}$$

The tensile load is applied along the y-axis. We shall assume that the tensile load is applied in the direction of the y-axis (see Figure X. 2), and the matrix and fibers are successively loaded. In this case the deformation of the composite ε_{yc} can be found as the sum of the fiber ε_{yf} and matrix ε_{ym} deformations, allowing for their volume fraction

$$\varepsilon_{yc} = \varepsilon_{yf} V_f + \varepsilon_{ym}(1 - V_f). \tag{X. 26}$$

The stresses in each of the components are equal to the external stress σ_y:

$$\sigma_{yf} = \sigma_{ym} = \sigma_y. \tag{X. 27}$$

By using the equations of Hooke's law, and (X. 26) and (X. 27), we can determine Young's modulus E_{yc} of the composite in the direction of the y-axis under the condition that the tensile load acts perpendicularly to the fiber orientation

$$E_{yc} = \frac{E_f E_m}{E_m V_f + E_f(1 - V_f)}. \tag{X. 28}$$

Poisson ratio. The Poisson ratio ν is the ratio between the material deformation in the direction perpendicular to the force vector and the deformation in the direction of action of the force.

If the tensile load is directed along the x-axis, the Poisson ratio, allowing for (X. 24) and (X. 26), is given by

$$\nu_x = \left|\frac{\varepsilon_{yc}}{\varepsilon_{xc}}\right| = \nu_f V_f + \nu_m(1 - V_f). \tag{X. 29}$$

If the tensile load acts in the direction of the y-axis, the Poisson ratio of the composite is

$$\nu_{yxc} = \left|\frac{\varepsilon_{xc}}{\varepsilon_{yc}}\right|. \tag{X. 30}$$

It follows from the condition that forces directed along the x-axis must be in equilibrium, and that $\varepsilon_{xm} = \varepsilon_{xf}$, that

$$\varepsilon_{xc} = -\frac{\nu_f V_f \frac{E_f}{E_m}\cdot\frac{\sigma_y}{E_f} + \nu_m(1-V_f)\frac{\sigma_y}{E_m}}{\frac{E_f}{E_m} - (1-V_f)\left(\frac{E_f}{E_m}-1\right)}. \qquad (X.31)$$

From Hooke's law and (X. 26), we obtain

$$\nu_{yxc} = \frac{E_f E_m[\nu_f V_f + \nu_m(1-V_f)]}{E_f V_f + E_m(1-V_f)[E_m V_f + E_f(1-V_f)]}. \qquad (X.32)$$

Modulus of shear. If the orthotropic plate is subject to shearing stresses in plane xy, the load is taken up successively by matrix and fibers, that is

$$\tau_{xy} = \tau_{xym} = \tau_{xyf}, \qquad (X.33)$$

where τ_{xym} and τ_{xyf} are the shearing stresses in matrix and fibers, respectively.

The shearing strain of the matrix is determined from

$$\gamma_{xyc} = \gamma_{xyf} V_f + \gamma_{xym}(1-V_f), \qquad (X.34)$$

where γ_{xyc}, γ_{xyf}, and γ_{xym} are the relative shearing strains in the composite, fibers, and matrix, respectively.

From (X. 33) and (X. 34), we find the modulus of shear of the plate in plane xy

$$G_{xyc} = \frac{G_f G_m}{G_f(1-V_f) + G_m V_f}, \qquad (X.35)$$

where G_f and G_m are the moduli of shear of fibers and matrix.

We see from (X. 25), (X. 28), (X. 29), and (X. 32), that

$$\frac{E_{yc}}{E_{xc}} = \frac{\nu_{yxc}}{\nu_{xyc}}, \qquad (X.36)$$

that is, the given model of the orthotropic material in the case of the two-dimensional problem in the elastic strain region is completely described by four elastic constants, namely, the modulus of shear and any of the three magnitudes of (X. 36).

Elastic constants during action of forces at an angle to the fiber orientation. The next stage in the solution of problems on the elastic constants of an orthotropic model is finding the elastic constants in directions differing from the main directions of the material.

If the orthotropic plate is subjected to normal (σ_x and σ_y) and shearing (τ_{xy} and τ_{yx}) stresses in two directions perpendicular to one another (Figure X. 7), the deformation in tension along the x and y axes (ε_{xc} and ε_{yc}) and the shearing strain γ_{xyc} are determined from

$$\varepsilon_{xc} = \frac{\sigma_x}{E_{xc}} - \nu_{yxc}\frac{\sigma_y}{E_{yc}}; \qquad (X.37)$$

$$\varepsilon_{yc} = \frac{\sigma_y}{E_{yc}} - \nu_{xyc}\frac{\sigma_x}{E_{xc}}; \qquad \text{(X. 38)}$$

and

$$\gamma_{xyc} = \gamma_{yxc} = \frac{\tau_{xy}}{G_{xyc}}. \qquad \text{(X. 39)}$$

We shall consider the case when the model is stressed at angle α to the fiber direction (Figure X. 8). From the values of σ_1, σ_2, τ_{12}, and τ_{21}, we find the moduli E_1, E_2, and G_{12} and the Poisson ratios ν_{12} and ν_{21}.

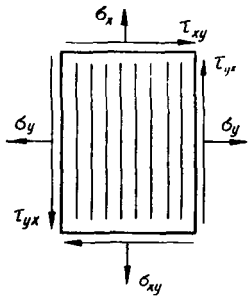

FIGURE X. 7. Diagram of an orthotropic plate subjected to normal and shearing stresses in two directions perpendicular to one another which coincide with the principal axes of the material.

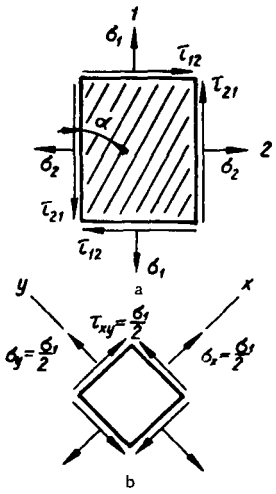

FIGURE X. 8. Diagram of an orthotropic plate subjected to normal and shearing stresses in two directions perpendicular to one another which do not coincide with the principal axes of the material:

a — equivalent stress system at $\alpha = 45°$, $\sigma_1 \neq 0$, and $\tau_{12} = 0$;
b — system of stresses directed along the main axis of the material.

We solve the problem in the general case as follows.

The stress sytem in axes 1 — 2 (Figure 8, a) leads to an equivalent stress system with reference to the x and y axes (see Figure X. 8, b). From (X. 37), (X. 38), and (X. 39), if we know the stresses with reference to the x and y axes, we can determine the corresponding strains, and then the strains with reference to axes 1 and 2. Finally, the elastic constants are calculated as shown in /31 — 34/.

We shall analyze only the main results obtained in these papers.

Simple tension ($\sigma_1 \neq 0$; $\sigma_2 = \tau_{12} = \tau_{21} = 0$). The dependence of strain ε_1 on tensile stress σ_1 is simple

$$\varepsilon_1 = \frac{\sigma_1}{E_1}. \tag{X. 40}$$

The required value of E_1 is determined from the known E_{xc} and E_{yc} values from

$$\frac{E_{xc}}{E_1} = \cos^4\alpha + \frac{E_{xc}}{E_{yc}}\sin^4\alpha + \frac{1}{4}\left(\frac{E_{xc}}{G_{xyc}} - 2\nu_{xyc}\right)\sin^2 2\alpha. \tag{X. 41}$$

The Poisson ratio ν_{12} is determined in terms of the elastic constants in axes x and y from

$$\nu_{12} = \frac{1}{E_{xc}}\left[\nu_{xy} - \frac{1}{2}\left(1 + 2\nu_{xyc} + \frac{E_{xc}}{E_{yc}} - \frac{E_{xc}}{G_{xyc}}\right)\sin^2 2\alpha\right]. \tag{X. 42}$$

The deformation of the plate along axis 2 is determined from

$$\varepsilon_2 = \nu_{12}\varepsilon_1, \tag{X. 43}$$

while the shearing strain caused by σ_1 is expressed by

$$\gamma_{12} = -m_1\frac{\sigma_1}{E_{xc}}, \tag{X. 44}$$

where m_1 is an interaction coefficient

$$m_1 = \sin 2\alpha\left[\nu_{xyc} + \frac{E_{xc}}{E_{yc}} - \frac{1}{2}\cdot\frac{E_{xc}}{G_{xyc}} - \cos^2\alpha\left(1 + 2\nu_{xyc} + \frac{E_{xc}}{E_{yc}} - \frac{E_{xc}}{G_{xyc}}\right)\right]. \tag{X. 45}$$

The characteristic difference between anisotropic and isotropic materials is that in the former shearing strain γ_{12} appears due to tensile stress σ_1.

Pure shear ($\sigma_1 = \sigma_2 = 0$; $\tau_{12} = \tau_{21} \neq 0$). In pure shear the shearing stresses lead to a tensile strain along axes 1 and 2

$$\varepsilon_1 = -m_1\frac{\tau_{12}}{E_{xc}};\quad \varepsilon_2 = -m_2\frac{\tau_{12}}{E_{xc}}, \tag{X. 46}$$

where m_1 is determined from (X. 45);

$$m_2 = \sin 2\alpha\left[\nu_{xyc} + \frac{E_{xc}}{E_{yc}} - \frac{1}{2}\cdot\frac{E_{xc}}{G_{xyc}} - \sin^2\alpha \times \left(1 + 2\nu_{xyc} + \frac{E_{xc}}{E_{yc}} - \frac{E_{xc}}{G_{xyc}}\right)\right], \tag{X. 47}$$

and also the shearing strain

$$\gamma_{12} = \frac{\tau_{12}}{G_{12}}. \tag{X. 48}$$

G_{12} is found from

$$\frac{G_{xyc}}{G_{12}} = \frac{G_{xyc}}{E_{xc}}\left[\left(1 + 2\nu_{xyc} + \frac{E_{xc}}{E_{yc}}\right) - \left(1 + 2\nu_{xyc} + \frac{E_{xc}}{E_{yc}} - \frac{E_{xc}}{G_{xyc}}\right)\cos^2 2\alpha\right]. \tag{X. 49}$$

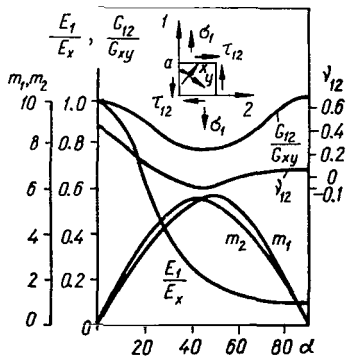

FIGURE X.9. Diagram of the elastic constants of a plate, made of material reinforced by fibers in a single direction, subjected to normal and shearing stresses at an angle α to the principal axes. The elastic constants are given with reference to the principal axes of the material:

$E_x = 0.35 \cdot 10^4$ kg/mm^2; $E_y = 0.035 \cdot 10^4$ kg mm^2; $G_{xy} = 0.0385 \cdot 10^4$ kg/mm^2; $\nu_{xy} = 0.45$; $\nu_{yx} = 0.045$.

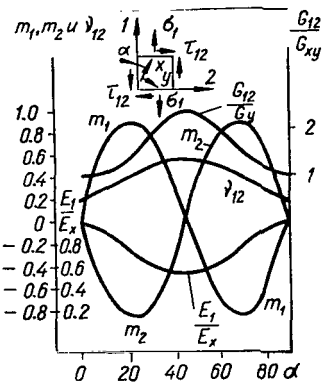

FIGURE X.10. Diagram of the elastic constants of a plate, made of material reinforced by the same amount of fibers in two directions perpendicular to one another, subjected to normal and shearing stresses at an angle α to the principal axes. The elastic constants are given with reference to the principal axes of the material:

$E_x = 0.21 \cdot 10^4$ kg/mm^2; $E_y = 0.21 \cdot 10^4$ kg/mm^2; $G_{xy} = 0.035 \cdot 10^4$ kg/mm^2; $\nu_{xy} = \nu_{yx} = 0.20$.

Overall two-dimensional stressed state ($\sigma_1 \neq \sigma_2 \neq 0$; $\tau_{12} = \tau_{21} \neq 0$). The diagram of the action of forces is shown in Figure X. 8. With the aid of Hooke's law, we shall determine strains ε_1 and ε_2 along axes 1 and 2, and the shearing strain γ_{12}:

$$\varepsilon_1 = \frac{\sigma_1}{E_1} - \nu_{21}\frac{\sigma_2}{E_2} - m_1\frac{\tau_{12}}{E_{xc}}; \qquad (X.50)$$

$$\varepsilon_2 = \frac{\sigma_2}{E_2} - \nu_{12}\frac{\sigma_1}{E_1} - m_2\frac{\tau_{12}}{E_{xc}}; \qquad (X.51)$$

and

$$\gamma_{12} = \frac{\tau_{12}}{G_{12}} = -m_1\frac{\sigma_1}{E_{xc}} - m_2\frac{\sigma_2}{E_{xc}}. \qquad (X.52)$$

E_1, m_1, m_2 and G_{12} are determined from (X.41), (X. 45), (X. 47), and (X. 49), and E_2 and ν_{21} from

$$\frac{E_{xc}}{E_2} = \sin^4\alpha + \frac{E_{xc}}{E_{yc}}\cos^4\alpha + \frac{1}{4}\left(\frac{E_{xc}}{G_{xyc}} - 2\nu_{xyc}\right)\sin^2 2\alpha; \qquad (X.53)$$

and

$$\nu_{21} = \frac{E_2}{E_1}\nu_{21} = \frac{E_2}{E_{xc}}\left[\nu_{xyc} - \frac{1}{2}\nu_{xyc} + \frac{E_{xc}}{E_{yc}} - \frac{E_{yc}}{G_{xyc}}\right)\sin^2 2\alpha\Big]. \qquad (X.54)$$

Figures X. 9 and X. 10 show the dependences of the elastic constants on α for a composite reinforced in a single direction and a material reinforced by the same amount of fibers oriented in two directions perpendicular to one another. The above equations were used for the calculation.

These dependences were derived from a idealized single-layer composite model. The plastic deformations of the material, layer interaction, technological defects in the material, destruction of the interfacial matrix-fiber bonds, etc., were not allowed for. Some deviations from the idealized state are considered in /35 – 40/. It should be noted that most of the theoretical and experimental research was performed on systems modeling reinforced plastics. It was shown that these solutions can be used for such materials if a computational estimate is required (it is here assumed that the working loads are much smaller than the ultimate strength of the composite). However, if we have to accurately determine the elastic constants, we must carry out tests in each case, since the simplifying assumptions taken when deriving the analytical equations introduce large errors into the calculation.

The range of application of the above equations is limited. They may satisfactorily describe the behavior of metallic systems within the elastic deformation range of both components. But usually the working loads are not within the proportional limit of the matrix. Therefore, when using reinforced metals we must carry out even more experimental and theoretical studies to explain the conditions under which the above equations can be applied.

5. Strength of materials with parallel discrete fibers

We shall consider the stressed state of a short fiber in the matrix, that is, we shall determine the tensile σ_f and shearing τ_m stresses arising in the composite when an external tensile load acts in a direction parallel to the fibers. The model of Outwater /10/ and Dow /29/ is the simplest for describing the stress distribution from the analytical and phenomenological points of view. This model (Figure X. 11) consists of a fiber of diameter d_f, mounted with constant clearance into a hollow cylinder of the matrix material. The wall thickness of the cylinder is equal to t. The cylinder itself is placed into an elastic body of sufficiently large size to have the average (effective) properties of the given composite. The tensile load is applied to this body. It is assumed that the matrix shell only transmits shearing stresses. The tensile stresses in the fiber arise because of the action of the shearing stresses on the fiber-matrix interface and both components of the material obey Hooke's law.

The equation of the force equilibrium for an element of the model of length dx (see (X. 11)) is

$$dN = c(u_f - u)\,dx, \qquad (X.55)$$

where N is the stress in the fibers; c is the shearing rigidity of the matrix

$$c = G_m \frac{b}{t};$$

b is the perimeter length of the fiber in the cross section; u_f is the axial displacement in the fiber; and u is the axial displacement in the matrix.

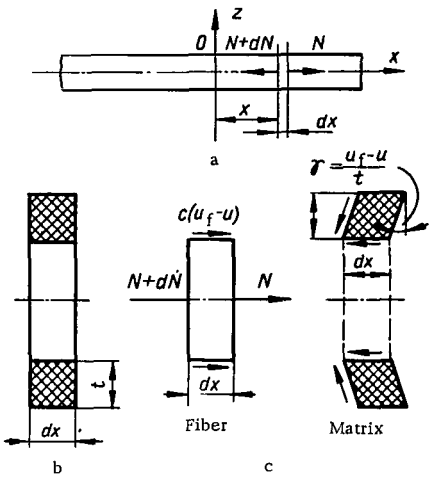

FIGURE X.11. The Outwater model:

a — stresses in fiber; b — element before loading; c — element under load.

According to Hooke's law

$$N = \frac{du_f}{dx} E_f F_f, \tag{X.56}$$

where F_f is the fiber cross section.

By inserting the values of c and N into (X.55), and dividing both sides by dx, we obtain

$$\frac{d^2u_f}{dx^2} - \frac{G_m}{E_f} \cdot \frac{b}{F_f t} (u_f - u) = 0, \tag{X.57}$$

or

$$\frac{d^2u_f}{dx^2} - \beta^2 (u_f - u) = 0, \tag{X.58}$$

where

$$\beta^2 = \frac{G_m b}{E_f F_f t}. \tag{X.59}$$

For a circular fiber

$$\beta^2 = \frac{4G_m}{t d_f E_f}. \tag{X.59a}$$

By solving the differential equation (X.58), we obtain an expression of type

$$u_f = u + A \operatorname{sh} \beta x + B \operatorname{ch} \beta x. \tag{X.60}$$

The boundary conditions for determining constants A and B when $x = \pm \frac{l}{2}$ are

$$\frac{du_f}{dx} = 0,$$

whence

$$u_f = u - \frac{\sigma}{E_c \beta} \cdot \frac{\operatorname{sh} \beta x}{\operatorname{ch} \beta \frac{l}{2}}. \tag{X. 61}$$

From (X. 56) and (X. 61) we find the tensile stress in the fiber

$$\sigma_f = \sigma \frac{E_f}{E_c} \left(1 - \frac{\operatorname{ch} \beta x}{\operatorname{ch} \beta \frac{l}{2}} \right), \tag{X. 62}$$

where σ is the applied axial stress; l is the fiber length, and E_c is the effective Young's modulus of the composite.

The shearing stresses in the fiber-matrix interface are

$$\tau_m = \sigma \frac{G_m}{E_c \beta t} \cdot \frac{\operatorname{sh} \beta x}{\operatorname{ch} \beta \frac{l}{2}}. \tag{X. 63}$$

The tensile stresses in the fibers when $x = 0$ have the maximum value

$$\sigma_{f\,max} = \sigma \frac{E_f}{E_c} \left(1 - \frac{1}{\operatorname{ch} \beta \frac{l}{2}} \right). \tag{X. 64}$$

If $l \to \infty$, that is, if the material is reinforced by continuous fibers, the normal stresses in the center of the infinitely long fiber are given by

$$\sigma_{f\infty} = \sigma \frac{E_f}{E_c}. \tag{X. 65}$$

The shearing stresses in the matrix at $x = \frac{l}{2}$ have a maximum value

$$\tau_{m\,max} = \sigma \frac{G_m}{E_c t \beta} \operatorname{th} \beta \frac{l}{2}. \tag{X. 66}$$

Thus, normal tensile stresses in the fiber increase from the ends to the middle, while the shearing stresses reach their maximum value at the fiber ends, and decrease almost to zero at half the critical length l_{cr}. The critical length of a discrete fiber is the length necessary to attain in the fiber a stress which is 97% of the stress on an infinitely long fiber. For the elastic model, the value of l_{cr} can be found as follows. The tensile stress in the fiber at distance δ from its center is determined from

$$\sigma_f \left(\frac{l}{2} - \delta \right) = \frac{\sigma E_f}{E_c} \left[1 - \frac{\operatorname{ch} \beta \left(\frac{l}{2} - \delta \right)}{\operatorname{ch} \beta \frac{l}{2}} \right]. \tag{X. 67}$$

The ratio of the stress at a point at distance δ from the fiber ends to the stress in the center of a continuous fiber is given by

$$\varphi = \frac{\sigma_f\left(\frac{l}{2} - \delta\right)}{\sigma_{f\infty}} = 1 - \operatorname{ch}\beta\delta + \operatorname{th}\beta\frac{l}{2}\operatorname{sh}\beta\delta, \qquad \text{(X. 68)}$$

where $\sigma_{f\infty}$ is determined from (X. 65).

For higher l values

$$\operatorname{th}\beta\frac{l}{2} = 1, \qquad \text{(X. 69)}$$

whence

$$\varphi = 1 - \operatorname{ch}\beta\delta + (\operatorname{ch}^2\beta\delta - 1)^{\frac{1}{2}}. \qquad \text{(X. 70)}$$

Consequently

$$\operatorname{ch}\beta\delta = \frac{1 - (1-\varphi)^2}{2 - (1-\varphi)}. \qquad \text{(X. 71)}$$

Rosen /28/ showed that the solution of (X. 71) for δ can be obtained as

$$\frac{\delta}{d_f} = \frac{1}{2}\left[\left(V_f^{-\frac{1}{2}} - 1\right)\frac{E_f}{G_m}\right]^{\frac{1}{2}} \operatorname{Arch}\left[\frac{1 + (1-\varphi)^2}{2(1-\varphi)}\right]. \qquad \text{(X. 72)}$$

When $\varphi = 0.97$

$$\operatorname{Arch}\frac{1 + (1-\varphi)^2}{2(1-\varphi)} \approx 3.5.$$

Thus

$$l_{cr} = 2\delta \approx 3.5\left[\left(V_f^{-\frac{1}{2}} - 1\right)\frac{E_f}{G_m}\right]^{\frac{1}{2}} d_f. \qquad \text{(X. 73)}$$

Dow /29/ studied various cases of uniaxial tension in such a model. If a small load is applied to a plastic matrix, and both components are elastically deformed, only a small fraction of the load is transmitted to the fiber, since the matrix deformation is too small to produce a large fiber deformation. But if the matrix is subjected to plastic deformation, at the same stress level the fibers receive a much larger part of the load. (The problem of stress distribution with allowance for plasticity was solved by Dow by reducing the nonelastic sections of the stress-strain curves to a series of pseudoelastic curves by means of the small stress method.) This is seen from the graphs given in Figure X. 12. The volume content of the whiskers is 1%, their Young's modulus is equal to 42,200 kg/mm^2, and their ultimate strength to 422 kg/mm^2. It can be seen from Figure X. 12 that at elastic-plastic behavior of the matrix, the effective length of the fiber receiving the load is larger than when the matrix behaves elastically. The load is transmitted to the fiber crystal on a length equal to 16 — 20% of its diameter.

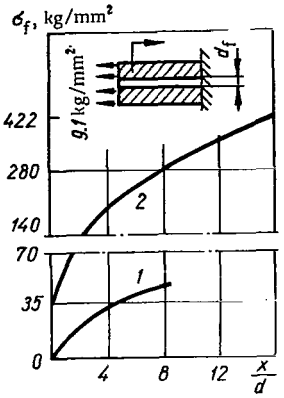

FIGURE X. 12. Rated values of the tensile stresses arising in fiber crystals of alumina during tension of the aluminum matrix under inelastic (2) and elastic (1) behavior $\left(\frac{V_m}{V_f} = 100\right)$.

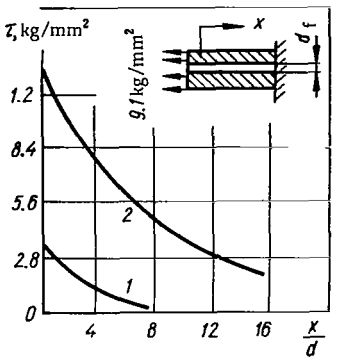

FIGURE X. 13. Rated values of the shearing stresses arising on the Al_2O_3 fiber crystal-aluminum matrix interface during tension of the matrix under elastic (1) and inelastic (2) behavior $\left(\frac{V_m}{V_f} = 100\right)$.

If both components are elastically loaded, the shearing stresses at the fiber ends are small. However, they increase sharply and become comparable with the tensile stresses applied to an aluminum matrix if the matrix is subjected to plastic deformation (Figure X. 13).

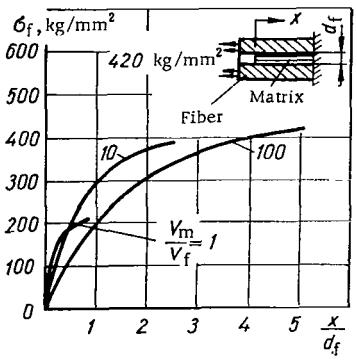

FIGURE X. 14. Tensile stresses arising in fibers on application of large stresses to an elastic high strength matrix.

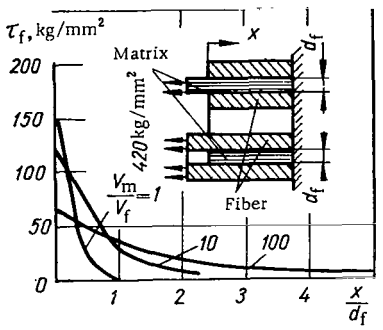

FIGURE X. 15. Shearing stresses arising between the high-strength fiber and the high-strength matrix on application of large stresses to matrix or fibers.

If in the matrix and fibers the Young's moduli and strengths are close to one another, the rated shearing stresses may be very large, even if both components behave elastically. The length of load transmission is small, and only about 4 — 6 fiber diameters (Figures X. 14, X. 15).

Thus, effective loading of the fibers is possible if plastic flow of the soft matrix occurs in the interfacial area, or if the matrix has a strength and rigidity sufficient to withstand large shearing stresses.

The elastic-plastic model describes the behavior of the composite more accurately than the elastic model. The critical fiber length for the elastic-plastic model can be estimated from the equilibrium of forces on the interfacial area

$$(\sigma_v)_f \frac{\pi d_f^2}{4} = \tau_m \pi d_f \frac{l_{cr}}{2}, \qquad (X.74)$$

whence

$$\frac{l_{cr}}{d_f} = \frac{(\sigma_в)_f}{2\tau_m}. \qquad (X.75)$$

If the length of the reinforcing fibers is smaller than the critical, the fibers are underloaded, and the composite will be destroyed because of the extraction of the fibers from the matrix and not because of their breaking.

The strength of the systems reinforced by discrete fibers can also be estimated from the additivity law, allowing for the so-called "end effect," that is, for inhomogeneities in the stress distribution along the fiber.

We shall now discuss the effect of the length of discrete fibers on the average tensile stress $\bar{\sigma}_f$ in them (Figure X.16) /30, 41/.

As the fiber length increases, the tensile stress at its center increases. If the length of the fiber is equal to the critical ($l = l_{cr}$), the stress at the center of the fiber reaches its maximum, which is approximately equal to the stress in the infinitely long fiber ($\sigma_{f\,max} \approx \sigma_{f\infty}$). With further increase in the fiber length, the maximum stress in the fiber remains constant, but the weighted mean stress in the fiber $\bar{\sigma}_f$ continues to increase, that is, for fibers of length $l_1 < l_2 < l_{cr} < l_4$ the following inequality will hold

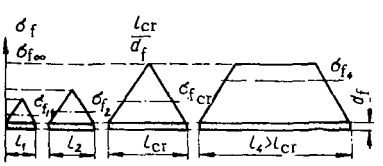

FIGURE X.16. Tensile stress cruves in fibers of different lengths.

$$\bar{\sigma}_{f1} < \bar{\sigma}_{f2} < \bar{\sigma}_{f\ cr} < \bar{\sigma}_{f4}.$$

We shall assume that the stress on the fiber end is equal to $\Omega(\sigma_в)_f$, where $1 > \Omega > 0$ (Ω is the load transmission coefficient). In this case, if the volume fraction of the fibers is V_f, a fraction of the fibers equal to $V_f \frac{l_{cr}}{l}$ carries stress $\Omega(\sigma_в)_f$, and the rest $\left(V_f \frac{l - l_{cr}}{l}\right)$ is subjected to stress $(\sigma_в)_f$.

If the weighted mean stress in the fibers $\bar{\sigma}_f$ is found from

$$\bar{\sigma}_f = \frac{\Omega(\sigma_в)_f V_f \left(\frac{l_{cr}}{l}\right) + (\sigma_в)_f V_f \left(\frac{l - l_{cr}}{l}\right)}{V_f}, \qquad (X.76)$$

or

$$\bar{\sigma}_f = (\sigma_в)_f \left[1 - (1 - \Omega)\frac{l_{cr}}{l}\right]. \qquad (X.77)$$

If, to a first approximation, we assume that over the critical length l_{cr}^{*} the tensile stress increases linearly, $\Omega = 0.5$. The total strength of the composite follows from the additivity law

$$(\sigma_в)_c = \bar{\sigma}_f V_f + \sigma_m(1 - V_f), \tag{X. 78}$$

or

$$(\sigma_в)_c = (\sigma_в)_f \left[1 - (1 - \Omega)\frac{l_{cr}}{l}\right] V_f + \sigma_m(1 - V_f). \tag{X. 79}$$

In the case of reinforcement by discrete fibers as in the case of reinforcement by continuous fibers, the critical volume fraction of the fibers is given by /11, 30/

$$V_{cr} = \frac{1}{1 + \frac{(\sigma_в)_f}{(\sigma_в)_m - \sigma_m}\left(1 - \frac{l_{cr}}{l}\right)}. \tag{X. 80}$$

It should be noted that V_{cr} is independent of the load transmission coefficient Ω, that is, the growth pattern of the stresses on the ends of the fibers.

In conclusion, it can be stated that if the oriented fibers are uniformly distributed over the matrix, the strength of the composite depends on the strength parameters of the components, volume fraction of the fibers, and efficiency of stress transmission from the matrix to the fibers. The last factor depends on the fiber length.

6. Statistical analysis of the fiber strength

In the preceding sections we assumed that the material is uniformly deformed over the bulk, and that it is broken after the limiting deformation of the fibers corresponding to the mean ultimate strength is exceeded. However, it was found by experiment that reinforced systems do not always behave in this manner, mainly because of the presence of internal defects, inhomogeneities in the stress distribution, insufficient bonding between fibers and matrix, and finally, differences in the fiber strength.

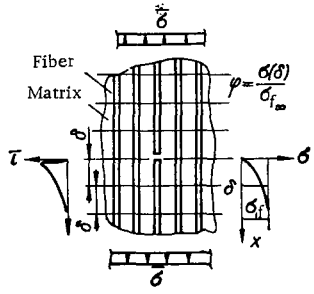

FIGURE X.17. Model of fracture of a composite during tension.

In practice, there are always defects in reinforced materials. They may appear during the technological process (scratches, flaws, nonmetallic inclusions, pores) or during loading of the material due to stress concentrations at the fiber ends.

These defects may lead to local disturbances in the fibers and matrix. Cracks appear and develop, and cause disturbance patterns differing from the pattern assumed for the idealized model.

In materials reinforced by continuous fibers, the fibers may begin to be fractured at the

defective sites long before the ultimate strength of the composite is reached. The stresses are redistributed near the sites of internal fracture (Figure X. 17). The internal fractures may accumulate over the fiber length until the remaining whole fibers are no longer able to receive the applied load or in other words, the whole material is fractured. This case was used by Rosen /13, 28/ as the basis of the statistical model of composite fracture during tension.

Before studying the statistical model of the reinforced composite, we shall carry out a brief statistical analysis of the strength of the individual fibers.

For a statistical analysis of the composite strength we must find the distribution function characterizing the probability of the fracture of fibers of length L, and their individual links of length δ, by a tensile stress less than or equal to the given stress σ.

If we consider a set of N fibers, and know that at a stress $\sigma_1 \leqslant \sigma$, n fibers are broken, for very large values of N the distribution function of the fiber strength $G(\sigma)$ is expressed by

$$G(\sigma) = \frac{n}{N}. \tag{X. 81}$$

If stress σ is insufficient to break even a single fiber, $G(\sigma) = 0$. But if all the fibers are broken, $G(\sigma) = 1$. In the general case, if n fibers are fractured by stress σ, a stress increase of $d\sigma$ increases the number of broken fibers to $n + dn$, while probability $g(\sigma)$ of fracturing fibers in the range from σ to $(\sigma + d\sigma)$ is

$$g(\sigma) = \frac{dn}{N}. \tag{X. 82}$$

The integral strength distribution function will be

$$G(\sigma) = \int_0^\sigma \frac{dn}{N} d\sigma = \int_0^\sigma g(\sigma)\, d\sigma. \tag{X. 83}$$

If we consider the fiber as a chain consisting of links of length δ, and assume that the strength of each link lies in the stress range between σ and $(\sigma + d\sigma)$ and is equal to $f(\sigma)\, d\sigma$, the probability of fracture of this link at a stress not exceeding σ is expressed by an integral function of the strength distribution of the link

$$F(\sigma) = \int_0^\sigma f(\sigma)\, d\sigma. \tag{X. 84}$$

Evidently, the probability that the link will not be fractured on application of a stress smaller than or equal to σ will be $[1 - F(\sigma)]$. The number of chain links is given by $n = \frac{L}{\delta}$. The probability of breaking the fiber $g(\sigma)$ consisting of n links in the stress range between σ and $(\sigma + d\sigma)$ is found as follows. If we know that at stresses smaller than or equal to σ the probability that one link is not fractured is $[1 - F(\sigma)]$, the probability that the other $(n - 1)$ links in the same stress range are not broken is equal to $[1 - F(\sigma)]^{n-1}$, according to the rule of probability addition.

The probability that a certain link is fractured between σ and $\sigma + d\sigma$ is given by product $f(\sigma)[1 - F(\sigma)]^{n-1}$. If we assume that fracturing a chain consisting of n links is equiprobable at each link, the differential function of the strength distribution is expressed according to the rule of probability addition by

$$g(\sigma) = nf(\sigma)[1 - F(\sigma)]^{n-1}, \tag{X. 85}$$

and the corresponding integral function in the form of

$$G(\sigma) = \int_0^\sigma g(\sigma)\, d\sigma = \int_0^\sigma nf(\sigma)[1 - F(\sigma)]^{n-1}\, d\sigma. \tag{X. 86}$$

By integrating (X. 86), we obtain

$$G(\sigma) = 1 - [1 - F(\sigma)]^n. \tag{X. 87}$$

From (X. 87) it is possible to determine the strength distribution function of the fiber $G(\sigma)$ from the known distribution function of the links $F(\sigma)$. The reverse problem, that is, the determination or $F(\sigma)$ and $f(\sigma)$ from given $G(\sigma)$ and $g(\sigma)$is solved by means of the following equations

$$F(\sigma) = 1 - [1 - G(\sigma)]^{\frac{1}{n}} \tag{X. 88}$$

and

$$f(\sigma) = \frac{g(\sigma)}{n}[1 - G(\sigma)]^{\frac{1}{n}-1}. \tag{X. 89}$$

If the strength distribution of the fibers obeys Weibulls law /24/, the correlation between fiber length L and fiber strength is given by

$$g(\sigma) = L\alpha\beta\sigma^{\beta-1}\exp(-L\alpha\sigma^\beta). \tag{X. 90}$$

By solving (X. 86), (X. 89), and (X. 90), and remembering that $L = n\delta$, we obtain

$$f(\sigma) = \alpha\delta\beta\sigma^{\beta-1}\exp(-\alpha\delta\sigma)^\beta. \tag{X. 91}$$

This equation contains two unknown constants α and β, which are found from strength tests on the fibers.

The average strength $\bar{\sigma}_f$ of a fiber of length L can be expressed as

$$\bar{\sigma}_f = \int_0^\infty \sigma g(\sigma)\, d\sigma. \tag{X. 92}$$

By integrating (X. 92), after substituting (X. 90) into it, we obtain

$$\bar{\sigma}_f = (L\alpha)^{-\frac{1}{\beta}}\Gamma\left(1 + \frac{1}{\beta}\right), \tag{X. 93}$$

where Γ is the gamma function.

Consequently, the graph of the fiber strength plotted against the length must be a straight line in logarithmic coordinates. Constants α and β are determined directly from this graph. Constant α determines the characteristic stress level $\alpha^{-\frac{1}{\beta}}$, while β is the reciprocal of the strength dispersion. It was shown by Cücer and Gurland /25/ that β-values between 2 and 4 correspond to brittle materials, and β-values of about 20 to plastic materials.

After this preliminary survey we can statistically analyze the composite strength as a whole.

7. Statistical model of the fracture of reinforced material in tension

The statistical model of the fracture of composite material in uniaxial tension was developed by Rosen /12, 13, 28/. This model consists of a row of parallel fibers uniformly distributed over the matrix (Figure X. 17). The strength and modulus of elasticity of the matrix are much higher in the matrix than in the fibers. It is supposed that the fiber strength is determined by a statistical distribution function, corresponding to the statistical distribution of defects along the fiber. Mechanical tests on thin fibers confirm that the assumption is correct, and show that the strength is a monotonically decreasing function of the length.

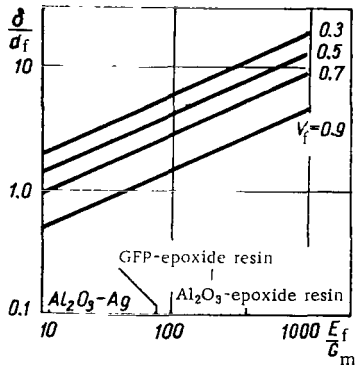

FIGURE X. 18. Noneffective fiber length in various composites when $\varphi = 0.9$.

According to this model, the composite fracture begins by the breaking of the fibers at defective sites at stresses much smaller than the ultimate strength of the composite. We shall assume that the bond on the fiber-matrix interface is sufficiently strong, and that the resistance of the composite against crack propagation is sufficiently high. Therefore, as the external tensile force increases, the fibers break at other defective sites. These fractures are statistically accumulated until in some of the remaining sections the fibers are no longer able to take the load, that is, the whole material is fractured.

Rosen introduced the term "noneffective fiber length" which means the part of the fiber length δ at the site of fracture which is unable to transmit the load. We know that at the site of fracture the tensile stresses in the fibers are zero, and gradually increase with distance from the torn end (Figure X. 17). As the noneffective fiber length we arbitrarily take the part of the fiber in which the mean stress is less than 90% of the stress in an indefinitely long fiber. δ can be approximately determined from (X. 72) where we put $\varphi = 0.9$.

The length of the noneffective part may change, depending on the component properties (Figure X. 18). Equation (X. 72) was derived by assuming that the matrix is purely elastic. If we assume that the stress-strain curve consists of two sections, namely, an ideally elastic until the yield point is reached, and an ideally plastic after the yield point has been exceeded, the results of an approximate analysis show that the noneffective fiber length increases, if we allow for the plastic state (Figure X. 19).

A composite in which some of the fibers are broken can be represented as one consisting of fibers with a height equal to the noneffective fiber length δ. Since the broken fibers within the layers are unable to transmit the load through the layer, the load is taken up by the whole fibers. The fiber is considered as a chain consisting of links of length δ, corresponding to the layer height. Each layer is treated as a bundle of such links, and the whole composite model is represented as a chain of such bundles.

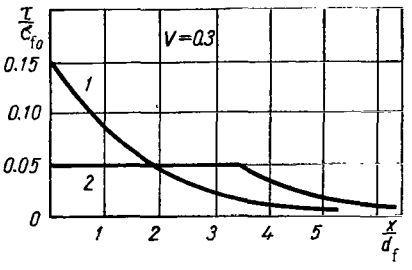

FIGURE X. 19. Change in the shearing stresses on the interface for glass fibers in a matrix with elastic (1) and elastic-plastic (2) pattern of the stress-strain curve.

The fiber length can be approximately determined from (X. 72) and the strength distribution function of the link $f(\sigma)$, provided that the fiber strength is described by the Weibull function, that is, from (X. 90), allowing for the experimental data on the dependence of the strength of individual fibers on their length.

The integral strength distribution function $F(\sigma)$ is found from the differential function by means of (X. 84).

From the known strength distribution $F(\sigma)$ we can find the strength distribution function of the bundle /25, 43/. Moreover, if we consider the composite as a chain made up of bundles of links, we can apply the statistical theorem of the weakest link, and obtain the strength distribution function of the composite.

When a large number of fibers N form a bundle, the probability of the approach of the mean breaking stress distribution $\bar{\sigma}_n$ to the Gaussian distribution is given by

$$\bar{\sigma}_n = \sigma_{max}[1 - F(\sigma)_{max}], \tag{X. 94}$$

where σ_{max} is the maximum stress in the fiber, which can be found from the conditions that the first derivative of the external force, which is equal to the number of unfractured fibers $[1 - F(\sigma)]$ multiplied by the stresses in the fiber σ, is zero:

$$\frac{d}{d\sigma}\{\sigma[1 - F(\sigma)]\}_{\sigma=\sigma_{max}} = 0. \tag{X. 95}$$

The standard deviation of the bundle is given by

$$\Psi_n = \sigma_{\max} \sqrt{\frac{F(\sigma_{\max})[1 - F(\sigma_{\max})]}{N}}. \qquad (X.96)$$

The distribution function of the bundle is given by

$$\omega(\sigma_n) = (1 - \psi_n)(2\pi)^{-\frac{1}{2}} \exp\left\{-\frac{1}{2}[(\sigma_n - \bar{\sigma}_n)/\Psi_n]^2\right\}, \qquad (X.97)$$

and the related integral distribution function has the form

$$\Omega(\sigma_n) = \int_0^{\sigma} \omega(\sigma_n)\, d\sigma_n. \qquad (X.98)$$

We shall now consider the composite model as a chain with links forming a fiber bundle of length δ, and apply to this chain the equations of the statistical strength theory. We can then find the distribution function of $\lambda(\sigma_{cr})$ of the main stress σ_{cr} in the fibers at the instant the whole composite is fractured, if we suppose that each link can be fractured

$$\lambda(\sigma_{cr}) = n\omega(\sigma_{cr})[1 - \Omega(\sigma_{cr})]^{n-1}. \qquad (X.99)$$

In this equation n is the number of bundles – links; $\omega(\sigma_{cr})\, d\sigma_{cr}$ is the probability of breaking of the bundle in the range from σ_{cr} to $\sigma_{cr} + d\sigma_{cr}$; $[1 - \Omega(\sigma)_{cr}]^{n-1}$ is the probability that the other $(n - 1)$ bundles do not break in this range.

After we have determined $\omega(\sigma_n)$ and $\Omega(\bar{\sigma}_n)$ from (X. 72), (X. 84), (X. 90), (X. 94) –(X. 96), and inserted them into (X. 99), we can find the strength distribution function of composite $\bar{\lambda}(\sigma)$, and the parameters which directly determine the the strength values of the composite.

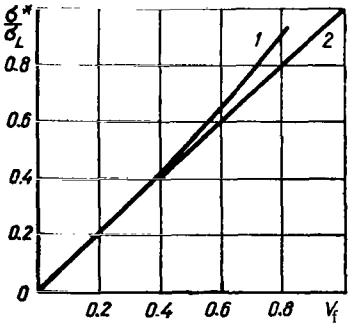

FIGURE X. 20. Dependence of the normalized tensile strength of the composite on the volume fraction of the fibers for the statistical model of fracture (line 1), and models derived from the combined action theory (line 2).

Thus, for example, the statistical mode σ^* of the composite is determined from

$$d\lambda/d\sigma = 0, \qquad (X.100)$$

which leads to

$$\sigma^* = V_в(\alpha\delta\beta e)^{-\frac{1}{\beta}}, \qquad (X.101)$$

where α and β are factors found from experimental data on the fiber strength (see (X. 93)); δ is the length of the noneffective fiber part; and e is the base of natural logarithms.

It is interesting to analyze the effect of the volume fraction of the fibers on the strength of the given model, and compare

it with the dependence of the strength on V_f obtained from the theory of combined action.

The expression for calculating the noneffective fiber length can be represented as

$$\delta = k\left(\frac{1 - V_f^{\frac{1}{2}}}{V_в^{\frac{1}{2}}}\right)^{\frac{1}{2}}, \qquad (X.102)$$

where k is a factor.

Expression (X.101), taking (X.102) into account, can be written as

$$\sigma^* = \sigma_{in} V_f \left[\frac{1 - V_f^{\frac{1}{2}}}{V_f^{\frac{1}{2}}}\right]^{-\frac{1}{2\beta}}, \qquad (X.103)$$

where σ_{in} is the initial strength level, which is a function of the matrix and fiber parameters.

Curve 1 in Figure X.20 was calculated from (X.103) for $\beta = 7.7$, which is characteristic of E-glass fibers, while curve 2 was calculated from equation

$$\sigma^* = \sigma_{in} V_f .$$

This dependence was found from the additivity law, neglecting the stresses in the matrix which is permissible for GFP.

For $V_f < 0.5$, curves 1 and 2 (see Figure X.20) almost coincide, and therefore from the correspondence between the mechanical test results and the theoretical results we cannot always determine by which mechanism the material was broken.

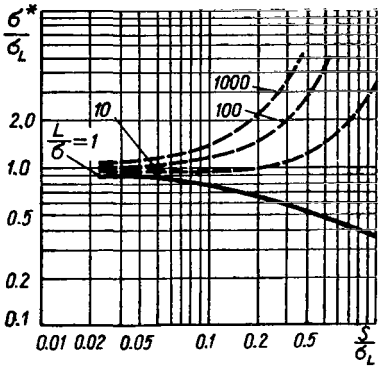

FIGURE X.21. Influence of the coefficient of variation in the fiber strength and the initial fiber length on the ratio of the composite strength (mode) to the mean fiber strength.

Photoelastic studies of single-layer composite models made of epoxide resins reinforced by δ-glass fibers showed that the fracturing mechanism agrees satisfactorily with that of the statistical model developed. The fracturing mechanism of a metal system has been very little investigated, but it is quite probable that it is similar to the mechanism under consideration.

The noneffective fiber length increases with increase in the plasticity of the matrix. It is clear that for a larger δ, we need less fibers for weakening the cross section; and therefore the composite must be broken at a lower stress level. Thus, when starting from the statistical model, it is not advisable to use a plastic

matrix. However, if we take into account that the material is broken because of separation into layers or crack propagation, the application of plastic matrices is suitable.

It is also interesting to consider the possible determination of the fiber strength in the composite. Rosen /13/ shows that the normalized composite strength (the ratio of the mode σ^* to the mean initial strength σ_L) can be written as

$$\frac{\sigma^*}{\sigma_L} = \left(\frac{\delta}{L}\right)^{-\frac{1}{\beta}} \frac{(\beta e)^{-\frac{1}{\beta}}}{\Gamma\left(1+\frac{1}{\beta}\right)}, \qquad (X.104)$$

while the coefficient of variation of the fiber strength, equal to the ratio of the standard deviation S to σ_L, can be written as

$$\frac{S}{\sigma_L} = \frac{\sqrt{\Gamma\left(1+\frac{2}{\beta}\right) - \Gamma^2\left(1+\frac{1}{\beta}\right)}}{\Gamma\left(1+\frac{1}{\beta}\right)}. \qquad (X.105)$$

The correlation between these two magnitudes for composites containing fibers of various lengths $\left(\frac{L}{\delta} = 1 - 1000\right)$ is shown in Figure X. 21. It follows from the diagram that when the material is reinforced with long fibers, the composite may have a mode larger than the mean fiber strength, and the normalized strength of such material must increase with increase in strength dispersion, characterized by the coefficient of variation. This is explained by the fact that even a single defect leads to fiber fracture, while the same defect does not necessarily affect the given composite as a whole. It must also be noted that for low coefficient of variation $(0.1 - 0.15)$, the mean strength of even very short fibers can be almost 100% utilized in the reinforced system. Therefore, the results of the study on reinforced materials showing that the fiber strength is fully realized can be explained by the theory of additivity and by the statistical model. The tests do not clearly establish which theory best describes the behavior of the material in tension. Until now, even in GFP the real strength is much lower than the theoretically predicted strength. This can be explained by the fact that during the production of the composite new defects appear in the fibers, which lower the strength. However, it is also possible that fracturing occurs by a different mechanism.

8. Types of composite fracture

We shall now analyze the possible variants of the fracture of a reinforced system in tension which differ from the case discussed above.

1. If Rosen's assumption on fiber fracture at defective sites by stresses much smaller than the ultimate stresses is true, the shearing stresses on the matrix-fiber interface at the fractured site must sharply increase and then decrease.

If the bond between matrix and fibers is not sufficiently strong, the shearing stresses lead to separation of the material into layers, or separation of the matrix from the fibers. Lamination may propagate without limit, and bring about fracture of the whole composite.

Melvin /14/ investigated the parameters affecting the tendency of the composite to separate into layers. The maximum shearing stresses developed on the interface gave a measure of this tendency.

If we assume that the matrix and fibers are elastic, the maximum shearing stress in the breaking site is expressed by

$$\tau_{max} = c\sigma_f \sqrt{\frac{G_m}{E_f} \cdot \frac{d_f}{S}}, \qquad (X.106)$$

where c is a factor equal to $0.1 - 1$, and S is the interfiber distance.

It follows from (X. 106) that to ensure a continuous and monolithic reinforced system during tension, a certain value of the $\frac{d_f}{S}$ ratio must be maintained. An increase in the volume content of the filler leads to an increase in this ratio, and hence to an increase in τ_{max}. The danger of separation of the composite into layers increases, especially if the clearance between the fibers is small. If the volume fraction of the fibers corresponds to $\frac{d_f}{S} = 10$, the maximum shearing stresses are three times their values when $\frac{d_f}{S} = 1$. Thus, one of the most important requirements in the technology of composite production is uniform fiber distribution in the matrix, and sufficient clearance between the fibers.

The tendency of the material to separate into layers can also be lowered by using a plastic matrix. By lowering the value of G_m, it is possible to achieve stress redistribution and a decrease in τ_{max}.

It follows from (X. 106) that for high strength of the fibers we must have the strongest possible bond between fiber and matrix.

2. If the bond between matrix and fiber is sufficiently strong so that it does not break immediately after formation of internal fracture in the fibers, the crack formed may propagate over the matrix in a direction perpendicular to the fiber orientation in accordance with Griffith's mechanism. As known, Griffith /15/ assumed that brittle bodies are fractured because of spontaneous propagation of microcracks and their conversion into macrocracks. The cracks propagate spontaneously when the work of the external forces exceeds the energy required for forming a new surface. Irwin /16/ and Orowan /17/ showed that the total work expended on fracture consists of the surface energy and the work of plastic deformation. Such an approach makes it possible to apply the concepts of Griffith to analyze the fracturing conditions of metals, which usually have a plastic safety factor.

The theory of crack propagation has not yet been applied to reinforced materials. It can be assumed that when the matrix is bonded with sufficient firmness to the filler, a microcrack formed at the site of fracture of the fiber will propagate in the matrix until it touches the adjacent fibers. These fibers may then be fractured by the crack because of stress concentration at their ends. The probability of fiber fracture increases, especially if the crack meets a defective site on its path.

3. Some authors /44—56/ believe that during tensioning of composites, two mechanisms of stress transmission exist in the reinforced fibers (at least in GFP): an adhesional mechanism acting before the bond between the phases is broken, and a frictional mechanism after cleavage of this bond. This assumption is based on theoretical calculations and experimental results. By comparing (X. 64) and (X. 66), we see that for numerous real materials

$$\tau_{m\max} = (0.25 — 1.25)\,\sigma, \qquad (X.\,107)$$

where σ is the stress applied to the composite.

However, the strength of the adhesional bonds and the shearing strength of the matrix are approximately one order of magnitude lower than the strength of composites. We can assume that the fiber-matrix bond is broken long before the ultimate strength of the system is attained, and that after cleavage of the elastic bond the load is transmitted to the fibers because of frictional forces (allowance for the elastic-plastic properties of the material leads, in principle, to the same results as the solution of the problem in elastic formulation /4/).

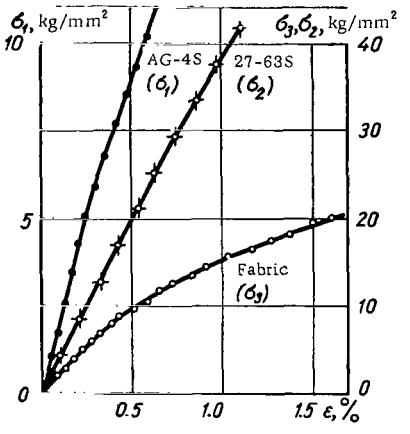

FIGURE X. 22. Stress-strain diagrams for various oriented GFP.

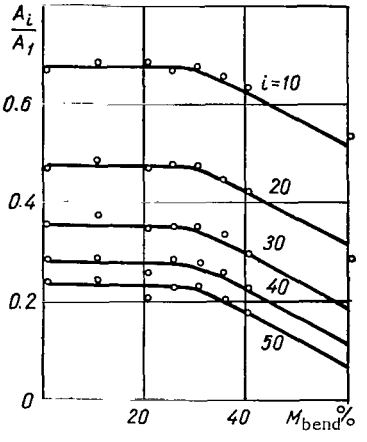

FIGURE X. 23. Dependence of the amplitude ratio $\frac{A_i}{A_1}$ on the preliminary load.

Frictional forces may appear during the production of the material because of the differences in the coefficients of linear expansion of matrix and fiber. Also, an additional squeezing of the fibers by the matrix is possible because of differences in the Poisson ratios.

The authors of /44—46/ assume that the frictional forces may be sufficiently large to load the fibers up to their ultimate strength.

This mechanism was confirmed by experiments on GFP by plotting the stress-strain diagram and processing the oscillogram of the damping

vibrations of the specimens. It was found that in the $\sigma - \varepsilon$ diagrams of the specimens a characteristic inflexion is obtained (Figure X. 22). The authors of /32/ and /46/ consider that this is an indication of qualitative changes in the mechanism of stress transmission (the lowering of the modulus of elasticity is explained by impairment of the interphase bonds).

A study of the oscillogram of the damping vibrations of specimens preliminarily loaded to bending by stepwise increase in the loads was started by assuming that the energy dissipation in the free damped vibration of a composite beam should be independent of the degree of preliminary loading, if the adhesional bonds are not cleaved. If these bonds are impaired, energy dissipation should increase because of its outlet over the friction surface. The test results shown in Figure X. 23 agree well with the data obtained from the stress-strain diagram, and the data calculated from (X. 66). This proved to the authors of /46/ that their proposed mechanism is correct.

Such a mechanism is completely possible. However, we should note that the test results obtained in these papers indicate the appearance of additional defects (cracks) in the material only after application of a load of a certain magnitude, but they do not prove that the frictional forces are sufficiently large to transmit loads to the fibers close to their ultimate strength.

Umanskii /47/ obtained interesting data when he studied mechanism of stress transfer from the matrix to the fibers by frictional forces. The author derived equations with which it is possible to calculate the length of the matrix-to-fiber load-transmitting section as a function of the initial pressure p_0 and the volume content of the filler.

We shall suppose that the elastic bonds between fiber and matrix are negligibly small, and only p_0 acts at the interface. This pressure may be due to differences in the coefficients of linear expansion and elastic constants of fiber and matrix. In this case, the initial pressure is estimated from the calculation of thermal stresses made by Karpinos and Tuchinskii /48, 49/. In reinforced plastics such pressure may also arise because of shrinkage during polymerization.

The problem is then one of analyzing the equilibrium conditions and strains in the composite cylinder (fiber-matrix) when a tensile stress $\bar{\sigma}$ is applied along the faces to the matrix.

The length δ of the load-transmitting section can be determined from /47/

$$\frac{\delta f}{d_f} = \frac{\varkappa(1-V_f)}{4\zeta V_f} \ln \frac{\nu_m + \varkappa \frac{p_0}{\bar{\sigma}}}{\frac{\nu_m - \nu_f}{(1-\lambda)\left[1 + \frac{E_f V_f}{E_m(1-V_f)}\right]} + \varkappa \frac{p_0}{\bar{\sigma}}}, \qquad (X.108)$$

where

$$\varkappa = (1-\nu_f)\frac{E_m}{E_f} + 1 + \nu_m + 2\frac{V_f}{1-V_f};$$

$$\zeta = \nu_m + \nu_f \frac{E_m}{E_f} \cdot \frac{(1-V_f)}{V_f};$$

$$\lambda = \frac{2\zeta^2}{\varkappa\left[1 + \frac{E_m}{E_f} \cdot \frac{(1-V_f)}{V_f}\right]} \cdot \frac{V_f}{1-V_f},$$

and f is the coefficient of dry friction.

It can be seen from (X. 108) that even if the initial pressures are low, the load is transmitted from the matrix to the fibers over a comparatively short section. Figure X. 24 shows the dependence of the length of the load-transmitting section on the ratio of p_0 to $\bar{\sigma}$ for a composite with $\nu_m = 0.33$; $\nu_f = 0.26$; $\frac{E_f}{E_m} = 4$; $V_f = 18.1\%$ and $l = 0.15$.

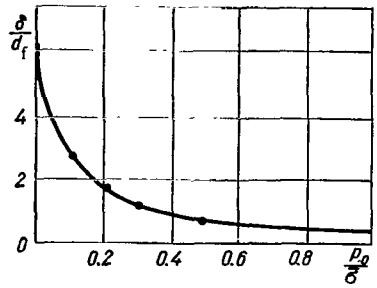

FIGURE X. 24. Dependence of the length of the load-transmitting section on the fiber on the initial pressure.

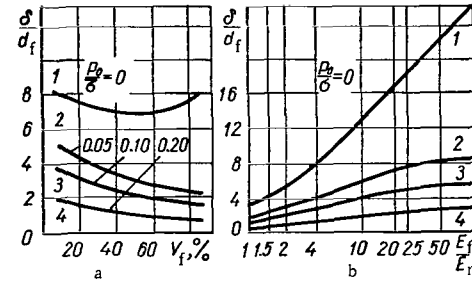

FIGURE X. 25. Dependence of the load-transmitting section on the fiber on the volume content of the fibers in the material (a) and the ratio of the Young's moduli of fibers and matrix (b):

$1 - \frac{p_0}{\bar{\sigma}} = 0$; $2 - \frac{p_0}{\bar{\sigma}} = 0.05$; $3 - \frac{p_0}{\bar{\sigma}} = 0.1$;

$4 - \frac{p_0}{\bar{\sigma}} = 0.2$.

If there is no initial pressure tensile stresses can be transmitted from the matrix to the fiber, but the length of the transmitting section will be fairly large ($\delta \approx 50\ d_f$). If an initial pressure appears $\frac{\delta_f}{d_f}$ will decrease according to the hyperbolic law. If $\frac{p_0}{\bar{\sigma}} = 0.3$, the length of the transmitting section will be about $8.5\ d_f$, that is, the critical fiber length in this case will be approximately $17\ d_f$. An increase in the volume fraction of the fibers has little effect on δ if $p_0 = 0$. However, when an initial pressure appears (Figure X. 25, a), an increase in the volume fraction of the filler leads to a decrease in the critical length of the fiber. An increase in the stiffness of the fibers will lead to an increase in the length of the load-transmitting section (Figure X. 25, b). These results show that the composite can only operate efficiently when purely frictional bonds exist between matrix and fibers.

9. Compressive strength of composites

To study the mechanism of fracture of composites on compression, most authors /13, 50/ consider the analytical two-dimensional model (Figure X. 26).

The model consists of stiff parallel plates, with fibers of equal thickness of length L and width h. These fibers are separated by a comparatively soft matrix of width $2c$. The composite is subjected to a compressive load in the direction of fiber orientation.

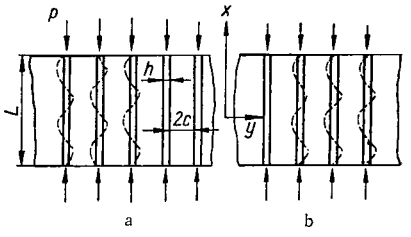

FIGURE X.26. Analytical model of compression of composite fiber with symmetric (a) and asymmetric (b) protrusion of fibers.

We shall assume that the fibers have an unlimited compressive strength, their deformation is purely elastic, and the shearing strain in the fibers is negligibly small compared with the shearing strain in the matrix.

The fracture in the model is studied after the fibers have been subjected to longitudinal bending. Two types of fracture may occur. In the first case adjacent fibers protrude in opposite directions symmetrically about the plane passing through adjacent fibers (Figure X.26, a). In this case the composite is fractured according to the so-called "way of tension," because the matrix is tensioned perpendicular to the fiber axis.

In the second type the fibers are bent in one phase, and then protrude asymmetrically about the symmetry plane (Figure X.26, b). In this case the composite is fractured in "way of shear," and the matrix is broken because of the shearing strain.

Symmetrical protrusion of fibers. If we assume that when the fibers protrude the lateral reaction of the matrix is replaced by transverse normal stresses, then we have a problem of rod compression on an elastic base /50, 51/.

The critical stress in the fibers can be determined from

$$\sigma_{f.\,s} = \frac{\pi^2 E_f h^2}{12L^2}\left(m^2 + \frac{12\beta' L^4}{m^2\pi^4 E_f h^3}\right), \qquad (X.109)$$

where β' is the elasticity coefficient of the base

$$\beta' = \frac{2E_m}{c}; \qquad (X.110)$$

and m is the number of waves in protruding fibers during longitudinal bending; and $\frac{E_f h^3}{12}$ is the bending rigidity of the rod.

The dependence of m on the rigidity is expressed by

$$m^2(m+1)^2 = \frac{12\beta' L^4}{\pi^4 E_f h^3}. \qquad (X.111)$$

If we assume that the fiber length L is much larger than the width of the matrix $2c$ and consequently m is large, we can obtain the approximate relationship

$$\left(\frac{12\beta' L^4}{\pi^4 E_f h^3}\right)^{\frac{1}{2}} = m(m+1) \approx m^2. \qquad (X.112)$$

By inserting (X. 110) and (X. 112) into (X. 109), we obtain

$$\sigma_{f.\,s} = \frac{2}{\sqrt{3}}\left(E_f E_{ma}\frac{h}{2c}\right)^{\frac{1}{2}}. \qquad (X.\,113)$$

If we allow for the work of the matrix in the axial direction, we can determine the critical stress of the composite at which it is fractured:

$$\sigma_{c.\,s} = \sigma_{f.\,s}\left[V_f + (1 - V_f)\frac{E_{ma}}{E_f}\right]. \qquad (X.\,114)$$

By substituting (X. 113) into (X. 114), and applying some transformations, we obtain

$$\sigma_{c\,s} = \frac{2}{\sqrt{3}} E_{ma} V_f \left[\frac{E_f}{E_{ma}} \cdot \frac{V_f}{1 - V_f}\right]^{\frac{1}{2}} \left[1 + \frac{1 - V_f}{V_f} \cdot \frac{E_{ma}}{E_f}\right]. \qquad (X.\,115)$$

Asymmetrical protrusion of fibers. It has already been mentioned that the composite is fractured because of the shearing strain of the matrix. In the given model the fibers lose their stability if the work ΔT expended on loading the fibers is equal to the change in the deformational energies of the matrix ΔW_{ma} and of the fibers ΔW_f, and if the system in compressive strain but without loss in stability passes into a state where the stability is lost during longitudinal bending.

The condition of loss of stability may be written as /13/

$$\Delta T = \Delta W_f + \Delta W_{ma}. \qquad (X.\,116)$$

We shall suppose that the shape of the curve is described by a sine wave, expressed as a series ϑ with a shift in the direction:

$$\vartheta = \sum_m a_m \sin \frac{m\pi x}{L}, \qquad (X.\,117)$$

where a_m is the protrusion amplitude.

If we assume that the shearing strain in the matrix is a function of the longitudinal coordinate x only, and is independent of the transverse coordinate y, we obtain

$$\left.\frac{\partial u_y}{\partial x}\right|_{ma} = \left.\frac{\partial u_y}{\partial x}\right|_f. \qquad (X.\,118)$$

The shearing strain in the matrix is given by

$$\gamma_{xy} = \frac{\partial u_y}{\partial x} + \frac{\partial u_x}{\partial y}. \qquad (X.\,119)$$

Since γ_{xy} is independent of y, we have

$$\frac{du_x}{dy} = \frac{1}{2c}\left[u_x(c) - u_x(-c)\right]. \qquad (X.\,120)$$

If we neglect the shearing strain in the fibers we can write

$$u_x(c) = \frac{h}{2} \cdot \frac{du_y}{dx}\Big|_f. \tag{X. 121}$$

By inserting (X. 120) and (X. 121) into (X. 119), and allowing for (X. 118), after the appropriate transformations we obtain

$$\gamma_{xy} = \left[1 + \left(\frac{h}{2c}\right)\right] \frac{du_y}{dx}\Big|_f. \tag{X. 122}$$

The shearing stress is given by

$$\tau_{xy} = G_{ma}\gamma_{xy}. \tag{X. 123}$$

The change in the deformational energy ΔW_{ma} is expressed by integral

$$\Delta W_{ma} = \frac{1}{2}\int_W \tau_{xy}\gamma_{xy}dW. \tag{X. 124}$$

By inserting (X. 117), (X. 122) and (X. 123) into (X. 124) we obtain

$$\Delta W_{ma} = G_{ma}c\left(1 + \frac{h}{2c}\right)^2\left(\frac{\pi^2}{2L}\right)\sum_m a_m^2 m^2. \tag{X. 125}$$

The change in the deformational energy of the fibers is expressed by /51/

$$\Delta W_f = \frac{P\pi^2}{4L}\sum_m m^2 a_m^2. \tag{X. 126}$$

Work ΔT expended on loading the fibers is determined from

$$\Delta T = \frac{P\pi^2}{4L}\sum_m m^2 a_m^2. \tag{X. 127}$$

Here P is the compressive load on one fiber

$$P = \sigma_f h,$$

where σ_f is the stress in the fiber.

By substituting (X. 125), (X. 126), and (X. 127), into (X. 116), we can determine the critical stress for asymmetric protrusion at which the composite breaks. The final result is

$$\sigma_{c.\,as} = \frac{G_{ma}}{1 - V_f}. \tag{X. 128}$$

The rated criterion of the compressive strength of the composite is the smaller value obtained from (X. 115) and (X. 128). By comparing (X. 115) and (X. 128), we get the boundary between the two types of fracture

$$\frac{E_f}{E_{ma}} = \left[\frac{16}{3}(1 + \nu_{ma})^2(1 - V_f)V_f^3\left(1 + \frac{E_{ma}}{E_f}\cdot\frac{1 - V_f}{V_f}\right)^2\right]^{-1}. \tag{X. 129}$$

Figure X. 27 shows the boundaries of the fracture regions calculated from (X. 129) for elastic ($\nu_{ma}= 0.3$) and plastic ($\nu_{ma}= 0.5$) behaviors of the matrix. It can be seen from the figure that at values $\frac{E_f}{E_{ma}}$ larger than 5, and sufficiently high volume fractions of the fibers ($V_f > 0.2$), the composite is fractured mainly asymmetrically. In this case the breaking stress on compression of the system depends only on the modulus of shear of the matrix and on the volume content of the filler, as follows from (X. 128). If the matrix behaves plastically, the modulus of shear is variable, and depends on axial strain. If the matrix is elastically-plastically deformed (X. 128) can be written as

$$\sigma_{c.\,as} = \frac{\bar{G}_{ma}(\varepsilon)}{1 - V_f}, \qquad \text{(X. 130)}$$

where $\bar{G}_{ma}(\varepsilon)$ is the fluid modulus of shear as a function of the axial strain ε of the matrix.

The fluid modulus of shear is determined for the concrete value of the axial strain of the matrix (it is assumed that the matrix remains isotropic in the fluid state also).

In symmetric and asymmetric behavior of composite fracture, the critical compressive stress depends only on the elastic-plastic properties of the components and their concentration, and is independent of the specimen size.

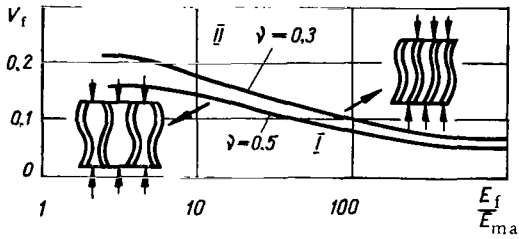

FIGURE X. 27. Regions of microstable fracture with symmetric (I) and asymmetric (II) protrusion of fibers.

The two-dimensional model can be considered as only a first approximation to the fracturing mechanism of real composites, because in practice the fracturing process of composites reinforced by cylindrical fibers is much more complex. Nevertheless, from our results we can conclude that the most important characteristic on which the compressive strength of the composite depends is the ability of the matrix to withstand shearing stresses. If the matrix can retain a high modulus of shear at fairly large shearing strains, we can produce reinforced systems, able to withstand very high compressive stresses.

Experimental studies on GFP /13/ and magnesium-boron fiber composites /50/ confirm our theoretical conclusions. However, the experimental data

are still so limited that it is impossible to come to definite conclusions. As in tension, fracture due to separation of the composites into layers, crack propagation etc., are possible besides the mechanism described.

10. Thermal stresses in composite fibers

When analyzing the behavior of composites we have to allow for the internal stresses in the material directly or indirectly due to technology of production. The study of thermal stresses is of special importance and they arise because of the differing thermal deformation of the components. Thermal stresses may affect short-term and creep strengths, thermal stability, and fatigue.

The term thermal stresses usually includes stresses produced by differences in the thermal expansions of separate parts of the body. In isotropic and homogeneous bodies, these stresses arise because of the unequal changes in temperature. But if the material is nonhomogeneous, or consists of several components with different thermal expansion coefficients or elastic constants, thermal stresses arise even if the temperature changes are uniform.

In brittle materials, under certain conditions even a small number of thermal cycles may lead to cracking. In plastic materials the thermal stresses arising from a single temperature change are not large, because of stress relaxation during plastic strain. However, repeated temperature variations may lead to an accumulation of plastic strains, and to fatigue fracture of the material. During the operation of heating systems of various types, petroleum distilling plants, turbines, nuclear reactors, and other installations, cyclic temperature gradients arise. Stresses and strains appearing in one half of the cycle reappear in the other half but with opposite sign.

In some cases thermal stresses may decrease the efficiency of the material even if the temperature is changed only once, and therefore they must be allowed for when developing a composite or manufacturing products from it.

In this section we shall discuss thermal stresses arising in the composite during uniform temperature changes because of differences in the Young's moduli, Poisson ratios, and linear expansion coefficients of the matrix and fibers.

We shall consider thermal stresses and deformations produced in a composite with the fibers oriented in a single direction. We shall assume that the composite is under one-dimensional stress, and that both components obey Hooke's law. Such a reinforced material can be represented as a system consisting of an assembly of individual elements, each of which includes a cylindrical core (fibers) and a shell (matrix). Both phases are isotropic, homogeneous, and firmly bound to one another at the interface, and no chemical reactions take place between fiber and matrix over the given temperature range.

It is evident that because of the identity of the individual elements, the temperature-induced changes will be equal in all.

To evaluate the stresses in the material, it is sufficient to consider the elastic strains and stresses within a single element. If the linear coefficients of thermal expansion and Young's moduli of the matrix, α_m and E_m, and of the fibers, α_f and E_f, are constant and equal over the given temperature range, then if the temperature is changed by ΔT, the compatibility conditions of the deformations can be written as

$$\alpha_m \Delta T + \frac{\sigma_{my}}{E_m} = \alpha_f \Delta T + \frac{\sigma_{fy}}{E_f}. \quad (X.131)$$

The force equilibrium conditions for composites containing V_f volume fractions of fibers is given by

$$\sigma_{fy} V_f + \sigma_{my}(1 - V_f) = 0. \quad (X.132)$$

By solving (X.131) and (X.132), we obtain the equations for the elastic stresses in the matrix (shell) σ_{my} and fiber (core) σ_{fy} when the composite is under linear stress /53—55/.

$$\sigma_{my} = -\frac{(\alpha_m - \alpha_f)\Delta T E_f V_f}{E_f V_f + E_m(1 - V_f)} E_m; \quad (X.133)$$

$$\sigma_{fy} = \frac{(\alpha_m - \alpha_f)\Delta T E_m(1 - V_f)}{E_f V_f + E_m(1 - V_f)} E_f. \quad (X.134)$$

According to Hooke's law, the elastic unit strains of matrix and fiber caused by thermal stresses are given by

$$\varepsilon_{my} = -\frac{(\alpha_m - \alpha_f)\Delta T E_f V_f}{E_f V_f + E_m(1 - V_f)}; \quad (X.135)$$

$$\varepsilon_{fy} = \frac{(\alpha_m - \alpha_f)\Delta T E_m(1 - V_f)}{E_f V_f + E_m(1 - V_f)}. \quad (X.136)$$

The relative unit strain of the composite e_y caused by the action of thermal stresses can be determined from

$$e_y = \alpha_f \Delta T + \varepsilon_{fy} \quad (X.137)$$

or

$$e_y = \frac{\alpha_m E_m(1 - V_f) + \alpha_f E_f V_f}{E_m(1 - V_f) + E_f V_f} \Delta T. \quad (X.138)$$

We shall now analyze in detail the significance of ΔT used in (X.131)—(X.138).

At high homologic temperatures, which are close to the melting point of the more readily fusible phase, this component is in the quasiviscous state. We can arbitrarily assume that at such temperatures the yield point of this phase is equal to zero, while the thermal stresses arising because of differences in the linear expansion coefficients are completely relaxed.

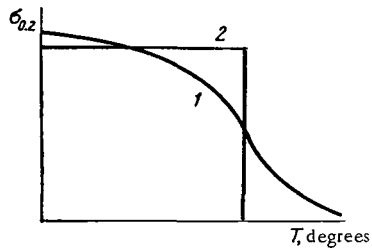

FIGURE X.28. Temperature dependence of the yield point:

1 — real; 2 — idealized.

As the readily fusible phase is cooled, it begins to display plastic properties. In practice the yield point gradually increases with decrease in temperature (Figure X.28). However, for calculations we can assume, to a first approximation, that at a certain temperature T_u the yield point increases jumpwise from zero to σ_T according to curve 2 of Figure X.28. At temperatures below T_u the matrix and fibers have purely elastic properties.

In the following discussion we shall term T_u the temperature of the initial stress distribution.

Thus, if the composite is cooled from the temperature of formation T_{f_0} to room temperature T_r, we have

$$\Delta T = T_r - T_u, \tag{X.139}$$

and not $T_r - T_{f_0}$

The value of T_u can be considered to be equal to the temperature at which the experimental curve expressing the temperature dependence of the yield point descends sharply.

With an accuracy sufficient for practical calculations, T_u can be characterized by the abscissa of the point where the linear temperature dependence of Young's modulus passes into a curvilinear one for the more plastic phase of the composite.

The technology of composites may include preliminary cooling of the fiber. In this case the composite will consist of three phases. The third phase may also arise during thermal treatment of the material because of component interaction, and in this case this phase is frequently very brittle.

The following equations can then be applied for thermal stresses

$$\sigma_{my} = \left[-\alpha_m + \frac{\alpha_m E_m V_m + \alpha_f E_f V_f + \alpha_n E_n V_n}{E_m V_m + E_f V_f + E_n V_n}\right] E_m \Delta T; \tag{X.140}$$

$$\sigma_{fy} = \left[-\alpha_f + \frac{\alpha_m E_m V_m + \alpha_f E_f V_f + \alpha_n E_n V_n}{E_m V_m + E_f V_f + E_n V_n}\right] E_f \Delta T; \tag{X.141}$$

$$\sigma_{ny} = \left[-\alpha_n + \frac{\alpha_m E_m V_m + \alpha_f E_f V_f + \alpha_n E_n V_n}{E_m V_m + E_f V_f + E_n V_n}\right] E_n \Delta T, \tag{X.142}$$

under the conditions that $V_m + V_f + V_n = 1$ (subscript n refers to the material of the new phase).

When the composite is heated or cooled, not only axial but also radial and circumferential strains may occur, that is, the composite is under three-dimensional stress. If an accurate calculation is required, we use the equations of the elasticity theory to determine the stresses in the composite cylinder at a constant temperature over the cylinder cross section consisting of core and shell.

The equations for calculating radial σ_{rm}, σ_{rf}, circumferential $\sigma_{\theta m}$, $\sigma_{\theta f}$ and axial σ_{zm}, σ_{zf} thermal stresses in oriented elastic composites as a function of the volume fractions of the fibers in hexagonal arrangement are given in /48, 52/.

On the matrix-fiber interface

$$\sigma_{rm} = \left(1 - \frac{1}{V_f}\right)\Phi; \tag{X.143}$$

$$\sigma_{\theta m} = \left(1 + \frac{1}{V_f}\right)\Phi; \tag{X.144}$$

$$\sigma_{zm} = \alpha_m E_m \Delta T V_f (\gamma - 1)\frac{\psi\delta(1+\nu_m) - 2(1-V_f)(1+\nu_f)(\nu_m-\nu_f)}{\psi(1+\nu_m)[1-V_f(1-\delta)] + 2V_f(1-V_f)(\nu_m-\nu_f)^2} + 2\nu_m\Phi. \tag{X.145}$$

In the fibers

$$\sigma_{rf} = \sigma_{\theta f} = -\frac{1-V_f}{V_f}\Phi; \tag{X.146}$$

$$\sigma_{zf} = -\frac{1-V_f}{V_f}\sigma_{zm}; \tag{X.147}$$

$$\gamma = \frac{\alpha_f}{\alpha_m}; \quad \delta = \frac{E_f}{E_m};$$

$$\Phi = \alpha_m E_m \Delta T V_f \frac{(\nu_m-\nu_f)[1-V_f(1-\gamma\delta)] - [1-V_f(1-\delta)][1+\nu_m-\gamma(1-\nu_f)]}{\psi(1+\nu_m)[1-V_f(1-\delta)] + 2V_f(1-V_f)(\nu_m-\nu_f)^2}; \tag{X.148}$$

$$\psi = 2(1-\nu_m)V_f + (1-V_f)[1-\delta_f + 2\delta_0(1-\nu_m)], \tag{X.149}$$

where

$$\delta_0 = \frac{E_m}{E_f}.$$

In practice, for most of the materials the Poisson ratios can be assumed to be equal, that is, $\nu_m = \nu_f = \nu$.

In this case the expressions for the thermal stresses are considerably simplified

$$\sigma_{rf} = \sigma_{\theta f} = c\delta(1-\gamma)(1-V_f)\alpha_m E_m \Delta T; \tag{X.150}$$

$$\sigma_{zf} = c\delta(1-\gamma)(1-V_f)\left[1 + \frac{\delta}{1-V_f(1-\delta)}\right]\alpha_m E_m \Delta T; \tag{X.151}$$

$$\sigma_{rm} = c\delta V_f(\gamma-1)\left(1 - \frac{1}{V_f}\right)\alpha_m E_m \Delta T; \tag{X.152}$$

$$\sigma_{\theta m} = c\delta V_f(\gamma-1)\left(1 + \frac{1}{V_f}\right)\alpha_m E_m \Delta T; \tag{X.153}$$

$$\sigma_{zm} = c\delta V_f(\gamma-1)\left[1 + \frac{\delta}{1-V_f(1-\delta)}\right]\alpha_m E_m \Delta T, \tag{X.154}$$

where

$$c = \frac{1}{2(1-\nu) - (1-\delta)[1+(1-2\nu)V_f]}.$$

These equations were derived by assuming that the linear expansion coefficients and the moduli of elasticity are constant in the ΔT range. The solution of the problem of thermal stresses, allowing for a linear temperature dependence of α and E, are given by Tuchinskii /52/.

An analysis of the equations shows that the magnitude of the elastic thermal stresses in composites depends on the elastic constants of the composite phases, their linear expansion coefficients, the transition temperature of matrix and fiber, and finally on the elastic state and volume content of the filler. In the matrix the circumferential stresses have the maximum absolute values, while in the fibers the maximum absolute values are displayed by the axial stresses. All three components of the thermal stresses in the fibers have the same sign, whereas in the matrix only the signs of the axial and circumferential stresses are equal.

The radial stresses are equal in both phases in magnitude and sign, while the circumferential stresses have opposite signs in matrix and fibers.

These equations are very important when designing composites consisting of brittle components (for tungsten or molybdenum fiber-reinforced ceramics). For such composites we can assume, with a fair accuracy, that both system components have a linear stress-strain diagram up to fracture, and hence the application of the equations derived from the theory of elasticity is justified.

Figure X. 29 shows the calculated curve of the dependence of the thermal stresses in molybdenum fiber-reinforced thorium dioxide on the volume content of the fibers. It can be seen that the circumferential thermal stresses may be larger than the ultimate strength of the matrix, and cause fracture. Crack formation on cooling was observed in ThO_2 specimens reinforced by tungsten fibers /56/.

In composites in which the matrix is much more plastic than the fibers, the thermal stresses are seldom higher than the ultimate strength, but exceed the yield point of the matrix. In this case the matrix is subjected to elastic-plastic deformations. The thermal stresses allowing for elastic-plastic deformations were calculated by Karpinos and Tuchinskii /49/ and by Tuchinskii /52/, who employed graphical-analytical methods with successive approximations. The ability of the matrix to be strengthened during plastic strain is of decisive importance. If the cold hardening of the composite is stronger, the stresses produced in the composite with variation in temperature are higher.

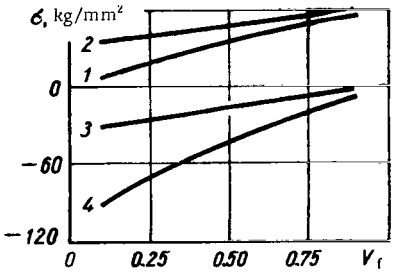

FIGURE X. 29. Dependence of thermal stresses on the volume fraction of the filler in the ThO_2-molybdenum fiber composite at room tempeature:
1 — σ_{zm}; 2 — $\sigma_{\theta m}$; 3 — $\sigma_{rm} = \sigma_{\theta f} = \sigma_{rf}$; 4 — σ_{zf}.

We shall now consider the effect of the thermal stresses on the parameters of the composite. We shall assume that the composite begins to break when the ultimate strength is reached by the maximum principal stress in any of the components. To employ concrete examples, we shall assume that the linear expansion coefficient of the matrix is higher than that of the fibers. In this case, when the material is cooled, the stress distribution in the matrix is such that $\sigma_{\theta m} > \sigma_{zm} > \sigma_{rm}$, and in the fibers $\sigma_{\theta f} = \sigma_{rf} > \sigma_{zf}$.

If no external force acts, the strength conditions may be written as

$$\begin{aligned} \sigma_{0f} &\leqslant (\sigma_B)_f; \\ \sigma_{0m} &\leqslant (\sigma_B)_m. \end{aligned} \qquad (X.155)$$

It is interesting to note that even for brittle materials creep and stress relaxation are observed on cooling. For this reason the actual stress level will be lower than the calculated. The extent of this difference will depend on the cooling rate of the material. If the cooling is slow, there is time for relaxation processes. A rapid temperature change leads to an increase in the thermal stresses, since the cooling period is insufficient for their relaxation. For this reason materials in which cracks are liable to form must be cooled and heated at the lowest possible rate.

The following feature is characteristic of composites: appearance of individual cracks does not lead to a catastrophic fracture of the total material. The fibers restrict crack propagation and the construction will continue to operate for a certain period. Therefore, the thermal stability of reinforced ceramic specimens is usually higher than of the nonreinforced material.

When an external tensile load is applied, the internal stresses are added to the external. If we make allowance for the external forces the strength condition is given by

$$\begin{aligned} \sigma_m + \sigma_{zm} &\leqslant (\sigma_B)_m; \\ \sigma_f + \sigma_{zf} &\leqslant (\sigma_B)_f. \end{aligned} \qquad (X.156)$$

Thus, in accordance with the first theory of strength, axial thermal stresses must have the strongest effect on the composite strength when external tensile stresses applied to the fibers act. Depending on the ratio of the external to the internal forces in the weak link of the composite, thermal stresses may increase or decrease the composite strength as a whole. Thus, in the regularly arranged system nickel-tungsten, where the matrix-fiber bond is sufficiently firm, the tungsten fibers are the first to begin to break when tensile forces are applied. The compressive thermal stresses appearing in the fibers on cooling should increase the ultimate strength of the whole composite.

For brittle matrices, which are less plastic than the fibers, fracture must occur when condition

$$\sigma_m + \sigma_{zm} \leqslant (\sigma_B)_m$$

is disturbed.

In such composites the strength at room temperature must decrease because of thermal stresses if $\alpha_f < \alpha_m$.

With increasing temperature the strength must increase because the thermal stresses are removed. Baskin et al. /57, 58/ found that the ultimate strength of molybdenum fiber-reinforced thorium dioxide increases with increasing temperature to a maximum value at 650°C.

If the thermal expansion coefficients of matrix and fibers are close to one another, the internal stresses will be smaller, and have almost no effect on the strength of the material as a whole; this was experimentally

confirmed with a composite based on mullite reinforced by tungsten and molybdenum /56/.

By selecting the matrix and fibers in such a way that preliminary compressive stresses are produced in the matrix, the strength of the material can be considerably increased.

Reinforced materials have still another characteristic feature: they are subject to thermal fatigue after uniform temperature changes. We shall consider a composite with a plastic matrix and elastic fibers.

We assume that the material operates at a large number of smoothly varying thermal cycles (temperature variation from T_1 to T_2). If the elastic-plastic deformation of the matrix after the first cooling is small (corresponding, for example, to point M on Figure X. 30), on heating from T_1 to T_2 the load removal will have an elastic character, and during successive thermal changes the stress-strain curve will be expressed by line MN.

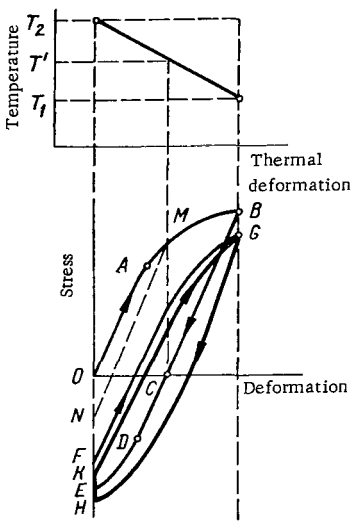

FIGURE X. 30. Hysteresis loop.

If the plastic strain after the first cooling corresponds to point B, during subsequent heating a curved section DE will follow the linear section BD. This means that during heating the matrix will also be elastically-plastically deformed. If the material is held at a high temperature T_2, partial stress relaxation will occur, indicated by section EF. When the next cycle starts, and the temperature begins to decrease, the strain will correspond to curve FG. If we neglect stress relaxation at the lower temperature T_1, it can be assumed that with a new temperature increase the stresses in the matrix will decrease, as shown by section GH. Then again, stress relaxation occurs (HK), and the subsequent cooling process is characterized by curve KG.

Finally, the behavior of the matrix during several cycles will be described by the steady hysteresis loop $KGHK$. The shape of this loop depends on the temperature gradient, holding time at the corresponding temperatures, heating and cooling rates, and also on the elastic and plastic properties of matrix and fiber, their ability to strengthen during plastic strain, etc. If we take into account the Bauschinger effect (the plastic deformation on compression during heating proceeds more rapidly than on tension during the first cooling of the material), it becomes evident how difficult it is to calculate the hysteresis loop in the general case. However, an approximate estimation of plastic strain per cycle is possible in each concrete case.

The presence of a hysteresis loop is an indication of the appearance of fatigue fracture of materials due to accumulation of plastic strains when the temperature is uniformly changed in cycles.

Bibliography

1. Beskorovainyi, N.M. and Ya.B.Fridman. Struktura i prochnost' metallov i splavov (Structure and Strength of Metals and Alleys).— In: Nauchnye Trudy Moskovskogo Mekhanicheskogo Instituta, 5, Moskva. 1953.
2. Kies, J.A. Strain Magnification Factors in the Resin.— Naval Res. Lab. Rep. January 1962.
3. Mc Abee, E. and M.Chmura.— Proc.16th Ann.SPI Conf.Reinforced Plastics Division. 1961.
4. Tarnopol'skii, Yu.M. and A.M.Skudra. Konstruktsionnaya prochnost' i deformativnost' stekloplastikov (Structural Strength and Deformability of Glass-Fiber Reinforced Plastics). Riga, Zinatne. 1966.
5. Ivanova, V.S. et al. Ustalost' i khrupkost' metallicheskikh materialov (Fatigue and Brittleness of Metallic Materials). Moskva, Nauka. 1968.
6. Dietz, A.G. Fiberglass Reinforced Plastics, N.Y., Reinhold Publ. Corp., 1954.
7. Kelly, A. and G.J.Davies.— Metal.Pevs., 10:37. 1965.
8. Sutton, W.— Raketnaya Tekhnika, 4, 1962.
9. Ustinov, L.M. Issledovanie mekhanicheskikh svoistv makromekhanizma razrusheniya medi, armirovannoi vol'framovymi voloknami (Study of Mechanical Properties and the Macromechanism of Fracture of Tungsten-Fiber Reinforced Copper). Author's Summary of Candidate's Thesis, Moskva, IMET, AN SSSR. 1968.
10. Outwater, J.O.— Ir. ASME Paper, 56-A-201. 1956.
11. Kelly, A.— Proc.Roy.Soc., A282, 1388, 63. 1964.
12. Rosen, B.W.— J.Amer.Inst.Aero Astron., 2, 1985, Nov. 1964.
13. Rosen, B.W.— In: Fiber-Composite Materials. Papers presented at a Seminar, Oct.17 and 18, 1965, Metals Park, Ohio, American Society for Metals. 1965.
14. Melvin, I.M. Effect of Resin Properties on the Fracture of FRP Laminate Models.— TAM Report in Preparation. Univ. of Illinois.
15. Griffith, A.A.— Phil.Trans., A221, 1921.
16. Irwin, I.R.— Trans. Amer. Soc. Metals, 40. 1948.
17. Orowan, E.— Rep.Progr.Phys., 12. 1948.
18. Dunin-Barkovskii, I.V. and N.V.Smirnov. Teoriya veroyatnostei i matematicheskaya statistika v tekhnike (Probability Theory and Mathematical Statistics in Engineering). Moskva, Gostekhizdat. 1965.
19. Dlin, A.M. Matematicheskaya statistika v tekhnike (Mathematical Statistics in Engineering). Moskva, Sovetskaya Nauka. 1958.
20. Hald, Anders. Statistike Metoder, København, Private Ingeniørfond. 1948.
21. Bolotin, V.V. Statisticheskie metody v stroitel'noi mekhanike (Statistical Methods in Building Mechanics). Moskva, Fizmatgiz. 1965.

22. Sorensen, S. V., V. S. Strelyaev, and G. P. Zaitsev. Statisticheskaya konstruktsionnaya prochnost' orientirovannykh stekloplastikov (The Statistical Strength of Glass-Fiber Reinforced Plastics in Design). Moskva, Stroizdat. 1962.
23. Pisarenko, G. S. and V. T. Troshchenko. Statystychni teoriyi mitsnosti ta yikh zastosuvannya do metalokeramichnykh materialiv (Statistical Strength Theories and Their Application to Cerments). — Kyyiv, Vydavnytstvo URSR. 1961.
24. Weibull, W. G.— Appl. Mech., 18:293. Sept., 1954.
25. Cücer, D. E. and J. J. Gurland.— Mech. Phys. Solids, **10**. 1962.
26. Ivanova, V. S. and L. M. Ustinov.— Metally, **5**. 1967.
27. Mekhanicheskie svoistva novykh materialov (Mechanical Properties of New Materials). Moskva, Mir. 1966.
28. Rosen, B. W.— Raketnaya tekhnika i kosmonavtika, **1**. 1964.
29. Dow, N. F.— Space Mechanics Meto, No. 102, Space Sciences Lab., Jan. 1961.
30. Kelly, A.— In: Mekhanicheskie svoistva novykh materialov. Moskva, Mir. 1966.
31. Korten, Kh. T. Razrushenie armirovannykh plastikov (Fracture of Reinforced Plastics). Moskva, Khimiya. 1967.
32. Bazhanov, V. L. et al. Soprotivlenie stekloplastikov (Resistance of Glass-Fiber Reinforced Plastics). Moskva, Mashinostroenie. 1968.
33. Rabinovich, A. L.— In: Trudy TsAGI, 582. Moskva. 1946.
34. Van Fo Fy, G. A.— Mekhanika Polimerov, 4. 1966.
35. Bolotin, V. V. Problemy armirovannykh sred (Problems Involved in Reinforced Media).— Doklady Nauchno-tekhnicheskoi Konferentsii MEI, podsektsiya dinamiki i prochnosti mashin. Moskva. 1965.
36. Tarnopol'skii, Yu. M., A. V. Rozen, and V. A. Polyakov.— Mekhanika Polimerov, **2**. 1965.
37. Bass, D. L.— Aircraft Prod., **25**:2. 1963.
38. Van Fo Fy, G. A. Osnovy teorii polimernykh tel s orientirovannoi armaturoi (The Foundations of the Theory of Polymer Bodies Reinforced by Oriented Fibers). Author's Summary of Candidate's Thesis. Institut Mekhaniki AN Ukrainskoi SSR, Kiev. 1965.
39. Bolotin, V. V.— Inzhenernyi Zhurnal. Mekhanika Tverdogo Tela, No. 3. 1966.
40. Tarnopol'skii, Yu. M., G. G. Portnov, and I. G. Zhgun.— Mekhanika Polimerov, **2**. 1967.
41. Tugoplavkie materialy v mashinostroenii (Refractory Materials in Mechanical Engineering. Reference book.). Moskva, Mashinostroenie. 1967.
42. Sutton, W. H. and J. Chorne.— In: Strengthening Mechanisms in Metals and Ceramics, p. 549. Syracuse University Press. 1966.
43. Daniels, H. E.— Proc. Royal Soc., 183, 405. 1945.
44. McAbee, E. and M. Chwea. Proc. Ann. SPI Conf. Reinforced Plastics Division. 1959.

45. Desai, M. B. and F. I. McGarry.—Proc. 14th Ann. SPI Conf. 45. Reinforced Plastics Division, 1959.
46. Tarnopol'skii, Yu. M. and T. Ya. Kintsis.— Mekhanika Polimerov, 1. 1965.
47. Umanskii, E. S.— Poroshkovaya Metallurgiya, 1. 1969.
48. Karpinos, D. M. and L. I. Tuchinskii.— Poroshkovaya Metallurgiya, 9. 1968.
49. Karpinos, D. M. and L. I. Tuchinskii.— Poroshkovaya Metallurgiya, 11. 1968.
50. Schuerch, H.— AIAA Journal, 4, No. 1. 1966.
51. Timoshenko, S. P. Theory of Elasticity, New York, McGraw-Hill. 1934.
52. Tuchinskii, L. I. Issledovanie uslovii polucheniya i svoistv kompozitsionnykh materialov armirovannykh tugoplavkimi voloknami (Study of Preparation and of the Properties of Composites Reinforced by Refractory Fibers). Authors Summary of Candidate's Thesis, IPM AN Ukrainskoi SSR, Kiev. 1968.
53. Gatewood, B. E. Thermal Stresses. New York, McGraw-Hill. 1957.
54. Abramov, V. V. Ostatochnye napryazheniya i deformatsii v metallakh (Residual Stresses and Strains in Metals). Moskva, Mashgiz. 1963.
55. Nikishin, V. S. Temperaturnye napryazheniya v sostavnom tsilindre (Thermal Stresses in Composite Cylinder).— In: Trudy vychislitel'nogo tsentra AN SSSR. Moskva, Nauka. 1964.
56. Wolton, J. and W. Corbett.— In: Voloknistye kompozitsionnye materialy, Moskva, Mir. 1967. (Russian translation).
57. Baskin, J., G. A. Arenberg, and I. H. Handwerk.— Amer. Cor. Soc., 33(7):345. 1959.
58. Baskin, J., G. A. Arenberg, and I. H. Handwerk.— Amer. Cor. Soc., 43(9):489. 1960.

Chapter XI

TECHNOLOGICAL PROCESSES FOR THE PRODUCTION OF COMPOSITE FIBERS AND THEIR PHYSICOMECHANICAL PROPERTIES

1. Production of composites by powder metallurgy

The materials used at present in industry operate at the limits of their potentialities. Austenitic refractory steels cannot be used at temperatures above 700°C, while the highest temperature at which Ni-based steels can be utilized is 1000°C. For the requirements of modern engineering, these parameters are insufficient. The refractory metals (W, Mo, Ta, Nb, and others) and the alloys based on them have high melting points, but are little resistant to slags. Therefore, they must be coated with special materials, able to withstand corrosive media at high temperatures. High-melting non-metallic materials such as carbides, borides, nitrides, and others, and also ceramic materials are refractory but their thermal stability, impact strength, and tensile strength are low. These drawbacks can only be eliminated by creating systems consisting of components with properties that supplement one another.

The best materials are composites. The fibrous structure of these materials makes it possible to combine the high strength and high melting point of the fibers with the high ductility of the metallic matrix or the high refractoriness of the ceramic matrix.

When selecting the method for producing composites, we must consider the properties of matrix and filler, conditions of their interaction, possibilities of obtaining the required properties, economics of the processes, availability of the equipment, etc.

The technology for the production of systems reinforced by fibers is still at the beginning stage. But after having realized the future of such composites, we must thoroughly investigate the various methods for their production to be able to select the optimum variants for each composite, and thus to ensure the large-scale application in industry.

When producing composites by the methods of powder metallurgy, the charge consisting of a mixture of matrix powder and fibers is subjected to pressing and sintering, hot pressing, rolling, or other treatment. After a mixture with short fibers is pressed, a structure with random fiber arrangement is formed. To obtain directed fiber orientation, the pressed briquettes are extruded. It is also possible to obtain oriented structures before pressing directly in the mold by vibration, or by a magnetic or

electrostatic field. This method is fairly simple and can be used to produce materials with the given porosity with a fiber concentration varying over a wide range. The method can easily be mechanized or automated. The number of composites produced by powder metallurgy is fairly large. The drawbacks of the method include the difficulties involved in attaining uniform distribution of the fibers in the matrix, because during mixing fiber clusters are formed. Another drawback is the possibility of damaging the threadlike crystals in the pressing process.

Preparation of the charge. The main difficulty involved in the production of reinforced composites by powder metallurgy is the mixing of the matrix powder uniformly with the fibers.

The properties of reinforced products are very dependent on the efficiency of mixing.

Two mixing methods exist in principle, the mechanical and chemical.

In mechanical mixing drums with an eccentric axis of rotation are used. The mixing effect is obtained by shaking the charge during revolution of the drum. The charge is also mixed in conical mixers or in mixers of the "intoxicated barrel" type, which is mostly used when the components must not be hardened or disintegrated by mixing.

The best mixing is apparently achieved by equipment of the tilting type, such as the double-cone mixer or the two-body mixer. The use of mixers producing slip of the material, ball mills or drum mixers, leads to cluster formation of the fibers. The length and thickness of fibers affect their agglomeration: the longer the fibers and the larger their diameter, the less clusters are formed.

In many cases wet mixing in alcohol, benzine, or water promotes a more uniform fiber distribution. It is evident that preparation of the charge by mechanical mixing is only possible if the fibers are discrete.

The chemical mixing method is based on deposition of various compounds of the matrix material, originally in solution, on the fiber-surface, followed by transfer of the fibers into the matrix. With the chemical method it is possible to obtain a fairly uniform component distribution.

After wet or chemical mixing, in most cases the charge must be dried at 100 – 110°C. If the mixture is not liable to oxidation it can be dried in air. Frequently vacuum furnaces are used. Mixtures consisting of components with large differences in their specific gravity must not be dried to a zero water content since during storage of the charge the components may separate according to their specific gravity.

Pressing followed by sintering consist in two operations. The pressing process is applied to compress the charge and thus impart the required shape and size. The material can be pressed in mold, by pressers or by large hammers, by the hydraulic method, extrusion, rolling, vibrational compression, explosion, etc.

If the material is pressed in molds, the pressure is transmitted to the charge through punches. After the pressure is removed, the product is squeezed out of the mold. During the pressing process frictional forces may arise between the outer layers of the powder and the mold walls, and these increase with increase in pressure. As a result, there is an appreciable fall in pressure over the height of the briquette. Frictional forces also arise between the surfaces of the punch and the briquette.

Uneven pressure distribution leads to an uneven compression of the charge in the briquette. Also comparatively stiff fibers hinder uniform matrix compression.

During the pressing process the fibers and powder particles are subjected to elastic and plastic deformation so that large stresses are accumulated in the briquette. After pressure removal, the briquette tends to expand because of these stresses.

The elastic stresses accumulated in the briquette after its removal from the mold lead to expansion, which in turn brings about packing defects.

The principle of hydrostatic pressing is as follows: the charge is filled into an elastic shell (rubber, lead), and is subjected to hydrostatic pressure from all sides. Hermetic chambers are used, and the liquids are oils, water, glycerol, etc. Absence of external friction is characteristic of hydrostatic pressing. The particles are shifted by hydrostatic pressure toward the center of the bar. In hydrostatic pressing, the density and hardness of the material are almost equal at all sections.

In cylindrical and spherical products the slight density drop from the periphery to the center may be due to the arch effect, that is, the formation of a layer which prevents further matrix compression.

Since no frictional forces act in hydrostatic pressing, the specific pressure is much lower than in conventional pressing. But because there is no interparticle displacement in hydrostatic pressing, the effective pressures applied must be higher than those in the mold at an equivalent density.

There is also another variant of hydrostatic pressing: the elastic, shell is placed into a rigid mold and thus plays two roles: that of the shell, and that of a medium for isostatic pressure transmission. This method is used for making tubes or rods. If it is possible to apply conditions which prevent fracture of the briquette when they are squeezed out of the mold, there are no restrictions on the length to diameter ratio of the product.

Extrusion of cermet bodies can be in two ways. In the first variant the fiber-powder mixture with binders (plasticizers), which are viscous liquids like bakelite solution, paraffin, etc., is pressed into a matrix and squeezed through a nozzle. To impart the required shape to such a charge, we need only a small degree of compression realized in the nozzle. The plasticizer binds the particles to be extruded and produces conditions favorable for the outflow of the mass from the nozzle.

In the second variant the heated intermediate product (consisting of the pressed or unpressed charge of the composite) is extruded from the nozzle. This method is used for producing various profiles: rods, pipes, angle brackets, etc. The advantage of extrusion is that it is possible to produce long products with uniform density from composites which are normally pressed with difficulty.

Rolling the charge has numerous advantages in comparison over normal pressing. By rolling we can produce larger products, the capacity of rolling mills is lower than that of presses, but their efficiency is higher. The rolling of cermets has all the advantages of powder metallurgy (production from high-purity materials, possibility of making details from refractory compounds). Moreover, compared to the rolling of cast metals, the capital investment for large equipment is less, the number of operations is smaller,

and the yield of the product is higher. The drawback of rolling is the restricted length of the tape, and the impossibility of obtaining products of complex configuration.

The conditions of charge deformation in rolling differ from those of deformation in pressing. In the latter case, if the charge is packed with nonuniform volume compression, plane stresses occur during rolling.

There are two additional ways of compressing the charge: impulse pressing (with hammers, by explosion, hydraulic impact, etc.) and vibrational compression. At present these methods are not applied on a large scale, though they have some advantages. By means of impulse pressing in some cases we can obtain complicated products without subsequent sintering, while vibrational compression makes it possible to obtain products with a directed fiber orientation. This is very important, since it allows maximum utilization of the fiber strength.

It is noteworthy that on pressing products in molds the fibers are oriented in planes which are normal to the compressive stresses, but the orientation in these planes is random. Extrusion and rolling make it possible to produce a composite with unidirectional fiber orientation, which is the important advantage of these methods.

During compression the physicochemical properties of the cermets begin to appear, but they become fully developed during sintering. Sintering of the composite means heat treatment of the mixture of initial materials pressed or formed by any of the above methods. Its purpose is to increase the density and attain the required physicomechanical parameters. The sintering operation includes heating to a temperature of $0.7-0.8\,T_{mp}$(in °K) of the matrix, and a certain residence at this temperature. The equipment used for sintering composites does not differ from that used to sinter conventional powder mixtures /1/. The operation is usually performed in atmospheres of hydrogen, inert gases, ammonia derivatives, gaseous hydrocarbons, or in vacuo. During sintering, the components form bonds, and are compressed and reinforced, but these components may dissolve in one another. For reinforced materials, we must maintain time and temperature limits during sintering which ensure sufficiently strong bonds without any appreciable dissolution. In some cases, after sintering the products are subjected to additional treatment, such as repeated pressing and sintering, heat, or heat-and-chemical treatment, in order to improve the physicomechanical parameters, protect the product surface against corrosion, or impart their final dimensions and form to the products.

Slip casting is as yet not as popular as pressing. However, this method is very promising, especially when producing composites with a high volume content of fibers. The method has three modifications. In the first the matrix powder and fibers are formed into a dross which is poured into a mold. The composite obtained is dried and burned. The fiber content in a composite obtained by this method is not higher than $5-10\%$. The liquid for producing the dross may be water with additions of $FeCl_3$, hydrochloric acid, ammonium alginate, and others /1/. The additives prevent the formation of agglomerations of particles, promote stable colloidal suspensions, and improve the wetting conditions. For slip casting of heavy powders, paraffin melt, glycerol, or other liquids are used. The usual particle size is not larger than $5-10\mu$, since larger particles do not yield a good suspension.

In the second variant, a felt is formed from the fibers, which is then immersed into a mold and finally impregnated with dross made of matrix powder.

Another modification of slip casting is the method in which a grid serves as the reinforcement. In this case, the reinforcement is first shaped, (for example the frontal edge of a wing), and the ceramic dough is applied to it.

Hot pressing. In hot pressing, the pressing and sintering processes are combined. The hot pressing temperature is usually $0.5-0.8\ T_{mp}$ (°K) of the matrix. Because of the heating, the compression process in hot pressing is much more intense than in pressing and sintering. With this method, it is possible to obtain almost poreless products. In hot pressing, the process is nearer to sintering than to pressing. But depending on the applied stresses and the imperfections in the crystal structure of the materials to be pressed, plastic strain, unsteady- or steady-state diffusional creep may be responsible for the density changes. The external pressure forces in hot pressing are added to the capillary pressures, and cause independent sintering of the briquettes. A very important advantage of hot pressing is the prevention of the fracture of brittle fibers during compression /2/. This is because in hot pressing, less pressure is required to obtain a material of the given density than in pressing together with sintering. Moreover, hot pressing is characterized by the application of lower temperatures, and a shorter time of residence, which in some cases prevents recrystallization and undesired chemical reactions. The most efficient process is dynamic hot pressing, based on impact compression of the preliminarily heated charge. Since the heating period is minimum, and only sufficient for heating the whole cross section (a few minutes), and the period of impact is also short (a few seconds), the diffusion processes are reduced to a minimum.

The drawback of the method of hot pressing is the comparatively low productivity of the process, restrictions on the size and shape of the products, and, finally, the necessity of employing complex equipment. But in spite of this, hot pressing will probably find wide application in the production of reinforced materials.

Impregnation. The technology of producing composites by impregnation is as follows. The pressed felt, consisting of cut wire, whiskers or long fibers, arranged in a certain order, are heated in vacuo or inert medium, impregnated with the fused metal matrix, and cooled in the furnace. Naturally, the melting point of the matrix must be lower than the melting point of the fibers.

Impregnation makes it possible to obtain almost poreless material, uniformly distribute the components, vary the volume contents of the fibers over a wide range, produce the required orientation, retain the initial form and size of the fibers, and use the standard equipment of thermal metallurgy.

However, the impregnation process cannot be employed for all matrix-fiber pairs. To obtain a good composite, we must ensure good wetting of the fibers by the liquid matrix. The wetting angle θ must be as small as possible to increase the bonding forces on the interface. If θ is larger than 90°, the composite cannot be prepared by impregnation.

For impregnation with refractory materials high temperatures are needed. But at elevated temperatures the fibers may become loosened or brittle, undergo polymorphic transformation, or dissolve in the matrix. These undesirable effects impair the quality of the composites.

The create better impregnating conditions, additives are introduced into the metal. These are adsorbed on the interface and decrease surface tension. Composite fibers can also be obtained by casting under pressure or casting in vacuo.

2. Application of coatings

In addition to the methods described composite can also be produced by applying alternating layers of matrix and fibers onto a support. The support is a mold and may differ greatly in configuration. After the coating is applied, the support is removed in some way (it is burnt, dissolved, fused, or mechanically removed). The result is a component part made of the reinforced material which has the same geometric shape as the support. Sometimes the structure requires high mechanical parameters in the surface layers of the part only. In this case a reinforced coating is produced on the product with the given properties. At present several methods of applying coatings exist.

Plasmatic coatings. The method of obtaining plasmatic coatings is very promising. Its advantages are especially obvious when spraying refractory metallic or nonmetallic coatings. The method consists in layer-by-layer spraying of the matrix material on the fibers, also introduced in individual layers. The composition of the sprayed coatings can be smoothly varied over the thickness of the sprayed layer by means of special batchers, or the coating may consist of layers of different materials. If required, the thickness of sprayed material and its properties may also be changed during the atomizing process.

The plasma-spray equipment is stable in its operations, and easy to handle. To improve the bond between the sprayed coating and the component part, the material to be reinforced (grids, band, rods) is riveted to the part.

The advantages of applying the coating by plasma spraying are the following:

the very high temperatures of the plasma stream make it possible to fuse and apply numerous materials with any melting point as coatings;

the stream of the plasma which does not contain oxygen makes it possible to reduce decomposition of the sprayed material and oxidation of the component part. If necessary, the coating can be sprayed in a controlled atmosphere chamber;

the high speed of the plasma stream leads to a high speed of the atomized particles. This increases the density of the coating and strengthens the bond between fiber and matrix;

the plasma stream makes it possible to apply complex and multilayer coatings;

with the aid of the plasma stream the coatings can be applied onto metals, ceramics, glass, plastics, wood, etc.

The energetic parameters of the plasma stream can be varied over a wide range according to the requirements of the technique.

The drawbacks of the method are the thermal stresses arising in the material under the effect of the plasma stream. In some cases they may lead to crack formation.

Electrolytic coatings. When the electrolytic method is used for the production of composite coatings the matrix is applied layer-by-layer onto the fibers. The matrix in plasma spraying is applied in an ionized gas stream, and in the electrolytic method from solutions or melts of the matrix material because of the potential difference.

In electrolytic processes, the coating is deposited at low temperatures without pressure. This makes it possible to reduce thermal effects and fiber fracture to a minimum during the technological process.

The method has a modification in the preparation of materials with retention of the threadlike crystals in the electrolyte in a suspended state. The matrix metal is deposited on the cathode, and the fibers in continuous contact with the cathode penetrate into the deposit and are uniformly distributed over it. The orientation of the threadlike particles in the plane is random. By changing the conditions of electrolysis we can control the fiber level, and the concentration and size of the dispersoid.

The drawback of this method is the following. It can only be applied to light short fibers, which can be kept in suspension. Long heavy fibers do not produce the required effect.

Other methods of applying reinforced coatings. Other methods can also be used to apply a coating of reinforced material. They include the electrode gas-flame methods, in which the material to be applied is fused in an electric arc or in the flame of gas burner, and applied by a gas stream onto the support with the fibers placed on it. These methods are simple and effective, but unsuitable for the application of refractory coatings. The coating can also be applied by precipitation from the gas phase, by vacuum emission, or by detonation methods. However, these methods are not very promising because of their low efficacy.

3. Directional crystallization

The use of directional crystallization of melts with the formation of a threadlike eutectic for the production of composite fibers makes it possible to reduce the laborious technological cycle. The $Cu-Cr$, $Al-Al_3Ni$, $Fe-FeS$, and other eutectics form needlelike parallel crystals distributed over the matrix. Such structures are usually obtained if the amount of matrix phase is much larger than that of the fibers. The needlelike crystals have properties resembling those of whiskers, and therefore the strength of controlled eutectics is very high /4/.

The disadvantage of this method is its restricted use, as it is suitable only for systems in which a eutectic reaction is possible. Moreover, it is difficult to obtain a large content of the fiber phase. But even allowing for these difficulties we know several systems in which we can produce eutectics with the required properties.

• [See Chapter XV.]

4. Composites based on copper or copper alloys

The first research workers to study the reinforcement of metals were Kelly, Tyson /6—8/, Cratchley /10, 33, 39/, and others. These authors investigated the reinforcement of copper by tungsten and molybdenum fibers. The advantage of these systems is that tungsten and molybdenum fibers are almost insoluble in copper, and are well wetted by it. Since tungsten passes from the brittle into the plastic state at 200—300°C, the tungsten-copper system is very suitable for studying composites reinforced by brittle and plastic fibers.

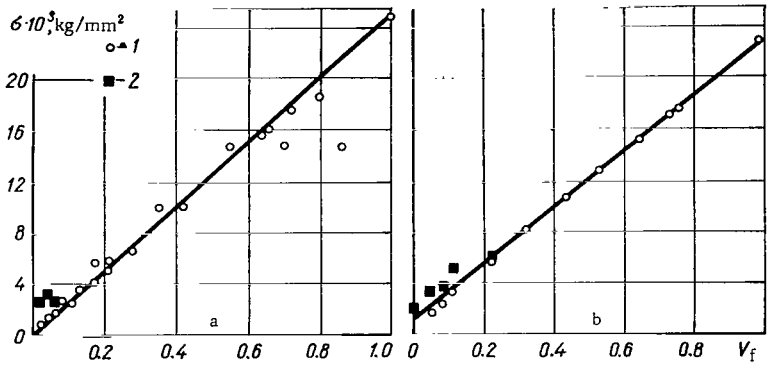

FIGURE XI.1. Dependence of the tensile strength parameters of reinforced copper on the volume fraction of tungsten fibers of 0.5 mm diameter at 20°C (a), and of 0.2 mm diameter at 250°C (b):

1 — yield point; 2 — ultimate strength.

These authors developed the technology of impregnating the fiber skeleton with copper, and studied the mechanical properties of the composite, and the effects of the volume content of the fibers and of the length-to-diameter ratio on the strength parameters of the aligned composite. Figure XI. 1 shows the dependence of the tensile strength parameters on the Cu — W system on the volume fraction of the tungsten fiber. The diameter of the fibers was 0.5 mm and the temperature 20°C. In another test the fiber diameter was 0.2 mm and the temperature 250°C. If the fiber content is higher than the critical one, this dependence is governed by the additivity law.

The dependence of the yield point of the composite on the fiber length is shown in Figure XI. 2. The tests were performed at 250°C. The fiber diameter was 0.5 mm. We see that with increase in the length of the fibers the yield point increases.

A decrease in the diameter of the fibers, and hence an increase in their strength, leads to a higher strength in the whole composite.

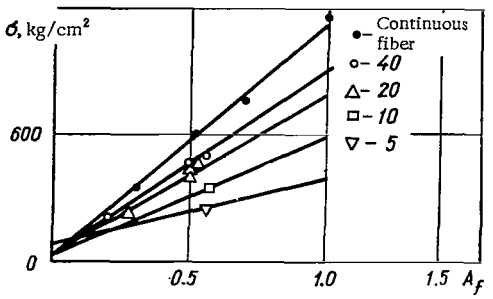

FIGURE XI.2. Yield of the Cu — W composite as a function of the volume fraction of continuous and discrete fibers. The figures next to the symbols show the length-to-diameter ratio.

The mechanism of macrofracture of copper reinforced by tungsten fibers was studied by Ustinov /11/. The author found the dependence of the number of fracturing cycles of the fibers on their initial length, diameter, and ultimate strength, for composites with a low filler level. The stress-strain diagrams of composites with a filler level of up to 7% are jagged curves because of the periodic falls and rises in the loads when the fibers are fractured. It was found that with increase in V_f over this range, the height of the first and subsequent peaks of the stress-strain curve increases and when V_f reaches a certain level, the height remains constant.

It was found that at a certain minimum volume fraction of the fibers V_{min} the reinforcing effect predominates over the weakening effect that is, when $V_f < V_{cr}$ the effect of reinforcement is positive. If $V_{min} < V_f < V_{cr}$, the composite is weaker than the pure matrix. This behavior is due to the fact that the fracturing processes of the fibers do not take place at the same time. Ustinov /11/ believes that the strength decrease when $V_f > V_{min}$ is due to increased impairment of the composite. The increases with increase in the level of the fiber, since the number of microcracks formed on fracturing of the fiber is proportional to the number of fibers.

The strength of the Cu — W system changes only slightly when the temperature increases from 20 to 400°C. This proves that in the given composite we can achieve transmission of stresses close to the ultimate strength from the matrix to the fiber. Since the main load is carried by the fibers, and the strength of tungsten is almost constant at such temperatures, the composite as a whole will be insensitive to temperature increases. This also explains the high long-term strength and low creep of the Cu — W composite. Copper reinforced by 12.5% of tungsten was not fractured at 400°C when a stress of 16 kg/cm² was applied for 1,700 hours, but zirconium alloyed with copper withstood this stress at the same temperature for only 700 hours.

Reinforced copper has not only higher short-term and long-term strengths, but also an increased resistance to fatigue fracture at room temperature /11/. This is explained by the fact that in reinforced copper the energy of crack generation and propagation is higher than in pure copper.

It was found that the fatigue limit of the Cu — W composite on the base of 10^7 cycles under repeated tension increases with increase in the volume

fraction of the fibers. For $V_f = 37.5\%$, the cyclic strength is 30 kg/mm², while for $V_f = 51\%$ it is 40 kg/mm²; this is 4 – 5 times the fatigue limit of pure copper. However, the introduction of W fibers of 1 mm diameter led to a somewhat lower cyclic strength than in copper. The ratio of the cyclic strength (10^7 cycles) to the static strength of the Cu – W system is approximately 0.5.

Ham and Place /13/ used the test results on the fatigue strength of reinforced copper, and concluded that a matrix which is scarcely hardened by variable loads is necessary in order to achieve a high fatigue strength. Moreover, bond continuity between matrix and fibers, residual thermal stresses, damage to the fibers during their production, and uniform distribution of fibers in the matrix, are other factors affecting the fatigue strength of reinforced copper.

The effect of alloying elements on the strength of the Cu – W composite was studied by Petrasek /14/. The specimens were prepared by impregnation. Alloying the copper matrix with nickel and chromium lowers the composite strength (Figure XI. 3), but this effect decreases with increase in temperature. The strength of reinforced material with chromium added is described by an equation obtained from the additivity law

$$(\sigma_в)_c = (\sigma_в)_f V_f + \sigma'_m V_m + \sigma'_a V_a, \qquad (XI.1)$$

where $(\sigma_в)_c$ is the ultimate strength of the composite; $(\sigma_в)_f$ is the ultimate strength of the fibers; σ'_m is the stress in the matrix at the moment the fibers are fractured; σ'_a is the stress in the alloyed zone of the fiber corresponding to the ultimate strength of the unalloyed zone; V_f, V_m, and V_a are the volume fractions of the fibers, matrix, and alloyed zone, respectively.

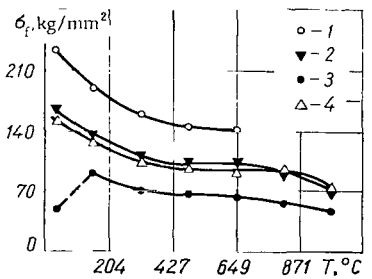

FIGURE XI.3. Temperature dependence of the ultimate strength of composites containing 70% of tungsten fibers:

1 – pure tungsten wire; 2 – pure copper matrix; 3 – Cu – Ni matrix; 4 – Cu – Cr matrix.

It is assumed that $V_f + V_m + V_a = 1$, and that the ductility of the alloyed zone is sufficient to prevent fracture of the zone when the ultimate strength of the unalloyed fiber is reached.

If the volume fraction of the fibers is less than the critical one, a system in which the copper is alloyed with 2% of Cr is stronger than systems with a pure copper matrix. This is because the matrix alloyed with chromium is stronger than the pure matrix, and with a low fiber content the main load is carried by the matrix.

Equation (XI. 1) is suitable for describing the strength of a system with a comparatively ductile alloyed zone. If the alloyed zone is brittle and increases the sensitivity of the fibers to stress concentrations, thus lowering their strength, equation (XI. 1) is unsuitable /15/.

The introduction of 10% of nickel into a copper matrix at room temperature leads to a sharp decrease in the fiber strength (and hence the composite strength), because brittle tungsten–nickel compounds are formed.

The strength of alloyed tungsten fibers decreases as the depth of penetration of the alloying element increases. Tungsten fibers alloyed with nickel are weaker than those alloyed with chromium, since nickel penetrates more deeply.

All these tests were performed on composites obtained by impregnation. The good wettability of tungsten by liquid nickel ensured a firm matrix-fiber bond. But when the same composite is prepared by other methods (electrolytic application of coatings /16/ or dynamic hot pressing /12/) the interfacial bond may be weak.

In this case, an equation of type

$$(\sigma_в)_c = (\sigma_в)_f V_f + \sigma'_m(1 - V_f) \qquad \text{(XI. 2)}$$

cannot describe the test results on the dependence of the composite strength on the volume fraction of the fibers. It was shown in /12/ that the ultimate strength of reinforced copper obtained by dynamic hot pressing at first increases with increase in the volume fraction of tungsten fibers, then passes through a maximum, and finally decreases again (Figure XI. 4). This is explained by the fact that the composite is fractured by lamination (fiber separation from the matrix) as can be seen in Figure XI. 5. The fiber-matrix bond cannot withstand the shearing stresses on the interface which appear when a tensile load is applied. The interface is the weak link in the composite, and cracks are formed at this weak link.

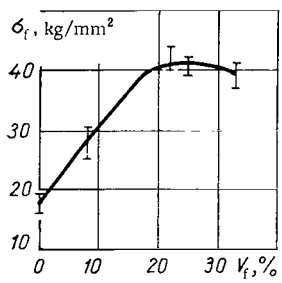

FIGURE XI.4. Effect of the volume content of parallel fibers on the strength of the Cu – W composite. The test temperature was 20°C and the fiber diameter 0.05 mm. The material was obtained by dynamic hot pressing.

FIGURE XI.5. Fracture of a copper specimen containing 33 vol % of parallel tungsten fibers. The specimen was obtained by dynamic hot pressing.

Greenstine /17/ describes the properties of the copper-boron fiber composite obtained by hot pressing. The volume content of the fibers was varied between 0 and 36%. These composites were stronger than pure copper; but when Young's modulus was close to the theoretical values, their strength was only 0.4 – 0.7 of the theoretical strength. It is evident that the high strength properties of the fibers were lost during the production of the material, because of mechanical damage during pressure application and fiber degradation at elevated temperatures.

It is also interesting to note that a composite material was obtained with directional crystallization of the eutectic Cu—Cr /18, 19/. The chromium fibers extracted from the composite had a high strength (up to 700 kg/mm^2). But because the fiber level was not higher than 2 vol %, that is, lower than the critical, no reinforcement was observed.

5. Composites based on silver or silver alloys

The silver matrix, like the copper matrix, does not react with tungsten and molybdenum fibers and a good wetting is observed. The effect of tungsten fibers on the strength parameters of reinforced silver was studied by Parikh /20, 21/. A felt of cut tungsten fibers was impregnated by silver. The bending strength of the sintered felt (without Ag) was 4.3 kg/mm^2 at a porosity of 84%. The same felt impregnated by silver had a bending strength of only 0.92 kg/mm^2. A 1% addition of lithium to the silver to improve wettability increases the strength to 1.4 kg/mm^2. Electrolytic coating of the fibers by nickel increased the ultimate bending strength to 4 kg/mm^2 at a porosity of the felt of 75%. It should be noted that the addition of magnesium and copper to the Ag—Li alloy lowers the strength.

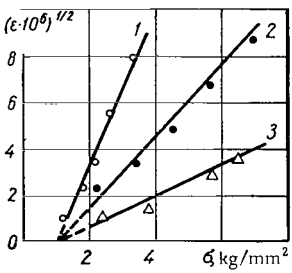

FIGURE XI.6. Relationship between stresses and small plastic strains for pure silver and silver-stainless steel wire composites:

1 — pure silver; 2 — silver with 30 vol % of wire; 3 — silver with 45 vol % of wire.

The creep of silver reinforced by parallel discrete tungsten fibers (length-to-diameter ratio 30—60) was studied by Kelly and Tyson /8/. The specimens were made by impregnation. The tests show that the introduction of fibers appreciably lowers the creep rate and decreases creep deformation prior to fracture.

Tests on reinforcing silver with molybdenum and stainless steel fibers (AISI-410 and AISI-430) /21/ showed that a continuous wire increases the strength much more effectively than short fibers with length-to-diameter ratio of about 100.

At a concentration of steel fibers of up to to 30 vol % the composite strength increases linearly with increase in the fiber content. With a further increase in the fiber content the reinforcing effect is inconsiderable, and the fracture is brittle. Parikh explains this by the imperfect technology.

Figure XI. 6 shows the relationship between stresses and small plastic deformations for silver in the silver-stainless steel wire composite. The yield point of such composites is described well by Petch's equation /22/. The equation

$$\sigma_y = \sigma_0 + kd^{-\frac{1}{2}}$$

(where σ_y is the yield point; σ_0 is the part of σ_y which is independent of the particle size; d is the clearance between the fibers; and k is a factor) applies to an oriented fiber level of 50 vol %.

For a unit strain of up to 10^{-6}, the yield point is independent of the fiber concentration, that is, the stress at the beginning of flow is equal for pure silver and for the reinforced silver matrix of the composite. But as the deformation increases, the fiber-matrix interfacial area begins to hinder the propagation of dislocations. The free path of the dislocations is reduced with increase in the fiber content, and therefore reinforced silver has a higher strengthening rate than pure silver. Thus, reinforcement with fibers has a strengthening effect which is similar to that of grain boundaries in polycrystalline bodies. At a unit strain of up to 10^{-4}, the rate of deformational strengthening is independent of the fiber type, and almost constant for composites reinforced by molybdenum or soft or cold-hardened steel fibers (Figure XI. 7).

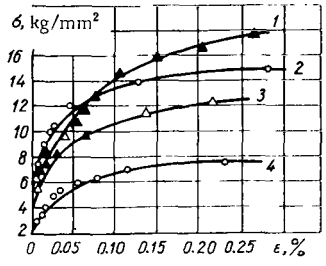

FIGURE XI.7. Stress-strain curves for silver composites with an equal content of reinforcing fibers made of different materials:

1 — silver-30 vol % of stainless steel fibers; 2 — silver-30 vol % of molybdenum fiber; 3 — silver-30 vol % of low-carbon steel fibers; 4 — pure silver.

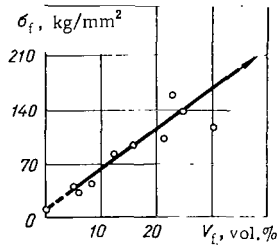

FIGURE XI.8. Effect of the fiber content on the ultimate strength of specimens made of silver reinforced by Al_2O_3 whiskers (extrapolation to 527 kg/mm² for 100% of whiskers).

During further deformation the properties of the reinforcing fibers begin to play a role; with increase in the strengthening rate of the fibers, the whole composite is reinforced more rapidly.

Sutton /23 — 25/ obtained a composite from silver reinforced by parallel Al_2O_3 whiskers. The filamentary crystals were first coated by platinum or nickel, and then placed into quartz capillaries to be impregnated by silver in vacuo. The strength of the microsample obtained obeys the mixing law. If the whisker level was 24 vol %, the strength of the composite was as high as 162 kg/mm² (Figure XI. 8), and the stress in the whiskers was about 600 kg/mm². The average strength of the separately investigated crystals was no higher than 700 kg/mm². Thus, in these composites the strength of the whiskers was utilized to about 90%. If the temperatures are close to the melting point of the silver, the material retains its high mechanical properties. Thus, at 930 ± 10°C the ultimate strength of the

specimens is 17.5 kg/mm^2. It is clear that the fibers give most of the strength, but the mechanism of load transmission from the weak matrix to the short whiskers is not yet clear.

The strength of silver reinforced by Al_2O_3 whiskers at high temperatures is higher than the strength of silver reinforced by disperse particles. At higher temperatures the advantages of the composite material become more obvious. Table XI. 1 shows the mechanical properties of pure silver and silver reinforced by disperse Al_2O_3 particles and filamentary Al_2O_3 crystals, and Table XI. 2 shows the properties of the $Ag - Al_2O_3$ whisker composite reinforced by whiskers of various diameters /26/.

TABLE XI.1. Mechanical properties during short-time tension of the composite $Ag - Al_2O_3$ and silver reinforced by Al_2O_3 particles

Specimen	Diameter, mm	Testing temperature, °C	σ_B, kg/mm^2	δ
Ag (99.95%)	0.434	24	12.0	48
	1.184	143	9.7	42
	1.022	202	8.0	45
	1.050	282	7.0	40
Ag + Al_2O_3 (disperse particles)	0.127	24	50.4	1–2
	0.127	316	39.9	–
	0.127	482	26.6	–
	0.127	649	16.8	–
Ag + Al_2O_3 (whiskers)	0.153	24	42.1	1
	0.521	302	37.1	1
	0.368	499	33.6	2
	0.226	760	31.2	2

Parrat /27/ studied the composite silver-silicon nitride whiskers. The material was obtained by hot pressing, and the volume content of the randomly arranged fibers was not higher than 15%. The specimens had a breaking strength of up to 28 kg/mm^2 and an elongation of up to 2%. However, the elastic limit of reinforced silver differed little from that of pure silver (Figure XI. 9). An addition of 1% of Si to Ag led to the formation of an $Ag - Si$ eutectic at the temperature 830°C of hot pressing. This improved the whisker-matrix bond, and hence, somewhat increased the ultimate strength. It is noteworthy that when the test temperatures were increased the weakening was much more intense. It is possible that this is due to imperfections in the technology.

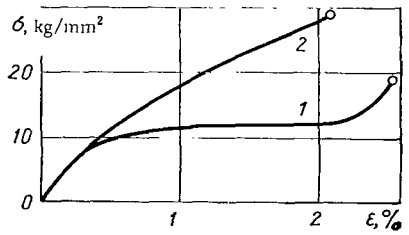

FIGURE XI.9. Stress-strain curves of pure silver (1) and silver reinforced by Si_3N_4 whiskers (2).

TABLE XI.2. Mechanical properties of the Ag – Al_2O_3 whisker composites as a function of the whisker diameter

Whisker diameter	V_f, vol %	Testing temperature, °C	σ_B, kg/mm^2
8–20	45.5	870	58.0
8–20	43.0	890	30.6
70–90	38.0	830	22.4
90	37.0	790	24.4
90	32.0	820	23.6

6. Composites based on aluminum or aluminum alloys

The first experiments on the preparation of aluminum alloy composites were carried out in the early fifties. Beskorovainyi and Fridman /28/ studied reinforcement of silumins by steel wire OVS ($\sigma_B = 150-200$ kg/mm^2) and steel-40 wire ($\sigma_B = 95-110$ kg/mm^2). The reinforced unmodified silumin had a 67–70% higher breaking strength, while the specific gravity increased by 15–21% only. The graph of the strength plotted against the volume content of the filler (3.8–13.4 vol %) was linear.

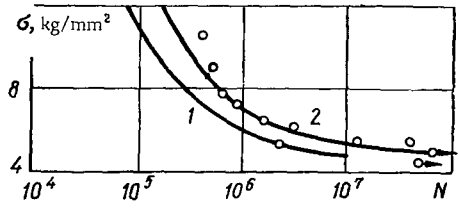

FIGURE XI.10. Fatigue failure curves of aluminum alloy (1) and the same alloy reinforced by 13.5 vol % of wire (in the form of a grid) made of stainless steel FV 520 B(2).

The reinforcement of aluminum by discrete stainless steel wires (stainless steel Kh18N9T was used) showed /29, 30/ that an increase in the length-to-diameter ratio of the wire increases the slope of the graph of the composite strength plotted against the volume content of the filler.

Forsith et al /31/ showed that when a grid of manganese ($\sigma_B = 245$ kg/mm^2) or stainless steel ($\sigma_f = 215$ kg/mm^2) is used as reinforcement, the rate of crack formation considerably decreases in fatigue tests on aluminum alloys.

The material was prepared by hot rolling aluminum sheets made of alloy DTD-687 (Al – Zn – Mg – Cu) or alloy L-73 (Al – Cu – Mg) together with steel grids. The fatigue curves of alloy L-73 reinforced by 13.5 vol % of FV520B stainless steel and of the nonreinforced matrix are fairly close to one another (Figure XI. 10). However, if the wires are positioned at an angle

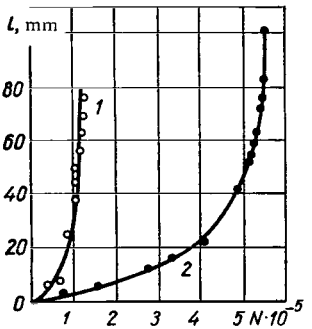

FIGURE XI.11. Dependence of the crack length l on the number of cycles in fatigue tests on aluminum alloy DTD-687A (1), and on the same alloy reinforced by one layer of stainless steel FV520B grid (2) (the grid wires are positioned at an angle of 45° to the axis of tension).

of 45° to the direction the load is applied, the number of cycles prior to fracture increases considerably (Figure XI. 11).

The short-term strength and ductility of alloy L-73 with 8% of tungsten or steel grids added are shown in Table XI. 3. To prevent cutting of the grid at the contact sites during rolling, the grids were produced so that the high-strength wires were placed in one direction and the aluminum wires perpendicular to them. Specimens made of alloy L-73 reinforced by 8 vol % of steel fibers of diameter 0.175 mm had a creep limit of $\sigma^{0.1}_{1000} = 35.7\,kg/mm^2$ at 150°C, while this parameter was $\sigma^{0.1}_{1000} = 7.9\,kg/mm^2$ for the pure alloy.

Parikh et al. /20/ used tungsten wire for reinforcing aluminum. The pressed briquettes obtained from aluminum powder and tungsten wire of 0.025 mm diameter were subjected to hot extrusion to produce a fiber orientation parallel to the specimen axis. Young's modulus changed linearly from $7 \cdot 10^3\,kg/mm^2$ for pure aluminum to $9 \cdot 10^3\,kg/mm^2$ at a filler level of 30 vol % (Figure XI. 12).

TABLE XI.3. Mechanical properties of the aluminum alloy L-73 reinforced by wire grids made of tungsten or FV 520B steel

Material	Testing temperature, °C	$\sigma_{0.1}$, kg/mm²	$\sigma_в$, kg/mm²	δ, %
Alloy L-73	20	40.0	43.5	10.0
	200	26.3	30.3	12.0
	250	10.0	12.0	20.0
	300	5.6	7.0	23.0
Alloy L-73 + 8 vol % of tungsten grid	20	59.0	68.0	—
	200	35.0	44.0	—
	250	22.3	29.6	3.5
	300	16.5	25.0	5.0
Alloy L-73 + 8 vol % of wire made of FV520B steel	20	51.0	56.0	8.0
	200	34.6	40.7	8.0
	250	21.8	25.0	4.5
	300	11.6	20.4	4.5

When the fiber level was 8 vol %, a 60% additional contraction increased the ultimate strength to 28 kg/mm², while after extrusion $\sigma_в$ was 17 kg/mm².

Morley /32/ prepared aluminum reinforced by silica fibers. The fibers were coated with a uniform aluminum layer by passing the fibers through the fused metal, and the mixture was pressed at high temperatures. The aluminum shells formed a continuous, almost poreless matrix. The

strength of such materials was more than 2.5 times that of SAP over the temperature range between 0 and 400°C (Figure XI. 13). The pseudoalloy 50% of Al — 50% of SiO_2 fibers had an ultimate strength of 77 kg/mm² at room temperature, and an ultimate strength of 38.5 kg/mm² at 400°C. In this case the composite strength was 20% of the rated strength.

Whitehurst et al. /34/ studied the mechanical properties of aluminum alloys reinforced by glass fibers. At temperatures higher than 370° C the alloy 2014-TG — 20 vol % of fibers had a higher strength than SAP-276. However, at room temperature the strength increase was slight.

It should be noted that the creep rate of aluminum alloys reinforced by glass fibers was one hundredth of that of pure aluminum /24/.

Papers /23, 24/ report data on the reinforcement of aluminum by randomly arranged ZrO_2 fibers. An addition of 9 vol % of ZrO_2 led to some weakening at room temperature. However, an increase in the fiber level to 19 vol % increased the strength. An addition of 5% of lithium to the aluminum — 13 vol % of ZrO_2 composite was introduced to improve the wettability of the fibers and to increase the fluidity of the metal, and this led to an appreciable increase in the ductility without impairing the strength parameters.

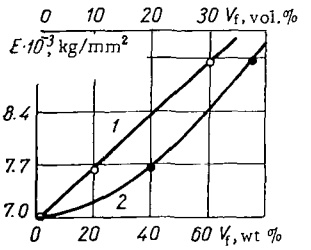

FIGURE XI.12. Effect of the volume (1) and weight (2) content of fibers on the Young's modulus of aluminum specimens reinforced by tungsten fibers.

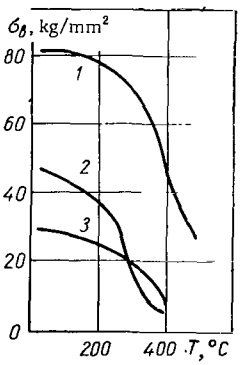

FIGURE XI.13. Temperature dependence of the ultimate strength of aluminum reinforced by SiO_2 fibers (1) of aluminum alloy RR58 (2) and SAP with 10% of Al_2O_3 (3).

Attempts were made to reinforce aluminum by thin graphite fibers of 5μ diameter /35/. However, these experiments were unsuccessful. The yield points and ultimate strength of the reinforced specimens were lower than those of the pure aluminum.

Hertzberg et al. /37/ prepared composites by cold pressing a mixture of aluminum powder and aligned boron and silicon carbide fibers, with subsequent sintering. The stiffness of the composite with the boron fibers was close to the theoretical. In some cases it was even higher, which is explained by the formation of borides, which have a high modulus of

elasticity but a low strength, on the interface. The ultimate strength of the reinforced material was 19 – 66% of the theoretical, because of the presence of borides and the weakening of fibers during the preparation of the specimens. The strength of composites reinforced by SiC was much nearer to the theoretical. Other specimens were also prepared by pressing aluminum sheets at 540°C for 30 min at a specific pressure of 2.1 – 2.8 kg/mm^2. The boron fibers were placed into parallel grooves etched into the aluminum. No chemical reactions were observed between matrix and fiber in the pressed material. In this case the strength was close to the rated one.

Sutton /24/ studied the reinforcement of aluminum by Al_2O_3 whiskers. The whisker bundle was impregnated with fused alumina, and the strength of the material was 113 kg/mm^2 at a fiber content of 35 vol %.

It is also possible to obtain a system based on aluminum containing 10 vol % of Al_3Ni whiskers by direct crystallization in aluminum /37 – 38/. If this alloy with random fiber distribution had an ultimate strength σ_s of 9.1 kg/mm^2 and a relative elongation of 15%, the eutectic with aligned filamentary crystals had a strength of 30 kg/mm^2 and a relative elongation of 2%. The strength of the whiskers etched out from the matrix was 210 – 230 kg/mm^2. Thus, in the eutectically hardened alloy the fiber strength was almost completely utilized.

The experiments of Cratchley /39/ are very interesting. He studied the deformation of aluminum alloys containing intermetallic compounds at temperatures above 0.6 T_m (in °K).

During deformation the intermetallic particles become filamentary, but if they are annealed for a long period, some of the particles become spherical.

7. Composites based on nickel or nickel alloys

Composites based on nickel have been studied less than composites with a low-melting matrix. Ceramic threadlike crystals are best for reinforcing the nickel matrix. Figure XI. 14 gives the theoretical values of the long-term strength of nickel reinforced with 50 vol % of Al_2O_3 whiskers.

This graph shows that the strength parameters of the nickel composites must be much higher than those of the better refractory alloys.

To increase the wettability between nickel and the ceramic it is recommended that titanium, chromium, etc., be introduced into the matrix /40, 41/. These elements are separated on the interface, and diffuse into Al_2O_3 or form a new phase on the surface of the filamentary crystals. However, because of the chemical interaction of titanium with the oxides, the whisker surface becomes rough and the strength decreases. This undesired effect is less pronounced when nickel is alloyed with chromium.

Sutton and Chorne /24/ report that for an additional decrease in the wetting angle between the Al_2O_3 whiskers and nichrome gallium salts, were added, and the composite was sintered at 1320°C (melting point of nichrome). The strength of the specimens was as high as 210 kg/mm^2, while the ultimate strength of the nichrome wire was only 130 – 150 kg/mm^2. The whisker level in the composite was varied between 0 and 9 vol %. Over this range the strength was linearly dependent on the filler level.

A nickel-palladium alloy reinforced with 9 vol % of filamentary Al_2O_3 crystals had an ultimate strength of 70 kg/mm^2, which was twice the strength of the nonreinforced material /24/.

The authors of patent /42/ developed a method for obtaining composites based on the nickel-chromium alloy reinforced by alumina whiskers. The plasticized mixture is extracted and subsequently sintered. It was found that that if no additives that improve wetting are introduced, the reinforcement will be inconsiderable. Solutions of alkaline-earth metals (Ca, Ba, Mg, for example, calcium chromate) served as the additives.

The reinforcement of the 50% of Ni—50% of Co alloy with thin (0.005 mm) graphite whiskers by sintering at a temperature above the melting point of the matrix did not give the desired effect /35/.

Greenstine /17/ also used boron fibers of 0.07 mm diameter for reinforcing nickel. The material was prepared by hot pressing. The experiments were not entirely satisfactory, because the maximum ultimate strength was not higher than 15.5 kg/mm^2 when the boron content was 6—10 vol %.

Reinforced nickel was also prepared by the electrolytical application of a coating onto silicon carbide and boron fibers /17/. The fibers were usually distributed in a nonuniform fashion and the bond between matrix and interface was not sufficiently firm. The ultimate strength of the Ni—B composite containing 34 vol % of B was only 84—85% of the theoretical. Specimens with SiC (30 vol %) had a strength of 72.2 kg/mm^2, which was 93% of the theoretical.

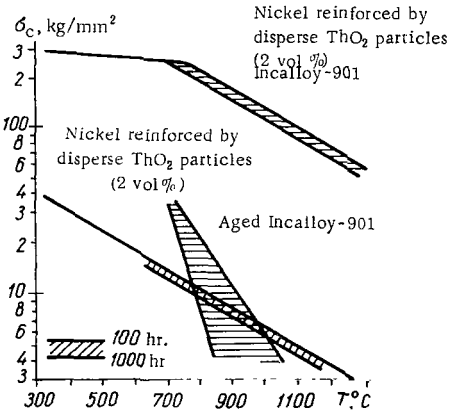

FIGURE XI.14. Comparison of the theoretical strengths of fiber-reinforced and disperse-particle-reinforced alloys.

Baskey /20/ studied reinforced material prepared from short tungsten wire and nichrome powder. The mixture was subjected to hot pressing. A temperature of 1150°C and a holding time of up 6 hr were insufficient for obtaining a monolithic material. The wire recrystallized, and partially dissolved in the matrix, and the reinforcing effect was very small. After the material was rolled the fiber phase became aligned, and the composite

strength increased to 7.9 kg/mm^2 at 1093°C, while the strength of the non-reinforced material was only 5.5 kg/mm^2.

Tuchinskii /12/ developed a technology for producing a composite on a nickel basis. The composites were reinforced by tungsten wires and grids made from these wires; they made it possible to prevent recrystallization of the fibers and their interaction with the matrix during the process. The specimens were prepared by dynamic hot pressing assemblies put together from alternate layers of thin nickel foil and fibers. The assemblies were placed into nickel containers to prevent oxidation of the material during heating. The material with container was placed into a furnace and kept at the given temperature (750—1200°C) for 8—10 min. It was then placed beneath a frictional hammer and impacted from a certain height.

Microstructural and X-ray structural analyses of the pressed composites showed that the matrix was in a recrystallized state and the fibers in the cold-hardened one. But metallographic, X-ray and microspectral analyses did not indicate the presence of a diffusion zone on the fiber-matrix interface.

It was found that in the given concentrational range of tungsten (13—35%), the dependence of the strength of nickel reinforced by parallel tungsten fibers on the volume fraction of the fibers is satisfactorily described by (XI.2) (Figure XI.15). The strength of the tungsten fibers in these components is 70% utilized at room temperature, while at 950 and 1100°C the degree of utilization is almost 100%.

The reinforcement of metals by grids makes it possible to control the anisotropy of the composite and ensure reliable operation of the materials under two-dimensional stress. Nickel was reinforced by grids, intertwined with 0.03—0.065 mm tungsten wire according to the "pouch-surface" type. The structure of the grids is such that their strength in the longitudinal direction (along the mesh columns) is 1.6 times that in the perpendicular direction (along the mesh rows). This is because in the given method of netting, about 62% of the fibers are parallel to the columns of the mesh and about 38% are longitudinal to the rows.

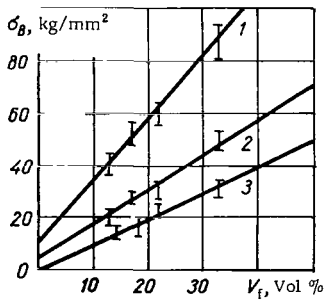

FIGURE XI.15. Effect of the volume fraction of fibers on the strength of the Ni—W composite:

1 — T = 20°C; 2 — T = 950°C; 3 — T = 1100°C.

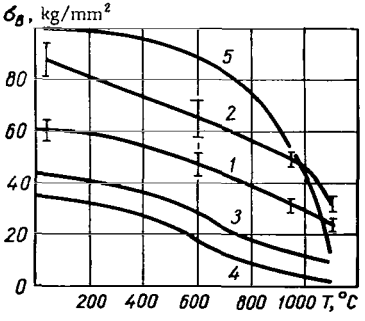

FIGURE XI.16. Temperature dependence of the ultimate strength:

1 — nickel + 33 vol % of continuous tungsten fibers of 0.065 mm diameter; 2 — nickel + 22 vol % of continuous tungsten fibers of 0.065 mm diameter; 3 — TD-nickel; 4 — pure nickel; 5 — Nimocast-258.

The results of strength tests showed that if the columns are aligned along the specimen axis, the composite strength is 1.4—1.7 times the strength when the rows are parallel to the tensile force. This indicates that the main fraction of the load is carried by fibers aligned along the tensile stress.

Nickel composites prepared by dynamic hot pressing have better indexes of short-term strength than the best contemporary refractory nickel alloys. Thus, for example, nickel reinforced with 33 vol % of tungsten wire (65μ in diameter) has a higher ultimate strength over the whole investigated temperature range (20—1100°C) than TD-nickel (Ni + 2 vol % of ThO_2) reinforced by disperse particles. It has rather lower strength parameters than the alloy Nimocast -258 at temperatures up to 950°C, but the composite at 1100°C has a strength 2.2 times that of the alloy under consideration (Figure XI. 16). However, because of the active diffusional interaction of nickel with tungsten, the system is unstable at high temperatures. The stability of such composites was evaluated by studying the kinetics of the growth of the diffusing zone appearing on the fiber-matrix interface during diffusional annealing. It was found that the thickness of the diffusional layer at 600—1100°C increases proportionally to the square of the isothermal holding time.

The temperature-dependence of the diffusion coefficient of the given s system is expressed by

$$D = 6 \cdot 10^{-5} \exp\left(-\frac{33000}{RT}\right). \qquad \text{(XI. 3)}$$

It has been proved that during annealing the diffusional flux is directed preferentially from tungsten into nickel, which agrees with the available published data.

Long-term annealing at 1100°C leads to crack formation in the material. It is assumed that the cracks are caused by thermal stresses appearing because of the different thermal strains in the components. The diffusion zone formed is very brittle, and appears to be unable to relax the thermal stresses (their value is higher than the ultimate strength).

The stability of a structure of composites with limited solubility of the components can be increased in two ways. In the first way a protective coating is given to the fibers which functions as a barrier against diffusional fluxes, and in the second way the thermodynamic stability of the matrix, preliminary saturated with alloying elements is used. The dissolving power of such a matrix should be reduced to a minimum.

Dean /43/ impregnated aligned tungsten fibers with liquid alloys Nimocast-258 and EPD-16 in vacuo. Because the process was so rapid (it lasted only a few seconds) dissolution of the fibers in the matrix could be greatly reduced. The thickness of the diffusional zone was a few μ. At temperatures below 900°C the strengthening effect was slight; at higher temperatures the strength of the material was close to the rated strength.

The long-term strength of the composite at 1100°C increases linearly with increase in the volume fraction of the fibers, and approaches the long-term strength of the tungsten wire.

Annealing tests (100 hr, 770°C) showed that the interdiffusion between matrix and fibers is inconsiderable. Annealing for 1000 hr resulted in a diffusion zone 0.025 mm thick.

Hot pressing a powder of alloy Hastelloy-X with W and Mo wires /44/ made it possible to obtain a composite which had an ultimate strength of 42 and 28 kg/mm^2, respectively, at 1090°C (the tungsten fiber content was 37 vol % and the molybdenum fiber content 36 vol %). The strength of the nonreinforced alloy was 7 kg/mm^2 at this temperature.

Ellison and Harris /45/ studied the short-term strength and creep of alloy Inconel-600 reinforced by tungsten fibers. When the fiber content was up to 27 vol % the ultimate strength increased only slightly. Ellison and Harris /45/ assumed that the critical fiber fraction was not attained in their tests. The yield point increased with increase in the volume content of the fibers, and the ductility decreased.

An increase in the fiber level leads to a longer service life of the specimens in creep tests and to a decrease in creep deformation. The positive effect appears even if the tungsten content is very low (0.42 vol %). Ellison and Harris believe that the fibers block the grain boundaries and inhibit crack propagation. With a higher fiber content the conventional reinforcing mechanism begins to act. The fibers take up the larger part of the load, and consequently strengthening is observed.

Vasilos and Wolf /46/ report the production of a nickel-tungsten fiber composite. The fibers were introduced into the matrix by electric molding. The authors do not give any details, and report only that the material was obtained at a low temperature, and that the nickel matrix was considerably reinforced (the ultimate strength was as high as 100 kg/mm^2).

8. Composites based on titanium

Jech et al. /20/ obtained very promising results in tests on the reinforcement of titanium or the alloy Ti—6Al—4V with molybdenum wires. The matrix powder-molybdenum wire mixture was pressed, sintered, subjected to hot electrolytic treatment, and finally rolled at elevated and room temperatures. The molybdenum fibers were drawn along the specimen axis. The titanium 20% of molybdenum composite had a higher temperature of pronounced weakening and better mechanical properties than the nonreinforced metal (Figure XI. 17).

At 538°C and a stress of 14 kg/mm^2, a composite of titanium — 10 vol % of molybdenum fibers was fractured after 100 hr, while pure titanium was fractured after 0.1 hr (Figure XI. 18).

The ultimate strength of the Ti—6Al—4V alloy containing 20 vol % of molybdenum wire at 760°C was 30 kg/mm^2, while the ultimate strength of the nonreinforced alloy was 9 kg/mm^2 (Figure XI. 19). The dependence of the modulus of elasticity on the volume fraction of the fibers is almost linear. An addition of 40 vol % of fibers increases Young's modulus by a factor of almost 2 at room temperature, and by a factor of more than 2.5 at 538°C.

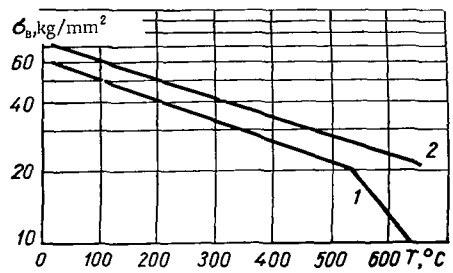

FIGURE XI.17. Temperature dependence of the ultimate strength of titanium (1) and of the titanium-20 vol % of molybdenum composite (2).

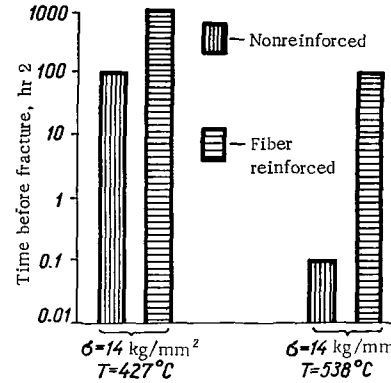

FIGURE XI.18. Comparison of the time before fracture of titanium and titanium reinforced by 10 vol % of molybdenum fibers.

Carlson and Tomalin /44/ studied a composite consisting of Ti – 6Al – 4V alloy and boron fibers. The composite was produced by hot pressing the matrix metal sheets between which the fibers were placed. The strength of the material which contained 20 vol % of boron did not attain the theoretical value; this is explained by deterioration during production. At temperatures above 705°C long-term residence under pressure leads to chemical reactions between the matrix and fibers, with the formation of the brittle compound TiB_2. The introduction of hydrides (TiH_2) made it possible to reduce the time of hot pressing to 10 min at 760°C (pressing without additives lasted 27 hr at 815°C).

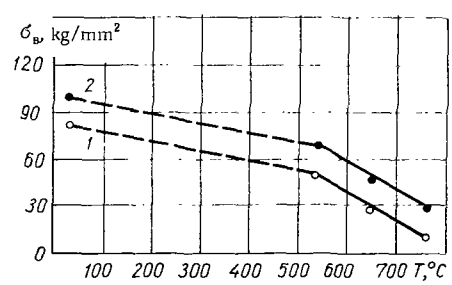

FIGURE XI.19. Temperature dependence of the ultimate strength of the alloy Ti – 6Al – 4V (1) and of the same alloy reinforced with molybdenum fibers (2).

9. Composites based on iron, nickel, magnesium, and their alloys

Kelsey, as reported in /24/, studied ways of reinforcing iron with filamentary crystals of alumina. The mixture of the iron powder and a felt of whiskers was fused in an argon atmosphere. The ultimate strength of the composite with 36 vol % of fibers was 166 kg/mm^2, which is almost three times the strength of the nonreinforced iron.

Beskorovainyi and Fridman /28/ described the properties of cast iron reinforced by steel wire. This material had an impact strength 2 — 4 times that of pure cast iron; the fatigue limit of the composite was 80% higher.

Colling /50/ studied iron alloys with 1.35 % of Si and 50% of Ni reinforced by tungsten fibers with a diameter between 30 and 250μ. The specimens were obtained by rolling the matrix sheets together with the wire. The fiber content was 8 — 15 vol %. The rolled specimens were coated with nickel and stress-relieved in a hydrogen atmosphere at 750°C. The composite strength increased with increase in the tungsten concentration.

This author also found that when an external magnetic field is perpendicular to the fibers, the coercive force increases linearly from 95 to 170 amp/m with increase in the tungsten level. But if the magnetic field is parallel to the fibers, the coercive force decreases from 95 amp/m for the pure matrix to 55 amp/m for the composite containing 8 vol % of tungsten, and then remains constant. Such materials can be used for the production of the rotors of electric motors in spacecraft.

A study of the compatibility of boron or silicon carbide fibers with iron, cobalt, and beryllium carried out by Schneidmiller and White /47/ showed that boron actively begins to react with the first two elements at temperatures above 700°C, while silicon carbide reacts above 800 — 850°C only. Because of the reactions on the interface, a new, very hard phase was formed. The stability of the matrix toward boron and silicon carbide increases in the sequence nickel—cobalt—iron—beryllium. The interaction of the fibers with beryllium was slight even when the composite was annealed for 100 hr at 1000°C.

Baskey /20/ studied the mechanical properties of pure cobalt and alloy L-605 (20% of Cr, 15 % of W, 10% of Ni, 0.1 % of C, remainder Co) reinforced by tungsten fibers. The ultimate strength of the hot-pressed composite with cobalt, containing 18 vol % of fibers, was 4 kg/mm^2 at 1093°C, compared to 1.9 kg/mm^2 for pure cobalt. The strength of alloy L-605 increased only after additional rolling, when the fibers became oriented.

Chuang /48/ reports on the high mechanical properties of the magnesium-boron fiber composite. The ultimate strength of magnesium reinforced by felt made of stainless steel /49/ increased five times, and the specific strength almost 3 times, when the material contained 27 vol % of fibers.

10. Fiber-reinforced ceramic materials

Ceramic materials are characterized by a high melting point, a high compressive strength retained at fairly high temperatures, and high

resistance to oxidation. These properties have been utilized for a long time in the production of furnace linings, refractory articles, etc.

In modern times, when ceramics are used as a structural material, they must have much better properties. Moreover, ceramic materials must have a high tensile strength, and a high impact strength, and must be able to withstand vibration and thermal shocks. Some metals have these properties. After the properties of ceramics and metals had been compared, composites were created in which the ceramic matrix was combined with metallic powder, which formed inclusions (cermets). Further research showed that an even better effect is achieved by introducing metal fibers into the ceramic matrix. Thus, for example to attain an equal thermal-shock stability, 3 times more metal powder had to be introduced than fibers with a length-to-diameter ratio of 20:1 /51/. Later, ceramic fibers were added to the ceramic matrix. At present, ceramic materials reinforced by metal or ceramic fibers are termed reinforced ceramics. In these materials the load is transferred from the weak matrix to the stronger fibers. But an increase in the ultimate tensile strength is not always observed in the reinforced materials. In some cases the reinforced material is weaker than the matrix. This is explained by the combination of a low plasticity with a high modulus of elasticity during tension in the ceramic material, so that the elongation of the matrix at its breaking stress is insufficient to transmit the larger part of the load to the fibers. This difficulty can be avoided by using fibers with a high modulus of elasticity, or by prestressing the fibers when they are quite firmly bound to the matrix. The fibers can be stressed either mechanically or thermally. Thermal stresses can be employed only if the thermal expansion coefficient of the fibers is larger than that of the matrix. In this case, if the system is cooled after heating, compressive stresses arise in the matrix. But if the thermal expansion coefficient of the fibers is less than that of the matrix, tensile stresses will appear in the matrix. These may lead to cleavage of the material, or the microcracks propagating from one fiber to another may lower the ultimate tensile strength of the composite without fracturing it.

The improvement in the impact strength of the reinforced ceramic is explained by a better distribution of mechanical stresses, and inhibition of crack propagation in the matrix by the fibers, which also explains the thermal-shock stability of the reinforced ceramic.

Reinforced ceramics are produced by hot pressing, or by pressing followed by sintering or slip casting. In every individual case the suitability of the method must be evaluated. Thus, when ceramic materials are produced by pressing and sintering composites reinforced by metal fibers, the fibers hinder the compression of the ceramic powder. When the pressure is removed, the products have a tendency to revert to their previous form. This is especially marked if the metal fibers have a large diameter, or their volume fraction is large.

We must also allow for the ability of metallic fibers to recrystallize at high temperatures. The fiber geometry is of great importance in the production of the composite. This is explained by the fact that not only diffusional and chemical processes but also purely mechanical ones affect the fiber-matrix bond. Bonding can be improved by producing rough surfaces by piling or by etching. The fibers and matrix react preferentially on the interfacial area. Metals (Cr, Fe, Co, Mo, Ni) which have surfaces

covered by an oxide film readily react with the ceramic to form spinels. If the oxygen level in the charge is decreased, the reactions take place less readily. In the Al_2O_3—Fe system the formation of spinel due to oxygen transfer occurs according to

$$Fe + O + Al_2O_3 \rightarrow FeAl_2O_4.$$

To ensure a better reaction between the matrix and the reinforcing metals or alloys which have no surface oxide film, catalysts must be used.

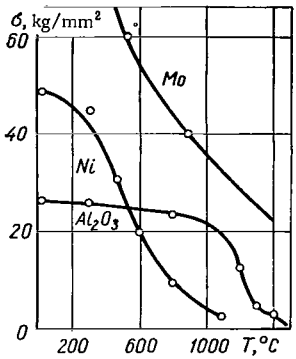

FIGURE XI. 20. Temperature dependence of the ultimate strength of Al_2O_3, Mo, and NI.

The mechanical strength of the composite depends also on the fiber diameter and the fiber level.

The corrosive resistance of a metal-fiber reinforced ceramic at high temperatures is determined by the corrosive resistance of the fibers at the same temperatures. It will increase at a lower gas permeability of the matrix, and if less cracks are present on the ceramic surface. Reinforced ceramics have a higher heat resistance than pure ceramics. The strength of the ceramic material at high temperatures does not decrease as much as that of the metal (Figure XI. 20).

Fiber alignment is very important. The fibers may be distributed over the matrix in an oriented fashion or randomly. The orientation of the fibers in a material must be known when selecting the conditions of operation.

At present, numerous materials are known based on a ceramic matrix and reinforced by fibers of various types obtained by different methods (Table XI. 4).

Reinforced ceramic coatings are becoming increasingly popular. When selecting materials we must allow for the thermal expansion coefficient of the matrix, fibers, and support, the operating temperatures of the coatings, and the corrosion resistance of the fibers during operation. An evaluation of stresses arising during operation of the coating is of importance. The requirements for fusibility at high temperatures depend on the depth at which the fibers are embedded in the matrix material. If the fibers are sensitive to corrosion, a protective coating must be applied to the fiber surface.

TABLE XI.4. Reinforced ceramics and methods for their production

Fiber	Matrix	Production process
Mo	Li_2O, Al_2O_3, $8SiO_2$	Hot pressing
Mo, steel	Al_2O_3, ZrO_2	" "
Nb	Al_2O_3 + 30% Cr	" "
W, Mo, Th	Al_2O_3	Slip casting
W, Mo	Kaolin, silicon, feldspar, Al_2O_3, ZrO_2, mullite, ThO_2	Hot pressing
W, Mo	Mullite + 20% Cr	" "
W	Si_3N_4, $ZrSiO_4$	Pressing and sintering
Mo	MgO, SiO_2	Hot pressing

Ceramic composites reinforced by ceramic fibers have many advantages over ceramic materials reinforced by metal fibers. These include: small differences in Young's moduli and thermal expansion coefficients; chemical affinity; the oxide fibers are not subjected to oxidation during production and operation of the composite.

11. Composites based on alumina and silica

Walton and Paulos /52/ report data on composite materials obtained by slip casting from alumina reinforced by steel-430 or nichrome fibers and from silica reinforced by the same fibers. The authors studied the changes in the modulus of elasticity as a function of the volume content of the fibers, and of the form in which the fibers were introduced into the matrix. It was found that the Young's modulus of composites reinforced by fibers is higher than the strength of these composites reinforced by "wool."

The bending strength of alumina reinforced by fibers is lower than that of the nonreinforced material. This is explained by the presence of microcracks which arise on heating because of the differences in the thermal expansion coefficients of the fiber and Al_2O_3. It was assumed that sintering at a higher temperature will help to eliminate the cracks. The strength of materials reinforced by nichrome fibers is higher than that of steel-fiber reinforced composites; this is because of the different fiber levels and the higher strengthening effect of the nichrome fibers.

Miller, Singleton and Wallace /53/ studied a hot-pressed composite consisting of a mullite matrix and W or Mo fibers. The authors found that 20 vol % of the fibers (diameter 5μ, length 1,500μ) increased the modulus of elasticity by 70% at 20°C. When tested for thermal stability the same composite had no fracture symptoms after 600 thermal cycles (maximum temperature 1315°C, minimum temperature 230°C, heating 5 sec, cooling 4 sec), while pure hot-pressed mullite was fractured after 180 cycles. The authors also studied composites reinforced by W and Mo fibers coated by diffusion with the silicides of the corresponding metals. These coatings slightly improve the oxidation resistance of the composites. After 30 min at 1,200°C the weight losses caused by the vaporization of molybdenum oxide were 2 and 3% for coated and uncoated fibers, respectively. Coating with silicides does not lead to fiber recrystallization (Figure XI. 21). However, after hot pressing grains begin to grow on the surfaces of the uncoated fibers; no microcracks appear in the mullite matrix, and recrystallization commences from the fiber surface (Figure XI. 22).

Complete recrystallization and considerable grain growth after hot pressing are observed in the composite with the coated tungsten fibers (Figure XI. 23), but no microcracks are found in the matrix. Figure XI. 24 shows the photomicrographs obtained by an electron microscope. The interphase layer ensures a firm mechanical bond between the mullite and the tungsten fibers.

In /51/ tests are described on composites consisting of a kaolin (50 wt %), silica (30 wt %), and feldspar (20 wt %) matrix Tungsten fibers (diameter 50μ, length 3.2 mm) were used for reinforcing. To prevent the oxidation of

FIGURE XI.21. Structure of *W* fibers coasted with WSi (× 450).

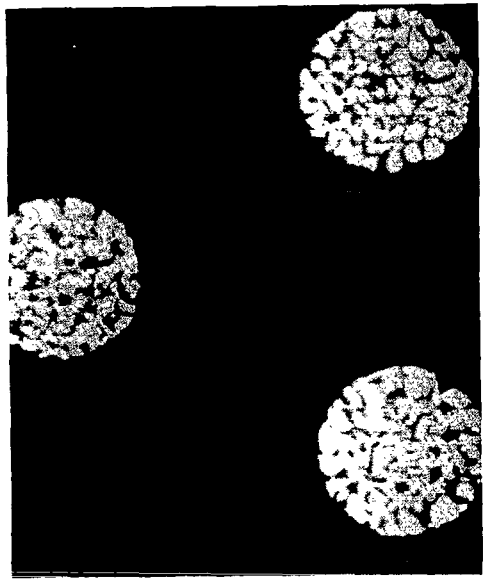

FIGURE XI.22. Structure of uncoated W fibers in a mullite matrix after hot pressing.

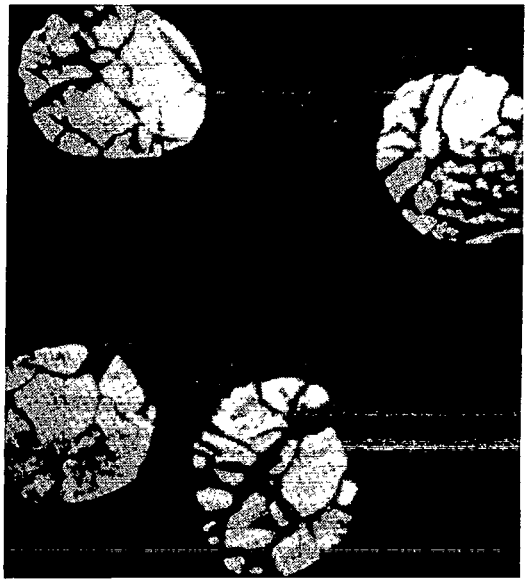

FIGURE XI.23. Structure of W fibers coated with WSi in a mullite matrix after hot pressing.

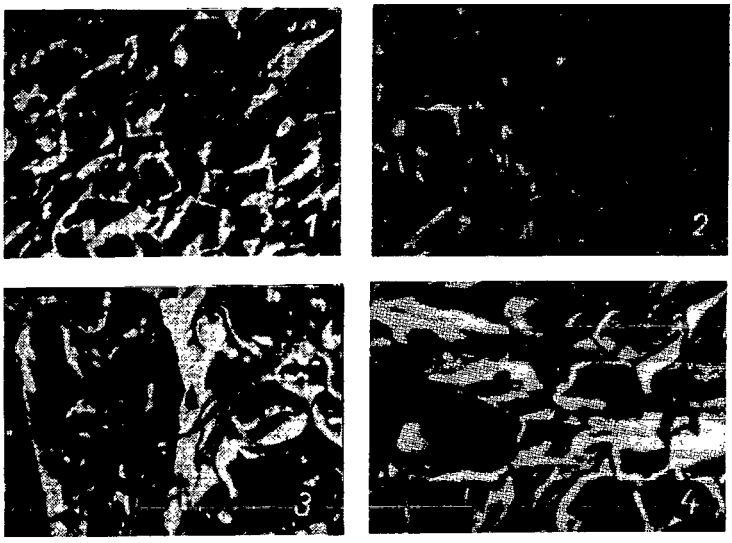

FIGURE XI.24. Structure of the composite mullite-tungsten fibers after hot pressing (× 2500):

1 — uncoated fibers; 2 — fibers coated with WSi_2; 3 — cracks in the interphase layer and tungsten fibers (fibers uncoated); 4 — cracks in the interphase layer (fibers coated with WSi_2).

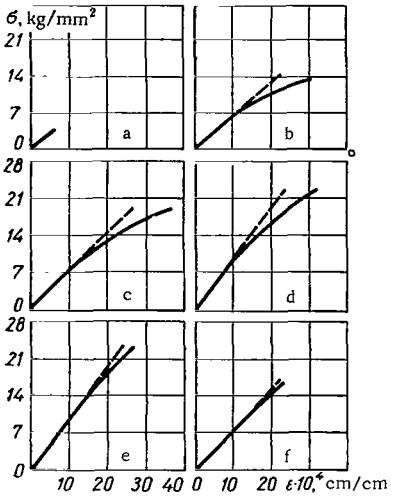

FIGURE XI.25. Stress-strain curves for the composite consisting of ceramic and tungsten fibers at various contents of tungsten (%):

0 (a); 10 (b); 20 (c); 30 (d); 40 (e); 50 (f).

tungsten, the ceramic was preliminarily heated. Figure XI. 25 shows the stress-strain curves for the these materials with various fiber levels. It can be seen that if the volume content of the fibers is higher than 40%, the strength properties of the composite deteriorate, apparently because of a decrease in the composite density due to the increasing fiber level.

Smica et al. /56/ obtained the relationship between the fiber concentration and the strength before and after thermal stability tests for a ceramic consisting of 58.5 vol % of mullite and 41.5 vol % of Al_2O_3 reinforced by molybdenum fibers (Table XI. 5). A higher fiber concentration increases the resistance to thermal shocks.

Data on the effect of the diameter of the fibers on the modulus of elasticity of the composite are shown in Table XI. 6.

Liva, Locke and Legget /57/ prepared a material consisting of alumina reinforced by corrugated stainless steel tapes. Aluminum phosphate was used as the binder. The thermal insulating properties of this material made it possible to increase the temperature of the combusion chamber of a jet motor by 260°C. This composite withstood several heating cycles up to 1,900°C.

TABLE XI. 5. Strength of composite alumina-mullite reinforced by molybdenum fibers

Size of fiber, mm	Content of fibers, vol %	Ultimate strength, kg/mm²	
		before thermal stability test	after four thermal cycles (heating to 1200°C, cooling in air)
0.05× 3.2	0	15.1	0
	4.2	16.8	1.0
	10	16.0	13.9
	20	16.6	14.6
	30	18.1	21.5
0.05× 12.7	10	10.2	8.3
	20	18.5	22.2
0.25× 3.2	10	14.3	8.0
	20	10.9	8.8
0.25× 12.7	10	15.0	6.2
	20	13.3	10.5

Moore et al. /58/ developed a method for preparing reinforced refractories by plasma spraying the refractory material, for example, alumina, onto a rotating metallic support. The reinforcing agent, tungsten wire, is simultaneously wound. The sire is fed through a tube filled with inert gas. The metallic base is then removed by chemical dissolution or blasting.

TABLE XI.6. Modulus of elasticity of ceramic alumina-mullite, reinforced by molybdenum fibers

Size of fiber, mm	Content of fibers, vol %	Modulus of elasticity, $\times 10^{-3}$ kg/mm^2		Modulus of elasticity after four thermal cycles, kg/mm^2	Fraction of total stress taken up by fibers (theoretical)	Stress in material (theoretical), kg/mm^2
		in practice. 20°C	theoretical			
0.203 × 6.3	30	28.3	25.0	19.5	35.0	12.7
0.050 × 3.1	30	24.9	25.0	21.5	35.0	14.0
0.150 × 6.3	43	25.5	26.1	25.8	48.8	13.2
0.150 × 76.2	25	24.7	25.0	22.4	29.0	15.9
0.50 × 1	42	22.5	23.9	9.8	5.2	Mean stress
Without fibers	—	23.3	—	—	—	14.0

Reinforced refractories can be used in induction coils or resistors intended for long service.

12. Composites based on other ceramic materials

Tinklepaugh et al. /54/ studied the modulus of elasticity of the $SrZrO_3$ system with 20 — 30 vol % of Mo fibers added. The fiber length was 1.6 mm and diameter 0.05 mm. It was found that with increase in the volume fraction of the fibers the modulus of elasticity increases from 1.4×10^6 to 1.7×10^6 kg/cm^2.

Miller et al. /53/ report data on the strength and thermal stability of strontium zirconate reinforced by 20 — 30 vol % of tungsten. These authors observed an increase in the strength and thermal stability of the composite which is proportional to the volume fraction of the fibers.

Liva, Locke and Legget /57/ described a composite based on zirconia with a phosphate binder. The composition of material with binder was as follows (wt %).

Base	Binder
ZrO_2 — 80	$NH_4H_2PO_4$ — 9
Cr_2O_3 — 15	H_2PO_3F — 5
ZrO_2 — 5	H_2O — 15

This mixture was applied onto a sheet consisting of alloyed Ti — Mo steel (0.5% Ti and Mo) to which corrugated tapes of molybdenum alloy were soldered. Under the influence of the plasma jet (temperature 2,300°C) no cracks were formed in the material. But, microcracks were observed in the system zirconia-tantalum fiber because of the large differences in the thermal expansion coefficients.

Baskin and Arenberg /59/ give the comparative characteristics of the thermal stability of a composite consisting of thoria and molybdenum fibers. It was found that specimens with such fibers are more resistant to thermal shocks than specimens containing approximately the same amount of molybdenum powder. Figure XI. 26 shows the temperature dependence of the thermal conductivity of pure ThO_2-based ceramic and of the same ceramic reinforced by molybdenum fibers. It can be seen that the thermal conductivity of the ThO_2 ceramics containing 10 vol % of molybdenum is higher than that of the nonreinforced ceramic.

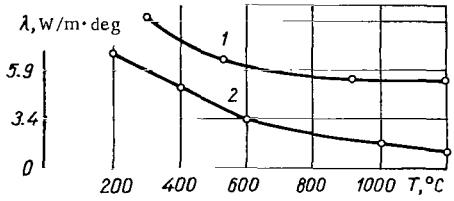

FIGURE XI.26. Temperature dependence of the thermal conductivity of ThO_2 and of ThO_2 reinforced by molybdenum:

1 — ThO_2 + 10 vol % of Mo; 2 — ThO_2.

Baskin et al. /60/ studied the hot-pressed composite made of pure ThO_2 reinforced by 2.5 — 20 wt % of molybdenum fibers. The fiber length was varied between 5 and 12.5 mm, and the fiber diameter between 0.05 and 0.0125 mm. It was found that after the addition of 2.5 — 10 wt % of molybdenum fibers, the compressive and bending strengths and Young's molecules are appreciably lower than those of pure thoria. If the fiber level increases above 10%, the properties of the material improve, but are nevertheless below those of pure ThO_2. A microscopic study of the reinforced material shows fine cracks on the ThO_2-molybdenum fiber interface, which close if the material is heated to 650°C. This leads to an increase in the modulus of elasticity.

Thermal conductivity is very important in industry, especially in the production of parts based on UO_2 for nuclear reactors. The thermal conductivity of uranium dioxide reinforced by molybdenum fibers is about 30% higher than that of the pure ceramic.

It can be seen from the above that the reinforcement of materials by fibers is very promising, and that it is worthwhile carrying out large-scale research in this direction.

Bibliography

1. Fedorchenko, I. M. and R. A. Andrievskii. Osnovy poroshkovoi metallurgii (Fundamentals of Powder Metallurgy). Kiev, Izdatel'stvo Ukrainskoi SSSR. 1963.

2. Karpinos, D. M. et al.— Poroshkovaya Metallurgiya, 5. 1968.
3. Ivanova, V. S., I. M. Kop'ev, and L. M. Ustinov. Itogi nauki metallovedenie i termicheskaya obrabotka, 1965. (Progress of Science, Physical Metallurgy and Heat Treatment). Moskva. VINITI. 1966.
4. Kraft, R. W.— J. Metals, 18:2. 1966.
5. Mekhanicheskie svoistva novykh materialov (Mechanical Properties of New Materials). Moskva, Mir. 1966.
6. Kelly, A. The Strengthening of Metals by Dispersed Particles.— Proceedings of the Royal Society. 1964.
7. Kelly, A. and W. R. Tyson.— J. Mech. Phys. Solids, 13:6. 1965.
8. Kelly, A. and W. R. Tyson.— J. Mech. Phys. Solids, 14:4. 1966.
9. Metallovedenie i termicheskaya obrabotka (Physical Metallurgy and Heat Treatment).— Ekspress-informatsiya, 4. 1965.
10. Cratchley, D.— Powder Metal, 11. 1963.
11. Ustinov, L. M. Issledovanie mechanicheskikh svoistv i makromekhanizma razrusheniya medi armirovannoi vol'framovymi voloknami (Study of the Mechanical Properties and Macromechanism of Fracture of Tungsten-Reinforced Copper). Author's Summary of Candidate's Thesis, IMET AN SSSR. Moskva. 1968.
12. Tuchinskii, L. I. Issledovanie uslovii polucheniya i svoistv kompozitsionnykh materialov, armirovannykh tugoplavkimi voloknami (Production Conditions and Properties of Composites Reinforced by High-Melting Fibers). Author's Summary of Candidate's Thesis, IPM AN Ukrainskoi SSR, Kiev. 1968.
13. Ham, R. H. and T. A. Place.— J. Mech. Phys. Solids, 14. 1966.
14. Petrasek, D. W.— Trans. AIME, 6. 1966.
15. Petrasek, D. W. and J. W. Weeton.— Trans. AIME, 230, 977. 1964.
16. Cooper, G. A.— J. Mech. Phys. Solids, 14:2. 1966.
17. Greenstine, R.— Metals Engng. Quart., 7:1. 1967.
18. Webb, W. and W. Forgeng.— Acta Met., 6. 1958.
19. Lemkey, F. D. and K. W. Kraft.— Rev. Sci. Instr., 33(8). 1962.
20. Metallovedenie i termoobrabotka (Physical Metallurgy and Heat Treatment).— Ekspress-informatsiya, 4. 1965.
21. Parikh, N.— In: Voloknistye kompozitsionnye materialy, Moskva, Mir. 1967 [Russian translation].
22. Petch, N. I.— J. Iron Steel Inst., 25. 1953.
23. Sutton, W. H.— Raketnaya tekhnika, 4, 1962.
24. Sutton, W. H. and J. Chorne.— In: Voloknistye kompozitsionnye materialy. Moskva, Mir. 1967. (Russian translation).
25. Sutton, W. H. and J. Chorne.— Metals Engng. Quart., 3:1. 1963.
26. Ivanova, V. S. et al. Ustalost' i khrupkost' metallicheskikh materialov (Fatigue and Brittleness of Metallic Materials). Moskva, Nauka. 1968.
27. Parrat, N. I.— Powder Metal., 7:14. 1964.
28. Beskorovainyi, N. M. and Ya. B. Fridman. Struktura i prochnost' metallov i splavov (Structure and Strength of Metals and Alloys).— In: Nauchnye Raboty Moskovskogo Mekhanicheskogo Instituta, 5, Moskva. 1953.
29. Vlasova, P. T. et al.— Alyuminievye splavy, 2. Moskva, Oborongiz. 1963.

30. Appl. Mater. Res., 3(3):148. 1964.
31. Forsith, P. I., R. W. George, and D. A. Ryder.— Appl. Mater. Res., 3(4):23. 1964.
32. Morley, I. G.— Proc. Royal Soc. A. 282, 1388, 43. 1964.
33. Cratchley, D. and A. A. Baker.— Metallurgia, 69:14. 1964.
34. Whitehurst, H. B., I. W. Michener, and P. A. Lockwood.— Proc. Sixth Sagamore Res. Conf., pp. 248—276, Aug. 1959.
35. Koppenaal, T. I. and N. M. Parikh.— Foundat. Chicago, 3:7. 1961.
36. Greenstine, R. B.— Metals Engng. Quart., 7:1. 1967.
37. Hertzberg, R. W., F. D. Lemkey, and J. A. Ford.— Trans. AIME, pp. 233—342. 1965.
38. Hertzberg, R. W.— In: Voloknistye kompozitsionnye materialy, Moskva, Mir. 1967. (Russian translation).
39. Cratchley, D.— Metal. Revs., 10:37. 1965.
40. Eremenko, V. N. and Yu. V. Naidich. Zmochuvannya ridkymy metalamy poverkhon' tugoplavkykh spoluk (Wetting of High-Melting Alloys by Liquid Metals), Kyyiv, Vydavnytstvo AN URSR. 1958.
41. Amstrong, W., A. Chaklader, and D. Clarke.— J. Amer. Cer. Soc., March, 1962.
42. Method of Production of Fiber-Reinforced Metals. US Patent, 29 — 420, 5, 3218697.
43. Dean, A. V.— J. Inst. Metals, 95:3. 1967.
44. Carlson, R. G. and D. S. Tomalin. Advanced Fibrous Reinforced Composites, F/45—F/69, North Hollywood, Calif. 1966.
45. Ellison, E. G. and B. Harris.— Appl. Mater. Res., 5:1. 1966.
46. Vasilos, V. and E. Wolf.— J. Metals, 18:5. 1966.
47. Schneidmiller, R. F. and J. E. White. F/53—F/62, North Hollywood, Calif. 1966.
48. Chuang, K. G. F/91—F/104, North Hollywood, Calif. 1966.
49. Read, R.— Mater. Design Engng., 50:7. 1959.
50. Colling, D. A.— J. Appl. Phys., Part 1, 39:2. 1968.
51. Voloknistye kompozitsionnye materialy (Fiber Composites). Moskva, Mir. 1967.
52. Walton, I. D. and N. E. Paulos.— J. Amer. Cer. Soc., 45:11. 1962.
53. Miller, D. G., K. H. Singleton, and A. V. Wallace.— J. Amer. Cer. Soc., 45:5. 1966.
54. Tinklepaugh, Funk, and Sullivan.— Metals Engng. Quart., 3:56. 1963.
55. Carroll-Proczynski, C. Z. Advanced Materials. Guilford, Astex Publishing Company. 1962.
56. Smica, J. J., W. R. Hoskyns, B. R. Goss, and J. H. Connor. WADC TR 58-452, Part 2, Jan., 1960.
57. Liva, A. V., S. R. Locke, and H. Legget. Composite Cer.— Metal. System, Astronautics, 58:27, April. 1961.
58. Moore, Norman, and Clement. US Patent CI 1B2B CYM, HIS (Co46), No. 95—3651.
59. Baskin, V. and C. Arenberg. Thoria Reinforced by Metal Fibers.
60. Baskin, V. and V. Harada.— J. Amer. Cer. Soc., 43:9. 1960.
61. Hoffmann, U. Faserverstärkte keramische Werkstoffe.— Deutsch. Cer. Ges., 43(25):337—345. Berlin. 1966.

Chapter XII

REINFORCED PLASTICS

1. Main principles of the production of reinforced plastics

Reinforced plastics are composites consisting of a filler of very strong fibers and a polymeric matrix.

The filler gives strength and rigidity to the system, and the polymeric matrix ensures a monolithic material which is moldable. Natural products (cotton, flax, jute, wood) and also synthetic (glass fibers, asbestos, and others) are used as the fiber material.

Materials consisting of two intrinsically differing components are required by modern engineering, which demands a combination of properties such as strength, low density, stiffness, and heat and corrosion resistance in structural materials. This combination is achieved by an intelligent selection of the materials for the matrix and filler and by arrangement of the fibers.

Short fibers of cellulose, asbestos, and staple glass fibers can be introduced into the composite without any pretreatment during molding. Moreover, before impregnation by the polymer, the short fibers can be combined by various methods: stable fibers into mats, natural and cellulose fibers into paper, and short natural fibers into threads for subsequent fabric production.

The fabrics used are prepared from threads of natural fibers, continuous synthetic fibers, and glass fibers.

Various thermoreactive and thermoplastic resins are used as the polymer matrix. The first reinforced plastics were prepared for the electrical industry; they were made of phenol resins and reinforced by fabric or paper /1 — 2/. At present phenol resins (polyesters, melamine, organosilicon, and epoxide) are being used on a large scale.

The reinforced plastics will have a wide variety of mechanical and technological properties depending on the type of reinforcement and the polymer matrix. According to the pressure under which the plastics are pressed, we distinguish high- (above 70 kg/cm^2), medium- and low-pressure (up to 28 kg/cm^2) plastics.

Plastics are widely applied in various engineering branches because of their good technological characteristics. The specific strength of plastics is frequently higher than that of metals. However, the increased brittleness and the frequently insufficient rigidity, low mechanical strength, and

thermal stability of popular laminated plastics used in industry such as textolite and getinax explain why these plastics have a limited use in structures subjected to mechanical and thermal loads. Therefore, the possible combination of fibers and polymer matrix, which have high structural and technological properties, into a single material is very important.

As mentioned by Kargin /5/, the idea of reinforcement was adopted directly from nature. Most animal and plant tissues consist of reinforced materials.

Glass-fiber reinforced plastics are very promising for the production of materials with high mechanical parameters /6/. The progress in polymer chemistry and the technology of high-strength (up 200 kg/mm^2), corrosion-resistant, fireproof, water- and mold-resistant fibers with a low weight density, and of different glass-fiber products made from them promoted the creation of glass-fiber reinforced plastics /8–26/. These materials have a high specific strength, and thermal stability, low thermal conductivity, and also good technological and electric insulation parameters. The specific strength of various glass-fiber reinforced plastics produced in the Soviet Union, and the strength of metals and other structural plastics are shown in Table XII. 1.

TABLE XII. 1. Specific strengths of various structural materials /6/

Material	Brand	Weight density, γ, g. cm^3	Young's modulus, kg mm^2	Specific strength		Specific rigidity
				tensile	compressive	
Chrome-nickel steel	30KhGSA	7.85	20000	15.3	13.4	2550
Duraluminum	D16T	2.80	7200	16.4	10.0	2570
Glass-fiber reinforced plastic	SVAM	1.90	3500	26.0	22.0	1840
Glass textolite	KAST-V	1.82	2200	16.5	10.4	1209
" "	EF-32-301	1.70	2200	24.0	17.0	1300
" "	ST-9IS	1.70	2000	23.5	8.8	1235
Structural textolite	PTK	1.35	1000	7.4	18.5	740
Plates of delta wood	DSP-10	1.35	3000	22.2	14.1	2222
Pine wood used for aircraft construction	DRS	0.52	1300	23.7	8.1	2500

The combination of a high mechanical strength with a low weight density, high chemical stability, and low thermal conductivity, makes it possible to use these materials in structures in which conventional materials are inefficient or even unsuitable.

2. Types and properties of glass fibers

Glass fibers have numerous advantages over other materials: they are prepared from raw materials which are in good supply; they have a high tensile strength (Table XII. 2) and a high modulus of elasticity; their resistance to fire and mold, and thermal stability are high; they are stable

in size; resistant to chemical agents and to the atmosphere; and have a low stretchability. They are used for the production of glass-fiber articles of various types.

TABLE XII. 2. Ultimate tensile strength of various fibers /6/

Material	Ultimate tensile strength, kg/cm^2	Material	Ultimate tensile strength, kg/cm^2
Glass	12600 – 22150	Wool	1200 – 1970
Asbestos	14060 – 21090	Natural silk	3200 – 5800
Jute	3100	Flax	3800
Cotton	2950 – 8790	Viscose rayon	2040 – 6200
Nylon	4570 – 8200		

For the production of glass fibers to serve as filler for polymers, borosilicate glass is used. The alkali content must not be higher than 2%; but the calcium-sodium glass sometimes used has an alkali content of 8 – 15%.

When selecting the glass type we must take into account the operating conditions of the product. Borosilicate glass is very stable in the atmosphere, and for this reason it is recommended as a filler for a polymer in a composite to be used in a wet environment. Moreover, borosilicate glass is used when high dielectric parameters are required or in the electrochemical industry.

Alkali-glass fibers have a rather low stability to moisture, but in acid media they are more stable than glass fibers made of borosilicate glass.

Glass fibers do not obey the fundamental laws of the strength theory derived for thin organic fibers; the strength of the latter is determined mainly by the high degree of orientation of the chain formations and the ordered structure.

When fibers are drawn from a glass melt, the fiber strength depends on the diameter; the thinner the fiber, the higher is its strength.

The determination of a correlation between the strength of glass fibers and the chemical composition of the glass is complicated, since the state of the surface of the glass fiber, the method of its production, the molding temperature, the cooling rate, and the test conditions may have a strong effect on the fiber strength.

The fiber strength also depends on the length of the test samples, but much less than on the diameter (Table XII. 3) /8 – 11/.

All the physical properties of glasses are the same in bulk and fiber samples; they depend mainly on the chemical composition of the glass.

The elastic properties are also a function of the chemical composition. For example, Young's modulus of quartz glass is between 10,000 and 12,000 kg/mm^2, Young's modulus of aluminoborosilicate glass (low alkali content) is 7,000 – 8,000 kg/mm^2, while Young's modulus for alkali glasses is between 4,000 and 6,500 kg/mm^2.

The mechanical (tensile) strength is much more dependent on the sample-size than on its chemical composition, and changes sharply from bulk to fiber samples.

TABLE XII. 3. Effect of fiber length on strength /12/

Fiber length, mm	Fiber diameter, mm	Tensile strength, kg/mm^2
5	9.0	150
10	9.5	122
20	10.0	121
45	9.0	115
90	9.7	76
185	9.7	87
1560	10.0	72

An attempt was made to explain the increase in the strength of the glass fibers by the orientation effect, as in the case of organic fibers /13/. Griffith explained that the increase in the strength of glass fibers with decrease in fiber diameter is due to the orientation of the molecular groups of the glass in the surface layer having a certain thickness. The author assumed that the molecular groups on the fiber surface are subjected to maximum attractive forces. Such a state ensures stability and strength of the surface layers of the glass fibers, and makes crack propagation difficult. However, the fundamental assumption of Griffith's theory, namely, that aligned molecular groups exist in the structure of thin glass fibers, is not confirmed, since if the assumption were true, the elastic properties of the fibers should also increase.

Reinkober /9, 14/ proved that the modulus of elasticity of quartz fibers increases with decrease in the fiber diameter: when the diameter was reduced from 80 to 5μ, the modulus of elasticity was doubled. Reinkober, like Griffith, considered that this strength increase is caused by the special properties of the surface. However, the data of Reinkober were disproved by the experiments of Aleksandrov and Zhurkov /15, 16/. These authors studied the elastic properties of quartz and glass fibers of different diameters, and concluded that the size factor has no effect on Young's modulus. Moreover, they also indicated the sources of error in the experiments of Reinkober. When they measured Young's modulus from the fiber elongation, Alexandrov and Zhurkov sighted two points on the fiber by two "coupled" microscopes to eliminate the effect of the unstressed section on the fiber deformation. Reinkober sighted only one point, and used only one microscope, and this led to the errors involved in measuring the elastic properties of the fibers.

Zak and Man'ko /17/ found that the Young's moduli are identical in large and small glass samples. Burov and Andreevskaya came to the same conclusion when they determined the modulus of elasticity of mirror glass /18/.

Thus, it was found from experimental data of various scientists that Young's modulus (for glasses of the same chemical composition) is the same for bulk samples and for fiber samples, irrespective of the fiber diameter.

Studies were also performed on the effect of the condition of the production of glass fibers /19 — 22/ and the effect of the environment /23 — 26/ on their mechanical strength.

If we summarize all these papers, we can conclude that the high strength of silicate fibers is due mainly to a reduction in the extent and number of dangerous defects (especially on the fiber surface). The formation of these defects depends on the method and conditions of production of the fibers, and on their chemical composition.

TABLE XII. 4. *Parameters of glass-fiber strands /6/*

Thread number	Designation of primary thread in metric system	Number of individual fibers in strand	Length of strand, m/kg	Fiber diameter, μ	Mean breaking stress of strand, kg
900	180	102	180000	4.5—5.6	0.272
450	90	204	90000	4.5—5.6	0.544
225	45	204	45000	6.3—7.6	1.088
150	30	204	30000	8.6—6.9	1.587

For the production of GFP, continuous glass-fibers are almost exclusively used. They are produced as follows. Glass in the form of sphere or glass face is placed into a platinum crucible fitted with an electric heater to melt the glass. The crucible has a perforated bottom with spinnerets (usually about 200). Under the action of its own weight the fused glass mass flows out of the spinneret, and when high-strength mechanical drawing is employed fibers of 4—5 μ diameter are obtained. After the fiber bundle leaves the crucible, it is subjected to sizing with a suitable agent. The fiber strand obtained is wound around a reel. The individual fibers combine to form a strand (Table XII. 4). The properties of the individual glass fibers are shown below /6/:

Property	
Weight density, g/cm^3	2.55
Coefficient of linear thermal expansion, $°C^{-1}$	0.0000049
Overall heat transfer coefficient, $W/m^2 \cdot deg$	1.009
Ultimate tensile strength, kg/cm^2	17550—22150
Young's modulus, kg/cm^2	700000
Relative elongation on tension, %	2—3

During the drawing process, the size is applied to the individual fibers. This process of sizing must protect the fibers against wear, combine the individual fibers into a single strand, the individual thread, and protect the threads from adhering to one another or to the reel. It should not complicate the removal of the strands from the reel, and should ensure that the individual threads are complete before they are used in subsequent processing into the fabric. The size must not dye the threads on aging, but should impart good adhesion to the glass surface, combine with any resin used for the preparation of laminated GFP, and protect the laminated GFP from environmental conditions (for example, moisture).

Up to the present no size has been produced which satisfies all the above requirements. For this reason, two fundamental types of sizing are

usually used. The first type, the so-called textile dressing, consists of a system of dextrin and oil emulsion, and leads to twisting and doubling of the strand.

The second type of sizing is based on polyvinyl acetate or an organic complex of chromium salts, or organic polysiloxanes. The dressed strand are suitable for processing into the corresponding yarn.

3. Types of reinforced plastics

The physicomechanical properties of reinforced plastics depend on the properties of the substance used for the reinforcing elements. From this point of view the following fundamental types are distinguished: getinaxes, in which the base is paper; textolites, in which the base consists of textile fibers and fabrics; wood plastics with the reinforcing material is made of plywood (delta-wood), chopped wood pieces, or sawdust.

The largest group of reinforced plastics are glass-fiber reinforced plastics (GFP). Their reinforcing structures are either glass fibers (SVAM, and others) or glass fabrics (glass textolites).

According to their structure, the GFP can be divided into the following three fundamental groups: glass textolites, unoriented and oriented GFP.

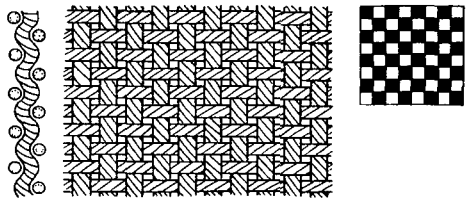

FIGURE XII. 1. Linen weaving.

Glass textolites. At present glass textolites are the most popular group of the widely applied GFP. They are used especially for products of complex configuration (hoods of automobile engines, ship hulls, etc.). The basis of this group is glass fabric. Its fibers (diameter $6-7\mu$) are subjected to the same textile treatment as conventional textile fibers. First threads are formed and then the fabrics are woven. The threads of the longitudinal (warp) and the transverse (weft) systems are interwoven so that the axial lines of the threads are curved. They form a "periodic" curve about the mean plane of the fabric. Figures XII. 1 – XII. 3 shows the main systems of reinforcing fabrics. Table XII. 5 gives the properties of typical fabrics used for reinforcing polymers.

The polymer matrix is applied to the fabric and fills the gaps between the threads. The filling is usually not complete, so that small voids remain which are filled with air or gases, usually released during pressing.

The glass fabric forms the layer element of the glass textolite. Various combinations of these layers make it possible to vary the properties of the glass textolite over a known range. The tensile strength of the glass

textolite is 30—50 kg/mm², while its ultimate compressive strength is 10—20 kg/mm² /28/. For the production of laminated plastics with the best mechanical properties, thin glass fabric is used. In some cases only the surface layers of the material are coated with glass fabrics. The strength of textolites decreases with increase in the thickness of the fabric used, which is best indicated by the values of the compressive strength. But the impact strength increases. This is probably because of the arrangement of the threads in the thick or thin fabric, and also in the fabric produced by linen or satin weaving.

In the fabric with linen structure, the crossed threads are undulated, and the action of the compressive stress is similar to the pressure upon a winding column, which deviates from the neutral axis and tends to break or bend.

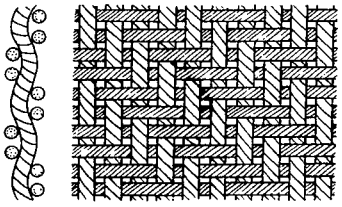

FIGURE XII. 2. Serge weaving.

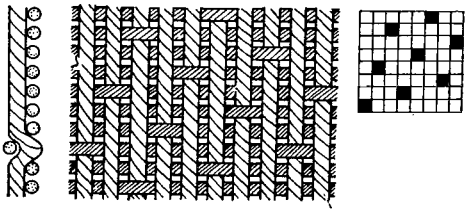

FIGURE XII. 3. 8-heald satin weaving.

To obtain stronger products we recommend either unidirectional (cord) fabrics or fabrics of 8-heald satin structure. In the first case the thick, most stressed threads are linear; such fabrics are weaker. If we use these fabrics with strong threads as the reinforcement in the direction in which the maximum stress is applied, the strength in the required direction is improved.

TABLE XII. 5. Main properties of fabrics of typical weaving types /6/

Property	Weaving type		
	linen	serge	8-heald satin
Nominal thickness, mm	0.15	0.28	0.20
Mean weight, g/m²	187	330	302
Density (number of threads per cm):			
warp	14.2	11.8	22.4
weft	12.2	11.8	21.3
Number of threads:			
warp	90—2/3	45—2/3	45—1/3
weft	90—2/3	45—2/3	45—1/3
Mean minimum breaking stress, kg:			
warp	83.4	127.4	122.5
weft	74.3	127.4	117.5

The so-called high-mode fabric consists of linear threads. This is achieved by using the system of the most loaded threads, consisting of two intersecting straight threads, which make up more than 90% of the glass fiber. The other 10% consists of threads interwoven in both directions around heavy threads, which imparts strength to the fibers. This phenomenon is of special importance when arranging the fabric by the positive method of contact forming (Figure XII. 4).

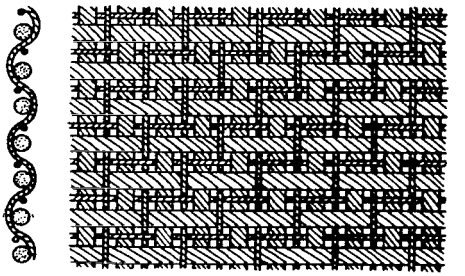

FIGURE XII. 4. Weaving of high-mode fabric.

The selection of fabrics used for laminated products depends on structural requirements.

Linen fabrics are employed if we have to ensure uniform strength of simply shaped products in all directions (especially in flat panels for electric insulation).

High-mode fabrics are used if we require good draping properties of the material, and a minimum shift of the threads.

Satin fabrics with a large number of threads in the repeat, and also serge fibers, are employed when good draping properties of the material are required (for example, when molding products with a double curvature), when we have to ensure strength in all directions together with a low weight and minimum expenditure of time and labor in the arrangement of the fabric on the form, and also when we want to obtain very strong laminated products. The advantages of such fabrics are their smooth surface and their nice appearance.

Cord fabrics are used for products with a maximum strength in a single direction when the load can be determined beforehand and the arrangement of the material must correspond to given requirements. These fabrics are also employed to impart additional stiffness to certain parts of the product, and to combine maximum strength in certain directions with a minimum weight.

For the preparation of structures with a crosswise (veneerlike) arrangement of the fabric, manual work is employed. This increases the cost of production.

Steklovoloknit is a plastic reinforced by glass mat. Mats are the most widely employed glass-fiber fillers after glass fabrics. Such a mat consists of chopped randomly distributed individual threads connected to one another by resin. Usually the length of the outer strands is 50 mm. Various

binders are used for mats employed for different purposes. The binder must combine the chopped strands, keep them in place, and impart sufficient strength to the glass-mat when packing it during the molding of the product. The binder must be neutral, that is to say, it must not accelerate or retard hardening of the resin. Finally, the binder used for the production of the mat must not affect the size.

We distinguish three main types of mats with a high, medium, and low solubility of the binder in the resin matrix.

1. Glass mats with a high solubility of the binder are used mainly for the production of transparent sheetlike material. The binder of a glass mat of such a type is readily dissolved in polyester resins, and remains soluble during curing. This property is of great importance in the production of transparent sheets of GFP. A glass mat of such type can be used for contact forming during manual or wet packing of the filler layers.

2. Glass mats with a medium solubility of the binder are used mainly for manual packing of the layers. The binder of the glass mat is slowly wetted by the resin. Therefore, the mat retains it strength during long-term packing when the products are molded.

3. Glass mats with a low solubility of the binder are not dissolved in the resin; this prevents excessive shift of the fibers during the pressing of GFP in metal molds.

The mechanically bound (sewn) mat is distinguished from the conventional mat made of chopped strands because its fibers are not bound by a binder, but mechanically, by mutually coupled fibers. For different molding processes glass mats of various types are used. Thus, a glass mat used for pressing in metallic molds by punch and die differs from a glass mat used for contact forming the product. Since for producing such a type of glass mat no binder is necessary, the mat is very quickly wetted by polyesters. This improves the quality of impregnation and helps to retain the strength of the GFP in the wet state. Moreover, a glass mat of such a type has very good draping properties, so that the material is rapidly shaped. In some cases this glass mat can be used in the uncut state for pressing in metallic molds and for vacuum forming.

The decorative mat is used for improving the surface of laminated plastic and consists of individual threads bound by a soluble binder. The decorative mat is a cloth 0.30 – 0.38 mm thick. To obtain a balanced laminated plastic, the mat is applied to both sides of the molded product.

Since glass-fiber materials in the form of mats are cheap, they are used when the cost of the product is of decisive importance (for example, when producing GFP sheets for roofs, hulls of boats, casks, etc.). However, the strength of fabrics and braids from strands is much lower than the sum total of the strengths of the component threads /29, 30/ because their parallel direction is impaired during meshing. Therefore, when a very high strength is required, plastics reinforced by individual fibers are used (oriented GFP).

Oriented glass-fiber reinforced plastics. Synthetic fibrous anisotropic materials (SFAM) were suggested by Burov as early as 1940. Structures of glass fibers oriented in a matrix, were originally intended as a steel substitute in the directed reinforcement of concrete constructions. The high

tensile strength (about $80-100\,kg/mm^2$ at a density of $1.8-1.9\,g/cm^3$) indicated a promising future, and the correctness of Burov's method.

Research at the Crystallographic Institute of the Academy of Sciences of the USSR made it possible to obtain oriented structures with very different properties: structural material with very good physicomechanical parameters, very thin electroinsulating films, systems of metallized glass and organic fibers able to conduct high-frequency currents and transmit light.

The materials produced by Burov were termed synthetic fibrous anisotropic structures, since these composites of man-made fibers, oriented in one or more given directions, showed very marked anisotropy in their mechanical properties.

The discovery in the last century of aligned structures in nature (animal bones, wood stems, bamboo, the chitin skeleton of insects), which were both strong and light, and the technological methods introduced at this period, led to the invention of orthotropic material, crossed plywood, at the end of the nineteenth century. However this material could be applied in constructions on a limited scale only, because of the rather poor physical and mechanical properties of the wood, and the great influence of moisture and solar radiation on the wood. Therefore, plywood was replaced by metals especially by light alloys, mainly in the aircraft industry.

Another step in the development of the principle of strength utilization of materials with a directed structure was the production of reinforced plastics which were not woven, and had many advantages over plywood.

Anisotropic structures which are not woven can be produced from various types of man-made fibers, oriented in different matrixes. The fiber material may be inorganic: glass, basalt, quartz, metals, silicates, or materials with a metallized surface. Organic and other fiber types can also be used. Organic polymers, organosilicon or organoaluminum can be used as the matrix. The variety in the properties of both components makes it possible to obtain materials with such different parameters that it is difficult to predict all the fields in which oriented structures will be applied.

The technology of oriented GFP consists of two main operations:

1) the glass fibers drawn from the glass-melting vessel are wound over a cylindrical drum or another receiving equipment, and the matrix, which preserves and fixes the parallel fiber orientation, is applied at the same time;

2) the sheets or tapes of GFP are processed into the required products.

The method for the production of not woven oriented GFP proposed by Burov /31 – 33/ has the following advantages over the process of spinning glass fabric and the production of glass textolites.

1. This method ensures reliable protection of the surface of glass fibers, which is easily damaged, against corrosive media (mainly atmospheric moisture), since the polymer matrix covers the surface of the clean, newly formed fibers, at the moment when they have not yet been able to absorb moisture from the air.

2. Good adhesion is ensured between the clean surface of the fibers and the polymer matrix, because the adhesive strength is very dependent on the surface state of the glass fiber.

3, The fibers are strictly aligned, and straightened, and their position is fixed in the polymer matrix. This leads to very favorable conditions of the simultaneous operation of the reinforcing fibers in thin polymer films.

Thus, by a correct selection of the polymer which has the required properties (high elastic parameters, strength, and adhesive power, with sufficient elasticity) we can utilize the strength of the individual fibers to the maximum extent.

This is because in such an oriented system the strength of the original fibers which are not subjected to mechanical damage and undesirable moisture effects is "conserved" and retained.

4. The technology for the production of GFP is very simple, and combines four operations in a single stage: drawing the glass fibers, their orientation and straightening, and the application of the polymer matrix.

5. In not woven oriented GFP, glass fibers of different diameters may be used: thin fibers (diameters $4-8\mu$) to very thick fibers (diameter $40-60\mu$ or larger). Such a gamut of fibers cannot be woven. This makes it possible to produce very cheap GFP.

6. When using thin fibers we can employ electroinsulating reinforced films with a crosswise structure. The thickness of these films is not larger than $15-20\mu$. The application of such thin dielectrics is very useful in many products of electrical and radio engineering.

The main disadvantage of the process of reeling the fibers over a rotating drum is that it is discontinuous: when the winding of the glass material is finished, the process has to be interrupted to cut the material from the drum.

The continuous method invented by E. S. Zelenskii /12/ is free of this disadvantage. The glass material is continuously removed from the drum and at the same time cut into strips (with the fiber orientation perpendicular to the axis of the strip) or into a tape (with the fiber orientation along the tape axis). The width of the strip is 1.5 m, the width of the tape 50 — 80 mm, and the thickness of both materials is 0.2 — 0.5 mm. The fibers in the continuous stock on the drum are oriented in one direction at an angle of 5° to one another. This small angle has no influence on the resulting strength of the products. In the continuous method, a fixed oven is employed. This makes it possible to produce the fibers in a single-stage process, and to put into one assembly line the manufacture of oriented GFP from the fusing of the glass mass to the preparation of some finished products (sheets, profiled products, etc.).

Several methods are known for the production of not woven oriented GFP from prepared glass threads. The first material of this type produced in the Soviet Union is AG-4S /37, 38/. Modifications of this material are glass tapes (for example, the material LOS), and materials made from glass plaits. These materials have been developed by Slobitsev and L'vov. Other glass-fiber materials of this group with oriented structure are known.

All these GFP are produced from already prepared glass fibers, combined into threads with the aid of various cementing agents or sizes.

The glass threads are oriented and straightened in the polymer matrix during the unwinding of the threads from the reels, bobbins or spools, and their drawing through the vat with the polymer matrix. The width of the

tape with aligned fibrous structure is determined by the number of spools or bobbins from which the glass threads are unreeled.

During slow unwinding and orientation of the threads, volatile products of the polycondensation of thermoreactive resins (or solvents) are removed, and the material is directly dried in the production process. Such a technology makes it possible to stretch the threads uniformly to form the tape. At the same time the long (almost continuous) tapes of different widths are suitable for the subsequent preparation of various articles by winding. This is the principle of the production of oriented GFP from previously prepared glass threads.

Thus, oriented GFP can be produced from individual fibers and from glass threads (twisted and untwisted), which are parallely arranged in various polymer matrices.

The production of oriented GFP from glass threads with thick ($25-30\mu$ or more) fibers is complicated, since the brittleness and low flexibility of the individual fibers lead to wear and damage to the fiber surface.

In one technique, the thick fibers are fixed immediately after their preparation in the stretched state by the resin in the drum, and it is convenient to use very thick threads in the production of SFAM.

The production of oriented GFP was started in 1954 – 1956. The first products were rods and tapes for high-strength structures for various purposes. At present, oriented GFP are produced from glass threads /39 – 44/ and individual fibers /45, 46/.

The table below shows the ultimate tensile strengths of some types of oriented GFP and glass textolites. For the oriented GFP we give the strength when the load is applied along the axis of the fibers (or threads), and for the glass textolites an arbitrary index, namely the overall strength, which is the sum of the strengths along the warp and weft of the glass fabric:

SFAM	170 – 180	"Highmode"	175
Glass tapes and glass braids	150 – 160	"Scotuply"	120 – 125
AG-4IS	90 – 100	Glass textolite	75 – 80

The strength of oriented GFP with a crosswise structure is approximately only half as great, since on application of the load only half of the fibers are stressed. Thus, by eliminating the weaving of glass fibers which are either brittle or have little wear resistance it is possible to obtain high-strength reinforced systems in which the strength of the original fibers is utilized to a high degree.

4. Plastics reinforced by high-melting fibers

Materials with high strength and thermal stability parameters can be produced by reinforcing polymers by high-strength fibers with a high melting point (for example, quartz fibers).

Plastics reinforced by quartz fibers are marketed under the name "Planeton." It is assumed that the use of these plastics instead of metals will reduce the weight of constructions by a factor of 10 /57 – 58/.

The data reported in Table XII. 6 indicate the strength characteristics of plastics reinforced by quartz fibers. Such materials are used as thermal insulating materials with a high stability to erosion /61, 62/.

TABLE XII. 6. Strength characteristics of plastic reinforced by quartz fibers /60/

Holding temperature, °C	Phenylsilane resin, reinforced by		Silicone resin reinforced by	
	quartz fiber	fibers with high SiO_2 content	quartz fiber	fibers with high SiO_2 content
	Flexural strength, kg/mm^2			
24	30.4	19.1	23.9	16.9
260	26.0	17.6	13.0	9.2
371	24.3	10.5	9.4	3.8
	Flexural modulus, kg/mm^2			
24	0.244	0.246	0.183	0.138
260	0.274	0.173	0.160	0.110
371	0.195	—	0.141	0.077
	Ultimate compressive strength, kg/mm^2			
24	32.8	11.2	15.8	15.5
260	23.0	8.0	6.6	5.5
371	7.7	5.4	4.1	3.4
	Ultimate tensile strength, kg/mm^2			
24	18.6	13.3	14.4	9.8
260	16.9	10.7	12.5	7.9
371	11.7	6.6	5.5	6.4

The firm "Fiberite Corporation" produces a composite reinforced by quartz fibers. The material contains quartz fibers of length of 0.4 — 0.6 mm, and a thermoresistant phenol resin with mineral filler /63/. The properties of this material termed "Fiberite" are given below:

Property	
Density, g/cm^3	1.78
Ultimate strength, kg/mm^2	21.1
on compression	21.1
on bending	9.8
on tension	7.0
on shear	9.8
Impact strength, kg/cm	0.034
Modulus of elasticity on bending, kg/mm^2	1400

Thermoprotective coatings have also been developed based on phenol-aldehyde plastics reinforced by quartz fibers. Such a coating withstands temperatures of up to 2,750°C at high pressures; the temperature of the protected body is not higher than 90°C /64/.

Ceramic fibers obtained from alumina and silica (Al_2O_3 level at least 45%) have good properties. The softening temperature of aluminosilicate fibers ("Fiberfrax") is 1,760—1,800°C, while the operating temperature is

up to 1,300°C. In the USA methods have been developed for the production of kaolin fibers ($Al_2O_3 \cdot 2SiO_2 \cdot 2H_2O$) with a softening point of about 1,500°C, and a high water resistance /65/. Research is also being carried out on the production of fibers from natural minerals, such as bauxite, andalusite, and others /66/.

Polymers reinforced by aluminosilicate fibers are successfully employed as materials operating at very high temperatures /67, 68/. The aluminosilicate fibers have found widest application for reinforcing fluorine plastics /69/. This material is used mainly in packings for equipment operating at high temperatures, and as a coating for materials operating under ablation conditions.

Table XII.7 shows the physicochemical and electrical properties of fluorine plastics reinforced by aluminosilicate fibers.

TABLE XII.7. Physicomechanical and electrical properties of polyterafluoroethylene plastics reinforced by aluminosilicate fibers /69/

Property	Pure plastic	Plastic + 40% of fibers
Ultimate tensile strength, kg/mm^2	10.5 — 21.0	18.2
Impact strength, $kjoules/m^2$	17	8
Shore hardness	50 — 65	66
Density, g/cm^3	2.1 — 2.1	1.9
Overall heat transfer coefficient, $W/m^2 \cdot deg$	242.8	318.2
Short-term electric strength, W/cm	16000 — 20000	6000
Volume resistivity, ohm/cm	10^{15}	4.6×10^{11}

Polymers reinforced by carbon or graphite fibers are also on the market. Fibers containing from 91 to 98% of carbon are termed carbon fibers, and fibers with more than 98% of C are termed graphite fibers. The fiber diameter is between 5 and 50μ.

The physical nature of carbonized fibers has not yet been established. It is assumed that the spiral shape of the crystallites of the original cellulose molecules is retained in the carbonized fibers, and is responsible for some flexibility and elasticity /70/.

Unlike graphite, which is highly crystallized, carbonized fibers have only a slightly ordered arrangement of the carbon atoms; for this reason the term "graphite" fibers is arbitrary.

Carbon and graphite fibers have a high thermal stability and infusibility, chemical resistance and a low density. Their drawback is their relatively high thermal conductivity (higher than in quartz and aluminosilicate fibers), and the fairly low mechanical properties /71/.

The strength of graphite fibers (8μ in diameter) at room temperature is about 40 — 70 kg/mm^2, and almost twice this at 1,700°C. Therefore, the utilization of graphite fibers for reinforcing polymers in rocket engineering (for example, reinforcement of plastics /63/) is very promising, since these materials are resistant to erosion in a very rapid gas stream at 2,000 — 3,000°C. The table on the next page shows the properties of graphite fiber-reinforced plastics.

At present, research is being carried out on the use of high-strength single crystal fibers and fibers consisting of needlelike crystals for reinforced plastics /72/.

Property	
Density, g/cm^3	1.4—1.5
Ultimate strength, kg/mm^2	
on compression	7.03
on bending	7.73
on tension	3.16
Impact strength, kjoule/m^2	190
Flexural modulus, kg/mm^2	980
Shearing strength, kg/mm^2	4.20

Tests on polyformaldehyde reinforced by filamentary single crystals of mullite are reported in /73, 74/.

The length of the mullite crystals was $100-150\mu$ and their diameter $3-4\mu$. The concentration of the mullite filler was varied from 0.1 — 60 wt %. The polyformaldehyde powder was mixed with the mullite, and specimens were pressed from the mixture. The temperature and pressure of pressing were 190°C and 1,200 kg/cm^2. The holding time at this temperature was 20 min. The specimens were cooled under pressure.

The pattern of the supermolecular structure was determined by metallographic microscope MIM-8M. Films of the specimens (thickness 100μ were etched in H_2SO_4 vapor and observed in reflected light.

To determine the effect of the filler on the mechanical properties of polyformaldehyde, the hardness of the specimens, their wear resistance, and their ultimate compressive strength were determined.

Pure polyformaldehyde has a structure consisting of fairly large individual spherolites of fibrous structure. The boundaries between the spherolites are sharp (Figure XII. 5, a). The introduction of the anisotropic mullite crystals produces grinding and "cross-linking" of spherolites with the formation of spherolite concretions, sometimes without sharp interfaces. The crystallization centers of these concretions are frequently the ends of the anisotropic particles (Figure XII. 5, b). Apparently, such a characteristic crystallization can be explained by the effect of fields of forces, concentrated on the needlelike mullite crystals.

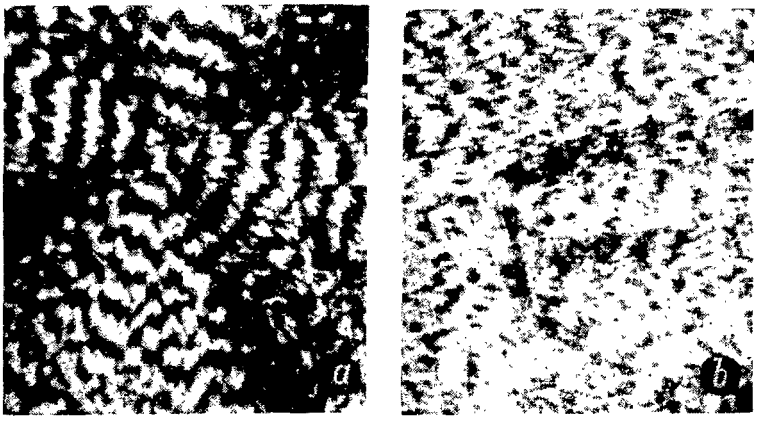

FIGURE XII. 5. Microstructure of pure polyformaldehyde (a) and polyformaldehyde filled with mullite (b) (× 200).

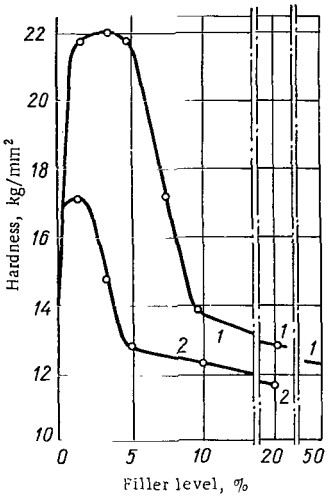

FIGURE XII.6. Dependence of the hardness of polyformaldehyde on the mullite (1) and Aerosil (2) levels.

The changes in the supermolecular structure of the polyformaldehyde have a considerable influence on the mechanical properties of the polymer. This is confirmed by the results of hardness, compressive strength, and wear resistance tests on the polymer.

Figure XII. 6 shows the dependence of the hardness of the polyformaldehyde on the filler level. It can be seen from this diagram that the maximum hardness occurs when 3% of filamentary mullite is introduced. An increase in the mullite level to 10% produces an abrupt decrease in hardness. If this filler level is exceeded, the hardness changes little.

The dependence of the wear resistance of polyformaldehyde on the fiber level (Figure XII. 7) was obtained after 30,000 revolutions of a steel disk, corresponding to a 5.65 km long path of friction. It can be seen that the wear resistance increases only when the filler level is low. The ultimate compressive strength is also increased when a small amount (3%) of filamentary mullite is added (Figure XII..8).

Thus, the mechanical properties of polyformaldehyde are improved when small amounts of mullite (0.5 – 3%) are introduced because of a modification in the supermolecular structure. If polyformaldehyde is filled with needlelike mullite crystals, the spherolite size decreases, and spherolite concretions with "cross-linked" interfaces are formed. The decrease in the mechanical strength with increase in the filler level is explained by aggregation of the filamentary mullite crystals.

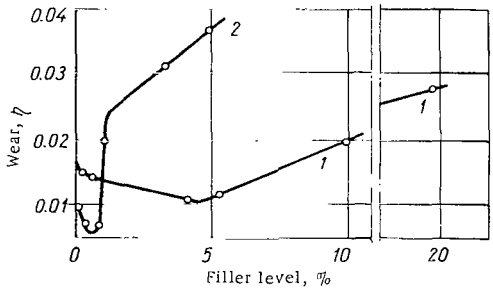

FIGURE XII.7. Dependence of the wear resistance of polyformaldehyde on the mullite (1) and Aerosil (2) levels.

The Institute of Material Sciences of the Ukrainian Academy of Sciences, together with the Institute of Chemistry of High-Molecular Compounds of

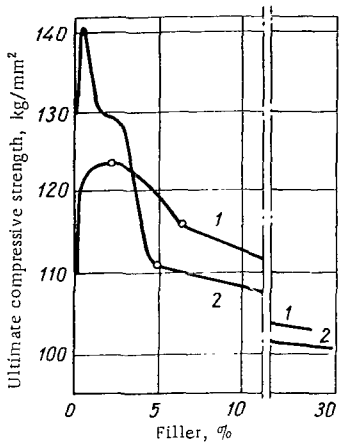

FIGURE XII.8. Dependence of the ultimate compressive strength of polyformaldehyde on the Aerosil (1) and mullite (2) levels.

the Ukrainian Academy of Sciences, developed a self-lubricating antifriction material from Ftoroplast-4.* The purpose of the research was the creation of an antifriction material with a low dry friction coefficient in various friction pairs, and a reduction in the linear wear of the material.

Five to ten wt % of filamentary mullite was introduced into the Ftoroplast-4. The mullite needles had a length of $150-1{,}000\mu$ and a diameter of $1-3\mu$. Both components were mixed in the dry state at $60-90°C$; then they were pressed into specimens of certain shapes and were sintered in closed molds under pressure.

The main properties of the material obtained are shown in Table XII.8. This table also contains the corresponding data for Ftoroplast-4 filled with colloidal graphite.

Ftoroplast-4 can be used for piston rings of small refrigerating machines.

The introduction of filamentary mullite single crystals eliminates the main disadvantages of the Ftoroplast: its fluidity in the cold. Thus, in breaking tests the relative elongation of the material was 24.13% while that of pure Ftoroplast under the same conditions was 250 – 500%.

Furthermore, in ablation coatings of Ftoroplast reinforced by glass fibers are more rapidly destroyed because of the dissolution of the glass fiber by the fluorides evolved. The filamentary mullite single crystals are insoluble in HF, and for this reason the material has a higher strength.

TABLE XII.8. Main properties of Ftoroplast*-4 reinforced by filamentary mullite single crystals

Propergy	Ftoroplast-4	
	filled with 30% of colloidal graphite	filled with 30% of filamentary mullite
Brinell hardness, kg/mm²	6.65	6.63
Strength, kg/mm², on		
tension	129	124
compression	300	271
Relative elongation on breaking, %	27	24
Specific impact strength kjoules/m²	1100	3122
Minimum wear, mm per 1 km path on steel 40 at:		
$v = 1.5$ m/sec, P_{imp} 20 kg/cm²	$15.1 \cdot 10^{-4}$	$4.6 \cdot 10^{-4}$
$v = 1.5$ " " 30 " "	$19.7 \cdot 10^{-4}$	$6.5 \cdot 10^{-4}$
$v = 1.5$ " " 40 " "	$30.5 \cdot 10^{-4}$	$13.0 \cdot 10^{-4}$
$v = 1.5$ " " 50 " "	$43.9 \cdot 10^{-4}$	$18.0 \cdot 10^{-4}$
Dynamic frictional wear coefficient on steel 40 at:		
$v = 1.5$ m/sec, P_{imp} 20 kg/cm²	0.23	0.11
$v = 1.5$ " " 30 " "	0.25	0.16
$v = 1.5$ " " 40 " "	0.28	0.17
$v = 1.5$ " " 50 " "	0.33	0.23

* [Polytetrafluoroethylene.]

5. Range of application of reinforced plastics

The combination of a high mechanical strength with low specific gravity, high chemical resistance, low thermal conductivity, and other valuable properties of plastic makes it possible to use reinforced plastics for structures in which conventional materials are not effective or even unsuitable. An analysis of the data in Table XII. 9 shows that the strength of anisotropic plastics is not lower than that of high-strength steel. Moreover, their weight is lower, and their specific strength is higher than that of the known structural materials. The high specific strength of GFP makes them very popular as a material in mechanical engineering.

Though the industrial production of GFP began fairly recently (about 10—12 years ago), they are being applied in all branches of industry. Table XII. 10 shows data on the use of reinforced plastics in various industries outside the Soviet Union.

Reinforced plastics are employed mainly in the building industry. Here GFP are used as corrugate sheets for roofings, panels, internal partitions, and decorative purposes. Moreover, GFP are widely employed in the building of residential houses for sanitary-technical equipment.

TABLE XII.9. Mechanical properties of some structural materials /4/

Property	High-strength steel	Aluminum alloy	Titanium	Plastics reinforced by		
				glass mat	glass fabric	aligned fibers
Weight density, g/cm^3 ..	7.9	2.5	4.5	1.5	1.7	2.1—2.2
Tensile strength, kg/mm^2	176	56	105	21	63	175—245
Specific impact strength, kjoule/m^2	—	—	—	11000	32500—43500	32500—43500
Young's modulus, $\times 10^{-4}$ kg/mm^2	2.10	0.77	1.12	0.055—0.140	0.125—0.350	0.350—0.490
Specific tensile strength, $\times 10^{-4}$cm	224	224	234	139	368	845—1113

TABLE XII.10. Utilization of reinforced plastics in 1957 /7/

Field	Fraction, %	Field	Fraction, %
Rocket engineering	15	Electrical engineering	3
Aircraft industry	3	Pipe lines, tanks, vessels	2
Shipping industry	15	Armatures	9
Building industry	15	Transport	20
Car industry	3		

Pipe lines and pump pipes made of glass textolite roving reinforced by a polyester matrix have good mechanical properties and can be used up to 200°C. The diameter and profile of the tubes can be of any desired size. Such pipe lines are especially suitable for chemical plants.

Tanks and various vessels made of GFP are applied in chemical industry, where metals are unsuitable for use in corrosive liquids and media /82, 83/.

GFP are widely used in the automobile, railroad coach, and shipping industries. Reinforced plastics are irreplaceable materials in the aircraft industry and rocket engineering.

In rocket engineering these materials may be more suitable than metals, but it should be emphasized that none of the above materials can withstand very high temperatures for a long period. Nonetheless, some of the reinforced plastics now being produced are sufficiently heat resistant to withstand such temperatures for a certain time without being destroyed.

A very important field where reinforced plastics are being applied is electrical engineering. In this branch plastics reinforced by graphite fibers are very effective /13/.

It should be noted that the strength of anisotropic GFP has not yet attained its limit. Therefore, these materials are still in the developing stage, and have a promising future. Further study on the physicochemical properties of reinforced plastics will doubtless extend their range of application.

GFP are widely employed in the furniture industry (chairs, armchairs, tables).

In the building industry GFP are also used for the production of molds for reinforced concrete. These molds can be used for a long time, and various concrete profiles can be produced on them. The cost of such products is low, regardless of the high cost of the molds.

Research is being carried out on the application of rods made of GFP (polyester resin serves as the matrix) for the preliminary stressing of concrete structures /78/. These materials have the following advantages over steel reinforcement: they are corrosion-resistant, especially at sites exposed on one side to water, and also light. This is especially important in constructions transported over wide distances.

The use of GFP for internal illumination systems is original. Window frames are made of glass-fiber reinforced polyester resin /79/. This system gives a shadowless illumination. The size of the window frame is 290 cm^2; the frames are placed over the whole area to be illuminated.

Another interesting field of application of GFP is the production of sliding doors of garages, with a low weight /80/. Because of the transparency of GFP, the garage is illuminated without the presence of windows.

A domed house was designed according to the geodesic principle, and constructed in Canada. It consists of 76 triangular transparent panels of glass fiber and transparent polyester resin /81/. Its cost was much lower than that of a house made of conventional materials. The skeleton of the building was made from laminated wood plastic on phenol resin.

Bibliography

1. Fiberglass Reinforced Plastics. Owens Corning Fiberglass Corp., August, 1962.
2. Brown, W.I. Fabric Reinforced Plastics, 3, London, Cleaver-Hume Press Ltd. 1947.

3. Sorrell, S. E. Paper Base Laminates, London, Cleaver-Hume Press, Ltd. 1950.
4. Korten, Kh. T. Razrushenie armirovannykh plastikov (Fracture of Reinforced Plastics). Moskva, Khimiya. 1967.
5. Kargin, V. A. Sovremennye problemy nauki o polimerakh (Contemporary Problems of Polymer Science). Moskva, Izdatel'stvo MGU. 1962.
6. Morgan, P. (editor). Glass Reinforced Plastics, 2nd. ed. New York, Philosophical Library. 1957. 3rd ed. New York, Intersience. 1961.
7. Duffen, D. I.— Laminated Plastics. N. Y. 1958.
8. Zak, A. F. Fiziko-khimicheskie svoistva steklyannogo volokna (Physicochemical Properties of Glass Fibers). Moskva, Gostekhizdat. 1962.
9. Reinkober, O.— Phys. Z., 6:243. 1931.
10. Anderegg, F.— Ind. Eng. Chem., 3:290. 1939.
11. Aslanova, M. S. Volokna, niti i tkani iz stekla (Fibers, Threads and Fabrics Made from Glass). Moskva, Gizlegprom. 1945.
12. Andreevskaya, G. D. Vysokoprochnye orientirovannye stekloplastiki (High-Strength Oriented Glass-Fiber Reinforced Plastics). Moskva, Nauka. 1966.
13. Griffith, A. A.— Phil. Trans. Roy. Soc., London, A-221:163. 1921.
14. Reinkober, G.— Phys. Z., 4:112. 1937.
15. Aleksandrov, A. P. and S. I. Zhurkov. Yavlenie khrupkogo razryva (Brittle Fracture). Moskva-Leningrad, Gostekhizdat. 1933.
16. Zhurkov, S. I.— ZhTF, 4:1640. 1934.
17. Zak, A. F. and Yu. P. Man'ko.—Nauchno-Tekhnicheskii Informatsionnyi Byulleten' VNII Steklovolokno. Moskva, Rostekhizdat. 1952.
18. Burov, A. K., M. V. Klassen-Neklyudova, and G. D. Andreevskaya.— ZhTF, **15**. 1945.
19. Bartenev, G. M. and A. N. Bovkunenko.— ZhTF, **29**. 1955.
20. Bartenev, G. M. and A. N. Bovkunenko.— ZhTF, **26**. 1956.
21. Aslanova, M. S.— Khimicheskaya Nauka i Promyshlennost', **3**. 1958.
22. Aslanova, M. S.— Steklo i Keramika, **11**:10. 1960.
23. Baker, T. and F. Preston.— J. Appl. Phys., **17**:26. 1946.
24. Preston, F. and T. Baker.— Phys. Abstr., **6**:581. 1946.
25. Grebenshchikov, I. V.— Izvestiya AN SSSR, Seriya Fizicheskaya, **4**. 1939.
26. Grebenshchikov, I. V.— Keramika i Steklo, 11(12):36. 1931.
27. Rabinovicz, A. L.— Trudy TsAGI, p. 582. 1946.
28. Kiselev, B. A. Stekloplastiki (Glass-Fiber Reinforced Plastics). Moskva, Goskhimizdat. 1961.
29. Meyer, O.— Kunststoff-Rundschau, 2(3):73—83, 1955; No. 4:109—116.
30. Meyer, O.— Kunststoff, 47(8):455—463. 1957.
31. Burov, A. K. Soviet Patent 66813.—Byulleten' Izobretenii, **11**. 1958.
32. Burov, A. K. Soviet Patent 69025.— Byulleten' Izobretenii, **11**. 1958.

33. Burov, A. K. and G. D. Andreevskaya. Soviet Patent 75081.— Byulleten' Izobretenii, 11. 1958.
34. Chernyak, M. G. (editor). Fiziko-tekhnicheskie svoistva steklovolokna i primenenie steklovoloknistykh materialov (Physical and Technical Properties of Glass Fibers, and Use of Glass-Fiber Materials). Moskva-Leningrad, Gizlegprom. 1949.
35. Delanova, M. S. Volokna, niti i tkany iz stekla (Fibers, and Fabrics Made from Glass). Moskva, Gizlegprom. 1945.
36. Kovalev, I. P.— In: Trudy Nauchno-Issledovatel'skogo Instituta Steklovolokna, 4. Moskva, Gosizdat. 1958.
37. Gulyaev, A. S.— In: Trudy Vsesoyuznogo soveshchaniya po stekloplastikam. Moskva, Gosizdat. 1959.
38. Goryainova, A. V. Stekloplastiki v mashinostroenii (Glass-Fiber Reinforced Fibers in Mechanical Engineering). Moskva, Goskhimizdat. 1961.
39. Levy, A.— Plast. World, 14:10. 1956.
40. Hennig, A.— Inst. Product. Engrs. J., 35. 1956.
41. Miller, W. H. and M. R. Alexander. US Patent 2910383. 1959.
42. Broonffeld, K. Y. and D. Prickthall.— Reinforced Plastics, 6. 1962.
43. Donaldson, A. L. and R. B. Vellen.— Mod. Plast., 35:133. 1957; 36:132. 1958.
44. Donaldson, A. L. and R. B. Vellen.— Mod. Plast., 36:132. 1959.
45. Case, J. and G. Robinson.— Mod. Plast., 32:151. 1955.
46. Stanley, F.— Mod. Plast., 32:121. 1954.
47. Judge, J.— Missiles and Rockets, 7:23. 1960.
48. Resato, D. V.— Brit. Plast., 33:348. 1960.
49. Caroll-Porczynski, C. Z. Inorganic Fibers, London, Nat. Trade Press. Ltd. 1958.
50. Gandin, M.— Compt. Rend. Acad. Sci., 8:678. 1839.
51. Stephenson, G. E.— J. Soc. Glass Techn., 39:186. 1955.
52. McBain, Baker.— J. Am. Chem. Soc., 48:690. 1926.
53. Gantler, A.— Compt. Rend. Acad. Sci., 130:816. 1900.
54. Luaritsen, C. C. and T. Lauritsen.— Rev. Sci. Instr., 8:438. 1937.
55. Neher, H. V.— Rev. Sci. Instr., 24:99. 1953.
56. Eberhardt, E., H. Kern, and H. Klamb.— J. Amer. Cer. Soc., 35:3. 1952.
57. Eng. Mater. Design, 10. 1959.
58. Mater. in Design Eng., 2. 1959.
59. Carrol-Porczynski, C. Z.— Eng. Mater. Design, 3(3):134. 1940.
60. Mater. Design Eng., 5:11. 1960.
62. Raech, H.— Glass Ind., 10. 1960.
63. Caroll-Porczynski, C. Z. Advanced Materials, Guildford, Astex Publishing Company. 1962.
64. Chem. Eng., 80, No. 3. 1960.
65. Fore, J.— Refractory J., 31. 1955.
66. Dixon, D.— Refractory J., 32. 1956.
67. Sherrard, G. H. and C. A. Murray.— Mach. Design, 35. 1963.
68. Murray, C. D.— West. Plast., 9:23. 1962.

69. Greenman, N. L. — Matėr. Design Eng., 10. 1959.
70. Schmidt, D. L. and W. C. Jones. — Chem. Eng. Progr., 58:42. 1962.
71. Davis, L. R. — Plast. World, 21:60. 1963.
72. Russel, K. C. and L. F. Morgan. US Patent 306591. 1962.
73. Gordienko, V. P. et al. — Khimicheskaya Promyshlennost' Ukrainy, 5. 1968.
74. Solomko, V. P. et al. — Fiziko-Khimicheskaya Mekhanika Materialov, 3. 1968.
75. Modern Plastics, 34:1. 1956.
76. British Plastics, 28:4. 1955.
77. Modern Plastics, 32:6. 1955.
78. British Plastics, 28. 1955.
79. Modern Plastics, 31:11. 1954.
80. Modern Plastics, 32(6):91. 1955.
81. Modern Plastics, 32(6):92. 1955.
82. British Plastics, 26. 1953.
83. Modern Plastics, 32:10. 1955.

Chapter XIII

FILTERS, TRANSPIRATORS, PACKERS, AND DAMPERS MADE OF FIBROUS MATERIAL

1. Methods for producing high-strength articles from fibers

The methods of powder metallurgy are used for the production of materials from fibers: pressing from one or two sides in the mold, hydrostatic pressing, rolling, and sintering in the solid or liquid phase. However, the specific features of the raw material (fibers) make it possible to employ special methods to process them into products.

The fiber diameter and length, and the quality of the surface, are selected according to the product design. Fibers obtained from wire are usually bent or curled to facilitate bonding during subsequent molding of the product. A correct selection of the fiber size facilitates the forming of a homogeneous structure of the material.

Because of the strong anisotropy in the size of the individual fibers, their poor friability, and low bulk weight, it is difficult to obtain semi-finished or finished products by the conventional methods of pressing, rolling, or extrusion. Frequently, after the fibers are degreased in trichloroethylene, sodium peroxide, or ammonium hydroxide, a felt is prepared. The method of felt production is taken from paper technology, and in principle is only a modification of slip casting. There are several variants of felt production: liquid, air, gravitation and vacuum.

In liquid felt production the fibers are placed into a viscous liquid (for example, glycerol), and the sludge obtained is poured into a porous mold (Figure XIII. 1), The mold has the form of the final product. It is exhausted, so that when the liquid is withdrawn the fibers settle randomly at the bottom and on the walls of the mold. They form a felt of bonded fibers.

In the settling process the density is self-regulating. Since in layers with increased density the permeability of the layer is reduced, the introduction of the suspension is slowed down and the settling of the layer is hindered on these sections. Conversely, at sites with a higher permeability and lower density, the fibers sediment until the density of the felt is equalized.

The size of the fibers, the settling medium, and the rate of sedimentation affect the felt density. The densest felt is obtained when short and thin fibers are used. The porosity of the felt obtained is usually 80 — 95%.

Continuous sheets can be obtained in a similar way /1/, The metal fiber suspension is placed into a supply tank (Figure XIII. 2), and from here it

passes to a sieve covered with filter paper. The sieve continuously moves on rollers passing through the chambers for liquid withdrawal. The felt formed is then passed through pressure rolls (this is compulsory when producing filter), and proceeds into the sintering furnace.

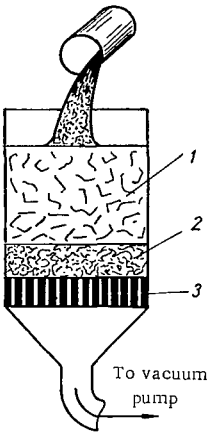

FIGURE XIII.1. Liquid felting process:

1 — fiber suspension in liquid; 2 — settled felt; 3 — porous bottom of mold.

For fibers made of metals which are readily oxidized (e.g., iron), glycerol or petroleum oils can be used as the suspension liquid. For fibers made of nickel, stainless steels, and other corrosion-resistant metals, water is used, with organic compounds added to increase the viscosity. The parameters to be controlled are the rate of movement of the tape, the feed rate of the suspension and the rate of liquid withdrawal. Mixing the suspension is important. The advantages of these methods of felt preparation are that they are simple and economical.

These products made of felt can have a complicated shape and large dimensions, and it is possible to produce large articles.

One of the variants of liquid felt preparation was used in the production of filters from copper fibers obtained by clipping wire /2/. The fibers were suspended in polyvinyl alcohol, and the suspension was poured into plaster of Paris molds. The material was dried at room temperature for 24 hours. The felt was extracted from the mold and subjected to further processing.

Felts can also be prepared from an air suspension (felt preparation in air). However, the adhesion and homogeneity of the felt is somewhat poorer than in liquid felt preparation.

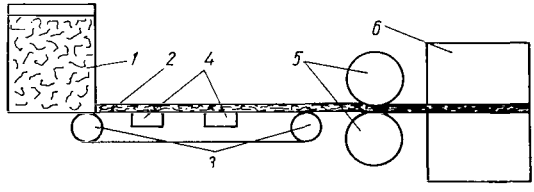

FIGURE XIII.2. Production of sheet material from metal fibers:

1 — supply tank with fiber suspension; 2 — screen with filter paper; 3 — rollers for shifting the screen; 4 — chambers for liquid withdrawal; 5 — pressure rolls; 6 — sintering furnace.

Recently, at the Baikov Metallurgical Institute of the Ukrainian Academy of Sciences a new method of felt preparation was proposed. It is a variant of the air suspension method. The dry fibers are sifted into a mold with a narrow hollow. The length or width of the hollow must be smaller than its height. The porosity of plates formed by this method is about 90%.

Other methods for felt preparation include molding in an electric or magnetic field, extrusion, and vibration treatment, which make it possible to obtain a felt with aligned fibers /3—6/. The method of vibration felting was studied in detail /5/. The tests were performed with nichrome (40—100μ diameter) and molybdenum (50μ diameter) fibers obtained by clipping wire. The fiber length was 5—12 mm. A mechanical rotational-pulse vibrator imparted the pulses. The felt was obtained as a cylindrical and bushing preparation. It was found that this method of felt production is most efficient at 50—100 Hz, amplitude 40—50μ, and pulse peaks must be applied. If the frequencies are low, the production of felt is retarded, and the application of higher frequencies is ineffective, and leads to excessive power consumption.

The rate of felting is dependent not only on the conditions of vibration but also on the fiber size. For example, nichrome fibers 5—7 mm long are felted twice as rapidly as the same fibers 10—12 mm in length. In vibrational felting the batch of the compressed fiber is proportional to the container cross section in which the felt is prepared. If the batch is increased, the felting process is retarded. The material of the fibers and size of the container have no effect on the process, but fiber orientation is determined by the geometrical forms of fibers and container. If the fibers are curved, they are randomly distributed; if the container diameter is several times larger than the container length, the fibers are preferentially oriented in a horizontal direction. By changing the fiber length and container diameter, a preferentially vertical fiber orientation can be obtained. An intermediate state exists, when the fibers are oriented in the bulk horizontally and in some places of the felt surface vertically.

The efficiency of the bond between the structural elements of the materials determines the physicomechanical parameters of the cermets. High pressures during pressing and high sintering temperatures, and additional pressing and sintering in the presence of a liquid phase, increase the strength of the bonds.

If fibers are used as the raw material it is possible to dispense with some treatments, because of the high quality and complexity of the bonds formed between the fibers after felting. A metal felt is like a continuous volume sieve, and has a sufficiently high "crude" strength without any additional treatment. According to the fiber size and the felt porosity, each fiber may have up to 100 bonds with the adjacent fibers. This is one order of magnitude higher than the number of interparticle bonds in powders, even when the particles are ideally arranged. It is thus possible to produce articles with an almost unlimited porosity from fibers, which is usually not attained by other methods.

After the felt has been prepared, further treatment may vary widely (Figure XIII. 3).

Because of the high initial porosity of the felt, and the low residual porosity of the articles made from fibers when the structural elements are ideally packed without deformation, (the porosity of spherical particle powders is about 25%, and of cylindrical fibers it is about 10%), the felt is strongly compressed during pressing. The pressure used for articles made of fibers is higher than that employed for the corresponding powder products, other conditions being equal (Table XIII. 1). For the preparation

of porous products from fibers, the pressure required is usually not higher than 5 – 35 kg/mm^2 (Figure XIII. 4).

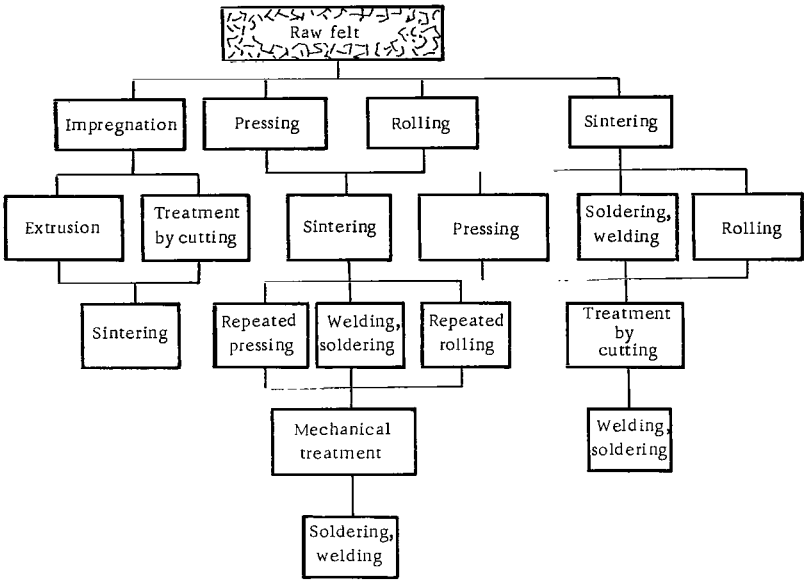

FIGURE XIII. 3. Scheme for processing metal felts into products.

TABLE XIII. 1. Comparative data on the pressing parameters of electrolytic copper powder and copper fibers obtained by clipping wire

Pressing pressure, kg/mm^2	Porosity, %	
	fiber	powder
20	30	36
25	24	30
30	20	26

The method of pressing applied is usually chosen according to the specifications for the final product. Pressing from one or two sides aligns the fibers in the direction of pressure application, while hydrostatic pressing reduces the anisotropy.

Tests on the pressing of products made by clipping wire /8/ showed that the elastic aftereffect in the pressed specimens is much higher than in powder briquettes. This is due to the spring effect of the long fibers (which are under high elastic strains), and their smooth and relatively small surface.

The elastic aftereffect is very marked during sintering, and leads to a size increase in the intermediate product; this must be taken into account in the production of articles of an exact size. Tests showed that with increase in the fiber diameter and porosity of the intermediate product, the elastic aftereffect increases after sintering (Figure XIII. 5).

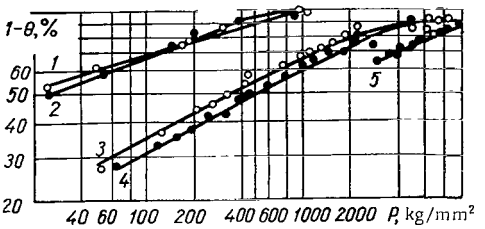

FIGURE XIII.4. Compressibility of porous products made from lead, silver and stainless steel during pressing (in logarithmic coordinates) /7/:

1 — lead fibers ($d = 120\mu$); 2 — lead fibers ($d = 550$—$600\,\mu$); 3 — silver fibers, ($d = 100\,\mu$, $l = 10$ mm); 4 — silver fibers ($d = 100\,\mu$; $l = 20$ mm); 5 — stainless steel fibers ($d = 200\,\mu$, $l = 5$ mm).

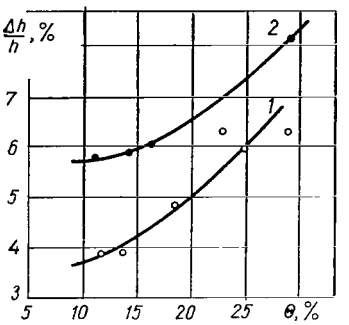

FIGURE XIII.5. Dependence of elastic aftereffect after sintering articles made from copper fibers on the porosity:

1 — wire diameter $40\,\mu$; 2 — wire diameter $100\,\mu$.

When porous products are made from extruded powderlike fibers, no elastic aftereffect is observed. After sintering, the product contracts. The extent of contraction depends on the sintering conditions chosen and the porosity of the intermediate product.

Rolling, in contrast to pressing, makes it possible to produce continuous single- or multilayer sheets with a controlled porosity from fibers. The thickness of the sheets varies between orders of about $10\,\mu$ and 10^2 mm. Ther permissible deformation depends on the fiber metal. It was found that a compression of about 75 % does not produce any appreciable decrease in the porosity /9/.

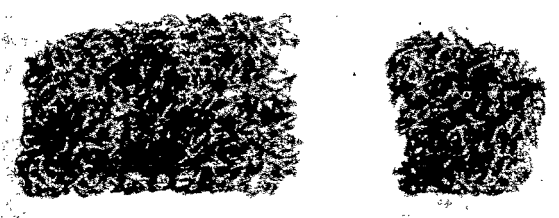

FIGURE XIII.6. Copper felt, obtained by sintering free-pouring extruded CuO fibers in hydrogen at 800°C. Sintering time 1 hr.

Extrusion can be used for the production of porous articles (tubes or cylinders of various sizes). The felt is preliminarily impregnated by wax, resin, or a salt mixture (44.5 % of KNO_3 and 55.5 % of $NaNO_3$ at 190°C). A similar impregnation method is used to retain the porosity of material cut from fibers. After extrusion or mechanical treatment the impregnating agent is removed.

We know of several methods for molding high-strength products from fibers, without felting. A method was developed by Kostornov and Fedorchenko and applied to articles produced from extruded fibers /10/. A plastic mass is prepared from a mixture of finely dispersed metal powder or metal oxide with a viscous matrix. This is then placed into a container and squeezed from spinnerets at a pressure between 2 and 3 kg/mm^2. The threads pass to a mobile mold, and are then sintered. To produce articles of complex form with a controlled porosity, one of the technological variants can be used: the threads squeezed from the spinnerets are divided into individual fibers after extrusion and fall into a mold. Here they are sintered, still in the free state. A felt is formed (Figure XIII. 6) which can be processed by one of the above procedures.

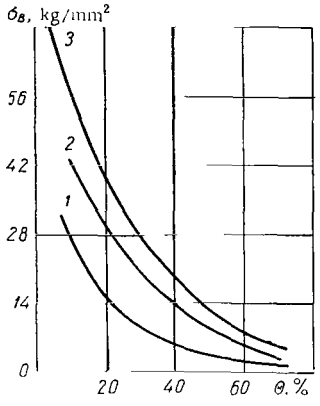

FIGURE XIII. 7. Dependence of the tensile strength of porous materials made of fibers on the porosity /12/: 1 — fibers of mild steel; 2 — fibers of stainless steel 434 A; 3 — fibers made of mild steel with copper additive.

Another method for producing porous articles from fibers without preliminary felting has been described in /6/. The tubular matrix is filled with the fibers, and heated after the addition of a thermoplastic resin. The intermediate product is evacuated, cooled and sintered. During sintering the resin is removed and a porous article formed.

In the production of articles from fibers sintering is usually employed to increase the strength. High sintering temperatures (93 % of the melting point (°K) of the fibers or more) are needed for fibers which are obtained by clipping wire and are structurally equivalent objects.

When studying the kinetics of the growth of contacts in specimens made from fibers obtained by tightly winding copper, nickel, or iron at temperatures close to the melting point (holding time 600 — 800 hr), it was found that the process rate is determined by volume diffusion and not by the presence of grain boundaries /11/.

Sintering in the presence of a liquid metal phase makes it possible to reduce the temperature and shorten the sintering period. For example, the addition of copper or bronze to steel, iron, or tungsten fibers or the addition of tin or zinc to copper fibers makes it possible to obtain high-strength products (Figure XIII. 7, Table XII. 2). When copper was added, heating for 1 hr up to 1,121°C was sufficient. Copper can be applied onto the fibers during felting by various methods (e.g., electrolytically or by deposition from gaseous phase). The amount of copper introduced determines the porosity and strength of the products. The strengthening effect is observed when only 5 wt % of copper is added, while a 10 % addition increases the tensile strength several times (Figure XIII. 8).

In addition to metals forming a liquid phase, powder additives can be introduced into the fiber products. After sintering, the product density changes only slightly, but the strength properties increase considerably (Table XIII. 3).

TABLE XIII.2. Effect of the liquid metal phase on the strength parameters of fiber products

Porosity, %	Ultimate tensile strength, kg/mm²					
	diameter of fibers of steel 1Kh18N9T sintered without the liquid phase at 1,250°C for 3 hr			diameter of fibers of bronze OTs 4-3 sintered with the liquid phase (20 vol %) at 980°C for 3 hr		
	100 μ	200 μ	300 μ	100 μ	200 μ	300 μ
30	7.8	6.2	4.5	13.4	11.0	9.7
40	5.2	4.0	2.2	10.1	5.6	5.3
50	3.7	2.3	0.8	7.5	4.0	—

TABLE XIII.3. Data on the impact strength of porous materials made of iron /13/

Porosity of material, %			Work expended for fracture, joule
from fiber	from mixture of fiber + powder	from powder	
18**	—	—	Above 34
27	—	—	8.3
45	—	17*	5.5
70	35	22	2.8
85*	—	30	1.4

* Obtained by extrapolation.
** Specimens were not fractured.

To reduce the sintering temperature and time for the production of fiber articles, the sintering process can be activated by introducing small amounts of activators. We know, for example, that if small amounts of metals of the iron group are added, the sintering temperature of tungsten and molybdenum is lowered. Thus, if nickel is added in an amount of 1 % to tungsten powder, it is possible to attain 95 % of the theoretical strength at a sintering temperature below 1,350°C. Activation is observed when nickel is added in amounts of 0.01 %, but the optimum activator level is about 0.25 %.

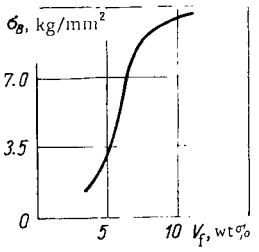

FIGURE XIII.8. Effect of copper additive on the strength of products made of mild low-carbon steel. Porosity of product 90% /9/.

The results of tests on the activation of the sintering of porous products made from molydenum fibers are reported by Sukhozhak and Skorokhod /14/. Fibers (length 8—10 mm, diameter 50 μ) obtained by clipping wire were pressed from two sides at a pressure of 35 kg/mm² to a porosity of 38—42 %. The products were sintered in a hydrogen atmosphere at 1,400°C for 2 hours. They were then impregnated by an aqueous solution of nickel nitrate, dried for 1 hr at 100°C, and again sintered under the same conditions*. It was found that

* When porous articles made of molybdenum fibers are sintered without activators, the following conditions are employed: annealing in hydrogen at 1,050°C for 2 hr, and then sintering at a reduced pressure, 10^{-3} mm Hg at 2,200—2,300°C for 2—20 hr.

when nickel was added in amounts up to 1 wt %, the density of the products was scarcely affected. A metallographic study of the structure showed that after nickel is added contact necks are formed between the fibers, that is considerable sintering occurs, which is almost unobserved in specimens without nickel (Figure XIII. 9). The fact that the sintering of molydenum fibers is activated by small amounts of nickel is confirmed by measuring Young's modulus on briquettes. For specimens of pure molybdenum fibers of 40 % porosity, the modulus was 2,620 kg/mm^2, and when 0.14 wt % of nickel was introduced, it was as high as 6,380 kg/mm^2. But the addition of nickel leads to an increase in the brittleness of the material and a reduction in the mechanical properties (e.g., impact strength); the reasons are not yet clear.

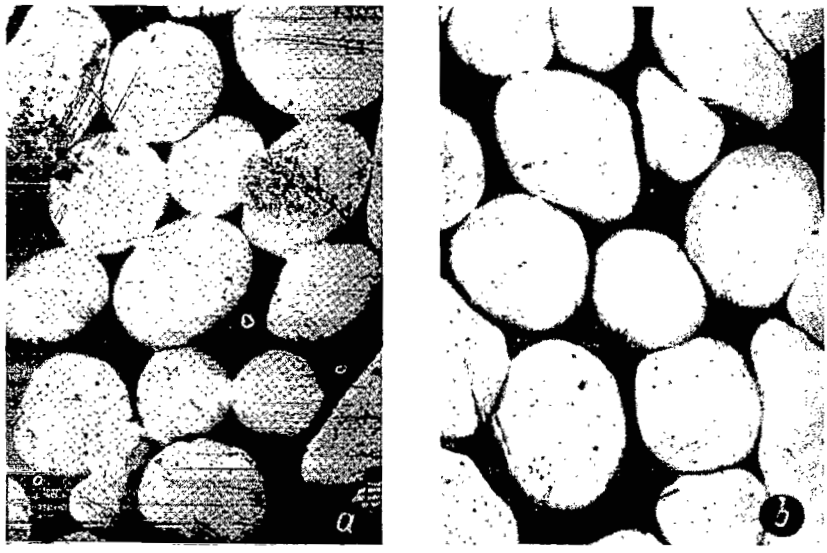

FIGURE XIII. 9. Structure of a porous briquette of molybdenum fibers after sintering at 1,400°C: a — with 0.3 wt% of Ni; b — without nickel.

TABLE XIII. 4. Effect of a protective gas atmosphere on the strength parameters of products made of stainless steel fibers. Porosity of product 40 % /9/

Sintering conditions, holding time 1 hr		Ultimate tensile strength, kg/mm^2	Work expended for breaking by impact (specimens without notches), joules
temperature, °C	protective gas		
1,343	Hydrogen, dry and free of oxygen	8.9	3.7
1,288	Dissociated ammonia	15.4	2.8
1,343	The same	22.0	4.1—5.5

When fiber products are sintered, the protective gas atmospheres recommended by powder metallurgy for powder products of similar composition are employed. When specimens made of fibers of stainless steel 430 are sintered, it was found that dissociated ammonia somewhat increases the tensile strength, but reduces the impact strength (Figure XIII. 4). As a protective atmosphere for sintering fiber products we recommend oxygen-free, dry hydrogen.

The German patent given in /15/ is interesting. It describes the sintering of fiber products by passing an electric current through them in pulses of constant or variable duration. The pulse power is higher than the mean power required for maintaining the sintering temperature; the pulse length and sequence correspond to the mean power. The pulse voltage is higher than 50 V. The current is passed in the direction of the largest dimension of the intermediate product. To break through the oxide films on the fiber surface, it is better to use an alternating current. The advantage of the method is that the sintering (welding) of the fibers lasts a short time at the points of contact, the original porosity is retained, and a strong fiber skeleton is formed. For example, in the sintering of 150×200 mm plates, made from steel fibers 10—100 μ thick and 3—20 mm long, the electric power was supplied for a total of 6—7 sec. Alterating current pulses (220 V) were passed every 50—100 milliseconds, and each pulse lasted 50 milliseconds.

Under exactly the same conditions, the sintering parameters (temperature, holding time) of fiber products are very dependent on the previous history of the fibers. Fibers obtained by clipping wire require the maximum sintering temperature. But extruded powderlike fibers, which have rough developed surface and unsymmetrical structure, are readily sintered under the conditions recommended for products from powders of corresponding composition. The sintering temperatures required are several hundred degrees lower in this case.

2. Filter materials made from fibers

Fiber materials are used in filters because of their high permeability, and the fact that there are almost no limits to the porosity obtainable in the products. Thus, in the production of filters from spherical powder particles, the upper porosity limit is 47%, and it may be as high as 98% in filter material made of fibers. Since there are almost no closed pores in such materials (if the porosity is higher than 10%), fiber filters are much more permeable than powder materials. For example, when filters made of stainless steel powders and of nickel fibers* were compared, it was found that at a porosity of 32% the permeability to air of fiber filters was four times as great (Figure XIII. 10). Higher porosity filters made of fibers are considerably stronger than filters made of powders, because of the higher number of points of contact per elementary particle, and the mechanical bond between the fibers (Table XIII. 5).

* To make the fiber surface similar to the surface state of the powder particles, the fibers were prepared by extrusion; the fiber diameter was equal to the particle diameter of the powder.

Thus, for high porosity and permeability, fiber filters are better than all other known filter media. Examples of the very high permeability and high strength of filters made of stainless steel fibers are shown in Table XIII. 6.

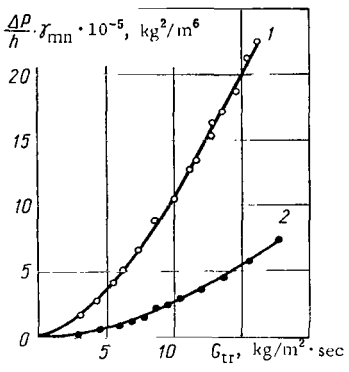

FIGURE XIII. 10. Dependence of the pressure drop on powder filters (1) and extruded fiber filters (2) on the air rate (ΔP— pressure drop, γ_{mn}.— mean density of air passed at test temperature; h — filter thickness; G_{tr} — true air rate at given pressure drop).

From the same fibers, filters can be produced with their permeability differing by the order of magnitude of 10^2, but their strength differs by the order of magnitude of 10° only. The geometrical dimensions and properties of the fiber considerably affect the permeability of filters. It can be seen from Table XIII. 6 that if we use thick fibers instead of thin ones the permeability increases several times. The dependence of the permeability of fiber filters on the fiber diameter is not linear for either liquids or gases. With an increase in the pressure drop on the filter the dependence of the filter permeability on the fiber diameter is greater (Figure XIII. 11).

A considerable increase in the permeability of filters* made from fibers of copper, stainless steel 1Kh18N9T and bronze OTs4-3 with increase in fiber diameter was observed when passing air (Figure XIII. 12, Table XIII. 7). In the general case, other conditions being equal, the ratio of the permeabilities to air of filters made of fibers related to the diameters of the fibers is given by

$$\frac{Q_1}{Q_2} = \left(\frac{d_1}{d_2}\right)^n, \qquad \text{(XIII. 1)}$$

where the theoretical value of n is 2.

TABLE XIII. 5. Data on strength of filters made of Fe powder and Fe fibers /13/

Ultimate tensile strength, kg/mm²	Porosity of filters, %	
	from fibers	from powder
5.3	50	32
7.7	40	29
10.5	30	23

In specimens with an open porosity (more than 10 %) this dependence has been experimentally confirmed. Thus, in the porosity range from 15 — 30 % the permeability of pressed copper fibers of 100 μ diameter (Figure XIII. 12, dashed lines) is four times that of specimens made from 50 μ diameter

* The filters of stainless steel and bronze were sintered in hydrogen at 980° for 3 hours; the copper filters were sintered for 2 hours at 950°C. The length of the initial fibers was 5 mm, the thickness of the filters was 5 mm, and their diameter 25 mm.

fibers (Figure XIII. 12, continuous lines). For specimens with a large closed porosity and specimens made of thick fibers (more than 100 μ) formula (XIII. 1) no longer applies (Table XIII. 7). One of the possible explanations is the higher packing anisotropy of the structural elements made from the thick fibers.

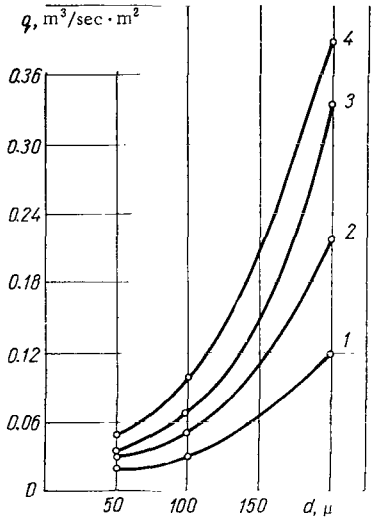

FIGURE XIII. 11. Dependence of the permeability of copper fiber filters on the fiber diameter:

1 — ΔP = 1 atm; 2 — ΔP = 2 atm; 3 — ΔP = = 3 atm; 4 — ΔP = 4 atm.

The pattern of gas flow through fiber filters is not the same as the pattern of liquid flow through the same filters. For example, when spindle oil was filtered through copper fiber filters (porosity 43 %, filter thickness 3 mm, length of initial fibers 12 ± 2 mm) the throughput increased by a factor of 8 at a pressure drop of 1 atm, and by a factor of 23 at a pressure drop of 4 atm when the fiber diameter was increased from 50 to 200 μ; the theoretical equation derived by Markov and Stryapko /2/ gives a 16-fold increase.

The fiber length has a much slighter effect on the permeability (Figure XIII. 13) than the diameter, because of the logitudinal fiber alignment perpendicular to the direction of the applied load. For this reason, changes in the fiber diameter affect the pore size more than changes in the fiber length.

The permeability of fiber filters is to a large extent a function of the fiber surfaces, depending on the production method. A maximum permeability is reached, usually on filters produced by cutting a smooth wire. The permeability of filters produced from metallic "wool" with a rough surface is minimal, for both gases and liquids. Thus, according to /17/ the permeability of filters made of smooth fibers of stainless steel (cut wire) with a porosity of 65 % is four times that of filters made of metallic "wool"; this applies to dry air and water (Figures XIII. 14, XIII. 15).

TABLE XIII. 6. Strength and permeability of fibers made of SAE-430 steel /16/

Ultimate tensile strength, kg/mm²	Permeability, × 10^{-10} cm²		
	fine fiber	*medium fiber*	*coarse fiber*
5.3	—	1,935	—
7.7	—	329	—
10.5	187	206	—
14.0	65	90	155
17.5	13	45	58
21.0	—	19	—
24.5		6	—

* SAE-430 — stainless steel of the ferrite group containing 14—16 % of Cr.

TABLE XIII.7. Permeability to air of filters made from stainless steel 1Kh18N9T and bronze OTs4-3 fibers

Porosity, %	Air rate, $m^3/sec\ m^2$											
	diameter of steel fiber, μ						diameter of bronze fiber, μ					
	100		200		300		100		200		300	
	0.05 atm	0.10 atm	0.05 atm	0.10 atm	0.05 atm	0.10 atm	0.05 atm	0.10 atm	0.05 atm	0.10 atm	0.05 atm	0.10 atm
30	0.37	0.95	1.14	2.30	1.20	2.42	0.23	0.94	1.30	2.08	1.32	2.62
40	0.90	1.76	1.47	2.76	1.64	2.96	0.58	1.50	1.84	3.00	1.18	3.58
50	1.53	3.06	1.98	3.50	2.22	3.80	0.93	2.50	2.50	4.28	3.04	5.04

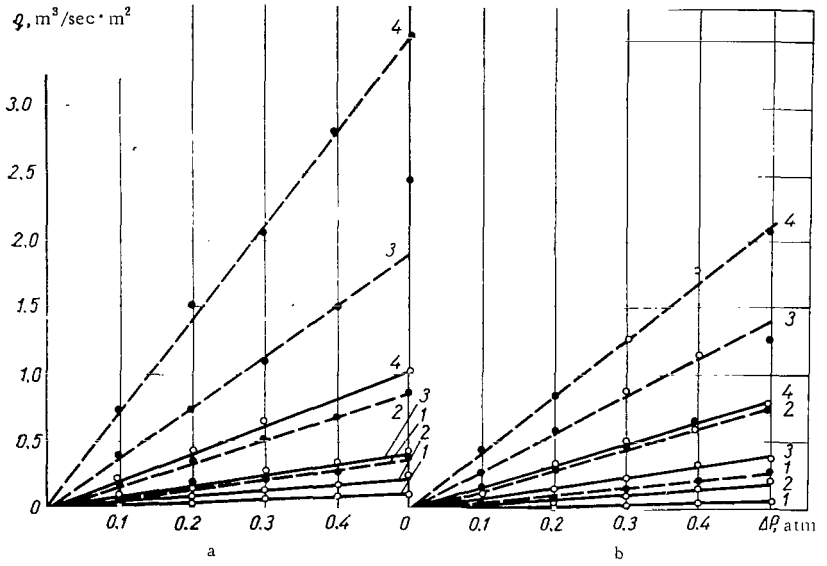

FIGURE XIII.12. Dependence of the permeability to air of filters of different porosities made of copper fibers of 50 μ (continuous line) and 100μ (dashed line) diameter after pressing (a) and after sintering (b) on the pressure drop:

1 — θ = 15%; 2 — θ = 20%; 3 — θ = 25%; 4 — θ = 30%.

Filters made from extruded fibers (Figure XIII.16, I) are also somewhat poorer than are similar filters made of smooth wire fibers (Figure XIII.16, II).

Very frequently, when pressing products from powders or fibers we observe a deformation of the structural elements in surface layers. The effect of this on the air and water penetrability in filters made from stainless steel fibers was studied by Sokol /7/. To obtain deformed fibers, smooth straight fibers were preliminarily subjected to a small pressure, and then the briquettes were fractured. Filters with certain parameters were prepared from these deformed fibers, and their permeability was compared with results obtained on filters made of unstrained fibers. It was found that the utilization of deformed fibers in filters considerably decreases their permeability to gas and liquids, especially if the porosity is lower than 50% (Table XIII.8).

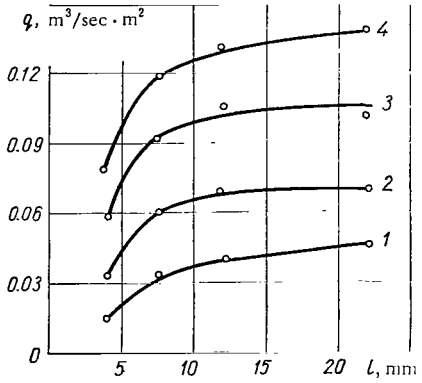

FIGURE XIII.13. Dependence of the permeability of filters made of copper fibers (porosity of filter 43%, filter thickness 3 mm, filter diameter 30 mm) on the fiber length:

1 — ΔP = 1 atm; 2 — ΔP = 2 atm; 3 — ΔP = 3 atm; 4 — ΔP = 4 atm.

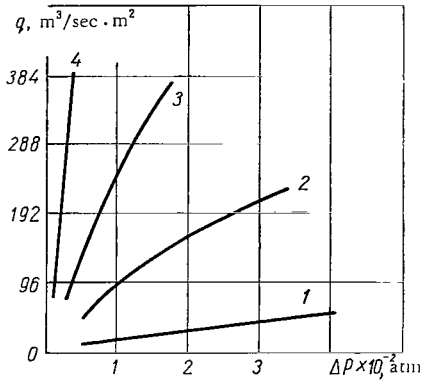

FIGURE XIII.14. Dependence of the permeability (to dry air) of filters made of stainless steel fibers on the pressure drop at 20°C:

1 — metal "wool", θ = 32%; 2 — metal "wool", θ = 50%; 3 — metal "wool", θ = 65%; 4 — wire fibers, θ = 65%.

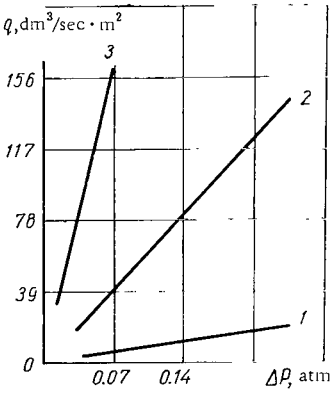

FIGURE XIII.15. Dependence of the permeability to water of filters made of stainless steel fibers on the pressure drop at 8°C:

1 — metal "wool", θ = 42%; 2 — metal "wool", θ = 65%; 3 — wire fibers, θ = 65%.

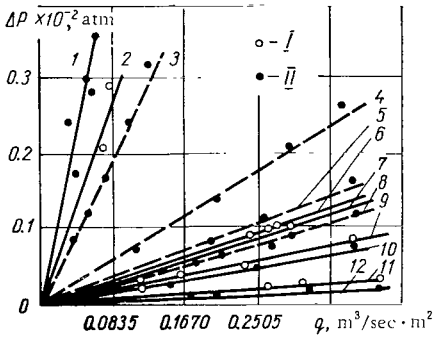

FIGURE XIII.16. Dependence of the pressure drop on the liquid rate through filters made of extruded nickel fibers (I) and nichrome fibers (II) (dashed lines — fiber diameter 100 μ; continuous lines — fiber diameter 200 μ):

1 — θ = 24%; 2 — θ = 25%; 3 — θ = 32%; 4 — θ = 40%; 5 — θ = 46%; 6 — θ = 40%; 7 — θ = 34%; 8 — θ = 53%; 9 — θ = 45%; 10 — θ = 47%; 11 — θ = 56%; 12 — θ = 50%.

The chemical composition of the fiber metal has almost no influence on the permeability. Thus, when the fiber diameter is 100 μ and the pressure drop 0.1 atm, the permeabilities of filters with a porosity of 30% made from stainless steel and bronze are very close (see Table XIII. 7).

TABLE XIII.8. Effect of the deformation of fibers made of stainless steel (diameter 200 μ, length 5 mm) on the properties of filters sintered in a hydrogen atmosphere at 1,300°C for 1 hr

Properties of fibers and porous products made from them	Type of fibers	
	not deformed	deformed
Free bulk weight of fibers, g/cm³	1.92	1.84
Bulk weight of fibers after shaking, g/cm³	2.58	2.47
Volatility of fibers through a 10 mm diameter hole	Not volatile	Not volatile
Density of products, g/cm³, after applying a pressure of, kg/cm²:		
4.8	5.38	5.62
6.4	5.95	6.09
Density of sintered products after applying a pressure, of, kg/cm²:		
4.8	5.58	5.70
6.4	5.90	6.04
Filtering time, sec, of 1 liter of water through filters 1 square inch in area, at a pressure drop of 400 mm H_2O after applying a pressure of, kg/cm²		
4.8	6	8
6.4	10	18
Pressure drop, mm H_2O, at an air rate of 1 m³/min · m² after applying a pressure of kg/cm²:		
4.8	20	20
6.4	140	320

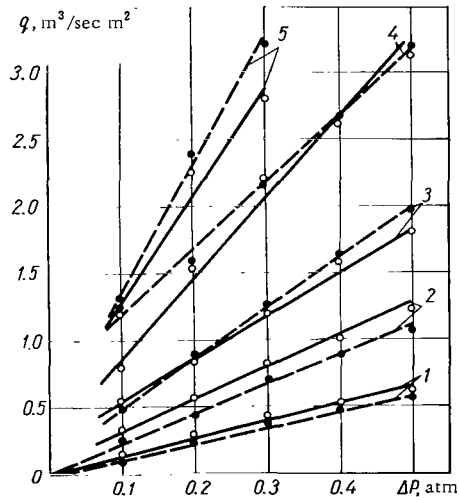

FIGURE XIII.17. Dependence of the air permeability of filters made from nickel fibers on the pressure drop after pressing (dashed lines) and sintering (continuous lines):

1 — θ= 15%; 2 — θ = 20%; 3 — θ= 25%; 4 — θ= 30%; 5 — θ= 35%.

Thus, the permeability of fiber filters depends on the parameters of the original fibers, and very strongly on their diameter and their surface state. The production technology has an especially large effect on the permeability of the filters.

A comparison of filters made by liquid felting and from fibers which have not been subjected to sedimentation shows that at an equal porosity the permeability in the first case is somewhat smaller. This is explained by the stronger local scattering in porosity, and consequently larger deviations in the pore size from the mean value, in products made from unfelted fibers.

Sintering fiber filters increases the interface between the fibers and usually lowers the permeability. This effect is very strong when the fibers are sintered in the presence of liquid phase. It follows from Table XIII. 7 that at equal porosities, pressure drops, and diameters of the initial fibers (100 μ), the permeability of bronze filters sintered in the presence of 20 vol % of a liquid phase is much smaller than that of filters made of stainless steel.

TABLE XIII. 9. Effect of the sintering conditions on the permeability of filters made from molybdenum fibers to air

Production conditions	Annealing in hydrogen at 1,050°C for 2 hr (1st stage)				Sintering in vacuo (10^{-3} mm Hg) at 2,200°C for 2 hr (2nd stage)			
	thick- ness, mm	*porosity,* %	*pressure* drop, atm	permea- bility, $m^3/sec \cdot m^2$	*thick-* ness, mm	*porosity,* %	*pressure* drop, atm	permea- bility, $m^3/sec \cdot m^2$
Pressed after preliminary felting	5.0	31.3	0.1	0.41	5.0	30.4	0.1	0.53
			0.2	0.87			0.2	0.98
			0.3	1.51			0.3	1.56
			0.4	1.78			0.4	1.94
			0.5	2.26			0.5	2.46
The same	3.1	31.8	0.1	0.46	3.1	30.3	0.1	0.41
			0.2	1.03			0.2	0.91
			0.3	1.54			0.3	1.33
			0.4	2.02			0.4	1.68
			0.5	2.52			0.5	2.12
Pressed without felting	5.0	26.9	0.1	0.25	5.0	26.1	0.1	0.24
			0.2	0.54			0.2	0.65
			0.3	0.90			0.3	0.89
			0.4	1.06			0.4	0.11
			0.5	1.38			0.5	1.42
The same	3.1	28.0	0.1	0.40	3.0	28.1	0.1	0.34
			0.2	0.89			0.2	0.93
			0.3	1.29			0.3	1.32
			0.4	1.67			0.4	1.67
			0.5	2.03			0.5	2.04

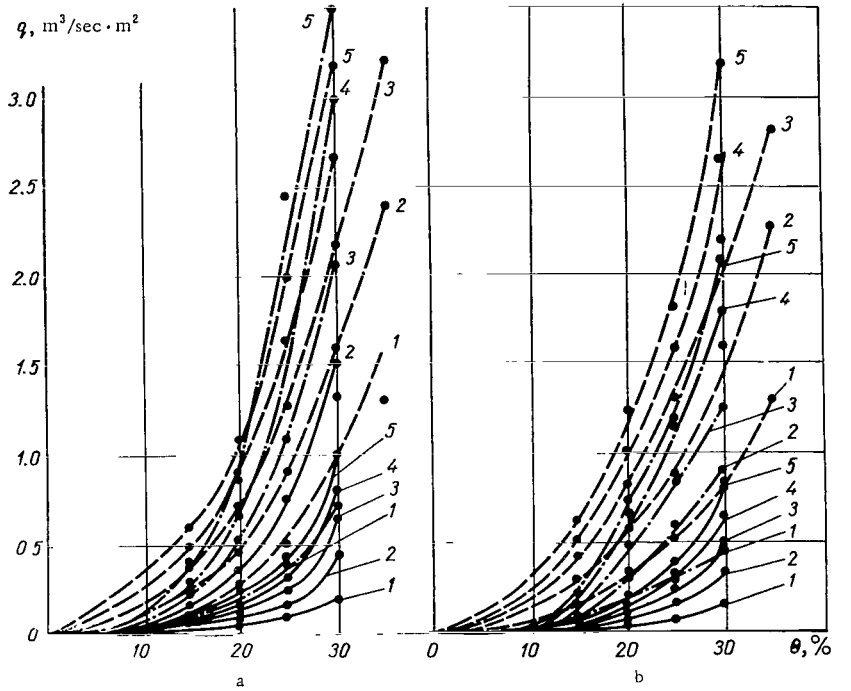

FIGURE XIII.18. Dependence of the permeability of fiber filters to air on the porosity after pressing (a) and after sintering (b):

1 — $\Delta P = 0.1$ atm; 2 — $\Delta P = 0.2$ atm; 3 — $\Delta P = 0.3$ atm; 4 — $\Delta P = 0.4$ atm; 5 — $\Delta P = 0.5$ atm.

In specimens made from thicker fibers (diameter 200 and 300 μ), sintering does not lead to the formation of interfiber contacts; for this reason the above effect is not observed.

Sintering filters made from nickel fibers of 180 μ diameter (Figure XIII.18, dashed lines) at 1,200°C for 2 hr leads to little increase in the interface. In this case the differences in the permeabilities of pressed and pressed plus sintered filters are almost nil (Figure XIII.17).

Thermal sintering conditions which do not lead to an appreciable increase in the interfacial area between the fibers have little effect on the permeability, even when the fibers are fairly thin. This is confirmed by tests on filters made from 70 μ molybdenum fibers (Table XIII.9).

Annealing filters of different thicknesses and porosities in hydrogen for 2 hr at 1,050° after they have been molded under different conditions and then sintered at 2,200°C for 2 hr ensures almost uniform permeability of molybdenum fiber filters. In this case, 2,200°C (2,473°K) is only 85% of the melting point of molybdenum expressed in Kelvin degrees, and clearly insufficient for sintering the fibers.

Sintering thin fiber filters at higher temperatures produces a considerable increase in the interparticle points of contact, and decreases the permeability. For example, after filters made of copper fibers of 50 and 100 μ diameter (Figure XIII.18, continuous and dashed lines) are sintered at 950°C (1,223°K, or 90% of the melting point of copper, expressed in degrees Kelvin), the permeability decreased by a factor of about 1.5.

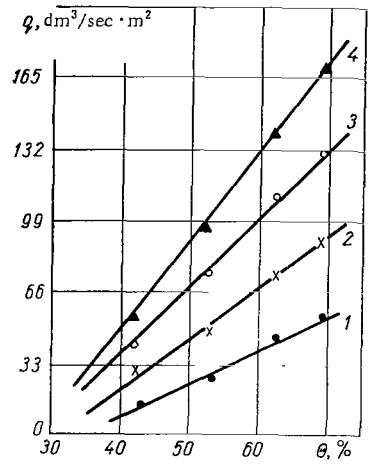

FIGURE XIII. 19. Dependence of the permeability of copper fiber filters (filter thickness 3 mm, fiber diameter 100 μ, fiber length 12 ± 2 mm) on the porosity in the filtering of spindle oil:

1 — ΔP = 1 atm; 2 — ΔP = 2 atm; 3 — ΔP = 3 atm; 4 — ΔP = 4 atm.

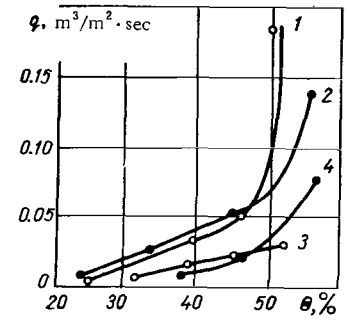

FIGURE XIII. 20. Dependence of the permeability of fiber filters on the porosity during the passage of oil AMG — 10 (for the water system of airplanes):

1 — fibers made of nichrome wire (d = 200 μ); 2 — extruded nickel fibers (d = 200 μ); 3 — fibers made of nichrome wire (d = 100 μ); 4 — extruded nickel fibers (d = 100 μ).

Tests on the effect of the geometrical parameters of products made of fibers and of the porosity on their permeability are reported in /2/ and /18/. The dependence of the permeability of filters made from copper, nickel, and nichrome fibers of various origin to gases and liquids (Figure XIII. 18, XIII. 19, and XIII. 20) on the porosity can generally be expressed by an exponential equation of type

$$Q = k\Theta^m, \qquad \text{(XIII. 2)}$$

where k is a factor depending on the conditions of the test; Θ is the porosity; m is an exponent determined by the slope of the straight line relative to the abscissa in logarithmic coordinates.

For pressed and sintered copper filters, when air is passed through m lies between 2.5 and 3.5; m increases with decrease in the fiber diameter. For example, for 100μ fibers m = 2 — 4, and for 40 μ fibers m = 4 — 8.

The dependence of the pressure drop (a magnitude proportional to the throughput) on the porosity was determined on filters made of lead fibers (porosity 35 — 80 %) and stainless steel fibers (porosity 25 — 45 %); it is also given by an exponential function (Figures XIII. 21, XIII. 22, Tables XIII. 10 and XIII. 11). At a given porosity of the filter, this dependence is very influenced by the state of the fiber surface and the specific gas rate. With increase in the gas rate and deformation or roughness of the fibers, the dependence of the pressure drop on the filter on its porosity becomes stronger.

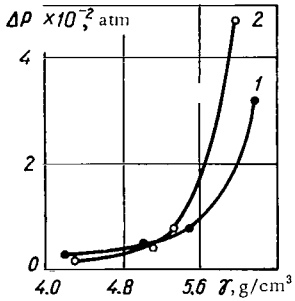

FIGURE XIII.21. Dependence of the pressure drop on filters made of stainless steel fibers of 200 μ diameter and 5 mm length on the density (air rate 0.167 m/sec, filter thickness after sintering about 5.3 mm):

1 — undeformed fibers; 2 — deformed fibers.

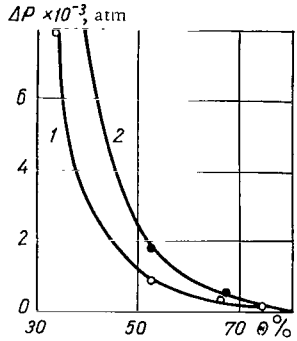

FIGURE XIII.22. Dependence of pressure drop on filters made of lead fibers (120 μ diameter) on the porosity:

1 — $q = 0.267\ m^3/sec \cdot m^2$; 2 — $q = 0.478\ m^3/sec \cdot m^2$.

TABLE XIII.10. Effect of the porosity of filters made of lead fibers (120 μ in diameter) on the pressure drop for various air rates

Filter parameters		Air rate, $m^3/sec \cdot m^2$	Pressure drop, $\times 10^{-4}$ atm
thickness, mm	porosity, %		
5.90	34.0	0.267	80
4.86	52.8	0.267	8
4.68	68.0	0.267	2
4.94	74.4	0.267	1
5.90	34.0	0.478	173
4.86	52.8	0.478	17
4.68	68.0	0.478	2.5
4.94	74.4	0.478	1.5

The thickness of the fiber also affects the filter permeability. It follows from tests performed on cermet filters with large and small retention limits (plugs, plates, disks) that up to a certain thickness the permeability decreases in proportion to the thickness. When it reaches a certain limit, the permeability begins to decrease much more rapidly than as given by the law of proportionality. Therefore, the filter thickness must be selected according to the required structural strength.

In the filtering of spindle oil the permeability decreases in direct proportion to the thickness if the pressure drop for 2 — 4 mm copper filters differs (Figure XIII.23). At a filter thickness larger than 3 mm, the graph of the pressure drop plotted against the filter thickness at a constant gas rate is no longer linear. This is shown on examples of the permeability to air of filters made of stainless steel fibers (Figures XIII.24 and Table XIII.12),

TABLE XIII. 11. Effects of the parameters of filters made of 100 μ diameter fibers on their porosity

Material and fiber diameter, μ	Filter thickness, mm	Filter density, g/cm³	Porosity, %	Pressure drop on filtering aerosol. Aerosol rate, m³/min · m²	Time (sec) of 100% permeation of 0.31 μ aerosol particles (initial aerosol concentration, 2.5 g/cm³)
Pb, 120	4.0	8.18	24.6	4.7	128.4
Pb, 120	4.1	7.14	34.8	2.0	32.4
Pb, 120	4.2	5.83	48.4	0.5	21.0
Al, 170	3.7	1.71	34.7	1.0	37.2

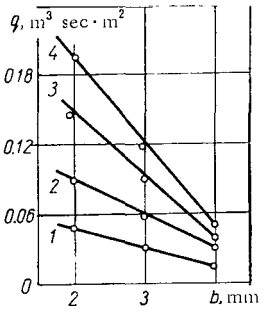

FIGURE XIII. 23. Dependence of the permeability of copper fiber filters on their thickness:

1 — $\Delta P = 1$ atm; 2 — $\Delta P = 2$ atm; 3 — $\Delta P = 3$ atm; 4 — $\Delta P = 4$ atm.

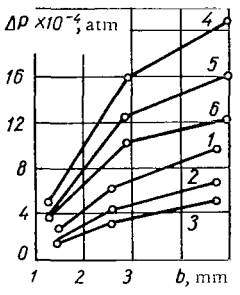

FIGURE XIII. 24. Dependence of the pressure drop on filters made of stainless steel on their thickness (air rate, 2 m³/sec · m²):

1 — $\gamma = 4.8$ g/cm³, $\frac{P_{abs}}{P_{atm}} = 0.2$; 2 — $\gamma = 4.8$ g/cm², $\frac{P_{abs}}{P_{atm}} = 0.6$; 3 — $\gamma = 4.8$ g/cm³, $\frac{P_{abs}}{P_{atm}} = 1.0$; 4 — $\gamma = 5.15$ g/cm³, $\frac{P_{abs}}{P_{atm}} = 0.2$; 5 — $\gamma = 5.15$ g/cm³, $\frac{P_{abs}}{P_{atm}} = 0.6$; 6 — $\gamma = 5.15$ g/cm³, $\frac{P_{abs}}{P_{atm}} = 1.0$.

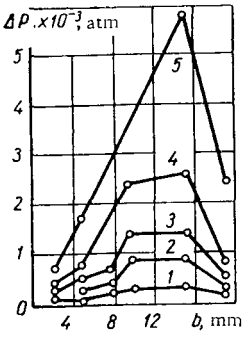

FIGURE XIII. 25. Dependence of the pressure drop on filters (porosity 53%) made of lead fibers 120 μ in diameter at various air rates:

1 — 0.054 m³/sec · m²; 2 — 0.106 m³/sec · m²; 3 — 0.160 m³/sec · m²; 4 — 0.267 m³/sec · m²; 5 — 0.478 m³/sec · m².

TABLE XIII.12. Effect of the density and thickness of filters of stainless steel fibers on the pressure drop at an air rate of 2 $m^3/sec \cdot m^2$

Filter parameters		Relative pressure losses for P_{abs}/P_{atm}, %		
thickness, mm	density, g/cm^2	1.0	0.6	0.2
1.50	4.61	1.75	2.00	2.70
2.62	4.85	3.35	4.13	6.25
4.65	4.83	5.25	6.70	9.80
1.37	5.15	3.90	4.25	5.25
2.95	5.22	10.5	12.60	16.10
5.00	5.12	12.40	16.10	20.90

TABLE XIII.13. Pressure drop on filters made of 120μ lead fibers at various air rates

Filter parameters		Pressure drop on filters, $\times 10^{-4}$ atm, at air rates of $m^3/sec \cdot m^2$					
porosity, %	thickness δ, mm	0.054	0.106	0.160	0.267	0.374	0.478
52.4	1.98	1.5	—	2.5	4.0	5.0	6.5
52.8	4.86	1.0	2.5	4.0	8.0	12.0	17.0
53.0	7.83	2.0	4.0	6.5	—	—	—
51.8	9.80	4.0	9.0	14.0	24.0	—	—
52.4	15.30	4.0	9.0	14.0	26.0	41.0	58.0
53.7	18.98	1.5	3.0	5.0	8.0	—	24.0

and of lead fibers (Figure XIII. 25 and Table XIII. 13). In the latter case the graph has a maximum; at filter thicknesses above 15 mm the pressure drop on lead filters decreases. But tests on the permeability to water of such filters showed that the filtering time of a constant liquid volume increases in proportion to the filter thickness provided that the pressure drop is constant (Figure XIII. 26). However, in repeated tests on the permeability to water of the same lead fiber filters, after preliminary drying, a considerable scattering of the results was observed every time. This invalidated the regularity found (Figure XIII. 27), though the measuring accuracy was adequate (Table XIII. 14). Therefore, the observed pattern of the permeability to water (its linear decrease with increase in filter thickness and increase in filter density (Figure XIII. 28)) through filters made of stainless steel and lead fibers cannot be applied to all fiber filters. It is evident that this pattern is characteristic of the given type of porous products only under given test conditions.

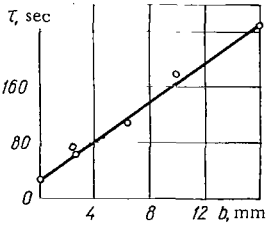

FIGURE XIII. 26. Dependence of the filtering time of 1 dm^3 of water through filters 1 sq in. in area on the filter thickness (filter material, 120 μ diameter lead fibers, porosity 38%, pressure drop 0.04 atm).

In general, the flow patterns of gases and liquid in fiber filters differ, just as in cermet filters. Since the permeability of fiber filters to gases was

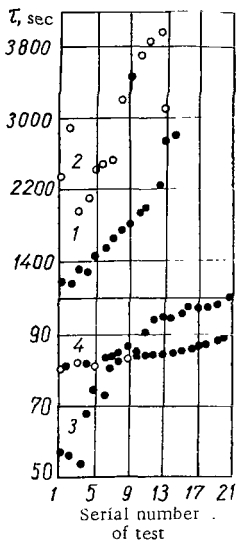

FIGURE XIII.27. Dependence of the filtering time of 1 dm^3 of water through a lead fiber filter (area 1 sq inch) on the serial number of experiment:

1, 2 — filter thickness, 2.6 mm; filter material, stainless steel fibers (diameter 200μ; length 5 mm); filter density 6.33 g/cm^3; 3, 4 — filter thickness, 2.2 mm; filter material, lead fibers (diameter 120μ); filter density, 7.0 g/cm^3; 1, 3 — data prior to drying of the filters; 2, 4 — data after drying the filters.

studied in greater detail, the pattern found can be generalized and theoretically described for this type of products.

TABLE XIII.14. Permeability of fiber filters to water at a pressure drop of 0.04 atm

Filter thickness b, mm	Relative density, %	Filtering time, sec, of 1 dm^3 of water through a filter 1 sq inch in area
2.3	59.2	24.8
2.3	59.4	20.9
2.3	60.7	20.9
2.2	61.7	27.6
2.4	61.8	24.4

At present, we consider that the effect of the thickness of fiber filters on its permeability to gas shows deviations from Darcy's law; the decrease in permeability is less than the value inversely proportional to the thickness. For example, at a constant porosity (26%) and a pressure drop of ~0.1 — 0.5 atm, the permeability of a 5 mm thick filter made of molybdenum fibers to air was 0.49 and 2.32 $m^3/sec \cdot m^2$, respectively, and of a 1 mm thick filter it was 0.77 and 3.99 $m^3/sec \cdot m^2$ (Table XIII.15). In other words, if the filter thickness decreases by a factor of 5, its permeability increases only 1.6 — 1.7 times. It is possible that one of the reasons for this deviation is the increase in the anisotropy of the structure with decrease in the filter thickness.

We have already mentioned that in filters made of stainless steel fibers (obtained by clipping wire) and lead fibers (obtained by spouting the melt) without preliminary felting, the permeability to water shows considerable scattering. In filters made from deposited fibers the deviations of the

permeability from the average values is less pronounced. For example, in filters made of thin copper wires the deviations of the permeability from the mean value obtained after repeatedly blowing air is only ± 6.5 %.

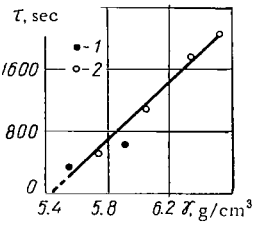

FIGURE XIII. 28. Dependence of the time of passage of 1 dm³ of water through a filter 1 sq inch in area (stainless steel fibers, diameter 200 μ, length 5 mm) on the density:

1 — undeformed fibers; 2 — deformed fibers.

The variance of data obtained in tests on the permeability of various filters made of thin copper fibers obtained by clipping wire is approximately equal to the variance of test data on the same filter.

One of the main properties of porous materials intended for filters is the retention limit; this term denotes the minimum dimension of the inclusion in liquid or gas which is completely retained by the filter.

The results of tests on the filtration of liquid fuel (kerosene) showed that fiber filters with a porosity corresponding to that of cermet filters have a 2- to 3-fold lower retention limit, while the thickness of the fiber filters is much smaller, and the permeability 4 — 5 times higher (Table XIII. 16).

Changes in the thickness, porosity, and length of the original fibers have little effect on the retention limit of the filter. But the fiber diameter greatly affects this parameter. For example, in the filtration of oil, filters with a fiber diameter of 200 μ retain 40 — 45 μ inclusions, while filters with a fiber diameter of 50 μ retain 8 μ inclusions.

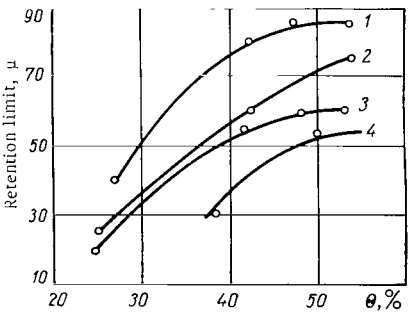

FIGURE XIII. 29. Dependence of the retention limit of 2 mm thick fiber filters on their porosity:

1 — nichrome wire fibers (d = 200 μ); 2 — extruded nickel fibers (d = 200 μ); 3 — nichrome wire fibers (d = 100 μ); 4 — extruded nickel fibers (d = = 100 μ).

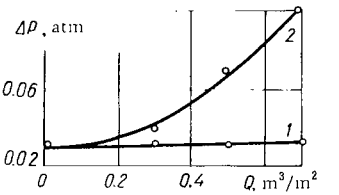

FIGURE XIII. 30. Dependence of the pressure drop over two-layer filters on the overall rate of contaminated liquid:

1 — direction of filtration: fiber-powder; 2 — direction of filtration: powder-fiber.

The retention limit of a filter depends to a large extent on the origin of the fibers. Figure XIII. 29 shows that the retention limit of filters from different fibers obtained by the same technology (pressing without preliminary

TABLE XIII.15. Effect of the thickness of molybdenum fiber filters on the permeability to air

Production conditions	Thickness b, mm	Porosity, %	Pressure drop, atm	Permeability to air, $m^3/sec \cdot m^2$
Pressed after preliminary felting	5.0	27.3	0.1	0.35
			0.2	0.78
			0.3	0.10
			0.4	1.38
			0.5	1.64
	3.0	26.7	0.1	0.49
			0.2	0.90
			0.3	1.28
			0.4	1.59
			0.5	1.98
Pressed without felting	5.0	26.0	0.1	0.49
			0.2	0.90
			0.3	1.48
			0.4	1.96
			0.5	2.32
	3.0	26.3	0.1	0.45
			0.2	0.94
			0.3	1.37
			0.4	1.72
			0.5	2.12
	2.0	26.8	0.1	0.77
			0.2	1.82
			0.3	2.59
			0.4	3.23
			0.5	3.99

TABLE XIII.16. Retention limit of filters made of fibers or powders in the filtration of liquid fuel

Filter material	Porosity, %	Filter thickness b, mm	Settling time of 2,500 cm^3 of fuel oil, sec	Retention limit, μ
Fibers	32	0.87	81	8
Powder	38	3.00	400	20
Fibers	45	0.87	64	12
Powder	45	3.00	266	40

felting and sintering) for oil AMG-10. Filters made of extruded fibers have a higher retaining power, because of the roughness of the fiber surface, which is specific for this fiber type. The surface roughness has almost no effect upon the permeability of the filters (see Figure XIII.20).

In practice the filters must also ensure the required operation reserve (dirt capacity) which is the time interval in the operation of the filter during which the pressure drop attains its maximum. The operation reserve is determined by the rate of clogging of the filter pores by the contaminant, and

TABLE XIII. 17. Properties of filters prepared from Fiberfrax fibers (aluminum silicate) /20/

Fiber	Filter thickness, mm	Packing density, g/cm³	Parameters of filtered gas			Filter resistance, $\times 10^{-4}$ atm	Retaining power, %
			velocity, m/sec	temperature, °C	aerosol concentration*, g/cm³		
Coarse	102	0.32	2.02	21	0.33	1.2	85
		0.48	2.02	760	0.72	1.7	83
		0.32	3.55	760	0.58	1.4	82
Medium	38	0.48	1.77	21	1.08	1.7	99
		0.48	2.02	538	1.21	2.2	94
		0.48	3.55	760	0.59	—	84
Fine	25	0.32	1.77	21	1.31	2.4	98
		0.32	2.02	760	1.23	2.3	91
		0.32	3.55	816	0.24	3.7	85
Mixture of coarse (l = =127 mm),	—						
		0.48	2.02	21	0.47	5.1	99
medium (l = 25 m),		0.48	2.02	760	0.39	5.3	99
and fine fibers (l = 3 mm)							

* Copper oxide (technical grade) with a particle size of 8.5μ was used as the aerosol.

decrease in its permeability to the permissible level. The operation reserve itself determines the necessary dimensions and weight of the filter.

We know from the cermet industry that to increase the operation reserve, the filters are produced in two layers. With correct operation of such a filter, depth (volume) filtration can be achieved, and thus the service life can be increased /19/.

Two-layer fiber filters have a much lower retention limit than similar monolayer filters. To produce such filters it is sufficient to apply a porous cermet layer onto a fiber filter. This does not affect the permeability, but ensures a sufficient retention limit. The combination of fiber and powder layers produces a permeable system with pores narrowing in the direction of liquid or gas flow; this also ensures conditions of depth filtration.

Two-layer filters can, in principle, be produced from fibers only, for example, by rolling.

Figure XIII. 30 shows the dependence of the pressure drop in a two-layer filter* on the total liquid rate during filtration of oil AMG-10. The service life of the filter is much longer if the coarse fiber layer is turned to receive the liquid flow than in the reverse case. The fiber layer is then used for rough purification, and the fine powder layer for fine filtration. The whole filter volume participates in the filtration process. But if the oil is fed from the powder to the fiber layer, only the former purifies the liquid. This leads to a rapid increase in the filter resistance to the passage of the oil.

* The filter is a disk consisting of two layers. One has a thickness of 2 mm, porosity of 40%; it is made from extruded nickel fibers 100μ in diameter. The second layer with 70% porosity and 0.5 mm thick consists of nickel carbonyl powder with a filler. The powder layer is sintered to the fiber layer.

TABLE XIII. 18. Composition and some properties of ceramic fibers /21/

Fiber material	Composition, vol %							Diameter, μ	Length, mm	Density, g/cm^3	Melting point, °C	Operating temperature, °C
	Al_2O_3	SiO_2	ZrO_2	B_2O_3	Na_2O	TiO_2	MgO+CaO+ $+Fe_2O_3$					
Aluminum silicate: Fiberfrax (long fiber)	51.3	45.3	3.4	—	—	—	—	4	13—254	2.73	Above 1,760	Up to 1,260
Fiberfrax (short fibers)	51.2	47.4	—	0.70	0.7	—	—	Up to 10 (mean 2.5)	(mean 50—75) Up to 3.8	2.73	Above 1,760	Up to 1,260
Fiberfrax (paper)	51.2	47.1	—	0.60	0.6	—	0.5	—	—	—	—	—
Kaowool	45.1	51.9	—	0.08	0.2	1.7	1.4	2.8	Up to 203	2.60	1,750	1,100 (long periods) 1,260 (short periods)
Kionite J—M	42.0	50.0	—	—	—	6.0	—	3—4	—	—	—	Up to 1.100
Potassium titanate: Tipersul ($K_2Ti_6O_{13}$)	—	—	—	—	—	—	—	1	0.2—30	3.60	1,371	1,200 (air and inert gases); 540 (hydrogen); 955 (75% H_2 + + 25% N_2 mixture); 980 (vacuum 10^{-5} mm Hg)

A modification of aluminum silicate fibers is Kaowool, produced as a bulky fibrous mass and felt /21/. Kaowool fibers which have a diameter of 3 μ and a maximum length of 200 mm are not changed by temperatures of 1,100°C acting for a long time, or by temperatures of about 1,260°C acting for a short time. The fibers are not destroyed by steam at high temperatures, but do not withstand contact with strong acids and alkalis for long periods. In short-term action, the resistance of Kaowool to cold acids is greater than to hot acids or hot and cold alkalis. Therefore, such material is most efficient for the filtration of hot gases.

Recently, thin flexible and long fibers (Kionite J — M), which resists temperatures up to 1,100°C, have been obtained from natural silica minerals. Felts (Thermoflex and Cerafelt) made from such materials are chemically pure, and suitable as a high-temperature filter material in the nuclear industry /21/.

Besides materials made of fibers used for the preparation of high-temperature gas filters, inorganic materials with a fibrous structure and resistant to corrosive media are also known. They include potassium titanate-base materials termed "Tipersul" /21/. Tipersul fibers have a high thermal stability at 1,090°C and a satisfactory stability at 1,200°C. Because of their resistance to fused acids, alkalies, salt solutions, and organic solvents, these fibers are a very good material for purifying corrosive liquids.

Materials from ceramic fibers are the most thermal-stable and refractory of known filter materials (Table XIII. 18).

A combined material made from fibers has recently been produced. It can be used for the filtration of hot gases. The initial product for such materials is a mixture of asbestos and glass or ceramic fibers, which are converted into various articles and paper. The combined materials are used for filtering air at 538°C or higher (it is assumed that such filters can be used to temperatures up to 982°C) /21/. These filters have a higher efficiency than ones produced from a single ceramic material made of fibers of fairly large diameter. Structural changes in the asbestos (when it is heated to a temperature above 482°C, chrysolite asbestos is transformed into olivine) do not affect the efficiency of the material since its fibrous structure remains unchanged.

If the preparation of continuous metal and nonmetal threads is not too complicated, these threads can and should be used as fabrics for filters. Examples include thermally stable fibers made of wire (glass fabrics with or without previous metallization) for cleaning hot liquids. For filtering some metal melts, fabrics of continuous graphite fibers are used; but the fibers must be pretreated, since graphite fibers are not wetted by most metals. Graphite filters can also be prepared unwoven as a felt from fibers of about 10 μ diameter. Such fibers are stable in air up to 370°C, and in neutral and reducing media up to 2,760°C. The strength of a graphite fiber felt at 1,650°C is twice as high as at 20°C.

3. Transpiration materials with a fibrous structure

The term transpiration materials is used for a material in which the liquid or gaseous agent is passed through the pores. Transpiration materials are used for the effective cooling of high-temperature installations, prevention of ice formation and control of the boundary layer in the aircraft industry, reactions in a fluidized bed, pneumatic transport of free-flowing bodies and melts, cooling or drying, mixing of liquids and gases, enrichment of mineral ores, etc.

There are few published data on the practical results of the use of materials as transpirators. Most of the information deals with so-called porous cooling.

The principle of porous cooling is heat dissipation when the cooling agent passes through the pores. When the rate of the cooling agent is sufficiently high, a liquid or gas film is formed on the surface of the porous walls and appreciably reduces the wall temperature. However, film cooling requires high rates of the cooling agent. When liquids are used as cooling agent, the wall temperature may also be reduced because of the heat consumed for liquid vaporization and possible dissociation.

The most effective cooling method is porous cooling with gases.

Tests on heat transfer in porous plates made of bronze and stainless steels between 100 and 200°C, with hydrogen, argon, or nitrogen as the cooling agents /22, 23/, showed that the molecular weight of the gases affects the cooling efficiency. At equal weight rates of the gases, hydrogen decreased the temperature most, and argon least. The heat transfer rate (internal heat exchange) without film conditions is also very dependent on the porosity.

Tests on porous cooling on bronze and stainless steel at temperatures up to 1,000°C showed that the process is independent of the material used. Porous stainless steel through which the cooling gas was blown withstood the combustion products of heavy fuel for 150 hr at gas and wall temperatures of 820 and 540°C, respectively. Because a boundary layer was formed near the wall, the clogging of the pores by the unburned particles was slight (after the tests the reduction in the permeability was only 10%).

Porous cooling has also been applied for nozzle and operating turbine blades /24—27/. The cooling agent was air, blown through at a rate of $0.7\ kg/sec \cdot m^2$ and the pressure drop was 1.4 atm. With a permeability coefficient of 0.49 darcy, the blade temperature was reduced from 800 to 450°C; the strength of the blades was $9—12\ kg/mm^2$.

Porous blades make it possible to elevate the temperature of gas from 840 to 1,200°C, and to increase the power by 10%. The power expended on air supply is 0.5—2.5%. (for air amounts of 1—5% of the gas amount). For example, hollow blades made of the alloy "Vitallium" can operate at 1,093°C for several hours. For the same time of service the temperature can be increased by 260°C; it is sufficient to blow 2% of air.

The equations for porous cooling by a liquid agent are reported in /28/.

In aircraft and rocket engineering, highly porous materials for vaporization cooling are being successfully used. The principle is the cooling of component parts or units by vaporizing a liquid with a low boiling point. For example, the outside surface of the German V 2 rocket was cooled to 815°C at a flying speed of 4,800 km/hr by this method.

In the first variant operation of a two-layer filter, the resistance remains for a long time on the level of a monolayer filter. At the same time, the retention limit is decreased by a factor of five, and amounts to 8 μ.

After the operation reserve has been exhausted, the filters are regenerated to restore the initial permeability and reserve. Reverse blowing or washing of the filters is the most widely applied recovery method.

However, according to available information, this method of regeneration does not yield the required effect for filters made of rough fibers. Filter regeneration employing ultrasound is very promising. High-frequency oscillators are the ultrasonic source. The filter is regenerated by forces arising at the instant the cavitational bubbles begin to be formed, after ultrasonic waves have impacted the washing liquid. In cavitational bubbles, a sharp local pressure increase occurs, while the temperature increases to 300 — 400°C; this considerably improves the cleaning. In ultrasonic regeneration the washing liquid must circulate; sodium nitrate solution is employed as the washing liquid,

After 20 min of regeneration and drying of the fiber filters, their permeability is restored to about 98 % of the initial value.

It can be concluded from the above that we now have fiber material available (stainless steel, nickel, molybdenum, aluminum, Monel metal) which can be employed for producing filters for a wide range of operating conditions. Not long ago, it was necessary to provide materials (including filter media) which are very resistant to high temperatures and corrosive gaseous and liquid media.

The raw material for these filters are nonmetallic fibers.

Usually aluminosilicate (Fiberfrax) fibers are used as filter material /20/. Such fibers are obtained by spraying the melt onto a rapidly rotating disk. The average length of the fibers is 50 — 75 mm, and their diameter is about 4 μ. Such fiber materials are convenient for trapping radioactive particles from hot gases formed in nuclear reactors, and for gas purification in chemical and metallurgical plants.

At present, in the ore-mining industry, technological processes are being developed which require filter materials employable at temperatures of about 390°C or higher. These processes include coal gasification in order to obtain hydrogen and carbon monoxide; coal gasification by the heat evolved during nuclear fission; filtration of the ignition products of coal used in gas turbines.

Research carried out in the USA showed that aluminum silicate fibers are suitable for long-term application in gas filtration at temperatures up to 980°C. The fiber material is absolutely inert to the filtered gases and the contaminants contained in them.

The technical parameters of Fiberfrax materials are summarized in Table XIII.17. From long Fiberfrax fibers mats are produced which are used as filters in nitric acid plants to trap particles of the very expensive Pt catalyst. The filters are mounted in the gas stream (temperature above 590°C) between the reactor and the operating boiler. Such filters are more effective than glas-fiber filters.

For the filtration of hot gases, corrugated paper made of Fiberfrax is also employed; the thickness of the paper is 0.5 — 2 mm.

Porous materials are now being used in pneumatic transport systems. In air troughs, the feed of compressed air imparts a high mobility to the free-flowing powder material. With a slope as low as 2 — 4° the material begins to move under gravity. In such systems the velocity of cement is about 1 m/sec; the air rate is 0.025 — 0.05 $m^3/m^2 \cdot$ sec at a pressure drop of 200 — 300 mm H_2O.

In the transport of fused glass from the furnace to the mold, porous metal troughs are used. Air is fed at such a rate that contact between the glass and trough walls is prevented. In this case, crack formation is avoided (the glass is, as it were, conveyed on an air cushion) /32/.

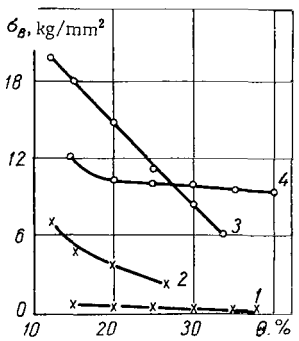

FIGURE XIII.31. Dependence of the strength of materials made from fibers and powders on the porosity /7/:

1 — pressed products made of iron sponge, particle size 0.06 — 0.15 mm; 2 — pressed products made of stainless steel fibers (d = 100 μ, l = 2.5 mm); 3, 4 — sintered products made of iron sponge and stainless steel fibers (sintering conditions: 1300°C, 1 hr).

Porous plates made of bronze or stainless steel are also used: for gas supply to liquids in the chemical, pharmaceutical, and food industries; choking of compressed gases to protect measuring instruments against pressure impacts /33/; production of uniform gas shielding in welding in an inert gas /34/; and uniform feed of oil in compressed air streams /35/.

Porous nickel caps are widely used for the passage of mercury which provides contact or ignition in mercury switches of radiolocation equipment /36/.

The application of porous materials in flotation machines for aeration of pulps in coal-processing plants is very promising. Compressed air (0.2 — 0.3 atm) is periodically fed. This sets a nickel membrane (porosity 30 — 35 %, thickness 4 — 5 mm), into motion. Air passing through the membrane aerates the pulp and floats the coal fines /37, 38/.

The above data show that transpiration materials can serve as multipurpose materials in engineering. However, up till now most of the transpiration materials used were cermet articles made of powders.

We shall now discuss the question of whether porous fiber products can be used as transpiration materials.

The transpirators must have a high strength, low hydraulic resistance, high thermal conductivity, and a uniform porous structure to ensure the required flow conditions for the coolant.

We shall determine how porous fiber products satisfy these requirements.

Skorokhod /39/ carried out a theoretical study of some properties of highly porous bodies. The author showed that if the porosity is high, the properties of fiber materials are much better than those of powder materials; the difference is more marked with increasing dependence of the property on porosity.

This is best seen on the strength parameters. The table below shows the ratio between strength parameters and porosity for articles made of iron fibers and iron powders /13/, when the strengths are the same for both materials.

Transpiration materials can be used for cooling the high-temperature combustion chambers of gas turbines, rocket motors, or magnetohydrodynamic generators /24, 29/. At a gas temperature of 2,000°C, and a cooling rate of the agent which is one tenth of the cooling rate in circulation cooling in conventional shells, the temperature of the wall can be reduced to 800°C if transpiration materials are used.

Refractory nickel and cobalt alloys are used as transpiration materials besides stainless steel.

The table below gives the parameters of porous stainless steel used as a transpiration material.

Pore size, μ	15
Porosity, %	20
Maximum thickness, mm	3
Air rate at a pressure drop of 0.07 atm, and a thickness of 1.5 mm, $m^3/m^2 \cdot sec$	0.03
Water rate under the same conditions $m^3/m^2 \cdot sec$	0.0017
Minimum tensile strength, kg/mm^2	17.5

Porous cooling materials should be coated by tungsten, cobalt, chromium or titanium to regulate the porous structure. By varying the thickness of the coatings the pore size can be controlled. The coatings are applied to the base material by pyrolysis, metallization or chemical methods /30/.

Thus, transpiration cooling makes it possible to increase the temperature limit of the efficiency of existing alloys, to obtain better operating parameters, to use the more abundant alloys for maintaining the required operating temperature and to control the temperature conditions in reactive motors.

Transpiration materials are also used to prevent the icing of airplanes. For this purpose, heated air or a special vaporizing liquid (antifreeze) is passed through porous plates placed at the frontal edges of the wings and the empennage.

The material used is porous bronze /31/ and stainless steel 316 /29/. The latter material is manufactured into 0.6 — 1.2 mm thick plates (porosity 15 — 20 %), tensile strength 21 — 35 kg/mm^2). A compressor feeds air through them at 350°C. The air rate is about 0.2 $m^3/m^2 \cdot sec$ at a pressure drop of 0.14 atm. Structures made of porous stainless steel are only half as heavy as equivalent compact material structures because of the higher strength of the steel. The design of the structure determines whether hot air or antifreeze is to be used. The use of porous materials against icing makes it possible to decrease antifreeze consumption by 50 %.

On landing and take-off of airplanes, air is sucked through porous materials mounted on the wings to improve the flight parameters. This prevents breaking off of the boundary layer and makes it possible to increase the lift of the wings. According to Pall /29/, the suction velocity must be 1.2 — 4.6 m/sec on an area of 0.280 — 0.744 m^2 at a pressure drop of 0.15 — 0.30 atm. To reduce the power consumption used for sucking the air it is better to produce porous plates with a certain porosity gradient, and not with a uniform porosity, corresponding to the pressure change in the air flowing past the wings.

Fiber products	Powder products
0.105	0.164
0.192	0.266
0.350	0.457

It can be seen from these data that the same tensile strength of powder and fiber materials is reached when the porosity of the fiber materials is 1.3 — 1.6 times that of the powder materials; hence the weight of the fiber material is correspondingly lower. Moreover, with increasing porosity of the fiber material these ratios will be still higher (Figure XIII.31).

TABLE XIII.19. Tensile strength and porosity of products made of metal fibers /16/

Ultimate tensile strength, kg/mm²	Porosity, %						
	Iron fiber products (P, S)	Products made of stainless steel 430 fibers					
		thin fibers (P, S)	thin fibers (F. P. S. G.)	thin annealed fibers (P, S)	thin fibers (F, P, S)	medium fibers (F, P, S)	coarse fibers (F, P, S)
3.50	—	55	—	—	—	—	—
5.25	50	49	—	—	—	54	—
7.70	40	39	—	34	—	40	—
10.50	30	31	—	25	38	34	36
14.00	—	20	—	16	32	28	25
17.50	—	13	25	—	27	24	16
21.00	—	—	16	—	—	21	9

Note: F — felting; P — pressing; S — sintering; G — gauging.

TABLE XIII.20. Dependence of the ultimate strength σ_B on the porosity and diameter of fibers of 1Kh18N9T steel and OTs4-3 bronze

Porosity, %	Ultimate tensile strength, kg/mm²					
	diameter of steel fibers,* μ			diameter of bronze fibers, ** μ		
	100	200	300	100	200	300
30	7.8	6.2	4.5	13.4	11.0	9.7
40	5.15	4.0	2.2	10.1	5.6	5.3
50	3.7	2.3	0.8	7.5	4.0	—

* Sintered at 1250°C for 3 hr.

** Sintered at 980°C for 3 hr (in the sintering process about 20% of liquid phase was formed).

Tables XIII.19 — XIII.21 and Figures XIII.32 — XIII.36 show the tensile strengths of porous products, made of different fibers by different technological processes.

It should first be emphasized that irrespective of the fiber material, felting before pressing and sintering considerably increases the ultimate tensile strength and decreases the scattering of its values, other conditions

being equal /18/. For example, a material obtained from copper fibers with preliminary felting, over a wide porosity range, has a tensile strength $1-3\ kg/mm^2$ higher than that of the same material obtained without felting (Figure XIII. 32).

TABLE XIII. 21. Tensile strength of materials made of copper fibers of various diameters sintered at 950°C for 3 hr after felting

Porosity, %	Ultimate strength, kg/mm^2	
	$d = 50\,\mu$	$d = 70\,\mu$
30	8.6	—
35	—	3.7—4.7
40	5.4	2.5—3.3
50	3.3	2.5
60	2.2	1.2—1.4

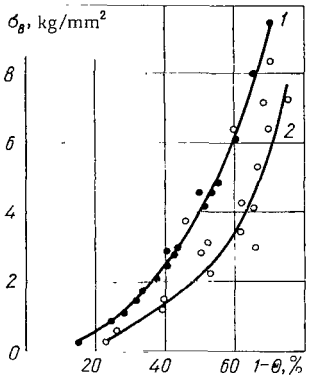

FIGURE XIII. 32. Dependence of the ultimate tensile strength of a material made of copper fibers ($d = 50\mu$, $l = 7$ mm) on the relative density (sintering conditions: 980°C, 3.5 hr):

1 — after felting; 2 — without felting.

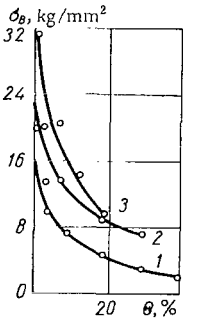

FIGURE XIII. 33. Dependence of the ultimate strength of a material prepared from copper fibers on the porosity /8/:

1 — pressed and sintered (980°C, 2 hr); 2 — pressed and sintered, repressed at the same pressure and sintered under the same conditions; 3 — pressed and sintered, repressed at a pressure twice as high as the first, and sintered.

The technological parameters during pressing and sintering appreciably influence the strength properties of porous fiber materials. This is illustrated by the data shown in Figure XIII. 33 and in Tables XIII. 19 and XIII. 20. Repeated pressing, sintering and gauging usually increase the strength properties (see Figure XIII. 33 and Table XIII. 19). The strength parameters of the fiber materials are very strongly affected by the sintering conditions.

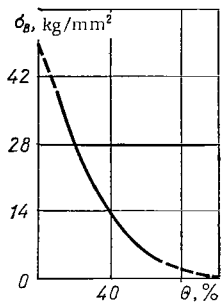

FIGURE XIII. 34. Dependence of the ultimate strength of a material made of stainless steel 1Kh18N9T (d = = 50 μ ; l = 6 mm) on the porosity (sintering conditions: 1,250°C, 3 hr).

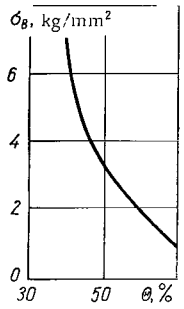

FIGURE XIII. 35. Dependence of the ultimate tensile strength of a material made of a "wool" of stainless steel 434 A of length 3.2 mm (sintering conditions: 1,345°C, 1 hr) on the porosity /9/.

For example, with the same fiber size and porosity, the strength of a bronze fiber material sintered in the presence of the liquid phase is twice as high as that of a material made of stainless steel fibers (Table XIII. 20), though in compact material there is a reverse relationship. Below, we give the tensile strength of a material made of stainless steel fibers 32 μ in diameter. The fibers were sintered for 3 hr at 1,250°C:

Porosity, %	Ultimate tensile strength σ_B, kg/mm^2
62.1	5.81
67.0	4.30
76.7	2.69
83.4	2.10

The fiber diameter affects the material strength, other conditions being equal (see Table XIII. 20). Thus, highly porous articles made of stainless steel fibers 32 μ in diameter are 3 to 4 times stronger than articles made of 50-μ diameter fibers (see Figure III. 34) while the strength of articles made of copper-fibers of 40 — 60 % porosity is 1.5 to 2 times higher when the fiber diameter is 50 μ than when the diameter is 70 μ (see Table XIII. 21).

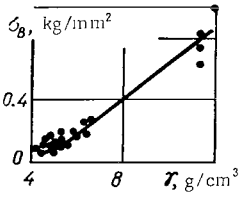

FIGURE XIII. 36. Dependence of the strength of pressed lead fibers on the density.

Finally, surface roughness of the fibers and their good bonding ability may lead to better strength properties than in materials made from smooth fibers (Figures XIII. 35). If we consider the bonding of rough lead fibers only in a material with 45 — 60 % porosity, 11 — 19 % of the strength of compact material is reached (see Figure XIII. 36).

Other strength parameters, besides the impact strength, are higher in porous materials than in powder materials. Below we give an example of the dependence of the yield point on the porosity during

the compression of a material made of copper fiber material (the fibers had a diameter of 50 μ and were sintered at 950°C for 3 hr):

Porosity, %	35.5	43.8	54.6	62.6	72.6
Yield point σ_y, kg/mm^2	3.46	2.44	1.57	0.87	0.61

TABLE XIII. 22. Impact strength of a material made of 100 μ copper fibers as a function of the porosity and production conditions

Sintering pressed felt (980°C, 2 hr)		Sintering pressed felt, repressing at the same pressure and sintering under same conditions		Sintering pressed felt, repressing at a pressure twice as high as the first, and sintering	
porosity, %	impact strength, joules/cm^2	porosity, %	impact strength, joules/cm^2	porosity, %	impact strength joules/cm^2
0	24.4	0	25	—	—
5	20.7	3	23	1	25
10	17.1	4	21	3	24
20	14.9	9	20	7	21
30	10.5	18	13	13	15
40	6.2	32	8	17	11

The advantages of porous fiber materials over porous powder materials are well marked when comparing their plasticity indexes and impact strengths. The impact strength and relative elongation of fiber materials with the same porosity as powder materials is at least one order of magnitude higher, and is scarcely dependent on porosity (Table XIII. 22). Thus, for materials made of 50 μ copper fibers, prepared by preliminary felting, the relative elongation is 8 — 12 % over a wide porosity range. Below, we give the impact strength of a material made of 50 μ molybdenum fibers:

Porosity, %	Impact strength, joules/cm^2
21	15.8
26	14.6
31	14.1
43	14.0

As in the case of other strength parameters, the impact strength of porous fiber materials is very dependent on the technology of their production. For example, specimens of materials of 50 % porosity made of 50 — 200 μ copper fibers (sintered in vacuo at 1,020 — 1,030°C for 1 hr) had an impact strength of 22.7 — 33.5 joules/cm^2. These values are much higher than those given in Table XIII. 8 for an analogous material prepared by another technological process.

Though we have no reports on the different strength parameters of fiber materials at higher temperatures, it is very probable that such materials will have a higher strength under high-temperature conditions than powder materials.

An analysis of the operation of materials in transpiration cooling shows that the materials must have not only a high load-carrying capacity, but also a high thermal conductivity.

TABLE XIII. 23. Dependence of the thermal conductivity coefficient λ, W/cm·deg and of temperature, and fiber diameter

Temperature, °C	Material made of 50μ diameter fibers of porosity, %							
	26		38		42		54	
	ρ	λ	ρ	λ	ρ	λ	ρ	λ
100	600	0.0345	1160	0.0170	1720	0.0150	—	0.0095
200	640	0.0345	1200	0.0175	1720	0.0150	—	0.0100
300	640	0.0355	1240	0.0175	1760	0.0150	—	0.0100
400	680	0.0360	1240	0.0175	1760	0.0150	—	0.0100
500	680	0.0360	1280	0.0180	1760	0.0150	—	0.0100
600	680	0.0365	1280	0.0180	1760	0.0150	—	0.0105
700	680	0.0370	1280	0.0185	1760	0.0150	—	0.0105
800	680	0.0375	1280	0.0190	1800	0.0155	—	0.0105

* The tests were carried out in vacuo (10^{-4} — 10^{-5} mm Hg). The material was prepared from for 2 hr.

We have very few data on the thermal conductivity of porous powder materials /40, 42/. There are no published results on heat transfer in porous materials made of metal fibers, though attempts have been made to apply the kinetic theory of gases to describe the thermal conductivity mechanism in porous fiber materials /42/.

Some regularities in the thermal conductivity of materials of different porosities made of nichrome fibers of different diameters at temperatures up to 800°C are shown in Table XIII. 23. First, we should mention the increase in the thermal conductivity coefficient with temperature characteristic of alloys. For all the investigated fiber diameters, the thermal conductivity coefficient decreases with increase in porosity, and other conditions being equal, it is also lower for thicker fibers. This last phenomenon is probably explained by the fact that under the same pressing and sintering conditions materials made of thick fibers are inferior in quality to those made of thin fibers. We can obtain some idea on the thermal conductivity by studying the electric conductivity, which can be determined with a higher accuracy. It can be seen from Table XIII. 23 that the general pattern of electrical conductivity variations in a material made of nichrome fibers with increase in fiber diameter and porosity is analogous to the pattern of changes in the thermal conductivity coefficient. Only the temperature dependence of the electrical conductivity is opposite to the temperature dependence of the thermal conductivity.

Many theoretical and experimental studies have been carried out by Russian and non-Russian scientists on the electrical conductivity of fiber materials. The first attempts to theoretically describe the correlation between electrical conductivity and the porosity of fiber materials was made by Skorokhod and Panichkina /43/. The authors applied the infinite cylinder model, arbitrarily oriented in space, and obtained a correlation between the above parameters, provided that no contact phenomena occur

$$\lambda = \frac{\lambda_1}{4}\left[1 - 3\Theta + \sqrt{(1-3\Theta)^2 + 8(1-\Theta)}\right], \qquad \text{(XIII. 3)}$$

where λ is the electrical conductivity of the material; Θ is the porosity of the material; and λ_1 is the electrical conductivity of the fibers.

the electrical resistivity ρ, μohm·cm of a material made of nichrome fibers on the porosity,

Material made of 100μ diameter fibers of porosity, %						Material made of 200μ diameter fibers of porosity, %			
25		42		63		26		38	
ρ	λ	ρ	λ	ρ	λ	ρ	λ	ρ	λ
760	0.0235	2860	0.0115	3180	0.0070	1880	0.0225	2280	0.0125
800	0.0240	2880	0.0115	3200	0.0075	1880	0.0225	2280	0.0125
820	0.0245	2900	0.0120	3240	0.0080	1920	0.0230	2300	0.0125
840	0.0250	2920	0.0120	3240	0.0085	1920	0.0235	2320	0.0125
860	0.0255	2920	0.0125	3260	0.0085	1940	0.0240	2320	0.0130
880	0.0260	2940	0.0130	3280	0.0090	1940	0.0245	2340	0.0135
880	0.0275	2960	0.0135	3280	0.0095	1960	0.0250	2360	0.0145
880	0.0275	2960	0.0145	3300	0.0100	1960	0.0255	2360	0.0150

4—6 mm long fibers without preliminary felting, and sintered at 1200°C in vacuo (10^{-3} mm Hg)

For an approximate allowance for contact phenomena, Skorokhod et al. proposed a simple expression

$$\lambda = \frac{\lambda_1}{4}\{1 - (2\xi + 1)\Theta + \sqrt{[1 - (2\xi + 1)\Theta]^2 + 8\xi(1 - \Theta)}\}, \qquad \text{(XIII. 4)}$$

where ξ is the relative linear dimension of the contact.

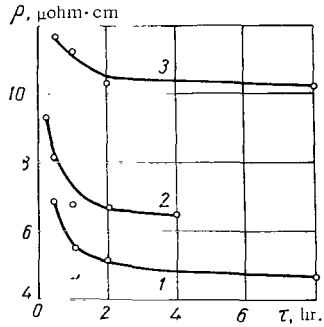

FIGURE XIII. 37. Dependence of the electrical resistivity of the material on the sintering time:

1 — θ = 48—50%; 2 — θ = 53—55%; 3 — θ = 64—65%.

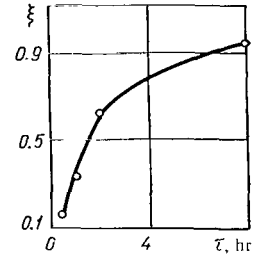

FIGURE XIII. 38. Values of the relative linear contact dimension of copper fiber material with 48—50% porosity.

At $\xi = 0$ the equation for the electrical conductivity of porous fiber-material is transformed into

$$\lambda = \frac{\lambda_1}{4}(1 - \Theta), \qquad \text{(XIII. 5)}$$

that is, it does not reduce to zero if there are no contacts between the fibers along the generatrix.

The equations were experimentally confirmed on materials obtained by pressing copper fibers (diameter 120μ, length 10—15 mm) on two sides and sintering at 1,000°C, with different holding times (Figure XIII. 37). From (XIII. 4) for the determination of materials with porosities of above 50%, it was impossible to obtain rationally justifiable results for long or short sintering times. Moreover, the theoretical results (Figure XIII. 38) do not agree with the experimental, It seems that the main reasons for this disagreement are the drawbacks of the selected model of the fiber material. Experimental data for materials with a porosity above 55%, irrespective of the sintering time, and for materials with a lower porosity, sintered for a short time, are better described by (XIII. 5). This equation was derived assuming that there are no contacts between the fibers along the generatrix (Figure XIII. 39). If the porosity of materials sintered for long periods is below 55%, the electrical conductivity data are described fairly well by (XIII. 4). If the porosity is higher than 45%, then irrespective of the sintering time, the electrical conductivity of sintered fiber materials is higher than that of the powder materials of the same porosity.

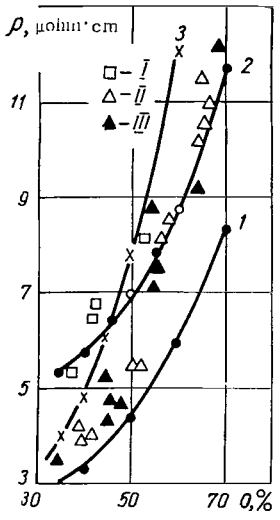

FIGURE XIII. 39. Dependence of the electrical resistivity of copper fiber material determined by equations (1 — (XIII. 3); 2 — (XIII. 5); 3 — for porous powder material /44/) and experimentally (I — sintering time 0.25 hr; II — sintering time 1 hr; III — sintering time 8 hr).

The errors in the theoretical equations in /43/ correlating the electrical conductivity of the material with its fiber structure and its porosity are caused by the imperfectly selected model. The errors were later eliminated by Skorokhod /39/. The determined pattern of variation in the relative conductivity as a function of the porosity of bodies prepared from powders of fibers is universal, that is, it is suitable over the total porosity range (Table XIII. 24). These data were obtained without allowing for contact phenomena. Therefore, by comparing them with experimental results for materials made of fibers, where interfiber contact is very important, it is possible to estimate the quality of production (especially sintering).

TABLE XIII. 24. Relative conductivity of porous bodies of various densities

Body type	Relative conductivity								
	0.1	0.2	0.3	0.4	0.5	0.6	0.7	0.8	0.9
Fiber	0.05	0.11	0.18	0.27	0.36	0.47	0.59	0.72	0.86
Powder	0.01	0.05	0.11	0.18	0.28	0.41	0.55	0.70	0.85

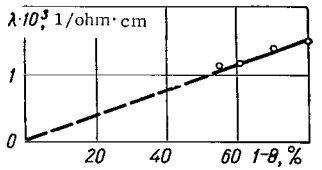

FIGURE XIII. 40. Electrical conductivity of a material made of 100μ diameter copper fibers as a function of the relative density.

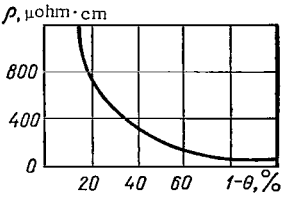

FIGURE XIII.41. Dependence of the electrical resistivity of a material made of stainless steel 430 fibers, diameter 62μ, on the relative density /45/.

It was shown in practice that the electrical conductivity of fiber materials (Figures XIII. 40, XIII. 41, and Tables XIII. 25 and XIII. 26) are very dependent on the properties of the selected fibers and the technology of production.

TABLE XIII. 25. Effect of the porosity on the electrical resistivity of a material made of copper fibers, diameter 50μ, length 7 mm

Sintered at 980°C for 3.5 hr		Sintered at 950°C for 3 hr	
porosity, %	electrical conductivity, μohm·cm	porosity, %	electrical conductivity, μohm·cm
10	2.09	—	—
20	2.63	—	—
30	3.47	31.9	3.45
40	4.36	39.9	4.12
50	5.98	50.1	5.71
60	9.12	60.6	9.53
70	11.82	70.0	16.3

TABLE XIII. 26. Dependence of the electrical resistivity of materials made of stainless steel 1Kh18N9T and bronze OTs 4-3 on the porosity and fiber diameter

Porosity, %	Electrical resistivity, μohm·cm					
	material made of steel fibers, diameter, μ			material made of bronze fibers, diameter μ		
	100	200	300	100	200	300
30	168	232	236	13.7	13.7	15.7
40	192	296	322	16.4	16.4	19.3
50	216	446	480	23.0	23.0	24.0

An increase in the temperature and time of sintering, and liquid-phase sintering, increases the electrical conductivity, while an increase in the fiber diameter decreases this parameter, though the effect of porosity on electrical conductivity is weaker than it is on the strength properties.

The efficiency of materials used as transpirators depends, as mentioned above, on the conditions applied in porous cooling. These conditions are

determined mainly by the hydraulic resistance of the material and by its uniform porous structure. When the hydraulic resistance coefficients are determined for porous materials, we simulate conditions of isothermal air flow through the pores over a wide range of air rates with fixed corresponding pressure drops on the specimens. Figure XIII. 42 gives a diagram of an apparatus for simulating the conditions required for the determination of the hydraulic resistance coefficient of porous material when a gas (air) stream passes through.

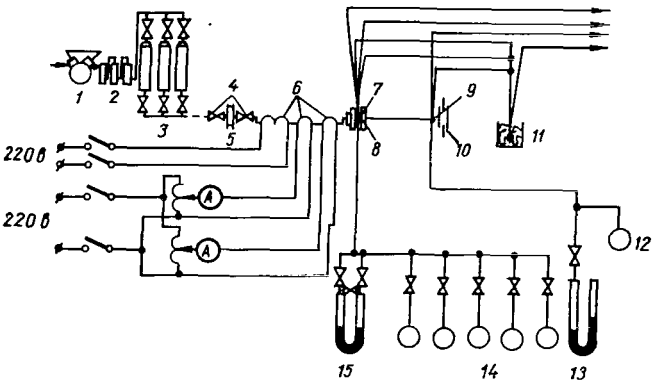

FIGURE XIII.42. Instrument for measuring the hydraulic resistance of porous materials:

1 — high-pressure compressor; 2 — air scrubbing systems after compressor; 3 — air cylinders (capacity 7.5 m^3, pressure 1.2 kg/mm^2); 4 — high-pressure valve for controlling air rate; 5 — filters for cleaning air after leaving cylinders; 6 — heating system for air; 7, 9 — thermocouples for measuring air temperature before specimen and membrane; 8 — head for fixing specimens; 10 — end diaphragm; 11 — vessel with ice for cold junction of thermocouple; 12, 14, 15 — mercury and pointer pressure gages; 13 — water column differential manometer.

The experimental data were processed by the conventional methods, using the two-term equation of gas flow through a porous material /46/

$$\frac{\Delta P}{h}\gamma_{mn} = \alpha\mu G_a + \frac{\beta}{g}G_a^2, \qquad \text{(XIII. 6)}$$

where ΔP is the pressure drop in the specimens; h is the specimen thickness; γ_{mn} is the density of the air blown through at the given temperature; G_a is the actual rate of the air at the given pressure drop; μ is the dynamic viscosity coefficient of air; g is the gravitational acceleration; α is the hydraulic resistance coefficient against laminar flow, determined by the friction of the air against the pore walls (viscous resistance coefficient); and β is the hydraulic resistance coefficient determined by the convolutions of the pores (inertial resistance coefficient).

The following conclusions can be drawn from the data in Table XIII. 27. The graph of the dependence of the hydraulic resistance coefficients on the porosity is approximately linear in logarithmic coordinates (Figure XIII. 43).

TABLE XIII.27. Hydraulic resistance coefficients of porous materials made of metal fibers

Fiber material	Fiber diameter, μ	Specimen porosity, %	Specimen thickness, mm	Hydraulic resistance coefficients		$\frac{\beta}{\alpha} \cdot 10^{-6}$, m
				$\alpha \cdot 10^{-11}$, m^{-2}	$\beta \cdot 10^{-5}$, m^{-1}	
Nickel* (extruded fibers), $l = 6-8$ mm	250	31.2	4.1	1.480	21.80	14.75
		31.3	4.1	1.590	16.40	10.30
		35.1	3.1	0.708	13.80	19.50
		36.4	3.8	0.556	6.29	11.30
		37.8	2.9	0.547	7.36	13.45
		37.9	3.9	0.490	7.75	15.80
		37.3	4.8	0.554	7.40	13.36
		37.4	4.8	0.664	7.83	11.80
		39.5	3.0	0.398	4.92	12.35
		45.6	3.7	0.202	2.14	10.60
		45.6	4.6	0.177	1.80	10.20
		48.1	2.9	0.170	1.51	8.88
		48.6	2.9	0.262	2.23	8.52
Molybdenum** , $l = 7$ mm	50	21.8	4—5	37,300	266.40	7.14
		50.0		1.230	1.72	1.40
		52.0		1.060	1.49	1.41
		76.0		0.168	0.13	0.77
Bronze† OTs 4-3, $l = 7$ mm	100	40.0	4—5	0.900	2.80	3.10
	200	40.0		0.570	1.40	2.50
	300	40.0		0.410	0.91	2.20
	100	50.0		0.210	0.86	4.10
	200	50.0		0.170	0.52	3.06

* Sintering temperature 1200°C, holding time 3 hr.
** Sintering temperature 2200°C, holding time 20 hr.
† Sintering temperature 980°C, holding time 3 hr.

Points 1 — 5 on this figure correspond to a specimen thickness of 3 mm; points 6 — 10 to a thickness of 4 mm, and 11 — 13 to a thickness of 5 mm. The hydraulic resistance coefficients are correlated to the porosity by exponential functions; with increase in porosity the coefficients decrease. For example for the above materials the following equations were obtained (the porosities are given as fractions): for materials from extruded nickel fibers by

$$\alpha = 2.4 \cdot 10^{8} \Theta^{-5.6};$$
$$\beta = 2.7 \cdot 10^{3} \Theta^{-5.6}; \qquad \text{(XIII. 7)}$$

and for molybdenum fiber materials by

$$\alpha = 68.2 \cdot 10^{8} \Theta^{-4.1};$$
$$\beta = 2.77 \cdot 10^{3} \Theta^{-6.0}. \qquad \text{(XIII. 8)}$$

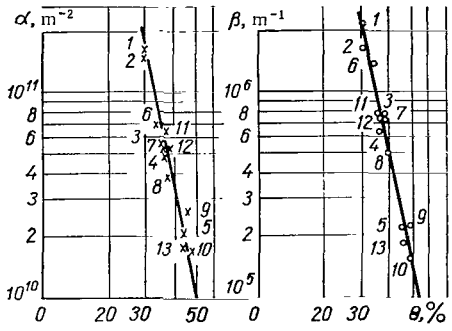

FIGURE XIII.43. Dependence of the hydraulic resistance coefficients of a material made of extruded nickel fibers on the porosity.

With increase in fiber diameter the hydraulic resistance coefficients also decrease (see Table XIII. 29). It should be noted that in the thickness range studied (Figure XIII. 43) changes in the thickness of specimens do not affect the hydraulic resistance coefficients.

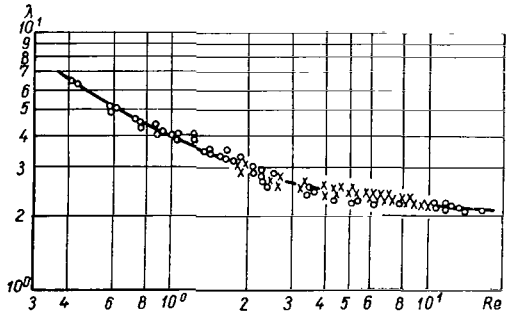

FIGURE XIII.44. Dependence of the analog of the friction coefficient on the Reynolds number.

The coefficient ratio used in the equation for the Reynolds number

$$\mathrm{Re} = \frac{\beta}{\alpha} \frac{G_a}{\mu g}, \qquad \text{(XIII. 9)}$$

may or may not change with porosity. Thus, the β/α ratio of a material made of extruded nickel fibers is independent of the porosity. But for molybdenum fiber material this ratio decreases with the porosity, and for bronze fiber material it increases. For thicker molybdenum and bronze fibers the β/α ratio decreases. Evidently this decisive parameter depends, other conditions being equal, on the internal structure of the material, and hence on its technological production.

TABLE XIII. 28. Hydraulic resistance coefficients of materials made of bronze powder and fiber ($\Theta = 40\%$)

Bronze fibers				Spherical bronze powder			
fiber diameter, μ	$\alpha \cdot 10^{10}, m^{-2}$	$\beta \cdot 10^{5}, m^{-1}$	$\frac{\beta}{\alpha} \cdot 10^{-6}, m$	particle diameter, μ	$\alpha \cdot 10^{10}, m^{-2}$	$\beta \cdot 10^{5}, m^{-1}$	$\frac{\beta}{\alpha} \cdot 10^{-6}, m$
200	5.7	1.40	2.5	−160+160	1.95	0.488	2.50
—	—	—	—	−250+200	0.78	0.350	4.50
300	4.1	0.91	2.2	−315+250	0.78	0.240	3.08

The experimental data used in (XIII. 6) may be represented in a dimensionless form

$$\lambda = \frac{2}{Re} + 2, \qquad \text{(XIII. 10)}$$

where λ is the analog of the friction coefficient inside the pores.

The dependence of this coefficient on the Reynolds number together with experimental data for materials obtained from extruded nickel fibers (diameter 250 μ, length 6 — 8 mm) are shown in Figure XIII. 44.

The fair agreement between the theoretical and experimental results (discrepancies less than 9%) justifies the application of (XIII. 10) for describing the flow of a gaseous coolant in transpiration materials made of fibers.

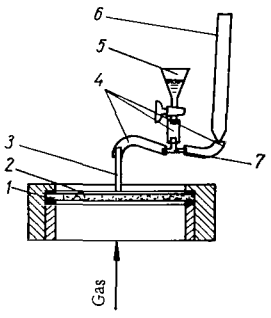

FIGURE XIII. 45. Instrument for measuring the local volume rate of gas:

1 — specimen; 2 — rubber tip; 3 — measuring probe; 4 — rubber tubes; 5 — funnel for soap solution; 6 — measuring burette; 7 — glass T-piece;

It is of interest to compare data on the hydraulic resistance of porous materials made of powders and fibers (Table XIII. 28).

This table shows that the β/α ratio at a given porosity is the same in both materials. For bronze made from spherical powders and materials made from extruded nickel fibers this ratio is almost independent of the porosity, but for materials prepared from bronze fibers it increases slightly with increase in porosity.

We can see from the above data that the hydraulic resistance of bronze made from fibers is 3 — 4 times that of bronze made from spherical powders. This is apparently because of the larger overall interfacial area of the fiber material and its structural anisotropy, since in the technological process no felting was applied, and the fiber axes of the material were perpendicular to the air flow.

A very important property of transpiration material is a constant hydraulic resistance over the surface, determined by the degree of uniformity of the porous structure. The results show that even a small change in the porosity affects the rate of the cooling agent. For example a decrease of 10% in the porosity of materials made from powders decreases the rate by 40%. Therefore, when producing a system with porous cooling we must take into account the deviations of the local values of the porosity, which

makes it possible to avoid local superheating of the material by increasing the overall rate of the cooling agent.

A method for determining local porosity values on the surface of flat articles was proposed by Dyban et al. /47/. The volume rates of the gaseous coolant are measured at various points over small surface areas of the specimen. The gas is discharged from the specimen surface through a tube (diameter 1.6 mm, wall thickness 0.15 mm) fitted with a thin rubber tip. The tube is connected to a T-piece by a rubber tube, and a soap solution is poured in. The gas passing through the tube entrains the soap films. The system is controlled in such a way that 1—2 soap films are present in the measuring tube. The time taken for a soap film to travel the distance between two marks notched on the measuring tube is determined. The gas velocities are chosen so that the inertial pressure losses can be neglected. In this case the flow equation (XIII. 6) is written as

$$\frac{\Delta P}{h}\gamma_{mn} = \alpha\mu G_a. \qquad \text{(XIII. 11)}$$

After transformations

$$\frac{\Delta P}{h}\gamma_{mn} = \alpha_L \mu v_{mn}\gamma\bar{v}_{al}. \qquad \text{(XIII. 12)}$$

where v_{mn} is the mean gas velocity at the outlet of the specimen; γ is the density of the gas at the outlet of the specimen; α_L is the local viscous coefficient of hydraulic resistance; $\bar{v}_{al}$ is the local relative gas velocity $\bar{v}_{al} = \frac{v_{al}}{v_{mn}}$.

The parameters which are constant during one experiment can be combined into a single constant. In this case

$$\alpha_L \bar{v}_{al} = \text{const}. \qquad \text{(XIII. 13)}$$

The local gas velocity is determined from experimental data

$$\bar{v}_{al\,i} = \frac{\sum_{1}^{n} t_i}{n t_i}, \qquad \text{(XIII. 14)}$$

where t_i is the time taken for the soap film to travel between two marks, and n is the number of measuring points.

The local value of the viscous coefficient of hydraulic resistance can be determined from

$$\alpha_{Li} = \frac{\alpha}{\bar{v}_{al\,i}} \qquad \text{(XIII. 15)}$$

according to (XIII. 6).

To calculate the local porosity from the local values of the viscous coefficient of hydraulic resistance we must know the porosity dependence of the mean viscous coefficient.

The above method was used to estimate the uniformity of the porous structure of materials made from nonspherical powders. The deviations from the mean porosity found in the individual sections of the specimen were confirmed by metallographic studies.

The same method was used to determine the uniformity of a porous material made from extruded nickel fibers 250 μ in diameter and 6 — 8 mm long. The material was produced without preliminary felting. The specimens 50 mm in diameter were divided into zones in which the volume rate of the gas was measured, as shown in Figure XIII. 46.

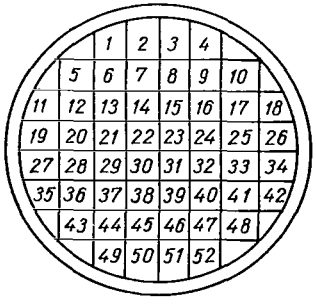

FIGURE XIII. 46. Distribution of measuring zones of the volume gas rate on the surface of a specimen made of extruded nickel fibers.

The results of measuring the relative (to the mean) weight gas rates over the zones of nickel specimens (porosity 45.6 %) and the local porosity values determined from them are summarized in Table XIII. 29. It can be seen that the maximum relative deviation of the local porosity from the mean porosity is 14 — 17 %, which is higher than corresponding data obtained on porous materials from nonspherical powders (4 — 11 %).

The comparison shows that to obtain fiber materials with uniform pore distribution over the bulk we must use sufficiently thin fibers, and felting, or any other molding operation ensuring a uniform structure in the fiber production.

For correct design of systems with porous cooling, data on the heat transfer within the materials applied are important. At present, we have no such data for fiber materials, though these materials appear to be the most interesting for use in transpirators.

To determine the heat transfer coefficient we studied porous specimens made from extruded nickel fibers, for which all the required parameters are known. The specimens were heated by an inductor, with air as the cooling agent. The temperature was measured with copper — constantan thermocouples (electrode diameters, 0.8 mm), welded by the contact method onto places of known porosity on the specimen surface.

The air rate at each point was determined by means of (XIII. 6) from the pressure drop measured. The arithmetic mean between the temperatures at the inlet and outlet of the gas was taken as the air temperature.

The heat transfer coefficient was determined from

$$\alpha_v = \frac{G_a c_p \Delta t_{ai}}{h \Delta t_L}. \qquad \text{(XIII. 16)}$$

Here c_p is the specific heat of coolant (air at constant pressure and temperature $\frac{t_{ai.\,in} + t_{ai.\,out}}{2}$); Δt_{ai} is the temperature gradient of the coolant at the outlet and inlet

$$\Delta t_{ai} = t_{ai.\,out} - t_{ai.\,in};$$

Δt_L is the logarithmic mean temperature gradient

$$\Delta t_L = \frac{\Delta t_2 - \Delta t_1}{\ln \frac{\Delta t_2}{\Delta t_1}},$$

where

$$\Delta t_1 = t_{01} - t_{\text{ai. in}}\,;\ \Delta t_2 = t_{02} - t_{\text{ai. out}},$$

and t_{01} and t_{02} are the temperatures of the specimen at inlet and outlet, respectively, in the direction of the flowing coolant.

TABLE XIII. 29. Relative volume rates of gas and local porosity in samples made from extruded nickel fibers at an average porosity of 45.6%

Measuring zone (Figure XIII. 46)	Relative volume rate of gas	Local porosity, %	Measuring zone (Figure XIII. 46)	Relative volume rate of gas	Local porosity, %
1	0.422	39.0	23	2.735	52.0
			24	1.092	46.0
2	0.570	41.0	25	2.050	50.5
3	1.280	46.7	26	0.432	39.0
			27	0.363	38.0
4	0.684	42.5	28	1.223	47.0
			29	1.820	50.5
5	0.719	43.0	30	2.410	51.3
6	1.580	49.0	31	1.959	50.7
			32	1.640	49.7
7	0.732	43.0	33	1.710	50.0
8	1.300	47.5	34	0.805	43.7
9	1.260	47.0	35	0.395	38.5
			36	0.590	41.0
10	0.682	42.5	37	1.092	46.0
11	1.820	50.5	38	1.640	49.5
12	1.520	49.0	39	1.580	49.0
13	1.410	48.5	40	1.640	49.5
			41	1.065	46.0
14	1.783	50.3	42	0.780	43.5
15	1.745	50.0	43	1.520	48.9
16	1.440	48.6	44	1.640	49.5
17	0.976	45.0	45	1.640	49.5
18	0.427	39.0	46	2.485	52.3
			47	2.155	51.0
19	1.170	46.7	48	0.513	40.5
20	1.640	48.0	49	0.965	45.0
21	1.365	47.5	50	1.365	48.0
22	2.160	51.0	51	0.864	44.0

From the data obtained the Nusselt number was determined

$$\mathbf{Nu} = \frac{\alpha_v}{\lambda_{ai}}\left(\frac{\beta}{\alpha}\right)^2 \qquad \text{(XIII. 17)}$$

(where λ_{ai} is the thermal conductivity coefficient at temperature $\frac{t_{\text{ai. in}} + t_{\text{ai. out}}}{2}$) and the dependence of Nu on Re was plotted; the Reynolds number was found from (XIII. 9).

The experimental results on heat exchange were processed and plotted into the graph shown in Figure XIII. 47.

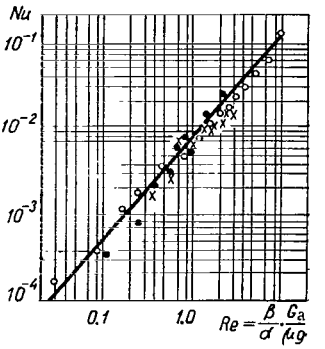

FIGURE XIII.47. Dependence of the mean Nusselt number for air flow in a porous material made from nickel fibers on the Reynolds number.

According to these data, the dependence of the Nusselt number on the Reynolds numbers is approximated by an exponential function

$$Nu = 4.25 \cdot 10^{-4} Re^{1.2}. \qquad (XIII.18)$$

Equation (XIII.18) can be applied to similar materials for Re between 0.04 and 10. The exponent of the Reynolds number in (XIII.18) remains constant for both viscous and inertial flow conditions.

4. Fiber-base packing materials

To ensure satisfactory functioning at high temperatures and pressures, packing materials must have an unusual combination of properties. They must display elasticity and flexibility (the ability to be compressed by a load, and to recover their former dimensions after load removal), and must be poreless when compressed. They must be chemically resistant to liquids used in industry, and finally, must have a low coefficient of friction, and not cause abrasive wear in the connected parts.

These requirements are satisfied by metallic elastic skeletons impregnated by soft metals. Such packing materials can withstand air pressures up to 210 — 350 kg/mm^2, and temperatures up to 538 — 660°C.

The base materials are stainless steel or molybdenum fibers 0.1 — 0.2 mm in diameter and 42 — 19 mm long. Sometimes the diameter is 3 — 18 μ and the length is 6 mm. Tin, silver, indium, magnesium and various polymers serve as the matrix.

To retain the stability of static packings during high-temperature operation the material of the skeleton and matrix must be compatible. This means, in principle, their minimum mutual solubility at high temperatures, and the absence of phase transformations or intermetallic compounds, which have a deletrious effect on the elasticity of the system (Table XIII.30).

The melting point of the impregnated material must not be very close to the temperature at which the packing operates, since otherwise recrystallization and dissolution of the skeleton in the matrix may occur. Since the

porosity of the packing material depends on the quality of impregnation (in the material to be impregnated all the cavities must be filled), the material of the skeleton must be thoroughly wetted by the matrix material.

TABLE XIII. 30. *Compatibility parameters* of some fiber of base and filler in packing materials

Impregnating material	Fiber base		Remarks
	Fe	Mo	
Al	Base dissolves to form intermetallic compounds	Compatible	
Ba	Compatible	"	
Cd	"	No data available	Cd produces toxic vapors
Cu	"	Compatible	Cu is strengthened because of cold hardening, it has a high yield point
In	No data available	No data available	
Pb	Compatible	Base dissolves to form intermetallic compounds	Pb produces toxic vapors and is oxidized
Mg	"	Compatible	Mg is brittle and has a high yield point
Ag	"	"	
Pb	"	"	

The following technique is employed for the production of fiber packings. The fiber skeleton is prepared by the method discussed for felting and is then impregnated. The products are molded from the skeleton. To impart the final form to the products, they are mechanically treated by cutting. Before the material is cut it should be cooled, since most of the metals used for impregnation are soft and tend to run.

If the mechanical treatment is carried out before impregnation, the methods discussed at the beginning of this chapter are employed.

The diagram of an impregnating chamber for metal fibers is shown in Figure XIII. 48. The impregnation method is chosen according to the type of impregnating agent.

If the skeleton is impregnated by tin, the metal is placed together with the felt into a crucible, which is tightly closed by a lid. To improve the wettability, air with argon or argon with

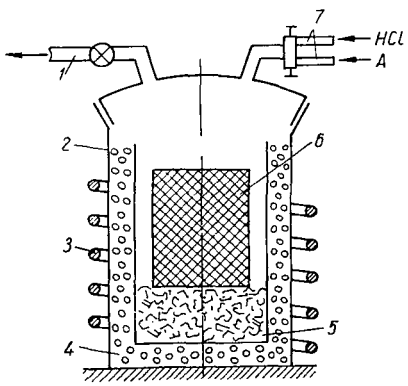

FIGURE XIII. 48. Diagram of chamber used for impregnating metal felt:

1 — suction pipe; 2 — Pyrex *vacuum vessel*; 3 — induction winding; 4 — alumina stuffing; 5 — felt; 6 — solid impregnating material; 7 — pipes for feeding HCl and A.

hydrogen chloride is blown through. Then, the crucible is heated to 400°C, kept at the boiling point of $SnCl_2$ to remove this compound from the fused tin, and the impregnation is completed under pressure in an argon atmosphere. No protective Al_2O_3 layer is required. If indium, silver or magnesium is used, an analogous method is employed with the following distinctive features.

TABLE XIII. 31. Composition and properties of the materials for high-temperature static seals based on metal fibers /49/

Composition of felt		Composition of impregnating agent		Density, g/cm^3	Brinell hardness, kg/mm^2	Modulus of elasticity on compression, 10^{-3} kg/mm^2	0.2% of yield point, kg/mm^2	Maximum permissible sealing temperature under a pressure of 350 atm, °C
metal	vol %	metal or polymer	vol %					
Mo	18.5	Sn	81.5	7.80	15.8	7.00	4.06	121
	39.4	Ag	60.6	10.36	67.3	9.80	10.50	649
	60.0	In	40.0	8.98	13.0	0.77	0.77	49
Stainless steel 430	26.9	Mg	73.1	3.63	46.7	9.1	17.50	538
	39.0	Sn	61.0	7.46	23.4	4.9	2.80	121
	47.0	$(PNCl_2)n$ *	53.0	—	—	—	—	438

* Polyphosphonitryl chloride, melting point 121°C, has the same properties as silicone elastomers.

If indium is used as the impregnating agent, the material need not be washed with hydrogen chloride, since indium has good wetting properties. Because of the low melting point of this material, no protective layer is necessary.

If silver is used as the impregnating agent the heating temperature is as high as 1,100°C, so that a protective Al_2O_3 layer is required. No washing with gaseous HCl is necessary.

In magnesium impregnation the heating temperature is 830°C and no washing with gaseous HCl is necessary. It should be noted, however, that small amounts of argon may be included by magnesium during impregnation, which may cause leakage in the material when operating under high pressure.

If an inorganic polymer is used as the impregnating material, at first crystals of the trimer $(PNCl_2)_3$ and tetramer $(PNCl_2)_4$ are deposited onto the felt, and are transferred together with it into the vessel with the lid, and heated to about 120°C. After the molten crystals have impregnated the metal felt, the lid is put on the vessel and the material is held at 300°C to facilitate the formation of a rubberlike polymer. The operating surface of the material is then treated to replace the unstable chlorine groups by stable groups, since the impregnating composition tends to hydrolyze.

Packing materials of this type are used in equipment which comes in contact with different chemical substances or fuels. The efficiency of these

materials is so high that they can be employed at high temperatures (when an inorganic polymer is used as the impregnating agent, the maximum temperature of operation is 582°C). It is reported in /48/ that packing rings with a wedge section made of molybdenum fibers show no liquid leakage. after 93 hr operation and 337,000 pulses at 540°C.

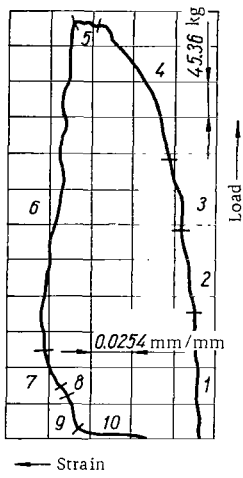

FIGURE XIII.49. Stress-strain diagram for a packing composite consisting of 18.5 vol % of molybdenum and 81.5 vol % of tin:

1—elastic range, the material obeys Hooke's law; 2—plastic strain, the slope of the curve is determined by the load; 3—reinforcement after the impregnating material begins to flow, the base remains rigid and is compressed until no pores are present; 4—continuation of strain, the load is higher than the yield point of the base; 5—the composite "creeps" and the load is reduced; 6—the base is very slowly restored because of the resistance of plastically reinforced impregnating material; 7, 9—the impregnating agent makes restoration of the material possible at a rather high rate, but nevertheless the material is restored much more slowly than when no load is present; 8—the compressed base material retards the strain of the tough impregnating agent, and reduces the compressive load; 10—the load is completely removed, and the material continues to be restored for a long time.

The component ratio (fiber skeleton to impregnating material) in high-temperature static packing may vary. It is determined by the specifications for these materials. The strength, creep resistance, and other properties are a function of the skeleton material, and the wetting properties are dependent on the soft impregnating material. However, the composite does not acquire the properties of the individual components in proportion to the amount of material present. For example, a composite consisting of 39.4 vol % of high-strength skeleton material (molybdenum) and 60.6 vol % of silver has only about twice the strength (yield point) of the impregnating material.

Table XIII.31 shows the properties and compositions of fiber-base packing materials. The most advantageous combination of properties is displayed by the systems Mo—Ag and stainless steel — Mg. These materials are successfully employed in fixed and mobile joints of airplanes, rockets and other machines.

To test the ability of such materials to be restored after applying a complex load, stress-strain curves were plotted up to stresses above the elastic limit. In analogy with the procedure adopted for a material consisting of cooled resin, with thin springs distributed over its bulk, the stress-strain curves were divided into 10 sections. Though this analogy is very arbitrary, it gives a certain idea of the behavior of the composite seal of fibrous structure.

The ability of the material of static packings to restore its shape after deformation is very important. Table XIII.32 shows some deformation values (up to 10%) of the most characteristic composites with a molybdenum or steel fiber skeleton. The liquid or gas pressure acting upon the packing greatly affects this parameter. This is confirmed by tests on various composite fibers for elasticity, when these are used as packings for air under higher pressure.

The best materials for static packings are those which have a low torque over a wide pressure range (Figure XIII.50).

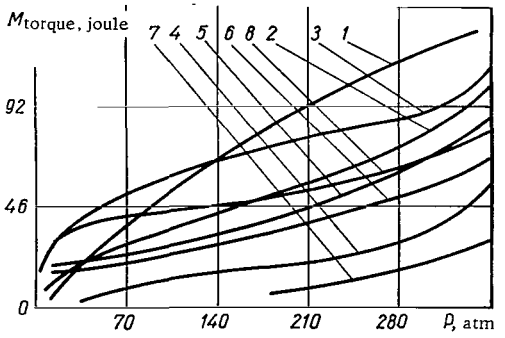

FIGURE XIII. 50. Parameters of packing composites:

1 — Mo—Sn; 2 — Mo—In; 3 — Mo—Ag; 4 — stainless steel—Sn; 5 — stainless steel—Mg; 6, 7 — stainless steel—monomer $PNCl_2$; 8 — pure Ag.

TABLE XIII. 32. Shape restoration of packing materials after deformation at room temperature

Number of composite	Composition	Deformation, %							
		stress, kg/cm²	degree of shape restoration, %	stress, kg/cm²	degree of shape restoration, %	stress, kg/cm²	degree of shape restoration, %	stress, kg/cm²	degree of shape restoration, %
1	18.5 vol % of Mo + 81.5 vol % of Sn	0.198	72	0.547	63	0.830	23	1.096	13
2	60 vol % of Mo + 40 vol % of In	0.183	59	0.187	46	0.870	32	1.607	14
3	39 vol % of Mo + 60 vol % of Ag	0.333	71	0.603	49	0.815	23	0.890	13
4	39 vol % of stainless steel 430 + 61 vol % of Sn	0.638	89	1.983	62	2.830	30	3.680	12
5	26.9 vol % of stainless steel 430 + 73.1 vol % of Mg	0.642	87	1.337	62	1.910	31	2.450	19

Packing composites of the metal-metal type are preferentially employed when temperature and pressure cycles act simultaneously. However, after the behavior of some inorganic polymers had been studied, it was realized that some of these can be employed as impregnating materials instead of metals. These polymers include polyphosphonitryl chloride (Table XIII. 31).

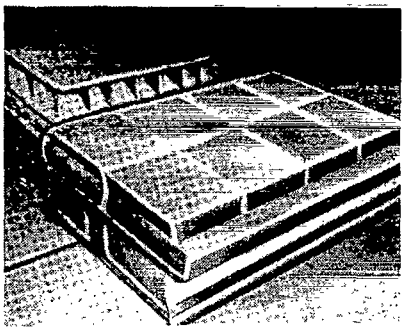

FIGURE XIII. 51. Fiberfrax lining.

We know of another nonmetallic impregnating material, Hermetic J-1-18. When this is applied to a skeleton of molybdenum or stainless steel fibers it forms a packing composite able to operate in fuel, mineral and synthetic oils at pressures up to 200 atm and temperatures up to 300°C.

Lining and stuffing materials. * We can use both single-phase and composite materials based on metallic and high-temperature nonmetallic fibers as raw material for linings and stuffings. For example, fibers made from aluminum silicate (Fiberfrax) as a loose fiber mass is a heat-resistant material for expanding joints in furnaces, boilers, etc. (Figure XIII. 51). Such material can retain its elasticity on long-term exposure to high temperatures.

The alloy Hastelloy is applied as strips onto Inconel rings, and used for producing stuffing boxes for turbines.

We know of some packing composites in which one of the components or even the base material is asbestos.

For valves operating in corrosive media at pressures up to 350 atm and temperatures of 650°C, heat-resistant stuffing materials are used consisting of asbestos and metal "wool" or wire. Such materials are produced as cords consisting of an asbestos covering and a flexible core made of asbestos and graphite (Figure XIII. 52). Another type of combined packing material has asbestos as the base material and one of the most heat-resistant plastics with a high melting point, of the fluorohydrocarbon type, namely polytetrafluoroethylene with the trade name Teflon or Fluon. This plastic is not only heat resistant but very stable to chemicals, and has a very low coefficient of friction. To obtain the material in an aqueous medium, colloidal Teflon (50 wt %) is mixed with finely ground dispersed asbestos (50 wt %) until a homogeneous mass is obtained. Then the polymer particles are coagulated, water is evaporated, and the mixture is dried. Instead of pure polytetrafluoroethylene, its copolymers with vinylidene fluoride can be employed. In this case the filler is asbestos.

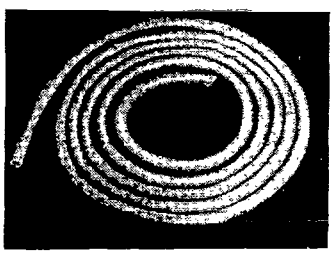

FIGURE XIII. 52. Asbestos-metal cord stuffing.

In the aircraft and rocket industries various packing materials based on asbestos composites are used. Stainless steel wool is sometimes added to increase the elastic properties. For elastic linings with specific properties, impregnating compositions of different types and copper shells have been used. Such packing material can operate at temperatures as high as 760°C.

* The materials and test results in this section were taken from Caroll—Porczynski /21/.

Metal fabrics are frequently employed as packings. For example, the lining materials for the heads of diesel engine cylinders are made of steel grids of cord weaving. The density is 11 threads per 1 cm along weft and warp. This grid reinforces the asbestos base coated with a thin layer of synthetic rubber.

Packing materials can also be produced from knitted fabrics made of aluminum, Monel Metal, Inconel, or silvered brass wires. From a fabric knitted from Inconel wires, a packing ribbon is prepared for aircraft and rocket engineering. The fabric is pressed and placed into an Inconel wire wheet and then formed into the required dimensions. The products are soft and elastic, and can be used at temperatures up to 1,100°C (Figure XIII. 53).

Packing materials made from knitted Inconel fabrics (for example, J-M 2559) as sheath are successfully employed for sealing nozzles, flange couplings of exhaust systems, rings and sealings of engines, various pipes, and control systems. These packings are resistant to most gases, alkalis and acids, keep their shape at high temperatures (up to 1,093°C), and are impermeable to hot gases if the pressure drops.

FIGURE XIII. 53. Packing material based on Inconel.

If a higher degree of hermetic sealing is required (for example, for sealing the sectional partitions of combustion chambers of reactive motors and fireproof partitions, or for isolating the compressor and the crew cabin from the exhaust system and the combustion chamber), a combined material consisting of Inconel and asbestos with graphite, is recommended. Depending on the operating conditions, the asbestos sheath for the Inconel fabric is impregnated with neoprene rubber, silicone resin, Teflon or aluminum, and reinforced with Inconel wire. This reduces flammability and keeps the core intact if the sheath is destroyed. Such a material can withstand temperatures of about 1,100°C for 15 min or longer. If the conventional band-type packing is ineffective, specially corrugated materials or materials of the "tadpole" type are used (Figure XIII. 54).

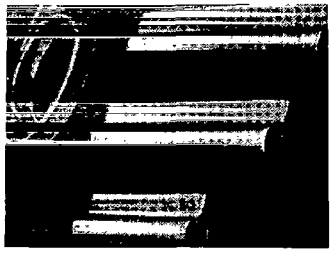

FIGURE XIII. 54. Special packing of the "tadpole" type.

FIGURE XIII. 55. Packing rings made of tungsten knitted fabric for rocket engines.

Some special types of packing materials have recently been developed for rocket engines (Figure XIII. 55). One of these materials (MX-4612) was produced from knitted tungsten and graphite fabric, impregnated with a fireproof compound. It is recommended for the nozzles of rocket engines at temperatures up to 2,760°C. Another material of similar composition (MX-4613) is used to prevent flame spreadings, and in various bearings, and other high-temperature component parts. ;

Packing materials made of fibers for steam and gas turbines. The above packing composites are not used for the radial packings of steam and gas turbines, since the operating conditions of radial and static seals differ appreciably.

According to the operating conditions of packings in turbines, the material used for the production of seals must satisfy the following criteria:

a) the properties and structure of the material must be stable during long-term operation;

b) the material must be resistant to oxidation and corrosion at the temperatures of operation;

c) the material must have an optimum mechanical strength, sufficient to prevent its breaking and to ensure smooth fitting of flanges at their moment of contact, and to reduce the wear to a minimum;

d) the material must not stick to the flanges;

e) the thermal expansion coefficients of the packing material and the turbine ring must be similar in value to prevent splitting during operation due to thermoelastic stresses.

The hardness of the packing material must not be too high. It was shown by tests that during operation the flanges of the packing wear away, and do not cut in when the hardness of the material is 100 H_v. The required hardness can be ensured by controlling the porosity of the material or introducing a soft filler with good antifriction properties. A study of the wear mechanism in the metal-metal pair showed that not only the hardness but also the toughness of the material is important. A high toughness is frequently the cause of setting during run in; for this reason a filler must be employed to decrease the toughness.

In the engine industry of the USSR, cermet packings are being used. They are based on nickel with graphite, boron nitride, and other fillers. Sometimes material is employed with a copper-base, such as bronze graphites. However, nickel-base seals have the following drawbacks: low impact strength of the materials, which does not exceed 4 joules/cm^2 in the initial state; increase in the hardness, decrease in the strength and embrittlement because of oxidation; low resistance to oxidation in the combustion products of various fuels because of the high graphite level, burning, and also shrinkage, during operation.

Bronze-graphite packings have some advantages over nickel-graphite seals; their structural and mechanical stability during operation is higher. These materials, however, are not used at high pressures and temperatues.

The application of fibers in packing materials appreciably increases the material strength and stability to impact loads during operations. The required effect can be attained with pseudofusible fibers of a given composition. The materials are produced from such fibers, or the fibers are used to reinforce a base material.

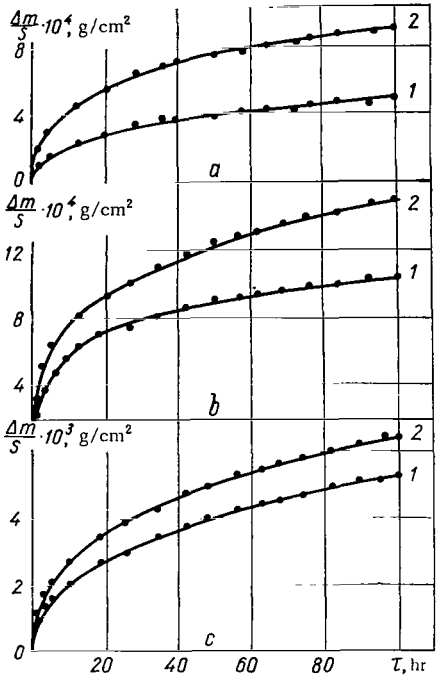

FIGURE XIII.56. Dependence of the weight increment on the oxidation period in air of material ($\theta = 30\%$) made of Ni + 5 wt % mica fibers at 600 (a), 700 (b), and 900°C (c):

1 — 6—10 mm long fibers; 2 — 2—5 mm long fibers.

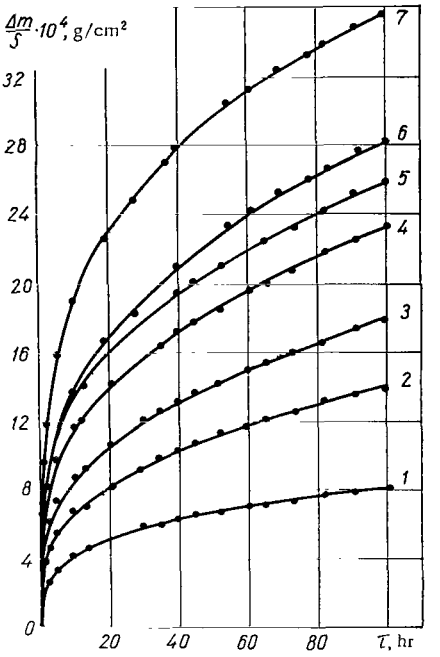

FIGURE XIII.57. Dependence of the weight increment on the oxidation period in air of materials of various porosities made of Ni + 5 wt % of mica fibers at 800°C (1 — 6: L = 6 — 10 mm; 7: L = 2 — 5 mm):

1 — $\theta = 6.5\%$; 2 — $\theta = 12.5\%$; 3 — $\theta = 16.5\%$; 4 — $\theta = 21.5\%$; 5 — $\theta = 26\%$; 6, 7 — $\theta = 30\%$.

At the Institute for Material Research of the Ukrainian Academy of Sciences, packing materials were developed from pseudofusible fibers. The base is nickel with 5 wt % of mica added. The charge made of nickel powder, mica, and organic plasticizer is extruded through spinnerets, and the fibers are then subjected to heat treatment.

One of the most important parameters determining the applicability of the material at high temperatures is its resistance to oxidation. This parameter was evaluated (after carrying out preliminary tests) by the weight increment after oxidation per unit of the total surface of the fibers.

The results showed that the oxidizability of the above material is a function of the initial fiber length. Figures XIII. 56 and XIII. 57 give data on the oxidation kinetics in air at 600 — 900°C of packing material made from pseudofusible fibers 2 — 5 and 6 — 10 mm long. In short-fiber products the weight increment is higher at all temperatures than in long-fiber products of the same porosity and size, because of the larger specific surface of the former. It was also found that the oxidation kinetics of this material obey the cubic law. In contrast, when materials from pure nickel fibers are oxidized, the weight increment is time dependent according to the

parabolic law. The rate constant of the oxidation of the nickel-mica material is in agreement with Arrhenius' law. Since the rate constant of high-temperature oxidation is satisfactorily described by Wagner's theory, and determined by diffusional processes, it can be assumed that the cubic law of oxidation noted involves time-dependent changes in the available oxidation surface.

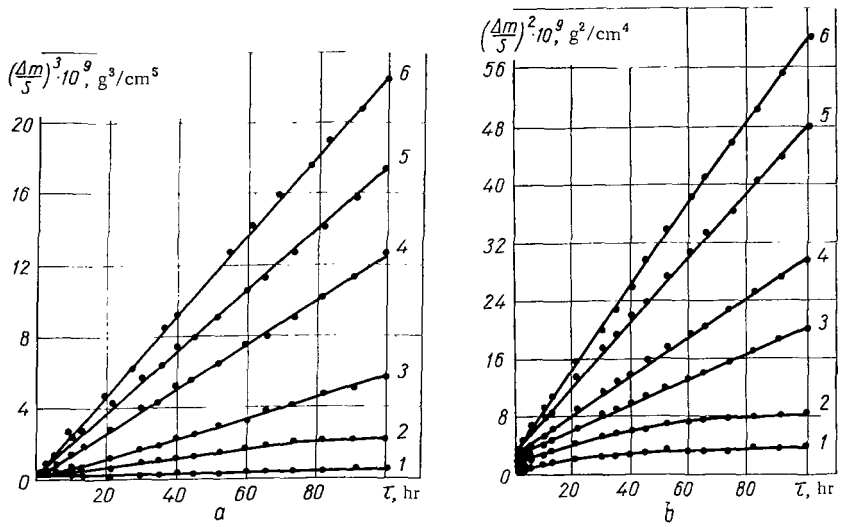

FIGURE XIII. 58. Special features of air oxidation of material made of Ni+ 5 wt % of mica fibers (a) and nickel fibers (b) at 800°C (L = 6 – 10 mm):

1 — θ = 6.5 — 7%; 2 — θ = 12 — 12.5%; 3 — θ = 15 — 16.5%; 4 — θ = 20.5 — 21.5%; 5 — θ = = 26 — 27%; 6 — θ = 30%.

Tests on the oxidation of products of various porosities showed that clogging of the pores is also observed in fiber materials. However, in powder materials pore clogging usually occurs in the porosity range between 10 and 40%, but in fiber materials this effect takes place in the lower porosity range because of the high permeability. Thus, for porosities below 12% we note deviations from the parabolic (nickel fibers) and cubic (nickel + 5% of mica fibers) laws, because of pore clogging (Figures XIII. 58, a, b), but at all porosities above 12% the oxidation kinetics are satisfactorily described by these laws.

Some special patterns of change in the physicomechanical properties of packing materials made from fibers are observed during high-temperature oxidation. We know that during the molding of powder materials, the interfacial area between the particles is very important. This area completely determines the strength properties and electrical conductivity of powder materials. Data for materials made from wire fibers show that the properties are determined mainly by the material itself, and depend less on interfacial factors.

Tests on materials made from pseudofusible (nickel-mica) fibers indicate that the properties are determined by both intraparticle and inter-

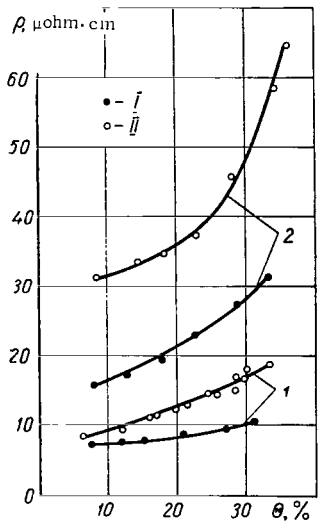

FIGURE XIII. 59. Dependence of the electrical resistivity of materials made of nickel fibers (I) and of nickel + 14 vol% of mica fibers (II) ($l = 6-10$ mm) on the porosity:

1 — made by pressing and sintering;
2 — made by pressing.

facial factors. It is thus possible to study structure-sensitive parameters such as the impact strength and electrical conductivity (Figure XIII. 59, Table XIII. 33).

Because of structural anisotropy, the fiber material is fractured on impact over the fiber cross section and not over the interfacial area. However, the state of the interface greatly affects the porosity. This is confirmed by the appreciable increase in the impact strength of fiber materials after sintering (it is twice as high for the nickel and four times as high for the pseudofusible materials). This is due to the formation of metallic contact between the fibers. The impact strength is also a function of the strength of the individual fibers. After material made of pseudofusible fibers has been sintered, its impact strength is only half that of the nickel fiber material (see Table XIII. 33). We must, however, note the very high impact strength of fiber materials even when the porosity is high; this is the considerable advantage of such materials.

The effect of the structure, and of contacts between fibers, on the properties of the materials is especially noticeable when the electrical resistivity is considered.

After fiber materials ($l = 6-10$ mm) have been sintered, their resistivity is only one third of that of materials which have only been pressed (Table XIII. 33). This large difference in the conductivity is due only to the quality of contact between the fibers.

TABLE XIII. 33. Impact strength and electrical resistivity of materials made from pseudofusible and metallic fibers

Fiber material ($d = 250$ μ)	Porosity of product, %	Impact strength, joules/cm², at $l = 6-10$ mm		Electrical resistivity, μohm·cm			
				pressed*		pressed and sintered**	
		pressed*	pressed and sintered**	$l = 2-5$ mm	$l = 6-10$ mm	$l = 2-5$ mm	$l = 6-10$ mm
Ni + 14 vol % of mica	30	3.5	12.5	122.0	55.0	21.0	17.5
Ni	30	12.7	26.0	59.5	31.0	11.0	10.5

* Pressed at 6 kilonewtons/cm².

** Pressed at 6 kilonewtons/cm², and then sintered in hydrogen at 1300°C for 2 hr.

In long-fiber materials ($l = 6-10$ mm), the resistivities after pressing and sintering differ by a factor of three, and in materials from short fibers of the same type ($l = 2-5$ mm) this parameter differs by a factor as high as about six. This is also due to the state of contact between the fibers in the material. In short-fiber products the number of such contacts is greater. Therefore, imperfections in the contacts after pressing affect the conductivity more than such imperfections after sintering.

Other conditions being equal, the resistivities of briquettes made from short and long fibers in the pressed state differ by a factor of about two. But after sintering, when the quality of contacts between the fibers is high, this difference almost vanishes.

Data on changes in the resistivity also indicate changes in the contacts between fibers when they are oxidized at high temperatures.

From a comparison between the resistivities of pressed, sintered, and oxidized fiber materials (Figure XIII. 60), we can conclude that during oxidation the contacts between the fibers are not completely destroyed; the products after oxidation have a lower resistivity than after pressing. In other words, oxidation for 100 hr at 800°C did not bring the contacts between the fibers in the material to such a qualitative state as the sintering process after pressing.

The kinetic curves of changes in the resistivity during oxidation at various temperatures shows that the sharp increase in this parameter is only found in the first oxidation stage; this may be due to the partial oxidation of the interfiber contacts. Later, the conductivity is a linear function of the oxidation period (Figure XII. 61).

With increase in the temperature the inflexion on the kinetic curves of resistivity vs oxidation periods shifts toward the left. In briquettes made from short fibers the electrical resistivity is much higher than in those made from longer fibers; this is due to the better oxidizability of the shorter fibers since their specific surface is larger. In material made from nickel fibers with 5 wt % of mica the maximum increase in the resistivity is found between 600 and 700°C.

The advantages of packing materials made from fibers over those made from powders are most distinctly seen when comparing the mechanical properties after long-term high-temperature oxidation. Figure XIII. 62 shows the impact strength of several materials and powders after oxidation at 800°C for 100 hr (except UPG-1) as a function of the porosity. The material UPG-1 was taken after sintering without oxidation.

The impact strength of fiber materials is less dependent on the porosity and oxidation temperature than that of powder material. The material made of Ni + 5 wt % of mica fibers has a higher impact strength in the given porosity range than powder material of the same composition. Even with a porosity as low as 17%, pseudofusible powder material has an impact strength close to zero, while at the same time analogous materials made from fibers have an impact strength after oxidation equal to $3-4$ joules/cm^2 in the porosity range of $17-30$%.

Thus, the impact strength, one of the most important mechanical parameters, is much higher in the nickel + 5 wt % of synthetic mica fiber product than in the better nickel-graphite or bronze-graphite packing materials. This applies to the original state and after oxidation. The fiber material also has a more stable impact strength with increase in oxidation temperature, especially above 700°C (Figure XIII. 63).

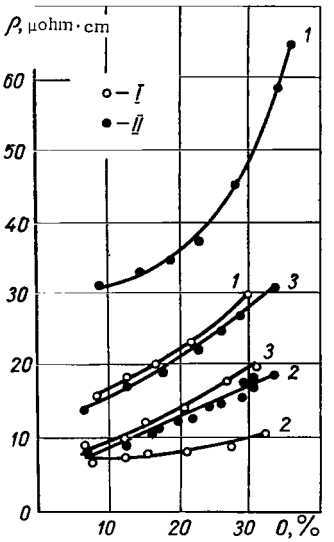

FIGURE XIII.60. Dependence of the electrical resistivity of materials made from nickel fibers (I) and nickel + 5 wt % of mica fibers (II) (l = 6—10 mm) on the porosity:

1 — products after pressing at 6 kilonewtons/cm^2; 2 — products after sintering in hydrogen at 1300°C for 2 hr; 3 — products after oxidation in air for 100 hr at 800°C.

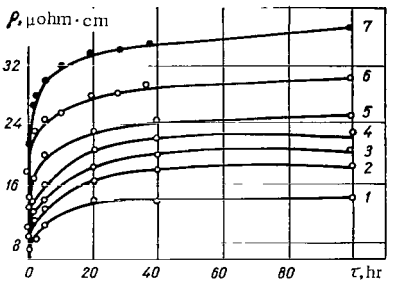

FIGURE XIII.61. Dependence of the electrical resistivity of materials made from fibers of the pseudo alloy Ni+ 5 wt % of mica fibers on the oxidation period in air at 800°C:

1 — θ = 6.5%; 2 — θ = 12.5%; 3 — θ = 16.5%; 4 — θ = 21.5%; 5 — θ = 26%; 6, 7 — θ = 30% (1—6; l = 6 — 10 mm; 7 — l = 2 — 5 mm).

Another very important parameter of the pseudofusible fiber material, the hardness, changes on oxidation within permissible limits (see Figure XIII. 63).

We have already mentioned that packing materials must be subject to little wear when the sealing flanges notch them. In other words they must have optimum antifriction properties. For crystalline mica on a base of synthetic potassium fluorophlogopite these properties were studied in detail by Belitskii et al. /50/, who proved that the introduction of synthetic mica into the material leads to a decrease in the coefficient of friction and to the elimination of undesirable hardening of surfaces after notching.

The antifriction properties of the pseudofusible material based on nickel+5 wt % of mica were studied by notching of a disklike counterbody into the surface of products subjected to oxidation in the air at 800°C for 100 hr. Powder samples of the same composition were also tested by notching a thin disk (0.5 — 1 mm) of EI-435 steel at a velocity of 100 m/sec under a load of 40 newtons /51/. The test time was 5 sec, and the depth of the notches 0.75 mm. The criteria characterizing the notching of disks into the material were the friction coefficient and wear of the notching counterbody. The results of tests on these parameters and comparative data for packing materials UPG-1 and M32 (without graphite added) in the initial state are shown in Table XIII. 34. It can be seen from these data that fiber materials give the lowest wear of the counterbody.

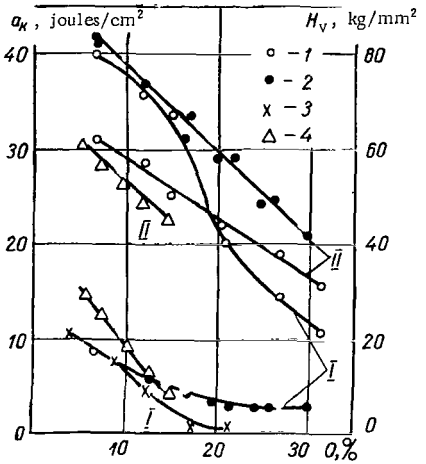

FIGURE XIII.62. Dependence of the impact strength and hardness of fiber materials on their porosity:

1 — briquettes made from nickel fibers; 2 — briquettes made from Ni + 5 wt % of mica fibers; 3 — briquettes made from Ni + 5 wt % of mica powder; 4 — briquettes made from material UPG-1 (Ni + 6 wt % of C):
I — impact strength; II — hardness.

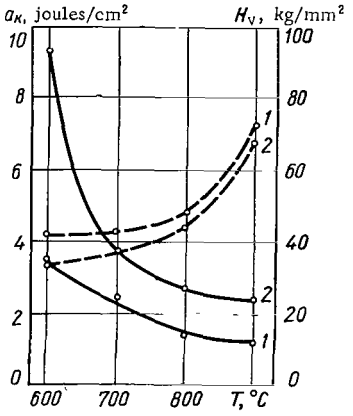

FIGURE XIII.63. Dependence of impact strength (continuous lines) and hardness (dashed lines) of material made of Ni + 5 wt % of mica fibers on the oxidation temperature (time of oxidation 100 hr, $\Theta = 30\%$):

1 — l = 2 — 5 mm; 2 — l = 6 — 10 mm.

The results of complex tests on packing materials made from pseudo-fusible fibers (nickel-mica) showed that these materials have a higher impact strength, lower hardness, higher stability of mechanical properties on heating than packing materials based on nickel and graphite with various fillers added (mainly graphite). Fiber materials are also free of additives which are burned when operating in oxidizing gaseous media. Their deformational properties are high and their running-in ability is good.

TABLE XIII.34. Notching tests on packing materials

Material	Porosity, %	Coefficient of friction	Wear of counterbody, mm
UPG-1	10	0.080	0.016
M32	8—10	0.015	Deposit 0.040
Ni + 5 wt % of mica (fibers)	12	0.080	0.008
Ni + 5 wt % mica (powder)	< 10	0.083	0.010

5. Dampers of mechanical and sonic vibrations

During the development process of metallic and nonmetallic fiber materials, new ranges of their application were detected. In particular, the mazelike structure of such materials, especially when their porosity is high, makes them very suitable for sound and vibration absorption.

TABLE XIII. 35. Sound-absorbing properties of fiber materials

Frequency, Hz	Sound absorption, %	
	material made from stainless steel fibers in the sintered state, plate thickness, 63 mm	glass fiber material, plate thickness, 76 mm
250	47	39
500	80	69
1000	94	83
2000	93	95

Tests on the sound absorption of materials made from stainless steel fibers showed that they are competitive with nonbonded glass fibers /52/.

At room temperature up 1000 Hz the sonic absorption coefficient of materials made from stainless steel fibers is about 8 — 11% higher than that of glass fibers. At higher frequencies the properties of both types of materials are equal; they ensure a 90% absorption of the sound energy (Table XIII. 35). But in contrast to glass fibers, metal felt material retains its high absorption power at higher temperatures also. For example, the same material made from stainless steel fibers at 475°C and audio-frequencies of 1,800 Hz had an absorption coefficient of sonic energy of 0.87, that is, only 7% lower than that at room temperature. The material also retains its satisfactory sound absorption properties when heated to 815°C.

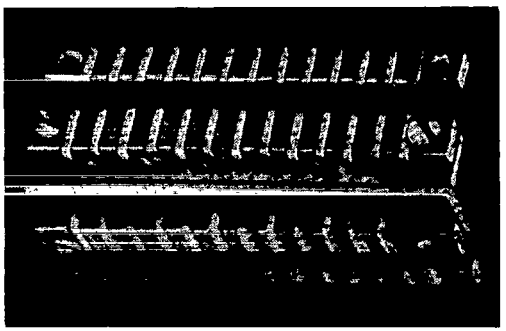

FIGURE XIII. 64. Stainless steel cable in an antivibration equipment.

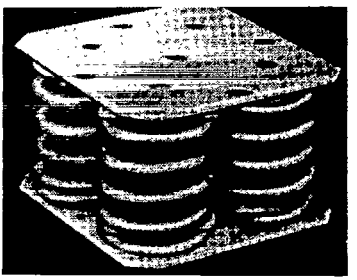

FIGURE XIII. 65. Antishock and antivibration padding.

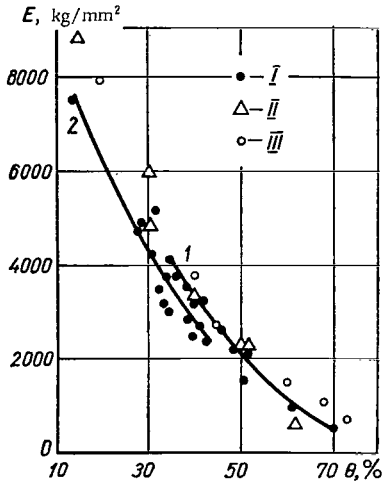

FIGURE XIII.66. Dependence of the dynamic modulus of elasticity on the porosity for material made from copper fibers of diameter 50μ and length 6—7 mm (sintering conditions: I — 950°C, 3 hr; II — 980°C, 3.5—4.0 hr; III — 1000°C, 4 hr):

1 — with preliminary felting; 2 — without preliminary felting.

Mechanical vibration are also readily absorbed by fiber materials. For example, a material made from stainless steel fibers (porosity 76 — 80%) had a damping power 2 to 6 times higher than aluminum sheet material, with an equal weight-to-surface ratio. In this case the required strength will certainly be reached, and the material can work at high temperatures in corrosive media /53/.

Because of their high antivibrational and sound adsorption properties, fiber materials are used as linings when assembling machines, for turbines, precision instruments, and electronic instruments, and also in space engineering (Figure XIII. 64).

Woven metal fabrics are generally used in vibration- and shock-absorbing components. The petallike structure of these materials ensures their high resistance against irreversible deformation at high temperatures and loads, since the heat evolved during bending is rapidly dissipated over the grid.

Damping parts have been produced from knitted metal fabrics. These are used for protecting electronic systems of airplanes and rockets, in radar aerials and other devices subject to rotation in operation /54, 55/.

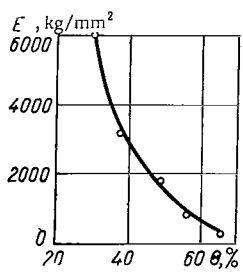

FIGURE XIII.67. Dependence of the dynamic modulus of elasticity on the porosity for material made from stainless steel 1Kh18NT fibers of diameter 50μ and length 6 mm (sintering conditions: 1250°C, 3 hr in very pure hydrogen after preliminary felting).

A new method for producing vibration isolating material with the trade name "Fibrashock Isolation" was developed in England /56/. This material is a knitted fabric made of stainless steel, which is crimped and rolled into cylindrical paddings. The form required imparted by pressing at a pressure above the elastic limit. Such paddings operate as steel springs which are subjected to minimum deformation on load increase without change in the vibrational frequency (Figure XIII. 65).

Pressed metallic knitted fabric is used for paddings in high-frequency electronic instruments to prevent emission of undesired frequencies /57/.

Published data also show that felts from high-temperature nonmetallic fibers can be used as damping materials. For example, fibers with a high silica (microquartz) content

gave very good results when tested for vibration resistance. After 48 hr of vibrations at 100 Hz at an amplitude of 0.5 mm a felt of such fibers 2.5 mm thick did not change its thermal conductivity; this indicates that the operating characteristics remain constant when the material is subjected to vibrations. Such a material is chemically very stable and is attacked by HF, hot H_3PO_4, and some metal oxides only /21/.

TABLE XIII.36. Elastic characteristics of a material made from copper fibers of 50μ diameter and 6 mm length obtained by sintering at 950°C for 3 hr

Porosity of material, %	Dynamic modulus of elasticity E, kg/mm^2		Damping ratio, $Q^{-1} \cdot 10^{-3}$	
	without impregnation	impregnated by bakelite varnish	without impregnation	impregnated by bakelite varnish
16.5	7512	7615	5.83	3.92
27.4	4785	4845	10.40	10.40
28.8	—	4917	6.80	11.80
30.0	4900*	—	—	—
31.1	4013	4486	16.50	19.00
33.5	—	4038	—	—
34.2	3625	3248	9.62	11.70
35.5	3114	3034	11.20	10.10
40.0	3300*	—	—	—
42.9	2457	2719	—	—
50.0	2200*	—	—	—
53.5	—	1374	—	25.0
53.8	—	1200	—	25.8
60.0	—	1550*	—	—
70.0	—	1000*	—	—
80.0	—	760*	—	—

* The data refer to materials obtained with preliminary felting.

Materials made from long aluminum silicate fibers (Fiberfrax and Kaowool) and mats produced from them have very good sound absorption properties, and high elasticity and vibration resistance. These properties are of especial importance when such materials are utilized for isolation of chambers on test stands of reactive and rocket engines, silencers of reactive motors, and in other cases where effective sound absorption is required /58/.

Lining material made from Fiberfrax paper has a high elasticity during long periods of high thermal action. It is used fro shock absorption when soldering honeycombed structures.

To protect the curved surfaces of various airplane parts (exhaust pipes, cones, jet chambers, etc.) from vibration, the materials Thermoflex and Cerafelt are used; they are produced from aluminum silicate fibers and placed into grids made from heat-reistant metal (for example, stainless steel or Inconel). These materials have good sound-absorbing properties and can also be used to reduce industrial noise /59/.

According to preliminary research, damping materials can be prepared from potassium titanate fibers. For example, Tipersul material combines good vibration resistance and sound isolation properties with high thermal and chemical stability /60/.

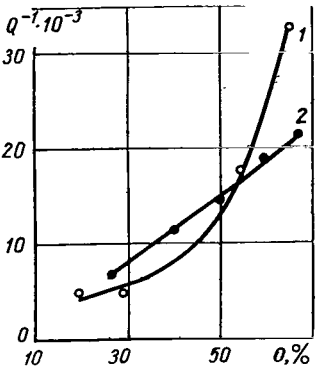

FIGURE XIII.68. Dependence of the damping ratio on the porosity of materials made from copper fibers (1) and stainless steel fibers (2) ($d = 50\mu$, $l = 6-7$ mm):

1 — sintering temperature 980°C, sintering time, 4 hr; 2 — sintering temperature 1250°C, sintering time, 3 hr.

As mentioned above, the high damping power of fiber materials is due to their mazelike structure and their high elastic parameters.

We shall now examine some experimental data on the properties of damping materials. Figures XIII.66 and XIII.67 show the dependences of the dynamic modulus of elasticity* on the porosity for materials made from copper and stainless steel fibers. It can be seen that with increase in porosity the modulus of elasticity decreases appreciably. For materials prepared with preliminary felting of fibers, sintered at higher temperatures for longer periods, the modulus of elasticity will be somewhat higher, other conditions being equal.

Not only porous fiber materials can be successfully used for sound and vibration absorption, but also composites based on fibers which contain components of various types applied as coatings or by impregnation. Examples of such materials are the vibration-absorbing mastic 2—20, polyfluoroethylene resins, and bakelite varnish. The impregnated material has a somewhat higher modulus of dynamic elasticity than an equal volume of nonimpregnated metallic component-fibers (Table XIII.36).

Interesting results are obtained by comparing data by means of the logarithmic damping ratio** (a number reciprocal to the number of vibrations at which the amplitude decreases $e = 2.71828$ times) for porous or impregnated fiber materials and compact materials. Thus, at a porosity of 17% the damping ratio for a copper fiber material is $4\cdot10^{-3}$, and at a porosity of 65% it is $33\cdot10^{-3}$. This is about 30 to 60 times the value for compact copper.

With increase in porosity the damping ratio increases appreciably: an increase in the porosity from 20 to 65% leads to a 4—7 times increase in the damping ratio (Figure XIII.68). These data indicate that it is advantageous and convenient to use porous materials made from fibers as sound and vibration absorbers.

Bibliography

1. British Patent No. 821690.
2. Markov, L.O. and V.P.Stryapko. Opyt izgotovleniya metallokeramicheskikh fil'trov (Attempts to Prepare Cermet Filters).— In: Tekhnologiya mashinostroeniya, 6. Moskva, Izdatel'stvo NIIMASh. 1965.

* The results were obtained with an instrument of the system Förster's "Elastomat."

** The damping ratio was determined by flexural vibrations.

3. U.S. Patent.— Cl. 29—183, 5, No. 3084421.
4. Lefer, H. Fiber Metallurgy for Controlled Density and Porosity.— Precision Metal Molding, 22:3. 1964.
5. Ivashchenko, V.V. et al. Izgotovlenie izdelii iz metallicheskogo volokna metodom vibratsii (Production of Articles from Metal Fibers by the Vibration Method).— Poroshkovaya Metallurgiya, 4. 1968.
6. Fiber Metallurgy. A New Process.— Precision Metal Molding, 16:1. 1958.
7. Sokol, L. Metal-Fibre Filters.— Powder Metal., 8:15. 1965.
8. Bal'shin, M. Yu. et al. Nekotorye voprosy metallurgiii volokna (Some Problems of Fiber Metallurgy).— Poroshkovaya Metallurgiya, 3. 1964.
9. Sump, C.H. and W. Pollack. Fiber Metallurgy.— Proceedings of 13th Annual Meeting at Metal Powder Association, April 30 — May 1, 1957. Volume 1. General Session on Powder Metallurgy, Chicago, Illinois.
10. Fedorchenko, I.M., A.G. Kostornov, and V.S. Pugin. Sposob polucheniya voloknistykh metallokeramicheskikh izdelii (Method for the Production of Fibrous Cermet Articles). Soviet Patent No. 198662.— Byulleten' Izobretenii, 14. 1967.
11. Pranatis, A.L. and L. Seigle. Powder Metallurgy, ed. Leszynsky. N.Y.— London. 1961.
12. Read, R.H., W. Pollack, and S.W. McGee. Fibre Metallurgy.— Precision Metal Molding, 16:4. 1958.
13. Metcalfe, A.G., C.H. Sump, and W.C. Troy.— Fiber Metallurg. Metal Progress, 67:3. 1955.
14. Sukhozhak, V.V. and V.V. Skorokhod. O spekaemosti poristykh briketov iz volokna molibdena s malymi dobavkami nikelya (The Sinterability of Porous Briquettes Made from Molybdenum Fibers with Small Nickel Additives).— Poroshkovaya Metallurgiya, 8. 1968.
15. GFR Patent No. 1206705.
16. Metcalfe, A.G. and C.H. Sump. Fiber Metals.— A New Metal Form.— Mater. Methods, 42:5. 1955.
17. Morden, J.F.C. Metallic Fibres.— Metal Industry, 96:25. 1960.
18. Poroshkovaya metallurgiya v novoi tekhnike (Powder Metallurgy in Modern Engineering). Moskva, "Nauka." 1968.
19. Gatushkin, A.A. and S.M. Solonin. Issledovanie fil'truyushchikh svoistv dvukhsloinykh metallokeramicheskikh fil'trov (Study of the Filtration Properties of Two-Layer Cermet Filters).— Poroshkovaya Metallurgiya, 7. 1966.
20. Walworth, C.B. Ceramic Fibres.— Fibers and Plastics, 22:6. 1961.
21. Carroll-Porczynski, C.Z. Advanced Materials, Refractory Fibres, Fibrous Metals, Composites. Guildford, Astex Publishing Company Ltd. 1962.
22. Druzhinin, S.A.— Teploenergetika, 9. 1961.
23. Eroshenko, V.M.— In: Fizicheskaya gazodinamika i teploobmen. Moskva, Izdatel'stvo AN SSSR. 1961.

24. Grootenhuis, P.— J.Roy.Aeron.Soc., 63(73):578. 1959.
25. Oliver, D., et al. Symposium on Powder Metallurgy, Spec.Rep., 58:180. London. 1956.
26. Lenel, F. and O.Reen. ASTM Spec.Techn.Publ., 140:42. Philadelphia. 1953.
27. Reeman, I. and R.Buswell.— Proc.Inst.Mech.Engrs., Sect.A, 167:341. 1953; Ainleg, D.— Proc.Inst.Mech.Engrs., Sect.A, 167:351. 1953.
28. Eisenclam, P., P.Grootenhuis, and H.Ziebland.— Chemical Engineering Practice, 11:609, Butterworth. 1956.
29. Pall, D.— Aeron.Eng.Rev., 13:7. 1954.
30. Chesin Hyman. Heat-Resistant Porous Structure. US Patent, Cl.29—191. 2, No.3161478.
31. Symposium on Powder Metallurgy, Spec.Rep., 38, 110. London. 1947.
32. Potel, M.— Air Compr. Votre Serv., 27:28. 1961.
33. Stempel, G.— VDV Zeit., 102:27. 1960.
34. Stempel, G.— Die Umschau, 59:6. 1959.
35. Langhammer, A. and P.Glick.— Product Engineering, 24:4. 1953.
36. Agte, K. and K.Otsetek. Metallokeramicheskie fil'try (Cermet Filters). Leningrad, Sudpromgiz. 1959.
37. Whelan, G.— Trans.Inst.Min.Engrs., 112:9. 1952—1953.
38. Zolotko, A.A.— Poroshkovaya Metallurgiya, 6. 1963.
39. Skorokhod, V.V. Nekotorye fizicheskie svoistva vysokoporistykh tel (Some Physical Properties of High-Porous Bodies).— Poroshkovaya Metallurgiya, 6. 1967.
40. L'vov, S.N. et al. Nekotorye teplovye i elektricheskie svoistva poristykh vol'framovykh i vol'framo-molibdenovykh katodnykh materialov (Some Thermal and Electrical Properties of Porous Tungsten and Tungsten-Molybdenum Cathode Materials).— Poroshkovaya Metallurgiya, 5. 1966.
41. Mal'ko, P.I. et al. Teplo- ielektroprovodnost' poristykh nikelya, zheleza i stali Kh17N2 (Thermal and Electrical Conductivity of Porous Nickel, Iron and Steel Kh17N2).— Poroshkovaya Metallurgiya, 1. 1969.
42. Pratt, A.W. Research Applied in Industry, 15:5. May. 1962.
43. Skorodhod, V.V. and V.V.Panichkina. Elektroprovodnost' poristykh i spechennykh materialov iz mednogo volokna (Electrical Conductivity of Porous Sintered Materials Made from Copper Fibers).— Poroshkovaya Metallurgiya, 3. 1965.
44. Skorokhod, V.V.— IFZh, 2:52. 1959.
45. Cobrin, C.L.— Iron Age, 191:4. 1963.
46. Il'in, Yu.V.— Izvestiya Vuzov. Aviatsionnaya Tekhnika, 4. 1959.
47. Dyban, E.P. et al. Opredelenie lokal'noi poristosti pronitsaemykh metallokeramicheskikh materialov (Determination of the Local Porosity of Permeable Cermets).— Poroshkovaya Metallurgiya, 8. 1968.
48. Fiber Metal Seals Take 5000 p.s.i. 1200°F.— Mat.Des.Eng., 53:4. 1961.

49. Sabanas, M. High-Temperature Static Seals from Metal Fibre Composites.— Product Engineering, 31:22. 1960.
50. Belitskii, M.E. et al. —In: Povyshenie iznosostoikosti i sroka sluzhby mashin (Increase in the Wear Resistance and Service Lives of Machines). Kiev. 1966.
51. Ponomarenko, N.E.— Vestnik Mashinostroeniya, 5. 1965.
52. Lorant, M. Fasermetallurgie.— Werkstoffe und Korrosion, 15:4. 1964.
53. Read, R. Mater. Design Eng., 50:7. 1959.
54. Flexible Metallic Mount. U.S. Patent No. 2687269.
55. Keetch, W.A. Vibration Control. Electron Equip., Jan. 1956.
56. Fibrashock Isolation.— Eng. Mater. Design, 4:10. 1961.
57. Kelly, S.G. Knitted Structures Have Unique Industrial Applications.— Mater. Methods, August, 1951.
58. Walworth, C.B. Ceramic Fibres.—Fibres and Plastics, 22:6. 1961.
59. Carroll-Porczynski, C.Z. Refractory Fibres in Modern Industry.— Eng. Mater. Design, 2:11. 1959.
60. Fibrous Potassium Titanate.— Techn. Inform. Bull. 1, 3 (E.J. du Pont de Nemours and Co. Inc.).

Chapter XIV

PRODUCTION OF REINFORCED MATERIALS AND THEIR PHYSICOMECHANICAL PROPERTIES

1. Mechanical methods

In the first stage in the development of any industrial branch the raw material is selected from that available. In fiber metallurgy these materials are fine-drawn wires and metal chips, "wool," obtained by scraping and shaving, or other types of treatment on machines giving continuous fiber strands.

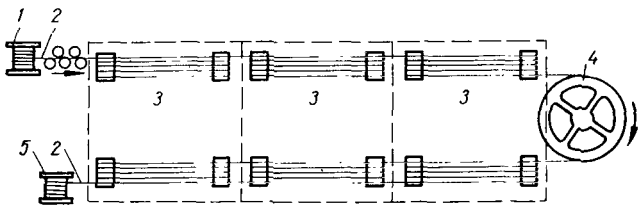

FIGURE XIV. 1. Shaving of wire in the production of metal wool.

The most popular method for producing metal wool is shaving on wiring machines. The wire is drawn through several shaving instruments, each of which removes part of the material in the form of a thin chip. The layout of the process is shown in Figure XIV. 1 /1 — 5/. Wire 2 is fed from drum 1 to the straightening apparatus, and then into several cutting machines 3, which strip off the shavings. The thinned wire passes through a reversing device and is coiled onto receiving drum 5.

Metallic wool has been used for a long time. As early as 1889, a machine for its production was designed in Germany, The wool obtained by shaving consists of 30 mm long fibers; their cross section is usually in the form of an acute-angled triangle. Wool can also be obtained from pipes or metal sheets on machines and during the processing of the involute profile of toothed wheels. Figure XIV. 2 shows a thin cross section of fibers made from stainless steel wool.

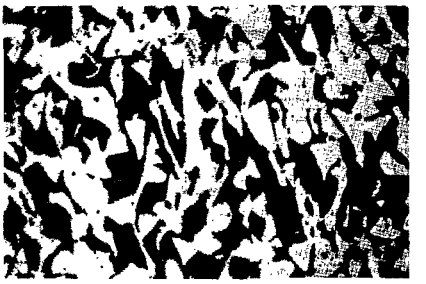

FIGURE XIV. 2. Thin cross section of fibers made from stainless steel wool.

Before the wire and the metal wool are used they are cut into pieces of a certain length on a special device (Figure XIV. 3). A correct selection of the fiber lengths helps to form homogeneous material structures.

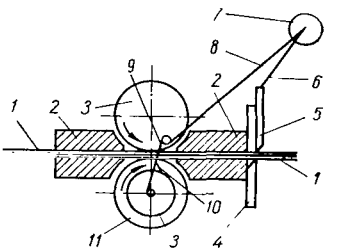

FIGURE XIV. 3. Diagram of a device for cutting wire into uniform fibers:

1 – wire braid; 2 – guiding spinnerets; 3 – drawing rolls; 4 – fixed part of guillotine; 5 – mobile part of guillotine; 6 – guide lever; 7 – crankshaft of reduction gear; 8 – 11 – hinge ratchet gearing for transmitting motion from the crank to the driving roll.

The methods for obtaining fibers by cutting wires and shaving are utilized for all technically important metals and alloys. The use of thin metallic shavings has advantages over the application of wire fibers from both the technological and economic points of view. Fibers from wool have a rough ribbed surface, and consequently, a good bonding power. This facilitates further technological processing. Therefore, when cutting wire it is very important to change the fiber configuration by bending or twisting, which makes the bonding parameters of the fibers close to those of wool. In some cases the wire is bent in a separate operation.

To obtain fibers from aluminum or copper alloys, foils are also cut (slitted); this method is used in the textile industry /6/. The foil is passed under the cutting edge of a microtome, and fibers with a rectangular cross section are obtained. Fibers produced mechanically are degreased in trichloroethylene, sodium peroxide, or aluminum hydroxide.

2. Preparation of fibers from fused metals

The methods for preparing fibers from melts are rather varied. In one of these the fused metal is extruded through holes /7/. The test equipment (Figure XIV. 4) consists of a cylindrical vessel with a protective coating for the molten metals. Two 25-mm diameter tubes pass through the vessels lid. One feeds gas, for example, nitrogen, onto the surface of the melt. The second tube is fitted at its end with a nozzle with holes, uniformly distributed over concentric circles. The fused metal is extruded through nozzle holes by the pressure exerted by the compressed gas on the metal surface.

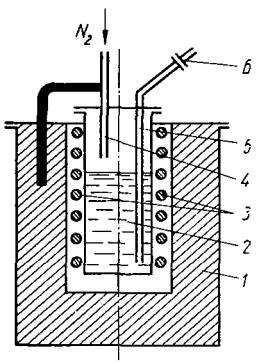

FIGURE XIV. 4. Diagram of the apparatus for preparing fibers from a metal melt extrusion:

1 – vessel with lining; 2 – metal melt; 3 – electric heater; 4 – tube for nitrogen supply; 5 – tube for extruding the liquid metal; 6 – nozzle with holes.

Aluminum and tin fibers were obtained on this equipment. The temperature of the molten aluminum was 700 – 750°C, while that of the molten tin was 400°C. The optimum hole diameter in the nozzle was 60 – 80μ for the extrusion of aluminum, while the pressure of the compressed nitrogen was not less than 6 atm. When the pressure was lower the aluminum fibers combined into thick strands when they left the nozzle. A higher pressure only ensured extrusion to a large distance from the nozzle; this cooled the fibers and prevented them from sticking together. When tin is extruded the pressure must be still higher because of the high specific gravity of the metal. The fibers obtained by this method have an undulated shape. Their length is between the orders of magnitude of 10^{-1} and 10^{1} mm and their diameter between 50 and 90μ.

The cross section along the fibers is nonuniform, and some thickenings are present which favor good bonding properties on further processing.

The surface film of Al_2O_3 formed on extrusion of aluminum is much thinner than in aluminum powders, since the fiber surface is about 30 % smaller than the surface of the spherical powder particles.

The extrusion efficiency through the holes is very high; at an extrusion speed of 1 m/sec from 28 holes in the nozzle, the maximum yield of the apparatus may be as high as 1 t/hr. By a similar method fibers from other metals and alloys can also be obtained, for example, from copper, bronze, brass and lead.

A modification of the extrusion method is that used to produce glass fibers. The fused charge is extruded through holes under the force of gravity. Attempts to employ this method for extrusion of fused aluminum were unsuccessful, since metal drops and not metal fibers were formed, due to the low viscosity of the melt /7/. However, we have information /8/ that it is possible to prepare metal fibers by spraying fused metal by means of a rapidly rotating disk with blades.

A method was developed for producing fibers by extruding a liquid metal onto a rapidly rotating disk. The centrifugal force produced by this disk

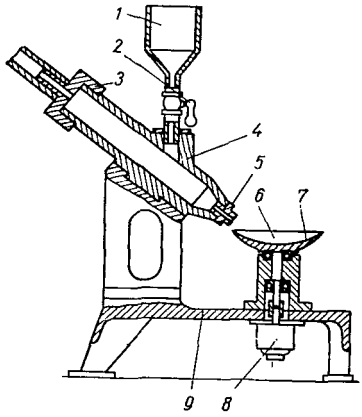

FIGURE XIV. 5. Diagram of the apparatus for preparing metal fibers by centrifuging.

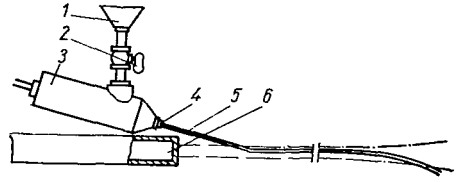

FIGURE XIV. 6. Diagram of the apparatus for preparing metal fibers by jet ejection.

forms fibers of 4 — 75μ diameter from the metal particles /9/. The apparatus (Figure XIV. 5) consists of a rapidly rotating cooling block 7 with a spherical polished surface 6 placed on base 9 (block 7 is driven by electric motor 8), and an ejecting tube 4 with nozzle 5 through which the fused metal is fed onto surface 6. The metal feed is actuated by the pressure supplied through head 3. Another part of the equipment is fusing vessel 1 with valve 2.

The pressure on the melt may be generated by pneumatic or mechanical methods. The hole size in the nozzle is controllable. At constant hole size and speed of the block the thickness of the fibers is a function of the temperature of the melt and the ejection rate.

The tested and approved methods for fiber production from metal melts include one based on the ejection of a metal jet /9/. The apparatus (Figure XIV. 6) is designed according to the principle of the ejection gas burner. A strong gas or air stream passing through nozzle 6 entrains the metal, fed as a continuous jet 5 from fusing vessel 1 by means of ejector 3 through a hole in spinneret 4. By controlling the feed rate of metal and gas by valve 2, short or long fibers can be obtained.

Methods which make it possible to produce continuous thin and very thin wires (diameter 50μ or less) or tangled wires as raw material in the technology of fiber metallurgy are interesting. They include spouting of metals and continuous extrusion (spinning) from melts. The spouting method was developed by Ulitovskii / 10/ as early as 1937. Aluminum, magnesium, copper, lead, zinc, tin and their alloys, and also some ferrous metals and their alloys, can be spouted. The spouting parameters of nonferrous metals for the production of thin cast wire, and the effect of the physicochemical properties of the spouted metals on the fibers obtained, are described in detail by Shpirnov /11, 12/.

A modification of spouting is the drawing of fibers from a drop. The principle of this method, also termed the Taylor method /13/, is the

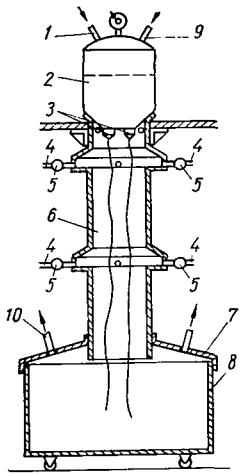

FIGURE XIV. 7. Diagram of the apparatus for preparing continuous metal fibers.

following: liquid metal drops fused in capillaries are drawn out together with the capillary into long and very thin threads.

The drawing out speed is 100 — 1,000 rpm of the winding drum. At a thread diameter of 10μ the yield of the apparatus is 0.1 — 1 g/min, or 0.1 — 1 kg/day. Such threads have a constant diameter, uniform surface, and small scattering of the strength parameters. They are almost continuous, and their cost is low.

The method of continuous extrusion from melts was developed fairly recently. The diagram of the apparatus for preparing continuous fibers by this method is shown in Figure XIV. 7 /14/.

The raw material in the molten state is fed through pipe 1 into a conical vessel with heating elements 2 which is connected to the fusing vessel. Under the pressure of the gas fed through pipe 9, the melt is extruded through the holes of nozzles 3 into chamber 6, filled with cooled air or inert gas. Gas is fed through pipe 4 by means of control valves 5. When the fiber passes through chamber 6 it becomes hard, and is then fed into receiving vessel 8. To ensure the required circulation of the gaseous coolant, the equipment is fitted with exhaust hood 7. The exhaust gas is led into the cooling equipment for reuse in chamber 6 through pipes 10. This method for obtaining continuous fibers from melts is the most economic and advanced.

3. Physicochemical methods

The above methods (mechanical and the preparation of fibers from melts) are the main ones employed in fiber metallurgy. Though they are far from perfect with regard to both efficiency and cost, they are nevertheless much better than most of the other known methods. The physicochemical methods for obtaining metallic and nonmetallic fibers are so far employed on a laboratory scale only, and most frequently for preparing filamentary crystals, so-called whiskers.

At present, whiskers can be prepared in very limited quantities only. Most of the whiskers are single crystals. Only few whiskers have a strength close to the theoretical, and they are used for various physical investigations. Because there are no methods so far available for using whiskers in fiber metallurgy, and their potential use is very problematical, we should not be deterred from looking for new approaches.

The main method for preparing metal whiskers is the reduction of various types of metal compounds. For example, when $SiCl_4$ is reduced by nickel at 800 — 1,000°C, silicon is obtained, and analogously in the reduction of $FeCl_2$ by hydrogen pure iron is produced. Under certain reduction conditions, long thin crystals begin to grow, namely whiskers. Thermodynamic and kinetic analyses show that the partial pressure of $SiCl_4$, $FeCl_2$,

or HCl determines the growth pattern of the whiskers. Widersich /15/ believes that the absorption of these components during reduction inactivates the growth of certain crystallographic planes, which leads to nucleation and growth of whiskers. Observations on whiskers of various metals when halides of Ag, Cu, Fe, Ni, Co and Mn were reduced /16/ made it possible to determine the activity of the metals. The maximum activity attained is about 100 units, which is two to four orders of magnitude lower than the results of thermodynamic calculations. It was also found by experiment that the halides are reduced on their surface, and that halide vapors ensure better transfer of matter in the gaseous phase during the growth of whiskers than metal vapors.

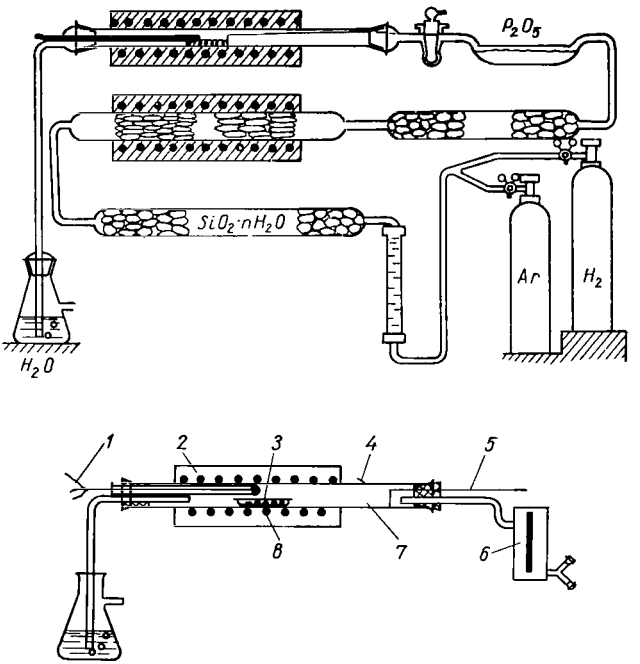

FIGURE XIV. 8. Diagram of apparatus for growing whiskers by reduction of halides:

1 – thermocouple for measuring temperature of compound; 2 – furnace; 3 – boat with halide; 4 – quartz or mullite tube; 5 – tungsten rod; 6 – flowmeter; 7 – cooling chamber; 8 – thermocouple for controlling furnace temperature.

Mazur and Rafalowicz /17/ believe that the growth mechanism of whiskers is ionic.

As material for the preparation of whiskers by reduction, sulfides /20/, chlorides /18, 21/, iodides /22/, and oxides /19/ can be used. The process of preparing whiskers by reduction of metal compounds by a gaseous or solid reducing agent is very simple. When a halide is reduced by hydrogen, the halide is placed into a boat, which is heated in an argon stream with a low hydrogen content. The tests are performed in a glass tube with cooled ends

on which the whiskers are deposited (Figure XIV. 8). The purity of the starring material and the reduction temperature have a great influence on whisker growth.

FIGURE XIV. 9. Copper whiskers obtained by reducing halides.

Under optimum conditions, the majority of crystals obtained are smooth and straight, and have a diameter of 1 — 20μ (Figure XIV. 9). Much more complicated shapes can be observed, such as spirals, plates, clubs, or beads, etc. An increase in the reduction temperature above the optimum leads to plate formation. With a further increase in temperature, large well-developed crystals grow, but no whiskers are formed. The optimum temperatures for reducing halides are shown in Table XIV. 1.

TABLE XIV. 1. Optimum temperatures of halide reduction for the production of filamentary crystals

Metal	Halide	Optimum temperature of reduction, °C	Maximum fiber length, mm
Copper	CuCl	650	50
	CuBr		
	CuI		
Silver	AgCl	800	10
	AgI		
Iron	$FeCl_2$	730°°	20
	$FeBr_2$	760°°	
Nickel	$NiBr_2$	740	2
Cobalt	$CoBr_2$	730†	3
Manganese	$MnCl_2$	940	0.25
Gold°	$AuCl_x$	550	2
Platinum°	$PtCl_x$	800	3
Palladium°	$PdCl_2$	960	10

° Thermal dissociation.

°° Weak hydrogen current.

† In a medium of 15% of H_2 and 85% of N_2.

Hauptman et al. /23/ describe a method for preparing needlelike cobalt crystals. The cobalt whiskers grown at 750 — 760°C had a cubic face-centered lattice, which was transformed into a hexagonal lattice at 400°C. Because of the phase transition, it is difficult to obtain crystals with a perfect surface. The whiskers were obtained by reducing dehydrated cobalt bromide, purified in vacuo (10^{-4} mmHg) by hydrogen. The hydrogen rate was 0.4 — 0.8 cm/sec. Because of phase transition, a relief was formed on the whiskers, similar to that produced by slip stages.

Because of the high strength parameters of defectless crystals, the theoretical papers which deal with growth mechansim of ideal whiskers are very important /24, 25/. Whiskers can grow by the inflow of atoms from the gaseous phase, and by atom diffusion from the melt (so-called basal growth). In both cases it is assumed that screw dislocation is present in the nucleus of the needlelike crystals /26, 27/. The dislocation can shift during crystal growth and distort the whisker shape, and thus lead to the formation of bent, twisted and laminated-helical single crystal whiskers /28, 29/.

An analysis of published data shows that the optimum growth temperature of needlelike crystals of metals belonging to the same group of the periodic table and with similar melting points are found on the partial pressure-temperature curves at points where the slopes of the tangents are equal. Hence from the $p = f(T)$ curves for two metals, and a knowlegde of its optimum conditions of the growth of needlelike crystals for one of them, we can predict the optimum growth conditions of whiskers for the second metal /30/.

A high degree of supersaturation is a condition for the growth of filamentary crystals from the gas phase. Under such conditions, the growth of screw dislocation steps can begin. In dislocations which are very distant from one another a growth cone is formed, and its edge begins to grow at the expense of the atoms used earlier for the growth of the base. Thus, from the apex of the screw dislocation, which functions as a vapor absorber for the given substance, a whisker grows. It is assumed that the whisker axis is a dislocation pair consisting of dislocations of opposite signs; for this reason it cannot always be observed /27/. With increasing temperature, the growth rate and diameter of the whiskers also increase.

Figure XIV. 10 shows an apparatus for growing whiskers from zinc, cadmium, silver, and cadmium sulfide during the condensation of these substances from the supersaturated vapor phase.

For work with zinc or cadmium, the vessels for crystal growth were made of Pyrex glass, and for work with silver or CdS from quartz glass. Before the vessel was sealed, gas was removed from it and the specimen. Furnaces 5 and 7 were tubular with a nichrome heater. Furnace 5 was open at both ends, and furnace 7 at one end. Chromel-alumel thermocouples were installed to control the furnace temperature.

At first the temperature in furnace 5 (T_2, was adjusted so that is was 250 degrees lower than the temperature in furnace 7 (T_1). The vessel was again put into the furnace and held there for about 30 min. The whiskers formed at the following furnace temperature (°C).

Material	T_1	T_2
Cd	330	250
CdS	810	800
Ag	940	850

Details on the preparation of filamentary crystals from triply distilled zinc are reported by Sears and Hudson /31/. When the whiskers were grown, the temperature of the bulk material was 418°C, and the ambient temperature of the growth finger was 430°C. A nitrogen stream flowing past the end of the needlelike crystal reduced its temperature to 415°C. The whisker length was 0.2 — 0.4 mm. When the nitrogen stream was interrupted, the crystals became fainter and then disappeared. Before the crystals vaporized, Brownian motion became stronger. The crystals vaporized at the rate of 10^{-8} cm/sec, which corresponded to a pressure difference of 10^{-6} mm Hg between the vapors of the whiskers and the zinc pressure in the vapor phase. Sears and Hudson concluded that the edges of the zinc whiskers serve as step sources.

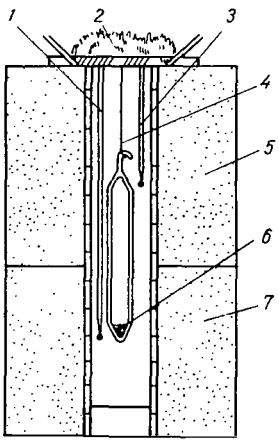

FIGURE XIV. 10. Diagram of apparatus for whisker growth in the vapor phase:

1, 3 — thermocouples; 2 — insulation; 4 — supporting wire; 5, 7 — furnaces; 6 — crystals.

Hauptman et al. /23/ report on the preparation of platinum whiskers obtained by vaporization of a platinum crucible. The following thermal conditions were applied: 1,350°C for 4 hr, 980°C for 10 days. The temperature gradient along the furnace axis was 50 — 80°C. The platinum fiber obtained has a $5 \times 10\mu$ cross section and 2 mm length.

Amonenko et al. /52/ obtained beryllium whiskers by vaporizing Be and then condensing its vapors in a column made of molybdenum sheet. Ribbon-shaped silicon whiskers $0.001 \times \times 0.1 \times (10 - 30)$ mm, can be grown from the vapor phase /53/.

Filamentary crystals can be obtained from several metals by electrolytic deposition. Iron, silver, and copper whiskers were deposited in this way /32, 33/. Tests on the electrolytic deposition of whiskers made it possible to obtain some theoretical ideas on the growth mechanism of whiskers during electrolysis.

Price et al. /34/ think that strongly adsorbed impurities hinder the steplike growth of whiskers if the distance between the impurities is comparable with the critical radius of curvature of the step. But if the impurity particles are very distant from one another, they no longer prevent whisker formation. During nucleation and growth of whiskers the impurity molecules are adsorbed at the lateral edges of the whiskers, and diffuse to the upper end. Therefore, the lateral edges do not grow, but the whiskers continue to grow at their ends. For steady crystal growth, a critical current density exists /35/ which is proportional to the diffusivity, concentration, and size of the impurities, and inversely proportional to the molecular concentration on the surface, whisker radius, size of the growth step, and surface of the atom of the deposited metal. At current densities less than the critical, the whiskers cease to grow. For the growth of whiskers, the condition of minimum metal ion concentration must be satisfied. This depends on the critical current density and also on the diffusivity of the metal ions.

Glazunova and Kudryavtsev /36/ studied the conditions of the spontaneous growth of filamentary tin crystals on electrolytic coatings. The authors

concluded that nucleation and subsequent growth of the whiskers is a special form of recrystallization of tin coatings.

We also know of a method for obtaining filaments and sharp points from alkali chlorides by controlled dissolution of crystals in aqueous solution. Single parallepiped crystals (3×3×10 mm) /37/ are immersed into an aqueous solution. By changing the depth of immersion of the crystals and the time of dissolution we can obtain either filaments of 10μ diameter and 1 cm length, or points with a tip radius of 1 — 5μ. Usually single crystals with a certain orientation are obtained. The thin threads are suitable for mechanical, electrical, and optical measurements.

Another method for obtaining filamentary crystals from alkali halides was described by Amelenckx / 38/. A slightly supersaturated salt solution is placed into cellophane containers and the surface becomes covered by crystalline whiskers after 24 hr. We also have data on the cultivation of whiskers of tungsten /54/, Al — Mg alloy /55/, and dendritic germanium crystals /56/. The so-called Fisher method, that is accelerated compression-induced growth of whiskers in solid phase, is of interest /39 — 41/. A steel plate (0.3 mm thick) is coated with a 5-μ electrolytic tin layer, and is then clamped between rigid steel plates. The edges of the specimens are ground and polished.

Because of the pressure applied to the steel plate, whiskers rapidly grow on the polished edges of the tin layer. An increase in temperature considerably accelerates the growth rate; the whiskers are as long as 5 mm when grown at 215°C. At this temperature and in an oxygen atmosphere the whiskers are thicker and longer than those grown at room temperatures. After the whiskers are removed from the surface, their growth begins again at the previous sites, which indicates some fixed whisker sources. In some cases, after the whiskers are removed, their growth sources become inactive for a certain time. When the initial sources are depeleted, the growth intensity can be rapidly restored by grinding off a thin surface layer of the metal. With increase in the thickness of the ground-off layer, the number of whiskers per unit area begins to increase, but at a depth of 20μ it is the same as in the freshly prepared specimen. Whiskers obtained in such a way are crystals of almost perfect structure. The whisker diameter is between 0.05 and 5μ. The whiskers usually consist of several parallel fibers with different cross-sectional shapes. It is assumed that the whiskers grow at the sites of action of the Frank-Read dislocation sources. Geometrically, the crystals are prisms traced by one of the inside petals of the dislocations. The growth of whiskers proceeds perpendicular to the surface because the diffusion of atoms is facilitated in the region of the Frank-Read source.

The force producing whisker growth in the solid phase is apparently the negative surface tension of the oxide film, according to Hardy /40/.

Besides Fisher's method, some other methods exist for growing whiskers in the solid phase. It was found that on the surface of many metal sheets (Fe, Cu, Ag, Au, Pt, Pb, Mg, W, brass, and others) filamentary crystals of 1 — 2μ diameter are formed /42/. The experiments were carried out with heating in air in a quartz tube. The temperature was between 200 and 700°C. The holding time was varied with a maximum of 2,500 hr. The chemical composition of the whiskers could not be accurately determined. Since the heating was performed in air, we can assume that oxide whiskers were formed. For this reason the study of the growth of filamentary crystals on heating noble metals is of special interest. Data

obtained on gold sheets showed no correlation between the growth rate and temperature, or maximum crystal size and the time necessary for considerable growth.

Sufficiently long metal whiskers can be obtained by periodic heating wire in vacuo when a current is passed through it. Iodide titanium wire was used as the test object /43/. The heating temperature was changed every 10 sec from 800 to 1,100°C. During this process, phase transition from a hexagonal close-packed structure below 400°C to a body-centered cubic structure above 900°C occurred 12 times per minute. Electromicrographs showed that periodic heating of the wire for about 30 hr leads to the formation of whiskers up to 100μ long. It is assumed that this is due to internal stresses which develop during the heating cycles.

The formation of metal whiskers was observed on electric component parts /44/, and when aluminum was ignited at 1,200 — 1,400°C with water vapor /45/. The hydrothermal growth of molybdenum whiskers was observed on the oxide base $MoO_3 - SiO_2$. The whiskers grew when small ampoules with a solid homogeneous mixture of MoO_3 and SiO_2 and water-filled capillaries were placed into a heated furnace.

The general growth conditions of filamentary crystals as a result of chemical reactions are reported by Morelock and Sears /47/. If several reactions are available to grow a given crystal phase, that reaction with the lowest entropy of reaction will allow the growth of near-perfect crystals at the largest temperature difference between source crystals and growing crystals.

Recently, because of the production of magnetic materials, the interest in filamentary iron crystals and their production methods has considerably increased. One of the known methods is as follows: copper in which the components are in the form of mixed crystals is subjected to strong deformation by rolling and drawing. In this case the iron inclusions become shaped as thin fibers, which can be separated by a solution which acts on copper only /48/.

Thin mechanical fibers can also be produced by chemical etching of wire until the required cross sections are reached /13/. For example, etching copper wire in HNO_3 gives fibers of a diameter less than 1μ. To obtain thin tungsten fibers, the method of electrolytical etching in an ac field can be employed. The etching agent is a 15 — 20% solution of sodium hydroxide /51/.

Methods for obtaining metal fibers in a maximum yield are very interesting in practical fiber metallurgy. Therefore, methods for extruding threads of diameter less than 1 mm are important. A method was recently introduced in fiber technology for producing filaments of electric bulbs /49/ The technological principle is as follows: fine disperse powder of metal or metal compound is transformed with a plasticizer into a doughlike plastic mass, which is then extruded through small holes. This filament is then subjected to various treatments depending on the type of plasticizer to eliminate side products and obtain a pure metal filament.

Depending on the type of plasticizer, we distinguish methods for applying organic matrices or inorganic matrices, the colloidal method and the method of metal amalgams. The following requirements must be borne in mind when selecting the matrices: complete elimination of the matrix after pressing, use in small amounts which impact a sufficient plasticity and strength to the mass and ensure slow hardening in air. These requirements are best satisfied by organic plasticizers.

In the first tests with tungsten extrusion, sugar, resin, collodion, or a solution of cotton in zinc chloride were used. In practice, a nitrocellulose

solution in amyl acetate with an admixture of castor oil, linseed oil, vaseline or wax was used, since the removal of carbon from the filament is easiest. The solution was mixed with fine tungsten powder in a weight ratio of 4 : 15. The mass was thoroughly ground and passed through special rolls to homogenize it. The homogenized mass was pressed on manual screw presses, or hydraulic presses in molds consisting of a matrix punch, and a diamond, with a hole in the mandrel. The extruded filament was placed onto a rocking mobile table of the press. The filaments were dried on thick cardboard sheets, and were then cut, and carbonized by heating in vacuo or in an inert gas atmosphere to make the filaments conductive. The carbonization process is terminated at 900°C, and is accompanied by partial dry distillation of organic compounds and conversion of their residues into carbon. In carbonization, the threads were placed in bundles into boats made of iron, nickel, copper, or quartz; the heating was carried out in tubular furnaces.

The next stage was the forming of the filaments to remove carbon, since its presence has a deletrious effect on the quality. The most widely applied method is oxidation of the carbon in the filaments under appropriate conditions. The process was carried out under a glass hood, through which hydrogen with admixtures of water vapor and nitrogen was blown. Each filament was heated to 1,100°C by passing an electric current. There are several ways of producing pure tungsten filament by pressing. All are characterized by the type of plasticizer applied. The plasticizer is chosen so that it can be removed either directly by dry distillation or by decomposition into pure tungsten metal and volatile gaseous compounds of other elements. Such plasticizers are solutions of camphor in alcohol, tungstic acid, and glycerol, compound $H_6W_2C_9O_3$, which decomposes $H_6W_2C_9O_3 = 3CO + C_6H_6 + W_2$. As a result of molding, the fiber length is reduced by 18 — 25%. In the final form tungsten filaments have a glossy metallic surface, but unlike drawn tungsten they remain brittle up to red heat.

In the extrusion of tungsten, inorganic plasticizers considerably shorten and simplify the technological process, because no carbon is in the mixture. The following inorganic plasticizers are being used: sulfur, sulfur compounds with ammonia or phosphorus, tungstic acid $H_2W_2O_{10}$, which forms a sticky mass with a small amount of water, and a concentrated solution of the ammonium salt of metatungstic acid $H_2W_4O_{13}$.

In the colloidal method, colloidal tungsten is used as the plasticizer. Pure tungsten metal is obtained from the plastic sticky mass of colloidal tungsten. After pressing and drying the threads are heated in vacuo. The process is terminated at white incandescence and accompanied by reduction in the length and diameter of the fibers. To increase the strength and plasticity of the filaments, oxides or hydroxides should be added to the colloidal mass together with colloidal tungsten nitrates. In this case, during thermal treatment a reducing gaseous phase must be present. The colloidal method is also applicable to other metals, for example, platinum, niobium, thorium, titanium, molybdenum, and osmium.

Together with the extrusion method for tungsten, another method, termed substitution method, was developed. The metallic filament is obtained by depositing the metal by electrolysis, or thermally, onto the surface of carbon filaments or platinum wire. After further ignition under appropriate conditions, such a thread is converted into one consisting of one of the

deposited metals. Substitution of tungsten from tungsten chlorides by direct heating with a current passing through the filament is much simpler but much less efficient than extrusion.

The production of molybdenum filaments by extrusion is similar to the production of tungsten filaments. However, unlike tungsten, pressed molybdenum is both flexible and soft. To obtain these properties the powder must be completely reduced and the threads thoroughly formed.

Three methods are available for extruding zirconium filaments. According to the first method finely dispersed zirconium hydride and zirconium carbide powders (50 : 45) are mixed with 5% of rhodium metal or rhodium oxide. Then, from this powder mixture a mass with an organic plasticizer is prepared, which is pressed into thin filaments. The pressed fibers are first calcined in vacuo up to 300°C, and then at a higher temperature in hydrogen or a hydrogen-hydrocarbon mixture. The principle of the second method is the utilization of a mixture of zirconium oxide and magnesium, reduced at a high temperature by hydrogen. The residue is ground and mixed with cellulose solution. After extrusion, the mixture is carbonized and formed in a hydrogen medium. According to the third method, a heated solution of zirconium nitrate is mixed with ammonium oxalate, and the gelatinlike zirconium oxalate is mixed with carbon to bind the oxygen during heating. Then, the mass is mixed with zirconium powder, pressed through thin holes, and the filaments obtained are sintered in hydrogen.

The production of boron and silicon fibers is based on the use of pure finely dispersed boron with a small amount of silicon. The filaments are extruded under high pressure. The matrix facilitates the pressing process, and because of the silicon which separates on decomposition, the strength of the filament material increases. Paraffin, nitrocellulose in a mixture with alcohol and ether, or cadmium amalgam can be used as plasticizers. The filaments must be formed until the carbon is completely removed. By using the colloidal method for boron and silicon, it is possible to obtain chemically pure filaments. The mass to be pressed is a pure colloid, or a mixture of the colloid and finely dispersed metal or metalloid.

The plasticizer in the production of titanium filaments is a casein solution in ammonia. A small amount of titanium nitrate is added to the mixture of the plasticizer with the titanium powder. After the filaments have been pressed and dried, they are calcined in vacuo at 1,200°C until all the carbon is removed. The final operation is calcination by passing an electric current through the filaments.

To obtain osmium filaments, the finely ground powder is mixed with sugar or another organic plasticizer and pressed through a diamond spinneret. The filaments are carbonized at high temperatures in a reducing medium. After oxidation and carbon removal, the filaments are sintered at the maximum permissible temperature. To obtain filaments of uniform length, the filaments are calcined again in a reducing medium with perosmic acid vapor. When an electric current passes through the filaments, the thinnest places are heated to a higher temperature. At these points osmium metal is deposited, and the cross section of the filaments become more uniform.

A method is known for producing iridium threads by pressing a mixture of iridium black with an appropriate plasticizer. Then the filaments are dried, and sintered by passing an electric current through them. The oxides are removed by ignition in hydrogen, and finally the filaments are decarbonized in air.

To obtain filaments by extrusion, not only pure metal powders but also metal oxides powders can be used. It is also possible to obtain filaments

from metallike compounds, such as carbides, and not only metal filaments. The general technology for the production of carbide filaments is as follows: three parts of carbide, either pure or with two parts of B, Mo or another high-melting metal, are ground into a fine powder and mixed with the plasticizer. The following plasticizers can be used: potassium or sodium water glass, paraffin, ceresine, turpentine oil, or cellulose solution. A small amount of graphite facilitates the process. After pressing and the other necessary operations, the filaments are formed in a hydrocarbon medium.

To obtain titanium carbide filaments, we can also use pure titanium with titanium acetate colloid, titanium oxide or titanium dioxide. A tragacanth solution is used as the plasticizer.

Metal filaments can also be produced without a plasticizer. For example, thorium and uranium fibers can be produced without plasticizers when a high high pressure (up to 20 t/cm^2) is applied.

We have mentioned above that the extruded tungsten filaments are brittle; this is explained by the coarse crystalline state. The problem of producing flexible filaments was solved by using the properties of alkaline earth and REE oxides to impart flexibility to filaments of high-melting metals. If the oxides of metals such as thorium or cerium are added in small amounts it is possible to obtain a flexible metallic filament which has all the properties of tungsten wire. To achieve uniform distribution of the parts of the mass, which is very important, a fine powder of tungsten trioxide is mixed with thorium nitrate or oxalate, and the mixture is heated on a water bath to complete dryness under continuous stirring. Then, the finely ground mass is heated to 300 — 400°C to decompose the thorium salts and to form thorium dioxide. The tungsten trioxide + thorium dioxide mixture is reduced by hydrogen. When the reduction is complete, the mixture should contain tungsten metal with 2 — 5% of thorium oxide. By mixing this powder with any organic plasticizer, we obtain a mass suitable for extrusion. The filaments are formed from the mass by conventional methods. The temperature of the final treatment is high and close to the melting point of tungsten.

The process for obtaining flexible tungsten filaments by this method can be explained in several ways. Some authors think that at the high molding temperature thorium oxide is reduced, and a thorium-tungsten alloy is formed. Another point of view is that thorium oxide acts as a catalyst in the reduction of the lower tungsten oxides which favor crystallization and increase the brittleness of tungsten. The second explanation is more plausible, since thorium metal with a melting point of 1,750°C would vaporize at the high temperature at which the Th — W alloy is formed by sintering.

The quality of filaments obtained by this method is so high that in some cases it exceeds the quality of drawn tungsten wire. The production of pressed flexible wires from tungsten is also possible by a method, analogous to the above, and known as the Pinch method /50/.

With this method we can obtain tungsten single crystals by powder metallurgy techniques. Finely dispersed tungsten powder (less than 0.5μ in diameter) is mixed with 0.75 — 2% of high-melting thorium oxide. Plasticizer is added until the mass forms a paste, which is then extruded as fibers. The fibers proceed continuously, surrounded by hydrogen, into a heated conical tungsten spiral. In the first temperature zone the fibers are dried; their porosity is 40%. In the second zone (temperature of 2,273 — 2,473 °K, that is 60% of the melting point expressed in °K) the

fibers are sintered. The fine and uniformly distributed thorium oxide particles inhibit the growth of tungsten grains until they enter the high-temperature zone.

Because recrystallization occurs during sintering, single crystal tungsten fibers are formed. The velocity of their passage through the thermal zones is 3 m/sec.

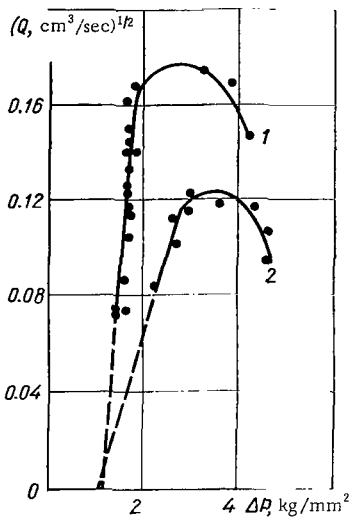

FIGURE XIV. 11. Output as a function of pressure in extrusion of fibers with degrees of squeezing 0.9993 (curve 1) and 0.9980 (curve 2).

During the last years, a detailed study was carried out on the production of metallic and nonmetallic fibers by extruding fine disperse powders with a plasticizer, followed by heat treatment. Some regularities could be revealed, which are interesting for the technologist. Kostornov et al. /57, 58/ show that in the first stage of fiber production, that is, extrusion, when the degree of squeezing is more than 98%, the output vs. pressure curve has a maximum. This means that the fibers must be extruded in a pressure range which includes the optimum pressure. Thus, in the extrusion of fibers from Cu, Ni, Fe, and some pseudoalloys, the maximum pressure is 2 — 3 kg/mm^2 (Figure XIV. 11) (at a yield point of the starting material of 4 kg/cm^2 and a plastic viscosity of 2,000 poise).

With increase in the degree of squeezing, that is, reduction of the hole diameter of the spinneret at a constant diameter of the matrix, the forces required to extrude the fibers grow exponentially, and are almost independent of the column height of the starting material in the mold. In practice, the forces are seldom higher than 1,000 kg.

If the plasticizer is correctly chosen (usually organic compounds), and its content in the starting material is optimum (up to 3 wt%), continuous filaments are obtained after extrusion which are readily wound on a reel.

The extruded fibers are sintered at comparatively high temperatures. For given fiber diameters, with values below the critical at the given temperature, the theoretical density can be obtained /59/.

Such fibers have a maximum strength, corresponding to cast material.

The range of nonmetallic fibers and the technological layouts for their production in both the discrete state (fiber mass) and as continuous filaments is fairly wide. Many of these fibers are produced on an industrial or semi-industrial scale, and others in the laboratory only. The high thermal and chemical stability in various gaseous and liquid corrosive media are fundamental properties, which make these fibers irreplaceable in refractory composites.

We shall now discuss existing methods for producing nonmetallic fibers.

Quartz fibers were first produced as early as 1838. At present, we know of sufficiently efficient schemes for producing woollike and continuous fibers from thin fused quartz rods by drawing. The layout of one of the continuous production processes is shown in Figure XIV. 12 /6/. Twenty quartz rods (diameter 6 — 7 mm) are fixed by clamps onto a

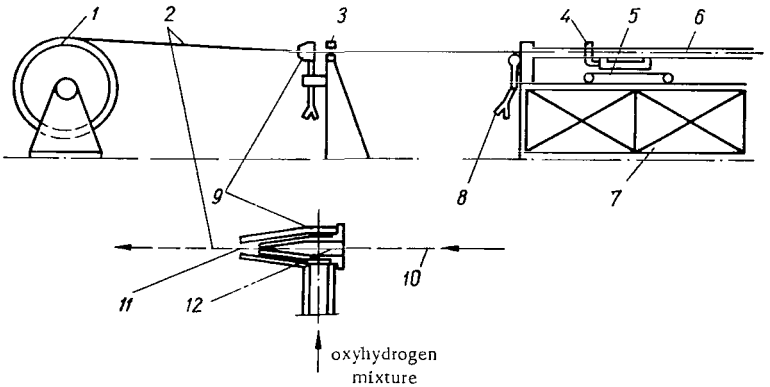

FIGURE XIV. 12. Flow sheet for the production of wool from quartz fibers:

1 – sieve drum; 2 – fibers of 4 – 10μ diameter; 3 – graphite guiding blocks with holes; 4 – clamps of carrier; 5 – carrier with chain drive; 6 – rods of 6 – 7 mm diameter; 7 – stand; 8 – burners; 9 – axial oxyhydrogen burner; 10 – fibers of 0.1 – 0.3 mm diameter; 11 – hole of 1.6 mm diameter; 12 – hole of 3 mm diameter.

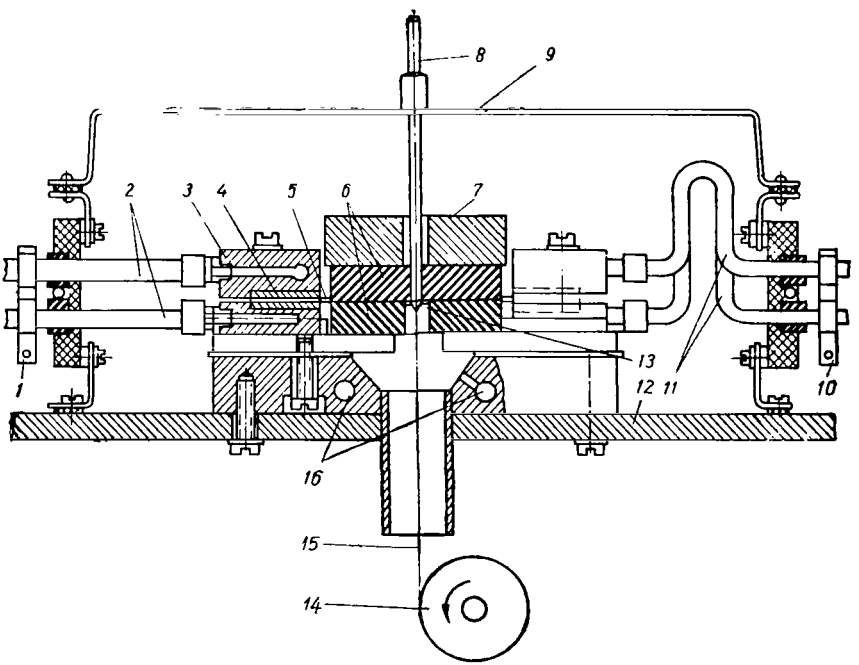

FIGURE XIV. 13. Apparatus for quartz fiber production.

carrier moved by motor along a sliding block. Each rod passes through the graphite block above a vertical oxyhydrogen burner so that the rod diameter is reduced to 0.2 mm. Then, the rods pass through another graphite block with 20 holes, placed in front of 20 axial oxyhydrogen burners. The rods are drawn out into short fibers, which are collected on a rotating drum.

A German patent /61/ discusses a method for producing wool from fused quartz. A gas jet is placed with the quartz into a chamber open at its front. The jet consists of an inert gas, at a temperature above the melting point of the quartz. The gas is supplied at a pressure of 1.4 — 1.9 atm. The quartz passing through the chamber is fused by the hot rapid stream, and is converted into fibers with a diameter between 2.5 and 40μ.

Ducati /136/ describes a very efficient method for obtaining fine fibers from vitreous high-melting materials. The melt is placed onto a conical vessel, narrowing at the bottom, which is made of refractory material and rotates around its vertical axis. The melt flows from this vessel as a thin stream into a chamber. Here, by combining an electric arc with a very rapid stream of compressed gas, a plasma jet is produced with a temperature of several thousand degrees. In the chamber very thin fibers are continuously formed, and fall into a receiver. The plasma jet can also be employed for producing fibers directly from thin rods or powder.

Recently, very thin continuous quartz fibers of uniform thickness have become popular. Such fibers are obtained as filaments by drawing them very rapidly from the softened end of quartz rods 0.2 — 2.0 mm thick, which are fed slowly at a uniform rate into a hydrogen or gas flame. The filaments are reeled onto drums with a polished surface /62/.

Figure XIV. 13 shows an apparatus with which it is possible to produce quartz fibers from both rods and powder mixtures /63/. In this apparatus a tungsten tape 5, covered by zirconium oxide is heated by an electric current fed through buses 2, 11 and terminals 1, 10. The tungsten tape is soldered into copper bushing 4 which is fastened between parts of block 3 by screws, and has a spinneret hole 13. To protect the tungsten against oxidation, the apparatus is placed into shell 9, fixed on plate 12. The block is thermally isolated by kieselguhr. Silica rod 8 is fed into the upper part of shell 9 through heat isolation layer 7. Rotating drum 14 designed for drawing the fibers 15 is placed underneath plate 13. Nitrogen is fed into channels 16, and thus the spinneret hole in tungsten tape 5 is surrounded by inert gas. As the tungsten tape is heated to 1,900°C, the end of the quartz rod resting in spinneret hole 13 begins to fuse. Drops of melt pass through the hole and are drawn into fibers by means of drum 14, over which the fibers are wound. The fiber thickness dpeneds on the drop temperature and size, and on the speed of the drum. If quartz powder is used instead of quartz rods, the powder is placed onto the tape. Several spinneret holes are bored into the tungsten tape to obtain a strand. The typical percent composition of quartz fibers is given below.

SiO_2	99.97	Fe_2O_3	0.0010
Al_2O_3	0.0150	K_2O	0.0007
CaO	0.0032	Li_2O	0.0003
Na_2O	0.0022	TiO_2	< 0.0001

To produce filaments and wool of high melting fibers from a mixture containing silica, the following apparatus can be used (Figure XIV. 14) / 64—66/.

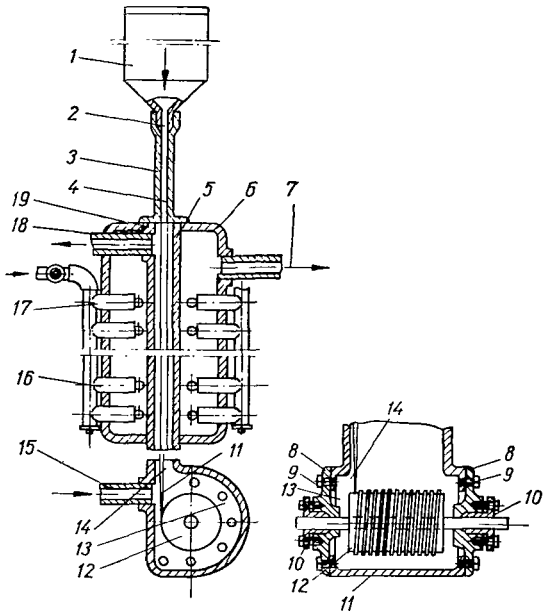

FIGURE XIV. 14. Diagram of apparatus for quartz fiber production.

First, a continuous rod is formed from the ground vitreous material in bin 1 by extrusion through hole 2. The rod passes through guiding tube 3 into reactor 19 fitted with muffle furnace 5 and burners 16 and 17. In the lower part of reactor 19 are placed chamber 13 with reel 12. Chamber 13 is closed by plate 8 fixed by screws 9 to its front. Reel 12 is mounted in chamber 13 on a shaft with stuffing box 10. Both sides of reactor 19 have inlet holes 15 and outlet holes 18. Tube 7 serves to remove the gases from furnace 6. After mass 4 is formed, it is sintered in reactor 19 into a strong block, which then enters the melting zone. By means of the tensile forces produced by reel 12 and its own weight, the thickness of the fused rod 4 is reduced. During its passage from reactor 19 into melting vessel 14 filament 11 is quickly cooled before being wound.

The quartz rods and filaments from them can be obtained in both induction furnaces and resistance furnaces. When the latter operate with protective gas and deflecting shields, better results are obtained. But the capacity of existing equipment limits the yield, and therefore not more than five filaments produced at present consist of 200 fibers with a diameter of 10μ. They contain 2 wt% of organic components, which can easily be removed by heat treatment at 340°C.

Recently, methods have been developed for applying metal coatings onto quartz fibers by decomposition in the gas phase /67, 68/, or by drawing the fibers issuing from the spinneret through a melt /69, 70/. These fibers have a high strength.

One of the most popular high-silica fibers (96 — 99% of SiO_2) produced in the USA and England during the last 20 years is the Refrasil fiber.

Such fibers (diameter 0.8 — 12μ) are obtained by treating glass fibers with acids (but not H_3PO_4 or HF), followed by dehydration. To reduce contraction and embrittlement which occurs during the process, the fibers are coated by an acidproof water-impermeable compound which does not hinder infiltration of the acid. For this purpose a dispersion of phenol-formaldehyde or phenol-furfural resin in water, or a solution of these resins in organic solvents, are used. After impregnation of the fiber mass by the resin, it is possible before leaching to use coatings of acid-resistant porous material which are permeable to acids. An example of such a material is borosilicate glass fabric, with a high content of lime and a low content of alumina. Before dehydration, the protective porous material is removed. Different acids can be used for leaching, but when treating glass fibers with a high lime content it is best to use hydrochloric or nitric acid, since H_2SO_4 forms insoluble calcium salts which retard the leaching process and complicate subsequent washing.

After the fibers are washed, they are heated at temperatures below their softening or melting points to dehydrate them. The temperatures applied are about 820°C.

If the ratio of silica to metal oxides is higher than 9 : 1, the fibers have sufficient strength to be processed into a fabric, which is then dehydrated.

Refrasil fiber is also obtained by leaching close-packed glass fibers by passing through them dilute acid until the silica-to-metal oxide ratio is 9 : 1 /71/.

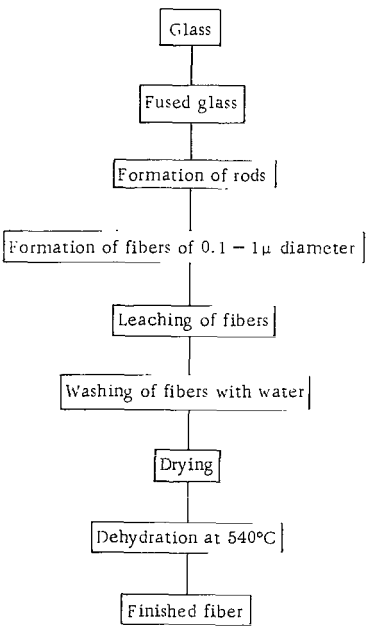

FIGURE XIV. 15. Scheme for producing fibers with high silica content.

The technology for obtaining high-silica fibers has numerous variations. Thin fibers (diameter 1μ or less) of sodium silicate glass (74.5% of SiO_2, 25% of Na_2O, and 0.5% of P_2O_5; or 78.2% of SiO_2, and 21.8% of Na_2O) are obtained as follows: the glass is melted and drawn into thin fibers, which after treatment in a hot gas stream (50 — 610 m/sec, 1,650 — 1,820°C) are leached. The leaching process is performed on a sieve immediately after, or not later than 48 hr after treatment by the hot gas, since long-term storage of the fibers lowers their strength.

The fibers are leached by hot water, solutions of mineral acids, a 5% solution of $CaCl_2$ /72/, or by NH_4Cl solution with a small amount of H_2PtCl_6 added /73/.

In the production of fibers with a high SiO_2 level, autoclave technology can successfully be employed. For example, from a glass mass containing, in wt%: 55 — 58 silicic acid, 15 — 30 boric acid, 3 — 12 alkali metal oxides, 0.5 — 3 alumina, 0 — 1 zirconium, titanium and barium oxides, fibers can be formed at a temperature of 800 — 1,100°C. After heat or heat cum chemical treatment in the autoclave, these fibers contain 98 — 99% of silica (all the other oxides are washed out). The properties of the fibers are not inferior to those of quartz glass /74/.

In the early fifties, one modification of high-silica fibers termed Microquartz (average fiber diameter 1μ) was first produced on an industrial scale in the United States.

The production of high-silica fibers can be represented by the scheme shown in Figure XIV.15.

Fibers which are now produced on an industrial scale include aluminum silicate termed Fiberfrax, Kaowool, and Kionite J-M. These refractory fibers are obtained from fused silica-alumina mixtures with small amounts of modifiers (such as boron glass). A compressed air stream (5.6 kg/cm^2) is blown onto a molten metal jet perpendicular to the jet direction. The fibers obtained in this way are collected on a screen, and cleaned from nonfibrous formations. The following initial mixture is recommended, wt% /75, 76/.

White aluminum ore with 98.9% of Al_2O_3	50
Silicon compounds (SiO_2)	50
Boron glass (sodium borate $Na_2B_4O_7$)	1.50

If modified fibers are to be produced, titanium slag is used instead of Al_2O_3, in the same amount. The purified fibers have the following composition, wt%:

SiO_2	46.99	B_2O_3	1.28
Al_2O_3	43.19	Fe_2O_3	0.56
TiO_2	7.55	Na_2O_3	0.43

If we have to produce long fibers with a comparatively low amount of nonfibrous formations, a jet of the melt is sprayed by the surface of a rapidly rotating disk (diameter 300 mm, speed 4,200 rpm). This method was originally developed for the production of metal fibers (see above). The most convenient composition of the mixtures is as follows, parts by wt%:

White aluminum ore A-1	42.75
White quartz sand	49.75
Zirconia	7.5

The fibers obtained have a diameter of about 4μ, and their chemical composition is as follows:

Al_2O_3	42.75
SiO_2	52.25
ZrO_2	5.0

Pure kaolin ($Al_2O_3 \cdot 2\,SiO_2 \cdot 2\,H_2O$) is the raw material for Kaowool. To prevent contamination by other refractory compounds, the melt is kept in unmelted kaolin before the fibers are produced. After spraying fibers of 3μ diameter and a maximum length of 200 mm are obtained on the conveyer in the form of a homogeneous mass. The composition of the mass, (wt%), is as follows /77/:

Al_2O_3	45.1	MgO	Traces
SiO_2	51.9	CaO	0.1
Fe_2O_3	1.3	Na_2O	0.2
TiO_2	1.7	B_2O_3	0.08

Research on the production of continuous kaolin fibers has been successful.

In the production of Kionite fibers, a mixture of natural minerals consisting of 100 parts of kionite ($Al_2O_3 \cdot SiO_2$) and 10 parts of SiO_2 is used. With such a mixture composition, a high yield of relatively long flexible fibers of 1 — 5 μ diameter are obtained /78/. For forming long fibers, we use an apparatus consisting of several rotating disks, and the centrifugal force produced converts the melt into thin fibers (Figure XIV. 16). The composition of the fibers is as follows, wt%:

Al_2O_3	42	TiO_2	6
SiO_2	50	Other components	2

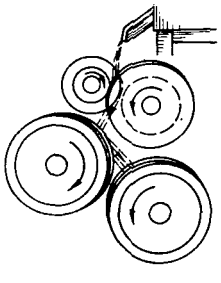

FIGURE XIV. 16. Diagram of apparatus for Kionite production by the centrifugal method.

The nonfibrous inclusions formed during production are removed by screening (short-fiber mass) or by a specially developed method (long-fiber mass) based on the effect of the impact of the fibers supplied by a rapid liquid stream onto a partition /79/.

Mullite ($3\,Al_2O_3 \cdot 2\,SiO_2$) is the only chemically stable compound in the $Al_2O_3 - SiO_2$ system; it melts congruently at 1,910°C. Its high melting point, chemical inertness, dielectric parameters, mechanical strength, and the absence of polymorphous transitions, make mullite a very valuable material in modern engineering. However, in spite of the fact that there are published papers on the preparation of mullite single crystals, the synthesis of mullite is still in the experimental stage.

All existing methods for preparing filamentary mullite single crystal have the same drawback, namely, the mullite yield is very low. Also, costly equipment and materials are required.

At the Institute of Plastic Materials of the Ukrainian Academy of Sciences, a method for producting filamentary mullite single crystals has been

developed. The yield is high and the technology simple. Filamentary mullite single crystals are obtained from fluorine-containing aluminum silicate melts, and the product is subsequently leached with HF.

The problem of producing filamentary mullite single crystals was solved in two stages. The first stage involved determination of the melt composition and crystallization conditions to ensure uniform distribution of mullite single crystals in the glass. In the second stage methods for separating the filamentary single crystals from the crystallized ingot were explored.

Published data on the crystallization of mullite showed that the mineral crystallizes from a melt with a composition close to the stoichiometric ($3\,Al_2O_3 \cdot 2\,SiO_2$). The melt must be cooled rapidly and held for a long time at low temperatures to prevent crack formation. Under such conditions a concretion of large mullite crystals (diameter up to 2 mm, length up to 7 mm) of prismatic form is obtained.

Crystallization of needlelike mullite from the melt is possible when the required number of crystallization sites are formed at which the filamentary single crystals are later grown.

The following compositions were taken as the raw material

$$2\,NaF \cdot 2\,B_2O_3 \cdot 15\,Al_2O_3 \cdot 18\,SiO_2;$$
$$2\,LiF \cdot 2\,B_2O_3 \cdot 15\,Al_2O_3 \cdot 18\,SiO_2.$$

These compositions were selected because they ensure the required crystallization of mullite in thin fibers; fluorine compounds accelerate the crystallization process, but the presence of borosilicate glass in the melt decreases the melting point without appreciably impairing the viscosity.

The raw materials for the corresponding charges were chemically pure reagents. The components were calcined at 400 — 800°C, weighed, introduced into the charge, and thoroughly mixed. The charge was fused in electrographite crucibles which are stable to corrosion by the fluosilicate melts.

The charges were fused and the melts crystallized in a high-temperature furnace with a graphite heater in an inert gas (A or N) (to present intense oxidation of the heater) under the following conditions: maximum possible rate of heating the charge to a temperature 70 — 80°C above the melting point of the charge; holding at this temperature for 45 — 70 min; and crystallization of the melt with rapid cooling in air.

The size of the mullite crystals depends on the cooling conditions of the melt: slow cooling leads to the formation of isometric crystals, and rapid cooling to the formation of needlelike mullite crystals. A rate of decrease in temperature of 32 — 35 deg/sec is the optimum. Under these cooling conditions the filamentary mullite crystals have a length of 250 — 1,000μ and a diameter of 0.3 — 1μ, that is, the length-to-diameter ratio is close to 1,000.

The studies showed that the first composition with NaF as the mineralizer is preferable for the following reasons: a) it is cheaper; b) it does not contain lithium salts, which are scarce; and c) the mullite obtained is of better quality. When mullite is crystallized from the composition containing LiF, up to 3 wt% of Li_2O is found in the final product.

To dissolve the vitreous phase between the mullite crystals which combines the crystals into a monolithic cast, hydrofluoric acid was used. The ground cast (particle size 0.75 — 4 mm) was treated with 18% HF. The vitreous phase dissolved completely in this acid in 3 — 4 days when the

particle size was 1.5 — 2.5 mm, and the dissolution proceeded without mixing. With mixing the rate of dissolution increases, but the mullite needles may be destroyed.

The fluorides formed are converted into soluble sulfites by treatment at 70 — 80°C for 1 — 1.5 hr with H_2SO_4 (specific gravity 1.84), diluted in 10 volumes of distilled water. The filamentary crystals are then filtered. During filtering they are washed with water at 70 — 80°C.

To discover the potentialities of mullite and some patterns of behavior of the filamentary crystals (at high temperature, under load, and in some corrosive media), the structure and some properties of mullite were studied.

The main properties of filamentary mullite single crystals are shown in Table XIV. 2, and also the properties of ordinary cast mullite.

TABLE XIV. 2. Properties of filamentary mullite single crystals

Property	Cast mullite (published data)	Filamentary mullite single crystals
Refractive indices:		
N_g	1.654	1.654
N_p	1.642	1.642
Birefringence	—	0.008
Angle $2v$	45 — 50°	52°
Lattice constants, Å:		
a	7.55	7.55
b	7.69	7.69
c	5.77	5.77
Crystal size, μ:		
length	up to 7,000	350 — 1,000
width	up to 20	3
Density, g/cm^3	3.05	3.10
Melting point, °C	1820	1,900 ± 20
Ultimate tensile strength, kg/mm^2	up to 10.5	up to 170.0

The behavior of filamentary mullite single crystals at high temperature in air or in vacuo is of special interest. It was found that mullite crystals do not change their structure when heat-treated in air up to 1,800°C. Heat treatment in vacuo (10^{-3} mm Hg) causes mullite to decompose at temperatures above 1,300°C; α-Al_2O_3 is formed, which retains its elongated form up to 1,400°C. Above this temperature α-Al_2O_3 loses its needlelike form and is converted into isometric corundum crystals.

The methods for producing ceramic, and in particular quartz fibers /64 — 66/ discussed above are based on the utilization of the heat released by exothermal reactions of the metals present in the initial mixture. Fibers can be obtained in this way from 44 parts by weight of SiO_2 and 29.6 parts by weight of Al powder. During combustion of this mixture a mass is formed with 56 wt % of Al_2O_3 and 44 wt % of SiO_2. The high-melting fibers are produced from this by the scheme shown in Figure XIV. 15. From a mixture of BaO, Mg, and Al, a three-component system BaO : Al_2O_3 : 2 SiO_2 can be obtained for the production of continuous aluminosilicate fibers. The high alumina content relative to the SiO_2 content will determine the refractoriness.

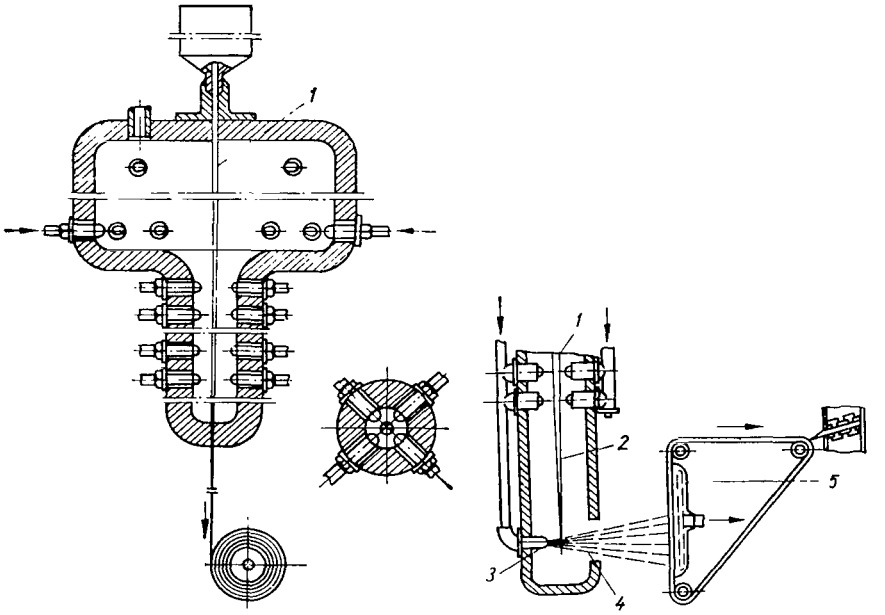

FIGURE XIV. 17. Schematic diagram showing the production of the composition from aluminosilicate fibers.

Bauxites and various boron-containing ores can be used as raw materials for fibers. For example, from a mixture of bauxite with ferric oxide and quartz, fibers with 23.8; 33.6; 44.6; 52.4; and 59% of SiO_2 can be obtained /80/. In this process the mixture is treated with a steam jet at a pressure of 8 atm. Fiber formation proceeds well at a $3\,Al_2O_3 : 2\,SiO_2$ ratio.

Good fibers were also obtained from a mixture of calcined bauxite (56.7%), calcined kaolin lumps (32%), and raw kaolin (20.3% in the air-dry state) /81/. The composition of the fibers, in %, is given below:

Al_2O_3	68.7	Fe_2O_3	2.1
SiO_2	26.5	TiO_2	2.7

The waste after enrichment of boron-containing ores can be used for the production of high-quality mineral fibers of the following composition (%):

SiO_2	42	MgO	11
CaO + FeO	28	$Al_2O_3 + B_2O_3$	15
		Other oxides	4

When the raw material is fused, limestone, dolomite, and coke are added /82/. The melt is processed into a fiber mass in the apparatus shown in Figure XIV. 17. Fiber 2 obtained from rod 1 by the action of a gas stream from nozzle 2 falls through hole 4 onto the screen conveyer of vacuum apparatus 5.

There are other methods besides the above. The melt can be fed in a pulsating steam or air jet, passed through a melt of metal wire, which directs the extruded molten mass and at the same time participates in the

exothermal reaction with excess oxygen to form an additional fiber component. In the industrial processes for fiber production potassium titanate fiber is marketed under the name Tipersul (the approximate composition of the material is $K_2Ti_6O_{13}$). The mean diameter of these fibers is about 1μ, and their length is about 0.2 mm. But under favorable conditions the fibers may be as long as 20 — 30 mm. It is assumed that the fibers have a laminated structure, and each layer consists of crystals with diameters of 0.1μ or less (Figure XIV. 18). Tipersul fibers are formed into articles without difficulty, and no matrix is necessary.

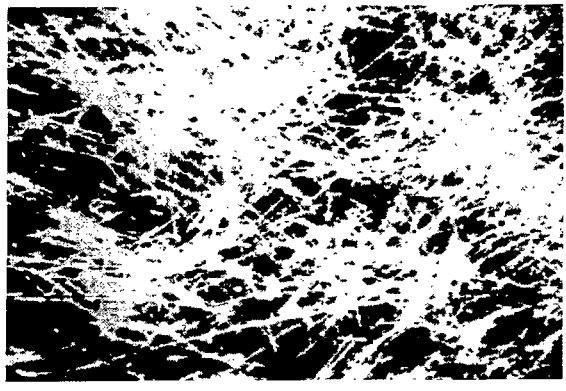

FIGURE XIV. 18. Potassium titanate fibers (Tipersul).

The production of highly refractory fibers has been successful. Some of these fibers are already being produced on a semi-industrial scale. They include polycrystalline oxide fibers obtained by vaporization and the continuous method, and by some other processes.

The production of fibers from oxides involves considerable difficulties. When the material is deposited on a hot wire, the wire must be made of a material which can be removed from the fibers after separation of the oxide. When the melt is drawn through the spinnerets, the material of the apparatus must withstand temperatures of 2,050 — 2,100°C, and must not react with the oxide.

The preparation of fibers by the vaporization of colloidal solutions is based on rapid drying of stabilized suspensions. Such fibers are then subjected to heat treatment to increase their strength and heat resistance. In this way, ZrO_2 fibers have been produced. The optimum conditions for the process are as follows: the ZrO_2 level in the suspension must be 5 wt%, and the pH of the suspension 3 — 5. Deviations from these values in either direction lead to deterioration in the fiber quality and yield. The fibers are ribbonlike; their length is between 6.35 and 50.8 mm, and their width 3.17 mm or less.

To stabilize the bulky ZrO_2 structure, calcium acetate or small amounts of MgO, SiO_2, BaO, TiO_2, and Cr_2O_3 are introduced into the suspension. The best stabilizer is CaO added in an amount of 5%. Figure XIV. 19, a

shows the appearance of ZrO_2 fibers produced by the above method. Fibers of SiO_2, ZrO_2+SiO_2 and $Al_2O_3+ThO_2$ can be produced by vaporizing colloidal solutions /83/.

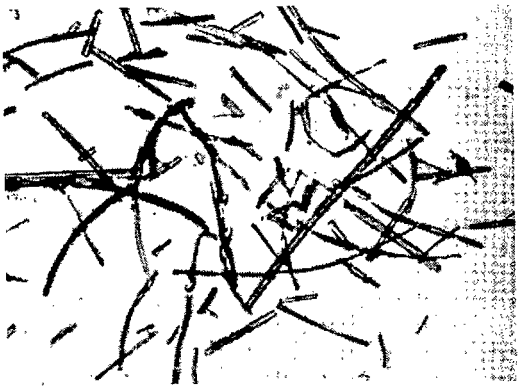

a

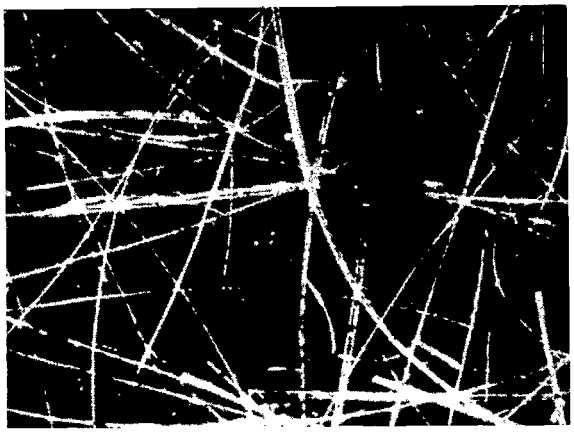

b

FIGURE XIV. 19. Fibers from zirconium dioxide obtained by vaporization of a colloidal solution (a) (× 400) and by the NITKO method (b) (× 40).

The production of fibers from colloidal solutions can be illustrated by the following examples. The main stages are /134/: mixing solutions of the initial components, application of a 10 — 50μ liquid layer onto a glass support, rapid heating to 100 —150°C, removal of the inorganic fibers formed by cracking of the film, and two heat treatments (at 500 — 600°C to remove the organic matter and at 900 — 1,500°C for 1 hr). The fibers are 25 — 203 mm long, and have a rectangular $(0.1-1.5)\cdot(2-30)\,\mu$ cross

section. They contain 5 — 15 wt% of SiO_2 and 45 — 85 wt% of the oxide of one of the following metals: Al, Sr, Hf, Th, Fe, Co, Mn, Ni, V, or REE. The oxides are introduced as salts of strong mineral or organic acids, with dissociation constants not lower than $1.5 \cdot 10^{-5}$. The oxide can also be added as a halogen derivative. The pH of the medium must be between 1 and 2, and is adjusted by adding HCl, HNO_3 or their salts. The addition of a sol of SiO_2 accelerates the formation of fibers and gives them a higher tensile strength and flexibility. For example, Wainer and Mayer /135/ dissolved 385 g of zirconium oxychloride octahydrate in 1,000 ml of water. When dissolution was complete, the solution was filtered, and 75 g of anhydrous Na_2CO_3 were added with continuous stirring. Then, 20 g of Na_2CO_3 were dissolved in 1,400 ml of water. The solution was added to the slightly alkaline ZrO_2 solution with vigorous stirring. The pH of the solution was 2.75. The solution was applied onto a Pyrex plate in a 10μ layer. The plates with the film were dried in ovens at 90°C. The dried film was a gel from which fibers started to form. The fibers were scraped off the glass plate and placed into a furnace at 150°C for 1 hr. The furnace temperature was increased at the rate of 200 deg/hr to 600°C. After a holding time of 1 hr at this temperature the fibers were removed from the furnace and cooled to about 20°C. The fibers were washed until completely free of chlorides. The washed fibers were dried at 150°C. During this process they turned completely opaque and remained sufficiently flexible. The fibers were placed into a furnace, and the temperature was increased to 1,400°C within 2 hr. The holding time was 1 hr at this temperature. After this heat treatment the fibers became completely transparent and contracted by 50%. The fiber structure was monoclinic. The length of the fibers was 2.5 — 152 mm, their width 5 — 25μ, and their thickness 0.2 — 1.5μ,

It was shown in /84/ that continuous ZrO_2 and Al_2O_3 fibers can be obtained from rods of the corresponding metal oxides when they are rotated at a high speed in the heating zone of a reverbatory furnace.

Circular polycrystalline fibers (diameter less than 25μ) can be obtained from various oxides by the NITKO process; no detailed description of this has so far been published. Figure XIV.19, b shows fibers made of zirconium dioxide by this process.

Polycrystalline fibers can also be obtained from molybdenum oxide by subliming the vapors formed on heating molybdenum wire to 500 — 550°C on a cold electrode. The potential difference between the wire and the brass electrode must be up to 4,000 V. If the voltage is low, molybdenum oxide is deposited as a uniform spongy layer. With increase in the voltage of the electric field the filament-forming process predominates. After the required fiber length is reached, the ends of the crystals are cut off. If the polarity of the field is reversed the fibers are completely destroyed /85/.

A method is being developed for producing polycrystalline refractory fibers. The method is based on the dispersion of finely ground inorganic material in an organic film-forming medium applied in a 127μ layer onto a glass plate. When the film is dry it immediately separates into fine fibers, which are calcined, and are then suitable for use /84/.

Several methods are known for producing alumina fibers. A method is described in which an alumina-thermoplastic mixture is drawn /133/. The mixture is subsequently heated, and during this process the plasticizer is volatilized and the alumina sintered. However, these threads are very short.

Fibers can also be produced from silicates with a high alumina content. In this case silica is reduced to Si, which is removed by vacuum evaporation. The filament formed is strengthened by sintering /133/.

Al_2O_3 fibers are also produced by the Taylor method. Instead of the metal, small alumina rods are placed into the capillary, and then fibers of 1μ diameter are obtained with the conventional equipment used in this method. The alumina melts in the heating zone (like the metal) and glass-coated filaments are produced.

It was found that because of the short heating period, there is little chemical reaction between Al_2O_3 and SiO_2. If the filament is heated after the quartz coatings have dissolved, weak lines of mullite are seen on the X-ray patterns.

Large amounts of Al_2O_3 can be obtained by this method. Such fibers are suitable for reinforcing metals and ceramics, and also for the production of the new high-temperature materials.

In one of the methods for producing alumina fibers the vapors of stable aluminum suboxide are sublimated; the suboxide is obtained when very pure aluminum melts are heated in moist hydrogen. The moisture in the hydrogen is a very important factor in fiber formation; this is illustrated in the data of Table XIV.3.

FIGURE XIV.3. Effect of the dew point on the growth of alumina fibers in hydrogen at 1,230°C

Duration of process, hr	Character of fleece	Character of whiskers	Dew point, °C
4	No fleece	No whiskers	+21
4	" "	" "	— 2
4	" "	" "	—25
4	Thickness, 3 mm	" "	—34
4	Thick	Whiskers appear	—43
9*	Dense	Dense	—59

* Excess time.

In the initial stage of the process a flexible fleece is formed. It consists of fibers of 1 — 7μ in diameter and up to 76 mm long. Long-term heating and high temperature increase the growth rate of the fibers, which are obtained as whiskers. The diameter of these whiskers is 80μ, and their length is up to 25 mm. The fibers are brittle.

The optimum temperature for the growth of fibers is 1,370°C for pure aluminum melt, and 1,510°C for aluminum-titanium melt.

To initiate fiber formation or to reduce the process temperature, small amounts of Ti, Cr, Si, Si compounds, or zirconium are added. The effect of these additives on the growth rate of the fibers is shown in Table XIV.4 /86/.

Needlelike TiO_2 can be obtained by oxidizing K_2TiCl_6 during crystallization in borate and cryolite, or by pseudoamorphous rearrangement of potassium hexatitanate fibers /87 — 90/.

Fibers with a diameter of less than 5μ and length of 0.2 — 5 mm or more can be obtained by acting on $TiCl_4$, $TiBr_4$, or TiI_4, with dry oxygen in the presence of the titanium halide melt, at a temperature of 600 — 800°C.

TABLE XIV.4. Effect of additives on the rate of formation of fibers

Starting material	Temperature of process, °C	Total fiber yield, mg	Rate of growth of fibers, mg/hr
Al	1,370	60	15
80 mole % of Al + 20 mole % of Ti	1,370	464	116
80 mole % of Al + 20 mole % of Ti	1,500	268	168
80 mole % of Al + 20 mole % of Cr	1,370	197	197
80 g of Al + 183 g of Si	1,500	354	177
80 mole % of Al + 20 mole % of Zr	1,500	185	61.6

The following process for producing TiO_2 fibers is described in the literature.* Dry air was passed through $TiCl_4$ at the rate of 30 cm^3/min. A mixture consisting of 12.3 g of KCl and 7.9 g of NaCl was placed into a quartz boat. The air — $TiCl_4$ mixture was added to the boat with the molten NaCl and KCl at a temperature of 650 — 675°C. The expenditure of $TiCl_4$ was 4.8 g in 208 hr. The mixture was cooled and extracted by water, and TiO_2 fibers were obtained with a diameter less than 5μ and a length of about 3 mm. X-ray analysis showed that the fibers are the crystalline modification of TiO_2, anatase. Of the candidate methods for fiber production, the technological processes for continuous fibers made from aggregated magnesium oxide are interesting. MgO is present in disperse phase in the system $Mg(CH_3COO)_2 - CH_3OH - H_2O$ /91/. The production of high-strength boron fibers of 100μ diameter and 210 m length /92, 93/ is worth noting.

Fibers from elemental boron are obtained by condensing boron halide vapors which have been reduced by hydrogen on incandescent tungsten wires. The reaction is as follows

$$BCl_3 + \tfrac{3}{2}H_2 \rightarrow B + 3HCl.$$

The boron layer (thickness up to 40μ) is continuously deposited on tungsten wire of 10 — 15μ diameter. Thus, two-layer fibers are obtained, in which the tungsten core is surrounded by a boron envelope. The strength of such fibers is high because they are tungsten reinforced. Because of the high temperature, tungsten boride is formed at a fairly high rate.

Fibers made of aggregated MgO are better than fibers obtained from MgO powder.

Silicon carbide fibers can be obtained by the thermal decomposition of gaseous compounds on the surface of a hot wire, as in the case of tungsten boride. For example, methyltrichlorosilane is decomposed as follows: $CH_3SiCl_3 \rightarrow SiC + 3HCl$.

SiC fibers can also be obtained by the reaction between $SiCl_4$ and any carbon-containing substance (for example, toluene or methane). SiC fibers can be prepared by reducing quartz with carbon, or by the action between silicon vapor and carbon vapor. Pultz /128/ describes the following method for preparing fibers of β-silicon carbide. A refractory boat containing a mixture of quartz sand and charcoal is placed into a ceramic tubular furnace with a temperature gradient supplied by a platinum heater. The molar ratio of the components is between 1:1 and 1:3.5. The furnace is heated to 1,770°C and exhausted. Then ammonia or a gaseous $N_2 + H_2$ mixture is introduced under pressure. The furnace temperature is reduced to 1,375 — 1,550°C, and the reaction mixture is held at this temperature for 3 — 12 hr.

* [No reference reported.]

When cool, the boat is removed from the furnace; the fibers obtained are light green to dark green. The crystal length is 25.4 mm, the length of individual fibers is up to 76 mm, and the fiber diameter is $2 - 4\mu$. X-ray analysis showed that the fibers consist of β-SiC.

Walworth /137/ describes the production of titanium carbide fibers. TiO_2 and colloidal carbon are placed into an alumina boat. The boat with contents is placed into a tubular muffle furnace. The furnace connected to a vacuum system and evacuated, and the temperature is increased to 1,250 — 1,500°C. When the reaction temperature is reached, gaseous chlorine is introduced into the furnace. As a result of the reaction titanium carbide fibers and the gaseous products $TiCl_4$, CO and CO_2 are formed. Below 1,250°C no fibers are obtained, and above 1,500°C chlorine strongly reacts with TiC and no fibers are observed. The optimum parameters for the preparation of TiC fibers are as follows: temperature 1,400°C. holding time 10 hr. X-ray diffraction patterns show that the main component of the fibers is TiC. The mean fiber diameter is $0.2 - 0.3\mu$, and the mean fiber length $7 - 15\mu$.

Of the different types of fibers, those made of asbestos, graphite, or carbon have very important properties.

Asbestos is the main raw material for a large number of materials. These are produced on an industrial scale. The most abundant and best type of asbestos chrysotile asbestos $3\,MgO \cdot 2\,SiO_2 \cdot 2H_2O$, which is found in nature as very flexible crystals with a maximum length of 5 cm (Figure XIV. 20). Individual asbestos fibers are tubular in form, and their inner structure is capillary in type /106/. Their diameter can be determined by an electron microscope only. The fibers have the following chemical composition (%)

SiO_2	37.28 – 41.96	Fe_2O_3	1.72 – 4.25
MgO	38.49 – 42.93	FeO	0.85 – 2.05
Al_2O_3	0.12 – 1.67	H_2O	12.28 – 14.08

The second type of asbestos forms a group of amphibolitic asbestos fibers (crocidolite, amosite, montezite). These fibers are less flexible but harder. Crocidolite $Na_2O \cdot 3\,FeO \cdot Fe_2O_3 \cdot 8\,SiO_2 \cdot H_2O$ consists of fibers 12 — 75 mm long, which are very strong. Amosite fibers contain iron, silica, magnesium, sodium, and calcium, and are very brittle. When heated to above 500°C, they lose water of crystallization, and this leads to a change in structure and reduction in strength.

Unlike the natural fibrous asbestos, graphite and carbon fibers are artificially produced. The first graphite fibers were prepared as early as 1883 by carbonization of nitrocellulose fiber. They were used for filaments in electric lamps /107/. At present, graphite fibers (Figure XIV. 21) are produced in electric furnaces at 2,700°C from cleaned and recovered cellulose materials. The carbonizaizon method is, in principle, the same as that used in /107/, but the production process is much more complex.

The main difference between graphite and carbon fibers lies in their molecular structure. Carbon filters are obtained at 800°C. Such fibers contain up to 8% of volatile products. Felts from these fibers have a specific surface of 150 m^2/g, which is 50 times the specific surface of graphite fiber felts. Various organic materials, mainly peat, are the raw materials for carbon fibers. First, moisture is removed, and then

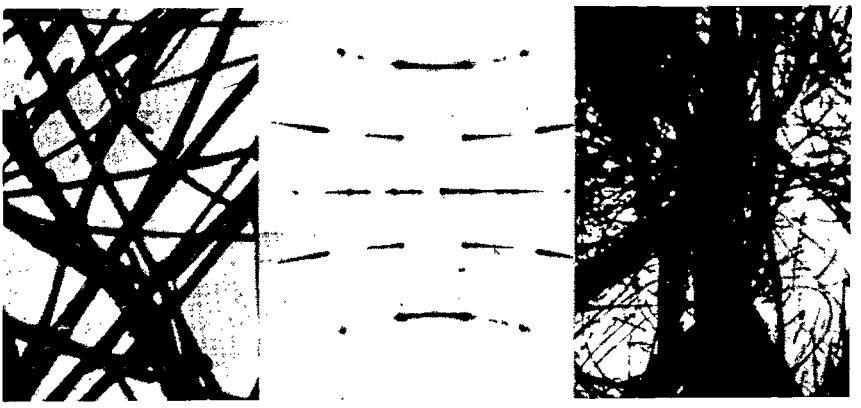

a b c

FIGURE XIV. 20. Chrysotile asbestos fibers:

a – × 2,000; b – X-ray powder pattern; c – × 30,000.

FIGURE XIV. 21. Graphite fibers, × 400

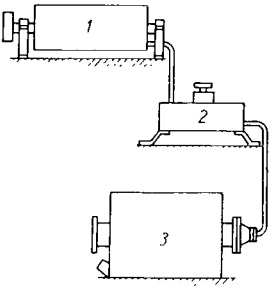

FIGURE XIV. 22. Technological process for production of carbon fibers:

1 – mill; 2 – rotating sieve; 3 – retort for carbonization.

the material is ground in a ball mill and carbonized at 450 – 500°C (Figure XIV. 22) /108 %/. Carbon fibers can be also obtained by slow pyrolysis of hydrocarbon vapors. Coke-oven gas containing about 30% of CH_4 and 55% of H_2 is passed through a heated silicon tube. The process temperature is 1,350°C, the flow rate of the gas is 0.322 liter/min, and the time of passage through the tube is 2 sec. From 8.37 g of CH_4, 4.2 g of carbon were recovered, and 7% of this was deposited in the tube and condensed in the form of fibers. The total amount of carbon in the methane was 62%.

Hydrogen sulfide can be used as a growth-promoting catalyst. A nichrome wire screen is used to disperse it in the apparatus. Some test results are shown in Table XIV. 5.

TABLE XIV. 5. Test data on the production of carbon fibers using hydrogen sulfide as catalyst*

Flow rate of coke-oven gas, liter/min	H_2S content, mole %	Reaction time, sec	Amount of CH_4 introduced	Fiber yield	
				g	% (relative to methane carbon)
0.33	0	1.5	8.6	0.20	3
0.46	0.13	1.1	4.4	0.13	4
0.45	0.23	1.1	4.9	0.19	5
0.45	0.37	1.1	3.9	0.42	14
0.38	0.42	1.4	3.3	1.03	41
0.39	0.45	1.3	4.2	1.14	37
0.42	0.47	1.2	4.4	1.24	37
0.46	4.0	1.1	7.6	0.79	14

* Test temperature, 1,350°C.

The diameter of the graphite fibers ranged from fractions of a micron to 100 μ, and the length from several μ to several centimeters /109/.

FIGURE XIV. 23. Pluton fibers.

The latest achievement in the production of new organic materials is the technology for preparing a new type of fibers, termed Pluton (Figure XIV. 23). So far, there are no data available on the production and chemical composition of Pluton. We only know that these fibers are noninflammable and nonconductors, and do not contain elemental carbon /110/.

We should also mention the processes for producing several nonmetallic fibers in the form of single crystal whiskers. Though the processes are complicated, and therefore have no industrial application, the fibers have unique strength parameters which are worth noting. Single crystal fibers include those of Al_2O_3 and MgO whiskers. The first are obtained by heating alumina up to 1,200 — 1,650°C in wet hydrogen. The aluminum vapors precipitate as high-strength whiskers /94/.

Single crystal whiskers from MgO are formed on deformation of MgO crystals under pressure at 20°C, because the edges of the planes are split off when the pressure is greater than the bonding forces /95, 96/. The whisker diameter is 1 — 3μ.

Another method for producing filamentary MgO crystals was proposed in /131, 132/. The initial material containing magnesium metal or magnesium hydroxide calcined at 500°C is mixed with graphite or soot, which functions as a reduction agent. A small amount of wax to act as plasticizer, and an appropriate amount of alcohol or benzine to dilute the plasticizer and

facilitate mixing, are introduced. The mixture is placed into a graphite crucible, and then heated to a temperature of at least 1,500°C. The mixture is heat-treated in a gaseous medium containing small amounts of oxygen in carbon dioxide, steam, nitrogen, or any other inert gas.

When Mg metal is introduced into the mixture, the metal begins to vaporize during heat treatment (boiling point, 1,103°C). At 1,500°C MgO is reduced by carbon to the metal, which also vaporizes. The magnesium vapors react with the oxygen present in the gas, and are condensed on the support as filamentary MgO crystals. The support is a ceramic containing mainly MgO and small amounts of Fe_2O_3 and SiO_2. In some cases the support may contain graphite also.

The rate of vaporization of MgO can be increased by heating to still higher temperatures.

MgO fibers obtained by the above method are transparent crystals with a circular cross section. Their diameter is not larger than 100μ, and they may be as long as 10 mm. An X-ray structural analysis showed that the fibers are stable, almost prefect MgO crystals.

The following variant for producing MgO fibers can be employed. MgO obtained from sea water and calcined at 600°C is mixed with carbon black in the molar ratio Mg: carbon black = 7 : 3. Beeswax mixed with benzine serves as the plasticizer. The components are mixed, and dried, and disks are extruded under a pressure of 1,000 kg/cm^2. The disks are placed into graphite crucibles, and covered by lids which serve as support. The lids are made of MgO with 10% of SiO_2 and 1% of Fe_2O_3. The crucible with the specimen is placed into an induction heater and heated at the rate of 15 deg/min to 1,650°C. The specimens are heated in CO_2, and white MgO fibers condense on the lid. After the fibers have grown to the required length, they are removed.

During the treatment of a mass with 10 g of MgO and 1.3 g of carbon black as the main components, 2 g of MgO fibers (diameter less than 100μ, length 20 mm) crystallize on the support within 10 minutes.

The production of high-strength graphite whiskers is described in /111/. An artificial graphite rod of 12.7 mm length is placed into a reactor made of stainless steel and lined with carbon. The reactor has a lid with a small tube for feeding an inert gas (argon) under a pressure of 93.4 atm. A graphite plate is mounted on the bottom of the reactor (the plate is made of a mixture of 80% of artificial graphite and 20% of carbon black, with coal tar as binder), and a carbon crucible is placed on it. Above the crucible there is a protective graphite sheet to prevent heat losses. The lid of the reactor is fitted with a conducting wire and a screw to control the feed and fix the graphite rod in the crucible. An arc is produced from a dc source (80 V); between the rod and block for 30 min, at a current density of about 10 A/cm^2. The growth rate of the whiskers if 254 mm/hr. The whiskers are precipitated on the plates as fibers of 0.5 — 5μ diameter and 150 mm length.

It was found that these crystals have a perfect structure near to single crystals. The whiskers obtained by the above method consist of large graphite plates rolled into one or more concentric tubes, each tube being in the form of a scroll /112, 113/.

We have also references in the literature on the possibility of producing filamentary crystals from the following compounds: Cr_3O_4 /97/; β-Ag_2S by the reaction between H_2S and silver at room temperature /98/; Cu_2Se and Cu_2Te by the reaction between Se or Te and copper at 380 — 600°C /99/;

γ-tungsten oxide /100, 101/; LiF by evaporating a two-component solution through a porous partition /102/; zinc sulfide from the gas phase /103/; Mn_5Si_3 and Si_3N_5 by chemical reactions; Cr_2N and Fe_3C by separation from the melts /104/; and quartz /105/.

Very fine γ-$W_{18}O_{49}$ fibers were produced as follows /129/. A porous crucible containing a tungsten crucible was placed into an induction coil. MgO was poured into the porous crucible and the inner hollow of the tungsten crucible. The whole equipment was covered by a hood (20 liters), and argon saturated with water vapor at 21°C was passed at the rate of 0.14 m^3/hr. The tungsten crucible was first heated to 1,200°C for one hour and then the temperature was increased to 1,600°C. During this process, inside the MgO powder at angles of 20 — 45° to the walls of the tungsten crucible, red-violet filaments began to grow. Their thickness was 0.1 — 1 μ and their length was up to 10 mm. The main factors determining the growth process are the partial vapor pressure, type of MgO powder, and the system geometry. The authors observed the growth of red-violet γ-$W_{18}O_{49}$ filaments, and of blue $WO_{2.96}$ and green WO_3 crystals.

In the production of silicon nitride fibers the process is carried out in a horizontal tubular furnace of 76.2 mm diameter, lined with carbon /130/. The furnace temperature is 1,400 — 1,410°C. 150 g finely dispersed (300 mesh) pure (99.9%) silicon is placed into the furnace and dry oxygen-free nitrogen is blown through at the rate of 500 ml/min. The silicon vapors react with nitrogen to form filamentary β-Si_3N crystals. The whole furnace is filled with the product in 5 — 7 days.

4. Metal-coated fibers

To increase the wear resistance, flexural and tensile strengths, and to obtain new high-melting and heat-reflecting materials, various metal coatings are applied to the glass fibers.

Several methods for the metallization of fibers have been developed.

Figure XIV. 24 shows the diagram of an equipment for coating fibers with metals in the gaseous phase /114, 115/. A carbon dioxide cylinder 1 fitted with valve 2 and reducing valve 3 is connected to spiral tube 5 by pipe 4. The spiral tube is connected by pipe with valve 6 to U-tube 7 and reactor 18. Reactor 18 has openings 15 and 24 for the passage of fibers 11 and gas outlet 16. The required temperature in reactor 18 is attained by means of induction heater 17. The fibers coated with a complex chromium salt move into the reactor and are heated by tubular heater 14 connected to the reactor. To ensure uniform application of the coating, the glass is vibrated by means of eccentric 20, fixed onto a roll-in jacket 21. After the coating is applied, the fibers pass through seal 23.

Seal 23 is a detachable metallic chamber with hole 24 for the outlet of the fiber, and with tube 22 for gas supply (for example, CO_2). The gas stream is adjusted by a valve according to the pressure gage reading so as to ensure sufficient gas in shell 21 of the eccentric, and in seal 23, and to prevent penetration of iron pentacarbonyl (after decomposition of this compound iron deposits on the fibers). A second seal 13 is placed in front of heater 14 to protect the system against penetration of air. The gases discharged from reactor 18 are suctioned off and condensed in spiral

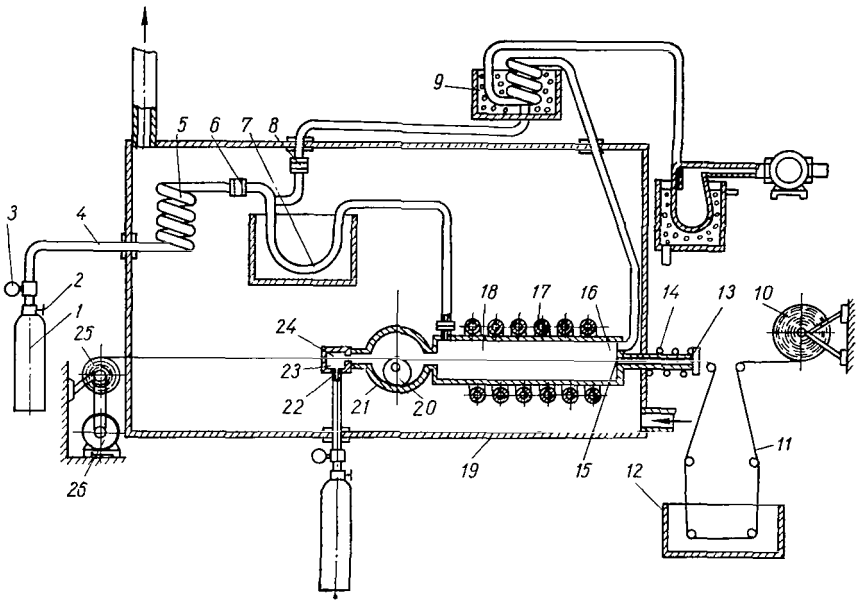

FIGURE XIV. 24. Diagram of setup for metallization of fibers in the gaseous phase.

tube 9, which is cooled by dry ice or other coolant. Valve 8 prevents the main gas stream from entering the condenser.

The penetration of spent gases into the reactor does not affect the quality of the final products if the process is carried out at atmospheric pressure. To avoid abrupt cooling of the processed fiber, shell 19 is used in which the required temperature is maintained. The unprocessed fibers are wound over reel 10. After the fiber has passed seal 23, it is wound over reel 25 driven by motor 26. The fibers are treated with a complex chromium salt in vessel 12 and then proceed to heater 14.

The approximate composition of the solution for treating the fibers before metallization in weight parts is as follows

Methacrylate-chromium chloride	20
Chromium	60
Isopropanol	45
Acetone	10
Water	169

Fibers can also be treated with heat-resistant silicone resin /116/.

To coat fibers, vapors of metals such as nickel, iron, molybdenum, zirconium, aluminum, etc., are employed.

We know of methods for the continuous application of coatings onto glass fibers at the moment they issue in the fused state from the pouring pipe of the spinning head. Figure XIV. 25 shows the setup for applying coatings onto fibers from the gaseous phase. The filament issuing from spinning head 2, placed at furnace outlet 1, passes through heater 3 and gas

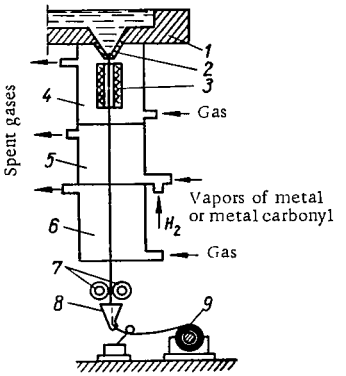

FIGURE XIV. 25. Diagram of setup for metallization of glass fibers in the vapor phase.

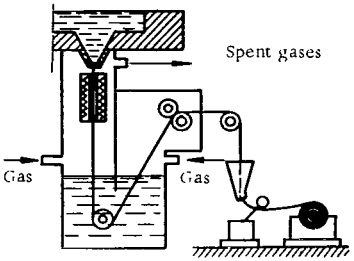

FIGURE XIV. 26. Diagram of setup for metallization of glass fibers.

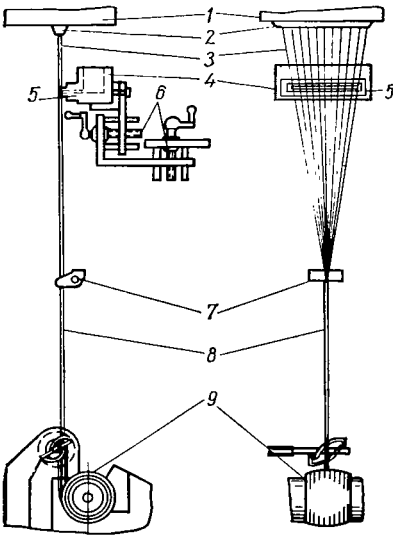

FIGURE XIV. 27. Diagram of apparatus for continuous forming and metallization of glass fibers.

chamber 4 into chamber 5, which is filled with metal vapor at a high temperature. After processing, the filament passes through reducing chamber 6. Finally, it proceeds through stretch rolls 7 and guiding device 8 to receiver 9. Instead of chambers 4, 5, and 6, we can use a single gas-filled chamber. The filament is metallized while it passes through this (Figure XIV.26) /117/.

Several variants of high-speed metallization exist. In one a roll system is employed for processing the fibers; the rate of forming is 900 — 3,000 m/min /118/. The optimum coating conditions are those at which the fibers are held at the temperature of the fused metal /119/.

The layout for high-speed metallization according to another variant is shown in Figure XIV.27. In this variant the filaments are not aligned when they pass through the fused metal /120/.

The apparatus is fitted with a fusing equipment with feeder 1. On the bottom of the feeder there are several holes through which jets of fused glass flow out in a single plane. Collector 7 combines the individual fibers into a single braid 8, and is installed between the fusing equipment and receiving drum 9. During forming, the fibers are drawn according to the speed of the drum. The metal is applied onto the fibers by devices 4 and 5 fitted with special adjusting screws 6.

Because of the coatings, the fibers may have very different properties. For example, by coating with chromium trioxide from aqueous solutions at room temperature, conventional glass fibers with a softening point of 482 — 650°C can be converted into high-melting materials /121, 122/. The efficiency of the coatings depends on the concentration of the solution and fiber diameter (Table XIV.6).

TABLE XIV.6. Melting point of borosilicate glass fibers* after coating with CrO_3

Fiber diameter, μ	Coating, g per g of fibers	Melting point of fibers, °C
0.18	0.063	1,100
0.18	0.084	1,320
0.18	0.105	1,650
2.5	0.069	1,650
9	0.087	1,100

*The melting point of pure glass is between 816 and 871°C.

The field of application of glass fibers can therefore be appreciably widened by coating the fibers.

5. Physicomechanical properties of reinforcing materials

TABLE XIV. 7. Physicomechanical properties of whiskers /123 – 127/

Whisker material	Ultimate tensile strength, kg/mm^2	Young's modulus, kg/mm^2	Maximum specific strength, $\times 10^{-6}$ cm	Ratio of ultimate tensile strength to Young's modulus
Fe	1,275 – 1,340	19,900 – 21,400	17.1	1/16
Al	392 – 400	–	14.8	–
W	2,260 – 2,300	–	11.9	–
Mo	2,260 – 2,300	–	22.6	–
Ag	165 – 180	7,550 – 7,800	1.71	1/43
Cu	294 – 320	12,100 – 12,600	3.58	1/39
Zn	220 – 225	10,000 – 10,500	3.16	1/47
Cd	89 – 92	6,850 – 7,100	1.06	1/77
Si	378 – 390	15,800 – 16,200	16.6	1/42
C	1,960 – 2,100	10,500*	84.0	1/50
Be	1,960 – 2.000	–	110.0	–
B	2,940 – 3,000	49,500	131.0	1/16
α-Al_2O_3	1,176 – 1,200	51,000 – 51,800	31.6	1/43
SiO_2	412 – 425	7,550 – 7,700	17.7	1/18
BeO	2,450 – 2,500	–	87.8	–
MgO	2,500	–	69.9	–
BN	35 – 87.5	2,800 – 8,400	2.53 – 3.8	1/96 – 1/32
Ni	340	–	3.82	–
Co	320	–	3.64	–
Au	140	–	0.725	–
Cu+Fe	400	–	–	–
Asbestos	500	–	15.62 – 25.0	–
β-Mn	310**	–	4.28	–
Si_3N_4	320**		10.00	–

* In s_{11} direction.
** Bending tests.

TABLE XIV. 8. Physicomechanical properties of fibers /139/

Fiber material	Ultimate tensile strength, kg/mm^2	Specific strength, $\times 10^{-6}$ cm
SiO_2	1,600	66.7
W	400	2.08
Mo	300	2.94
Ti	210	4.67
B	176	7.65
BeO	1,336	46.9
Glass	500	–
Carbon steel	450	–
Asbestos	300	9.37 – 12.0
Fe_3C	800*	10.42
Al_4N_3	700	–
Cu_6Sn_5	125	–

* Bending tests.

TABLE XIV. 9. Physicochemical properties of some nonmetallic fibers /138/

Fiber material	Melting point, °C	Density, g/cm³	Length, mm	Diameter, μ	Strength, kg/mm²	Young's modulus, kg/mm²	Coeff. of thermal conductivity, W(cm · deg)	Specific heat, kjoules (kg · deg)	Temperature, °C, of		Chemical resistance temperature of application of fiber
									recrystallization	strength loss	
Quartz (fused silica)	1,667 (softening)	2.20	Variable	0.8 10.1	650 280–422	7,030	1.38	0.691	1,140	1,070	Insoluble in all acids, except HF and hot H_3PO_4, soluble in strong alkalis
Glass E	1,149 (871–915 softening)	2.53	Variable	–	210.9	8,928	–	0.732	720	675	
Fiberfrax	>1,760	2.73	Up to 3.8 13 – 254 (Average 50 – 75)	Up to 10 (average 2.5)	126.54	–	–	–	–	–	Heat resistant up to 1,260°C; should not be used in contact with strong acids or alkalis for long periods
Kaowool	1,750	2.60	Up to 203	Average 2.8	–	–	–	–	–	–	Chemical resistance the same as that of other aluminosilicate fibers, heat resistant up to 1,100°C for long periods and up to 1,260°C for short periods
Tipersul	1,371	3.60	0.2	Average 1.0	16.3	2,800	–	0.921	–	–	Resistant to boiling alkalis at concentrations up to 30%, and to cold dilute acids (10 wt%); 1,200°C – air, inert gas, 955°C – 75% of H_2+25% of N_2 mixture, 980°C – vacuum of 10^{-5} mm Hg, 540°C – pure H_2
ZrO_2+5%CaO	2,590	5.90	6.35–50.8 6.3 –300	– 2.5–12.5	<38.6 140	–	–	–	–	–	Refractory up to 1,650°C
Asbestos	1,193 – –1,521		Up to 75	–	126–351	–	–	–	–	–	
Graphite (carbon)	>3.600	1.5	Variable	7.6	42.5–76.3 280	300–980 35,000	4.19–159.0	0.670	–	>447	400°C – air, 700°C – steam, 900°C – CO_2, up to 2,760°C – neutral and reducing media

Bibliography

1. Schaefer, G. German Patent No. 78671.
2. Muller, K. Swiss Patent No. 32688.
3. Marti, J. Swiss Patent No. 32668.
4. Steinbart, W.A. Brit. Patent No. 242894.
5. British Patent No. 268244.
6. Modern Materials, I. Sect. E, p. 180, New York. 1958.
7. Krátký, L. — Hutnické Listy, 14(6):499 — 500. 1959.
8. Modern, J.F.C. Metallic Fibres. — Metal Industry, 96(25):495 — 499. 1960.
9. British Patent No. 814490.
10. Ulitovskii, A.V. — Stal', 11. 1937.
11. Shpirnov, V.A. Fontanirovanie zhidkogo metalla (Liquid Metal Spouting). — TsITEIN, PNTPO, M-59-484/48. 1959.
12. Shpirnov, V.A. Poluchenie i primenenie litoi provoloki i profil'nogo lit'ya (Production and Application of Cast Wire and Profile Casting). — GOSINTI, PNTPO, M-62-197/22. 1962.
13. Eisenkolb, F. Grundlagen des Festigkeitsverhaltens von Metallen. Akademie Verlag. Berlin. 1965.
14. U.S. Patent No. 2976590.
15. Wiedersich, H. — J. Electrochem. Soc., 106(9):810 — 815. 1959.
16. Webb, W.W. and E.F. Riebling. — J. Chem. Phys., 28(6) 242 — 1245. 1958.
17. Mazur, J. and J. Rafalowicz. — Brit. J. Appl. Phys., 12(10): 569 — 571. 1961.
18. Wayman, C.M. — J. Appl. Phys., 32:1844. 1961.
19. Cech, R.E. The Nucleation of Nickel Whiskers. — Acta Met, 7(12): 787 — 792. 1959; 9(5):459 — 463. 1961.
20. Wagner, C. — Trans. Amer. Inst. Min. Met. Eng., 194, 214. 1952.
21. Brenner, S.S. — Acta Met., 7(10):677 — 678. 1959; 2(7):519. 1959.
22. Morelock, C.R. and G.W. Sears. — J. Chem. Phys., 31(4):926 — 928. 1959.
23. Hauptmann, Z., J. Kacer, and R. Temperle. — In: Růst krystalů [Russian translation. 1961.]
24. Burton, W.K. and N. Cabrera. — Disc. Farad. Soc., 5:33 — 40. 1949.
25. Frank, F.C. — Advances in Physics, 1:91. 1952.
26. Burton, W., N. Cabrera, and F. Frank. — Phil. Trans. Roy. Soc., 243:299. 1953.
27. Oding, I.A. and I.M. Pop'ev. — Metallovedenie i termoobrabotka, 7:2 — 7. 1961; 9:44 — 49. 1961.
28. Chernov, A.A. Sloisto-spiral'nyi rost kristallov (Laminar-Spiral Growth of Crystals). — UFN, 73:277. 1961.
29. Amelenckx, S. On Whisker Growth Shapes. — Philos. Mag., 3(29):425 — 428. 1958.
30. Mazur, J. and J. Rafalowicz. — Acta Phys. Polon., 21(4):365 — 370. 1962.
31. Sears, G.W. and J.B. Hudson. — J. Chem. Phys., 35:1509 — 1510. 1961.
32. Meulen, P. and H. Lendstrom. — Trans. Electrochem. Soc., 103:390. 1956; 104:607. 1957.

33. Muller, H.G. — Report on the Second International Conference on Powder Metallurgy in Eisenach (German version, pp. 23 — 42. Berlin, Akademie Verlag. 1962).
34. Price, P., D.A. Vermilyca, and W.W. Webb. — Acta Met., 6(8):524 — 531. 1958.
35. Hoffman, G.A., I. Mazur, I. Nikliborc, and J. Rafalowicz. — Brit. J. Appl. Phys., 12(11):635 — 636. 1961.
36. Glazunova, V.K. and N.T. Kudryavtsev. — ZhPKh, 36:3. 1963.
37. Mc Nulty, I. M. Silver, and R. Witte. — Rev. Scient. Instr., 8(31):904 — 905. 1960.
38. Amelenckx, S. — Physica, 24:390 — 392. 1958.
39. Franks, I. — Acta Met., 6:103 — 109. 1958.
40. Hardy, N.K. — Progr. Metal. Phys., 6:45. 1956.
41. Sines, G. — J. Phys. Soc. Japan, 15(7):1199 — 1210. 1960.
42. Arnold, S.M. and E.S. Koonce. — J. Appl. Phys., 27(8):964. 1956.
43. Russele, A.M. and R.C. Abott. — J. Appl. Phys., 29(7):1130 — 1131. 1958.
44. Arnold, S. Obrazovanie metallicheskikh usikov na elektricheskikh detalyakh (Metal Whisker Formation on Electric Component Parts). — In: Radioelektronika za rubezhom, 33(59). TsBNTI. Moskva. 1960.
45. Lachma, W.L., I.P. Sterry, and H.I. Thompson. — Chem. Eng. Progr., 37. 1962.
46. Callahan, I.L., R.H. Petrucci, and C.A. Brown. — J. Col. Sci., 15(5):418 — 426. 1960.
47. Morelock, C.R. and G.W. Sears. — J. Chem. Phys., 34(3):1008 — 1009. 1961.
48. Anonym. — Metal Ind., 15(1):104. 1964.
49. Ivanov, A.P. Elektricheskie lampy i ikh izgotovlenie (Electric Lamps and Their Production). Nauchnoe khimichesko-tekhnicheskoe izdatel'stvo. Petrograd. 1923.
50. Meerson, G.A. Sovremennoe sostoyanie teorii osnovnykh protsessov poroshkovoi metallurgii (Advances in the Theory of the Fundamental Processes of Powder Metallurgy). — In: Voprosy poroshkovoi metallurgii. 1955.
51. Chemical "Drawing" Produces Tungsten Filaments. Abstract from Product Eng., 15. 1961.
52. Amonenko, V.M. et al. — Fizika Metallov i Metallovedenie, 13:6. 1962.
53. Silicon Crystals in "Ribbon" Form. — Bell Lab. Record, 39(12):448. 1961.
54. Ahlborn, H. and G. Wassermann. — Acta Met., 8(12):897 — 898. 1960.
55. Forsyth, P.I., P.G. Partridge, and D.A. Ryder. — Philos. Mag., 4(40):447 — 450. 1959.
56. Andle. Dendritický růst krystalů germania. — Českosl. Časop. Fys., 11(5):397 — 400. 1961.
57. Kostornov, A.G. and A.I. Raichenko. — Poroshkovaya Metallurgiya, 12(48):37 — 42. 1966.
58. Kostornov, A.G. and E.T. Denisenko. — DAN UkrSSR, Seriya A, 4. 1967.

59. Kostornov, A.G. and V.V. Skorokhod.— Poroshkovaya Metallurgiya, 11(71):21 — 24. 1968.
60. British Patent No. 507951.
61. GFR Patent No. 1108388.
62. Eberhardt, E. and H.Klumb. —Glastech. Ber., 27, 134. 1954.
63. Loosli, H. British Patent No. 765632.
64. Silverman, A. U.S. Patent No. 2736141.
65. Silverman, A. U.S. Patent No. 2822579.
66. Silverman, A. U.S. Patent No. 2838882.
67. U.S. Patent No. 2699415.
68. U.S. Patent No. 2928716.
69. Nachtman, I.S. U.S. Patent No. 2940866.
70. U.S. Patent No. 2934458.
71. GFR Patent No. 1026925.
72. Labidno, D. U.S. Patent No. 2823117.
73. Labino, D. U.S. Patent No. 2843461.
74. GFR Patent No. 1072367.
75. U.S. Patent No. 2557834.
76. U.S. Patent No. 2686821.
77. British Patent No. 638876.
78. U.S. Patent No. 2699397.
79. U.S. Patent No. 2968069.
80. British Patent No. 495654.
81. Refractory Fibers from Kaolin. U.S. Patent No. 2674559.
82. Smith, H.C. Can. Patent No. 455781.
83. Mechanism of Growth and Physical Properties of Refractory Oxide Fibers. Report PB 171520 (U.S. Dept. of Commerce. April, 1960).
84. Candidate Materials for High Temperature Fabrics. WADC Tech. Rep., pp. 59 — 155 (U.S. Dept. of Commerce. September, 1959).
85. Lewowski, T. and B. Sujak.— Molybdänoxyd — Fadenbildung. Zs. Naturforsch., 15a(1):89 — 90. 1960.
86. British Patent No. 171520.
87. British Patent No. 861802.
88. Mellor, I.W. U.S. Patent No. 2980510.
89. Mergault, P. and G. Branch.— C.R. Acad. Sci., 238, 914. 1954.
90. Berry, K.L. and H.S. Young.— J. Inorg. Nucl. Chem., 14:231. 1960.
91. Florentine, R.A., I.W. Simmons, and I. Mockrin. Magnesium Oxide in Fiber Form by Extrusion Methods, PB 171939, AD 243205 (U.S. Dept. of Commerce. August, 1960).
92. Boron Filaments.— Mater. Design Eng., 54(7):7. 1961.
93. Missiles and Rockets, 9(16):16. 1961.
94. De Vries, R.C. and G.W. Sears.— J. Chem. Phys., 31:1256 — 1257. 1959.
95. Hulse, C.O.— J. Amer. Cer. Soc., 14(11):572. 1961.
96. Hulse, C.O. and I.A. Pask.— J. Amer. Cer. Soc., 113:373. 1960.
97. Hilty, D.C., W.D. Forgeng, and R. Folkman.— Trans AIME, 203:253. 1955.
98. Drott, I.— Acta Met., 8(1):19 — 22. 1960.
99. Arkharov, V. and S. Mordnikov.— DAN SSSR, 3, 517.

100. Takaji, R. — J. Electronomicroscopy, 3:18. 1953.
101. Hashimoto, H., K. Tanaka, E. Ioda, and H. Araki. — Acta Met., 8:559. 1958.
102. Nadgornyi, E.M. — Fizika Tverdogo Tela, 3(3):957 — 958. 1961.
103. Samelson, H. — J. Appl. Phys., 32:309. 1961.
104. Webb, W.W. and W.D. Forgeng. — Acta Met., 6(7):462 — 469. 1958.
105. Iaccodine, R.I. and R.K. Kline. — Nature, 189(4761). 1961.
106. Pundsack, F.L. — J. Phys. Chem., 65 :30. 1961.
107. Swan, I.W. British Patent No. 5978.
108. Pickard, I.A. U.S. Patent No. 2822321.
109. U.S. Patent No. 2796331.
110. Carrol-Porczynski, C.Z. — Eng. Mat. Design, 4(7): 418. 1961.
111. U.S. Patent No. 2957756.
112. Sears, G.W. — J. Chem. Phys., 31(2):358 — 360. 1959.
113. Bacon, R. — J. Appl. Phys., 31(2):283 — 290. 1960.
114. U.S. Patent No. 2862783.
115. U.S. Patent No. 2744255.
116. U.S. Patent No. 2847322.
117. U.S. Patent No. 2699415.
118. U.S. Patent No. 2835221.
119. U.S. Patent No. 2928716.
120. U.S. Patent No. 2963739.
121. Can. Patent No. 564671.
122. Labino, D. Can. Patent No. 564670.
123. Missiles and Rockets. 16(9):16. 1961.
124. Detert, K. — Metall., 19(5):471 — 473. 1965.
125. Lytle, A. — SAE Journal, 67(5):59. 1959.
126. Strength from Whiskers. — Eng. Mat. Design, 3(5):300, 303. 1960.
127. Williams, M.L., G. Gerard, and G.A. Hoffman. — 9th International Astronautical Congress, Stockholm, 1960. Paper 18.
128. Pultz, W.W. U.S. Patent 3161473; French Patent No. 1419728.
129. Wolf, E.G. — J. Amer. Cer. Soc., 48(4):221 — 222. 1965.
130. British Patent No. 998167.
131. U.S. Patent No. 3314759.
132. Wolf, E.G. and T.D. Coskren. — J. Amer. Cer. Soc., 48(6):279 — 285. 1965.
133. Nixdorf, J. — Ber. Deut. Keram. Ges., 45(4):141 — 148. 1968.
134. Beasby, R.M. and H. Johns. U.S. Patent No. 3082099.
135. Wainer, E. and E.F. Mayer. U.S. Patent No. 3096144.
136. Ducati, A. U.S. Patent No. 3099548.
137. Walworth, C.B. — Text. Manufacture, 87(1040):315 — 316. 1961.
138. Carroll-Porczynski, C.Z. Advanced Materials, Refractory Fibers, Fibrous Metals, Composites, Astex Publishing Company, Ltd., Guildford. 1962.
139. Poroshkaya metallurgiya v novoi tekhnike (Powder Metallurgy in Modern Engineering). Moskva, "Nauka." 1968.

Chapter XV.

PRODUCTION OF FIBROUS STRUCTURES BY DIRECTIONAL CRYSTALLIZATION OF EUTECTIC ALLOYS AND HEAT TREATMENT OF SOLID SOLUTIONS

1. Properties of cast composites

The idea of reinforcing metals by filamentary crystals to obtain structural materials with good strength properties was first conceived in the fifties. At that time the unique mechanical properties of whiskers which could withstand stresses close to the theoretical were first noted /1/. Since then, wide research has been carried out on the growth process, properties, and perfectness of whiskers. The authors of /2, 3, 4/ are experts in this field and consider that filamentary crystals are very promising materials for reinforcing metals, ceramics, or plastics.

But for the application of whiskers numerous new problems must be solved, such as, the cultivation of a sufficient amount of high-strength crystals, their grading according to strength, provision of sufficient bonding with the matrix, and development of techniques for introducing the whiskers into the matrix. A very important problem involved in the production of whisker-reinforced materials is the development of a technique for distributing the whiskers uniformly over the composites. This is a complicated task, even when the size of the material is small. The alignment of the fibers in the matrix is of special importance in reinforced materials, since the maximum strengthening effect can be achieved when the fibers are oriented in the direction of the external applied load. In contrast to the numerous conventional methods of reinforcement based on retarding and moving dislocations, reinforcement by fibers is possible because the load applied to the composite is sustained by the fibers, while the role of the matrix is only transmission of the load and maintaining the form of the structure.

In 1952, Salkind /5/ was the first to study directional eutectic crystallization to investigate the hardening process. Later Kraft /6/ and Chadwick /7/ studied directional eutectic crystallization in order to obtain anisotropic structures. During the eutectic reaction, a liquid of a certain (eutectic) composition is transformed into two solid phases at a certain constant temperature. The existence of such forms of eutectic structures, both platelets and needles, has been known for a long time /8 – 12/.

Davies /13/ studied the possibility of producing fiber-reinforced materials by directional crystallization from a solution of needlelike dendritic structures. From the morphological point of view, dendritic fibers are similar to whiskers. At high temperatures and high stresses they keep their stable form in the tough matrix formed from the same melt. A preliminary investigation of materials obtained in such a way showed that their properties are similar to those of fiber-reinforced materials. This research confirmed the hypothesis of the strengthening of such material by dendritic fibers. A new approach was found for the production of high-strength materials of a new type. Under mechanical loads such materials behave similarly to reinforced materials produced from separately prepared fibers and matrix. The production of composite materials by directional crystallization of eutectic alloys is the simplest way of preparing specimens.

However, alloys prepared by directional crystallization have not only advantages but also numerous disadvantages when they are compared with composites prepared in the conventional way.

There are more than 1000 alloys containing metals, ceramic and intermetallic compounds. By directional cooling many of these single-phase alloys can be formed into structures consisting of a matrix containing fibers or other aligned formations. But comparatively few of these have been studied. The following systems have been investigated in the greatest detail.

$Al - Al_3Ni$ system. This system was studied by Hertzberg /14/ and Lemkey /15/. The eutectic alloy consisting of an Al matrix and 10 vol % of Al_3Ni is the most interesting. After directional crystallization this eutectic behaves like aluminum reinforced by filamentary crystals, and its ultimate tensile strength is much higher than the strength of the cast eutectic. In the cast state when the whiskers in the alloys are randomly oriented the ultimate strength is 9.1 kg/mm^2 and the relative elongation 15%. If this alloy is subjected to directional crystallization at a speed of 2 – 10 cm/hr, its strength is increased by a factor of 3.5 (30 kg/mm^2 or more), while the relative elongation is reduced to about 2%. It is interesting to note that the ultimate strength of aluminum is only about 3.5 kg/mm^2.

Filamentary crystals chemically isolated from the $Al - Al_3Ni$ alloy had $\sigma_B = 35\ kg/mm^2$. Though this strength level cannot be considered high compared to that of some composites (the Cu – W composite has a strength of more than 175 kg/mm^2 /38/), the strength-to-density ratio is 10, so that this composite is comparable with the most promising high-strength alloys such as Cu – W /26/.

Because the strength of the $Al - Al_3Ni$ composite was sufficiently high, and the calculated strength of the whiskers composites was equal to the experimentally determined strength of the individual whiskers separated from the matrix, we can conclude that the matrix does not impair the strength of the whiskers. The flexural strength of these whiskers is about twice their tensile strength. It can be statistically expected that whiskers must have a higher flexural strength than tensile strength, because in the former case a smaller area of the whisker is subjected to the maximum applied stress, and therefore there must be less defects in the region of maximum loading.

The quality of load transmission by the matrix to the whiskers was checked by electron diffraction studies of the fractures. It was reliably established by Hertzberg /16/ that the composite begins to break with fracture of the whisker and not at the whisker-matrix interface. Preliminary studies on the creep of Al reinforced by Al_3Ni or $CuAl_2$ showed that the creep of alloys reinforced by filamentary crystals ($Al-Al_3Ni$) differs from that of alloys with platelike structures ($Al-CuAl_2$). Whisker-reinforced materials have a lower creep rate and a higher ductility on fracture. But metals reinforced by plates have a higher creep rate and lower ductility on fracture. These differences in the two structural types have also been observed for eutectic $Nb-Nb_2C$ reinforced by whiskers, and for eutectic $Ni-NiMg$ in which the second phase consists of plates. A study of the plastic properties of reinforced materials showed that $Al-Al_3Ni$ can be cold rolled with a deformation of about 95%. The direction of deformation is perpendicular to the orientation of the whiskers, and this makes it possible for the matrix to flow around the crystals without producing stresses round the filamentary crystals. Rolling in a direction parallel to the whiskers leads to cleavage, while the deformation is small. Because of the high thermal stability of these materials, sheets can be bonded by diffusional methods /18/.

$Al-CuAl_2$ system. The eutectic alloy of this system contains approximately equal volume fractions of the Al solid solution and the intermetallic compound $CuAl_2$. After directional crystallization, microstructures consisting of alternating plates of each phase are formed. It is worth noting that alloys of the $Al-Al_3Ni$ type are reinforced more than alloys of the $Al-Al_2$ type, which contain plates, and not fibers reinforcing the matrix. The reinforcing effect of the $CuAl_2$ plate is much lower than that of the $Al-Al_3Ni$ fiber, although the $Al-CuAl_2$ alloy contains more than 40% of the strengthening phase, while the content of the strengthening phase in the $Al-Al_3Ni$ system is 10 vol %. Thus, the strength of alloy $Al-CuAl_2$ was $\sigma_в \approx 28\,kg/mm^2$ /17/, while the strength of the $Al-Al_3Ni$ alloy containing one quarter of the strengthening phase was $35\,kg/mm^2$.

The $Al-CuAl_2$ system has been studied by numerous authors /14, 19, 20/. The first task in the selection of the eutectic alloy for studying its suitability as a composite is to determine the presence of the phases and the volume fraction occupied by each in the composite. It is not altogether clear /22/ why in one case fibers are formed which are precipitated in the matrix phase, while in the other case plates. The following tentative explanation can be given, which was obtained from observations made when studying many eutectic alloys. If the volume fraction of one phase does not exceed about 20–28%, this phase precipitates as thin rods ingrained in the matrix, which is the second phase. But if the volume fraction of a phase is 35–50%, it is very probable that the alloy will have a platelike structure. According to the theory of Tiller /21/ the distance between the particles of the separated phase (plates or particles of another form) is determined by

$$\lambda = Av^{-\frac{1}{2}},$$

where λ is the distance between the particles; v is the freezing velocity; and A is a magnitude depending on numerous factors

$$A = \left\{\frac{8\gamma_{\alpha\beta}T_E D_B\left(\frac{1}{m_\alpha} - \frac{1}{m_\alpha}\right)}{M_\alpha \Delta H (1 - K_\alpha) C_E}\right\}^{\frac{1}{2}},$$

where $\gamma_{\alpha\beta}$ is the free energy of formation of the α/β phase boundary; T_E is the eutectic temperature; D_B is the liquid diffusion coefficient of the B-atoms; m_i is the liquidus slope of the i-phase; ΔH is the latent heat of fusion per unit volume; K_α is the solute partition coefficient with respect to the α-phase; C_E is the eutectic concentration; and M_α is a shape parameter between 0.5 and 2.

For reasonable values of these and $\gamma_{\alpha\beta}$ $200 - 400$ ergs/cm^2, A is expected to be about 10^{-5} cm$^{3/2}$sec$^{-1/2}$.

According to experimental data, λ is usually $0.5 - 10\mu$.

Tiller /21/ studied the systems Pb – Sn, Zn – Sn, and Cd – Zn to determine the effect of the freezing velocity on the dimensions of the crystallizing eutectic phases. From materials preliminarily zone-refined, specimens 20 cm in length and 0.9 cm in diameter were prepared. Then, along the specimens zones of material were separated which were frozen at certain rates. The individual zones were separated from one another by zones of quenched material. The author obtained good confirmation of his theoretical conclusions. The zones frozen at a very high rate had phases separated in the form of grains and not of plates, which was also predicted by his theory.

For the same purpose, Mamura /22/ subjected alloys Al – Cu and Al – Si of eutectic composition to directional crystallization at rates: 0.5; 3.5, and 5 cm/hr (air freezing), and 0.3, 3, and 30 m/hr (water freezing). The specimens were fused in stainless steel vessels, coated inside by 20μ titanium foils. In eutectic Al – $CuAl_2$ alloys, platelike structures were formed in all cases. When the specimens are frozen in water, λ is very small (about $0.4 - 0.5\mu$). After crystallization of the eutectic Al – Si alloy, the eutectic has a very fine crystal structure, with $\lambda = 1.8 - 3.0\mu$, and in the eutectic modified by Na, $\lambda = 3.3\mu$. Thus, crystallization of eutectic alloys $CuAl_2$ – Al and Al – Si in water and modification procedures make it possible to reduce λ to the order of magnitude of 1μ.

It is clear that the high strength properties of the specimens obtained by directional crystallization are in the direction coinciding with that of the reinforcing element. Salkind /18/ reports that the alloy Al – $CuAl_2$ crystallized by the conventional method with a random distribution of the reinforcing $CuAl_2$ phase has a compressive strength of about 21 kg/mm^2, while with unidirectional solidification this parameter increases to 63 kg/mm^2. The mechanical properties at angles of 90 and 45° to the direction of freezing in the eutectic Al – $CuAl_2$ were lower than in the direction parallel to the platelets, but higher than in the alloy obtained by conventional methods. If 28 kg/mm^2 is the compressive strength perpendicular to the plate orientation, the tensile strength is much lower, and usually less than 14 kg/mm^2. It is, however, interesting that after extrusion this strength increased to 28 kg/mm^2. The individual coarse grains of the two-phase eutectic make it possible to study the anisotropy of the

mechanical properties by four-point bending as a function of the angle between the direction of the bending stress and the plane of the plates /14/. It was shown that the maximum stress in the external fibers of the microspecimen is reduced by a factor of 2.5 when the plates return from the position parallel to the direction of the bending stress to the position perpendicular to it.

Lemkey /15/ carried out another experimental series with the eutectic, and attained a maximum strength of 52.5 kg/mm^2 with plates which were 1μ thick. This result confirms the size dependence of the strength of whiskers, according to which smaller whiskers have a higher strength than larger ones.

Electron diffraction and metallographic studies /14/ showed that the platelike Al — $CuAl_2$ structure is broken in the same way as the eutectic alloy Al — Al_3Ni. The main process is slip which fractures the more rigid and brittle intermetallic phase. The soft aluminum plates are destroyed by tension. Thus, on the fracture surface alternating zones of slip and tensile fractures are observed.

Al — Si system. This system was studied in /22, 23, 24/. If the initial elements are fairly well purified, the structure of the eutectic alloy can be controlled by unidirectional freezing. According to Bell /23/, the crystallized alloy has a structure consisting of long parallel rods ingrained into the matrix.

The distance between the particles of the separated phase is controlled by the freezing rate of the melt /22/.

Cu — Cr system. The eutectic alloy Cu — Cr is a system containing 2 vol % of Cr whiskers, distributed over the matrix. Although the chromium whiskers isolated chemically from the alloy subjected to directional crystallization have $\sigma_B = 700$ kg/mm^2, which corresponds approximately to E/30 /25/, the alloy itself is not stronger than the randomly crystallized alloy /26/. The absence of any reinforcing effect is apparently due to the low volume fraction of the whiskers in the alloy. The chromium whiskers isolated from a randomly crystallized Cu — Cr eutectic have a high strength /27/.

When this alloy was studied, a very important fact was discovered of the nature of the bond on the whisker-matrix interface. Investigations on deformations show that this bond ensures satisfactory load transmission, and that the composite is fractured at the whiskers themselves, and not on the interface /28/. Such a fracturing mechanism was found in all the systems studied. It should be noted that one of the main advantages of eutectic melts obtained by directional crystallization is the presence of a firm bond between the two phases. The electron diffraction patterns of the fractures in specimens of the Cu — Cr melt showed the presence of longitudinal pits, each of which is bonded to half of the fractured Cr whisker.

Mg — Mg_2Sn system. It should be noted that even under directional crystallization, not all the eutectic melts are able to form an ordered microstructure. Kraft /29/ carried out metallographic and X-ray studies of the Mg — Mg_2Sn eutectic (the alloy contained 63.5 wt % of Mg and 36.5 wt % Sn); 99.8 — 99.95% of pure Mg and spectrally pure Sn were used for the preparation. With directional crystallization of the melt no strictly oriented structures arise, but nevertheless a certain trend of the plates of the solid Mg solution and the Mg_2Sn phase to align in the direction of crystallization is observed. The ingot consists of zones, fairly clearly

delineated. Within these zones the plates of the solid solution and of the Mg_2Sn phase are more or less parallel, but differently oriented with reference to the direction of the crystallization. Sometimes several systems of parallel plates are observed within a single zone. In comparison with the eutectic formed by directional crystallization, the eutectic formed by conventional crystallization is characterized by a large number of systems of parallel plates. In the case of directional crystallization, crystallographic correspondence $\{220\}Mg_2Sn \| \{1011\}$ of the solid solution is usually noted between the plates of the solid Mg-base solution and the Mg_2Sn phase. It is possible that the crystallographic correspondence found between the plates of the solid solution and the Mg_2Sn phase in the eutectic corresponds to the minimum surface energy at the interface. It is worth noting /24/ that in every case the single crystals in the eutectic are very imperfect, and consist of a large number of mosaics.

$Nb - Nb_2C$ and $Ta - Ta_2C$ systems. According to Salkind /17/, the $Nb - Nb_2C$ eutectic contains 31 vol % of filamentary crystals, and has a higher strength-to-weight ratio than other niobium alloys.

The eutectic $Ta - Ta_2C$ contains 29 vol % of filamentary crystals, and at temperatures above 1093°K has a higher strength than other tantalum alloys. Kurilo et al. /31/ employed microstructural, electron microscope, and X-ray structural methods, and finally mechanical tests, to study the effect of carbide whiskers obtained by directional crystallization on the mechanical properties of the eutectic alloys $Nb - Nb_2C$ (carbon level 1.45 wt %) and $Ta - Ta_2C$ (carbon level 0.8 wt %). Directional crystallization was attained by electron-beam zone melting of deformed, pressed rods. To increase the heat flux in the axial direction, the end of the rod was shielded and cooled.

The microstructures of both alloys before directional crystallization consisted of globular hexagonal carbides, randomly arranged in the matrix, which was a solid solution of carbon in niobium or tantalum. After two or more cycles of directional crystallization (rate 1—50 cm/hr, temperature gradient 900 — 1000 deg/cm) the carbides acquired a fibrous structure, and the fibrous whiskers became narrower as the rate of crystallization increased. Electron microscope studies showed that the whiskers had a rectangular cross section. The whiskers grow preferentially in direction [1010], while the preferential position of the faces was in direction (1210). The mechanical properties of the alloys are $\sigma_B = 98 - 120\,kg/mm^2$, and $\delta \leqslant 1.2 - 1.7\%$ in the direction of alignment after directional crystallization, and $\sigma_B = 35 - 45.5\,kg/mm^2$ and $\delta = 4 - 1.8\%$ only after crystallization. In the $Nb - Nb_2C$ alloy, 31% of Nb_2C whiskers are present, and at a temperature of 1400°K, σ_B is five times that of pure niobium. $Nb - Nb_2C$ alloys retain their stable structure at 1370°K after a holding time of 264 hr.

Salkind also reports /17/ that $Ta - Ta_2C$ alloy was subjected to cold rotational treatment with a deformation of 66%; after this treatment the strength of the material increased again. Because of their structural stability, whisker-reinforced materials can be combined by diffusional welding, and it is possible to obtain products with various alignments of the reinforcing phase.

Ni — NiMo system. According to Salkind /17/, the Ni — NiMo eutectic with 40% of NiMo has $\sigma_B > 39.9\,kg/mm^2$ at 1093°K. This is much higher than the strength of the existing simple Ni — Mo alloys. This stability of the

composites is in sharp contrast to the poor stability of composites in which the matrix is reinforced by whiskers obtained from the vapor phase. Salkind also reports /17/ that experiments are being carried out on the casting of complex profiles with a given oriented structure. For example, turbine blades are cast from platelike Ni — NiMo.

Pb — Sn, Sn — Zn, and Zn — Cd systems. These systems were studied by Kraft /29/.to determine the effect of freezing on the distance between the platelets in the eutectic. The Sn — Zn system was also studied by Kurilo et al. /31/. The authors were able to retain the homogeneity of the eutectic composition along the specimen by drawing the fibers from the melt. The melt temperature was kept only a little higher than the eutectic temperature. Impairment of the melt was prevented, since each component in excess (with reference to the eutectic) was separated in the crucible as primary crystals, and thus the eutectic composition was restored. When the the drawing speed was 40 — 80 mm/hr, a unidirectional discontinuous separation of zinc in the tin matrix was achieved. The matrix remained in the single-crystal state, as was indicated by the simultaneous extinction and transmission observed in an optical microscope on rotation of the polarizer. There is, however, a difficulty involved in the preparation of fiber materials from the melt, namely, the trend of the fibrous deposits to form spheres near the melting point. This was noticed by Kurilo et al. /31/, who, however, report that Davies, Kraft, and their co-workers considerably increased the resistance against sphere formation by reducing the interfacial energy in the composition to a minimum, and ensuring the low solubility of the reinforcing phase in the matrix.

ZnSb—Sb system. The eutectic of this system consists of approximately equal amounts of antimony rods and matrix, which is the chemical compound ZnSb /32/. The whisker size of antimony decreases with increase in the crystallization rate, which agrees with the theory of eutectic crystallization. The side of the triangle is $a = 5 \cdot 10^{-3}$ to $5 \cdot 10^{-4}$ cm, depending on the freezing rate. The whiskers grow in the direction parallel to the hexagonal axis in the crystal lattice of antimony, and parallel to direction $<111>$ in the crystal lattice of ZnSb. The direction of the side of the triangle in the cross section of the Sb whiskers is parallel to direction $<110>$ in the crystal lattice of ZnSb.

The physical properties of the specimens are anisotropic. For example, the electrical resistance can change by a factor of 10, depending on the direction.

The anisotropy of the physical properties of materials which have been subjected to directional crystallization can be used in various engineering branches. If the composite contains two phases, one of which is a conductor and the other an insulator, then in a certain direction the material will be a conductor and in the direction perpendicular to it an insulator. This phenomenon may find application in electric engineering. Another example is given by alloys of type Fe — FeS, with one phase ferromagnetic and the other not. Kraft /24/ reports that the Fe — FeS alloy containing iron fibers of 2μ diameter is an example of a good material for the production of permanent magnets.

Pall and Weiss /33/ report the anisotropy of the transmission power in the infrared range of alloys consisting of fibers of the chemical compound NiSb,

ingrained into the chemical compound ZnSb. The authors suggest that these materials be used as polarization filters.

Ni — Au system. We have hitherto considered the properties of alloys obtained by the directional crystallization of eutectics. However, such alloys have some disadvantages. One of them is the fixed amount of the reinforcing phase obtained during crystallization. Ordone /34/ proposed a method with which it is possible to eliminate this drawback. This method is based on the utilization of the solid state reaction, and it was tested on the Ni — Au system.

Specimens of the equiatomic alloy were heated to 900°C, at which the solid Ni — Au solution is formed. Then, the specimens were quenched, and later tempered at different temperatures. It was found that at a temperature not much higher than 400°C the nonequilibrium solid solution formed on quenching decomposed into equilibrium phases, which nucleated on the grain boundary. At 600°C the reaction rate was highest.

Electron microscope analysis of the decomposition products of the solid solution showed that at a temperature below 700°C the separating phase is a nickel-rich solid solution. Its spherical particles (diameter about 1000 Å) are distributed over the matrix which is a gold-rich solid solution. With increase in the temperature of reaction, the particle diameter increases, and at 700°C the particles that separate are no longer spherical but fibrous.

The separated phase is fibrous; the fiber diameter is about 1μ and the length several microns. It should, however, be noted that the strengthening effect by spherical particles is greater than the effect of fibers; this is probably because the low volume content of fibers.

The volume content of the fibers can, however, be increased by using alloys richer in nickel. To obtain fiber orientation, we must apply directional heat treatment or heat treatment in a magnetic field.

2. Advantages and disadvantages of cast composites

Cast composites have numerous advantages and disadvantages compared with materials obtained from individually growing fibers and a matrix. We must mention some special features which appear when these two material types are compared.

1. In composites the problem of bonding between filler (mainly filamentary crystals) and the matrix material is very important. The problem is complicated because filamentary nitride, boride, carbide and oxide (especially sapphire) crystals are not wetted by the majority of metals. To improve wettability and adhesion, the whiskers must first be treated with dressing compositions, or thin metal films must be applied by chemical deposition or vacuum spraying. For example, in the system Ag — Al_2O_3 a 0.1μ nickel or platinum layer was applied onto sapphire whiskers. In the system Al — Al_2O_3 the whiskers were aluminized, and in the system Ni — Al_2O_3 the whiskers were nickel-coated by simultaneous electrolytic deposition from a sapphire whisker and nickel suspension. The wettability can be improved by introducing active additives into the matrix to reduce

the tension on the fiber-liquid metal interface. For example, titanium, zirconium, and chromium in nickel increase the wettability of sapphire by fused nickel.

In the preparation of eutectic alloys these problems do not occur, since a natural process takes place during the crystallization or the separation reaction of the strengthening phase from the matrix, so that good bonding between matrix and fibers is automatically achieved. It has already been mentioned that when investigating composites of type $Al - Al_3Ni$, $Al - CuAl_2$ and $Cu - Cr$ by metallographic or electron diffraction studies of the fractures, it was found that the composite begins to break in the whiskers and not on the whisker-matrix interface. This indicates a satisfactory transmission of the load by the matrix to the very strong whiskers, and hence the good bond between matrix and the reinforcing phase.

2. The production of natural composites by directional crystallization of a eutectic or the solid phase reaction is the simplest method for preparing specimens. When this method is used there is no need, as in other methods to prepare special whiskers, so that all operations involved in the preparation of whiskers are eliminated, which is a great advantage.

To enhance the uniform distribution of the filamentary crystals in the matrix, forced mixing and circulation are applied, which also complicates production of composites. In the crystallization of the alloy, high-strength whiskers are formed which are uniformly distributed parallel to the growth of the ingot. At low crystallization rates /31/ it is possible to segregate the crystallizing phases according to their specific gravity, but to maintain the eutectic homogeneous along the whole specimen is complicated. In this case we must select optimum crystallization methods and conditions.

To attain high quality of the natural composite, we must use very pure starting materials, which involves certain difficulties. For this reason this process is not suitable at present. In fact, high purity of the materials is a prerequisite for a planar interface between the solid and liquid during crystallization. If insufficiently pure materials are used, the planar interface becomes honeycombed, so that fanlike whiskers or plates are formed, which impart a columnar structure to the eutectic. Consequently, the strengthening phase no longer spreads in the direction of freezing.

3. Every eutectic alloy has its characteristic, strictly determined volume fraction of the high-strength phase. The volume fraction is obtained by calculating the content of each phase, and then dividing the result by the phase density. The phases are determined from the phase diagram. An important drawback of eutectic alloys is that the volume fraction of the high-strength phase is constant for the given eutectic composition. Consequently, the properties of the eutectic alloy cannot be improved by changing the volume fractions of the components in the eutectic mixture.

At the same time the effect of the high strength of the filamentary crystals can be completely realized only when a material is produced /35/ in which the fibers take up the whole load, while the soft matrix serves for transmission only. This can be achieved with a certain volume fraction of the fibers, an optimum length, and the most advantageous length-to-diameter ratio. The fiber dimensions can be controlled in directional crystallization by varying the freezing velocity of the alloy, but the volume fraction is a constant property of every eutectic composite.

Davies /13/ proved that it is possible to increase the volume fraction of the strengthening phase by forced crystallization of an alloy with a composition above the eutectic. Consequently, under certain conditions needlelike pseudoeutectic particles of the harder phase are formed. For the eutectic system $Cu - Cu_6Sn_5$ the author found that the pseudoeutectic component Cu_6Sn_5 has a needlelike structure, and tensile properties similar to those of whiskers. A disadvantage of the Cu_6Sn_5 system is the very complex form of the cross section of the pseudoeutectic needles. At many sites stress concentrations are produced, which lower the high strength inherent in this compound. The above method cannot be applied to all eutectic alloys. For example, alloys of the system $Cu - Cr$, in which the volume fraction of the high-strength phase is insufficient to reinforce the alloy very much, cannot be strengthened by using pseudoeutectic particles of the high-strength phase, since in alloys of such systems the pseudoeutectic components are formed as dendrites and not as oriented needlelike particles.

As mentioned above, Ordone /34/ proposed a method for producing natural composites by separating the reinforcing phase as fibers of diameter about 1μ and length of several microns after tempering preliminarily quenched alloys. The authors illustrated this method on the $Ni - Au$ alloy. It is quite probable that after further development of the method it will be possible to control the composition of the corresponding composites.

4. High-temperature stability is a very important property of eutectic composites. In spite of the fact that among alloys consisting of several elements eutectic alloys have the lowest melting point, they have a high thermal stability. Some specimens obtained by directional crystallization of eutectic alloys of the systems $Al - Al_3Ni$, $Al - CuAl_2$ and $Cu - Cr$ /16/ were kept hundreds of hours at temperatures of about 60° below their melting point without any considerable spheroidization or overall destruction of the whiskers or plates. Graham (as communicated by Kraft /24/) studied the coagulability of some eutectic alloys after he had obtained information on their high thermal stability. The author found that such alloys retain their structure after long-term holding at temperatures close to their melting point. Even if some of the individual plates coagulate, they retain their high anisotropy.

Libermann /32/ and Kraft /36/ also report on the high thermal stability of natural composites. This very high thermal stability is apparently due to the minimum surface energy on the interface because of the unusual crystallographic correspondence between the phases. These features also make such alloys very suitable for high temperatures. We must, however, note the following. If in natural composites spherical crystallographic correspondences between two phases are produced /21, 22/, the dislocations are able to penetrate from the matrix into the whiskers. They thus reduce the initial strength, even if the whiskers extracted from the matrix are sufficiently strong. For example, even if the eutectic alloy of the Ag—Cu system contains 26 vol % of copper, no reinforcement is observed /16/. This may be due to the crystallographic correspondence between the copper whiskers and the matrix, which enables the dislocations to pass from the face-centered cubic lattice of the silver matrix into the face-centered cubic lattice of the copper whisker. It should be noted that since natural composites are applied mainly for high-temperature operation, a property such as refractoriness is of the utmost importance.

The production of external dislocation barriers appears to be one of the most promising methods for increasing refractoriness /37/. If the cross sections are small (fibers, particles), high refractoriness can be achieved by preventing the dislocations from emerging to the surface by the barrier effect of oxide films on the surface. It was hitherto assumed that the main role of artificial coatings or oxide films is protection against oxidation. But according to the dislocation theory it can be stated that the strengthening effect of films and coatings is due not only to the reduction of the action of oxidizing processes but also to the prevention of the emergence of dislocations to the surface, that is, to the functioning of surface films or coatings as external dislocation barriers. The highest inhibiting effect should be observed in deformations of thin cross sections, since in this case the efficiency of the oxide films or coatings as dislocation barriers is higher. However, the good bonding on the interface of the two phases in natural composites is explained by the fact that there are no intermediate oxide layers between the two phases since both phases are formed simultaneously from the melt, or the strengthening phase is formed under conditions preventing the appearance of an oxide film (when separated in the solid state). Hence, if the above is correct, the problem of producing refractory natural composites is fairly complicated, and the high thermal stability of these materials must be combined with their high refractoriness.

5. The ability to undergo cold and hot deformation, and also the possibility of producing complex articles, are some of the properties required of structural materials.

But by the methods now used for producing composite materials, only specimens of the simplest shape such as rods or plates can be made. However, as reported by Hertzberg /16/, it is possible to grow eutectic grains along the edge of specimens. We can therefore hope that we shall be able to grow ingots of more complex shapes in the future.

The communication of Salkind /17/ is interesting. The author reports that experiments are under way on casting complex profiles with a given oriented structure. In particular, turbine blades will be produced from the Ni — NiMo alloy, which has a platelike structure. Moreover, for the production of complex articles, diffusion welding can be used, because of the high thermal stability of the natural composites.

The same author also reports that the alloy Ta — Ta_2C was subjected to cold rotational treatment with a degree of deformation of 66%; and the strength of the material increased. It appears that mechanical deformations have no unfavorable effect on the strength of the Ta_2C whiskers, and that the overall increase in strength of the Ta — Ta_2C alloy might be due to cold hardening of the matrix.

Bibliography

1. Herring, C. and J.K. Galt. — Phys. Rev., 85:1060. 1952.
2. Rosen, B.W. — In: Fiber Composite Materials; Papers Presented at a Seminar, October 17 and 18, 1965. Metals Park, Ohio, American Society for Metals.1965.

3. Sutton, W.H. and J.Chorne. Voloknistye kompozitsionnye materialy (Fiber Composite Materials). 1967. [Russian translation].
4. Sutton, W.H.— Am. Rocket Soc., 32(4):593. 1962.
5. Salkind, M.— Internat. Sci. Techn., 63, 52—57. 1967.
6. Kraft, R.W.— Trans AIME, 221:95.. 1961.
7. Chadwick, G.A.— Progr. Mater. Sci., 12:2. 1968.
8. Bochvar, A.L. Issledovanie mekhanizma i kinetiki kristallizatsii splavov evtekticheskogo tipa (Study of the Crystallization Mechanism and Kinetics of Eutectic Alloys).— ONTI. 1935.
9. Pines, B.Ya.— ZhTF, 18:6. 1948.
10. Chadwick, G.A.— J. Inst. Metals, No. 5:298. 1963.
11. Davies, V.de L.— J. Inst. Metals, No. 9:10. 1964.
12. Hunt, J.D.— J. Inst. Metals, No. 6:338. 1963.
13. Davies, G.I. Phil. Mag., 9(102):953. 1964.
14. Hertzberg, R.W.— Trans. AIME, 233:342. 1965.
15. Lemkey, F.D.— Trans. AIME, 233:334. 1965.
16. Hertzberg, R.W. Voloknistye kompozitsionnye materialy (Fiber Composite Materials). "Mir" 1967. [Russian translation].
17. Salkind, M. Advanced Fibrous Reinforced Composites. North Hollywood. 1966.
18. Salkind, M.J.— J. Metals, 20(3):30. 1968.
19. Kraft, R.W.— Trans. AIME, 224:65. 1962.
20. Kraft, R.W.— Trans. AIME, 224:1176. 1962.
21. Tiller, W.A.— J. Appl. Phys., 34(12):3639. 1963.
22. Mamura, U.M.— J. Japan Inst. Metals, 30(11):1005. 1966.
23. Bell, J.F.— J. Inst. Metals, 93(11):1005. 1966.
24. Kraft, R.W.— J. Metals, 18(2):192. 1966.
25. Lemkey, F.D.— Rev. Scient., 33(8):846. 1962.
26. Hertzberg, R.W.— Trans. AIME, 57, 434. 1964.
27. Webb, W.W.— Acta Met., 6:462. 1958.
28. Hertzberg, R.W.— Trans. AIME, 227:580. 1963.
29. Kraft, R.W.— Trans. AIME, 227(2):398. 1963.
30. Kraft, R.W.— Trans. AIME, 224:65. 1962.
31. Kurilo, Yu.P. et al.— In: Fiziko-khimicheskie osnovy polucheniya novykh zharostoikikh materialov. 1966.
32. Libermann, W.K.— J. Appl. Phys., 34(9):2653
33. Pall, B. and H.Weiss.— Electronic News, 12:42. 1964.
34. Ordone, Z.J.— Nature, 217:3,442. 1968.
35. Ivanova, V.S.— In: Fizika i Khimiya Obrabotki Materialov, 1:75-78. 1967.
36. Kraft, R.W.— Trans. AIME, 227:540. 1963.
37. Ivanova, V.S.— In: Fiziko-khimicheskie osnovy polucheniya novykh zharostoikikh neorganicheskikh materialov. 1966.
38. McDanels, D.L.— Metal Progress, 78(6):118. 1960.

EXPLANATORY LIST OF ABBREVIATED NAMES OF USSR INSTITUTIONS AND PERIODICALS APPEARING IN THIS BOOK

Abbreviation	Full name (transliterated)	Translation
AN SSSR	Akademiya Nauk SSSR	Academy of Sciences of the USSR
AN UkrSSR	Akademiya Nauk Ukr SSR	Academy of Sciences of the Ukrainian SSR
DAN SSSR	Doklady Akademii Nauk SSSR	Reports of the Academy of Sciences of the USSR
DAN UkrSSR	Doklady Akademii Nauk Ukrainskoi SSR	Proceedings of the Academy of Sciences of the Ukrainian SSR
GITTL	Gosudarstvennoe Izdatel'stvo Tekhnicheskoi i Teoreticheskoi Literatury	State Publishing House of Technical and Theoretical Literature
GOSNITI	Gosudarstvennyi Vsesoyuznyi Nauchno-Issledovatel'skii Tekhnologicheskii Institut Remonta i Ekspluatatsii Mashinno-Traktornogo Parka	State All-Union Technological Institute for Repairs and Operation of Tractors and Machinery
IPM	Institut Prikladnoi Metallurgii	Institute of Applied Metallurgy
ONTI	Otdel Nauchno-Tekhnicheskoi Informatsii	Department of Scientific and Technical Information
PMM	Prikladnaya Matematika i Mekhanika	Applied Mathematics and Mechanics
TsAGI	Tsentral'nyi Aerogidrodinamicheskii Institut imeni N. E. Zhukovskogo	Central Aerohydrodynamic Institute im. Zhukovskii
TsITEIN	Tsentral'nyi Institut Tekhniko-Ekonomicheskoi Informatsii	Central Institute of Information on Technology and Economics
UFN	Uspekhi Fizicheskikh Nauk	Advances in Physical Sciences
VINITI	Vsesoyuznyi Institut Nauchnoi i Tekhnicheskoi Informatsii	All-Union Institute for Scientific and Technical Information
ZhPKh	Zhurnal Prikladnoi Khimii	Journal of Applied Chemistry

National Aeronautics and Space Administration
WASHINGTON, D. C. 20546

OFFICIAL BUSINESS

Penalty For Private Use, $300.00

POSTAGE AND FEES PAID
NATIONAL AERONAUTICS AND
SPACE ADMINISTRATION

014 001 C3 U 18 720321 S00903DS
DEPT OF THE AIR FORCE
AF WEAPONS LAB (AFSC)
TECH LIBRARY/WLOL/
ATTN: F LOU BOWMAN, CHIEF
KIRTLAND AFB NM 87117

5980

Printed in Jerusalem, Israel

TT 71-50050
NASA TT F-675